University of Windsor
Scholarship at UWindsor

Electronic Theses and Dissertations | Theses, Dissertations, and Major Papers

7-7-2020

Petrogenesis and tectonic setting of Archean anorthosite-bearing layered intrusions, Western Superior Province, Canada

Paul Sotiriou
University of Windsor

Follow this and additional works at: https://scholar.uwindsor.ca/etd

Recommended Citation

Sotiriou, Paul, "Petrogenesis and tectonic setting of Archean anorthosite-bearing layered intrusions, Western Superior Province, Canada" (2020). *Electronic Theses and Dissertations*. 8400.
https://scholar.uwindsor.ca/etd/8400

This online database contains the full-text of PhD dissertations and Masters' theses of University of Windsor students from 1954 forward. These documents are made available for personal study and research purposes only, in accordance with the Canadian Copyright Act and the Creative Commons license—CC BY-NC-ND (Attribution, Non-Commercial, No Derivative Works). Under this license, works must always be attributed to the copyright holder (original author), cannot be used for any commercial purposes, and may not be altered. Any other use would require the permission of the copyright holder. Students may inquire about withdrawing their dissertation and/or thesis from this database. For additional inquiries, please contact the repository administrator via email (scholarship@uwindsor.ca) or by telephone at 519-253-3000ext. 3208.

Petrogenesis and tectonic setting of Archean anorthosite-bearing layered intrusions, Western Superior Province, Canada

By

Paul Sotiriou

A Dissertation

Submitted to the Faculty of Graduate Studies

through the School of the Environment

in Partial Fulfilment of the Requirements for

the Degree of Doctor of Philosophy at the

University of Windsor

Windsor, Ontario, Canada

2020

© 2020 Paul Sotiriou

Petrogenesis and tectonic setting of Archean anorthosite-bearing layered intrusions, Western Superior Province, Canada

by

Paul Sotiriou

APPROVED BY:

_____

P. Hollings, External Examiner
Lakehead University

_____

K. Tepe
Department of Electrical and Computer Engineering

_____

J. Gagnon
School of the Environment

_____

I. Samson
School of the Environment

_____

A. Polat, Advisor
School of the Environment

April 30, 2020

Declaration of Co-Authorship/Previous Publication

I. Co-Authorship

I hereby declare that this thesis incorporates material that resulted from joint research, as follows:

Chapter 1 of this thesis was supervised by Dr. Ali Polat (30%). Chapter 2 of this thesis was co-authored by Dr. Robert Frei (10%) under the supervision of Dr. Ali Polat (25%). Chapters 3 and 4 of this thesis were co-authored by Dr. Robert Frei (8%), Dr. Xue-Ming Yang (5%) and Mr. James van Vessem (2%) under the supervision of Dr. Ali Polat (25%). Dr. Robert Frei performed radiogenic isotope analyses and provided feedback on Chapters 2-4, Dr. Xue-Ming Yang provided assistance in the field and provided feedback on Chapters 2-4, and Mr. James van Vessem assisted the author in the procurement of scanning electron microscope energy dispersive X-ray spectroscopy (SEM-EDS) and Raman spectrometer analyses.

I am aware of the University of Windsor Senate Policy on Authorship and I certify that I have properly acknowledged the contribution of other researchers to my thesis and have obtained written permission from each of the co-authors to include the above material in my thesis.

I certify that, with the above qualification, this thesis, and the research to which it refers, is the product of my own work.

II. Previous Publication

This thesis includes three original papers that have been previously published/submitted for publication in peer reviewed journals, as follows:

Thesis Chapter	Publication title/full citation	Publication status
Chapter 2	**Sotiriou, P.** (65%), Polat, A. (25%), Frei, R. (10%), 2019a. Petrogenesis and geodynamic setting of the Neoarchaean Haines Gabbroic Complex and Shebandowan greenstone belt, southwestern Superior Province, Ontario, Canada. Lithos 324-325, 1-19.	Published in Lithos

Chapter 3	**Sotiriou, P.** (60%), Polat, A. (25%), Frei, R. (8%), Yang, X.M. (5%), van Vessem, J. (2%), 2019b. A back-arc origin for the Neoarchean megacrystic anorthosite-bearing Bird River Sill and the associated greenstone belt, Bird River subprovince, Western Superior Province, Manitoba, Canada. International Journal of Earth Sciences108(7), 2177-2207.	Published in the International Journal of Earth Sciences
Chapter 4	**Sotiriou, P.** (60%), Polat, A. (25%), Frei, R. (8%), Yang, X.M. (5%), van Vessem, J. (2%), Evidence for Neoarchean hydrous arc magmatism, the anorthosite-bearing Mayville Intrusion, Western Superior Province, Canada. Lithos 362-363, 105482, https://doi.org/10.1016/j.lithos.2020.105482.	Published in Lithos

I certify that I have obtained a written permission from the copyright owner(s) to include the above published material(s) in my thesis. I certify that the above material describes work completed during my registration as a graduate student at the University of Windsor.

III. General

I declare that, to the best of my knowledge, my thesis does not infringe upon anyone's copyright nor violate any proprietary rights and that any ideas, techniques, quotations, or any other material from the work of other people included in my thesis, published or otherwise, are fully acknowledged in accordance with the standard referencing practices. Furthermore, to the extent that I have included copyrighted material that surpasses the bounds of fair dealing within the meaning of the Canada Copyright Act, I certify that I have obtained a written permission from the copyright owner(s) to include such material(s) in my thesis.

I declare that this is a true copy of my thesis, including any final revisions, as approved by my thesis committee and the Graduate Studies office, and that this thesis has not been submitted for a higher degree to any other University or Institution.

Abstract

Field relationships, petrographic observations, mineral chemistry, and whole-rock major and trace element and Sm-Nd and Pb radiogenic isotope geochemistry of Neoarchean megacrystic anorthosite-bearing layered intrusions and spatially and temporally associated volcanic and sedimentary rocks in Archean greenstone belts in the western Superior Province of Ontario and Manitoba, Canada, were utilised to constrain their petrogenesis, and the tectonic settings in which they formed. Thoroughly determining the petrogenesis and tectonic settings of these Archean megacrystic anorthosite-bearing layered intrusions and spatially associated greenstone belt volcanics has very important implications for whether modern-style plate tectonics processes operated in the western Superior Province during the Neoarchean.

The Neoarchean Haines Gabbroic Complex, Bird River Sill and Mayville Intrusion include megacrystic anorthosites and leucogabbros and gabbros, melagabbros, pyroxenites, peridotites and chromitites and intrude or are closely spatially associated with pillow basalts in the Neoarchean Shebandowan and Bird River greenstone belts of Ontario and Manitoba, respectively. These layered intrusions and pillow basalts are intruded by tonalite-trondhjemite-granodiorite (TTG) batholiths, represent oceanic crust, and formed in an oceanic setting proximal to pre-existing continental crust. The pillow basalts were erupted onto pre-existing Neoarchean-Mesoarchean TTG batholiths and the Bird River Sill and Mayville Intrusion were emplaced into the pre-existing Mesoarchean Maskwa Lake TTG Batholith I. Basaltic to rhyolitic volcanic rocks were erupted onto the Haines Gabbroic Complex and Bird River Sill and constitute part of volcanic and sedimentary formations that formed after the emplacement of these layered intrusions.

The Haines Gabbroic Complex, Bird River Sill and Mayville Intrusion and their host greenstone belts have undergone greenschist- to amphibolite-facies metamorphism and variable alteration and deformation (shearing). The primary mineralogy of the Haines Gabbroic Complex has been largely altered to metamorphic plagioclase and actinolite, however, its cumulate textures are still preserved. The primary mineralogy and cumulate textures of the Bird River Sill and Mayville Intrusion are variably well-preserved and consist of calcic plagioclase (An_{63-99}), clinopyroxene, orthopyroxene, olivine, chromite and magnesiohornblende. Oikocrystic magnesiohornblende envelops cumulus calcic plagioclase in the megacrystic anorthosites and leucogabbros.

The Haines Gabbroic Complex, Bird River Sill and Mayville Intrusion are of tholeiitic affinity and crystallised from hydrous Ca- and Al-rich tholeiitic parental magmas. The hydrous nature of these parental magmas is demonstrated by the occurrence of magmatic amphibole (magnesiohornblende) and calcic plagioclase megacrysts in the megacrystic anorthosites and leucogabbros of the Bird River Sill and Mayville Intrusion. The hydrous Ca- and Al-rich tholeiitic parental magmas to these layered intrusions fractionated from hydrous boninitic-like or primitive arc tholeiitic parental magmas that were derived by variable degree partial melting of variably depleted mantle sources (ε_{Nd} = +0.53 to +4.72). The parental magmas to the Bird River Sill and Mayville Intrusion underwent minor contamination by pre-existing Mesoarchean crust (Maskwa Lake TTG Batholith I). The Mayville Intrusion was cogenetic with the pillow basalt-bearing Mayville Assemblage into which it intrudes. The Haines Gabbroic Complex was not cogenetic with the spatially and temporally associated Greenwater and Burchell assemblages. The anorthosites, leucogabbros and peridotites of the Bird River Sill were not cogenetic with the Northern Lamprey Falls Formation into which it intrudes, whereas the gabbros of this layered intrusion were cogenetic with this formation.

Geological relationships, lithological associations, mineral chemistry and whole-rock trace element geochemistry (e.g., negative Nb-Ti anomalies) indicate that the Haines Gabbroic Complex, Bird River Sill and Mayville Intrusion, and the pillow basalts that they intrude or are closely spatially associated with, formed in continental back-arc geodynamic settings akin to the modern Circum-Pacific subduction zones. The Neoarchean Peterson and Bird River formations in the Bird River greenstone belt and the spatially associated Mesoarchean Maskwa Lake TTG Batholith I formed in a continental arc setting. The Neoarchean Burchell Assemblage in the Shebandowan greenstone belt formed in a mature intra-oceanic continental arc setting. Modern-style plate tectonics processes operated in the western Superior Province during the Neoarchean and hydrous arc magmatism has occurred since this time.

Dedication

This dissertation is dedicated to my mum, my stepdad, my sister, my dad, my family, and my friends who have provided ample encouragement, support, and love throughout my geological education. I could not have done this without you.

Acknowledgments

I would like to sincerely thank my supervisor, Dr. Ali Polat, for giving me the opportunity to come to Canada to do my Ph.D. and work with him at the University of Windsor. My research was funded by an NSERC Discovery research grant awarded to Ali, for which I am very grateful. I would like to thank Ali for the encouragement, support, advice, knowledge, humour, and enthusiasm that he provided throughout the course of my research. Ali's emphasis on fieldwork and field observations in research on Archean terrains, in combination with petrography, mineral chemistry and whole-rock geochemistry, is a methodology that has been critical to my research and has been responsible for the emphasis that I have placed on conducting geological sound and meaningful research. I could not have done my research without Ali's support.

I want to thank my departmental committee members, Dr. Iain Samson, and Dr. Joel Gagnon, for their agreeing to be on my committee and the encouragement and the support that they have provided during my Ph.D. I would also like to thank my internal committee member (Dr. Kemal Tepe) and external examiner (Dr. Pete Hollings, Lakehead University) for their agreeing to be on my committee. Joe Hackl is thanked for providing drill core samples from the Haines Gabbroic Complex and Greenwater Assemblage. I would also like to thank Gossan Resources Limited for permitting fieldwork on its property in the Bird River Sill. I also want to thank Melissa Price for the great support and enthusiasm that she provided during my time on the petrographic microscope and Raman spectrometer. Similarly, I would like to thank Sharon Lackie from the Great Lakes Institute for Environmental Research for the obliging support that she provided whilst I used the SEM and Raman spectrometer. James van Vessem is thanked for spending countless hours working with me on the SEM and Raman spectrometer to acquire mineral chemistry and Raman spectra data. The faculty, staff and past and present graduate students at the School of the Environment are sincerely thanked for their support, encouragement, humour, banter, and interesting conversations. A special shout out must go to my fellow graduate students for all of the fun times and laughs that we have had together.

Last but not least, I would like to warmly thank my mum, stepdad, sister and dad for the love, support and encouragement that have made possible my achievements and got me to where I am today.

Table of Contents

List of Tables

List of Figures

List of Appendices

List of Abbreviations

Act	Actinolite
Alb	Albite
Amp	Amphibole
Apt	Apatite
Aug	Augite
BIF	Banded iron formation
BSE	Backscatter electron
Cpy	Chalcopyrite
Chl	Chlorite
Chr	Chromite
Cpx	Clinopyroxene
Czs	Clinozoisite
Diop	Diopside
EDS	Energy dispersive X-ray spectrometer
Ens	Enstatite
Epd	Epidote
Fsp	Feldspar
Hbl	Hornblende
HFSE	High-field strength element (Nb, Zr, Ta, Hf)
HREE	Heavy rare-earth element (Gd, Dy, Yb, Lu)
ICP	Inductively coupled plasma
ICP-MS	Inductively coupled plasma mass spectrometer
LILE	Large-ion lithophile element
LREE	Light rare-earth element (La, Ce, Pr, Nd)
MORB	Mid-ocean ridge basalt
Mt	Magnetite
N-MORB	Normal mid-ocean ridge basalt
Ol	Olivine
Op	Opaque mineral
Plag	Plagioclase
Px	Pyroxene
Qtz	Quartz

REE	Rare-earth element
SEM	Scanning electron microscope
SEM-EDS	Scanning electron microscope energy dispersive X-ray spectroscopy
Ser	Sericite
Serp	Serpentine
TAS	Total alkali-silica
TIMS	Thermal ionisation mass spectrometry
Tlc	Talc
Trem	Tremolite
TTG	Tonalite-trondhjemite-granodiorite
Ttn	Titanite
Zo	Zoisite

Chapter 1: Introduction

1. 1. Introduction

Archean anorthosite-bearing layered intrusions occur on every continent and constitute a minor yet important part of Archean cratons (Ashwal, 1993, 2010; Ashwal and Myers, 1994; Ashwal and Bybee, 2017). These layered intrusions intrude spatially and temporally associated pillow basalt-bearing volcanic rocks in greenstone belts comprise volcanic, intrusive, and sedimentary rocks that underwent greenschist- to granulite-facies metamorphism (Ashwal, 1993, 2010; Ashwal and Myers, 1994; Ashwal and Bybee, 2017; Polat et al., 2018a). Archean anorthosite-bearing layered intrusions and the volcanic rocks into which they intrude are intruded by tonalite-trondhjemite-granodiorite (TTG) batholiths that predominate Archean cratons (Percival et al., 2006, 2012; Windley and Garde, 2009; Polat et al., 2018a). Given that Archean anorthosite-bearing layered intrusions occur in most Archean cratons, are closely spatially and temporally associated with pillow basalt-bearing volcanic rocks and that both are intruded by TTG batholiths, it is very important to understand how these layered intrusions formed and the tectonic settings in which they formed. This has major implications for the style of tectonics that operated in the Archean, Archean crustal growth and evolution mechanisms, and Archean magma genesis and evolution.

Anorthosites occur on all of Earth's seven continents, have formed throughout Earth history and range from being volumetrically minor to major (Ashwal, 1993, 2010; Ashwal and Bybee, 2017). Despite this, the petrogenesis of anorthosites has been the subject of considerable debate since the 'anorthosite problem' was first identified over a century ago by Bowen (1917). The petrogenesis of anorthosites remains enigmatic, with numerous models proposed for their genesis (Ashwal, 1993, 2010; Ashwal and Bybee, 2017). Elucidating the petrogenesis of anorthosites has major implications for crustal evolution and growth processes, the evolution of the Earth's mantle, magma chamber processes and the genesis of cumulate rocks. There is still considerable debate about the petrogenesis and tectonic settings of Archean anorthosite-bearing layered intrusions, with numerous petrogenetic models and tectonic settings having already been proposed for these layered intrusions (Ashwal, 1993, 2010; Ashwal and Myers, 1994; Ashwal and Bybee, 2017; Polat et al., 2018a).

1.2. Archean megacrystic anorthosite-bearing layered intrusions

Archean megacrystic anorthosite-bearing layered intrusions form a minor yet important component of most Archean cratons worldwide (Ashwal, 1993, 2010; Ashwal and Myers, 1994; Ashwal and Bybee, 2017; Polat et al., 2018a). Megacrystic anorthosite-bearing layered intrusions contain calcic megacrystic anorthosites and leucogabbros and are largely thought to be restricted to the Archean (Ashwal, 1993, 2010; Ashwal and Myers, 1994; Ashwal and Bybee, 2017; Polat et al., 2018a). These anorthosites and leucogabbros are dominated by calcic (An_{80-100}) plagioclase megacrysts up to 45 centimetres in diameter (Simmons et al., 1980; Ashwal, 1993, 2010; Ashwal and Myers, 1994; Ashwal and Bybee, 2017; Polat et al., 2018a). Archean megacrystic anorthosite-bearing layered intrusions comprise anorthosites, leucogabbros, gabbros, melagabbros, pyroxenites, troctolites, peridotites and chromitites (Ashwal, 1993, 2010; Ashwal and Myers, 1994; Jobin-Bevans, 1997; Good et al., 2009; Polat et al., 2011, 2018a; Ashwal and Bybee, 2017). These layered intrusions vary in size from <1 km^2 to 2200 km^2 and range from Neoarchean to Eoarchean (2500-3927 Ma) in age (Ashwal, 1993, 2010; Ashwal and Myers, 1994; Ashwal and Bybee, 2017).

Well known Archean megacrystic anorthosite-bearing layered intrusions occur in the Superior Province, and the North Atlantic, Dharwar, Yilgarn, São Francisco, Kaapvaal and Kola cratons (Ashwal, 1993, 2010; Ashwal and Myers, 1994; Ashwal and Bybee, 2017; Polat et al., 2018a). These include the Doré Lake, Bad Vermilion Lake, Shawmere, Pipestone Lake, Bird River and Mayville intrusions of the Superior Province (Simmons et al., 1980; Jobin-Bevans, 1997; Yang and Gilbert, 2014; Zhou et al., 2016; Polat et al., 2018b), the Fiskenæsset Complex of the North Atlantic Craton (Polat et al., 2011), the Sittampundi Complex of the Dharwar Craton (Mohan et al., 2013), the Manfred Complex and Windimurra Intrusion of the Yilgarn Craton (Ahmat and de Laeter, 1982; Myers, 1988; Ivanic et al., 2010), the Lagoa da Vaca Complex of the São Francisco Craton (Paixão and Oliveira, 1998), the Messina Complex of the Kaapvaal Craton (Barton Jr., 1996), and the Kolmozero Complex of the Kola Craton (Vrevskii, 2016).

The petrogenesis and geodynamic setting of Archean megacrystic anorthosite-bearing layered intrusions has been debated for decades, with numerous tectonic settings and petrogenetic models proposed for these layered intrusions since the 1970s (Windley and Smith, 1976; Wiener, 1981; Windley et al., 1981; Ashwal et al., 1983; Ashwal, 1993, 2010; Ashwal and Myers, 1994; Ashwal and Bybee, 2017). A variety of subduction-related and subduction-unrelated tectonic settings have been proposed for Archean megacrystic anorthosite-bearing

layered intrusions. The subduction-related tectonic settings proposed for these layered intrusions include island arc (Hoffmann et al., 2012; Acosta-Gongora et al., 2018), continental arc (Piaia et al., 2017), and back-arc (Wiener, 1981) settings. The subduction-unrelated tectonic settings proposed for these layered intrusions include mantle plume (Ivanic et al., 2010; Spath et al., 2015), mantle plume-derived continental rift (Ivanic et al., 2010), continental rift (Sandeman et al., 2001; Hartlaub et al., 2004), quasi-platform (Vrevskii, 2016), and passive continental margin (Paixão and Oliveira, 1998) settings. Recently, Polat et al. (2018a) proposed that Archean megacrystic anorthosite-bearing layered intrusions in the Superior Province (Canada) and North Atlantic Craton (Greenland) formed in a back-arc or an intra-arc rift tectonic setting.

There is some debate over whether Archean anorthosite-bearing layered intrusions were cogenetic with spatially and temporally associated volcanic rocks in their host greenstone belts. Polat et al. (2011) proposed that the Fiskenæsset Complex was not cogenetic with the amphibolite-facies tholeiitic basalts into which it intruded. In contrast, Polat et al. (2018b) postulated that the gabbros and mafic dykes of the Doré Lake Complex were cogenetic with the tholeiitic basalts and gabbros of the Obatogamau Formation in the Abitibi greenstone belt. The studies of Polat et al. (2011, 2018b) are the only recent studies that have established whether Archean anorthosite-bearing layered intrusions were cogenetic with volcanic rocks in their host greenstone belts. Ashwal (1993) accounted for why Archean megacrystic anorthosite-bearing layered intrusions are spatially and temporally associated with mafic volcanic rocks in their host greenstone belts by concluding that they both formed in an oceanic setting on the basis that the latter contain pillow basalts. The composition of the parental magmas to Archean anorthosite-bearing layered intrusions has been the subject of substantial debate (Ashwal, 1993, 2010; Ashwal and Myers, 1994; Ashwal and Bybee, 2017). A Ca- and Al-rich tholeiitic parental magma is generally proposed for these layered intrusions, however, more primitive basaltic, picritic or komatiitic parental magmas have also been proposed (Ashwal, 1993, 2010; Ashwal and Myers, 1994; Ashwal and Bybee, 2017).

The Superior Province of Canada contains more Archean megacrystic anorthosite-bearing layered intrusions than any other Archean craton worldwide, with the western Superior Province having the greatest concentration of these layered intrusions (Ashwal, 1993, 2010; Ashwal and Myers, 1994; Ashwal and Bybee, 2017; Polat et al., 2018a). Only the Doré Lake and Bad Vermilion Lake complexes in the eastern and western Superior Province, respectively, have been studied in detail (Zhou et al., 2016; Polat et al., 2018b). These layered intrusions

were interpreted to have formed in back-arc basin and volcanic arc settings, respectively (Zhou et al., 2016; Polat et al., 2018b). Studying other Archean megacrystic anorthosite-bearing layered intrusions in the western Superior Province offers an ideal opportunity to test the various subduction-related and subduction-unrelated tectonic settings proposed for these layered intrusions and whether they are cogenetic with spatially and temporally associated volcanic rocks in their host greenstone belts. The study of these layered intrusions can also constrain why they are spatially and temporally associated with volcanic rocks in their host greenstone belts. The study of the Archean megacrystic anorthosite-bearing layered intrusions in the western Superior Province also provides the opportunity to constrain the composition of the parental magmas to these layered intrusions. The Wawa and Bird River subprovinces contain the Haines Gabbroic Complex, and Bird River Sill and Mayville Intrusion, respectively (Osmani, 1997a; Corfu and Stott, 1998; Gilbert et al., 2008; Yang and Gilbert, 2014). These Archean megacrystic anorthosite-bearing layered intrusions have not been studied through a combination of fieldwork, petrography, and high-precision modern analytical techniques. These layered intrusions provide an ideal opportunity to resolve the questions outlined above surrounding the petrogenesis and tectonic setting of Archean megacrystic anorthosite-bearing layered intrusions.

1.3. Style of tectonics that operated in the western Superior Province in the Neoarchean

Despite numerous studies of Archean cratons worldwide, including the Superior Province, there is still no overarching consensus on whether horizontal (plate) or vertical tectonics operated in the Archean or whether either of these tectonic styles dominated over the other (Bédard et al., 2003, 2013; Bédard, 2006, 2018; Polat et al., 2015; Kusky et al., 2018; Hastie and Fitton, 2019; Roman and Arndt, 2019). There is a growing consensus that some form of horizontal (plate) tectonics (e.g., subduction, mid-ocean ridge spreading), and even modern-style plate tectonics, has operated in the Superior Province and other cratons since the Archean (Hollings and Kerrich, 2000; Hollings et al., 2000; Percival et al., 2006, 2012; Polat et al., 2015; Kusky et al., 2018; Hastie and Fitton, 2019; Roman and Arndt, 2019). Despite this, vertical tectonics (e.g., sagduction, subcretion, catalytic delamination) has been proposed as an alternative in recent years (Bédard et al., 2003, 2013; Bédard 2006, 2018). Proponents of vertical tectonics have discounted horizontal or modern-style plate tectonics operating in the Archean on the basis that the negative Nb and Ti anomalies indicative of sub-arc mantle wedge

melting in modern subduction zones cannot be used as evidence for Archean subduction and may reflect trace element mobility or crustal contamination (Bédard et al., 2003, 2013; Bédard 2006, 2018; Guice et al., 2018). The fact that higher heat flow and degrees of partial melting in the Archean resulted in thicker oceanic crust (30 km thick) than today's oceanic crust has been interpreted by advocates of vertical tectonics to indicate that subduction could not have occurred (Bédard et al., 2003, 2013; Bédard 2006, 2018). Lin (2005) proposed that vertical tectonics operated in the western Superior Province prior to a transition period during which synchronous vertical and horizontal tectonics operated before horizontal tectonics dominated. Given that Archean megacrystic anorthosite-bearing layered intrusions are ubiquitous in and constitute a minor yet important part of Archean greenstone belts, studying these layered intrusions may have major implications for whether vertical tectonics or horizontal tectonics akin to modern-style plate tectonics operated in the western Superior Province in the Neoarchean in particular and in the Archean in general. This would constrain the mechanism that facilitated Archean crustal growth and evolution in both the western Superior Province and in other Archean cratons.

1.4. Archean megacrystic anorthosites and the secular evolution of the Earth

Megacrystic anorthosites are thought to be restricted to the Archean and reflect processes that only occurred early in the Earth's history due to their ubiquity in Archean greenstone belts and their perceived scarcity in younger greenstone belts (Ashwal, 1993, 2010; Ashwal and Myers, 1994; Ashwal and Bybee, 2017). This has posed two intriguing questions: 1) Why are megacrystic anorthosite-bearing layered intrusions restricted to the Archean?; and 2) Is there a relationship between anorthosite petrogenesis and the secular evolution of the Earth? Rollinson et al. (2010) proposed that the Fiskenæsset Complex and Archean megacrystic anorthosite-bearing layered intrusions in general formed by partial melting of a depleted, harzburgitic sub-arc mantle wedge that was metasomatised and refertilised by siliceous Al-rich oceanic slab melts in a subduction zone setting. Rollinson et al. (2010) concluded that Archean megacrystic anorthosite-bearing layered intrusions largely ceased to form at the end of the Archean when the main crustal growth process switched from the melting of subducting oceanic crust to melting of the sub-arc mantle wedge. Polat et al. (2018a) postulated that Archean megacrystic anorthosite-bearing layered intrusions crystallised from shallow large magma chambers that formed by large degree partial melting of a very depleted sub-arc mantle wedge. The higher

mantle potential temperatures and degree of partial melting of the mantle in the Archean are thought to have been critical for the formation of Archean megacrystic anorthosites and leucogabbros and their calcic plagioclase megacrysts (Polat et al., 2018a). When these elevated mantle potential temperatures and the higher degree of partial melting of the mantle dropped below a certain level, the formation of megacrystic anorthosite-bearing layered intrusions largely ceased (Polat et al., 2018a). Slab melting has been shown to have occurred more efficiently and more often in the Archean as a result of the higher mantle potential temperatures and higher degree partial melting of the mantle that prevailed on the early Earth relative to the remainder of Earth history (Polat and Kerrich, 2006; Rollinson et al., 2010). The megacrystic anorthosite-bearing Haines Gabbroic Complex, Bird River Sill and Mayville Intrusion will be studied to test the aforementioned models and constrain how Archean megacrystic anorthosite-bearing layered intrusions formed and why they largely stopped forming at the end of the Archean. This will be done to constrain why megacrystic anorthosite-bearing layered intrusions are thought to be restricted to the Archean and if there is a relationship between anorthosite petrogenesis and the secular evolution of the Earth.

1.5. Geological setting

1.5.1. Superior Province

The Neoarchean Haines Gabbroic Complex, and Bird River Sill and Mayville Intrusion occur in the Wawa and Bird River subprovinces of the western Superior Province, respectively (Corfu and Stott, 1998; Percival et al., 2012; Yang and Gilbert, 2014). These subprovinces are typical of the west-east-trending volcano-plutonic subprovinces in the western Superior Province that predominantly comprise TTG batholiths and subordinate greenstone belts (Card and Ciesielski, 1986; Percival et al., 2012). The greenstone belts in these greenschist- to amphibolite-facies volcano-plutonic subprovinces host Archean megacrystic anorthosite-bearing layered intrusions (Percival et al., 2012; Polat et al., 2018a). Archean megacrystic anorthosite-bearing layered intrusions also occur in high-grade gneiss terranes that underwent granulite-facies metamorphism (Simmons et al., 1980; Ashwal, 1993; Peck et al.,1996; Hartlaub and Kuiper, 2004). The volcanic-plutonic subprovinces of the western Superior Province alternate with west-east-trending plutonic and metasedimentary subprovinces (Card and Ciesielski, 1986; Percival et al., 2012).

1.5.1.1. Haines Gabbroic Complex

The Neoarchean Haines Gabbroic Complex is located adjacent to the shores of Upper and Middle Shebandowan lakes in northwestern Ontario in the Shebandowan greenstone belt of the Wawa subprovince, and is spatially and temporally associated with the volcano-sedimentary Greenwater and Burchell assemblages (Farrow, 1993; Corfu and Stott, 1998; Lodge et al., 2015; Lodge, 2016). The Haines Gabbroic Complex is intruded by the Shebandowan Lake Pluton (Corfu and Stott, 1998; Lodge et al., 2015).

1.5.1.2. Bird River Sill

The Neoarchean Bird River Sill is located to the north of the Bird River and partly straddles the northern shores of Bird Lake in southeastern Manitoba (Gilbert et al., 2008). The Bird River Sill occurs in the southern arm of the Bird River greenstone belt in the Bird River subprovince and is located along the southern margin of the Neoarchean-Mesoarchean Maskwa Lake Block (Gilbert et al., 2008; Yang and Gilbert, 2014). The Maskwa Lake TTG Batholith II intrudes the Bird River Sill (Gilbert et al., 2008).

1.5.1.3. Mayville Intrusion

The Neoarchean Mayville Intrusion is located ~25 kilometres to the north of Bird Lake and the Bird River in southeastern Manitoba (Yang et al., 2013; Yang and Gilbert, 2014). The Mayville Intrusion occurs in the northern arm of the Bird River greenstone belt in the Bird River subprovince and is located along the northern margin of the Neoarchean-Mesoarchean Maskwa Lake Block (Yang et al., 2013; Yang and Gilbert, 2014). The Maskwa Lake TTG Batholith II intrudes the Mayville Intrusion (Yang et al., 2013; Yang and Gilbert, 2014).

1.6. Research objectives

The following key hypotheses will be tested to resolve the unresolved questions outlined above:

1) The Archean megacrystic anorthosite-bearing layered intrusions in the western Superior Province formed through modern-style plate tectonic processes at subduction zone tectonic settings.

2) Archean anorthosite-bearing layered intrusions formed through sagduction processes (Van Kranendonk et al., 2004; Johnson et al., 2017; Bédard, 2018).
3) These layered intrusions were cogenetic with spatially and temporally associated volcanic rocks in their host greenstone belts.

The overarching objective is: To test these key hypotheses.

The overarching objective will be met through the following sub-objectives:

1) To better constrain the petrogenesis and tectonic settings of the Haines Gabbroic Complex, Bird River Sill and Mayville Intrusion.
2) To place the petrogenesis and tectonic setting(s) of these anorthosite-bearing layered intrusions in the context of the evolution and assembly of the Superior Province and regional scale geological processes.
3) To place the petrogenesis and tectonic setting of these anorthosite-bearing layered intrusions in the context of Archean crustal evolution and continental growth mechanisms.
4) To better constrain the nature of plate tectonics in the Archean and ascertain whether modern plate tectonic-like processes did exist in the Archean based on the findings of this study.

These objectives will also be used to address the following outstanding questions:

1) Why are Archean megacrystic anorthosite-bearing layered intrusions spatially and temporally associated with greenstone belts?
2) What are the implications of anorthosite studies for the geodynamic evolution of the western Superior Province and continental growth in the Archean?
3) Why are megacrystic anorthosite-bearing layered intrusions restricted to the Archean?
4) Is there a relationship between anorthosite petrogenesis and the secular evolution of Earth?

This dissertation consists of six chapters. Chapters 1 and 5 are the Introduction and Conclusion, respectively, and Chapters 2, 3 and 4 are manuscripts. Chapters 2 and 3 have been published in Lithos and the International Journal of Earth Sciences, respectively. Chapter 4 has been published in Lithos.

The study combines detailed field, microscope, scanning electron microscope (SEM) and Raman spectroscopy petrographic observations, SEM-EDS (energy dispersive X-ray spectroscopy) mineral chemistry, whole-rock inductively coupled plasma mass spectrometry (ICP-MS) and Fusion-ICP major and trace element data, thermal ionisation mass spectrometry (TIMS) radiogenic Sm-Nd and Pb isotope geochemistry data, and pre-existing literature data. In *Chapter 2*, the field relationships, and petrographic observations for the Haines Gabbroic Complex and Shebandowan greenstone belt are described. Whole-rock major and trace element and radiogenic Sm-Nd and Pb isotope geochemical data for the Haines Gabbroic Complex and Shebandowan greenstone belt are presented and interpreted to determine their petrogenesis, whether they are cogenetic and the tectonic setting in which they formed. The effects of alteration on these data are assessed to ascertain whether they are suitable for valid petrogenetic and tectonic setting interpretation.

In *Chapter 3*, the field relationships and petrographic observations for the Bird River Sill and Bird River greenstone belt are described. Whole-rock major and trace element and radiogenic Sm-Nd and Pb isotope geochemical data for the Bird River Sill and Bird River greenstone belt are presented and interpreted to determine their petrogenesis, the tectonic setting in which they formed and whether they are cogenetic. The effects of alteration on these data are assessed to ascertain whether they are suitable for valid petrogenetic and tectonic setting interpretation. Scanning electron microscope mineral chemistry and Raman spectroscopy data are presented and interpreted to determine their mineralogy and chemistry in order to place constraints on the petrogenesis and tectonic setting of the Bird River Sill and Bird River greenstone belt.

In *Chapter 4*, the field relationships and petrographic observations for the Mayville Intrusion and Bird River greenstone belt are described. Whole-rock major and trace element and radiogenic Sm-Nd and Pb isotope geochemical data for the Mayville Intrusion and Bird River greenstone belt are presented and interpreted to determine the tectonic setting in which they formed, their petrogenesis and whether they are cogenetic. The effects of alteration on these data are assessed to ascertain whether they are suitable for valid petrogenetic and tectonic setting interpretation. In order to place constraints on the petrogenesis and tectonic setting of the Mayville Intrusion and Bird River greenstone belt, SEM-EDS mineral chemistry and Raman spectroscopy data are presented and interpreted to determine their mineralogy and mineral chemistry. Parental magma composition calculations and modelling are employed to better constrain the composition of the parental magma to the Mayville Intrusion.

1.7. References

Acosta-Gongora, P., Pehrsson, S.J., Sandeman, H., Martel, E., Peterson, T., 2018. The Ferguson Lake deposit: an example of Ni–Cu–Co–PGE mineralization emplaced in a back-arc basin setting?. Canadian Journal of Earth Sciences 55(8), 958-979.

Ahmat, A.L., de Laeter, J.R., 1982. Rb-Sr isotopic evidence for Archaean-Proterozoic crustal evolution of part of the central Yilgarn Block, Western Australia: Constrains on the age and source of the anorthositic Windimurra Gabbroid. Journal of the Geological Society of Australia 29(1-2), 177-190.

Ashwal, L.D., 1993. Anorthosites. Springer-Verlag: Berlin, Germany, Minerals and Rocks 21, 422p.

Ashwal, L.D., 2010. The temporality of anorthosites. The Canadian Mineralogist 48(4), 711-728.

Ashwal, L.D., Bybee, G.M., 2017. Crustal evolution and the temporality of anorthosites. Earth-Science Reviews 173, 307-330.

Ashwal, L.D., Morrison, D.A., Phinney, W.C., Wood, J., 1983. Origin of Archean anorthosites: Evidence from the Bad Vermilion Lake Anorthosite Complex, Ontario. Contributions to Mineralogy and Petrology 82, 259-273.

Ashwal, L.D., Myers, J.S., 1994. Archean anorthosites. In: Condie, K.C. (ed.). Archean Crustal Evolution. Elsevier: Amsterdam, Developments in Precambrian Geology 11, 315-355.

Barton Jr, J.M., 1996. The Messina layered intrusion, Limpopo belt, South Africa: an example of in-situ contamination of an Archean anorthosite complex by continental crust. Precambrian Research 78(1-3), 139-150.

Bédard, J.H., 2006. A catalytic delamination-driven model for coupled genesis of Archaean crust and sub-continental lithospheric mantle. Geochimica et Cosmochimica Acta 70(5), 1188-1214.

Bédard, J.H., 2018. Stagnant lids and mantle overturns: Implications for Archaean tectonics, magmagenesis, crustal growth, mantle evolution, and the start of plate tectonics. Geoscience Frontiers 9(1), 19-49.

Bédard, J.H., Brouillette, P., Madore, L., Berclaz, A., 2003. Archaean cratonization and deformation in the northern Superior Province, Canada: an evaluation of plate tectonic versus vertical tectonic models. Precambrian Research 127(1-3), 61-87.

Bedard, J.H., Harris, L.B., Thurston, P.C., 2013. The hunting of the snArc. Precambrian Research 229, 20-48.

Bowen, N.L., 1917. The problem of the anorthosites. Journal of Geology 25, 209-243.

Card, K.D., Ciesielski, A., 1986. Subdivisions of the Superior Province of the Canadian Shield. Geoscience Canada 13(1), 5-13.

Corfu, F., Stott, G.M., 1998. Shebandowan greenstone belt, Western Superior Province: U-Pb ages, tectonic implications, and correlations. Geological Society of America Bulletin 110, 1467-1484.

Dilek, Y., Furnes, H., 2011. Ophiolite genesis and global tectonics: Geochemical and tectonic fingerprinting of ancient oceanic lithosphere. GSA Bulletin 123(3-4), 387-411.

Farrow, C.E.G., 1993. Base metal sulphide mineralization, Shebandowan greenstone belt. In: Baker, C.L., Dressler, B.O., deSouza, H.A.F., Fenwick, K.G., Newsome, J.W., Owsiaki, L. (eds.). Summary of Field Work and Other Activities 1993. Ontario Geological Survey, Miscellaneous Paper 162, 87–96.

Gilbert, H.P., Davis, D.W., Duguet, M., Kremer, P., Mealin, C.A., MacDonald, J., 2008. Geology of the Bird River Belt, southeastern Manitoba (parts of NTS 52L5, 6). Manitoba Science, Technology, Energy and Mines, Manitoba Geological Survey, Geoscientific Map MAP2008-1, scale 1:50,000.

Good, D., Mealin, C., Walford, P., 2009. Geology of the Ore Fault Ni-Cu Deposit, Bird River Sill Complex, Manitoba. Exploration and Mining Geology 18(1-4), 41-57.

Guice, G., McDonald, I., Hughes, H., Schlatter, D., Goodenough, K., MacDonald, J., Faithfull, J., 2018. Assessing the validity of negative high field strength-element anomalies as a proxy for Archaean subduction: evidence from the Ben Strome Complex, NW Scotland. Geosciences 8(9), 338.

Hartlaub, R.P., Heaman, L.M., Ashton, K.E., Chacko, T., 2004. The Archean Murmac Bay Group: evidence for a giant archean rift in the Rae Province, Canada. Precambrian Research 131(3-4), 345-372.

Hartlaub, R.P., Kuiper. Y.D., 2004. Geology of central and north Split Lake (parts of NTS 54D4, 5 and 64A1, 8), Manitoba. Manitoba Industry, Economic Development and Mines, Manitoba Geological Survey, Preliminary Map PMAP2004-1, scale 1:25000.

Hastie, A.R., Fitton, J.G., 2019. Eoarchaean tectonics: New constraints from high pressure-temperature experiments and mass balance modelling. Precambrian Research 325, 20-38.

Hoffmann, J.E., Svahnberg, H., Piazolo, S., Scherstén, A., Münker, C., 2012. The geodynamic evolution of Mesoarchean anorthosite complexes inferred from the Naajat Kuuat Complex, southern West Greenland. Precambrian Research 196, 149-170.

Hollings, P., Kerrich, R., 2000. An Archean basalt-Nb-enriched basalt-adakite association: the 2.7 Ga Confederation assemblage of the Birch-Uchi greenstone belt, Superior Province. Contributions to Mineralogy and Petrology 139, 208-226.

Hollings, P., Stott, G., Wyman, D., 2000. Trace element geochemistry of the Meen-Dempster greenstone belt, Uchi subprovince, Superior Province, Canada: back-arc development on the margins of an Archean protocontinent. Canadian Journal of Earth Sciences 37, 1021-1038.

Ivanic, T.J., Wingate, M.T.D., Kirkland, C.L., Van Kranendonk, M.J., Wyche, S., 2010. Age and significance of voluminous mafic–ultramafic magmatic events in the Murchison Domain, Yilgarn Craton. Australian Journal of Earth Sciences 57(5), 597-614.

Jobin-Bevans, L.S., 1997. Geology, mineral chemistry and petrogenesis of the Pipestone Lake anorthosite complex. University of Manitoba, Winnipeg, Manitoba, M.Sc. thesis, 269p.

Johnson, T.E., Brown, M., Gardiner, N.J., Kirkland, C.I., Smithies, R.H., 2017. Earth's first stable continents did not form by subduction. Nature 543, 239-242.

Kusky, T.M., Windley, B.F., Polat, A., 2018. Geological evidence for the operation of plate tectonics throughout the Archean: Records from Archean paleo-plate boundaries. Journal of Earth Science 29(6), 1291-1303.

Lin, S., 2005. Synchronous vertical and horizontal tectonism in the Neoarchean: Kinematic evidence from a synclinal keel in the northwestern Superior craton, Canada. Precambrian Research 139(3-4), 181-194.

Lodge, R.W.D., 2016. Petrogenesis of intermediate volcanic assemblages from the Shebandowan greenstone belt, Superior Province: Evidence for subduction during the Neoarchaean. Precambrian Research 272, 150-167.

Lodge, R.W.D., Gibson, H.L., Stott, G.M., Franklin, J.M., Hudak, G.J., 2015. Geodynamic setting, crustal architecture, and VMS metallogeny of ca. 2720 Ma greenstone belt assemblages of the northern Wawa subprovince, Superior Province. Canadian Journal of Earth Sciences 52(3), 196-214.

Mohan, M.R., Satyanarayanan, M., Santosh, M., Sylvester, P.J., Tubrett, M., Lam, R., 2013. Neoarchean suprasubduction zone arc magmatism in southern India: Geochemistry, zircon U-Pb geochronology and Hf isotopes of the Sittampundi Anorthosite Complex. Gondwana Research 23(2), 539-557.

Myers, J.S., 1988. Oldest known terrestrial anorthosite at Mount Narryer, Western Australia. Precambrian Research 38(4), 309-323.

Osmani, I.A., 1997a. Geology and mineral potential: Greenwater Lake area, west-central Shebandowan greenstone belt. Ontario Geological Survey, Report 296, 135 p.

Paixão, M.A.P., Oliveira, E.P., 1998. The Lagoa da Vaca complex: an Archaean layered anorthosite body on the western edge of the Uauá Block, Bahia, Brazil. Revista Brasileira de Geociencias 28(2), 201-208.

Peck, D.C., Cameron, H.D.M., Layton-Matthews, D., Bishop, A., 1996. Geological investigations of anorthosite, gabbro and pyroxenite occurrences in the Pikwitonei granulated domain and the Cross Lake region (parts of NTS 63I/6, 63 J/7, 63 J/8, 63P/5, 63P/6,63P/7, 63P/8, 63P/9, 63P/10, 63P/11 and 63P/12). In: Report of Field Activities1996. Manitoba Energy and Mines, Minerals Division, 85–90.

Percival, J.A., Sanborn-Barrie, M., Skulski, T., Stott, G.M., Helmstaedt, H., White, D.J., 2006. Tectonic evolution of the western Superior Province from NATMAP and Lithoprobe studies. Canadian Journal of Earth Sciences, 43(7), 1085-1117.

Percival, J.A., Skulski, T., Sanborn-Barrie, M., Stott, G.M., Leclair, A.D., Corkery, M.T., Boily, M., 2012. Geology and tectonic evolution of the Superior Province, Canada. Tectonic styles in Canada: The Lithoprobe Perspective, Special Paper 49, 321-378.

Paixão, M.A.P., Oliveira, E.P., 1998. The Lagoa da Vaca complex: an Archaean layered anorthosite body on the western edge of the Uauá Block, Bahia, Brazil. Revista Brasileira de Geociencias 28(2), 201-208.

Piaia, P., Oliveira, E.P., Valeriano, C.M., 2017. The 2.58 Ga São José do Jacuipe gabbro-anorthosite stratiform complex, Itabuna-Salvador-Curaçá Orogen, São Francisco Craton, Brazil: Root of the Neoarchaean Caraiba continental arc?. Journal of South American Earth Sciences 79, 326-341.

Polat, A., Frei, R., Longstaffe, F.J., Woods, R., 2018b. Petrogenetic and geodynamic origin of the Neoarchean Doré Lake Complex, Abitibi subprovince, Superior Province, Canada. International Journal of Earth Sciences (Geol Rundsch) 107(3), 811-843.

Polat, A., Fryer, B.J., Appel, P.W., Kalvig, P., Kerrich, R., Dilek, Y., Yang, Z., 2011. Geochemistry of anorthositic differentiated sills in the Archean (~ 2970 Ma) Fiskenæsset Complex, SW Greenland: Implications for parental magma compositions, geodynamic setting, and secular heat flow in arcs. Lithos 123(1-4), 50-72.

Polat, A., Kerrich, K., 2006. Reading the geochemical fingerprints of Archean hot subduction volcanic rocks: Evidence for accretion and crustal recycling in a mobile tectonic regime.

In: Benn, K., Mareschal, J.C., Kondie, K.C. (eds.). Archean Geodynamics and Environments. AGU Geophysics Monograph Series 164, 189-213.

Polat, A., Longstaffe, F.J., Frei, R., 2018a. An overview of anorthosite-bearing layered intrusions in the Archaean craton of southern West Greenland and the Superior Province of Canada: implications for Archaean tectonics and the origin of megacrystic plagioclase. Geodinamica Acta 30(1), 84-99.

Polat, A., Wang, L., Appel, P.W.U., 2015. A review of structural patterns and melting processes in the Archean craton of West Greenland: Evidence for crustal growth at convergent plate margins as opposed to non-uniformitarian models. Tectonophysics, 662, 67-94.

Rollinson, H.R, Reid, C., Windley, B.F., 2010. Chromitites from the Fiskenæsset anorthositic complex, West Greenland: clues to late Archaean mantle processes. In: Kusky, T.M., Zhai, M.-G., Xiao, W. (eds.). The Evolving Continents: Understanding Processes of Continental Growth. Geological Society of London, Special Publications 338, 197-212.

Roman, A., Arndt, N., 2019. Differentiated Archean oceanic crust: its thermal structure, mechanical stability and a test of the sagduction hypothesis. Geochimica et Cosmochimica Acta, https://doi.org/10.1016/j.gca.2019.07.009.

Sandeman, H.A., Brown, J., Studnicki-Gizbert, C., MacHattie, T., Hyde, D., Johnstone, S., Greiner, E., Plaza, D., 2001. Bedrock mapping in the Committee Bay belt, Laughland Lake area, central mainland, Nunavut. Natural Resources Canada, Geological Survey of Canada, 28p.

Simmons, E.C., Hanson, G.N., Lumbers, S.B., 1980. Geochemistry of the Shawmere anorthosite complex, Kapuskasing structural zone, Ontario. Precambrian Research 11(1), 43-71.

Spath, C.S. III, Lesher, C.M., Houlé, M.G., 2015. Hybridized ultramafic rocks in the Black Label hybrid zone of the Black Thor intrusive complex, McFaulds Lake greenstone belt, Ontario, In: Ames, D.E., Houlé, M.G. (eds.). Targeted Geoscience Initiative 4: Canadian Nickel-Copper-Platinum Group Elements-Chromium Ore Systems - Fertility, Pathfinders, New and Revised Models. Geological Survey of Canada, Open File 7856, 103–114.

Van Kranendonk, M.J., Collins, W.J., Hickman, A., Pawley, M.J., 2004. Critical tests of vertical vs. horizontal tectonic models for the Archaean East Pilbara Granite-Greenstone Terrane, Pilbara Craton, Western Australia. Precambrian Research 131(3-4), 173-211.

Vrevskii, A.B., 2016. Age and sources of the anorthosites of the Neoarchean Kolmozero-Voron'ya greenstone belt (Fennoscandian Shield). Petrology 24(6), 527-542.

Wiener, R.W., 1981. Tectonic setting, rock chemistry, and metamorphism of an Archean gabbro–anorthosite complex, Tessiuyakh Bay, Labrador. Canadian Journal of Earth Sciences 18(9), 1409-1421.

Windley, B.F., Bishop, F.C., Smith, J.V., 1981. Metamorphosed layered igneous complexes in Archean granulite-gneiss belts. Annual Review of Earth and Planetary Sciences 9, 175-198.

Windley, B.F., Garde, A.A., 2009. Arc-generated blocks with crustal sections in the North Atlantic craton of West Greenland: crustal growth in the Archean with modern analogues. Earth-Science Reviews 93(1-2), 1-30.

Windley, B.F., Smith, J.V., 1976. Archaean high grade complexes and modern continental margins. Nature 260, 671-675.

Yang, X.M., Gilbert, H.P., 2014. Mineral chemistry of chromite in the Mayville intrusion: evidence for petrogenesis and linkage to the Bird River sill in the Neoarchean Bird River greenstone belt, southeastern Manitoba (NTS 52L5, 6, 12). In: Report of Activities 2014. Manitoba Mineral Resources, Manitoba Geological Survey, 32–48.

Yang, X.M., Gilbert, H.P., Houlé, M.G., 2013. Cat Lake-Euclid Lake area in the Neoarchean Bird River greenstone belt, southeastern Manitoba (parts of NTS 52L11, 12): preliminary results of bedrock geological mapping and their implications for geodynamic evolution and metallogeny. In: Report of Activities 2013. Manitoba Mineral Resources, Manitoba Geological Survey, 70-84.

Zhou, S., Polat, A., Longstaffe, F.J., Yang, K., Fryer, B.J., Weisener, C., 2016. Formation of the Neoarchean Bad Vermilion Lake Anorthosite Complex and spatially associated granitic rocks at a convergent plate margin, Superior Province, Western Ontario, Canada. Gondwana Research 33, 134-159.

Chapter 2: Petrogenesis and geodynamic setting of the Neoarchaean Haines Gabbroic Complex and Shebandowan greenstone belt, Southwestern Superior Province, Ontario, Canada

2.1. Introduction

The Neoarchean greenstone belts of the formerly contiguous Wawa and Abitibi subprovinces of the southern Superior Province (Fig. 2.1) in Canada contain prime examples of Archean megacrystic anorthosite-bearing layered intrusions. The Doré Lake Complex (Abitibi subprovince; Polat et al., 2018a) and the Haines Gabbroic Complex (Wawa subprovince; Farrow, 1993; Osmani 1996, 1997a; Corfu and Stott, 1998) share textural, lithological, geochemical and geodynamic setting similarities with other Archean megacrystic anorthosite-bearing layered intrusions in Greenland (Polat et al., 2011; Hoffmann et al., 2012), Canada (Wu et al., 2016; Zhou et al., 2016), India (Mohan et al., 2013), South Africa (Mouri et al., 2009), Russia (Vrevskii, 2016), Brazil (Paixão and Oliveira, 1998) and Australia (Myers, 1988).

The Haines Gabbroic Complex in the Shebandowan greenstone belt of the Wawa subprovince in Canada has received relatively little study (see Williams et al., 1991; Farrow, 1993; Osmani, 1996, 1997a; Corfu and Stott, 1998) compared to other Archean megacrystic anorthosite-bearing layered intrusions and its petrogenesis and geodynamic setting have not been studied using a combination of fieldwork, petrography, and whole-rock major and trace element and isotope geochemistry. A petrological and geochemical study of the Haines Gabbroic Complex offers an ideal opportunity to test the intra-oceanic arc rift models put forward by Corfu and Stott (1998), Lodge et al. (2015) and Lodge (2016) for the geodynamic setting of the Shebandowan greenstone belt and can explain the evolution of this belt within the context of the evolution of the Wawa subprovince. The Haines Gabbroic Complex is located in the central part of the Shebandowan greenstone belt and temporally and spatially associated with the mafic volcanic rocks of the Greenwater and Burchell assemblages and is spatially associated with and intruded by the Shebandowan Lake tonalite pluton. Therefore, studying the Haines Gabbroic Complex offers a great opportunity to test the aforementioned tectonic setting models proposed for the Shebandowan greenstone belt. Furthermore, the models of Lodge et al. (2015) and Lodge (2016) represent the most recent studies on this belt and invoke the involvement of a mantle plume in the generation of the Shebandowan greenstone belt, a hypothesis that is yet

to be tested. Moreover, studying the Haines Gabbroic Complex and the Shebandowan greenstone belt using a multi-disciplinary approach and modern high-precision analytical methods will determine whether the Haines Gabbroic Complex is genetically related to the spatially associated Greenwater and Burchell assemblages. Addressing these questions about the petrogenesis, geodynamic setting and evolution of the Haines Gabbroic Complex and the Shebandowan greenstone belt will also have implications for the geodynamic evolution of the western Superior Province, Archean crustal growth and evolution, the operation of plate tectonics in the Archean, and the petrogenesis of Archean megacrystic anorthosite-bearing layered intrusions.

This study differs from the previous investigations on the Shebandowan greenstone belt in that it presents extensive new field, petrography, and whole-rock major and trace element (21 samples) and Sm-Nd and U-Th-Pb isotope (10 samples) geochemical data from the Haines Gabbroic Complex to address the petrogenetic and geodynamic questions outlined above. In addition, new whole-rock major and trace element (29 samples), and Sm-Nd and U-Th-Pb isotope (16 samples) geochemistry data are presented for basalts, basaltic andesites, andesites, picrites, serpentinites, gabbros, pyroxenites and peridotites from the Greenwater and Burchell assemblages of the Shebandowan greenstone belt (Figs. 2.2 and 2.3) to assess their petrogenesis and geodynamic setting(s).

2.2. Regional geology

2.2.1. Superior Province

The Superior Province is the largest and, quite possibly, the most studied Archean craton in the world (Fig. 2.1) (Card and Ciesielski, 1986; Card, 1990; Williams et al., 1991; Card and Poulsen, 1998; Percival, 2007; Percival et al., 2012). The Superior Province comprises a number of volcanic-plutonic, plutonic, metasedimentary, and high-grade gneissic subprovinces (Fig. 2.1) (Percival et al., 2006, 2012). In the western and central Superior Province, volcanic-plutonic subprovinces of Neoarchean to Paleoarchean age are separated by plutonic and metasedimentary subprovinces of Neoarchean to Eoarchean and Neoarchean to Mesoarchean age, respectively (Percival et al., 2012). At the margins of the Superior Province, there are Neoarchean to Paleoarchean high-grade gneissic subprovinces (Percival et al., 2012). The subprovinces of the western and eastern Superior Province trend from west to east, however,

alternating Neoarchean to Paleoarchean plutonic subprovinces and Neoarchean to Mesoarchean high-grade gneissic subprovinces in the northeastern Superior Province trend from northwest to southeast through the Superior orocline (Percival et al., 2012).

The volcano-plutonic subprovinces of the Superior Province are comprised of greenstone belts and TTG batholiths (Fig. 2.1) (Percival et al., 2006, 2012; Percival, 2007). These greenstone belts consist of ultramafic to felsic volcanic rocks, metasedimentary rocks and mafic to ultramafic sills and intrusions that are often layered (Percival et al., 2006, 2012; Percival, 2007). Some of these layered mafic to ultramafic intrusions (e.g., Bad Vermillion Lake, Wabigoon; Doré Lake, Abitibi; Bird River, Mayville and Euclid Lake, Bird River; Pipestone Lake, Island Lake; Haines and Shawmere, Wawa) contain megacrystic anorthosites and leucogabbros (Simmons et al., 1980; Osmani, 1997a; Peck et al., 1999a; Yang et al., 2011, 2013; Yang and Gilbert, 2014; Zhou et al., 2016; Polat et al., 2018a, b). These intrusions are known as Archean megacrystic anorthosite-bearing layered intrusions (Ashwal, 1993, 2010; Ashwal and Bybee, 2017; Polat et al., 2018b).

2.2.2. Wawa subprovince

The Wawa subprovince in the southwestern Superior Province (Figs. 2.1 and 2.2) is a granite-greenstone belt terrain in which granitoid rocks surround disparate units and well-defined greenstone belts comprising metamorphosed komatiite, basalt, dacite, rhyolite, andesite, associated metasedimentary rocks and layered mafic-ultramafic intrusions (Williams et al., 1991; Card and Poulsen, 1998; Percival et al., 2006, 2012). There are at least three stages of supracrustal development preserved in the Wawa subprovince, dated at 2.70 Ga, 2.75 Ga and 2.89 Ga (Williams et al., 1991). The Wawa subprovince was amalgamated with the Quetico accretionary prism to the north by plate convergence and transpressive interaction during the late Neoarchean ~2695 Ma Shebandowanian orogeny (Pan and Fleet, 1993; Zaleski et al., 1999; Davis and Lin, 2003; Percival et al., 2006, 2012; Percival, 2007).

2.2.3. Shebandowan greenstone belt

The arcuate Shebandowan greenstone belt in the Wawa subprovince (Figs. 2.1 and 2.2) extends from Thunder Bay to the Ontario–Minnesota (U.S.A.) border and from the Quetico subprovince boundary to the 2750 Ma Northern Light tonalite-trondhjemite-granodiorite

(TTG) Gneiss Complex (Fig. 2) (Osmani, 1996; Corfu & Stott, 1998; Lodge et al., 2015). The Shebandowan greenstone belt contains Neoarchean (2680-2722 Ma) volcanic rocks ranging in composition from komatiite to trachyte, the Haines Gabbroic Complex, ultramafic, pyroxenitic, gabbroic and anorthositic sills, and syn-to post-tectonic TTGs and granitoid plutons (Figs. 2.2 and 2.3) (Watkinson and Irvine, 1964; Corfu and Stott, 1986, 1998; Williams et al., 1991; Osmani et al., 1992; Farrow, 1993; Osmani and Payne, 1993; Osmani, 1996, 1997a; Hart, 2007; Lodge and Chartrand, 2013; Lodge et al., 2015; Lodge, 2016; Hinz, 2018). The 2719-2722 Ma Greenwater Assemblage is the predominant assemblage within the Shebandowan greenstone belt and consists of ultramafic to felsic volcanic rocks, anorthosite, gabbro, peridotite and pyroxenite sills, banded iron formations (BIFs), sandstones, greywackes and conglomerates (Figs. 2 and 3) (Williams et al., 1991; Corfu and Stott, 1998; Hart, 2007; Lodge and Chartrand, 2013; Lodge et al., 2015; Lodge, 2016). The 2716-2719 Ma Burchell Assemblage contains basaltic to rhyolitic volcanic rocks, mafic intrusions, and BIFs (Fig. 2.2 and 2.3; Williams et al., 1991; Lodge, 2016). The mafic volcanic rocks of the Greenwater Assemblage have arc-, backarc- and MORB-like affinities and were partly erupted onto the Northern Light TTG Gneiss Complex (Williams et al., 1991; Corfu and Stott, 1998; Santaguida, 2001; Lodge et al., 2015). The Shebandowan greenstone belt underwent three phases of deformation (D_1-D_3) and folding (F_1-F_3) between ~2695 and 2680 Ma (Williams et al., 1991; Corfu and Stott, 1998; Lodge et al., 2015; Lodge, 2016).

2.2.4. Haines Gabbroic Complex

The 2722 ± 2 Ma Haines Gabbroic Complex (Farrow, 1993; Corfu and Stott, 1998) comprises medium-grained, mesocratic gabbro with subordinate melanocratic gabbro, anorthosite, leucogabbro, anorthositic gabbro, hornblendite, and gabbroic pegmatite (Williams et al., 1991; Osmani, 1996). The Haines Gabbroic Complex is strongly altered and is cut by numerous dykes, sills and small intrusions related to the 2696 ± 2 Ma Shebandowan Lake Pluton (Figs. 1 and 2) (Williams et al., 1991; Farrow, 1993; Osmani, 1996, 1997a; Corfu and Stott, 1986, 1998). Along both its northern and southern margins, the Haines Gabbroic Complex is in unconformable contact with basaltic to rhyolitic volcanic rocks of the younger Burchell Assemblage (Fig. 2.2) (Williams et al., 1991; Corfu and Stott, 1998; Lodge et al., 2015; Lodge, 2016). Megacrystic anorthosite (with plagioclase megacrysts up to 2 cm in diameter) occurs

1.2 kilometres to the west of Upper Shebandowan Lake and proximal to the Haines Gabbroic Complex (Osmani, 1997a).

2.3. Sampling

Due to a lack of accessible surface exposure, samples of the Neoarchean Haines Gabbroic Complex were obtained from the drill core library of Joe Hackl. Drill-core samples from the Haines Gabbroic Complex included seven anorthosites, five leucogabbros and nine gabbros (Figs. 2.2 and 2.3; Appendix 1.1). These drill-core samples enabled representative sampling to be done from the top to the bottom of the Haines Gabbroic Complex in order to understand the genetic relationships between the different lithologies within it. Three pyroxenite, three peridotite and three picrite drill-core samples were obtained from the Greenwater Assemblage (Figs. 2.2 and 2.3; Appendix 1.2). The picrites were primarily distinguished from basalts after geochemical analyses. Field-based sampling was also conducted in the spatially and temporally associated Greenwater and Burchell assemblages of the Shebandowan greenstone belt (Figs. 2.2 and 2.3; Appendix 1.2). Two basalts, two basaltic andesites, three gabbros and four serpentinites were sampled from the Greenwater Assemblage and three andesites and six gabbros were sampled from the Burchell Assemblage (Figs. 2.2 and 2.3; Appendix 1.2). The field samples' weights ranged from 2 to 4 kg. The Global Positioning System (GPS) coordinates for the sample locations are given in Appendices 1.1 and 1.2.

2.4. Analytical methods

A Leitz Laborlux 12 Pol polarising microscope and an Olympus BX51 petrographic microscope, equipped with a Luminera Infinity 1 high resolution digital camera with image capture software, were used to study the petrography of the samples. Samples were also analysed for major and trace elements, and for Nd and Pb isotopes. Details of the whole-rock major and trace element and Sm-Nd and U-Th-Pb isotope analysis procedures are given in Polat et al. (2016) and Wu et al. (2016). As such, only short summaries of the analytical procedures are provided here.

2.4.1. Major and trace elements

Major elements were analysed using a Fusion-ICP at Activation Laboratories Ltd. (Actlabs) in Ancaster, Ontario, Canada, and trace elements were analysed at Geoscience Laboratories (Geo Labs) in Sudbury, Ontario, Canada by inductively-coupled plasma mass spectrometry (ICP-MS). For the major element analyses, the samples were reduced to a powder using an agate mill. The loss-on-ignition (LOI) values were calculated based on weight loss resulting from heating the samples for 3 hours at 1100°C. Following this, the samples were melded with a lithium metaborate and lithium tetraborate commixture and then poured into a 5% nitric acid solution for dissolution. The totals for major element oxides were found to be 100 ± 1.5 wt.%. The reproducibility of the analyses was found to be better than ±5% of the amount present. Detection limits and the results of standard and duplicate analyses are given in Appendix 1.3. The analytical procedures outlined in Schweyer (2006) and Burnham (2008) were used for the trace element ICP-MS analyses. Multi-acid techniques (method code IMC-100) were used to digest the samples. The reproducibility of most of the trace element analyses was determined to be generally better than ±10% of the amount present (see Polat et al., 2012, 2016). The methods for calculating anomalous element ratios stipulated in Taylor and McLennan (1985) were used to calculate Eu/Eu*, Nb/Nb*, Zr/Zr* and Ti/Ti* ratios. Mg-numbers (#) were calculated using the molecular ratio of $Mg/(Mg + Fe^{2+})$, where Fe^{2+} is assumed to be 90% of total Fe (Gill, 2010; Zhou et al., 2016). Trace elements were normalised to normal mid-ocean ridge basalt (N-MORB) and chondrite values (Sun and McDonough, 1989) for petrogenetic interpretation.

2.4.2. Sm-Nd and U-Th-Pb isotope analyses

A VG Sector 54 IT thermal ionisation mass spectrometer (TIMS) at the Geological Institute (IGN), University of Copenhagen, Copenhagen, Denmark, was used to analyse 26 samples for Sm-Nd and Pb isotope compositions. The sample selection was representative of the sampled lithology types and included only samples with coherent chondrite-normalised rare-earth element (REE) and N-MORB-normalised trace element patterns. Prior to acid digestion, powder samples were mixed with a $^{150}Nd/^{147}Sm$ spike. Savillex™ beakers containing concentrated HNO_3, HCl and HF were placed on a hotplate heated to 130°C for 3 days to dissolve the powder samples (see Frei and Polat, 2013; Wu et al., 2016). Separation of REEs was conducted using chromatographic separation columns charged with 12 ml AG50W-X 8 (100-200 mesh) cation resin. Smaller chromatographic columns containing Eichrom's™ LN

resin SPS (Part#LN-B25-S) were used to enhance the separation of Sm and Nd. Conventional glass and miniature glass stem anion exchange columns containing 1 ml and 200 μl of 100-200 mesh Bio-Rad AG 1 x 8 resin, respectively, were used to separate Pb. A triple Ta-Re-Ta filament assembly was used to collect Sm and Nd isotopes in a multi-dynamic routine and a static multi-collection mode, respectively. A $^{146}Nd/^{144}Nd$ ratio of 0.7219 was used to correct the measured Nd isotope ratios for mass bias. Throughout the period of analyses, measurements of the JNdi standard yielded a mean value of $^{143}Nd/^{144}Nd = 0.512095 \pm 11$ (2σ; $n = 6$). The precision of the $^{147}Sm/^{144}Nd$ ratios was found to be better than 2% (2σ).

A static multi-collection mode was used to measure the Pb isotope compositions of the samples. Repeated analysis of the NBS 981 standard was conducted to control fractionation (using the values of Todt et al., 1993). Insignificant total procedural blanks (<200 pg Pb) indicate that common Pb isotope ratios were not influenced beyond the significant third digit. Samarium, Nd and Pb isotopic ratios and Sm and Nd isotopic dilution concentrations were determined from the dissolved powder aliquots.

2.5. Petrography

Almost all the primary igneous minerals have been extensively recrystallised and replaced in the Haines Gabbroic Complex and the Greenwater and Burchell assemblages (Figs. 2.4 and 2.5). In spite of this extensive recrystallisation and replacement, primary plagioclase, pyroxene, and olivine crystals and pseudomorphs of cumulus plagioclase, pyroxene and olivine and interstitial pyroxene crystals are locally preserved. Transmitted light petrographic microscope observations indicate that the altered, primary plagioclase crystals were extensively recrystallised and replaced by metamorphic plagioclase, epidote, zoisite, sericite and calcite through saussuritisation. Many pyroxene crystals have been replaced by secondary amphibole and/or epidote whereas most olivine crystals have been serpentinised to serpentine minerals, tremolite and talc. Pseudomorphs of primary, megacrystic plagioclase crystals (Fig. 2.5) occur in the anorthosites and leucogabbros of the Haines Gabbroic Complex. The presence of these megacrystic plagioclase crystals indicates that the Haines Gabbroic Complex is an Archean megacrystic anorthosite-bearing layered intrusion. The occurrence of megacrystic anorthosite (with plagioclase megacrysts up to 2 cm in diameter) 1.2 kilometres to the west of Upper Shebandowan Lake and proximal to the Haines Gabbroic Complex (Osmani, 1997a) indicates that there are other occurrences of megacrystic anorthosites in the vicinity of this complex. Due

to the lack of accessible surface exposures of the Haines Gabbroic Complex, it was hard to determine whether outcrop-scale cumulate textures are well preserved in the anorthosites, leucogabbros, and gabbros. However, Osmani (1996) observed compositional grading on Boyes Island in Upper Shebandowan Lake. The anorthosites are composed mainly of plagioclase + sericite + zoisite ± actinolite ± ilmenite ± magnetite ± hematite ± calcite ± quartz ± chalcopyrite ± pyrrhotite ± pyrite (Fig. 2.5). The leucogabbros are mineralogically similar to the anorthosites, consisting mainly of plagioclase + sericite + zoisite ± actinolite ± olivine ± quartz ± chalcopyrite ± pyrrhotite ± pyrite (Fig. 2.5). Many of the recrystallised plagioclase crystals have a cloudy appearance (Fig. 2.5). The gabbros are characterised by plagioclase + sericite + actinolite ± epidote ± zoisite ± quartz ± chalcopyrite ± magnetite ± ilmenite ± hematite ± pyrite (Fig. 2.5). Primary plagioclase in the anorthosites, leucogabbros and gabbros is mainly replaced by metamorphic plagioclase, epidote and zoisite (Fig. 2.5). Primary pyroxene and olivine are rare to absent.

Basalts, basaltic andesites and gabbros from the Greenwater Assemblage are composed predominantly of epidote + chlorite + actinolite + plagioclase + quartz ± zoisite ± talc ± calcite ± sericite ± olivine ± magnetite ± pyrite ± ilmenite ± chalcopyrite (Fig. 2.5). As a result of extensive deformation and metamorphic recrystallisation, relict igneous textures are rarely preserved, and quartz veins are pervasive. Picrites from the Greenwater Assemblage consist of tremolite + actinolite + talc + chlorite + sericite + epidote + magnetite + hematite + pyrite + chalcopyrite + rutile. The serpentinites in the Greenwater Assemblage are comprised of serpentine + tremolite + olivine + talc + actinolite + epidote + magnetite + chalcopyrite + pyrite ± chlorite (see Fig. 2.5). Despite pervasive serpentinisation, euhedral olivine comprises 2 to 5% of the samples with some crystals showing no sign of serpentinisation and others having a serpentinised rim (Fig. 2.5). The gabbros of the Greenwater Assemblage consist of actinolite + plagioclase + epidote + sericite + chlorite + opaques ± calcite ± olivine ± quartz (Fig. 2.5). The pyroxenites of the Greenwater Assemblage consist mainly of tremolite + actinolite + serpentine + chlorite + talc + epidote + chalcopyrite + pyrite + magnetite ± pyroxene ± olivine ± albite (Fig. 2.5). The harzburgites of the Greenwater Assemblage are comprised of serpentine + tremolite + actinolite + magnetite (Fig. 2.5). Serpentinisation is pervasive and no primary minerals are observed. Magnetite-rich bands outline the boundaries of pseudomorphs of olivine (Fig. 2.5). The andesites and gabbros from the Burchell Assemblage are composed of actinolite + plagioclase ± epidote + chlorite + quartz ± zoisite ± talc ± calcite ± sericite ± olivine ± magnetite ± pyrite ± ilmenite ± chalcopyrite.

2.6. Geochemical results

2.6.1. Major and trace elements

2.6.1.1. Haines Gabbroic Complex

The anorthosites from the Haines Gabbroic Complex are characterised by high Al_2O_3 (24.0-26.9 wt.%) and CaO (13.2-15.7 wt.%), and low to moderate MgO (1.2-3.1 wt.%), $Fe_2O_3^T$ (2.2-4.6 wt.%) and TiO_2 (0.13-0.41 wt.%) contents (Fig. 2.6; Appendix 1.1; Gill, 2010, and references therein). These anorthosites have low SiO_2 (47.9-50.4 wt.%) contents, and moderate Mg# (47-60) (Appendix 1.1). High-field strength elements (HFSE) are depleted relative to REE, as shown by the presence of negative Nb, Ti and Zr anomalies on the N-MORB-normalised trace element diagram (Figs. 2.7 and 2.8a; Appendix 1.1). Furthermore, the anorthosites have pronounced positive Eu anomalies and LREE-enriched patterns (Figs. 2.8a and 2.9a, Appendix 1.1).

The leucogabbros from the Haines Gabbroic Complex have high Al_2O_3 (18.4-23.9 wt.%) and CaO (12.3-16.6 wt.%), moderate to high $Fe_2O_3^T$ (3.6-5.8 wt.%), low to high MgO (1.1-5.8 wt.%), low to moderate TiO_2 (0.13-0.39 wt.%) and low SiO_2 (48.4-49.5 wt.%) contents, and moderate to high Mg# (37-67) (Fig. 2.6; Appendix 1.1). These leucogabbros are depleted in Nb, Ti and Zr relative to REE, generating negative HFSE anomalies on the N-MORB-normalised trace element diagram (Fig. 2.8b; Appendix 1.1). The leucogabbros have pronounced positive Eu anomalies and near-flat to slightly LREE-enriched patterns (Fig. 2.8b and 2.9b; Appendix 1.1). Sample SP04-002-11 was deemed anomalous on the basis of its higher SiO_2 and Na_2O and lower $Fe_2O_3^T$, MgO and CaO contents relative to the other leucogabbros and being more visibly altered than these leucogabbros. As such, this sample has not been included in this section, Figs. 2.6-2.9 and the petrogenetic interpretation below (Appendix 1.1).

The gabbros from the Haines Gabbroic Complex are characterised by moderate to high Al_2O_3 (13.7-17.9 wt.%), high CaO (11.6-13.6 wt.%), MgO (7.0-10.1 wt.%) and $Fe_2O_3^T$ (6.0-8.5 wt.%), low TiO_2 (0.18-0.30 wt.%) and SiO_2 (43.5-49.8 wt.%) contents, and primitive Mg# (69-70) (Fig. 2.6; Appendix 1.1; Gill, 2010, and references therein). These gabbros exhibit pronounced negative Nb, Ti and Zr anomalies, resulting in HFSE depletion relative to REE on the N-MORB-normalised trace element diagram (Fig. 2.8c; Appendix 1.1). On the chondrite-normalised diagram (Fig. 2.9c), the gabbros largely display HREE-enriched patterns and

positive Eu anomalies (Appendix 1.1). Sample SP04-002-21 was deemed to be anomalous on the basis of its lower SiO_2 and higher MgO contents and higher Zr/Y, Nd/Sm and La/Yb_{cn} ratios relative to the other gabbros and has not been included in this section, Figs. 2.6-2.9 and the petrogenetic interpretation below (Appendix 1.1).

2.6.1.2. Greenwater Assemblage

The basalts from the Greenwater Assemblage are characterised by high MgO (6.4-6.8 wt.%), $Fe_2O_3^T$ (13.9-14.4 wt.%) and TiO_2 (1.10-1.23 wt.%), moderate Al_2O_3 (13.0-14.1 wt.%) and CaO (7.0-10.0 wt.%) and low SiO_2 (47.9-50.3 wt.%) contents, and moderate Mg# (47-49) (Fig. 2.6; Appendix 1.2). These basalts have La/Yb, Zr/Y and Th/Yb ratios that are consistent with a tholeiitic affinity (Appendix 1.2; see Ross and Bédard, 2009). Negative Nb, Ti and Zr anomalies indicate that HFSE are depleted relative to REE on the N-MORB-normalised trace element diagram (Fig. 2.8d; Appendix 1.2). The basalts have negative Eu anomalies and exhibit near-flat, slightly LREE-enriched patterns (Figs. 2.8d and 2.9d; Appendix 1.2).

The basaltic andesites/andesites from the Greenwater Assemblage were identified based on the Zr/Ti versus Nb/Y immobile element total alkali-silica (TAS) proxy diagram (Fig. 2.10; see Winchester and Floyd, 1977). These rocks are characterised by high $Fe_2O_3^T$ (12.9-14.7 wt.%), MgO (5.8-6.6 wt.%) and TiO_2 (1.25-1.48 wt.%), moderate Al_2O_3 (12.7-13.9 wt.%), moderate to high CaO (7.2-9.2 wt.%) and low to moderate SiO_2 (50.6-53.9 wt.%) contents, and low to moderate Mg# (44-50) (Fig. 2.6; Appendix 1.2). The Zr/Y, La/Yb and Th/Yb ratios of these basaltic andesites are indicative of a tholeiitic to transitional affinity (Appendix 1.2; see Ross and Bédard, 2009). The HFSE exhibit negative anomalies relative to REE on the N-MORB-normalised trace element diagram, as shown by the presence of variably pronounced negative Nb, Ti and Zr anomalies (Fig. 2.8e; Appendix 1.2). On the chondrite-normalised REE diagram, the basaltic andesites display negative Eu anomalies and slightly LREE-enriched patterns (Fig. 2.9e; Appendix 1.2).

The picrites from the Greenwater Assemblage are typified by high MgO (14.5-16.1 wt.%) and $Fe_2O_3^T$ (12.0-13.5 wt.%), moderate Al_2O_3 (10.3-11.2 wt.%), TiO_2 (0.51-0.65 wt.%) and CaO (9.4-9.8 wt.%) and low SiO_2 (46.0-46.8 wt.%) contents, and primitive Mg# (71-72) (Fig. 2.6; Appendix 1.2). These picrites have a tholeiitic affinity (see Ross and Bédard, 2009), based on their La/Yb, Zr/Y and Th/Yb ratios (Appendix 1.2). High-field strength elements are depleted relative to REE in these picrites, on the basis of negative Nb, Ti and Zr anomalies on the N-MORB-normalised trace element diagram (Fig. 2.8g; Appendix 1.2). The chondrite-

normalised REE diagram for the picrites exhibits slightly positive Eu anomalies and gently sloping, slightly HREE-enriched patterns (Fig. 2.9g; Appendix 1.2).

The serpentinites from the Greenwater Assemblage are characterised by high MgO (20.3-31.1 wt.%) and $Fe_2O_3^T$ (11.9-14.3 wt.%), low to moderate CaO (2.4-7.7 wt.%), Al_2O_3 (3.3-9.2 wt.%) and TiO_2 (0.20-0.35 wt.%) and low SiO_2 (37.7-44.6 wt.%) contents, and high Mg# (77-81) (Fig. 2.6; Appendix 1.2). The serpentinites have negative Nb, Ti and Zr anomalies on the N-MORB-normalised trace element diagram, negative Eu anomalies and slightly HREE-enriched patterns (Figs. 2.8g and 2.9g; Appendix 1.2). Sample SD2016-02 was deemed anomalous on the basis of its higher Zr/Y, La/Yb_{cn} and Nd/Sm ratios and lower SiO_2 and higher MgO contents relative to the other serpentinites and has not been included in this section, Figs. 2.6, 2.7, 2.8 and 2.9 and the petrogenetic interpretation below (Appendix 1.2).

The gabbros from the Greenwater Assemblage are characterised by high $Fe_2O_3^T$ (8.2-15.3 wt.%) and MgO (6.9-8.0 wt.%), moderate to high Al_2O_3 (13.8-18.5 wt.%), CaO (8.7-11.7 wt.%) and TiO_2 (0.49-1.44 wt.%) and low SiO_2 (48.0-50.9 wt.%) contents, and moderate to high Mg# (47-63) (Fig. 2.6; Appendix 1.2). The gabbros are depleted in HFSE relative to REE on the N-MORB-normalised trace element diagram, as shown by Nb, Ti and Zr exhibiting negative anomalies (Fig. 2.8f; Appendix 1.2). On the chondrite-normalised REE diagram, there are negative Eu anomalies and gently sloping, LREE-enriched patterns (Fig. 2.9f; Appendix 1.2). Sample SD2016-43 has some dioritic affinities (Figs. 2.6, 2.7, 2.8d and 2.9d; Appendix 1.2).

The pyroxenites from the Greenwater Assemblage have high MgO (17.7-21.2 wt.%), $Fe_2O_3^T$ (11.9-15.5 wt.%) and TiO_2 (0.88-1.08 wt.%), moderate to high CaO (7.2-11.4 wt.%) and low Al_2O_3 (6.0-7.9 wt.%) and SiO_2 (43.8-48.9 wt.%) contents, and primitive Mg# (73-75) (Fig. 2.6; Appendix 1.2). Their N-MORB-normalised trace element patterns show depletion in HFSE relative to REE, with Nb, Ti and Zr exhibiting negative anomalies (Fig. 2.8h; Appendix 1.2). The pyroxenites have negative Eu anomalies and LREE-enriched patterns (Fig. 2.9h; Appendix 1.2).

The peridotites from the Greenwater Assemblage are characterised by high MgO (27.9-30.2 wt.%) and $Fe_2O_3^T$ (13.0-14.2 wt.%) and low SiO_2 (39.2-40.3 wt.%), Al_2O_3 (3.7-4.6 wt.%), CaO (1.6-3.0 wt.%) and TiO_2 (0.28-0.29 wt.%) contents, and primitive Mg# (81) (Fig. 2.6; Appendix 1.2). The peridotites have negative Nb and Ti and negative to positive Zr anomalies on the N-MORB-normalised trace element diagram (Fig. 2.8h; Appendix 1.2). Chondrite-normalised REE patterns are slightly LREE-enriched and have negative Eu anomalies (Fig. 2.9h; Appendix 1.2).

2.6.1.3. Burchell Assemblage

The andesites from the Burchell Assemblage were identified based on the Zr/Ti versus Nb/Y immobile element TAS proxy diagram (Fig. 2.10; see Winchester and Floyd, 1977). They are characterised by high $Fe_2O_3^T$ (7.5-9.2 wt.%), MgO (4.6-8.4 wt.%) and TiO_2 (0.71-1.13 wt.%), moderate to high Al_2O_3 (14.1-17.5 wt.%) and moderate CaO (4.4-7.0 wt.%) and SiO_2 (52.9-57.5 wt.%) contents, and moderate to high Mg# (49-65) (Fig. 2.6; Appendix 1.2). These andesites have an overall calc-alkaline affinity, based on their Zr/Y, La/Yb and Th/Yb ratios (Appendix 1.2; see Ross and Bédard, 2009). High-field strength elements, such as Nb and Ti, are depleted relative to REE on the N-MORB-normalised trace element diagram, however, there are slightly positive Zr anomalies (Fig. 2.8e; Appendix 1.2). There are slightly negative Eu anomalies and moderately-sloping, LREE-enriched patterns (Fig. 2.9e; Appendix 1.2).
The gabbros of the Burchell Assemblage are characterised by high $Fe_2O_3^T$ (7.3-12.3 wt.%), MgO (4.9-7.7 wt.%), CaO (8.6-12.0 wt.%) and TiO_2 (0.68-1.49 wt.%), moderate Al_2O_3 (13.7-16.8 wt.%) and low to moderate SiO_2 (46.9-55.7 wt.%), and moderate Mg# (48-60) (Fig. 2.6; Appendix 1.2). These gabbros have negative Nb, Ti and Zr anomalies on the N-MORB-normalised trace element diagram and slightly positive Eu anomalies (Figs. 2.8f and 2.9f; Appendix 1.2). On the chondrite-normalised REE diagram, the gabbros exhibit gently-sloping, LREE-enriched patterns (Fig. 2.9f; Appendix 1.2). Samples SD2016-23 and SD2016-30 have dioritic major and trace element characteristics (Figs. 2.6 and 2.7; Appendix 1.2).

2.6.2. Radiogenic isotopes

2.6.2.1 Sm-Nd isotopes

The anorthosites (ε_{Nd} = +3.1 to +4.7), leucogabbros (ε_{Nd} = +3.3 to +5.0) and gabbros (ε_{Nd} = +4.0 to +4.1) from the Haines Gabbroic Complex have variably positive, depleted initial $\varepsilon_{Nd\ 2720\ Ma}$ values (Fig. 2.11a; Table 2.1). Furthermore, these anorthosites, leucogabbros and gabbros have overlapping, depleted $^{147}Sm/^{144}Nd$ ratios (Fig. 2.11a; Table 2.1). Leucogabbro sample SP04-002-31 (ε_{Nd} = +5.0; T_{DM} = 2495 Ma; $^{147}Sm/^{144}Nd$ = 0.1846) is anomalous (see below; Table 2.1).

The basalts (ε_{Nd} = +2.8), basaltic andesites (ε_{Nd} = +2.1), picrites (ε_{Nd} = +3.8 to +4.1), serpentinites (ε_{Nd} = +2.8 to +4.1), pyroxenites (ε_{Nd} = 1.8), gabbros (ε_{Nd} = +3.2) and peridotites (ε_{Nd} = +2.1 to +2.7) from the Greenwater Assemblage have variably positive, depleted initial $\varepsilon_{Nd\ 2720\ Ma}$ values (Fig. 2.11a; Table 2.1). Moreover, these basalts, basaltic andesites, picrites, serpentinites, gabbros, pyroxenites and peridotites have overlapping, depleted $^{147}Sm/^{144}Nd$ ratios (Fig. 2.11a; Table 2.1). Basaltic andesite sample SD2016-15 from the Greenwater Assemblage has an atypical ε_{Nd} value (+5.0), T_{DM} age (2569 Ma) and $^{147}Sm/^{144}Nd$ (0.1716) ratio (see below; Table 2.1). The T_{DM} model ages of the serpentinites (2846-3177 Ma) and peridotites (2991-3188 Ma) from the Greenwater Assemblage overlap with those of the Haines Gabbroic Complex (2745-3011 Ma) (Fig. 2.11a; Table 2.1).

The andesites (ε_{Nd} = +2.0 to +3.0) and gabbros (ε_{Nd} = +2.6 to +3.7) of the Burchell Assemblage have positive, depleted initial $\varepsilon_{Nd\ 2720\ Ma}$ values and similar, depleted $^{147}Sm/^{144}Nd$ ratios (Fig. 2.11a; Table 2.1). The andesites of the Burchell Assemblage have juvenile T_{DM} model ages (2861-2963 Ma) that are like those of the Haines Gabbroic Complex, however, they differ from the more ancient T_{DM} model ages (2846-3213 Ma) of the Greenwater Assemblage (Fig. 2.11a; Table 2.1). The gabbros of the Burchell Assemblage have T_{DM} model ages (2824-3471 Ma) that overlap with yet are older than those of the Haines Gabbroic Complex, Greenwater Assemblage and Burchell Assemblage andesites (Fig. 2.11a; Table 2.1).

2.6.2.2 Pb isotopes

The anorthosites, leucogabbros and gabbros of the Haines Gabbroic Complex display very similar present-day $^{207}Pb/^{204}Pb$ isotope ratios (Fig. 2.11b; Table 2.2). The anorthosites of the Haines Gabbroic Complex have present-day $^{208}Pb/^{204}Pb$ and $^{208}Pb/^{204}Pb$ isotope ratios that vary greatly, whereas those of the leucogabbros and gabbros have narrower variations (Fig. 2.11b; Table 2.2). The pyroxenites and basaltic andesites of the Greenwater Assemblage have large variations in present-day $^{206}Pb/^{204}Pb$ isotope ratios, whereas the picrites, serpentinites, and peridotites exhibit only minor to moderate variations (Fig. 2.11b; Table 2.2). Similarly, the picrites, serpentinites, pyroxenites and peridotites exhibit very similar present-day $^{207}Pb/^{204}Pb$ isotope ratios. The basaltic andesites and pyroxenites of the Greenwater Assemblage have large variations in present-day $^{208}Pb/^{204}Pb$ isotope ratios, on the other hand, those of the picrites, serpentinites, and peridotites exhibit minor to moderate variations (Fig. 2.11b; Table 2.2). The andesites and gabbros of the Burchell Assemblage have largely invariable present-day $^{206}Pb/^{204}Pb$, $^{207}Pb/^{204}Pb$ and $^{208}Pb/^{204}Pb$ ratios (Fig. 2.11b; Table 2.2).

2.7. Discussion

2.7.1. Effects of metamorphism on element mobility

Petrographic observations indicate that the Haines Gabbroic Complex and the Greenwater and Burchell assemblages were extensively recrystallised under greenschist-facies metamorphic conditions (Figs. 2.4 and 2.5). All samples analysed for this study record the effects of a metamorphic overprint; however, field, and petrographic observations indicate that there is sample to sample variation in the degree of metamorphic alteration. Primary igneous minerals have been extensively replaced by secondary metamorphic minerals (Figs. 2.4 and 2.5). Many plagioclase crystals appear clouded due to the presence of Fe-bearing minerals (Fig. 2.5). This has been attributed to the exsolution of Fe - originally contained in the plagioclase crystals in solid solution - due to thermal metamorphism (see Deer et al., 2013). Accordingly, the effects of metamorphic alteration on the geochemistry of the Haines Gabbroic Complex and the Greenwater and Burchell assemblages must be assessed before any petrogenetic and geodynamic interpretation can be made. Following the approach of Guice et al. (2018), major and trace elements were plotted against Zr and Yb in bivariate plots (Fig. 2.7) and the corresponding correlation coefficients were calculated to test the mobility of these elements during metamorphism. The major elements (except TiO_2), LILE, and transition metals (e.g., Ni, Cu and Co) do not correlate well with Zr and Yb, indicating that they were significantly affected by metamorphic alteration. The presence of Ni- and Cu-bearing magmatic sulphides (pyrrhotite and chalcopyrite) in the Haines Gabbroic Complex and Greenwater Assemblage indicate that magmatic sulphide formation may have also had an influence on the variability of Ni and Co abundances, rendering these elements inadequate for petrogenetic interpretation. The HFSE and REE correlate well with Zr and Yb, suggesting that they were not significantly affected during metamorphism and are suitable for valid petrogenetic and geodynamic interpretation (Fig. 2.7). The LILE and major elements (except TiO_2) are not as suitable for petrogenetic interpretation and only the latter will be used in any way for this purpose.

Despite the pervasive nature of the metamorphic alteration that affected the Haines Gabbroic Complex and the Greenwater and Burchell assemblages, their Sm-Nd and U-Th-Pb isotope systems are considered useful for petrogenetic interpretation. There is no significant variability in the Sm, Nd and Pb compositions of the Haines Gabbroic Complex and the Greenwater and

Burchell assemblages (Fig. 2.11; Tables 2.1 and 2.2), indicating that their Sm-Nd and U-Th-Pb systems were not significantly open during metamorphism and that these isotope systems can be used for petrogenetic interpretation. This is corroborated by the $^{147}Sm/^{144}Nd$-$^{143}Nd/^{144}Nd$ (2765 +110/-280 Ma and 3108 +120/-380 Ma, respectively) and $^{206}Pb/^{204}Pb$-$^{207}Pb/^{204}Pb$ (2903 ± 350 Ma and 2642 ± 140 Ma, respectively) errorchron ages of the Haines Gabbroic Complex and the Greenwater Assemblage. These errorchron ages, within uncertainty, overlap with the ~2720 Ma U-Pb zircon ages of the Haines Gabbroic Complex and the Greenwater Assemblage (Fig. 2.11c) (see Corfu and Stott, 1998; Lodge and Chartrand, 2013). These errorchron ages indicate that the Sm-Nd and U-Th-Pb isotope systems were relatively robust during metamorphic recrystallisation and alteration. The Sm-Nd errorchron ages of the Haines Gabbroic Complex and the Greenwater Assemblage correlate with the T_{DM} ages presented in this contribution. This suggests that the Sm-Nd isotope system was more robust than the U-Th-Pb isotope systems used in this study, however, the large uncertainty in the errorchron ages of the Haines Gabbroic Complex and the Greenwater Assemblage indicates that even this system was slightly reset during metamorphism. Samples SD2016-15 and SP04-002-31 have initial ε_{Nd} values of +5.0 (Table 2.1), which most likely were a consequence of Sm/Nd fractionation during metamorphism and deformation (cf. Lahaye and Arndt, 1996; Lahaye et al., 1995) rather than small-scale heterogeneities in the mantle or very-depleted mantle source domains beneath the Shebandowan greenstone belt during the Neoarchean. This is supported by these samples being more visibly altered and recrystallised than the other lithologies of the Haines Gabbroic Complex and Greenwater Assemblage, suggesting that their anomalous initial ε_{Nd} values are due to metamorphism. Moreover, this is also supported by the Neoarchean mafic volcanic rocks of the Shebandowan greenstone belt having significantly lower ε_{Nd} values of +1.5 to +2.7 (Lodge and Chartrand, 2013) than these anomalous initial ε_{Nd} values, indicating that there were no small-scale heterogeneities in the mantle or very-depleted mantle source domains beneath the Shebandowan greenstone belt (Lahaye and Arndt, 1996) beneath the Shebandowan greenstone belt when they formed. Filtering out these anomalous initial ε_{Nd} values indicates that the Haines Gabbroic Complex and Greenwater Assemblage have initial ε_{Nd} values of +3.0 to +4.1 and +1.8 to +4.1, respectively (Fig. 2.11a).

2.7.2. Degree of crustal contamination

The mafic volcanic rocks of the Greenwater Assemblage are in unconformable contact with the 2750 Ma Northern Light TTG Gneiss Complex, which therefore represents basement to the Shebandowan greenstone belt (Corfu and Stott, 1998; Santaguida, 2001; Lodge et al., 2015; Lodge, 2016). This, combined with the occurrence of basaltic pillow lavas (Fig. 2.4a) and VMS deposits (e.g., Vanguard, Wye Lake, Calvert-Stares, Mud Lake) in the Greenwater and Burchell assemblages, indicates that these mafic volcanic rocks most likely formed in an oceanic setting proximal to TTG crust (Lodge et al., 2015; Lodge, 2016). The juvenile, uncontaminated nature of the Haines Gabbroic Complex and the ultramafic to intermediate extrusive and intrusive rocks of the Greenwater and Burchell assemblages is indicated by their positive, depleted initial ε_{Nd} (+3.0 to +4.1, +1.8 to +4.1 and +2.0 to +3.7, respectively) values (Fig. 2.11a; Table 1). Furthermore, there is no correlation between their initial ε_{Nd} values and Th and Zr contents or La/Sm_{cn} and $^{147}Sm/^{144}Nd$ ratios, suggesting that there was little or no contamination of their parental magmas (see Vervoort and Blichert-Toft, 1999). Both the La/Yb_{cn} versus $^{206}Pb/^{204}Pb$ and Nb/Th_{pmn} versus $^{206}Pb/^{204}Pb$ diagrams indicate that minimal contamination of the parental magmas to the Haines Gabbroic Complex and Greenwater and Burchell assemblages by older continental crust occurred (Fig. 2.12; Lodge et al., 2015). These observations indicate that the initial ε_{Nd} values of the Haines Gabbroic Complex and Greenwater and Burchell assemblages are representative of their mantle source compositions.

2.7.3. Petrogenesis and mantle source characteristics

The major and trace element geochemistry of the Haines Gabbroic Complex indicates that it crystallised from a Ca- and Al-rich tholeiitic parental magma(s) (Figs. 2.6 and 2.7; Appendix 1.1). The anorthosites, leucogabbros and gabbros of the Haines Gabbroic Complex (Fig. 2.9) display more than one REE pattern, an observation which suggests that these lithologies were derived from multiple magma batches or crystal mushes of variable composition. The highly-depleted nature of the N-MORB-normalised trace element patterns of the Haines Gabbroic Complex suggests that its parental magmas fractionated from a more primitive (boninitic-like) parental magma (see Dilek and Furnes, 2014; Pearce, 2014; Ishizuka et al., 2014; Polat et al., 2018b). Polat et al. (2018b) found that Archean megacrystic anorthosite-bearing layered intrusions crystallised from hydrous parental magmas in a subduction zone setting. Given the fact that there are petrographic (Figs. 2.4c and 2.4d), field (see Osmani, 1996, 1997a) and geochemical (Figs. 2.6-2.9; Appendix 2.1) similarities between the Haines Gabbroic Complex

and other Archean megacrystic anorthosite-bearing layered intrusion, this suggests that this complex may have also crystallised from hydrous parental magmas in a subduction zone setting (see Polat et al., 2018b). This is supported by the fact that Archean megacrystic anorthosite-bearing layered intrusions have predominantly been interpreted to have formed from hydrous magmas in subduction zone settings (Rollinson et al., 2010; Polat et al., 2011, 2018b; Ashwal and Bybee, 2017).

Major and trace element variations diagrams, N-MORB- and chondrite-normalised diagrams and initial ε_{Nd} values (Figs. 2.6-2.11a) indicate that the parental magmas to the Haines Gabbroic Complex were derived from different, more depleted mantle sources than the Greenwater and Burchell assemblage mantle sources. This geochemical evidence also demonstrates that the Haines Gabbroic Complex and the Greenwater Assemblage are not cogenetic and that they were both derived by partial melting of different, variably-depleted mantle sources. The gabbros of the Haines Gabbroic Complex are more depleted and HREE-enriched compared to their associated anorthosites and leucogabbros (Figs. 2.6-2.11a), signifying that their parental magmas formed by the partial melting of a separate, more depleted mantle source. Such an observation illustrates that the gabbros are not cogenetic with the anorthosites and leucogabbros and crystallised from more primitive (boninitic-like) parental magmas that formed by greater degree partial melting of a more depleted mantle source.

The ultramafic to intermediate extrusive and intrusive rocks of the Greenwater Assemblage formed from tholeiitic to transitional parental magmas (Figs. 2.6-2.9; Appendix 1.2). The basalts and gabbros (*sensu stricto*) of the Greenwater Assemblage have more evolved and less primitive and depleted major and trace element, N-MORB- and chondrite-normalised and Nd isotope composition characteristics that are quite distinct from those of the picrites, serpentinites and peridotites of the Greenwater Assemblage (Figs. 2.6-2.11a; Appendix 1.2). These differences strongly suggest that these basalts and gabbros formed from distinct parental magmas and depleted mantle sources to these lithologies and are not cogenetic with the picrites, serpentinites and peridotites. The gabbros of the Greenwater Assemblage display more than one REE pattern (Figs. 2.8 and 2.9), indicating that they were derived from multiple magma batches or crystal mushes of variable composition.

The less depleted initial ε_{Nd} values (Fig. 2.11a) of the pyroxenites and their major and trace element characteristics (Figs. 2.6-2.11a; Appendix 1.2) indicate that they are genetically distinct from the other Greenwater Assemblage lithologies, the Burchell Assemblage and the Haines Gabbroic Complex. The pyroxenites crystallised from a distinct, tholeiitic parental magma derived by partial melting of a depleted mantle source that was more enriched than the

mantle sources to the other Greenwater Assemblage lithologies, the Burchell Assemblage and the Haines Gabbroic Complex.

The picrites, serpentinites and peridotites of the Greenwater Assemblage formed from primitive, tholeiitic parental magmas and are petrogenetically distinct from the other Greenwater Assemblage lithologies, the Burchell Assemblage and the Haines Gabbroic Complex (Appendix 1.2). Their major and trace element abundances, Nd isotope compositions and N-MORB- and chondrite-normalised trace element patterns indicate that these lithologies were derived from separate parental magmas and depleted mantle sources (Figs. 2.7-2.11a; Tables 2.1 and 2.2; Appendices 1.1 and 1.2).

The trace element geochemistry (Appendix 1.2) and trace element patterns (Figs. 2.8 and 2.9) of the picrites, serpentinites and peridotites of the Greenwater Assemblage are more primitive and depleted than the other Greenwater Assemblage lithologies and the Burchell Assemblage. The Haines Gabbroic Complex exhibits more depleted trace element patterns (Figs. 2.8 and 2.9) and trace element abundances than these picrites, serpentinites and peridotites, signifying that it is petrogenetically distinct. The peridotites have less depleted initial ε_{Nd} values than the picrites and serpentinites (Table 2.1), indicating that they were derived from a less depleted mantle source and that their parental magma may have been petrogenetically distinct from the parental magmas to these lithologies.

The andesites and gabbros of the Burchell Assemblage formed from calc-alkaline and tholeiitic to transitional parental magmas, respectively (Figs. 2.6-2.9; Appendix 1.2). The andesites are petrogenetically distinct from the gabbros of the Burchell Assemblage, the Greenwater Assemblage, and the Haines Gabbroic Complex. The andesites have distinctly more evolved major and trace element abundances, N-MORB- and chondrite-normalised trace element patterns, and higher Zr/Ti and Nb/Y ratios (Figs. 2.6-2.9; Appendix 1.2). The geochemical evidence outlined above indicates that the andesites formed from a distinct parental magma and depleted mantle source.

The dioritic gabbros of the Burchell Assemblage have similar major and trace element characteristics to the dioritic gabbro and basaltic andesites belonging to the Greenwater Assemblage (Figs. 2.6-2.9; Appendix 1.2), signifying that these lithologies are genetically related and crystallised from similar parental magmas that were derived from the same depleted mantle source. The gabbros (*sensu stricto*) of the Burchell Assemblage share similar geochemical characteristics with the basalts and gabbros of the Greenwater Assemblage, connoting that these lithologies are genetically related and were derived from the same depleted mantle source.

The Haines Gabbroic Complex and the Greenwater and Burchell assemblage have large positive, variably depleted initial ε_{Nd} values, consistent with long-term depleted mantle source compositions (Fig. 2.11a; Table 2.1). These depleted initial ε_{Nd} values corroborate with existing initial ε_{Nd} values (ε_{Nd} = +1.5 to +2.7; Lodge and Chartrand, 2013) for the mafic volcanic rocks of the Greenwater Assemblage. Furthermore, these depleted initial ε_{Nd} values are similar to the juvenile initial ε_{Nd} values (ε_{Nd} = +0.8 to +2.9) of the mafic volcanic rocks in the other greenstone belts (Vermilion, Winston Lake and Manitouwadge) of the Wawa subprovince (Lodge and Chartrand, 2013; Lodge et al., 2015; Lodge, 2016). These are indicative of considerably depleted mantle sources and are inconsistent with substantial contamination of their mantle-derived parental magmas by older continental crust (see Polat and Kerrich, 2002; Polat, 2009). Despite the proximity of the Haines Gabbroic Complex and Greenwater and Burchell assemblages to the Northern Light TTG Gneiss Complex and the fact that the mafic volcanic rocks of the Greenwater Assemblage were partly erupted onto the latter (Williams et al., 1991; Corfu and Stott, 1998; Santaguida, 2011; Lodge et al., 2015; Lodge, 2016), these lithologies were not significantly contaminated by spatially associated TTGs and are reflective of their variably-depleted mantle sources.

2.7.4. Geodynamic setting

The N-MORB-normalised trace element patterns and negative HFSE anomalies of the Haines Gabbroic Complex, and the Greenwater and Burchell assemblages (Fig. 2.8), the spatial and temporal field relationships between these lithologies, the proximity of these lithologies to the Northern Light TTG Gneiss Complex, and lithological associations are broadly consistent with a Japan-style mature intra-oceanic continental arc that had a large volume of TTGs (Fig. 2.13; Moreno et al., 2016; Taira et al., 2016). This interpretation corroborates with the arc rift geodynamic setting interpretations of Corfu and Stott (1998), Lodge et al. (2015) and Lodge (2016). Furthermore, the andesitic to rhyolitic volcanic rocks of the Greenwater and Burchell assemblages occur as tuffs and have negative HFSE anomalies, characteristics consistent with explosive pyroclastic volcanic activity in an active volcanic arc setting (see Corfu and Stott, 1998; Lodge et al., 2015; Lodge, 2016). Geochronological, geochemical and field evidence indicate that intra-oceanic arc magmatism occurred in the Shebandowan greenstone belt along the central northern margin of its associated arc (which will henceforth be referred to as the Shebandowan arc) as early as ~2726 Ma (Corfu and Stott, 1998), with earlier intra-oceanic arc

magmatism occurring along the central section of this arc (e.g., Northern Light TTG Batholith) at 2750 Ma (Corfu and Stott, 1998; Lodge and Chartrand, 2013).

The Greenwater Assemblage lithologies typically have variably negative Nb, Ti and Zr anomalies and flat to gently sloping (LREE-enriched) REE patterns and field relationships that are most likely consistent with a suprasubduction zone back-arc geodynamic setting (Murphy, 2007). The basaltic andesites and a dioritic gabbro from the Greenwater Assemblage have moderately sloping, LREE-enriched patterns and negative HFSE anomalies. These characteristics and geological relationships suggest that these lithologies may have formed in an active volcanic arc environment in a mature intra-oceanic continental arc geodynamic setting. The pyroxenites of the Greenwater Assemblage also have sloping, LREE-enriched patterns and enriched, P-MORB-like trace element patterns suggesting that they probably formed as a result of a mantle plume (Sproule et al., 2002; Pearce, 2014). The lithologies of the Burchell Assemblage have near-flat to steep REE patterns and negative HFSE anomalies and geological relationships consistent with both back-arc and active volcanic arc environments in a mature intra-oceanic continental arc setting. The geochemical characteristics of the Burchell Assemblage andesites signify that they are high-magnesian andesites that formed in a 'hot' subduction zone environment (see Lodge et al., 2015; Lodge, 2016)

The N-MORB-normalised trace element patterns and negative HFSE anomalies of the Haines Gabbroic Complex and geological relationships are also consistent with a back-arc setting in a rifted Japan-style mature intra-oceanic continental arc suprasubduction zone that had a large volume of TTGs (Fig. 2.13). This is corroborated by the Haines Gabbroic Complex being spatially and temporally associated with calc-alkaline basaltic to rhyolitic volcanic rocks that were interpreted by Lodge et al. (2015) and Lodge (2016) to have formed in a 'hot' subduction zone environment with a low-angle subducting slab. Furthermore, the inferred hydrous nature of the parental magmas to the Haines Gabbroic Complex and its initially boninitic-like parental magmas also point to a subduction zone setting (see Dilek and Furnes, 2014; Polat et al., 2018b). The Haines Gabbroic Complex has trace element patterns and initial ε_{Nd} values that are more depleted than the lithologies in the Greenwater and Burchell assemblages. The Haines Gabbroic Complex's highly-depleted trace element patterns and initial ε_{Nd} values indicate that the parental magmas to the complex were extracted from a mantle source that had already been depleted by an earlier melt extraction event. Given that the picrites, serpentinites and the gabbros of the Greenwater Assemblage have similarly-depleted ε_{Nd} values, these lithologies must have also formed from a parental magma derived from partial melting of a harzburgitic sub-arc mantle wedge source that had also been depleted by earlier melt extraction. The back-

arc setting proposed here for both the Haines Gabbroic Complex and the picrites, serpentinites, and gabbros of the Greenwater Assemblage indicates that the parental magmas to these lithologies were contemporaneously extracted from multiple sources in a highly-depleted, harzburgitic sub-arc mantle wedge.

A mantle plume most likely accentuated mature intra-oceanic continental back-arc rifting of the central northern section of the Shebandowan arc (Fig. 2.13). As the komatiites and ultramafic sills (including pyroxenites) formed during the second volcanic cycle of the Greenwater Assemblage, they post-date the Haines Gabbroic Complex (first volcanic cycle) and are contemporaneous with the mafic volcanics and intrusives of the second volcanic cycle (Williams et al., 1991). These geological relationships indicate that the back-arc of the northern central section of the Shebandowan arc in which the Haines Gabbroic Complex and the first volcanic cycle Greenwater Assemblage gabbro sills formed was not generated by a mantle plume. The plume-derived komatiites and ultramafic sills formed after these intrusions, implying that another mechanism, such as slab rollback, caused the intra-oceanic continental back-arc rifting that led to the formation of the Haines Gabbroic Complex and the spatially associated gabbro sills of the Greenwater Assemblage. Therefore, a mantle plume caused further intra-oceanic continental back-arc rifting, leading to the generation of the komatiites, pyroxenites, basalts, gabbros, serpentinites and peridotites of the second cycle of the Greenwater Assemblage.

Initial intra-oceanic continental volcanic arc magmatism between 2750 Ma and 2722 Ma formed the Northern Light TTG Batholith (2750 Ma) and the calc-alkaline basalts to rhyolites of the first volcanic cycle of the Greenwater Assemblage (Fig. 2.13) (between 2726 Ma and 2722 Ma). Slab rollback-driven back-arc rifting of the Japan-style mature Shebandowan intra-oceanic continental arc formed the Haines Gabbroic Complex and the first volcanic cycle Greenwater Assemblage gabbro sills. Contemporaneous arrival of a mantle plume accentuated the earlier back-arc rifting and directly resulted in the formation of the Greenwater Assemblage pyroxenites. The second volcanic cycle basalts, picrites, serpentinites, and peridotites of the Greenwater Assemblage formed in the more extensive back-arc environment adjacent to the active Shebandowan volcanic arc. The basaltic andesites and dioritic gabbro of the second volcanic cycle of the Greenwater Assemblage formed in the active Shebandowan volcanic arc. Following this, the andesites and dioritic gabbros of the Burchell Assemblage formed in the active Shebandowan volcanic arc, representing magmatism that was contemporaneous with the formation of the Burchell Assemblage gabbros (*sensu stricto*) in the adjacent back-arc. Based on field relationships, the Greenwater and Burchell assemblages formed consecutively as the

Shebandowan arc prograded in association with slab rollback and trench retreat (Figs. 2.2 and 2.13). The Burchell Assemblage arc-back-arc lithologies were erupted onto the older Greenwater Assemblage arc-backarc lithologies and the Haines Gabbroic Complex.

The petrographic, field and geochemical observations presented in this study and pre-existing geological relationships and lithological associations indicate that the Haines Gabbroic Complex, and the Greenwater and Burchell assemblages of the Shebandowan greenstone belt represent a dismembered Neoarchean suprasubduction zone ophiolite (see Dilek and Furnes, 2011) that marks a suture zone between the Wawa terrane and the Quetico and Wabigoon terranes to the north that accreted/collided together during the Shebandowan orogeny at ~2695 Ma (Percival et al., 2006, 2012; Percival, 2007). This further substantiates plate tectonics-based accretion models proposed for the Superior Province (e.g., Percival et al., 2006, 2012, Percival, 2007). The location of the Haines Gabbroic Complex and Shebandowan greenstone belt in the northern central section of the Shebandowan arc suggests that the subduction zone that they formed above had a present-day south-dipping subducting plate (Fig. 2.13).

2.8. Conclusions

1. The Haines Gabbroic Complex and the Greenwater and Burchell assemblages of the Shebandowan greenstone belt experienced widespread metamorphic recrystallisation and hydrothermal alteration.
2. The Haines Gabbroic Complex crystallised from hydrous Ca- and Al-rich tholeiitic parental magmas that fractionated from more primitive, hydrous boninitic-like parental magmas.
3. The Haines Gabbroic Complex, and Greenwater and Burchell Assemblages formed from several distinct parental magmas that were derived by variable partial melting of variably-depleted mantle sources.
4. The ultramafic to intermediate extrusive and intrusive rocks of the Haines Gabbroic Complex and the Greenwater and Burchell assemblages have large positive initial ε_{Nd} values, indicating that their parental magmas were extracted from long-term depleted mantle sources.
5. The parental magmas to the Haines Gabbroic Complex and Greenwater and Burchell assemblages were not contaminated by older continental crust and originated in an intra-oceanic setting.

6. The Haines Gabbroic Complex and the ultramafic to intermediate extrusive and intrusive rocks of the Greenwater and Burchell assemblages formed in a back-arc to arc setting at a Japan-style mature rifted intra-oceanic continental arc that had a large volume of TTGs. Back-arc rifting of the Shebandowan arc was most likely triggered by slab rollback followed by mantle plume emplacement. As such, they represent a dismembered Archean suprasubduction zone ophiolite that marks a suture zone between the Wawa and Wabigoon subprovinces that formed during the Shebandowanian orogeny at ~2695 Ma.

2.9. References

Ashwal, L.D., 1993. Anorthosites. Minerals and Rocks Series 21, Springer-Verlag: Berlin, 422p.

Ashwal, L.D., 2010. The temporality of anorthosites. The Canadian Mineralogist 48, 711-728.

Ashwal, L.D., Bybee, G.M., 2017. Crustal evolution and the temporality of anorthosites. Earth Science Reviews 173, 307-330.

Bowen, N.L., 1917. The problem of the anorthosites. Journal of Geology 25, 209-243.

Burnham, O.M., 2008. Trace element analysis of geological samples by inductively coupled plasma mass spectrometry (ICP-MS) at the Geoscience Laboratories; Revised capabilities due to method improvements. In: Summary of Field Work and Other Activities 2008. Ontario Geological Survey, Open File Report 6226, 38-1 - 38-10.

Card, K.D., 1990. A review of the Superior Province of the Canadian shield, a product of Archaean accretion. Precambrian Research 48, 99-156.

Card, K.D., Ciesielski, A., 1986. Subdivisions of the Superior province of the Canadian Shield. Geoscience Canada 13, 5-13.

Card, K.D., Poulsen, K.H., 1998. Geology and mineral deposits of the Superior Province of the Canadian shield. In: Lucas, S.B., St-Onge, M.R. (eds.). Geology of the Precambrian Superior and Grenville Provinces and Precambrian Fossils in North America. Geological Survey of Canada, Geology of Canada 7, 13-194.

Corfu, F., Stott, G.M., 1986. U-Pb ages for late magmatism and regional deformation in the Shebandowan Belt, Superior Province, Canada. Canadian Journal of Earth Sciences 23, 1075-1082.

Corfu, F., Stott, G.M., 1998. Shebandowan greenstone belt, Western Superior Province: U-Pb ages, tectonic implications, and correlations. Geological Society of America Bulletin 110, 1467-1484.

Davis, D.W., Lin, S., 2003. Unravelling the geologic history of the Archaean Hemlo gold deposit, Superior Province, Canada: A U-Pb geochronological study. Economic Geology 98, 51-67.

Deer, W.A., Howie, R.A., Zussman, J., 2013. An Introduction to the Rock-Forming Minerals. 3rd edition. The Mineralogical Society: London, 498p.

Dilek, Y., Furnes, H., 2011. Ophiolite genesis and global tectonics: Geochemical and tectonic fingerprinting of ancient oceanic lithosphere. GSA Bulletin 123(3-4), 387-411.

Dilek, Y., Furnes, H., 2014. Ophiolites and their origins. Elements 10(2), 93-100.

Farrow, C.E.G., 1993. Base metal sulphide mineralization, Shebandowan greenstone belt. In: Baker, C.L., Dressler, B.O., deSouza, H.A.F., Fenwick, K.G., Newsome, J.W., Owsiaki, L. (eds.). Summary of Field Work and Other Activities 1993. Ontario Geological Survey, Miscellaneous Paper 162, 87–96.

Frei, R., Polat, A., 2013. Chromium isotope fractionation during oxidative weathering - implications from the study of a Paleoproterozoic (ca. 1.9 Ga) paleosol, Schreiber Beach, Ontario, Canada. Precambrian Research 224, 434-453.

Friedman, E., Polat, A., Thorkelson, D.J., Frei, R., 2016. Lithospheric mantle xenoliths sampled by melts from upwelling asthenosphere: The Quaternary Tasse alkaline basalts of southeastern British Columbia, Canada. Gondwana Research 33, 200-230.

Gill, R.G., 2010. Igneous Rocks and Processes: A Practical Guide. John Wiley & Sons Ltd.: Chichester, U.K., 428p.

Guice, G.L., McDonald, I., Hughes, H.S.R., Schlatter, D.M., Goodenough, K.M., MacDonald, J.M., Faithfull, J.W., 2018. Assessing the validity of negative high field strength-element anomalies as a proxy for Archaean subduction: Evidence from the Ben Strome Complex, NW Scotland. Geosciences 8(9), 338, 1-32.

Hart, T.R., 2007. Geochronology of the Hamlin and Wye Lakes Area, Shebandowan Greenstone Belt, Thunder Bay District. In: Summary of Field Work and Other Activities 2007. Ontario Geological Survey, Open File Report 6213, 9-1 - 9-8.

Henry, P., Stevenson, R.K., Gariepy, C., 1998. Late Archaean mantle composition and crustal growth in the Western Superior Province of Canada: neodymium and lead isotopic evidence from the Wawa, Quetico and Wabigoon subprovinces. Geochimica et Cosmochimica Acta 62, 143-157.

Hinz, S.L.K., 2018. Geochemistry and petrography of the ultramafic metavolcanic rocks in the eastern portion of the Shebandowan greenstone belt, north western Ontario. M.Sc. thesis, Lakehead University, Thunder Bay, Ontario, Canada, 167p.

Hoffmann, J.E., Svahnberg, H., Piazolo, S., Scherstén, A., Münker, 2012. Geodynamic evolution of Mesoarchaean anorthosite complexes inferred from the Naajat Kuuat Complex, southern West Greenland. Precambrian Research 196-197, 149-170.

Ishizuka, O., Tani, K., Reagan, M.K., 2014. Izu-Bonin-Mariana forearc crust as a modern ophiolite analogue. Elements 10(2), 115-120.

Lahaye, Y., Arndt, N., 1996. Alteration of a komatiite flow from Alexo, Ontario, Canada. Journal of Petrology 37, 1261-1284.

Lahaye, Y., Arndt, N., Byerly, G., Chauvel, C., Fourcade, S., Gruau, G., 1995. The influence of alteration on the trace-element and Nd isotopic compositions of komatiites. Chemical Geology 126, 43-64.

Lodge, R.W.D., 2016. Petrogenesis of intermediate volcanic assemblages from the Shebandowan greenstone belt, Superior Province: Evidence for subduction during the Neoarchaean. Precambrian Research 272, 150-167.

Lodge, R.W.D., Chartrand, J.E., 2013. Establishing regional geodynamic settings and the metallogeny of volcanogenic massive sulphide mineralization of greenstone belt assemblages (circa 2720 Ma) of the Wawa Subprovince via geochemical comparisons. Ontario Geological Survey, Miscellaneous Release - Data 306.

Lodge, R.W.D., Gibson, H.L., Stott, G.M., Franklin, J.M., Hudak, G.J., 2015. Geodynamic setting, crustal architecture, and VMS metallogeny of ca. 2720 Ma greenstone belt assemblages of the northern Wawa subprovince, Superior Province. Canadian Journal of Earth Sciences 52(3), 196-214.

Mohan, R.M., Satyanarayanan, M., Santosh, M., Sylvester, P.J., Tubrett, M., Lam, R., 2013. Neoarchean suprasubduction zone arc magmatism in southern India: Geochemistry, zircon U-Pb geochronology and Hf isotopes of the Sittampundi Anorthosite Complex. Gondwana Research 23, 539-557.

Moreno, T., Wallis, S., Kojima, T., Gibbons, W., 2016. The Geology of Japan. The Geological Society, London, 536p.

Mouri, H., Whitehouse, M.J., Brandl, G., Rajesh, H.M., 2009. A magmatic age and four successive metamorphic events recorded in zircons from a single meta-anorthosite sample in the Limpopo Belt, South Africa. Journal of the Geological Society of London 166, 827-830.

Murphy, J.B., 2007. Igneous Rock Associations 8. Arc magmatism II: Geochemical and isotopic characteristics. Geoscience Canada 34(1), 7-35.

Myers, J.S., 1988. Oldest known terrestrial anorthosite at Mount Narryer, Western Australia. Precambrian Research 38, 309-323.

Osmani, I.A., 1996. Geology and mineral potential of the upper and middle Shebandowan Lakes area, west-central Shebandowan greenstone belt. Ontario Geological Survey, Open File Report 5938, 82 p.

Osmani, I.A., 1997a. Geology and mineral potential: Greenwater Lake area, west-central Shebandowan greenstone belt. Ontario Geological Survey, Report 296, 135 p.

Osmani, I. A., Payne, J., 1993. Geology of Begin, Lamport and parts of Haines and Hagey Townships, District of Thunder Bay. In: Baker, C.L., Dressler, B.O., deSouza, H.A.F., Fenwick, K.G., Newsome, J.W., Owsiaki, L. (eds.) Summary of Field Work and Other Activities 1993. Ontario Geological Survey, Miscellaneous Paper 162, 237–242.

Osmani, I.A., Payne, J., Lavigne, M.J., 1992. Geology of the western Greenwater Lake area, District of Thunder Bay, Ontario. In: Dressler, B.O., Baker, C.L., Blackwell, B. (eds.). Summary of Field Work and Other Activities 1992. Ontario Geological Survey, Miscellaneous Paper 160, 218–227.

Paixão, M.A.P., Oliveira, E.P., 1998. The Lagoa da Vaca Complex: An Archaean layered anorthosite body on the western edge of the Uauá Block, Bahia, Brazil. Revista Brasileira de Geociencias 28(2), 201-208.

Pan, Y., Fleet, M.E., 1993. Polymetamorphism in the Archaean Hemlo-Heron Bay greenstone belt, Superior Province: P-T variations and implications for tectonic evolution. Canadian Journal of Earth Sciences 30, 985-996.

Pearce, J.A., 2014. Immobile element fingerprinting of ophiolites. Elements 10(2), 101-108.

Peck, D.C., Halden, N.M., Jobin-Bevans, S., Cameron, H.D.M., Theyer, P., 1999a. Summary of metallogenetic and petrogenetic features of Archaean anorthosites and associated mafic and ultramafic rocks in the Superior Province, Manitoba (parts of NTS 63I, 63J, 63P and 64A). In: Report of Activities 1999. Manitoba Industry, Trade and Mines, Geological Services, 94-96.

Percival, J.A., 2007. Eo- to Mesoarchaean terranes of the Superior Province and their tectonic context. In: Van Kranendonk, M.J., Smithies, R.H., Bennett, V.C. (eds.). Earth's Oldest Rocks. Elsevier BV: Amsterdam, Developments in Precambrian Geology 15, 1065-1085.

Percival, J.A., Sanborn-Barrie, M., Stott, G.M., Helmstaedt, H., Skulski, T., White, D.J., 2006. Tectonic evolution of the Western Superior Province from NATMAP and Lithoprobe studies. Canadian Journal of Earth Sciences 43, 1085-1117.

Percival, J.A., Skulski, T., Sanborn-Barrie, M., Stott, G.M., Leclair, A.D., Corkery, M.T., Boily, M., 2012. Geology and tectonic evolution of the Superior Province, Canada. Tectonic styles in Canada: The Lithoprobe Perspective, Special Paper 49, 321-378.

Polat, A., 2009. The geochemistry of Neoarchaean (ca. 2700 Ma) tholeiitic basalts, transitional to alkaline basalts, and gabbros, Wawa Subprovince, Canada: Implications for petrogenetic and geodynamic process. Precambrian Research 168, 83-105. Science: Dordrecht, Modern Approaches in Solid Earth Sciences 7, 127-147.

Polat, A., Frei, R., Longstaffe, F.J., Woods, R., 2018a. Petrogenetic and geodynamic origin of the Neoarchaean Doré Lake Complex, Abitibi subprovince, Superior Province, Canada. International Journal of Earth Sciences 107, 811-843.

Polat, A., Fryer, B.J., Appel, P.W.U., Kalvig, P., Kerrich, R., Dilek, Y., Yang, Z., 2011. Geochemistry of anorthositic differentiated sills in the Archaean (~2970 Ma) Fiskenæsset Complex, SW Greenland: Implications for parental magma compositions, geodynamic setting, and secular heat flow in arcs. Lithos 123, 50-72.

Polat, A., Kerrich, R., 2002. Nd-isotope systematics of ~2.7 Ga adakites, magnesian andesites, and arc basalts, Superior Province: evidence for shallow crustal recycling at Archaean subduction zones. Earth and Planetary Science Letters 202, 345-360.

Polat, A., Kokfelt, T., Burke, K.C., Kusky, T., Bradley, D., Dziggel, A., Kolb, J., 2016. Lithological, structural, and geochemical characteristics of the Mesoarchaean Târtoq greenstone belt, South-West Greenland, and the Chugach-Prince William accretionary complex, southern Alaska: Evidence for uniformitarian plate-tectonic processes. Canadian Journal of Earth Sciences 53, 1336-1371.

Polat, A., Longstaffe, F.J., Frei, R., 2018b. An overview of anorthosite-bearing layered intrusions in the Archaean craton of southern West Greenland and the Superior Province of Canada: implications for Archaean tectonics and the origin of megacrystic plagioclase. Geodinamica Acta 30(1), 84-99.

Polat, A., Longstaffe, F.J., Weisener, C., Fryer, B.J., Frei, R., Kerrich, R., 2012. Extreme element mobility during transformation of Neoarchaean (ca. 2.7 Ga) pillow basalts to a Paleoproterozoic (ca. 1.9 Ga) paleosol, Schreiber Beach, Ontario, Canada. Chemical Geology 326-327, 145-173.

Ross, P.S., Bédard, J.H., 2009. Magmatic affinity of modern and ancient subalkaline volcanic rocks determined from trace element discriminant diagrams. Canadian Journal of Earth Sciences 46, 823-839.

Santaguida, F., 2001. Precambrian geology compilation series - Thunder Bay sheet. Ontario Geological Survey, Map 2664, 1:250000.

Schweyer, J., 2006. QA/QC: Summary of 2005-2006 quality control data at the Geoscience Laboratories. In: Summary of Field Work and Other Activities 2006. Ontario Geological Survey, Open File Report 6192, 40-1 - 40-4.

Simmons, E.G., Hanson, G.N., Lumbers, S.B., 1980. Geochemistry of the Shawmere Anorthosite Complex, Kapuskasing Structural Zone, Ontario. Precambrian Research 11, 43-71.

Sproule, R.A., Lesher, C.M., Ayer, J., Thurston, P.C., and Herzberg, C.T., 2002. Spatial and temporal variations in the geochemistry of komatiitic rocks in the Abitibi greenstone belt. Precambrian Research 115, 153-186.

Sun, S.S., McDonough, W.F., 1989. Chemical and isotopic systematics of oceanic basalts: implications for mantle composition and processes. In: Saunders, A.D., Norry, M.J. (eds.). Magmatism in the Ocean Basins. Geological Society of London: London, Special Publication 42, 313-345.

Taira, A., Ohara, Y., Wallis, S.R., Ishiwatari, A., Iryu, Y., 2016. Geological evolution of Japan: an overview. In: Moreno, T., Wallis, S., Kojima, T., Gibbons, W. (eds.). The Geology of Japan. The Geological Society, London, 1-24.

Taylor, S.R., McLennan, S.M., 1985. The continental crust: its composition and evolution. Blackwell: Oxford, 312p.

Todt, W., Cliff, R.A., Hanser, A., Hofmann, A.W., 1993. Re-calibration of NBS lead standards using ^{202}Pb+ ^{205}Pb double spike. Terra Abstracts 5, 396.

Vervoort, J.D., Blichert-Toft, J., 1999. Evolution of the depleted mantle: Hf isotope evidence from juvenile rocks through time. Geochimica et Cosmochimica Acta 63(3-4), 533-556.

Vrevskii, A.B., 2016. Age and sources of the anorthosites of the Neoarchaean Kolmozero-Voron'ya greenstone belt (Fennoscandian Shield). Petrology 24(6), 527-542.

Watkinson, D.H., Irvine, T. N., 1964. Peridotitic intrusions near Quetico and Shebandowan, northwestern Ontario: A contribution to the petrology and geochemistry of ultramafic rocks. Canadian Journal of Earth Sciences 1, 63–98.

Williams, H.R., Stott, G.M., Heather, K.B., Muir, T.L., Sage, R.P., 1991. Wawa Subprovince. In: Thurston, P.C., Williams, H.R., Sutcliffe, R.H., Stott, G.M. (eds.). Geology of Ontario. Geological Survey of Ontario, Special Volume 4 (Part 1), 485-539.

Winchester, J.A., Floyd, P.A., 1977. Geochemical discrimination of different magma series and their differentiation products using immobile elements. Chemical Geology 20, 325-343.

Wu, T., Polat, A., Fryer, B.J., Yang, K., Kusky, T. M., 2016. Geochemistry, Nd, Pb and Sr isotope systematics of the Neoarchaean Bad Vermilion Lake Greenstone Belt and spatially associated granitic rocks, Western Superior Province, Canada. Precambrian Research 97, 27-42.

Yang, X.M., Gilbert, H.P., 2014. Mineral chemistry of chromite in the Mayville intrusion: evidence for petrogenesis and linkage to the Bird River sill in the Neoarchaean Bird River greenstone belt, southeastern Manitoba (NTS 52L5, 6, 12). In: Report of Activities 2014. Manitoba Mineral Resources, Manitoba Geological Survey, 32-48.

Yang, X.M., Gilbert, H.P., Corkery, M.T., Houlé, M.G., 2011. The Mayville mafic-ultramafic intrusion in the Neoarchaean Bird River greenstone belt, southeastern Manitoba (part of NTS 52L12): preliminary geochemical investigation and implication for PGE-Ni-Cu-(Cr) mineralization. In: Report of Activities 2011. Manitoba Innovation, Energy and Mines, Manitoba Geological Survey, 127-142.

Yang, X.M., Gilbert, H.P., Houlé, M.G., 2013. Cat Lake-Euclid Lake area in the Neoarchaean Bird River greenstone belt, southeastern Manitoba (parts of NTS 52L11, 12): preliminary results of bedrock geological mapping and their implications for geodynamic evolution and metallogeny. In: Report of Activities 2013. Manitoba Mineral Resources, Manitoba Geological Survey, 70-84.

Zaleski, E., van Bremen, O., Peterson, V.L., 1999. Geological evolution of the Manitouwadge greenstone belt and Wawa-Quetico subprovince boundary, Superior Province, Ontario, constrained by U-Pb zircon dates of supracrustal and plutonic rocks. Canadian Journal of Earth Sciences 36, 945-966.

Zhou, S., Polat, A., Longstaffe, F.J., Yang, K., Fryer, B.J., Weisener, C., 2016. Formation of the Neoarchean Bad Vermilion Lake Complex and spatially associated granitic rocks at a convergent plate margin, Superior Province, Western Ontario, Canada. Gondwana Research 33, 134-159.

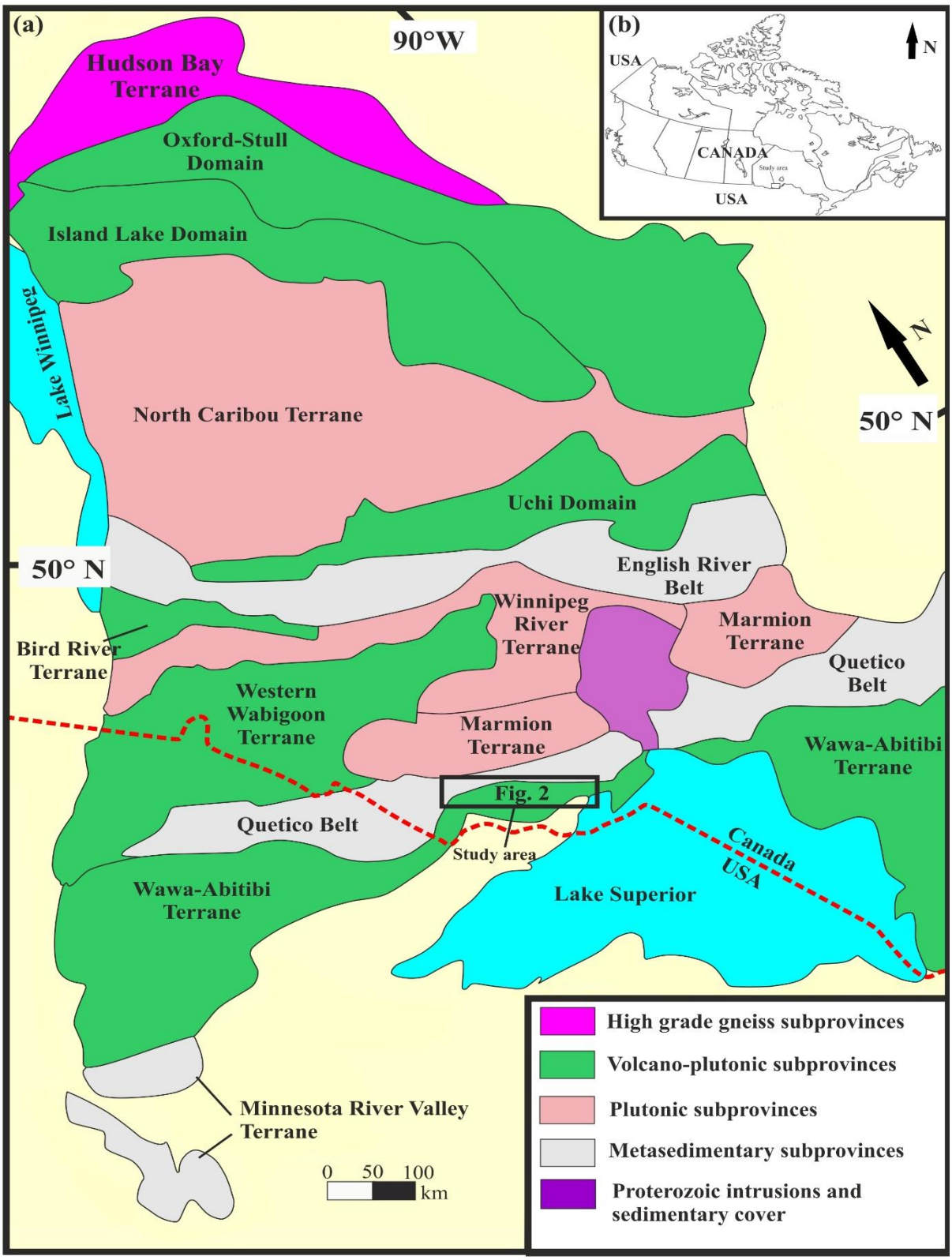

Fig. 2.1. (**a**) Simplified tectonic map of the western Superior Province (modified after Percival et al., 2012). (**b**) Simplified geographical map of Canada showing the location of the study area.

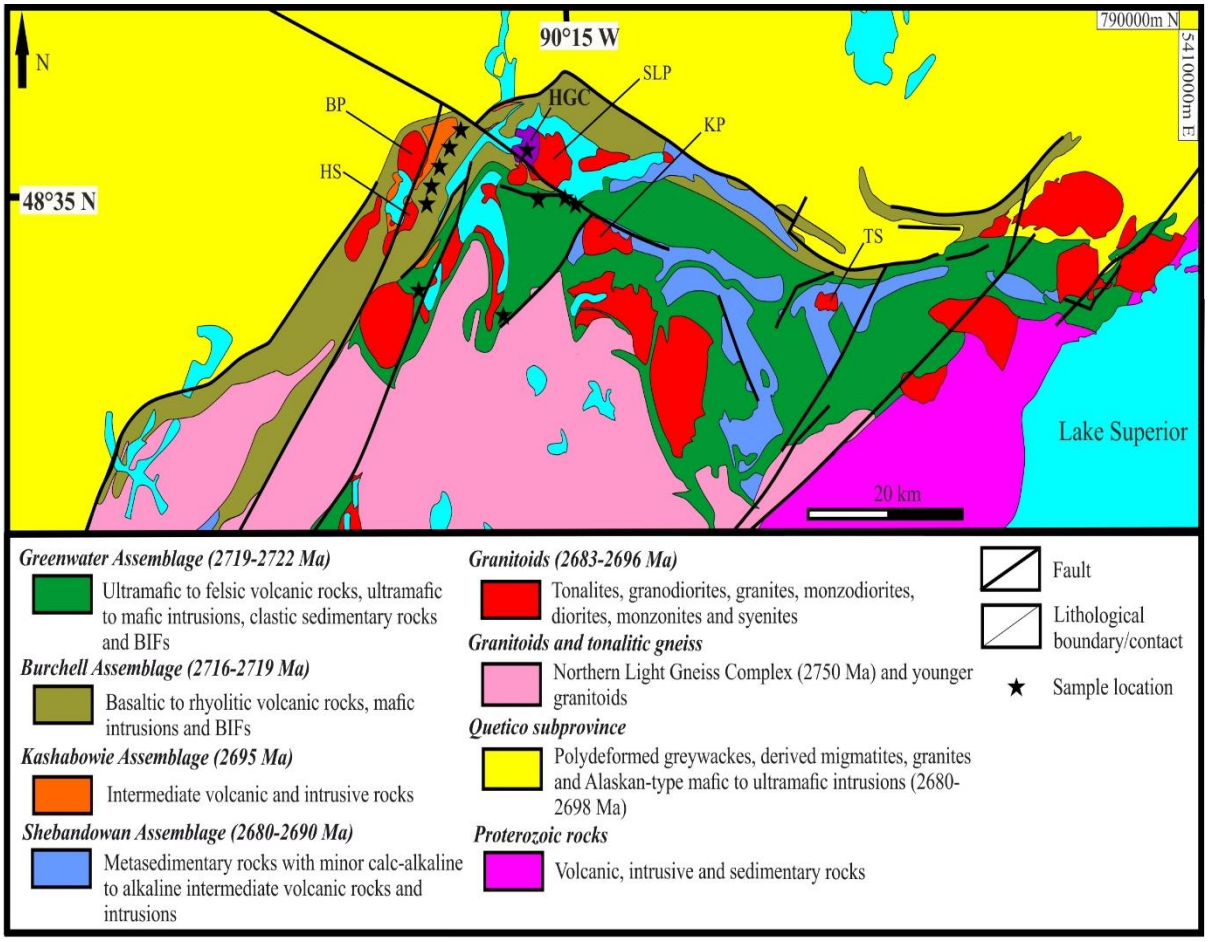

Fig. 2.2. Simplified geological map of the Shebandowan greenstone belt (modified and simplified from Lodge et al., 2015, and constructed based on information from Williams et al. (1991), Corfu and Stott (1998), Lodge et al. (2015) and Lodge (2016). HGC: Haines Gabbroic Complex; SLP: Shebandowan Lake Pluton; BP: Burchell Pluton; KP: Kekekuab Pluton; HS: Hermia Stock; TS: Tower Stock.

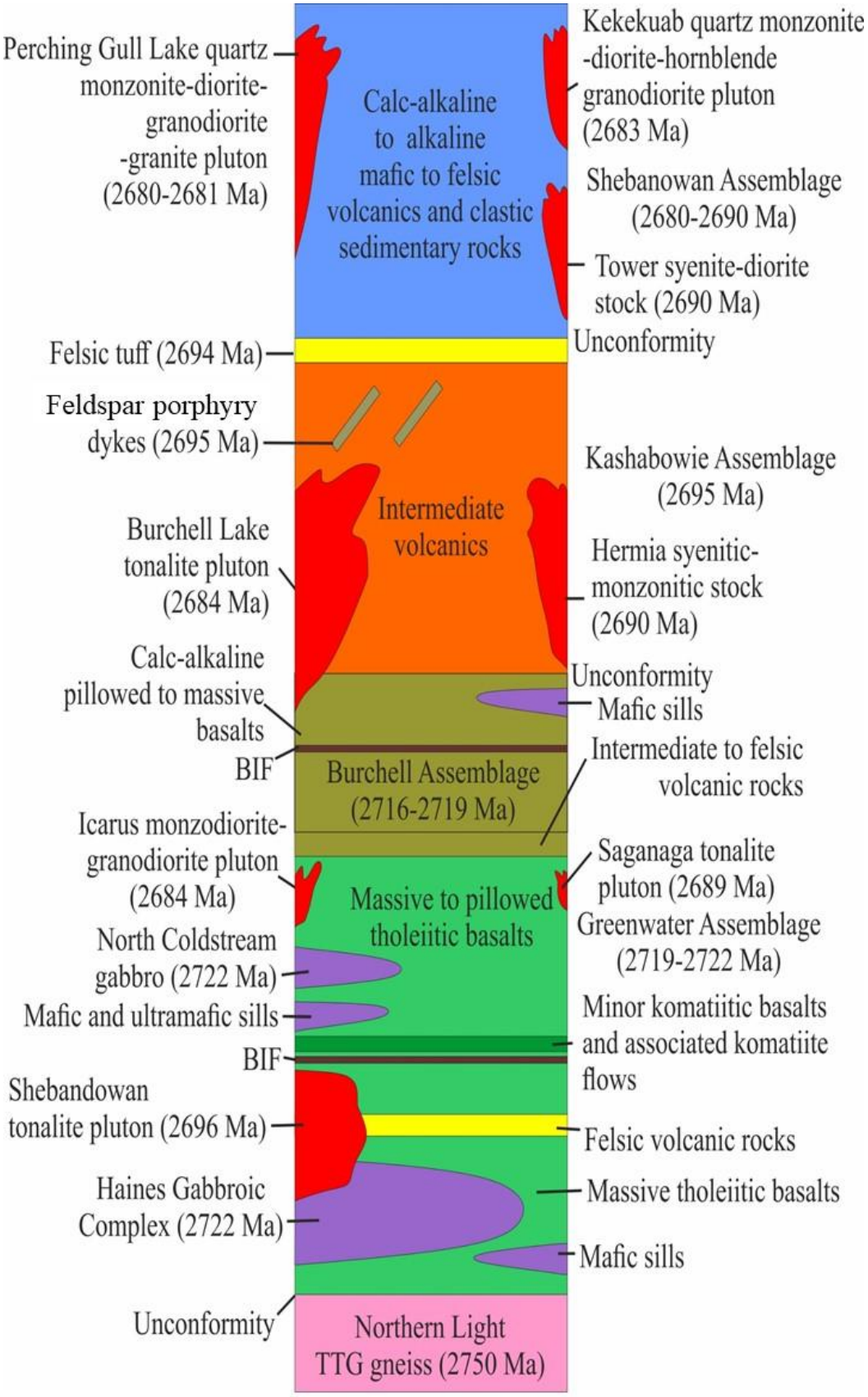

Fig. 2.3. Lithostratigraphy of the Shebandowan greenstone belt (constructed based on information from Williams et al. (1991), Corfu and Stott (1998), Lodge et al. (2015) and Lodge (2016).

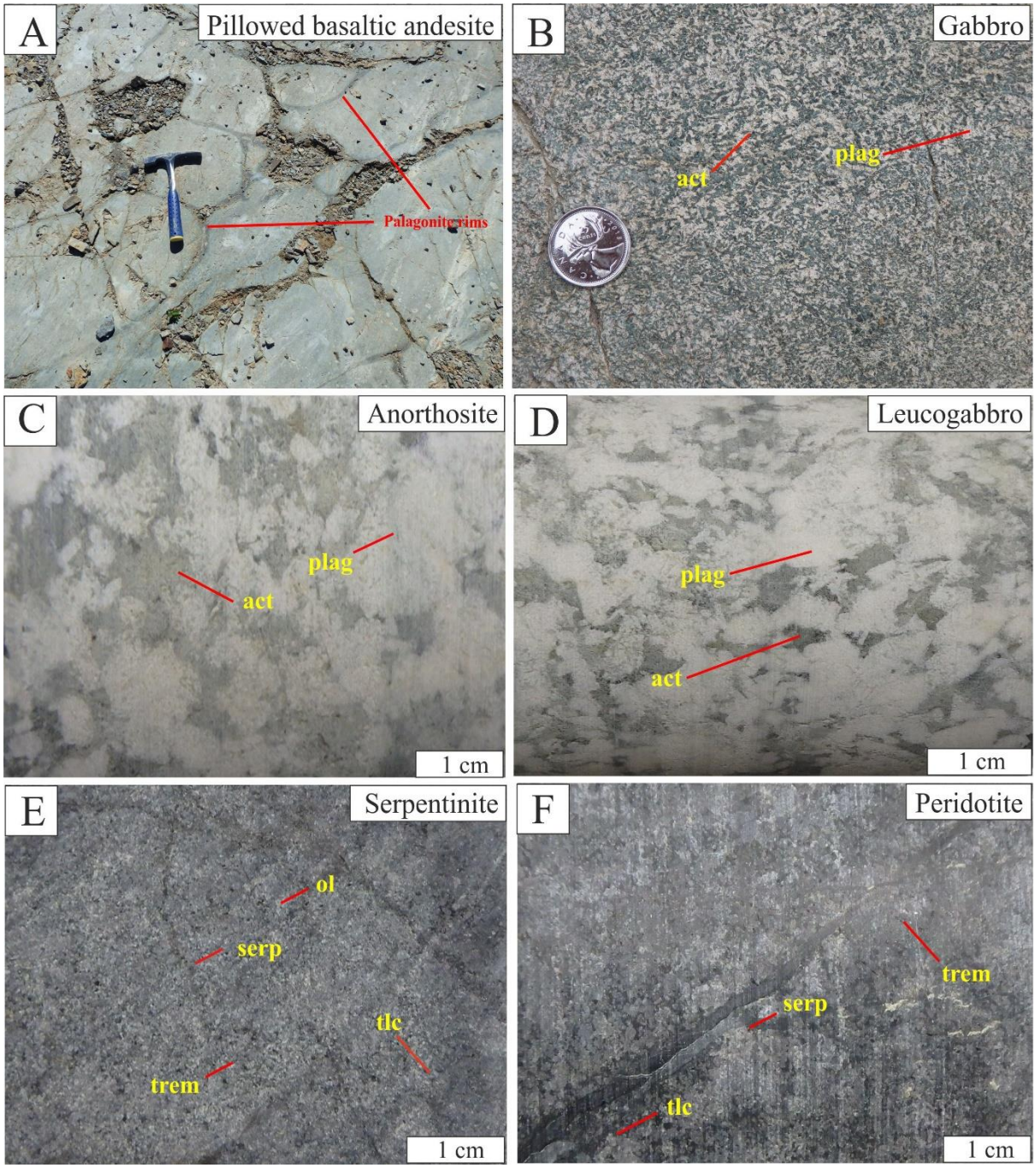

Fig. 2.4. Field and drill-core sample photographs of lithologies from the Haines Gabbroic Complex. (**a**) Pillowed basaltic andesite from the Greenwater Assemblage with palagonite rims around individual pillows. (**b**) An outcrop of gabbro from the Greenwater Assemblage. (**c**) A megacrystic anorthosite drill-core sample from the Haines Gabbroic Complex. (**d**) A megacrystic leucogabbro drill-core sample from the Haines Gabbroic Complex. (**e**) A serpentinite drill-core sample from the Greenwater Assemblage. (**f**). A peridotite drill-core sample from the Greenwater Assemblage. plag: plagioclase; act: actinolite; serp: serpentinite; trem: tremolite; ol: olivine; tlc: talc.

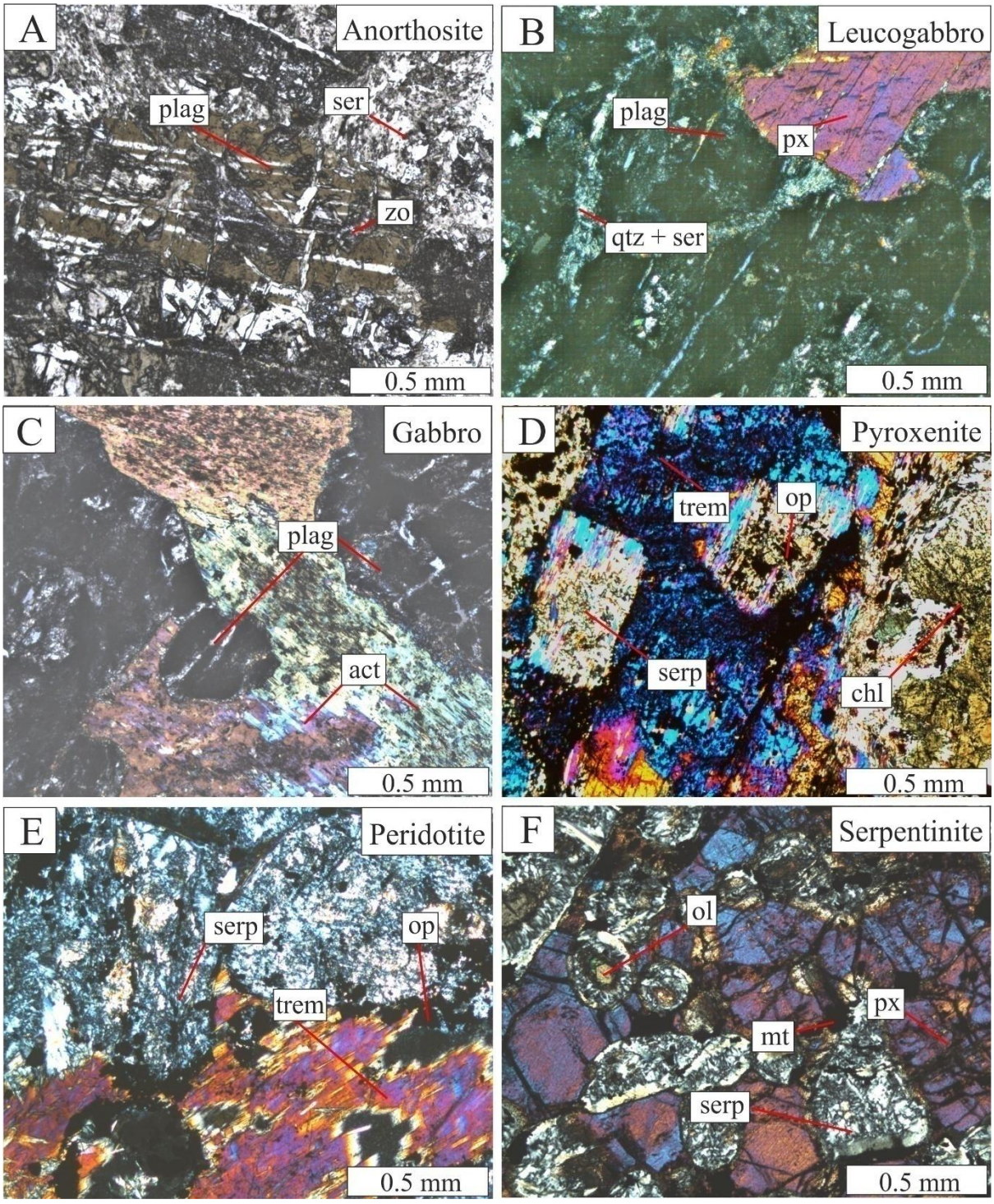

Fig. 2.5. Photomicrographs of the lithologies from the Haines Gabbroic Complex and the Greenwater Assemblage. Anorthosite (**a**), leucogabbro (**b**) and (**c**) gabbro from the Haines Gabbroic Complex and (**d**) pyroxenite, (**e**) peridotite and (**f**) harzburgite from the Greenwater Assemblage. These lithologies exhibit relict cumulate textures. Primary minerals are rarely preserved. zo: zoisite; plag: plagioclase; ser: sericite; op: opaque; qtz: quartz; act: actinolite; px: pyroxene; serp: serpentine; trem: tremolite; chl: chlorite; ol: olivine; mt: magnetite.

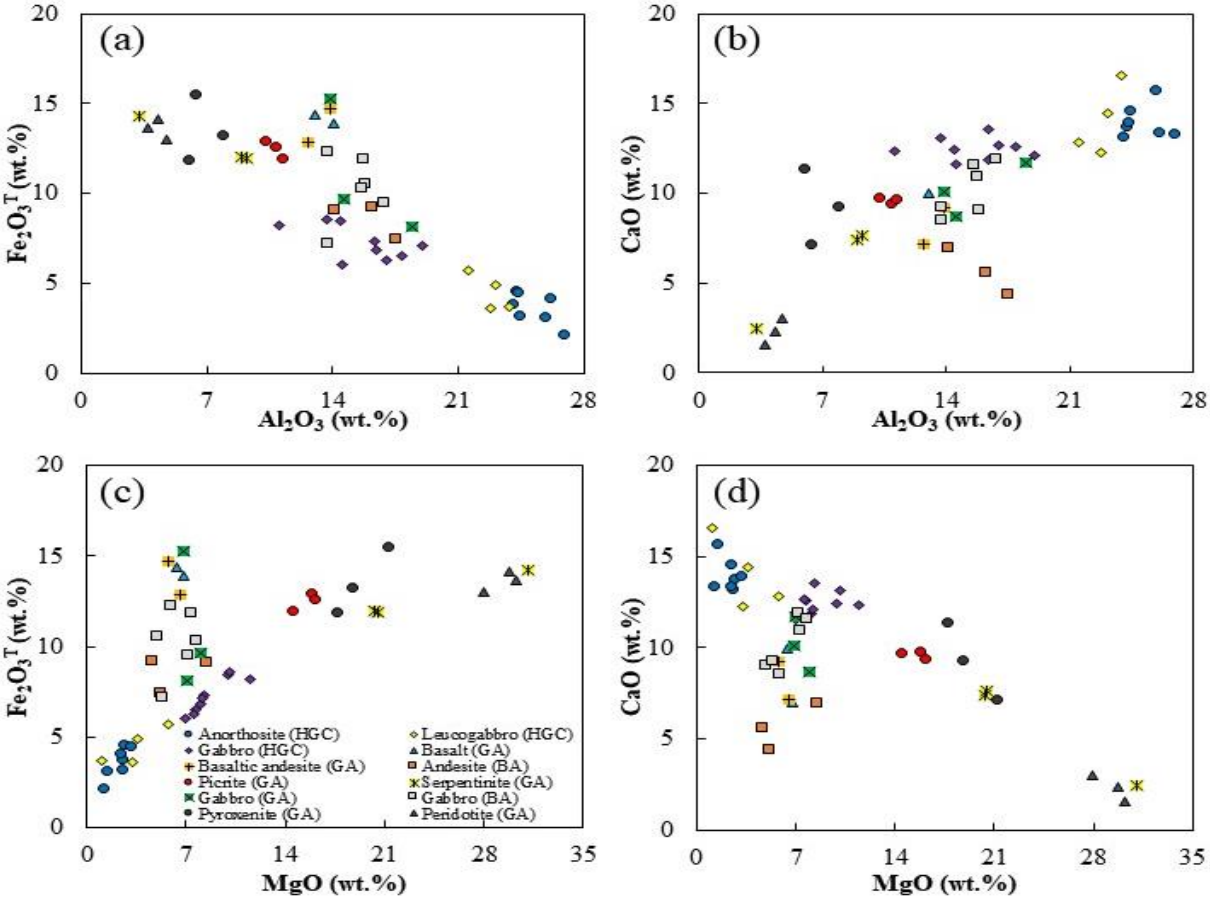

Fig. 2.6. Major and trace element variation diagrams for the Haines Gabbroic Complex (HGC) and the Greenwater (GA) and Burchell (BA) assemblages of the Shebandowan greenstone belt. (**a**) $Fe_2O_3^T$ versus Al_2O_3, (**b**) CaO versus Al_2O_3, (**c**) $Fe_2O_3^T$ versus MgO and (**d**) CaO versus MgO.

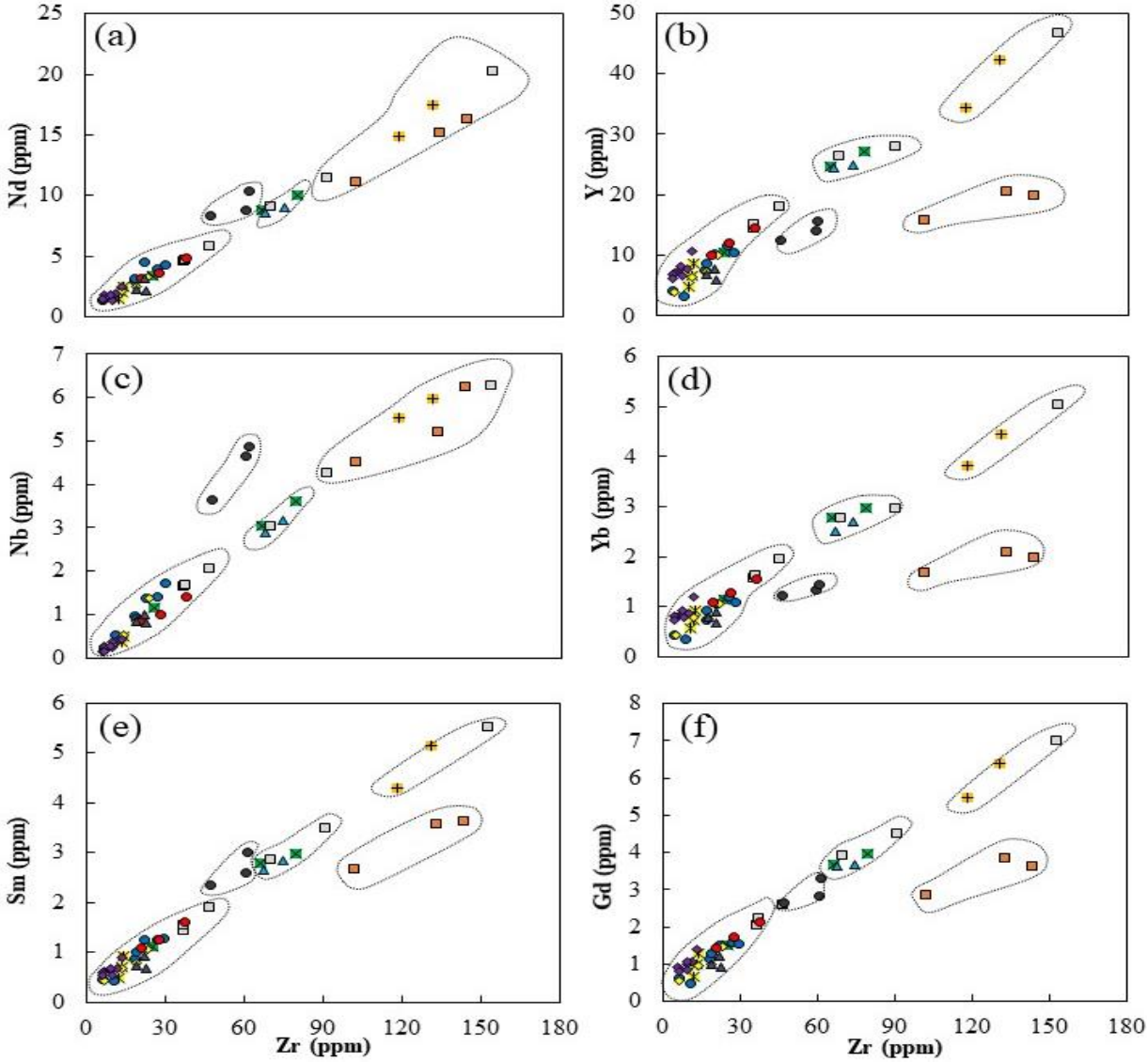

Fig. 2.7. Zr versus (**a**) Nd, (**b**) Y, (**c**) Nb, (**d**) Yb and (**e**) Sm and (**f**) TiO_2 trace element variation diagrams for the Haines Gabbroic Complex (HGC) and the Greenwater (GA) and Burchell (BA) assemblages of the Shebandowan greenstone belt. The symbols are the same as for Fig. 2.6.

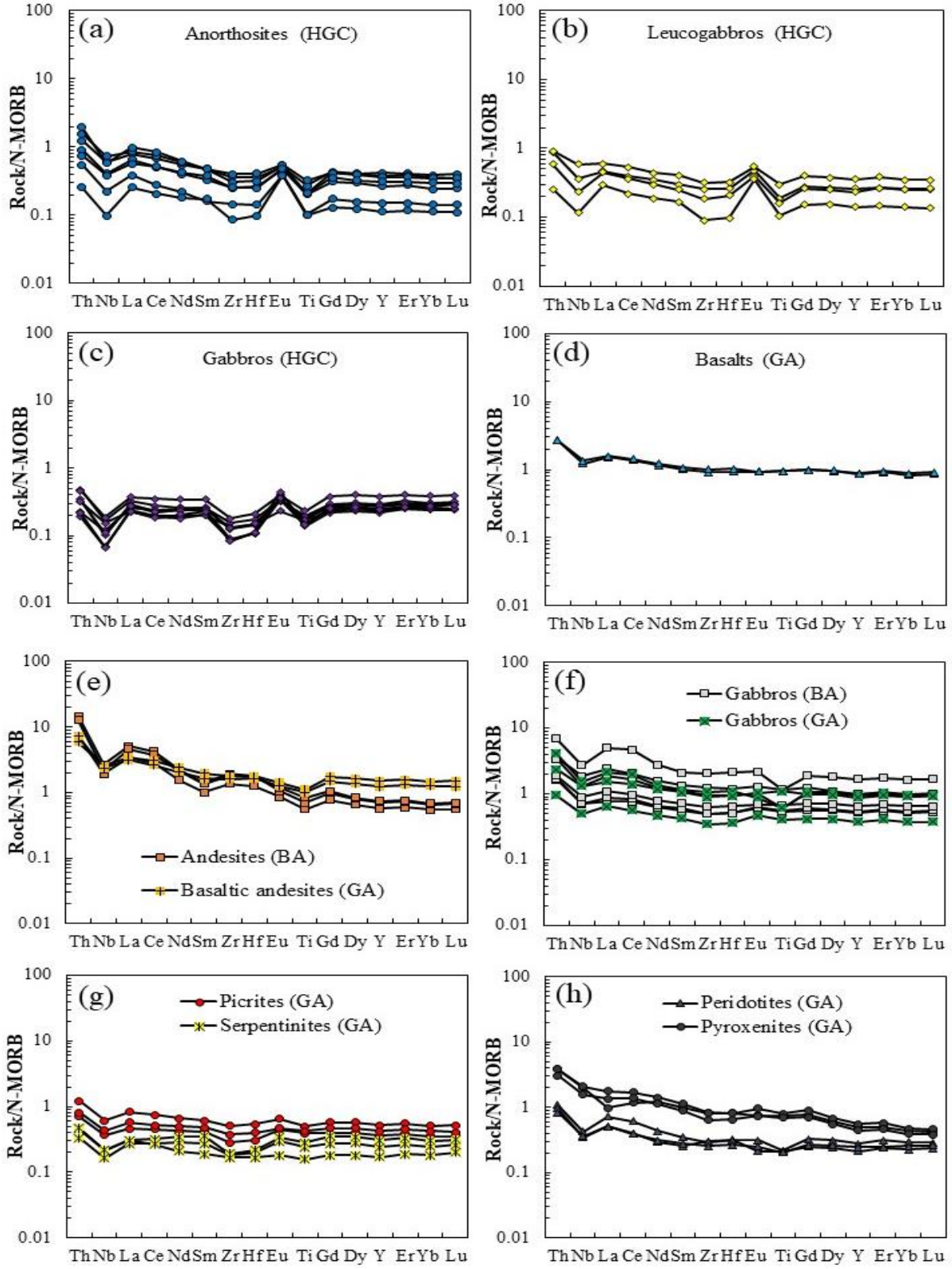

Fig. 2.8. N-MORB-normalised trace element diagrams for the lithologies of the Haines Gabbroic Complex (HGC), and Greenwater (GA) and Burchell (BA) assemblages. (**a**) Anorthosites, Haines Gabbroic Complex. (**b**) Leucogabbros, Haines Gabbroic Complex. (**c**) Gabbros, Haines Gabbroic Complex. (**d**) Basalts, Greenwater Assemblage. (**e**) Andesites and basaltic andesites from the Burchell and Greenwater assemblages, respectively. (**f**) Gabbros,

Burchell and Greenwater assemblages. (**g**) Picrites and serpentinites, Greenwater Assemblage. (**h**) Peridotites and pyroxenites, Greenwater Assemblage. Normalisation values are from Sun and McDonough (1989).

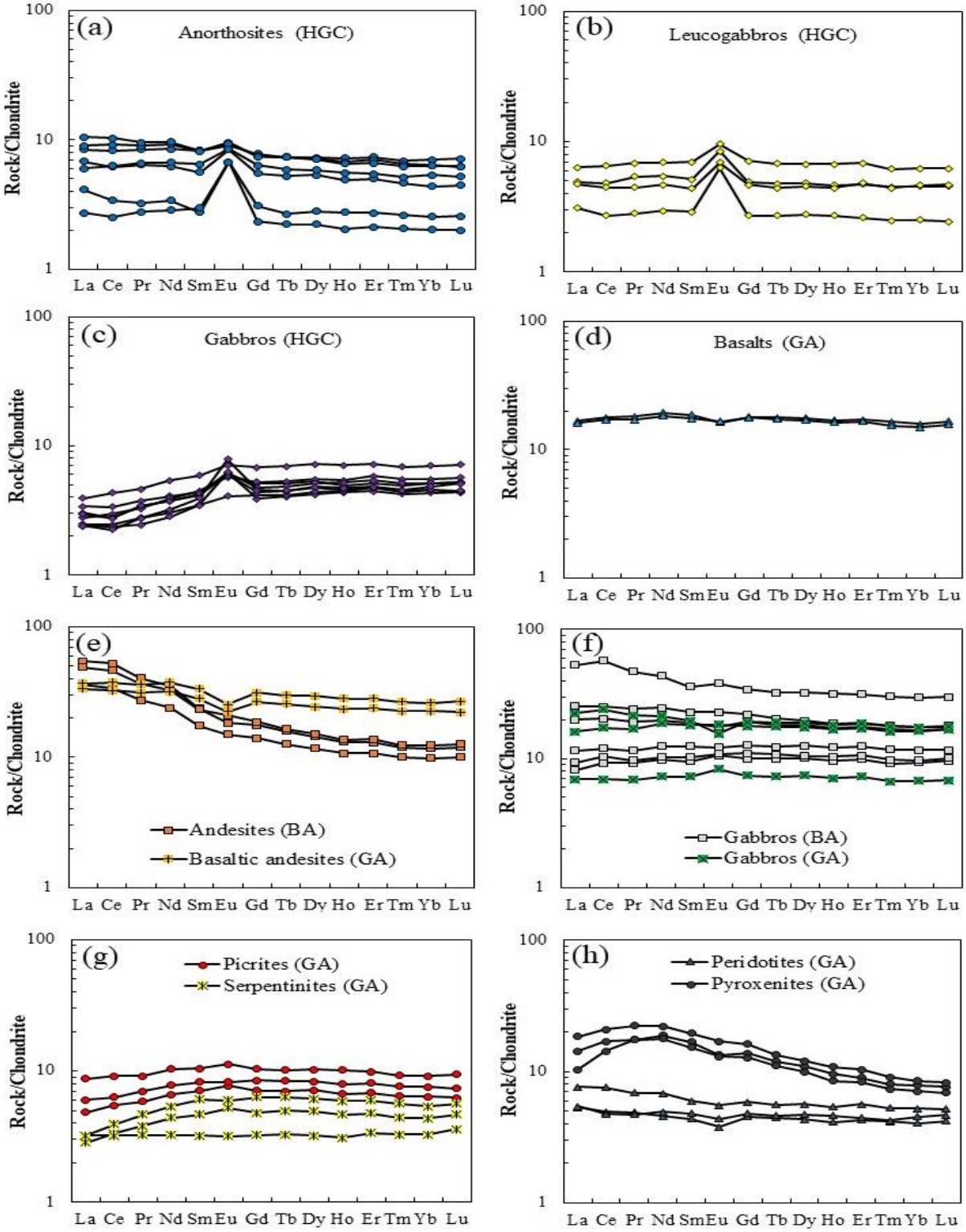

Fig. 2.9. Chondrite-normalised REE diagrams for the lithologies of the Haines Gabbroic Complex (HGC), and Greenwater (GA) and Burchell (BA) assemblages. (**a**) Anorthosites, Haines Gabbroic Complex. (**b**) Leucogabbros, Haines Gabbroic Complex. (**c**) Gabbros, Haines Gabbroic Complex. (**d**) Basalts, Greenwater Assemblage. (**e**) Andesites and basaltic andesites from the Burchell and Greenwater assemblages, respectively. (**f**) Gabbros, Burchell and Greenwater assemblages. (**g**) Picrites and serpentinites, Greenwater Assemblage. (**h**)

Peridotites and pyroxenites, Greenwater Assemblage. Normalisation values are from Sun and McDonough (1989).

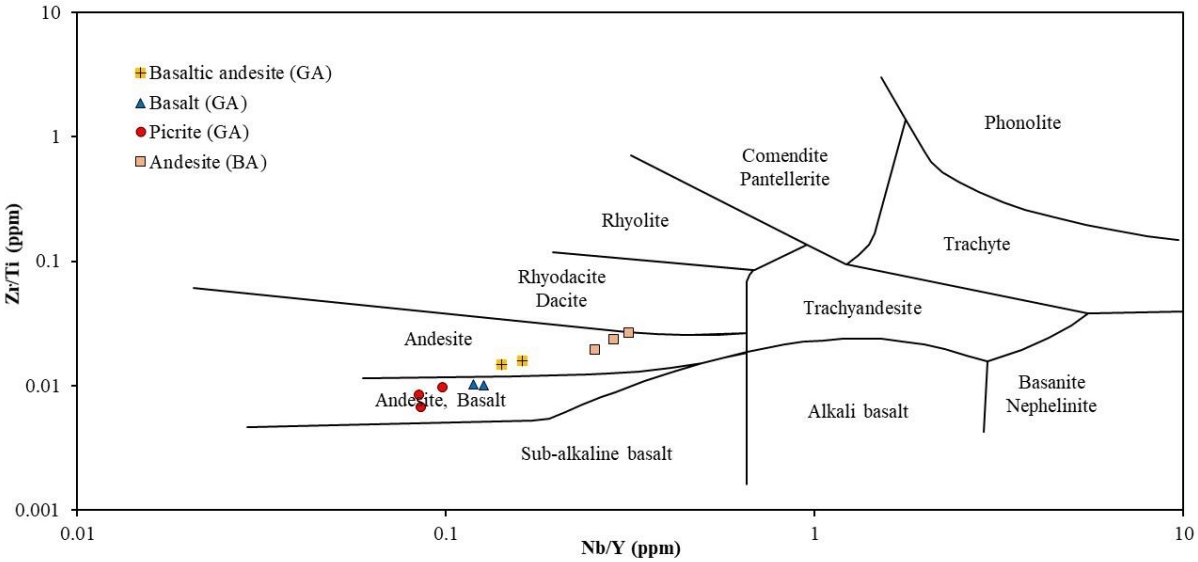

Fig. 2.10. Basaltic andesites, basalts and picrites of the Greenwater Assemblage (GA) and andesites of the Burchell Assemblage (BA) plotted on a Zr/Ti versus Nb/Y diagram (after Winchester and Floyd, 1977).

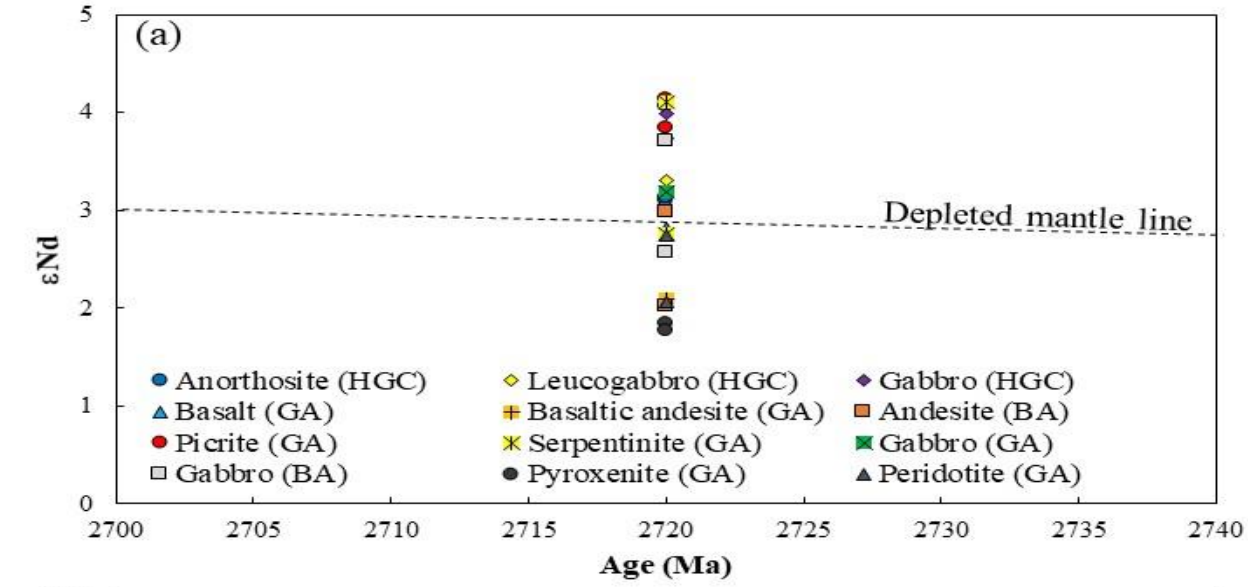
(a)
εNd
Depleted mantle line
Anorthosite (HGC)
Leucogabbro (HGC)
Gabbro (HGC)
Basalt (GA)
Basaltic andesite (GA)
Andesite (BA)
Picrite (GA)
Serpentinite (GA)
Gabbro (GA)
Gabbro (BA)
Pyroxenite (GA)
Peridotite (GA)
Age (Ma)

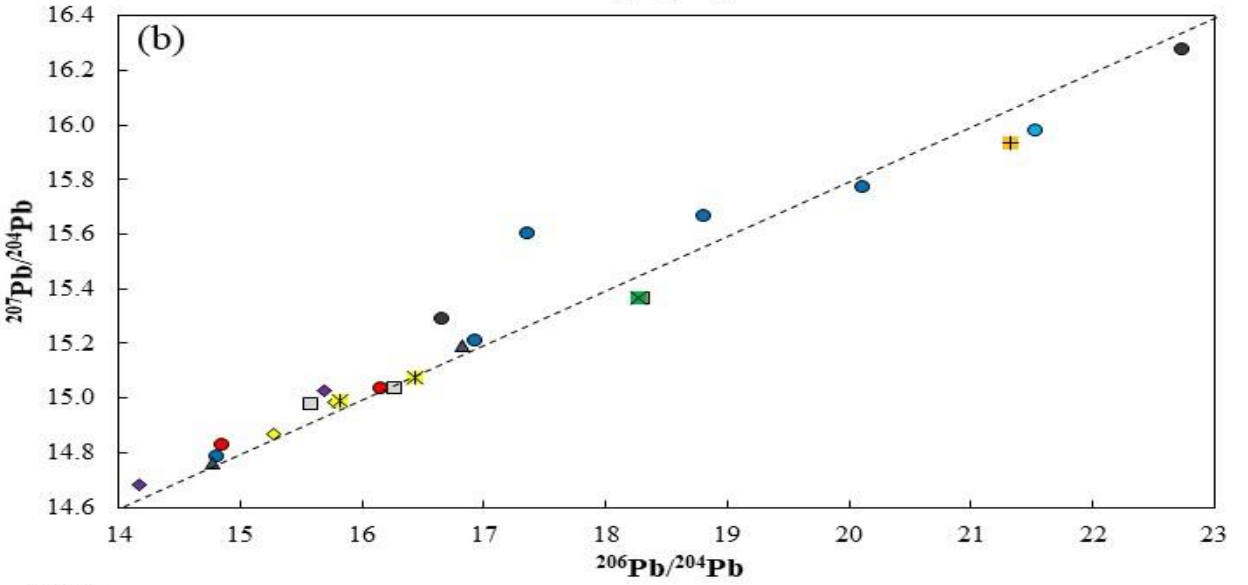
(b)
$^{207}Pb/^{204}Pb$
$^{206}Pb/^{204}Pb$

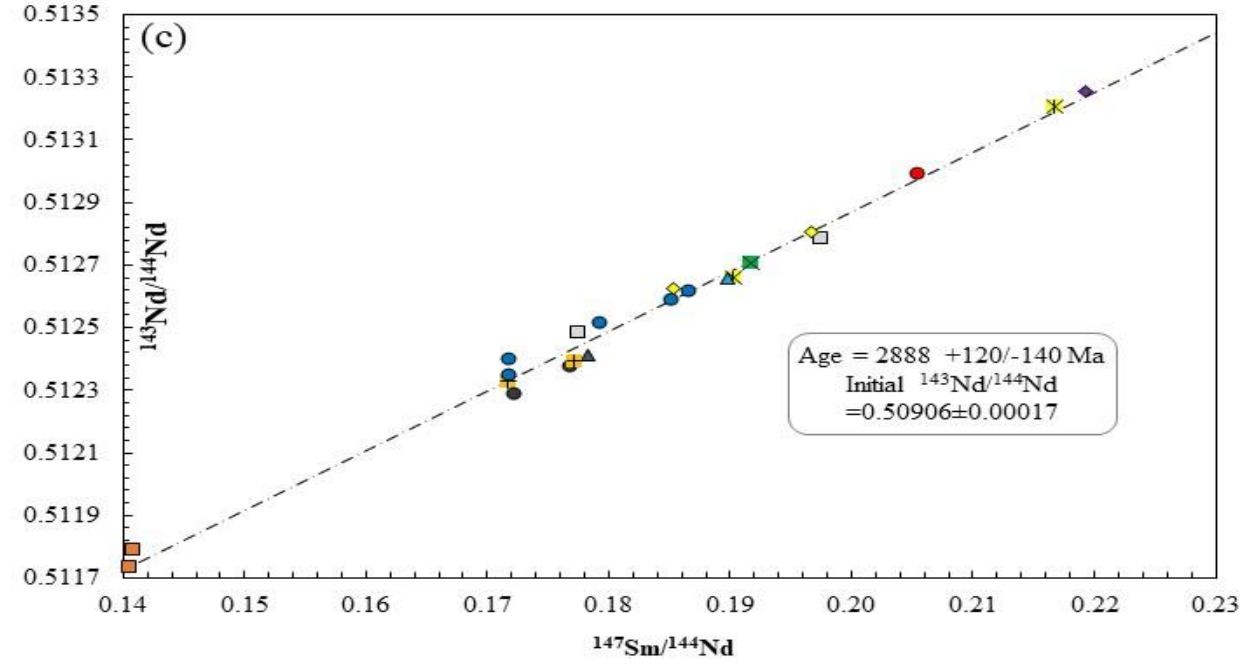
(c)
$^{143}Nd/^{144}Nd$
$^{147}Sm/^{144}Nd$
Age = 2888 +120/-140 Ma
Initial $^{143}Nd/^{144}Nd$
=0.50906±0.00017

Fig. 2.11. (a) Age (Ga) versus $\varepsilon_{Nd\ (2720\ Ma)}$ diagram for the Haines Gabbroic Complex (HGC) and the Greenwater (GA) and Burchell (BA) assemblages of the Shebandowan greenstone belt (modified from Henry et al., 1998). (**b**) $^{207}Pb/^{204}Pb$ vs. $^{206}Pb/^{204}Pb$ ratio diagram showing the present day Pb isotope compositions of the Haines Gabbroic Complex, and the Greenwater and Burchell assemblages. (**c**) Sm/Nd isochron plot for the Haines Gabbroic Complex, and the Greenwater and Burchell assemblages.

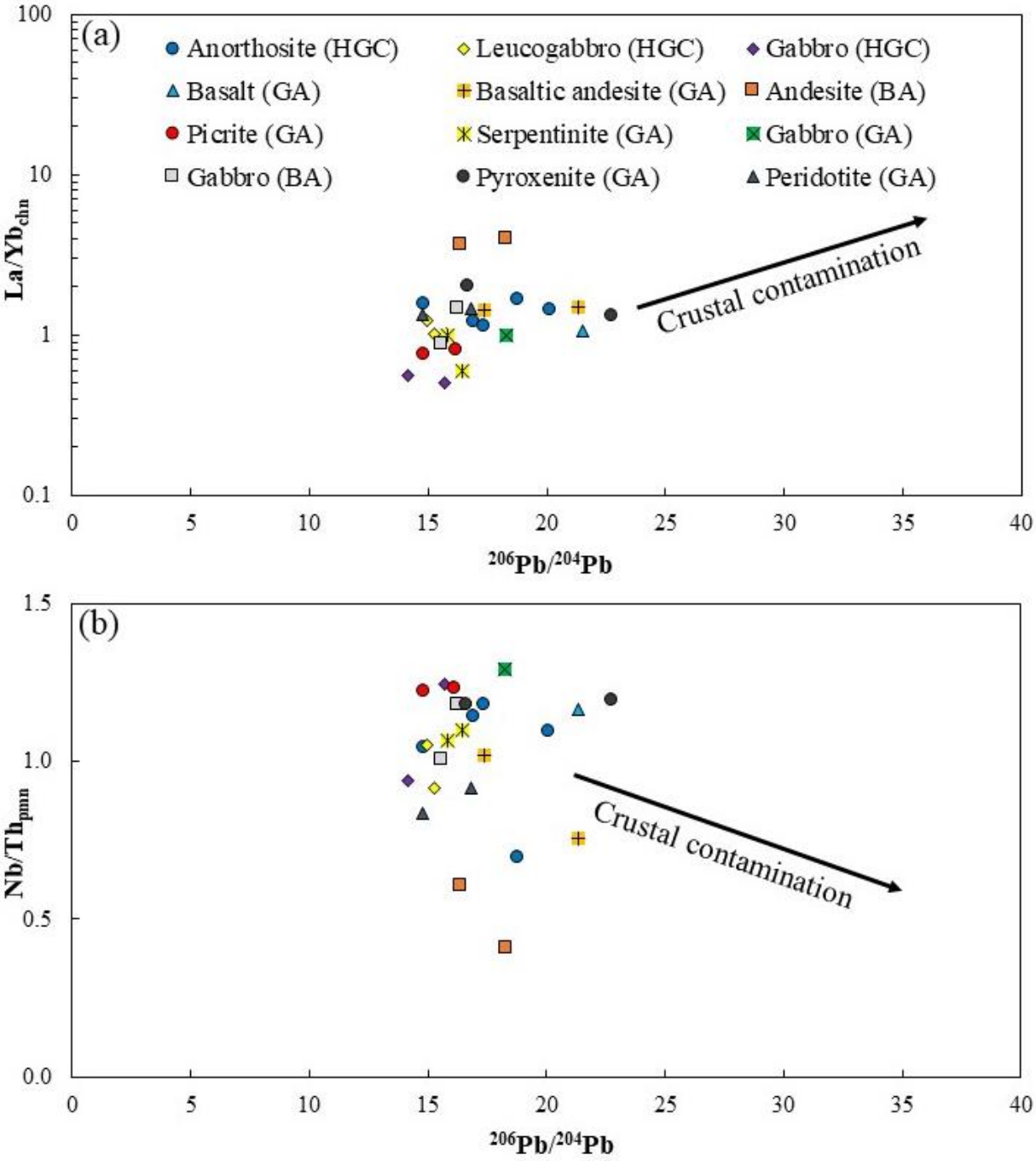

Fig. 2.12. $^{206}Pb/^{204}Pb$ ratio versus (**a**) chondrite-normalised La/Yb ratio and (**b**) primitive mantle-normalised Nb/Th ratio plots for the Haines Gabbroic Complex (HGC) and Greenwater (GA) and Burchell (BA) assemblages of the Shebandowan greenstone belt (modified after Lodge et al., 2015).

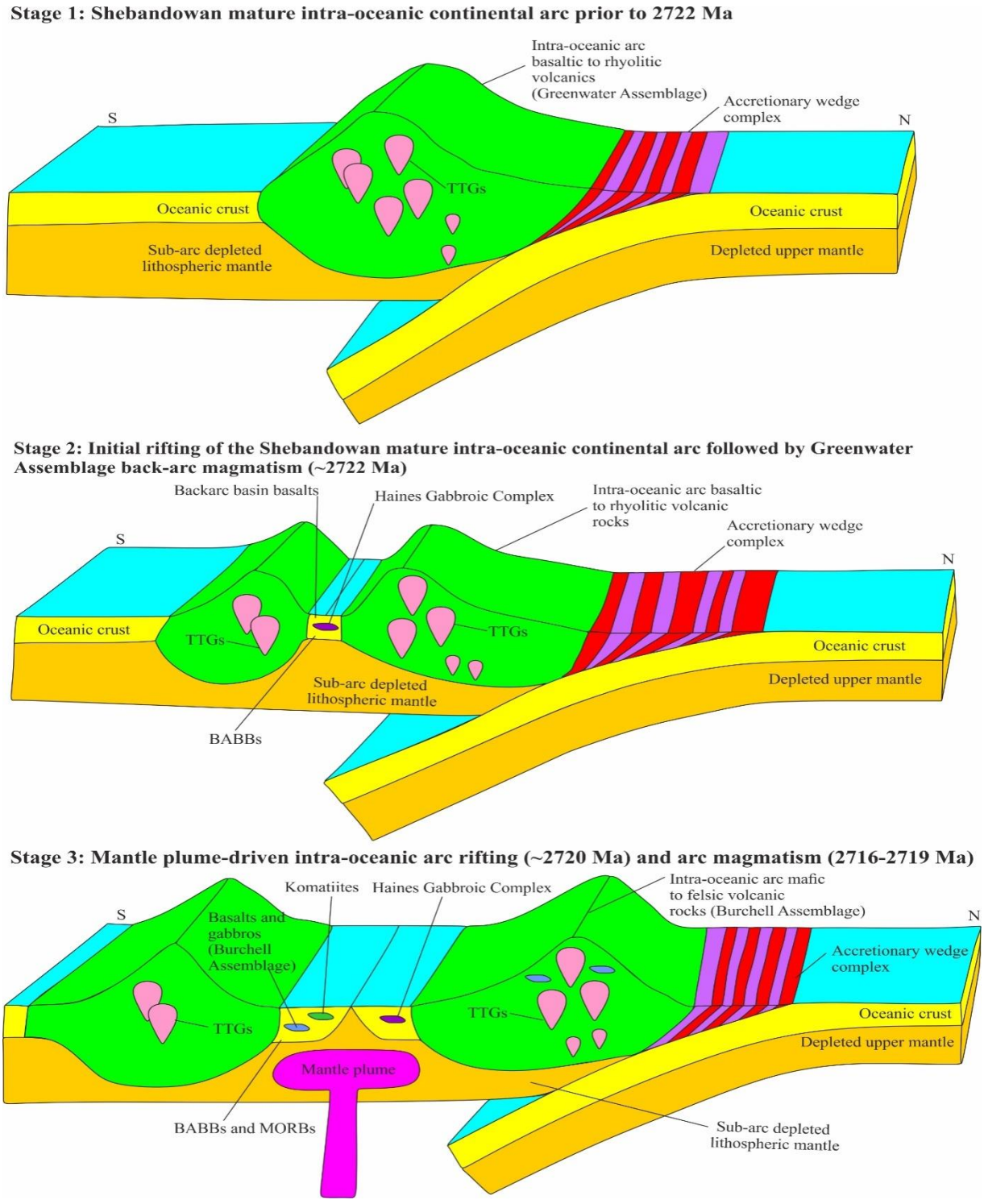

Fig. 2.13. Schematic diagram showing the three stages in the evolution of the geodynamic setting of the Shebandowan mature intra-oceanic continental arc and the Shebandowan greenstone belt. Stage 1: Prior to 2722 Ma, basaltic to rhyolitic volcanic rocks (Cycle 1, Greenwater Assemblage) formed in a Japan-style mature intra-oceanic continental arc setting and were erupted onto the 2750 Ma Northern Light TTG Batholith at the northern margin of the Shebandowan arc. Stage 2: At ~2722 Ma, incipient intra-oceanic continental arc rifting had occurred alongside continuing intra-oceanic continental arc magmatism. The Haines Gabbroic Complex and numerous mafic sills had formed as a result alongside contemporaneous back-

arc basin basalts (BABB) volcanics (Cycle 1, Greenwater Assemblage). Stage 3: By ~2720 Ma, a mantle plume accentuated earlier incipient intra-oceanic arc rifting and resulted in the formation of komatiites, mafic to ultramafic sills, back-arc basin basalts (BABB) and mid-ocean ridge basalts (MORB; Cycle 2, Greenwater Assemblage). Contemporaneous arc and back-arc magmatism occurred between 2716 Ma and 2719 Ma, forming the andesites and gabbros of the first cycle of the Burchell Assemblage. Please refer to the text for more details.

Sample ID	Lithology	Location	Sm (ppm)	Nd (ppm)	$^{147}Sm/^{144}Nd$	$^{143}Nd/^{144}Nd$	ε_{Nd} (2720 Ma)	T_{DM} (Ma)*
SD2016-09	Serpentinite	Greenwater Assemblage	0.969	2.705	0.2168	0.513207±06	4.1	2846
SD2016-11	Serpentinite	Greenwater Assemblage	0.526	1.673	0.1903	0.512663±07	2.8	3177
SP04-007-42	Peridotite	Greenwater Assemblage	0.712	2.509	0.1717	0.512329±07	2.7	2991
SP04-007-43	Peridotite	Greenwater Assemblage	0.517	1.755	0.1783	0.512413±07	2.1	3188
SP06-015-32	Pyroxenite	Greenwater Assemblage	2.162	7.399	0.1769	0.512376±07	1.8	3213
SP06-003-40	Pyroxenite	Greenwater Assemblage	2.162	7.598	0.1722	0.512288±07	1.8	3177
SP05-006-34	Picrite	Greenwater Assemblage	1.020	3.010	0.2050	0.512998±07	4.1	2691
SP06-004-39	Picrite	Greenwater Assemblage	1.220	3.594	0.2055	0.512992±06	3.8	2953
SD2016-15	Basaltic andesite	Greenwater Assemblage	5.275	18.607	0.1716	0.512443±06	5.0	2569
SD2016-16	Basaltic andesite	Greenwater Assemblage	3.578	12.220	0.1772	0.512395±09	2.1	3163
SD2016-18	Basalt	Greenwater Assemblage	2.720	8.675	0.1898	0.512657±06	2.8	3153
SD2016-27	Andesite	Burchell Assemblage	2.573	11.052	0.1409	0.511788±09	3.0	2861
SD2016-36	Andesite	Burchell Assemblage	3.410	14.676	0.1406	0.511734±06	2.0	2963
SD2016-14	Gabbro	Greenwater Assemblage	2.484	7.845	0.1916	0.512709±05	3.2	3051
SD2016-21	Gabbro	Burchell Assemblage	3.118	10.632	0.1775	0.512482±05	3.7	2824
SD2016-25	Gabbro	Burchell Assemblage	1.576	4.828	0.1976	0.512785±06	2.6	3471
SP04-002-25	Gabbro	Haines Gabbroic Complex	0.795	2.124	0.2265	0.513377±08	4.0	2698
SP04-002-27	Gabbro	Haines Gabbroic Complex	0.910	2.499	0.2193	0.513254±08	4.1	2842
SP04-002-14	Leucogabbro	Haines Gabbroic Complex	0.619	2.021	0.1854	0.512625±08	3.7	2835
SP04-002-24	Leucogabbro	Haines Gabbroic Complex	1.001	3.080	0.1966	0.512805±06	3.3	3088
SP04-002-31	Leucogabbro	Haines Gabbroic Complex	0.388	1.271	0.1846	0.512676±06	5.0	2495
SP04-002-1	Anorthosite	Haines Gabbroic Complex	1.134	3.708	0.1852	0.512589±05	3.1	3010
SP04-002-6	Anorthosite	Haines Gabbroic Complex	0.762	2.573	0.1793	0.512515±05	3.7	2825
SP04-002-23	Anorthosite	Haines Gabbroic Complex	1.214	4.277	0.1718	0.512397±07	4.1	2745
SP04-002-26	Anorthosite	Haines Gabbroic Complex	1.155	4.068	0.1718	0.512346±09	3.0	2938
SP04-002-29	Anorthosite	Haines Gabbroic Complex	0.991	3.215	0.1866	0.512616±05	3.1	3011

Table 2.1. Sm-Nd isotope compositions of anorthosites, leucogabbros and gabbros from the Haines Gabbroic Complex, and the basalts, basaltic andesites, andesites, picrites, serpentinites, gabbros, pyroxenites and peridotites from the Greenwater and Burchell assemblages of the Shebandowan greenstone belt. The 2σ uncertainty values represent absolute values.

Sample ID	Lithology	Location	$^{206}Pb/^{204}Pb$	± 2σ	$^{207}Pb/^{204}Pb$	± 2σ	$^{208}Pb/^{204}Pb$	± 2σ	r_1**
SD2016-09	Serpentinite	Greenwater Assemblage	16.437	0.024	15.077	0.023	35.150	0.055	0.982
SD2016-11	Serpentinite	Greenwater Assemblage	15.821	0.035	14.990	0.034	35.980	0.084	0.984
SP04-007-42	Peridotite	Greenwater Assemblage	16.830	0.026	15.192	0.024	36.492	0.061	0.980
SP04-007-43	Peridotite	Greenwater Assemblage	14.779	0.018	14.763	0.019	34.794	0.047	0.960
SP06-015-32	Pyroxenite	Greenwater Assemblage	22.748	0.058	16.272	0.042	43.425	0.117	0.989
SP06-003-40	Pyroxenite	Greenwater Assemblage	16.661	0.025	15.285	0.024	35.863	0.060	0.966
SP05-006-34	Picrite	Greenwater Assemblage	14.858	0.031	14.829	0.032	34.528	0.082	0.976
SP06-004-39	Picrite	Greenwater Assemblage	16.166	0.038	15.031	0.036	35.871	0.089	0.988
SD2016-15	Basaltic andesite	Greenwater Assemblage	17.396	0.036	15.218	0.033	37.540	0.083	0.984
SD2016-16	Basaltic andesite	Greenwater Assemblage	21.325	0.048	15.935	0.037	41.340	0.097	0.988
SD2016-18	Basalt	Greenwater Assemblage	21.536	0.043	15.977	0.033	41.742	0.089	0.981
SD2016-27	Andesite	Burchell Assemblage	16.406	0.036	15.031	0.034	36.110	0.083	0.982
SD2016-36	Andesite	Burchell Assemblage	18.321	0.009	15.360	0.010	38.662	0.030	0.963
SD2016-14	Gabbro	Greenwater Assemblage	18.272	0.037	15.367	0.032	38.219	0.082	0.984
SD2016-21	Gabbro	Burchell Assemblage	16.276	0.022	15.033	0.022	36.026	0.054	0.975
SD2016-25	Gabbro	Burchell Assemblage	15.592	0.033	14.975	0.033	35.190	0.078	0.988
SP04-002-25	Gabbro	Haines Gabbroic Complex	15.690	0.032	15.029	0.032	35.572	0.077	0.980
SP04-002-27	Gabbro	Haines Gabbroic Complex	14.175	0.015	14.685	0.017	34.026	0.042	0.939
SP04-002-14	Leucogabbro	Haines Gabbroic Complex	15.280	0.033	14.868	0.033	35.095	0.078	0.984
SP04-002-24	Leucogabbro	Haines Gabbroic Complex	15.770	0.027	14.983	0.026	35.626	0.064	0.982
SP04-002-31	Leucogabbro	Haines Gabbroic Complex	14.952	0.040	14.818	0.040	34.800	0.097	0.990
SP04-002-1	Anorthosite	Haines Gabbroic Complex	16.935	0.032	15.206	0.030	36.547	0.073	0.985
SP04-002-6	Anorthosite	Haines Gabbroic Complex	14.815	0.031	14.784	0.032	34.702	0.076	0.984
SP04-002-23	Anorthosite	Haines Gabbroic Complex	20.121	0.032	15.768	0.026	40.247	0.070	0.980
SP04-002-26	Anorthosite	Haines Gabbroic Complex	18.813	0.023	15.664	0.020	38.413	0.053	0.980
SP04-002-29	Anorthosite	Haines Gabbroic Complex	17.364	0.011	15.601	0.012	36.577	0.031	0.969

Table 2.2. Pb isotope compositions of anorthosites, leucogabbros and gabbros from the Haines Complex, and the basalts, basaltic andesites, andesites, picrites, serpentinites, gabbros, pyroxenites and peridotites from the Greenwater and Burchell assemblages of the Shebandowan greenstone belt. The 2σ uncertainty values represent absolute values. r_1^{**} = $^{206}Pb/^{204}Pb$ vs. $^{207}Pb/^{204}Pb$ error correlation.

Chapter 3: A back-arc origin for the Neoarchean megacrystic anorthosite-bearing Bird River Sill and the associated greenstone belt, Bird River subprovince, Western Superior Province, Manitoba, Canada

3.1. Introduction

Greenstone belts in the upper to middle crustal sections of Archean cratons such as the Superior Province and the Dharwar, Kaapvaal and North Atlantic cratons retain important information about Archean geodynamics and crustal growth processes (Windley,1995; Windley and Garde, 2009; Percival et al., 2012). These cratons are thought to have coalesced through accretion of island arcs, accretionary prisms, orogenic sedimentary rocks and continents (Windley, 1995; Hollings and Kerrich, 2004; Windley and Garde, 2009; Percival et al., 2012; Kusky et al., 2018) and contain Archean megacrystic anorthosite-bearing layered intrusions (Fig. 3.1) that have been interpreted to have formed in an intra-arc rift or a back-arc setting (Polat et al., 2018a). Despite this, Archean megacrystic anorthosite-bearing layered intrusions are postulated to have formed in a wide range of settings, including arc (Ashwal, 1993, 2010; Ashwal and Bybee, 2017; Polat et al., 2018a; Sotiriou et al., 2019), mantle plume-derived continental rift (Ivanic et al., 2010), passive continental margin (Paixão and Oliveira, 1998), quasi-platform (Vrevskii, 2016), mid-ocean ridge (Ashwal, 1993, 2010), oceanic plateau (Ashwal, 1993, 2010), mantle plume (Spath et al., 2015) and continental rift (Sandeman et al., 2001; Hartlaub et al., 2004) settings.

The geodynamic setting, growth, and evolution of the Bird River subprovince of Manitoba in the western Superior Province, however, are not as well-constrained as the Hudson Bay terrane and Sachigo, Abitibi and Wawa subprovinces (Dostal and Mueller, 1997; Card and Poulsen, 1998; Lodge et al., 2015). The well-studied Bird River greenstone belt forms part of the Bird River subprovince (Figs. 3.2 and 3.3), and its location between the Winnipeg River and English River subprovinces makes it critical for understanding the evolution and growth of the western Superior Province. Despite numerous studies on the Bird River greenstone belt (e.g., Gilbert, 2005, 2006, 2007, 2008; Duguet et al., 2005, 2006, 2007, 2009; Gilbert et al., 2008; Yang et al., 2011, 2012, 2013; Yang and Gilbert, 2014), the petrogenesis and geodynamic setting of the Archean megacrystic anorthosite-bearing Bird River Sill are still not fully resolved. Addressing the unresolved questions outlined above will have major implications for the crustal evolution and growth of the Bird River greenstone belt, Bird River subprovince and western Superior

Province, and the petrogenesis and geodynamic setting of the Bird River Sill, in particular, and Archean anorthosite-bearing layered intrusions in general.

This study employs a multi-analytical technique and multi-disciplinary approach to address the geodynamic and petrogenetic questions outlined above. New field, petrographic, mineral chemistry, and whole-rock major and trace element geochemical data for anorthosites, gabbros, leucogabbros, peridotites and chromitites from the Bird River Sill are presented (Appendix 2.1). Furthermore, we present new field, petrographic, whole-rock major and trace element geochemical data from the Northern Lamprey Falls, Peterson Creek and Booster Lake formations and 'Diverse arc assemblage' (previously the Peterson Creek Formation) of the Bird River greenstone belt and the Maskwa Lake Batholith I (Appendix 2.2). New whole-rock Sm-Nd and U-Th-Pb isotope data are presented for a total of 28 samples, including peridotites, gabbros, leucogabbros and anorthosites from the Bird River Sill, basalts and a gabbro from the Northern Lamprey Falls Formation, andesites and greywackes from the 'Diverse arc assemblage', rhyolites from the Peterson Creek Formation and tonalites from the Maskwa Lake Batholith I (Tables 3.1 and 3.2). The new field, petrographic and geochemical data are integrated with existing data to construct a new geodynamic model for the Bird River Sill and its spatially associated extrusive, intrusive, and sedimentary rocks.

3.2. Regional geology

3.2.1. Superior Province

The Superior Province comprises numerous volcanic-plutonic, plutonic, metasedimentary, and high-grade gneissic subprovinces (Fig. 3.2) (Percival et al., 2012). The western margin of the Superior Province contains several Archean megacrystic anorthosite-bearing layered intrusions (Fig. 3.1) (Ashwal, 1993, 2010; Yang et al., 2013). These layered intrusions usually form part of greenstone belts that underwent greenschist- to amphibolite-facies metamorphism (e.g., Bird River, Mayville, Euclid Lake, Pipestone Lake; Ashwal, 1993; Gilbert et al., 2008; Duguet et al., 2009; Yang et al., 2013), or they are associated with granulite-facies high-grade gneiss terrains (e.g., Cauchon Lake, Split Lake; Ashwal, 1993; Peck et al., 1996; Hartlaub and Kuiper, 2004). These Archean megacrystic anorthosite-bearing layered intrusions form a

volumetrically minor yet important part of their respective subprovinces (Ashwal, 1993, 2010; Percival et al., 2012).

3.2.2. Bird River subprovince

The Mesoarchean to Neoarchean Bird River subprovince occurs as a wedge-shaped granite-greenstone terrain between the predominantly plutonic Winnipeg River subprovince to the south and the metasedimentary English River subprovince to the north (Figs. 3.2 and 3.3) (Card and Poulsen, 1998; Yang et al., 2011; Percival et al., 2012). The Bird River subprovince comprises the volcano-sedimentary Neoarchean Bird River greenstone belt, and its eastward extension, the Separation Lake greenstone belt, the Mesoarchean to Neoarchean Maskwa Lake TTG (tonalite-trondhjemite-granodiorite) Batholith, and Neoarchean granitoid plutons (Baadsgaard and Černý, 1993; Wang, 1993; Gilbert, 2006, 2007, 2008; Gilbert et al., 2008; Yang, 2014; Yang et al., 2018).

3.2.3. Bird River greenstone belt

The Neoarchean Bird River greenstone belt is located along the northern and southern margins of the Maskwa Lake Block (Fig. 3.3) (Wang, 1993; Gilbert et al., 2008; Yang et al., 2012, 2013).The southern arm of the Bird River greenstone belt along and adjacent to the southern margin of the Maskwa Lake Batholith has been interpreted to have formed in arc and MORB tectonic settings and consists of ca. 2.72-2.74 Ga volcanic and sedimentary rocks and mafic to ultramafic intrusions, which are separated into northern and southern panels by the Booster Lake Shear Zone (Figs. 3.3 and 3.4) (Gilbert, 2005, 2006, 2007, 2008; Gilbert et al., 2008; Duguet et al., 2009; Yang et al., 2011, 2013; Yang and Gilbert, 2014). The volcanic and sedimentary formations and mafic to ultramafic intrusions of the Bird River greenstone belt are separated by unconformities or faults (Figs. 3.3 and 3.4) (Card and Poulsen, 1998; Gilbert et al., 2008; Yang et al., 2011). The northern panel comprises the Northern Lamprey Falls Formation (‘Northern MORB-type Formation’ of Gilbert et al., 2008), Bird River Sill, Peterson Creek Formation and ‘Diverse arc assemblage’ (previously the Peterson Creek Formation) (Fig. 3.3) (Wang, 1993; Gilbert, 2006, 2007, 2008; Duguet et al., 2007; Gilbert et al., 2008; Scoates and Scoates, 2013). The southern panel consists of the Booster Lake, Bernic Lake and

Southern Lamprey Falls formations ('Southern MORB-type Formation' of Gilbert et al., 2008), with the latter two formations being intruded by the Birse Lake Pluton (Fig. 3.3) (Gilbert et al., 2008). The Flanders Lake Formation truncates the eastern edge of the northern panel of the Bird River greenstone belt and is juxtaposed against the Euclid Lake Formation of the northern arm of the Bird River greenstone belt to the northeast (Fig. 3.3) (Gilbert, 2006; Gilbert et al., 2008). The Northern Lamprey Falls Formation, Bird River Sill, 'Diverse arc assemblage' (previously the Peterson Creek Formation of Gilbert, 2007, 2008) and Peterson Creek Formation were erupted onto or, in the case of the Bird River Sill, emplaced into the 2844 ± 12 Ma phase of the Maskwa Lake TTG Batholith (Fig. 3.3) (Wang, 1993; Duguet et al., 2007; Gilbert et al., 2008; Yang, 2014).

3.2.4. Bird River Sill

The 2743 ± 0.5 Ma Bird River Sill is located in the southern arm of the Bird River greenstone belt (Fig. 3.3) (Peck and Theyer, 1998; Gilbert et al., 2008; Yang et al., 2011, 2012, 2013; Scoates and Scoates, 2013) and is 15 to 25 kilometres long and 800 metres thick. The Bird River Sill was emplaced into the Northern Lamprey Falls Formation as multiple east-trending, sub-concordant igneous bodies that have been significantly disrupted by faults (Fig. 3.3) (Ashwal, 1993, 2010; Gilbert et al., 2008). The Bird River Sill occurs at and was emplaced along the southern margin of the Mesoarchean to Neoarchean Maskwa Lake Block (Fig. 3.3) (Gilbert, 2005, 2006, 2007, 2008; Gilbert et al., 2008; Yang et al., 2013).

The Bird River Sill consists of the Marginal Mafic, Ultramafic, Transition and Mafic Series (Good et al., 2009). The Ultramafic Series constitutes the lower 200 metres of the Bird River Sill and consists of strongly serpentinised ultramafic cumulates (dunite, peridotite, troctolite and minor pyroxenite) with subordinate chromite-rich layers (Fig. 3.5), whereas the 600-metre-thick Mafic Series consists of layered gabbro, hornblende gabbro, quartz gabbro, leucogabbro, anorthosite, anorthositic gabbro, diorite and tonalite (Fig. 3.5) (Trueman, 1971; Scoates, 1983; Scoates et al., 1989; Theyer, 1991; Peck and Theyer, 1998; Mealin, 2008; Good et al., 2009; Yang and Gilbert, 2014). The Mafic Series is separated from the underlying Ultramafic Series by the 1 to 5-metre-thick Transition Series, which comprises interlayered peridotite and gabbro (Trueman, 1971; Scoates, 1983; Mealin, 2008; Good et al., 2009). The Marginal Mafic Series occurs at the bottom of the Ultramafic Series (Trueman, 1971; Mealin, 2008; Good et al., 2009)

and consists of a 12-metre-thick olivine gabbro unit with a chilled margin visible at the contact between the Ultramafic Series and the Northern Lamprey Falls Formation (Mealin, 2008; Good et al., 2009).

3.3. Field relationships

The Ultramafic Series includes peridotite and chromitite, with the former being strongly serpentinised and extensively sheared. Cumulate textures and magmatic layering in the associated chromitites are locally well preserved (Fig. 3.5). The chromitite layers are largely disrupted by shearing, and, in some cases, the chromites in the chromitites have been fragmented and broken up by shearing (Fig. 3.5). The Mafic Series includes gabbros, leucogabbros and anorthosites (Fig. 3.5). The gabbros have well-preserved cumulate textures yet have very little primary mineralogy remaining due to alteration (Fig. 3.5). The leucogabbros and anorthosites have well-preserved cumulate textures, large magmatic plagioclase megacrysts and amphibole oikocrysts (Fig. 3.5). The Bird River Sill was emplaced into the Maskwa Lake Batholith I and intruded by the Maskwa Lake Batholith II (Figs. 3.3 and 3.4).

The section of the southern arm of the Bird River greenstone belt to the north of the Booster Lake Shear Zone consists of the Northern Lamprey Falls Formation, 'Diverse arc assemblage' (henceforth referred to as the Bird River Formation; see below) and Peterson Creek Formation (Fig. 3.3). The Northern Lamprey Falls Formation comprises basalts and synvolcanic gabbros and is in fault contact with the overlying felsic volcanic rocks of the Peterson Creek Formation (Figs. 3.3 and 3.4). The Bird River Formation consists of mafic to felsic volcanic rocks and siliciclastic sedimentary rocks and unconformably overlies the Peterson Creek Formation (Figs. 3.3 and 3.4). The Peterson Creek Formation is separated from the siliciclastic sedimentary rocks of the Booster Lake Formation by the Booster Lake Shear Zone (Fig. 3.3). The Northern Lamprey Falls, Peterson Creek and Bird River formations are emplaced into the Maskwa Lake TTG Batholith I. The Northern Lamprey Falls, Bird River and Peterson Creek formations are intruded by the Maskwa Lake TTG Batholith II (Figs. 3.3 and 3.4).

3.4. Sampling

Samples were obtained from the Neoarchean Bird River Sill and greenstone belt (Figs. 3.3 and 3.4) during fieldwork conducted in the Bird River area of southeastern Manitoba. Representative sampling of the cumulate textures and lithologies of the Bird River Sill was conducted during traverses from the top to the bottom of the intrusion to understand the genetic relationships between the different lithologies within it. Three anorthosites, eight leucogabbros and four gabbros were collected from the Mafic Series of the Bird River Sill. Eight peridotites and four chromitites were sampled from the Ultramafic Series of the Bird River Sill. Two basalts and one synvolcanic gabbro (Northern Lamprey Falls Formation), three rhyolites (Peterson Creek Formation), two greywackes (Booster Lake Formation), and a volcaniclastic greywacke and a greywacke (Bird River Formation) were sampled from the Bird River greenstone belt. The Northern Lamprey Falls Formation (Duguet et al., 2005, 2006, 2007; Gilbert, 2005, 2006) was renamed as the Northern MORB-type Formation by Gilbert et al. (2008), however, this name has genetic connotations and the name Northern Lamprey Falls Formation will consequentially be used in this contribution instead. Similarly, the Bird River Formation will be used instead of the 'Diverse arc assemblage' (Gilbert, 2007), which was initially referred to as the Peterson Creek Formation by Duguet et al. (2007). The 'Diverse arc assemblage' has genetic connotations and the Peterson Creek Formation of Duguet et al. (2007) may be confused with the Peterson Creek Formation of Gilbert (2007, 2008). Two tonalite samples were collected from the southern margin of the Maskwa Lake TTG Batholith. The location of these tonalite samples suggests that they most likely came from the 2844 ± 12 Ma phase of this batholith (Wang, 1993; Gilbert et al., 2008). The proximity of the Northern Lamprey Falls Formation gabbro indicates that it was emplaced into this phase of the batholith (Fig. 3.3 and 3.4; Wang, 1993; Gilbert et al., 2008). This field-based sampling was supplemented by obtaining additional samples from the Geological Survey of Manitoba in Winnipeg, Manitoba, where 4 samples were selected, described, and cut for petrographical and whole-rock geochemical analysis. Two andesite dykes from the Bird River Formation and two chromitites from the Ultramafic Series of the Bird River Sill were selected. Samples ranging from having minor to major alteration were obtained to test the effect of alteration on element mobility within the samples. The samples' weights ranged from 2 to 4 kg. The Global Positioning System (GPS) coordinates for the field sample locations are given in Appendices 2.1 and 2.2.

3.5. Analytical methods

The petrography and textures of the samples from the Bird River Sill, the adjacent formations in the Bird River greenstone belt and the Maskwa Lake TTG Batholith I were studied using a Leitz Laborlux 12 Pol polarising microscope, an Olympus BX51 petrographic microscope, equipped with a Luminera Infinity 1 high-resolution digital camera with image capture software, a FEI Quanta 200 FEG scanning electron microscope (SEM) and a WiTec confocal Raman spectrometer at the University of Windsor. Samples were analysed for major and trace elements, and for Nd and Pb isotopes. Detailed descriptions of the whole-rock major and trace element, and Sm-Nd and U-Th-Pb radiogenic isotope analysis procedures are given in Polat et al. (2016) and Wu et al. (2016). As such, only short summaries of the analytical procedures are provided here.

3.5.1. Major and trace elements

At the beginning of the major element analysis procedure, the samples were reduced to a powder using an agate mill and then heated for 3 hours at 1100°C, resulting in weight loss that was used to calculate loss-on-ignition (LOI) values. Following this, a lithium metaborate and lithium tetraborate commixture was used to fuse the samples, which were then dissolved by being poured into a 5% nitric acid solution. Subsequently, major elements were analysed using a Fusion-ICP at Activation Laboratories Ltd. (Actlabs) in Ancaster, Ontario, Canada. Major element oxides totals are 100 ± 1.5 wt.%. There was a reproducibility better than ±5% for the samples analysed. Appendix 2.3 contains detection limits for the major elements and the results of standard and duplicate analyses.

The analytical procedure used for the trace element inductively-coupled plasma mass spectrometry (ICP-MS) analyses is described in detail in Burnham (2017) and Hargreaves (2017). The technique used for powder sample dissolution involved multiple acids. Following this, trace elements were analysed using ICP-MS at Geoscience Laboratories (Geo Labs) in Sudbury, Ontario, Canada. The use of this technique resulted in a generally better than ±10% reproducibility for the majority of the trace element analyses (Polat et al., 2012, 2016). For petrogenetic interpretation, trace elements were normalised to normal mid-ocean ridge basalt (N-MORB) and chondrite values reported in Sun and McDonough (1989). Nb/Nb*, Zr/Zr*, Hf/Hf*, Ti/Ti*, Eu/Eu* and Ce/Ce* anomalous element ratios were calculated based on the

methods set out in Taylor and McLennan (1985). The molecular ratio of $Mg/(Mg + Fe^{2+})$ was used to calculate Mg# based on the assumption that Fe^{2+} is 90% of total Fe (Gill, 2010; Zhou et al., 2016).

3.5.2. Sm-Nd and U-Th-Pb radiogenic isotope analyses

Twenty-eight samples were selected for Sm-Nd and U-Th-Pb isotope composition analysis based solely on lithology types and their coherent chondrite-normalised rare-earth element (REE) and N-MORB-normalised trace element patterns. A VG Sector IT Thermal Ionisation Mass Spectrometer (TIMS) at IGN, University of Copenhagen, Copenhagen, Denmark, was used to determine Sm, Nd and Pb isotopic ratios and Sm and Nd isotopic dilution concentrations from the dissolved powder aliquots. Prior to acid digestion, powders of the samples were mixed with a $^{150}Nd/^{147}Sm$ spike. Concentrated HNO_3^-, HCl^- and HF^--bearing Savillex^{TM} beakers were placed on a hotplate heated at 130°C for 3 days to dissolve the powder samples (Frei and Polat, 2013; Wu et al., 2016). The separation of REEs was performed using 12 ml AG50W-X 8 (100-200 mesh) cation resin-charged chromatographic separation columns. Smaller chromatographic columns bearing Eichrom's^{TM} LN resin SPS (Part#LN-B25-S) were used to facilitate separation of Sm and Nd. Conventional glass and miniature glass stem anion exchange columns containing 1 ml and 200 µl, respectively, of 100-200 mesh Bio-Rad AG 1 x 8 resin were used for the purpose of Pb separation. The Sm and Nd isotopes were measured in a multi-dynamic routine and a static multi-collection mode, respectively. A $^{146}Nd/^{144}Nd$ ratio of 0.7219 had to be used to correct the measured Nd isotope ratios for mass bias. Throughout the duration of the analytical period, measurements of the JNdi standard were made and yielded a mean value of $^{143}Nd/^{144}Nd = 0.5120948 \pm 0.0000089$ (2σ; $n = 8$). There was a better than 2% (2σ) precision for the $^{147}Sm/^{144}Nd$ ratio analyses. A static multi-collection mode was employed to quantify the Pb isotope compositions of the samples. During the Pb isotope ratio analyses, repeated analysis of the NBS 981 standard was done to control fractionation (using the values of Todt et al., 1993). <200 pg Pb total procedural blanks demonstrate that Pb isotope ratio compositions were not influenced beyond the significant third digit.

3.5.3. Scanning electron microscope energy dispersive X-ray spectroscopy (SEM-EDS) analyses

A FEI Quanta 200 field emission gun (FEG) scanning electron microscope (SEM) at the Great Lakes Institute for Environmental Research, University of Windsor, was used to complement petrographical observations made on the polarising microscope. A spot size of 3.9 μm, a voltage of 15 kV and an analysis duration of 30 seconds per analysis spot were used to acquire qualitative and scanning electron microscope energy dispersive X-ray spectroscopy (SEM-EDS) quantitative data on the chemistry and textures of plagioclase, amphibole, chromite, and chromite-hosted mineral inclusions from the Bird River Sill. The error percentage values for these minerals are inversely proportional to their weight percentage values.

3.5.4. Raman spectrometer analyses

A WiTec confocal Raman spectrometer at the Great Lake Institute for Environmental Research, University of Windsor, was used to corroborate data obtained using petrographic and scanning electron microscopy. Operating conditions included a 10 to 40 mW laser power, a laser spot size of 7 μm and a 532 nm excitation wavelength. The spots analysed were chosen based on the location of the SEM-EDS analysis spots.

3.6. Petrography

3.6.1. Bird River Sill

3.6.1.1. Ultramafic Series

The peridotites of the Ultramafic Series are medium to coarse grained (2-4 mm) and are comprised of anhedral to subhedral serpentine (55-90%), subhedral to euhedral olivine (5-20%), orthopyroxene (10-15%) and clinopyroxene (5-20%) and anhedral to euhedral opaque magnetite (5-20%) and chromite (2-20%) (Fig. 3.6). The predominance of orthopyroxene over clinopyroxene in some of the peridotites (Fig. 3.6) indicates that they are harzburgites. Secondary serpentine pervasively replaces and pseudomorphs primary olivine. Pyroxene is partly replaced by serpentine/bastite. Talc occurs within serpentine masses that pseudomorph olivine (Fig. 3.6). Secondary tremolite forms ≤1% of these peridotites. Primary olivine, orthopyroxene and clinopyroxene occur as relicts or pristine grains (Fig. 3.6). Some peridotites

are cut by serpentine veins that form 10 to 15% of these rocks (Fig. 3.6). Opaque minerals (chromite and magnetite) mark out the round edges of the serpentine masses that pseudomorph olivine (Figs. 3.6). Chromite occurs in both cumulate and interstitial form. In some peridotites, clinopyroxene oikocrysts envelop numerous serpentine pseudomorphs of poikilitic olivine chadacrysts. The chromitites of the Ultramafic Series are fine grained (≤2 mm) and comprise 50 to 60% serpentine (pseudomorphs and replaces olivine) and 40 to 50% opaque, subhedral to euhedral chromite (Figs. 3.5 and 3.6). Some chromite crystals have vein-filled fractures and/or have small pyroxene, plagioclase, and olivine inclusions (Figs. 3.5 and 3.6). Pyroxene (<1%) is not very abundant. Serpentine pseudomorphing olivine forms 15 to 20% of the chromitites (Figs. 3.5 and 3.6). Chromite is usually interstitial to olivine crystals pseudomorphed by serpentine (Figs. 3.5 and 3.6). The serpentine pseudomorphs are ≤6 mm in diameter. The peridotites and chromitites are variably preserved, just as with the anorthosites, leucogabbros and gabbros from the Mafic Series (Figs. 3.5 and 3.6) and the volcanic and sedimentary lithologies of the Bird River greenstone belt (Fig. 3.7). Raman spectroscopy and SEM-EDS analyses indicate that chromite-hosted inclusions in the peridotites and chromitites of the Ultramafic Series of the Bird River Sill consist of clinopyroxene, orthopyroxene, albite, chalcopyrite, and calcite (Figs. 3.8 and 3.9; Appendices 2.4 and 2.5).

3.6.1.2. Mafic Series

The primary cumulate textures and mineralogy of the anorthosites, leucogabbros and gabbros are generally well preserved and contain varying proportions (25-95%) of coarse (<1 cm) to megacrystic (≤2.5 cm) plagioclase (Figs. 3.5 and 3.6). The anorthosites and leucogabbros contain interstitial primary clinopyroxene, orthopyroxene and amphibole, whereas the gabbros have cumulus clinopyroxene and orthopyroxene (Figs. 3.5, 3.6 and 3.8). Some of the interstitial primary clinopyroxene and amphibole in the anorthosites and leucogabbros occur as large oikocrysts that envelop plagioclase chadacrysts (Fig. 3.6). A magmatic origin for the amphiboles is strongly indicated by their optical continuity, whole-grain extinction, and their serrated, igneous grain boundaries with cumulus plagioclase (Fig. 3.6; Claeson and Meurer, 2004). The gabbros are more visibly altered than the anorthosites and leucogabbros with secondary actinolite, chlorite, sericite and epidote replacing clinopyroxene, orthopyroxene and plagioclase (Fig. 3.6). In the anorthosites and leucogabbros, plagioclase is partly replaced by sericite, clinozoisite and epidote, whereas clinopyroxene, orthopyroxene and amphibole are

partly replaced by actinolite (Fig. 3.6). Based on SEM-EDS analyses, the magmatic amphibole identified in the anorthosites and leucogabbros is magnesiohornblende (Appendix 2.4).

The gabbros of the Mafic Series are fine to coarse grained (1-7 mm) and have variably well-preserved primary igneous textures and primary igneous minerals (Figs. 3.5 and 3.6). These gabbros are comprised of 25 to 40% plagioclase, 1 to 5% clinopyroxene, 1 to 5% orthopyroxene and 2 to 5% opaques (all primary), however, secondary, subhedral to euhedral actinolite (20-40%), chlorite (10-15%), sericite (~5%) and epidote (1-5%) partly replace euhedral, primary clinopyroxene, orthopyroxene and plagioclase. The ferromagnesian minerals are more altered than plagioclase (Figs. 3.5 and 3.6). In some cases, intrusion of quartz veins has altered the primary minerals in these gabbros (Figs. 3.5 and 3.6).

The leucogabbros of the Mafic Series are generally very fresh, have well-preserved cumulate textures and primary igneous mineralogy and have grain sizes ranging from medium grained (3 mm) to megacrystic (≤2 cm; Figs. 3.5 and 3.6). These leucogabbros consist of ~40 to 85%, subhedral to euhedral, primary plagioclase (3mm to ≤2 cm), 1 to 30%, subhedral to anhedral, primary hornblende (≤2 mm), euhedral (<2 mm), primary clinopyroxene (1-25%) and orthopyroxene (1-35%) and 1 to 10% euhedral, secondary clinozoisite (Figs. 5 and 6). Fine-grained opaques (≤2 mm) are a significant constituent (1-15%) of these leucogabbros and occur within and between larger primary plagioclase, hornblende, clinopyroxene and orthopyroxene crystals and secondary actinolite porphyroblasts. Plagioclase megacrysts (≤2 cm) comprise numerous, finer-grained (≤1 cm) plagioclase crystals (Figs. 3.5 and 3.6). Hornblende occurs as oikocrysts that envelop numerous, poikilitic plagioclase chadacrysts, forming an ophitic texture (Figs. 3.5 and 3.6). Plagioclase inclusions occur within orthopyroxene, clinopyroxene and hornblende, and plagioclase crystals contain both altered (now actinolite) and fresh hornblende, clinopyroxene and orthopyroxene inclusions. Clinozoisite (1-10%) and epidote (<1%) partly replace some plagioclase megacrysts. Actinolite (1-3%) partly replaces clinopyroxene and orthopyroxene. Hornblende is not completely pristine and is partly replaced by secondary actinolite. Sericite (after plagioclase) forms 1 to 3% of the leucogabbros.

The anorthosites of the Mafic Series have a coarse-grained (≤5 mm) to megacrystic (≤2 cm by ≤1.5 cm plagioclase megacrysts) texture and are very well preserved in terms of their primary, igneous textures and primary igneous mineralogy (Fig. 3.6). These anorthosites are dominated by euhedral, primary plagioclase (60-95%), with subordinate, fine- to coarse-

grained (1-6 mm), primary clinopyroxene (5-10%), orthopyroxene (10-15%) and hornblende (<1%) and opaque (<1%) minerals (Fig. 3.6). The plagioclase megacrysts consist of numerous, coarse-grained (≤7 mm) plagioclase crystals (Fig. 3.6). These primary minerals generally have well-defined grain boundaries (Fig. 3.6). Numerous, poikilitic plagioclase chadacrysts are, in some instances, surrounded by larger clinopyroxene and orthopyroxene oikocrysts, thereby forming an ophitic texture (Fig. 3.6). Plagioclase contains small, primary clinopyroxene, orthopyroxene and hornblende inclusions (Fig. 3.6). Some plagioclase megacrysts are partly replaced by sericite and clinozoisite (1-2%), and secondary actinolite (1-2%) partly replaces some clinopyroxene (Fig. 3.6).

3.6.2. Bird River greenstone belt

The fine- to coarse-grained intrusive, volcanic, and sedimentary rocks of the Northern Lamprey Falls, Peterson Creek, Bird River and Booster Lake formations are variably altered but their primary cumulate, volcanic, and sedimentary textures are preserved (Figs. 3.7 and 3.10). The clastic sedimentary textures of the sedimentary rocks of the Booster Lake and Bird River formations are also preserved (Figs. 3.7 and 3.10).

3.6.2.1. Northern Lamprey Falls Formation

The gabbro from the Northern Lamprey Falls Formation is medium grained (≤3 mm) and is generally not very well preserved. This gabbro has a well-preserved cumulate texture but has lost most of its primary igneous mineralogy (Fig. 3.7). Euhedral plagioclase (45-50%) is the dominant mineral, followed by 1 to 3 mm secondary actinolite (50-55%) and minor relict pyroxene (Fig. 3.7). Opaque minerals form 3 to 4% of this gabbro (Fig. 3.7).

The basalts of the Northern Lamprey Falls Formation are fine to medium grained (1-3 mm) and comprise elongate, euhedral, primary plagioclase (~50%), and euhedral clinopyroxene (~15%) and orthopyroxene (~15%) (Fig. 3.7). Secondary actinolite (~20%) partly replaces both clinopyroxene and orthopyroxene and partly comprises the finer-grained (<1 mm) groundmass of the basalts (Fig. 3.7). Fine-grained opaques are minor (<1%) and are finer grained than primary plagioclase, clinopyroxene and orthopyroxene and secondary actinolite porphyroblasts. Clinopyroxene and orthopyroxene occur as relicts and can be near pristine (Fig. 3.7).

3.6.2.2. Bird River Formation

The volcaniclastic greywacke from the Bird River Formation is very fine grained and has a fine-grained matrix made up of clay minerals (25-30%) and lithic fragments (10-15%), with coarser-grained hornblende porphyroblasts (30-40%), plagioclase (10-15%) and quartz (10-15%) phenocrysts/xenocrysts comprising the remainder of the sample (Fig. 3.7). The clay minerals within this volcaniclastic greywacke are most likely illite and smectite (Fig. 3.7). Opaques are minor (<1%) and are most likely detrital zircons.

3.6.2.3. Peterson Creek Formation

The rhyolites of the Peterson Creek Formation have a distinctive porphyritic texture with ≤4 mm quartz and ≤2 mm feldspar phenocrysts forming 5-10% and 5% of these rocks, respectively (Fig. 3.7). Finer-grained (<1 mm) quartz (15-30%), biotite (15-20%), clinopyroxene (<1%), feldspar (15-30%) and sericite (15-30%) make up the fine-grained groundmass (Fig. 3.10). Fine-grained (<1 mm) opaques form ≤2% of these porphyritic rhyolites. Most of the primary minerals in these rhyolites are fresh but are altered in some cases. Sericite and epidote partly replace feldspar, and actinolite (<2%) partially replaces clinopyroxene. Quartz veins occur within the porphyritic rhyolites and some quartz phenocrysts are cut by these quartz veins.

3.6.2.4. Booster Lake Formation

The quartzitic greywackes of the Booster Lake Formation predominantly (70%) consist of a fine-grained (<1 mm) matrix of quartz (~20%), feldspar (~20%), sericite (~10%), chlorite (≤5%), opaques (≤1%) and clay minerals (~20%), with coarser-grained (≤2 mm) quartz (~20%) and lithic fragments (1-5%) being subordinate (Fig. 3.7). Sericite has partly replaced feldspar and chlorite most likely replaced a ferromagnesian mineral. The fine-grained opaques are most likely detrital zircons. Numerous thin (<1 mm-thick) quartz veins penetrate these quartzitic greywackes (Fig. 3.7). Some quartz grains have quartz veins cutting through them and linear cracks lined with Fe-oxide staining.

3.6.3. Maskwa Lake TTG Batholith I

The tonalites of the Maskwa Lake TTG Batholith I are coarse grained (≤4 mm) and comprised of euhedral, primary quartz (20-25%), plagioclase (50-60%), biotite (10-15%), and alkali feldspar (0-20%) and opaque (<1%) minerals (Fig. 3.7). These tonalites are predominantly fresh yet have been slightly altered with minor actinolite replacing a ferromagnesian mineral. Quartz exhibits undulose extinction, suggesting that these tonalites underwent significant strain (Fig. 3.7).

3.7. Geochemical results

3.7.1. Chromite, plagioclase, amphibole, and chromite-hosted mineral inclusions mineral chemistry

3.7.1.1. Chromite

The cores of the chromite grains from the chromitites of the Bird River Sill have variable Al (3.83-14.53 wt.%), Cr (26.02-38.92 wt.%), Mg (0.00-8.94 wt.%) and Fe (17.34-34.82 wt.%) contents, and variable Cr# (48-82) and Mg# (0-57) (Appendix 2.4). The rims of these chromite grains have similar, variable Al (1.91-13.97 wt.%) and Cr (26.66-40.15 wt.%), lower Mg (0.00-4.30 wt.%) and higher Fe (24.11-44.20 wt.%) contents and overlapping Cr# (50-89) and lower Mg# (0-31) (Appendix 2.4). The rims bordering the inclusions of these chromite grains have variable Al (3.84-15.99 wt.%), Cr (24.67.06-42.04 wt.%), Mg (2.32-11.18 wt.%) and Fe (13.92-33.44 wt.%) contents, and variable Cr# (44-85) and Mg# (12-62) (Appendix 2.4). There are chromites with a Mg# of 0 that are associated with distinctly bright rims and fracture rims on SEM images, which may have been a consequence of hydrothermal alteration (Fig. 3.8; Appendix 2.4). The chemistry of the chromite cores from the Bird River Sill indicate that they are of chromite *sensu stricto* to magnesiochromite to hercynite composition (Appendix 2.4; Deer et al., 2013).

3.7.1.2. Plagioclase

The cores of plagioclase grains from leucogabbro sample BR2017-19 from the Bird River Sill are characterised by narrow-ranging Ca (11.26-13.71 wt.%), Na (1.39-2.21 wt.%), Al (18.39-19.09 wt.%) and Si (20.96-22.06 wt.%) contents and have high An (76-85) contents, indicating that they are of bytownite composition (Appendix 2.4). The rims of these plagioclases have

similar, narrow-ranging Ca (11.54-13.58 wt.%), Na (1.53-2.79 wt.%), Al (18.16-19.00 wt.%) and Si (21.11-22.46 wt.%) contents and similarly high An (70-83) contents, indicating that they are also of bytownite composition (Appendix 2.4).

3.7.1.3. Amphibole

The cores of amphibole grains from a leucogabbro (BR2017-19) from the Bird River Sill have narrow-ranging Mg (9.95-11.30 wt.%), Al (0.63-2.85 wt.%), Fe (7.20-8.69 wt.%), Si (24.96-26.38 wt.%), Ca (9.79-10.12 wt.%), and Na (0.26-0.48 wt.%) contents, and high Mg# (75-80) (Appendix 2.4). The rims of these amphibole grains have overlapping, slightly variable Mg (9.12-11.55 wt.%), Al (1.13-4.02 wt.%), Fe (6.54-9.39 wt.%), Si (24.21-26.04 wt.%) and similar, narrow-ranging Ca (9..87-10.23 wt.%) and Na (0.14-0.40 wt.%), and similarly high Mg# (71-82) (Appendix 2.4). Based on their mineral chemistry, these amphibole grains are magnesiohornblende (Appendix 2.4; Leake et al., 1997).

4.7.1.4. Chromite-hosted mineral inclusions

The chromite-hosted clinopyroxene inclusions in the chromitites of the Bird River Sill have variable Al (0.55-9.19 wt.%), Si (16.20-29.13 wt.%), Ca (4.10-17.79 wt.%) and Mg (6.65-19.84 wt.%) and narrow-ganging Na (2.97-4.11 wt.%) contents (Appendix 2.4). The chromite-hosted orthopyroxene inclusions have variable Si (29.71-39.24 wt.%) and narrow-ranging Mg (21.03-23.38 wt.%) contents (Appendix 2.4). The chromite-hosted plagioclase inclusions have variable Al (8.02-11.28 wt.%), Si (30.26-35.44 wt.%) and Na (6.29-11.26 wt.%) contents and sodic An (0-23) contents, indicating that they are predominantly albite, with oligoclase being subordinate (Appendix 2.4). The chromite-hosted calcite inclusions have narrow-ranging Ca (47.72-48.78 wt.%) contents (Appendix 2.4).

3.7.2. Major and trace elements

3.7.2.1. Bird River Sill

The peridotites have high MgO (25.6-35.0 wt.%) and $Fe_2O_3^T$ (9.3-16.0 wt.%) and low Al_2O_3 (4.1-8.8 wt.%), CaO (0.4-5.5 wt.%), TiO_2 (0.04-0.17 wt.%) and SiO_2 (33.1-38.6 wt.%) contents, and high Mg# (74-87) (Fig. 3.11; Appendix 2.1; Gill, 2010). The peridotites have

very low trace element contents and display near-flat to LREE-enriched patterns and positive Eu anomalies on the chondrite-normalised diagram, and variably negative Nb and negative to positive Ti, Zr, and Hf anomalies on the N-MORB-normalised trace element diagram (Figs. 3.12-3.14; Appendix 2.1).

The chromitites have high $Fe_2O_3^T$ (14.4-21.8 wt.%) and MgO (16.1-23.0 wt.%), moderate Al_2O_3 (12.9-17.2 wt.%) and low SiO_2 (13.2-20.6 wt.%), CaO (0.1-0.7 wt.%) and TiO_2 (0.14-0.37 wt.%) contents, and moderate to high Mg# (59-74) (Fig. 3.11; Appendix 2.1).

The gabbros are characterised by high MgO (6.0-9.8 wt.%), $Fe_2O_3^T$ (10.6-12.0 wt.%), CaO (9.4-10.7 wt.%) and TiO_2 (0.54-1.07 wt.%), low to moderate SiO_2 (48.8-54.1 wt.%) and moderate Al_2O_3 (13.3-15.9 wt.%) contents, and moderate Mg# (47-59) (Fig. 3.11; Appendix 2.1). The gabbros exhibit variably negative Nb, Ti, Zr, and Hf anomalies on the N-MORB-normalised trace element diagram and near-flat to LREE-enriched patterns and positive Eu anomalies on the chondrite-normalised diagram (Figs. 3.13 and 3.14; Appendix 2.1).

The leucogabbros have high Al_2O_3 (17.3-24.0 wt.%) and CaO (11.4-15.3 wt.%), moderate to high $Fe_2O_3^T$ (4.3-10.1 wt.%), TiO_2 (0.19-0.55 wt.%) and MgO (3.7-7.3 wt.%) and low SiO_2 (45.4-51.2 wt.%) contents, and moderate to high Mg# (53-72) (Fig. 3.11; Appendix 2.1). The leucogabbros have near-flat to LREE-enriched patterns and pronounced positive Eu anomalies on the chondrite-normalised diagram, and negative to positive Ti, Zr and Hf and variably negative Nb anomalies on the N-MORB-normalised trace element diagram (Figs. 3.13 and 3.14; Appendix 2.1).

The anorthosites have high Al_2O_3 (25.1-28.9 wt.%) and CaO (13.2-14.6 wt.%), and low MgO (2.5-3.3 wt.%), $Fe_2O_3^T$ (3.7-3.9 wt.%), TiO_2 (0.22-0.29 wt.%) and SiO_2 (44.9-49.6 wt.%) contents, and moderate Mg# (54-61) (Fig. 3.11; Appendix 2.1). The anorthosites display pronounced positive Eu anomalies and near-flat to LREE-enriched patterns on the chondrite-normalised diagram, and variably negative Nb and negative to positive Ti, Zr and Hf anomalies on the N-MORB-normalised trace element diagram (Figs. 3.13 and 3.14; Appendix 2.1).

3.7.2. Bird River greenstone belt

3.7.2.1. Northern Lamprey Falls Formation

The basalts from the Northern Lamprey Falls Formation are characterised by high $Fe_2O_3^T$ (9.8-13.9 wt.%), MgO (6.3-6.8 wt.%), CaO (10.6-10.8 wt.%) and TiO_2 (0.85-1.02 wt.%), moderate Al_2O_3 (14.5-15.9 wt.%) and low SiO_2 (49.8-51.5 wt.%) contents, and moderate Mg# (47-53) (Fig. 3.11; Appendix 2.2). The basalts exhibit negative Nb, Ti, Zr and Hf anomalies on the N-MORB-normalised trace element diagram, and near-flat to slightly HREE-enriched and LREE-depleted patterns and positive Eu anomalies on the chondrite-normalised diagram (Figs. 3.13 and 3.14; Appendix 2.2).

The synvolcanic gabbro has high MgO (7.5 wt.%), $Fe_2O_3^T$ (13.7 wt.%), CaO (10.1 wt.%) and TiO_2 (0.91 wt.%), moderate Al_2O_3 (15.4 wt.%) and low SiO_2 (48.7 wt.%) contents, and a moderate Mg# (50) (Fig. 3.11; Appendix 2.2). This gabbro displays a negative Eu anomaly and a near-flat to HREE-enriched and LREE-depleted pattern on the chondrite-normalised diagram, and negative Nb, Ti and Zr anomalies on the N-MORB-normalised trace element diagram (Figs. 3.13 and 3.14; Appendix 2.2).

3.7.2.2. Peterson Creek Formation

The rhyolites from the Peterson Creek Formation are characterised by high SiO_2 (69.2-70.4 wt.%), moderate Al_2O_3 (12.9-13.1 wt.%), TiO_2 (0.57-0.62 wt.%) and $Fe_2O_3^T$ (5.3-5.6 wt.%) and low MgO (1.2-1.3 wt.%) and CaO (2.4-2.8 wt.%) contents, and low Mg# (28-31) (Fig. 3.11; Appendix 2.2). The chondrite-normalised diagram for these rhyolites shows negative Eu anomalies and strongly LREE-enriched patterns, and variably negative Nb and Ti and slightly positive Zr and Hf anomalies are shown on the N-MORB-normalised trace element diagram (Figs. 3.13 and 3.14; Appendix 2.2). The rhyolites are classified as dacites or rhyodacites, based on where they plot on the Zr/Ti versus Nb/Y diagram of Winchester and Floyd (1977) (Fig. 3.15). Rhyolite sample BR2017-21 was deemed anomalous based on its significantly higher SiO_2 content (81.35%) and Mg# (57) and lower La/Yb_{cn}, Zr/Y and Nd/Sm ratios relative to the dacites, as such it has not been included and will not be taken into consideration in the petrogenetic interpretation below (Appendix 2.2).

3.7.2.2.3. Bird River Formation

The andesite dykes from the Bird River Formation have high MgO (5.2-6.6 wt.%) and $Fe_2O_3^T$ (6.6-7.0 wt.%), moderate Al_2O_3 (14.9-16.0 wt.%), CaO (5.1-9.9 wt.%) and TiO_2 (0.44-0.49 wt.%) and moderate SiO_2 (54.2-60.1 wt.%) contents, and moderate to high Mg# (59-63) (Fig.

3.11; Appendix 2.2). These andesite dykes exhibit variably negative Nb, Ti and Hf and negative to positive Zr anomalies on the N-MORB-normalised trace element diagram, and strongly LREE-enriched patterns and negative to positive Eu anomalies on the chondrite-normalised diagram (Figs. 3.13 and 3.14; Appendix 2.2). Based on their high MgO contents and where they plot on the Zr/Ti versus Nb/Y diagram (Winchester and Floyd, 1977), the andesites are classified as high-magnesian basaltic andesites and andesites (Figs. 3.11 and 3.15; Appendix 2.2).

The volcaniclastic greywacke from the Bird River Formation has high $Fe_2O_3^T$ (6.5 wt.%) and MgO (5.3 wt.%), moderate SiO_2 (61.1 wt.%), Al_2O_3 (15.6 wt.%) and TiO_2 (0.49 wt.%) and low CaO (2.5 wt.%) contents, and a moderate Mg# (59) (Fig. 3.11; Appendix 2.2; Taylor and McLennan, 1985). This volcaniclastic greywacke displays a slightly negative Eu anomaly and a steep, LREE-enriched pattern on the chondrite-normalised diagram, and variably negative Nb, Ti, Zr and Hf anomalies on the N-MORB-normalised trace element diagram (Figs. 3.13 and 3.14; Appendix 2.2).

The greywacke from the Bird River Formation has high $Fe_2O_3^T$ (7.0 wt.%) and MgO (6.0 wt.%), moderate SiO_2 (60.7 wt.%), Al_2O_3 (14.8 wt.%) and TiO_2 (0.51 wt.%) and low CaO (3.9 wt.%) contents, and a moderate to high Mg# (61) (Fig. 3.11; Appendix 2.2). This greywacke exhibits negative Nb, Ti, Zr and Hf anomalies on the N-MORB-normalised trace element diagram and a LREE-enriched pattern with a slightly negative Eu anomaly on the chondrite-normalised diagram (Figs. 3.13 and 3.14; Appendix 2.2).

3.7.2.2.4. Booster Lake Formation

The quartzitic greywackes from the Booster Lake Formation are characterised by high SiO_2 (72.6-79.0 wt.%), moderate Al_2O_3 (10.8-12.8 wt.%), low to high TiO_2 (0.10-1.57 wt.%) and low $Fe_2O_3^T$ (1.4-2.4 wt.%), MgO (0.16-0.20 wt.%) and CaO (0.9-2.3 wt.%) contents, and low Mg# (13-17) (Fig. 3.11; Appendix 2.2). These quartzitic greywackes display negative Eu anomalies and strongly LREE-enriched patterns on the chondrite-normalised diagram, and variably negative Nb, Ti and Hf and negative to positive Zr anomalies on the N-MORB-normalised trace element diagram (Figs. 3.13 and 3.14; Appendix 2.2).

3.7.2.3. Maskwa Lake TTG Batholith I

The tonalites from the Maskwa Lake TTG Batholith I have high SiO_2 (70.4-71.6 wt.%), moderate Al_2O_3 (14.2-14.3 wt.%), $Fe_2O_3^T$ (3.5-3.7 wt.%) and TiO_2 (0.35-0.38 wt.%) and low MgO (1.3-1.5 wt.%) and CaO (1.8-2.2 wt.%) contents, and low Mg# (40-42) (Fig. 3.11; Appendix 2.2). These tonalites show variably negative Nb and Ti and variably positive Zr and Hf anomalies on the N-MORB-normalised trace element diagram, and negative Eu anomalies and strongly LREE-enriched patterns on the chondrite-normalised diagram (Figs. 3.13 and 3.14; Appendix 2.2).

3.7.3. Radiogenic isotopes

3.7.3.1. Sm-Nd isotopes

3.7.3.1.1. Bird River Sill

The majority of samples from the Bird River Sill have positive $\varepsilon_{Nd\ (2743Ma)}$ values, although some negative values are also evident (Fig. 3.16; Table 3.1). The peridotites have a wide range of $\varepsilon_{Nd\ (2743\ Ma)}$ (-0.99 to +9.47) values. The gabbros have positive, variably-depleted $\varepsilon_{Nd\ (2743\ Ma)}$ (+0.35 to +3.63) values. The leucogabbros have positive, variably-depleted $\varepsilon_{Nd\ (2743\ Ma)}$ (+1.36 to +4.72) values. The anorthosites have positive, variably-depleted $\varepsilon_{Nd\ (2743\ Ma)}$ (+1.96 to +3.75) values.

3.7.3.1.2. Bird River greenstone belt and Maskwa Lake TTG Batholith I

Samples collected from the Bird River greenstone belt display dominantly positive ε_{Nd} values (Fig. 3.16; Table 3.1). The synvolcanic gabbro sampled from the Northern Lamprey Falls Formation has a positive $\varepsilon_{Nd\ (2743\ Ma)}$ (+1.40) value. The basalts from the Northern Lamprey Falls Formation have positive, variably-depleted $\varepsilon_{Nd\ (2743\ Ma)}$ (+1.96 to +2.66) values. The high-magnesian andesites from the Bird River Formation have weakly positive $\varepsilon_{Nd\ (2725\ Ma)}$ (+0.14 to +0.20) values. The greywackes from the Bird River Formation have negative to positive $\varepsilon_{Nd\ (2706\ Ma)}$ (-0.96 to +0.31) values. The dacites from the Peterson Creek Formation also have weakly positive $\varepsilon_{Nd\ (2731\ Ma)}$ (+0.58 to +0.59) values. Notably, the Mesoarchean tonalites from the Maskwa Lake TTG Batholith I have more juvenile, positive $\varepsilon_{Nd\ (2844\ Ma)}$ values (+1.44 to +1.73) (Fig. 3.16; Table 3.1).

3.7.3.2. U-Th-Pb isotopes

3.7.3.2.1. Bird River Sill

The peridotites, gabbros and leucogabbros have quite variable $^{206}Pb/^{204}Pb$ (13.755-18.445, 14.002-27.476, and 14.909-21.721) and $^{208}Pb/^{204}Pb$ (33.552-37.982, 33.800-46.764, and 34.404-40.778) ratios but narrow $^{207}Pb/^{204}Pb$ (14.710-15.614, 14.764-17.232 and 14.841-16.151) ratio variations (Fig. 3.16; Table 3.2). The $^{206}Pb/^{204}Pb$ (14.314-14.717), $^{207}Pb/^{204}Pb$ (14.810-14.888) and $^{208}Pb/^{204}Pb$ (33.805-34.061) ratios of the anorthosites show little variation (Fig. 3.16; Table 3.2).

3.7.3.2.2. Bird River greenstone belt and Maskwa Lake TTG Batholith 1

The $^{206}Pb/^{204}Pb$ (14.923-15.481), $^{207}Pb/^{204}Pb$ (14.921-15.028) and $^{208}Pb/^{204}Pb$ (34.074-34.939) ratios of the basalts from the Northern Lamprey Falls Formation show little variation (Fig. 3.16; Table 3.2). The high-magnesian andesites and greywackes from the Bird River Formation and dacites from the Peterson Creek Formation show only minor variation in their $^{206}Pb/^{204}Pb$ (15.893-15.959, 17.748-19.205, and 19.205-19.740), $^{207}Pb/^{204}Pb$ (15.050-15.091, 15.401-15.620, and 15.746-15.829) and $^{208}Pb/^{204}Pb$ (35.544-36.327, 36.988-37.222, and 39.454-39.534) ratios (Fig. 3.16; Table 3.2). The tonalites from the Maskwa Lake TTG Batholith I have highly variable $^{206}Pb/^{204}Pb$ (36.525-44.586) and $^{208}Pb/^{204}Pb$ (49.834-54.943) ratios and only slightly variable $^{207}Pb/^{204}Pb$ (18.844-20.294) ratios (Fig. 3.16; Table 3.2).

3.8. Discussion

3.8.1. Effects of metamorphism on element mobility

Given the Neoarchean age of the Bird River Sill and the Bird River greenstone belt and the fact that both were subjected to greenschist-facies metamorphism (Ashwal, 1993; Wang, 1993; Peck et al., 1999a; Yang et al., 2011; Yang and Gilbert, 2014) during the Uchian Orogeny (2720-2700 Ma; Percival et al., 2006, 2012; Percival, 2007), the effects of this metamorphism on the geochemistry of the rocks selected for geochemical analysis must be determined before any petrogenetic and geodynamic interpretations can be made. Ytterbium, Zr and Nb were

plotted against the major elements, transition metals, large-ion lithophile elements (LILE), high-field strength elements (HFSE) and REE (only Zr versus HFSE and REE are shown in Fig. 3.12) and the corresponding coefficient correlations were calculated to determine the degree of element mobility in the Bird River Sill and Bird River greenstone belt samples (Guice et al., 2018). These plots and correlation coefficients indicate that some major elements, transition metals and LILE were mobilised in both the Bird River Sill and the rocks of the Bird River greenstone belt. These elements do not correlate well with Yb, Zr and Nb, making them unsuitable for petrogenetic and geodynamic setting interpretation. The HFSE and REE correlate far better with Yb, Zr and Nb (Fig. 3.12), particularly in the case of the Bird River Sill, an observation that confirms their suitability for the petrogenetic and geodynamic setting interpretations to follow.

Field and petrographic observations, major and trace element and Nd isotope data indicate that the peridotites and, to a lesser extent, gabbros of the Bird River Sill and the synvolcanic gabbro from the Northern Lamprey Falls Formation were strongly affected by metamorphism and hydrothermal alteration (Figs. 3.5, 3.6 and 3.16; Table 3.1; Appendices 2.1 and 2.2). Despite the fact that the Bird River Sill and Bird River greenstone belt were affected by greenschist-facies metamorphism, hydrothermal alteration and deformation had a greater effect on the peridotites and synvolcanic gabbro, perhaps reflecting localised cases of greater hydrothermal fluid flow and shearing. Consequentially, their respective Sm-Nd and Pb isotopic systems were reset during metamorphism. Moreover, the Sm-Nd isotopic system for the peridotites was reset during alteration and deformation (Figs. 3.5, 3.6 and 3.16; Table 3.1; Lahaye et al., 1995; Lahaye and Arndt, 1996). As such, the petrogenetic interpretations presented below for this lithology will be based solely on their HFSE compositions. Based on their coherent N-MORB- and chondrite- normalised trace element patterns and their relatively well-preserved igneous and sedimentary textures and primary mineralogy, the Bird River Sill anorthosites and leucogabbros, Northern Lamprey Falls Formation basalts, Bird River Formation high-magnesian andesites and greywackes, Peterson Creek Formation dacites and Maskwa Lake TTG Batholith I tonalites, however, have not been affected as much by metamorphism. Consequently, their Sm-Nd isotope systems were not reset by metamorphism and will be used alongside their HFSE and REE compositions in the petrogenetic and geodynamic setting interpretations to follow. Despite the alteration that affected the Bird River Sill and the adjacent formations of the Bird River greenstone belt, Pb-Pb isochron ages of 2691 ± 43 Ma for the

former and 2833 ± 130 Ma for the latter broadly agree, within uncertainty, with their published U-Pb zircon ages (Gilbert et al., 2008; Scoates and Scoates, 2013).

3.8.2. An assessment of the degree of crustal contamination

The occurrence of pillow basalts with hyaloclastite between individual pillows within the Northern Lamprey Falls Formation (Gilbert, 2008) is suggestive of the eruption and emplacement of this formation in a subaqueous, oceanic setting. The Northern Lamprey Falls Formation was emplaced into and is in unconformable contact with the Maskwa Lake TTG Batholith I and occurs to the present-day south of the latter (Gilbert et al., 2008). Based on these observations, the parental magmas to the Northern Lamprey Falls Formation basalts and the Bird River Sill formed in an oceanic setting near the southern margin of the Neoarchean-Mesoarchean Maskwa Lake Block, which will henceforth be referred to as the Maskwa Lake microcontinent and formed through the formation of the Maskwa Lake TTG Batholiths I and II over a period of 133 Ma (Gilbert et al., 2008; Yang et al., 2011, 2012, 2013). This suggests that the parental magmas to the Northern Lamprey Falls Formation and the Bird River Sill would not have been significantly contaminated by the older continental crust of the Maskwa Lake microcontinent. Gilbert et al. (2008), however, reported mafic dykes within the Maskwa Lake TTG Batholith I that are compositionally similar to the Northern Lamprey Falls Formation and suggested that these dykes may be synvolcanic feeder dykes. The field relationship between the mafic dykes and the Maskwa Lake TTG Batholith I, as well as the interpretation of Gilbert et al. (2008), suggests that the parental magma(s) to the Northern Lamprey Falls Formation and Bird River Sill formed in an oceanic setting proximal to the pre-existing continental crust of the Maskwa Lake microcontinent. The positive $\varepsilon_{Nd\ (2743\ Ma)}$ values of the anorthosites (+1.96 to +3.75) and leucogabbros (+1.36 to +4.72) of the Bird River Sill and the basalts (+1.96 to +2.66) of the Northern Lamprey Falls Formation, coupled with their depleted N-MORB-normalised trace element patterns argue against extensive contamination of their parental magmas by Mesoarchean continental crust, and indicate that they were derived from depleted mantle sources (Fig. 3.16). Fig. 3.16 shows that two gabbros and one leucogabbro from the Bird River Sill have lower primitve mantle-normalised Nb/Th_{PM} and higher $^{206}Pb/^{204}Pb$ and chondrite-normalised La/Yb_{cn} ratios than other samples from the sill and plot along a crustal contamination trend. This observation, coupled with these gabbros and leucogabbro having lower $\varepsilon_{Nd\ (2743\ Ma)}$ values (+0.53 to +1.77 and +1.36, respectively) and more

enriched N-MORB- and chondrite-normalised trace element patterns relative to the other samples from the Bird River Sill and $\varepsilon_{Nd\ (2743\ Ma)} < +2.0$ values (Figs. 3.13-3.14 and Fig. 3.16), indicates that the parental magma(s) from which these samples crystallised may have been contaminated by pre-existing crust, namely the ca. 2858-2782 Ma Maskwa Lake microcontinent (Gilbert et al., 2008; Yang et al., 2011; Lodge et al., 2015). This is further corroborated by the $\varepsilon_{Nd\ (2743\ Ma)}$ values of these gabbros and leucogabbro being well below the expected depleted mantle $\varepsilon_{Nd\ (2743\ Ma)}$ (+2.8) value (Henry et al., 1998).

The weakly positive $\varepsilon_{Nd\ (2725\ Ma)}$ values (+0.14 to +0.20) of the Bird River Formation high-magnesian andesites indicate that their parental magma(s) was contaminated by pre-existing continental crust or derived by partial melting of slab sediment melt metasomatised mantle (Fig. 3.16; Kay, 1978; Tatsumi and Hanyu, 2003; Kelemen et al., 2003; Polat and Kerrich, 2006; Suzuki and Tatsumi, 2006; Polat et al., 2009). The weakly positive $\varepsilon_{Nd\ (2731\ Ma)}$ values (+0.58 to +0.59) of the Peterson Creek Formation dacites suggest that their parental magma(s) was derived by partial melting of lower arc crust or sediment-bearing subducted oceanic crust (Fig. 3.16; Hoffmann et al., 2011; Huang et al., 2013). The negative to positive $\varepsilon_{Nd\ (2725\ Ma)}$ values (-0.96 to +0.31) of the Bird River Formation greywackes indicate that they were derived by erosion of pre-existing crustal material (Fig. 3.16; Gilbert et al., 2008). The tonalites of the Maskwa Lake Batholith have positive $\varepsilon_{Nd\ (2844\ Ma)}$ values (+1.44 to +1.73), indicating that their parental magma(s) was derived from a juvenile source and was not modified by pre-existing continental crust (Fig. 3.12; Hoffmann et al., 2011; Huang et al., 2013). This is supported by the fact that Archean TTG batholiths are predominantly interpreted to represent juvenile crust derived by melting of hydrous mafic rocks (Martin and Moyen, 2002; Condie, 2005; Martin et al., 2005; Moyen and Martin, 2012).

3.8.3. Petrogenesis and source characteristics

The depleted N-MORB-normalised patterns (Fig. 3.13) and low Dy/Yb (1.54-1.60 and 1.35-1.77), Nd/Sm (2.86-3.14 and 2.63-3.50) and La/Nb (1.12-1.26 and 0.91-3.80) ratios (Appendices 2.1 and 2.2) of the Northern Lamprey Falls Formation and the Bird River Sill are consistent with depleted mantle sources (Saunders et al., 1980; Hofmann, 1988; Stern et al., 2003). However, the Bird River Sill exhibits differing trends in major and trace element variation diagrams and variable N-MORB-normalised trace element and chondrite-normalised

REE patterns (Figs. 3.11-3.14). There are four possible explanations for this: (1) derivation from more than one depleted mantle source; (2) derivation from a depleted mantle source that became progressively more depleted over time; (3) crystallisation of a single parental magma from a large magma chamber and (4) cumulates formed by crystallisation of magma batches derived from the same depleted mantle source and emplaced as sills. Major element variation diagrams (Fig. 3.11) show that the Bird River Sill lithologies do not plot along the same linear trend, indicating that they did not crystallise from a single parental magma in a large magma chamber (Polat et al., 2011, 2018a). The variably-preserved cumulate textures exhibited by the lithologies of the Bird River Sill, coupled with their differing major and trace element variation diagram trends and variably positive $\varepsilon_{Nd\ (2743\ Ma)}$ values, signify that these lithologies crystallised from different magma batches that formed by variable partial melting of a mantle source depleted to varying degrees by at least one prior melting event (Stern et al., 2003; Polat et al., 2011, 2018b; Golowin et al., 2017). These magma batches were emplaced as sills to form the Bird River Sill, as proposed for other Archean megacrystic anorthosite-bearing layered intrusions by Polat et al. (2018a). The Mafic Series leucogabbros and gabbros and Northern Lamprey Falls Formation basalts each have at least two different REE patterns, implying that they crystallised from at least two magma batches or crystal mushes of variable composition (Sotiriou et al., 2019). The Mafic Series gabbros have more similar N-MORB-normalised trace element patterns and trace element geochemistry to the basalts and synvolcanic gabbro from the Northern Lamprey Falls Formation than the Mafic Series anorthosites and leucogabbros and Ultramafic Series peridotites, indicating that they were cogenetic with the former but not the latter (Figs. 3.11-3.14). Similarly, the anorthosites, leucogabbros and peridotites of the Bird River Sill were not cogenetic with the basalts and synvolcanic gabbro of the Northern Lamprey Falls Formation.

The low Zr/Y (1.51-4.17 and 2.19-2.58), La/Yb (0.72-3.18 and 1.09-1.41) and Th/Yb (0.06-0.51 and 0.11-0.17) ratios of the Bird River Sill and Northern Lamprey Falls Formation signify that their parental magmas were tholeiitic in affinity (Ross and Bédard, 2009). The anorthosites and leucogabbros of the Bird River Sill have highly-depleted N-MORB-normalised trace element patterns and negative Nb, Ti and Zr anomalies (Figs. 3.13 and 3.14; Appendix 2.1), indicating that the parental magma(s) to these lithologies was generated by large degree partial melting of a highly-depleted, sub-arc harzburgitic mantle wedge source (Stern et al., 2003; Golowin et al., 2017). Furthermore, the observation of magmatic amphibole (magnesiohornblende) in the anorthosites and leucogabbros (Fig. 3.6) strongly suggests that

the Bird River Sill crystallised from a hydrous parental magma (Claeson and Meurer, 2004). The amphibole oikocrysts in the anorthosites and leucogabbros most likely formed as a result of an interstitial melt reacting with plagioclase, based on an analogy with oikocrystic amphiboles in arc gabbroic cumulates from the 1.79 Ga Eriksberg gabbroic intrusion in southern Sweden that were interpreted to have formed through this reaction (Meurer and Claeson, 2002; Claeson and Meurer, 2004). The anorthosites and leucogabbros of the Bird River Sill have high Al and Ca contents, highly-depleted N-MORB-normalised trace element patterns, low HFSE and REE abundances and negative Nb and Ti anomalies, characteristics that resemble the primitive arc tholeiitic parental magmas to gabbronorites from the suprasubduction zone Puerto Plata Ophiolite in the Dominican Republic (Fig. 3.13; Escuder-Viruete et al., 2014). These findings indicate that the parental magma to the Bird River Sill anorthosites and leucogabbros was most likely a hydrous primitive arc tholeiitic magma that subsequently fractionated to a hydrous, Ca- and Al-rich tholeiitic parental magma (Polat et al., 2011; Escuder-Viruete et al., 2014). The primitive arc tholeiitic parental magma to the Puerto Plata Ophiolite formed by high-degree partial melting of depleted MORB mantle (Escuder-Viruete et al., 2014). Based on the broad geochemical similarity between the anorthosites and leucogabbros of the Bird River Sill and the gabbronorites of the Puerto Plata Ophiolite, the initial parental magma to the Bird River Sill may have also formed by high-degree partial melting of a depleted MORB mantle source (Escuder-Viruete et al., 2014).

The fact that the Bird River Sill intrudes the tholeiites of the Northern Lamprey Falls Formation implies that the extraction of the parental magma to the latter from a sub-arc harzburgitic mantle wedge source led to the depletion of the source of the parental magma to the former (Rollinson et al., 2010). The sequential formation of mantle wedge-derived tholeiites (i.e. Northern Lamprey Falls Formation), accompanying mantle wedge depletion and melting of a sub-arc harzburgitic mantle wedge (Bird River Sill) is similar to recent models proposed for the formation of other Archean megacrystic anorthosite-bearing layered intrusions that formed from hydrous parental magmas in a subduction zone setting (Rollinson et al., 2010; Polat et al., 2011; Yang and Gilbert, 2014; Sotiriou et al., 2019). As shown by Claeson and Meurer (2004), the anorthosite-bearing Paleoproterozoic Eriksberg and Rymmen gabbroic intrusions in Sweden have highly-depleted N-MORB-normalised trace element patterns and crystallised from a hydrous basaltic parental magma(s). This suggests that the Bird River Sill anorthosites and leucogabbros could have formed by high-degree partial melting of a highly depleted sub-arc mantle wedge source that was not fertilised by slab-derived melts (Ishizuka et al., 2006,

2014; Escuder-Viruete et al., 2014). However, the high Al_2O_3 contents of these lithologies suggest that slab sediment- and/or subducting oceanic crust-derived melts may have refertilised this highly-depleted mantle wedge source before it underwent high-degree partial melting (Rollinson et al., 2010; Polat et al. 2011; Yang and Gilbert, 2014, Woelki et al., 2018; Wyman, 2019).

The major and trace element geochemistry of the Peterson Creek Formation dacites, Bird River Formation high-magnesian andesites and Maskwa Lake TTG Batholith tonalites (Appendix 2.2), together with major and trace element variation diagrams (Figs. 3.11 and 3.12; Appendix 2.2) and N-MORB- and chondrite-normalised trace element patterns (Figs. 3.13 and 3.14), indicate that these lithologies were derived from distinctive parental magmas. These lithologies plot as separate clusters on major and trace element variation diagrams (Fig. 3.11), indicating that they formed from different parental magmas (Sotiriou et al., 2019). Based on the similar major and trace element geochemistry (Figs. 3.8-3.11; Appendix 2.2) of the Bird River Formation greywackes and high-magnesian andesites, the greywackes may have been derived from the erosion of arc volcanic rocks (Gilbert et al., 2008). Indeed, these clastic sedimentary rocks were found to have been derived from erosion of the arc-derived Bird River Formation and back-arc-derived Bird River Sill and Northern Lamprey Falls Formation (Gilbert et al., 2008). The varying major and trace element geochemistry (Figs. 3.11 and 3.12; Appendix 2.2) and N-MORB- and chondrite-normalised trace element patterns (Figs. 3.13 and 3.14) of the Booster Lake Formation quartzitic greywackes indicate that local sedimentary processes, such as sorting or grading, could have played a role in their genesis (Taylor and McLennan, 1985).

The high La/Yb (15.85-16.47), Zr/Y (9.82-10.76) and La/Yb_{cn} (11.37-11.82) ratios and weakly positive $\varepsilon_{Nd\ (2731\ Ma)}$ (+0.58 to +0.59) values of the Peterson Creek Formation dacites suggest that their calc-alkaline parental magma(s) formed by partial melting of hydrated basalts in the lower arc crust (Ross and Bédard, 2009; Hoffmann et al., 2011; Huang et al., 2013). The high-magnesian andesites from the Bird River Formation also have high La/Yb_{cn} (9.28-19.60) and La/Yb (12.94-27.32) ratios, low Y (10-12 ppm) and Yb (0.97-1.31 ppm) contents, moderate to high Mg# (59-63), and weakly positive $\varepsilon_{Nd\ (2725\ Ma)}$ (+0.14 to +0.20) values. These geochemical characteristics suggest that these high-magnesian andesites may have been derived by extensive hybridisation of subducting oceanic crust- and slab sediment-derived melts with mantle wedge peridotite (Kay, 1978; Tatsumi and Hanyu, 2003; Kelemen et al., 2003; Polat and Kerrich, 2006; Suzuki and Tatsumi, 2006; Polat et al., 2009).

The greywackes of the Bird River Formation have moderate to high Mg# (59-61) and high La/Yb (15.64-19.17), La/Yb_{cn} (11.22-13.75) and Zr/Y ratios (10.07-10.82), consistent with their derivation by erosion of intermediate igneous rocks (Taylor and McLennan, 1985; Ross and Bédard, 2009). The quartzitic greywackes of the Booster Lake Formation most likely represent sediments derived by erosion of silica-rich igneous rocks (Taylor and McLennan, 1985). This is supported by the low Mg# (13-17) and high La/Yb (18.62-32.62), Zr/Y (5.06-15.46) and La/Yb_{cn} (13.36-23.39) ratios of these quartzitic greywackes (Taylor and McLennan, 1985, Ross and Bédard, 2009). However, enrichment of quartz by local sedimentological processes cannot be ruled out (Taylor and McLennan, 1985). The tonalites from the Maskwa Lake TTG Batholith I have high La/Yb (16.00-15.36) and La/Yb_{cn} (11.48-36.84) ratios and low Mg# and Y (10-12 ppm) and Yb (0.81-1.31 ppm) contents. These characteristics, combined with their positive $\varepsilon_{Nd\ (2844\ Ma)}$ (+1.44 to +1.73) values, negative Nb and Ti anomalies and high Zr/Y (17.45-21.86) and Th/Yb (4.50-9.36) ratios, are consistent with their derivation by partial melting of juvenile lower arc hydrated basalts (Pearce and Peate, 1995; Murphy, 2007; Pearce, 2008; Ross and Bédard, 2009; Hoffmann et al., 2011; Huang et al., 2013).

3.8.4. Geodynamic setting

Several different geodynamic settings have been proposed for Archean megacrystic anorthosite-bearing layered intrusions (Ashwal, 1993, 2010; Paixão and Oliveira, 1998; Ivanic et al., 2010; Spath et al., 2015; Vrevskii, 2016; Ashwal and Bybee, 2017; Polat et al., 2018a; Sotiriou et al., 2019). The negative Nb, Zr and Ti anomalies and near-flat to LREE-enriched patterns of the Bird River Sill anorthosites, leucogabbros, gabbros and peridotites, coupled with geological relationships and the occurrence of spatially and temporally associated pyroclastic and plutonic continental arc rocks and back-arc pillow lavas (Gilbert et al., 2008; Yang et al., 2011, 2012, 2013; Yang and Gilbert, 2014) indicate that they may have formed in a continental back-arc geodynamic setting that may have been broadly similar to the Chilean-style continental back-arc setting in which the Jurassic Rocas Verdes Ophiolite formed (Fig. 3.17; Pearce and Peate, 1995; Stern and de Wit, 2003; Murphy, 2007; Pearce, 2008). The N-MORB-normalised trace element patterns of these lithologies suggest that they formed in an intra-arc rift to back-arc setting. The basalts and synvolcanic gabbro of the Northern Lamprey Falls Formation also have negative Nb, Ti and Zr and near-flat to HREE-enriched trace element patterns (Figs. 3.13 and 3.14) that are suggestive of a suprasubduction zone back-arc

geodynamic setting (Pearce and Peate, 1995; Pearce, 2008). The anorthosites (Th/Nb = 0.69-1.46 and La/Nb = 1.02-1.61), leucogabbros (Th/Nb = 0.68-3.49 and La/Nb = 0.91-2.98), gabbros (Th/Nb = 1.33-3.58 and La/Nb = 1.46-1.84) and peridotites (Th/Nb = 0.60-1.91 and La/Nb = 1.20-3.80) from the Bird River Sill and basalts (Th/Nb = 1.04-1.16 and La/Nb = 1.54-1.60) from the Northern Lamprey Falls Formation all have narrow-ranging low Th/Nb and La/Nb ratios that may reflect their derivation from depleted, sub-arc mantle wedge sources (Saunders et al., 1980, Saccani, 2015). The subduction zone geodynamic setting interpretation presented here for both the Bird River Sill and Northern Lamprey Falls Formation is corroborated by several studies on the Bird River greenstone belt proposing that they formed in a back-arc setting and the mafic to felsic volcanic rocks of the Peterson Creek, Bird River, Bernic Lake and Southern Lamprey Falls Formation formed in arc to back-arc to intra-arc rift geodynamic settings (Gilbert, 2008, Gilbert et al., 2008; Yang et al., 2011, 2012, 2013).

The Bird River Sill and the 92 Ma Neyriz back-arc suprasubduction zone ophiolite in Iran both have anorthosite sections that are up to hundreds of metres thick (Sarkarinejad, 2003; Good et al., 2009; Furnes et al., 2014; Moghadam et al., 2014; Attarzadeh et al., 2017). Given this, and considering that the Neyriz Ophiolite also has broadly comparable N-MORB-normalised trace element patterns and chromite compositions, the Bird River Sill may have also formed in a back-arc suprasubduction zone geodynamic setting (Fig. 3.13; Appendix 2.4; Sarkarinejad, 2003; Furnes et al., 2014; Moghadam et al., 2014; Yang and Gilbert, 2014; Attarzadeh et al., 2017). The 59 Ma Marum suprasubduction zone ophiolite in Papua New Guinea has 10 to 50 centimetre-thick anorthosite dykes with megacrystic (1-3 centimetres) calcic plagioclase (An_{87-91}) and clinopyroxene, which are texturally very similar to the Bird River Sill and indicate that it also may have formed in a suprasubduction zone geodynamic setting by high-degree partial melting of a shallow, hydrous depleted mantle source (Kaczmarek et al., 2015).

Scanning electron microscope energy dispersive X-ray spectroscopy analyses of plagioclase megacrysts (An_{70-85}) from the Bird River Sill overlap with those of plagioclase megacrysts (An_{61-94}) in other Archean megacrystic anorthosite-bearing layered intrusions that have been interpreted to have formed in a subduction zone setting (Appendix 2.4; Ashwal, 1993; 2010; Ashwal and Bybee, 2017; Polat et al., 2018a). Chromite SEM-EDS compositions indicate that the Bird River Sill chromitites have arc (Alaskan-type mafic-ultramafic intrusion, suprasubduction zone and boninitic) and MORB affinities (Fig. 3.18; Appendix 2.4; see Kiseleva and Zhmodik, 2017; Lay et al., 2017; Xiong et al., 2017). Moreover, the chromites in Fig. 3.18b plot along a similar trend to the Bird River Sill chromites in Fig. GS-3-7 of Yang

and Gilbert (2014), who proposed that the Bird River Sill formed in a back-arc setting. These findings are in accordance with the subduction zone geodynamic setting proposed here for the Bird River Sill and Northern Lamprey Falls Formation and strengthens the link between subduction zones, Archean megacrystic anorthosite-bearing layered intrusions and hydrous primitive arc tholeiitic magma generation.

The dacites of the Peterson Creek Formation and the high-magnesian andesites and greywackes of the Bird River Formation have negative Nb and Ti anomalies and steep, LREE-enriched patterns that are consistent with a continental arc geodynamic setting (Pearce and Peate, 1995; Murphy, 2007; Pearce, 2008; Gilbert et al., 2008). The continental arc affinity of the Peterson Creek Formation dacites and Bird River Formation high-magnesian andesites is further suggested by their occurrence as pyroclastic flows (Gilbert et al., 2008, and references therein). This interpretation is supported by a continental arc setting being proposed for the Peterson Creek and Bird River formations by Gilbert et al. (2008) on the basis of trace element geochemistry and field relationships. The quartzitic greywackes of the Booster Lake Formation have very similar geochemical characteristics to these lithologies, indicating that they were likely derived from igneous rocks that formed in a continental arc geodynamic setting (Gilbert et al., 2008). The tonalites of the Maskwa Lake TTG Batholith I have pronounced negative Nb and Ti anomalies and steep, LREE-enriched patterns, consistent with a continental arc setting (Pearce and Peate, 1995; Murphy, 2007; Pearce, 2008; Yang et al., 2011, 2012, 2013; Yang, 2014).

Based on the findings of this study and the existing literature, the southern arm of the Bird River greenstone belt formed at a continental arc to intra-arc rift or back-arc setting along the southern margins of the Maskwa Lake microcontinent and what will henceforth be referred to as the Birse Lake juvenile continental arc (Gilbert et al., 2008; Duguet et al., 2009). It is not known whether the Maskwa Lake microcontinent was derived from the rifting of the North Caribou terrane to the north or the Winnipeg River terrane to the south or whether it is an isolated micro-continental block. The first interpretation is more plausible with the North Caribou terrane being the most likely source of this cratonic block based on its contemporaneity with the Maskwa Lake microcontinent (Card and Poulsen, 1998; Gilbert et al., 2008; Percival et al., 2012). Continental arc TTG magmatism lasted from 2940 Ma to 2850 Ma in the North Caribou terrane, with the occurrence of 2858 Ma to 2782 Ma continental arc magmatism recorded by the Maskwa Lake TTG Batholith I, suggesting that continental arc magmatism occurred along the southern margin of the North Caribou terrane from 2940 Ma to 2782 Ma

(Wang, 1993; Card and Poulsen, 1998; Percival et al., 2006, 2012; Gilbert, 2008; Gilbert et al., 2008; Duguet et al., 2009; Yang et al., 2011, 2012, 2013). The rifting and creation of the Maskwa Lake microcontinent from the North Caribou terrane occurred at ~2743 Ma, resulting in the formation of the Bird River Sill and Northern Lamprey Falls Formation in a continental back-arc basin (Fig. 3.17; Wang, 1993; Gilbert et al., 2008; Duguet et al., 2009). The Bird River greenstone belt subsequently formed along and around the margins of the Maskwa Lake microcontinent and Birse Lake juvenile continental arc, which most likely subsequently collided during the Uchian Orogeny at ~2698 Ma (Gilbert et al., 2008; Duguet et al., 2009; Percival et al., 2012). Structural evidence indicates that the nearby Birse Lake arc was thrusted over the edge of the Maskwa Lake microcontinent during the Uchian Orogeny (Gilbert et al., 2008; Duguet et al., 2009; Percival et al., 2012) with the Booster Lake Shear Zone representing a suture zone that marks this collisional event.

Models for the geodynamic evolution of the Bird River greenstone belt have been proposed by a number of workers recently (e.g., Gilbert, 2008; Gilbert et al., 2008; Yang et al., 2011); however, the geodynamic evolution of the Bird River subprovince and its relationship with adjacent subprovinces in the Superior Province have largely been neglected (Percival et al., 2006, 2012). Based on the findings of this study, the Bird River Sill and the Northern Lamprey Falls Formation mark a transition from a continental arc to a continental back-arc geodynamic setting along the southern active margin of the North Caribou terrane at ~2743 Ma (Fig. 3.17). The continental arc affinities of the Peterson Creek Formation dacites, Bird River Formation high-magnesian andesites and greywackes, Booster Lake Formation greywackes and Maskwa Lake TTG Batholith I tonalites suggest that continental arc magmatism occurred along the southern margin of the North Caribou terrane from 2844 Ma to 2782 Ma and the Maskwa Lake microcontinent from 2731 Ma to 2725 Ma, resulting in the growth of the Bird River greenstone belt (Fig. 16; Percival et al., 2012; Yang et al., 2012, 2013). Despite the continental arc setting of the Peterson Creek and Bird River formations, crustal contamination was not involved in their petrogenesis (Gilbert et al., 2008).

The geodynamic evolution and location of the Maskwa Lake microcontinent and Birse Lake juvenile continental arc between the Winnipeg River subprovince to the south and the English River subprovince to the north suggest that the Bird River subprovince may be analogous to the setting of the Cretaceous-Tertiary Kohistan arc in the Pakistan Himalaya. The Kohistan arc is wedged between the Indian plate to the south and the Eurasian plate to the north and is separated from these plates by suturing thrust faults (Fig. 3.19) (Treloar et al., 1996; Peterson

and Treloar, 2004; Jagoutz et al., 2007; Petterson, 2018), a scenario that bears some similarities to the Bird River subprovince and its adjacent, larger subprovinces.

Based on field observations and geochemical data, the Bird River Sill and Bird River greenstone belt seem to conform to the definition of Dilek and Furnes (2011) for an ophiolite as "a suite of temporally and spatially associated ultramafic to felsic rocks related to separate melting episodes and processes of magmatic differentiation in particular tectonic environments." This definition is more reflective of the lithological, structural, and geochemical complexity of ophiolites than the typical Penrose ophiolite (Anonymous, 1972) definition (Dilek and Furnes, 2011). Furthermore, Furnes et al. (2015) concluded that Precambrian greenstone belts represent different ophiolite types. Collectively, geological observations and relationships indicate that the Bird River Sill and the southern Bird River greenstone belt represent a dismembered subduction-related Archean ophiolite that marks a suture zone between the Winnipeg River subprovince and the Maskwa Lake microcontinent. The subduction zone setting proposed here for the Bird River Sill and Bird River greenstone belt corroborates recent interpretations proposing that Archean granitoid-greenstone terrains formed in convergent margin settings (Windley and Garde, 2009; Furnes et al., 2015; Lodge et al., 2015; Furnes and Dilek, 2017; Cox et al., 2018; Hastie and Fitton, 2019).

3.9. Conclusions

1. The megacrystic anorthosites and leucogabbros of the Neoarchean Bird River Sill are quite well preserved. The Bird River Sill gabbros, peridotites and chromitites, Neoarchean Northern Lamprey Falls Formation basalts and synvolcanic gabbro, Peterson Creek Formation dacites, Bird River Formation high-magnesian andesites and greywackes, Booster Lake Formation quartzitic greywackes and the Mesoarchean Maskwa Lake TTG Batholith I tonalites underwent variable metamorphic recrystallisation and hydrothermal alteration. The Bird River Sill peridotites were strongly serpentinised and sheared during alteration and deformation, causing their Sm-Nd and Pb isotopic systems to be reset.
2. The Bird River Sill anorthosites and leucogabbros formed through shallow crystallisation of a hydrous, Ca- and Al-rich tholeiitic parental magma that fractionated from a hydrous primitive arc tholeiitic parental magma.

3. The Bird River Sill gabbros were cogenetic with the Northern Lamprey Falls basalts and synvolcanic gabbro but not the Bird River Sill anorthosites, leucogabbros and peridotites, which were not cogenetic with the latter.
4. The parental magmas to the Bird River Sill and Northern Lamprey Falls Formation basalts and gabbro were derived by variable partial melting of variably depleted mantle sources. Samples with $\varepsilon_{Nd\ (2743\ Ma)} < +2.0$ may reflect variable minor crustal contamination from the 2858-2782 Ma Maskwa Lake microcontinent.
5. The parental magma to the Bird River Formation high-magnesian andesites was derived by partial melting of subducting oceanic crust and slab sediments and extensively interacted with sub-arc mantle wedge peridotite. The parental magmas to the Peterson Creek Formation dacites and Maskwa Lake TTG Batholith I tonalites crystallised from parental magmas derived by partial melting of juvenile lower arc crust hydrated basalts.
6. The Bird River Sill and Northern Lamprey Falls Formation basalts and gabbro formed in a back-arc geodynamic setting at the southern active continental margin of the North Caribou terrane. The Peterson Creek Formation dacites and Bird River Formation high-magnesian andesites and Maskwa Lake TTG Batholith I tonalites formed in a continental arc setting along the southern active continental margins of the Maskwa Lake microcontinent and North Caribou terrane, respectively.
7. The southern Bird River greenstone belt records back-arc rifting of the southern active continental margin of the North Caribou terrane, the consequent formation of the Maskwa Lake microcontinent, and accretion of the Birse Lake juvenile continental arc to this microcontinent.
8. The Bird River Sill and the southern Bird River greenstone belt represent a dismembered Archean subduction-related ophiolite that marks an Archean suture zone between the Winnipeg River subprovince and the Maskwa Lake microcontinent.

3.10. References

Anonymous, 1972. Penrose field conference on Ophiolites. Geotimes 17, 24-25.

Ashwal, L.D., 1993. Anorthosites. Minerals and Rocks Series 21, Springer-Verlag: Berlin, 422p.

Ashwal, L.D., 2010. The temporality of anorthosites. The Canadian Mineralogist 48, 711-728.

Ashwal, L.D., Bybee, G.M., 2017. Crustal evolution and the temporality of anorthosites. Earth Science Reviews 173, 307-330.

Attarzadeh, P., Karimi, M., Yazdi, M., Khankahdani, K.N., 2017. Geochemistry of chromitites in eastern part of Neyriz Ophiolite Complex (Southern Iran). Open Journal of Geology 7, 213-233.

Baadsgaard, H., Černý, P., 1993. Geochronological studies in the Winnipeg River pegmatite populations, southeastern Manitoba. Geological Association of Canada-Mineralogical Association of Canada, Joint Annual Meeting, Program with Abstracts 18, A5.

Burnham, O.M., 2017. Inductively coupled plasma mass spectrometry analysis of trace elements in geological sample after *Aqua Regia* extraction at the Geoscience Laboratories: Revised capabilities resulting from new instrumentation In: Summary of Field Work and Other Activities 2017. Ontario Geological Survey, Open File Report 6333, 31-1 - 31-10.

Card, K.D., Poulsen, K.H., 1998. Geology and mineral deposits of the Superior Province of the Canadian shield. In: Lucas, S.B., St-Onge, M.R. (eds.). Geology of the Precambrian Superior and Grenville Provinces and Precambrian Fossils in North America. Geological Survey of Canada, Geology of Canada 7, 13-194.

Condie, K.C., 2005. TTGs and adakites: are they both slab melts?. Lithos 80 (1-4), 33-44.

Cox, D., Kerr, A.C., Hastie, A.R., Kakar, M.I., 2018. Petrogenesis of plagiogranites in the Muslim Bagh Ophiolite, Pakistan: implications for the generation of Archean continental crust. Geological Magazine 156(5), 874-888.

Claeson, D.T., Meurer, W.P., 2004. Fractional crystallization of hydrous basaltic "arc-type" mamas and the formation of amphibole-bearing gabbroic cumulates. Contributions to Mineralogy and Petrology 147, 288-304.

Deer, W.A., Howie, R.A., Zussman, J., 2013. An Introduction to the Rock-Forming Minerals. 3rd edition. The Mineralogical Society: London, 498p.

Dilek, Y., Furnes, H., 2011. Ophiolite genesis and global tectonics: Geochemical and tectonic fingerprinting of ancient oceanic lithosphere. GSA Bulletin 123(3-4), 387-411.

Dostal, J., Mueller, W.U., 1997. Komatiite flooding of a rifted Archean rhyolitic arc complex: geochemical signature and tectonic significance of the Stoughton-Roquemaure Group, Abitibi greenstone belt, Canada. The Journal of Geology 105(5), 545-564.

Duguet, M., Gilbert, H.P., Corkery, M.T., Lin, S., 2006. Geology and structure of the Bird River Belt, southeastern Manitoba (NTS 52L5 and 6). In: Report of Activities 2006, Manitoba Science, Technology, Energy and Mines, Manitoba Geological Survey, 170-183.

Duguet, M., Lin, S., Davis, D.W., Corkery, M.T., McDonald, J., 2009. Long-lived transpression in the Archean Bird River greenstone belt. western Superior Province, southeastern Manitoba. Precambrian Research 174(3-4), 381-407.

Duguet, M., Lin, S., Gilbert, H.P., Corkery, M.T, 2005. Preliminary results of geological mapping and structural analysis of the Bird River greenstone belt, southeastern Manitoba (NTS 52L5 and 6). In: Report of Activities 2005. Manitoba Industry, Economic Development and Mines, Manitoba Geological Survey, 117-124.

Duguet, M., Lin, S., Gilbert, H.P., Corkery, M.T., 2007. Structural geology and kinematic evolution of the Bird River greenstone belt, English River Subprovince, Manitoba (NTS 52L5, 6). In: Report of Activities 2007. Manitoba Science, Technology, Energy and Mines, Manitoba Geological Survey, 144-154.

Escuder-Viruete, J., Castillo-Carrión, M., Pérez-Estaún, A., 2014. Magmatic relationships between depleted mantle harzburgites, boninitic cumulate gabbros and subduction-related tholeiitic basalts in the Puerto Plata ophiolitic complex, Dominican Republic: Implications for the birth of the Caribbean island-arc. Lithos 196, 261-280.

Frei, R., Polat, A., 2013. Chromium isotope fractionation during oxidative weathering - implications from the study of a Paleoproterozoic (ca. 1.9 Ga) paleosol, Schreiber Beach, Ontario, Canada. Precambrian Research 224, 434-453.

Furnes, H., de Wit, M., Dilek, Y., 2014. Four billion years of ophiolites reveal secular trends in oceanic crust formation. Geoscience Frontiers 5, 571-603.

Furnes, H., Dilek, Y., 2017. Geochemical characterization and petrogenesis of intermediate to silicic rocks in ophiolites: A global synthesis. Earth-Science Reviews 166, 1-37.

Furnes, H., Dilek, Y., de Wit, M., 2015. Precambrian greenstone sequences represent different ophiolite types. Gondwana Research 27, 649-685.

Gilbert, H.P., 2005. Geological investigations in the Bird River area, southeastern Manitoba (parts of NTS 52L5N and 6N). In: Report of Activities 2005. Manitoba Industry, Economic Development and Mines, Manitoba Geological Survey, 125-139.

Gilbert, H.P., 2006. Geological investigations in the Bird River area, southeastern Manitoba (parts of NTS 52L5N and 6). In: Report of Activities 2006. Manitoba Science, Technology, Energy and Mines, Manitoba Geological Survey, 184-205.

Gilbert, H.P., 2007. Stratigraphic investigations in the Bird River greenstone belt, Manitoba (part of NTS 52L5, 6). In: Report of Activities 2007.Manitoba Science, Technology, Energy and Mines, Manitoba Geological Survey, 129-143.

Gilbert, H.P., 2008. Stratigraphic investigations in the Bird River greenstone belt, Manitoba (part of NTS 52L5, 6). In: Report of Activities 2008. Manitoba Science, Technology and Mines, Manitoba Geological Survey, 121-138.

Gilbert, H.P., Davis, D.W., Duguet, M., Kremer, P., Mealin, C.A., MacDonald, J., 2008. Geology of the Bird River Belt, southeastern Manitoba (parts of NTS 52L5, 6). Manitoba Science, Technology, Energy and Mines, Manitoba Geological Survey, Geoscientific Map MAP2008-1, scale 1:50,000.

Gill, R.G., 2010. Igneous Rocks and Processes: A Practical Guide. John Wiley & Sons Ltd.: Chichester, U.K., 428p.

Golowin, R., Portnyagin, M., Hoernle, K., Sobolev, A., Kuzmin, D., Werner, R., 2017. The role and conditions of second-stage mantle melting in the generation of low-Ti tholeiites and boninites: the case of the Manihiki Plateau and the Troodos ophiolite. Contributions to Mineralogy and Petrology 172(11-12): 104.

Good, D., Mealin, C., Walford, P., 2009. Geology of the Ore Fault Ni-Ce deposit, Bird River Sill Complex, Manitoba. Exploration and Mining Geology 18(1-4), 41-57.

Guice, G.L., McDonald, I., Hughes, H.S.R., Schlatter, D.M., Goodenough, K.M., MacDonald, J.M., Faithfull, J.W., 2018. Assessing the validity of negative high field strength-element anomalies as a proxy for Archaean subduction: Evidence from the Ben Strome Complex, NW Scotland. Geosciences 8(9), 338, 1-32.

Hargreaves, J.C., 2017. Summary of quality control data for the Geoscience Laboratories methods EMP-100, IMC-100, 1MO-100 and ISE-R01. instrumentation In: Summary of Field Work and Other Activities 2017. Ontario Geological Survey, Open File Report 6333, 32-1 - 32-15.

Hartlaub, R.P., Heaman, L.M., Ashton, K.E., Chacko, T., 2004. The Archean Murmac Bay Group: evidence for a giant archean rift in the Rae Province, Canada. Precambrian Research 131(3-4), 345-372.

Hartlaub, R.P., Kuiper, Y.D., 2004. Geology of central and north Split Lake (parts of NTS 54D4, 5 and 64A1, 8), Manitoba. In: Manitoba Geological Survey, Preliminary Map PMAP2004-1, scale 1:25000.

Hastie, A.R., Fitton, J.G., 2019. Eoarchean tectonics: New constraints from high pressure-temperature experiments and mass balance modelling. Precambrian Research 325, 20-38.

Hébert, R., Rezard, R., Guilmette, C., Dostal, J., Wang, C.S., Liu, Z.F., 2012. The Indus-Yarlung-Zangbo ophiolites from Nanga Parbat to Namche Barwa syntaxes, southern Tibet:

First synthesis of petrology, geochemistry, and geochemistry with incidences on geodynamic reconstruction of Neo-Tethys. Gondwana Research 22, 377-397.

Henry, P., Stevenson, R.K., Gariepy, C., 1998. Late Archean mantle composition and crustal growth in the Western Superior Province of Canada: neodymium and lead isotopic evidence from the Wawa, Quetico and Wabigoon subprovinces. Geochimica et Cosmochimica Acta 62, 143-157.

Hoffmann, J.E., Münker, C., Næraa, T., Rosing, M.T., Herwartz, D., Garbe-Schönberg, D., Svahnberg, H., 2011. Mechanisms of Archean crust formation inferred from high-precision HFSE systematics in TTGs. Geochimica et Cosmochimica Acta 75, 4157-4178.

Hoffmann, J.E., Svahnberg, H., Piazolo, S., Scherstén, A., Münker, C., 2012. The geodynamic evolution of Mesoarchean anorthosite complexes inferred from the Naajat Kuuat Complex, southern West Greenland. Precambrian Research 196-197, 149-170.

Hofmann, A.W., 1988. Chemical differentiation of the Earth: the relationship between mantle, continental crust, and oceanic crust. Earth and Planetary Science Letters 90, 297-314.

Hollings, P., Kerrich, R., 2004. Geochemical systematics of tholeiites from the 2.86 Ga Pickle Crow assemblage, northwestern Ontario: arc basalts with positive and negative Nb–Hf anomalies. Precambrian Research 134(1-2), 1-20.

Huang, H., Polat, A., Fryer, B.J., 2013. Origin of Archean tonalite-trondhjemite-granodiorite (TTG) suites and granites in the Fiskenæsset region, southern West Greenland: Implications for continental growth. Gondwana Research 23, 452-470.

Ishizuka, O., Kimura, J.I., Li, Y.B., Stern, R.J., Reagan, M.K., Taylor, R.N., Ohara, Y., Bloomer, S.H., Ishii, T., Hargrove III, U.S., Haraguchi, S., 2006. Early stages in the evolution of Izu–Bonin arc volcanism: New age, chemical, and isotopic constraints. Earth and Planetary Science Letters 250(1-2), 385-401.

Ishizuka, O., Tani, K., Reagan, M.K., 2014. Izu-Bonin-Mariana forearc crust as a modern ophiolite analogue. Elements 10(2), 115-120.

Ivanic, T.J., Wingate, M.T.D., Kirkland, C.L., Van Kranendonk, M.J., Wyche, S., 2010. Age and significance of voluminous mafic–ultramafic magmatic events in the Murchison Domain, Yilgarn Craton. Australian Journal of Earth Sciences 57(5), 597-614.

Jagoutz, O., Müntener, O., Ulmer, P., Pettke, T., Burg, J.-P., Dawood, H., Hussain, S., 2007. Petrology and mineral chemistry of lower crustal intrusions: the Chilas Complex, Kohistan (NW Pakistan). Journal of Petrology 48(10), 1895-1953.

Kaczmarek, M.-A., Jonda, L., Davies, H.L., 2015. Evidence of melting, melt percolation and deformation in a supra-subduction zone (Marum ophiolite complex, Papua New Guinea). Contributions to Mineralogy and Petrology 170: 19.

Kay, R.W., 1978. Aleutian magnesian andesites: Melts from subducted Pacific Ocean crust. Journal of Geothermal and Volcanic Research 4, 117-132.

Kelemen, P.B., Yogodzinski, G.M., Scholl, D.W., 2003. Along-strike variation in the Aleutian island arc: Genesis of high Mg# andesite and implications for continental crust. In: Eiler, J. (ed.). Inside The Subduction Factory. American Geophysical Union, Geophysical Monograph Series 138, 223-276.

Kiseleva, O., Zhmodik, S., 2017. PGE mineralization and melt composition of chromitites in Proterozoic ophiolite complexes of Eastern Sayan, Southern Siberia. Geoscience Frontiers 8(4), 721-731.

Kusky, T.M., Windley, B.F., Polat, A., 2018. Geological evidence for the operation of plate tectonics throughout the Archean: Records from Archean paleo-plate boundaries. Journal of Earth Science 29(6), 1291-1303.

Lahaye, Y., Arndt, N., 1996. Alteration of a komatiite flow from Alexo, Ontario, Canada. Journal of Petrology 37, 1261-1284.

Lahaye, Y., Arndt, N., Byerly, G., Chauvel, C., Fourcade, S., Gruau, G., 1995. The influence of alteration on the trace-element and Nd isotopic compositions of komatiites. Chemical Geology 126, 43-64.

Lay, A., Graham, I., Cohen, D., Privat, K., González-Jimenez, J.M., Belousova, E., Barnes, S.J., 2017. Ophiolitic chromitites of Timor Leste: Their composition, platinum group element geochemistry, mineralogy, and evolution. The Canadian Mineralogist 55(5), 875-908.

Leake, B.E., Woolley, A.R., Arps, C.E.S., Birch, W.D., Gilbert, M.C., Grice, J.D., Hawthorne, F.C., Kato, A., Kisch, H.J., Krivovichev, V.G., Linthout, K., Laird, J., Mandarino, J.A., Maresch, W.V., Nickel, E.H., Rock, N.M.S., Schumacher, J.C., Smith, D.C., Stephenson, N.C.N., Ungaretti, L., Whittaker, E.J.W., Youzhi, G., 1997. Nomenclature of amphiboles: Report of the subcommittee on amphiboles of the International Mineralogical Association, Commission on New Minerals and Mineral Names. The Canadian Mineralogist 35, 219-246.

Lodge, R.W., Gibson, H.L., Stott, G.M., Franklin, J.M., Hudak, G.J., 2015. Geodynamic setting, crustal architecture, and VMS metallogeny of ca. 2720 Ma greenstone belt

assemblages of the northern Wawa subprovince, Superior Province. Canadian Journal of Earth Sciences 52(3), 196-214.

Martin, H., Moyen, J.F., 2002. Secular changes in tonalite-trondhjemite-granodiorite composition as markers of the progressive cooling of Earth. Geology 30(4), 319-322.

Martin, H., Smithies, R.H., Rapp, R., Moyen, J.F., Champion, D., 2005. An overview of adakite, tonalite–trondhjemite–granodiorite (TTG), and sanukitoid: relationships and some implications for crustal evolution. Lithos 79(1-2), 1-24.

Mealin, C.A., 2008. Geology, geochemistry and Cr-Ni-Cu-PGE mineralization of the Bird River sill: evidence for a multiple intrusion model. University of Waterloo, Waterloo, Ontario, Unpublished M.Sc. thesis, 155p.

Meurer, W.P., Claeson, D.T., 2002. Evolution of crystallizing interstitial liquid in an arc-related cumulate determined by LA-ICP-MS mapping of a large amphibole oikocryst. Journal of Petrology 43, 607-629.

Moghadam, H.S., Zaki Khedr, M., Chiaradia, M., Stern, R.J., Bakhshizad, F., Arai, S., Ottley, C.J., Tamura, A., 2014. Supra-subduction zone magmatism of the Neyriz ophiolite, Iran: constraints from geochemistry and Sr-Nd-Pb isotopes. International Geology Review 56(11), 1395-1412.

Moyen, J.F., Martin, H., 2012. Forty years of TTG research. Lithos 148, 312-336.

Murphy, J.B., 2007. Igneous Rock Associations 8. Arc magmatism II: Geochemical and isotopic characteristics. Geoscience Canada 34(1), 7-35.

Paixão, M.A.P., Oliveira, E.P., 1998. The Lagoa da Vaca complex: an Archaean layered anorthosite body on the western edge of the Uauá Block, Bahia, Brazil. Revista Brasileira de Geociencias 28(2), 201-208.

Pearce, J.A., 2008. Geochemical fingerprinting of oceanic basalts with applications to ophiolite classification and the search for Archean oceanic crust. Lithos 100, 14-48.

Pearce, J.A., Peate, D.W., 1995. Tectonic implications of the composition of volcanic arc magmas. Annual Review of Earth and Planetary Sciences 23, 251-286.

Peck, D.C., Cameron, H.D.M., Layton-Matthews, D., Bishop, A., 1996. Geological investigations of anorthosite, gabbro and pyroxenite occurrences in the Pikwitonei granulated domain and the Cross Lake region (parts of NTS 63I/6, 63J/7, 63J/8, 63P/5, 63P/6, 63P/7, 63P/8, 63P/9, 63P/10, 63P/11 and 63P/12). In: Report of Field Activities 1996. Manitoba Energy and Mines, Minerals Division, 85-90.

Peck, D.C., Halden, N.M., Jobin-Bevans, S., Cameron, H.D.M., Theyer, P., 1999a. Summary of metallogenetic and petrogenetic features of Archean anorthosites and associated mafic

and ultramafic rocks in the Superior Province, Manitoba (parts of NTS 63I, 63J, 63P and 64A). In: Report of Activities 1999. Manitoba Industry, Trade and Mines, Geological Services, 94-96.

Peck, D.C., Theyer, P., 1998. PGE-copper-nickel potential of mafic-ultramafic intrusions in the Bird River greenstone belt (parts of NTS 52L). In: Report of Activities 1998. Manitoba Energy and Mines, Geological Services, 151-160.

Percival, J.A., 2007. Eo- to Mesoarchean terranes of the Superior Province and their tectonic context. In: Van Kranendonk, M.J., Smithies, R.H., Bennett, V.C. (eds.). Earth's Oldest Rocks. Elsevier BV: Amsterdam, Developments in Precambrian Geology 15, 1065-1085.

Percival, J.A., Sanborn-Barrie, M., Stott, G.M., Helmstaedt, H., Skulski, T., White, D.J., 2006. Tectonic evolution of the Western Superior Province from NATMAP and Lithoprobe studies. Canadian Journal of Earth Sciences 43, 1085-1117.

Percival, J.A., Skulski, T., Sanborn-Barrie, M., Stott, G.M., Leclair, A.D., Corkery, M.T., Boily, M., 2012. Geology and tectonic evolution of the Superior Province, Canada. Tectonic styles in Canada: The Lithoprobe Perspective, Special Paper 49, 321-378.

Petterson, M.G., 2018. The plutonic crust of Kohistan and volcanic crust of Kohistan-Ladakh, north Pakistan/India: lessons learned from deep and shallow arc processes. In: Treloar, P.J., Searle, M.P. (eds.). Himalayan Tectonics: A Modern Synthesis. Geological Society, London, Special Publications 483, SP483-4.

Petterson, M.G., Treloar, P.J., 2003. Volcanostratigraphy of arc volcanic sequences in the Kohistan arc, North Pakistan: volcanism within island arc, back-arc-basin, and intra-continental tectonic settings. Journal of Volcanology and Geothermal Research 130, 147-178.

Piaia, P., Oliveira, E.P., Valeriano, C.M., 2017. The 2.58 Ga São José do Jacuipe gabbro-anorthosite stratiform complex, Itabuna-Salvador-Curaçá Orogen, São Francisco Craton, Brazil: Root of the Neoarchaean Caraiba continental arc? Journal of South American Earth Sciences 79, 326-341.

Polat, A., Appel, P.W., Fryer, B., Windley, B., Frei, R., Samson, I.M. and Huang, H., 2009. Trace element systematics of the Neoarchean Fiskenæsset anorthosite complex and associated meta-volcanic rocks, SW Greenland: evidence for a magmatic arc origin. Precambrian Research 175(1-4), 87-115.

Polat, A., Fryer, B.J., Appel, P.W.U., Kalvig, P., Kerrich, R., Dilek, Y., Yang, Z., 2011. Geochemistry of anorthositic differentiated sills in the Archean (~2970 Ma) Fiskenæsset

Complex, SW Greenland: Implications for parental magma compositions, geodynamic setting, and secular heat flow in arcs. Lithos 123, 50-72.

Polat, A., Kerrich, R., 2006. Reading the geochemical fingerprints of Archean hot subduction volcanic rocks: Evidence for accretion and crustal recycling in a mobile tectonic regime. In: Benn, K., Mareschal, J.C., Condie, K.C. (eds.). Archean Geodynamics and Environments. American Geophysical Union, Geophysical Monograph Series 164, 189-213.

Polat, A., Kokfelt, T., Burke, K.C., Kusky, T., Bradley, D., Dziggel, A., Kolb, J., 2016. Lithological, structural, and geochemical characteristics of the Mesoarchean Târtoq greenstone belt, South-West Greenland, and the Chugach-Prince William accretionary complex, southern Alaska: Evidence for uniformitarian plate-tectonic processes. Canadian Journal of Earth Sciences 53, 1336-1371.

Polat, A., Longstaffe, F.J., Frei, R., 2018a. An overview of anorthosite-bearing layered intrusions in the Archaean craton of southern West Greenland and the Superior Province of Canada: implications for Archaean tectonics and the origin of megacrystic plagioclase. Geodinamica Acta 30(1), 84-99.

Polat, A., Longstaffe, F.J., Weisener, C., Fryer, B.J., Frei, R., Kerrich, R., 2012. Extreme element mobility during transformation of Neoarchean (ca. 2.7 Ga) pillow basalts to a Paleoproterozoic (ca. 1.9 Ga) paleosol, Schreiber Beach, Ontario, Canada. Chemical Geology 326-327, 145-173.

Rollinson, H., Reid, C., Windley, B.F., 2010. Chromitites from the Fiskenæsset anorthositic complex, West Greenland: clues to late Archaean mantle processes. In: Kusky, T.M., Zhai, M.-G., Xiao, W. (eds.). The Evolving Continents: Understanding Processes of Continental Growth. Geological Society, London, Special Publications 338, 197-212.

Ross, P.-S., Bédard, J.H., 2009. Magmatic affinity of modern and ancient subalkaline volcanic rocks determined from trace-element discriminant diagrams. Canadian Journal of Earth Sciences 46, 823-839.

Saccani, E., 2015. A new method of discriminating different types of post-Archean ophiolitic basalts and their tectonic significance using Th-Nb and Ce-Dy-Yb systematics. Geoscience Frontiers 6(4), 481-501.

Sandeman, H.A., Brown, J., Studnicki-Gizbert, C., MacHattie, T., Hyde, D., Johnstone, S., Greiner, E., Plaza, D., 2001. Bedrock mapping in the Committee Bay belt, Laughland Lake area, central mainland, Nunavut. Natural Resources Canada, Geological Survey of Canada, 28p.

Santosh, M., Shaji, E., Tsunogae, T., Mohan, M.R., Satyanarayanan, M., Horie, K., 2013. Suprasubduction zone ophiolite from Agali hill: petrology, zircon SHRIMP U–Pb geochronology, geochemistry and implications for Neoarchean plate tectonics in southern India. Precambrian Research 231, 301-324.

Sarkarinejad, K., 2003. Structural and microstuctural analysis of a palaeo-transform fault zone in the Neyriz ophiolite, Iran. In: Dilek, Y., Robinson, P.T. (eds.). Ophiolites in Earth History. Geological Society, London, Special Publications 218, 129-145.

Saunders, A.D., Tarney, J., Weaver, S.D., 1980. Transverse geochemical variations across the Antarctic Peninsula: Implications for the genesis of calc-alkaline magmas. Earth and Planetary Science Letters 46, 344-360.

Scoates, R.F.J., 1983. A preliminary stratigraphic examination of the ultramafic zone of the Bird River Sill, southeastern Manitoba. In: Report of Field Activities 1983. Manitoba Department of Energy and Mines, Mineral Resources Division, 70-83.

Scoates, J.S., Scoates, R.F.J., 2013. Age of the Bird River Sill, southeastern Manitoba, Canada, with implications for the secular evolution of layered intrusion-hosted stratiform chromite mineralization. Economic Geology 108, 895-907.

Scoates, R.F.J., Williamson, B.L., Eckstrand, O.R., Duke, J.M., 1989. Stratigraphy of the Bird River Sill and its carboniferous zone, and preliminary geochemistry of the chromitite layers and PGE-bearing units, Chrome property, Manitoba. In: Galley, A.G. (ed.). Investigations by the Geological Survey of Canada in Manitoba and Saskatchewan during the 1984-1989 Mineral Development Agreements. Geological Survey of Canada, Open File 2133, 69-82.

Sotiriou, P., Polat, A., Frei, R., 2019. Petrogenesis and geodynamic setting of the Neoarchaean Haines Gabbroic Complex and Shebandowan greenstone belt, Southwestern Superior Province, Ontario, Canada. Lithos 324-325, 1-19.

Souders, A.K., Sylvester, P.J., Myers, J.S., 2013. Mantle and crustal sources of Archean anorthosite: a combined in situ isotopic study of Pb-Pb in plagioclase and Lu-Hf in zircon. Contributions to Mineralogy and Petrology 165, 1-24.

Spath, C.S. III, Lesher, C.M., Houlé, M.G., 2015. Hybridized ultramafic rocks in the Black Label hybrid zone of the Black Thor intrusive complex, McFaulds Lake greenstone belt, Ontario, In: Ames, D.E., Houlé, M.G. (eds.). Targeted Geoscience Initiative 4: Canadian Nickel-Copper-Platinum Group Elements-Chromium Ore Systems - Fertility, Pathfinders, New and Revised Models. Geological Survey of Canada, Open File 7856, 103–114.

Stern, R.J., de Wit, M.J., 2003. Rocas Verdes ophiolites, southernmost South America: remnants of progressive stages of development of oceanic-type crust in a continental margin

back-arc basin. In: Dilek, Y., Robinson, E.T. (Eds.), Ophiolites in Earth History: Geological Society of London Special Publication 218, 665–683.

Stern, R.J., Fouch, M.J., Klemperer, S.L., 2003. An overview of the Izu-Bonin-Mariana subduction factory. In: Eiler, J. (ed.). Inside The Subduction Factory. American Geophysical Union, Geophysical Monograph 138, 175-222.

Sun, S.S., McDonough, W.F., 1989. Chemical and isotopic systematics of oceanic basalts: implications for mantle composition and processes. In: Saunders, A.D., Norry, M.J. (eds.). Magmatism in the Ocean Basins. Geological Society of London: London, Special Publication 42, 313-345.

Suzuki, K., Tatsumi, Y., 2006. Re-Os systematics of high-Mg andesites and basalts from the Setouchi volcanic belt, SW Japan: Implications for interaction between wedge mantle and slab-derived melt. Geochemical Journal 40, 297-307.

Tatsumi, Y., Hanyu, T., 2003. Geochemical modelling of dehydration and partial melting of subducting lithosphere: Toward a comprehensive understanding of high-Mg andesite formation in the Setouchi volcanic belt, SW Japan. Geochemistry, Geophysics, Geosystems 4 (9), doi: 10.1029/2003GC000530.

Taylor, S.R., McLennan, S.M., 1985. The continental crust: its composition and evolution. Blackwell: Oxford, 312p.

Theyer, P., 1991. Petrography, chemistry, and distribution of platinum and palladium in ultramafic rocks of the Bird River Sill, SE Manitoba, Canada. Mineralium Deposita 26, 165-174.

Todt, W., Cliff, R.A., Hanser, A., Hofmann, A.W., 1993. Re-calibration of NBS lead standards using $^{202}Pb+ ^{205}Pb$ double spike. Terra Abstracts 5, 396.

Treloar, P.J., Petterson, M.G., Jan, M.Q., Sullivan, M.A., 1996. A re-evaluation of the stratigraphy and evolution of the Kohistan arc, Pakistan Himalaya: implications for magmatic and tectonic arc-building processes. Journal of the Geological Society of London 153, 681-693.

Trueman, D.L., 1971. Petrological, structural and magnetic studies of a layered basic intrusion - Bird River Sill, Manitoba. University of Manitoba, Winnipeg, Manitoba, Unpublished M.Sc. thesis, 67p.

Vrevskii, A.B., 2016. Age and sources of the anorthosites of the Neoarchean Kolmozero-Voron’ya greenstone belt (Fennoscandian Shield). Petrology 24(6), 527-542.

Wang, X., 1993. U-Pb zircon geochronology study of the Bird River Greenstone Belt, Southeastern Manitoba. University of Windsor, Windsor, Ontario, Unpublished M.Sc. thesis, 121p.

Winchester, J.A., Floyd, P.A., 1977. Geochemical discrimination of different magmas series and their differentiation products using immobile elements. Chemical Geology 20, 325-343.

Windley, B.F., 1995. The evolving continents. 3rd edition. John Wiley & Sons: Chichester, UK, 526p.

Windley, B.F., Garde, A.A., 2009. Arc-generated blocks with crustal sections in the North Atlantic craton of West Greenland: Crustal growth in the Archean with modern analogues. Earth Science Reviews 93, 1-30.

Woelki, D., Regelous, M., Haase, K.M., Romer, R.H., Beier, C., 2018. Petrogenesis of boninitic lavas from the Troodos Ophiolite, and comparison with Izu–Bonin–Mariana fore-arc crust. Earth and Planetary Science Letters 498, 203-214.

Wu, T., Polat, A., Fryer, B.J., Yang, K., Kusky, T. M., 2016. Geochemistry, Nd, Pb and Sr isotope systematics of the Neoarchean Bad Vermilion Lake Greenstone Belt and spatially associated granitic rocks, Western Superior Province, Canada. Precambrian Research 97, 27-42.

Wyman, D.A., 2019. 2.8 Ga Subduction-related magmatism in the Youanmi Terrane and a revised geodynamic model for the Yilgarn Craton. Precambrian Research 327, 14-33.

Xiong, Q., Henry, H., Griffin, W.L., Zheng, J.P., Satsukawa, T., Pearson, N.J., O'Reilly, S.Y., 2017. High- and low-Cr chromitite and dunite in a Tibetan ophiolite: evolution from mature subduction system to incipient forearc in the Neo-Tethyan Ocean. Contributions to Mineralogy and Petrology 172:45.

Yang, X.M., 2014. Granitoid rocks in southeastern Manitoba: preliminary results of reconnaissance mapping and sampling. In: Report of Activities 2014. Manitoba Mineral Resources, Manitoba Geological Survey, 49-63.

Yang, X.M., Drayson, D., Polat, A., 2018. S-type granites in the western Superior Province: a marker of Archean terrane boundaries. Canadian Journal of Earth Sciences. https://doi.org/10.1139/cjes-2018-0056

Yang, X.M., Gilbert, H.P., 2014. Mineral chemistry of chromite in the Mayville intrusion: evidence for petrogenesis and linkage to the Bird River sill in the Neoarchean Bird River greenstone belt, southeastern Manitoba (NTS 52L5, 6, 12). In: Report of Activities 2014. Manitoba Mineral Resources, Manitoba Geological Survey, 32-48.

Yang, X.M., Gilbert, H.P., Corkery, M.T., Houlé, M.G., 2011. The Mayville mafic-ultramafic intrusion in the Neoarchean Bird River greenstone belt, southeastern Manitoba (part of NTS 52L12): preliminary geochemical investigation and implication for PGE-Ni-Cu-(Cr) mineralization. In: Report of Activities 2011. Manitoba Innovation, Energy and Mines, Manitoba Geological Survey, 127-142.

Yang, X.M., Gilbert, H.P., Houlé, M.G., 2012. Geological investigations of the Cat Creek area in the Neoarchean Bird River greenstone belt, southeastern Manitoba (part of NTS 52L12): new insights into PGE-Ni-Cu-Cr mineralization. In: Report of Activities 2012. Manitoba Innovation, Energy and Mines, Manitoba Geological Survey, 32-53.

Yang, X.M., Gilbert, H.P., Houlé, M.G., 2013. Cat Lake-Euclid Lake area in the Neoarchean Bird River greenstone belt, southeastern Manitoba (parts of NTS 52L11, 12): preliminary results of bedrock geological mapping and their implications for geodynamic evolution and metallogeny. In: Report of Activities 2013. Manitoba Mineral Resources, Manitoba Geological Survey, 70-84.

Zhou, S., Polat, A., Longstaffe, F.J., Yang, K., Fryer, B.J., Weisener, C., 2016. Formation of the Neoarchean Bad Vermilion Lake Complex and spatially associated granitic rocks at a convergent plate margin, Superior Province, Western Ontario, Canada. Gondwana Research 33, 134-159.

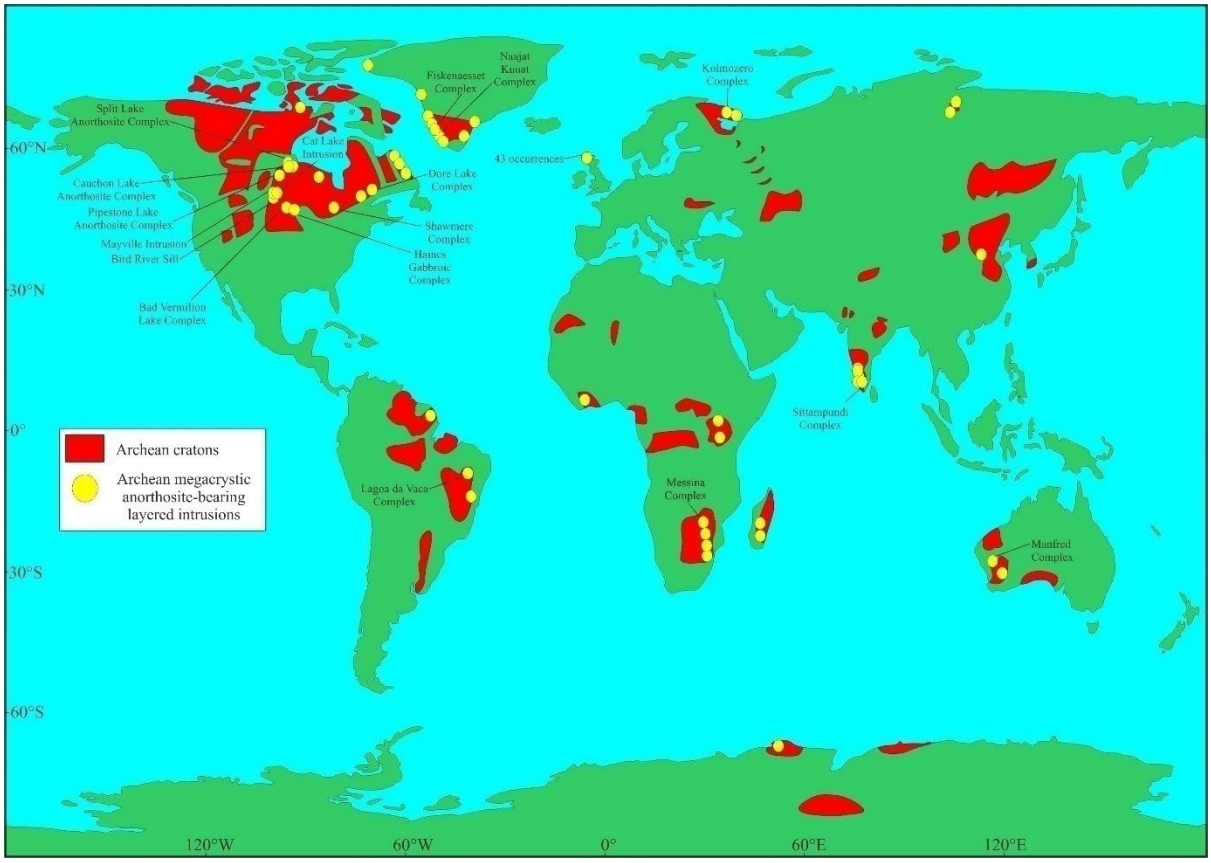

Fig. 3.1. Map showing Archean anorthosite-bearing layered intrusions around the world (modified after Furnes et al., 2015; Ashwal and Bybee, 2017). The Archean anorthosite-bearing layered intrusion occurrences are from Ashwal (1993, 2010), Hoffmann et al. (2012), Santosh et al. (2013), Souders et al. (2013), Yang et al. (2013), Yang and Gilbert (2014), Ashwal and Bybee (2017), Piaia et al. (2017), Polat et al. (2018a) and Sotiriou et al. (2019).

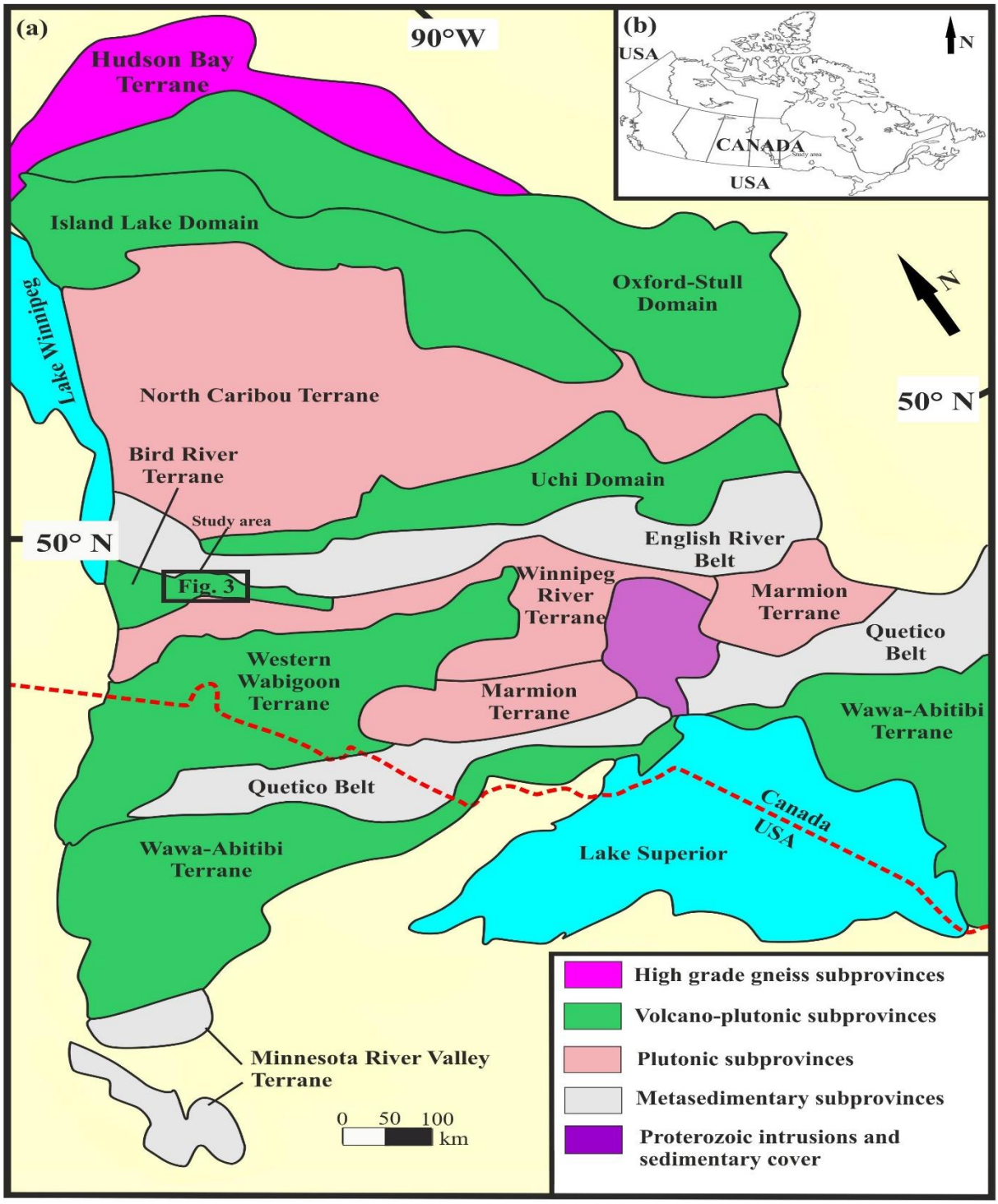

Fig. 3.2. (**a**) Simplified tectonic map of the western Superior Province (modified after Percival et al., 2012). (**b**) Simplified map of Canada showing its location in North America and the location of the study area.

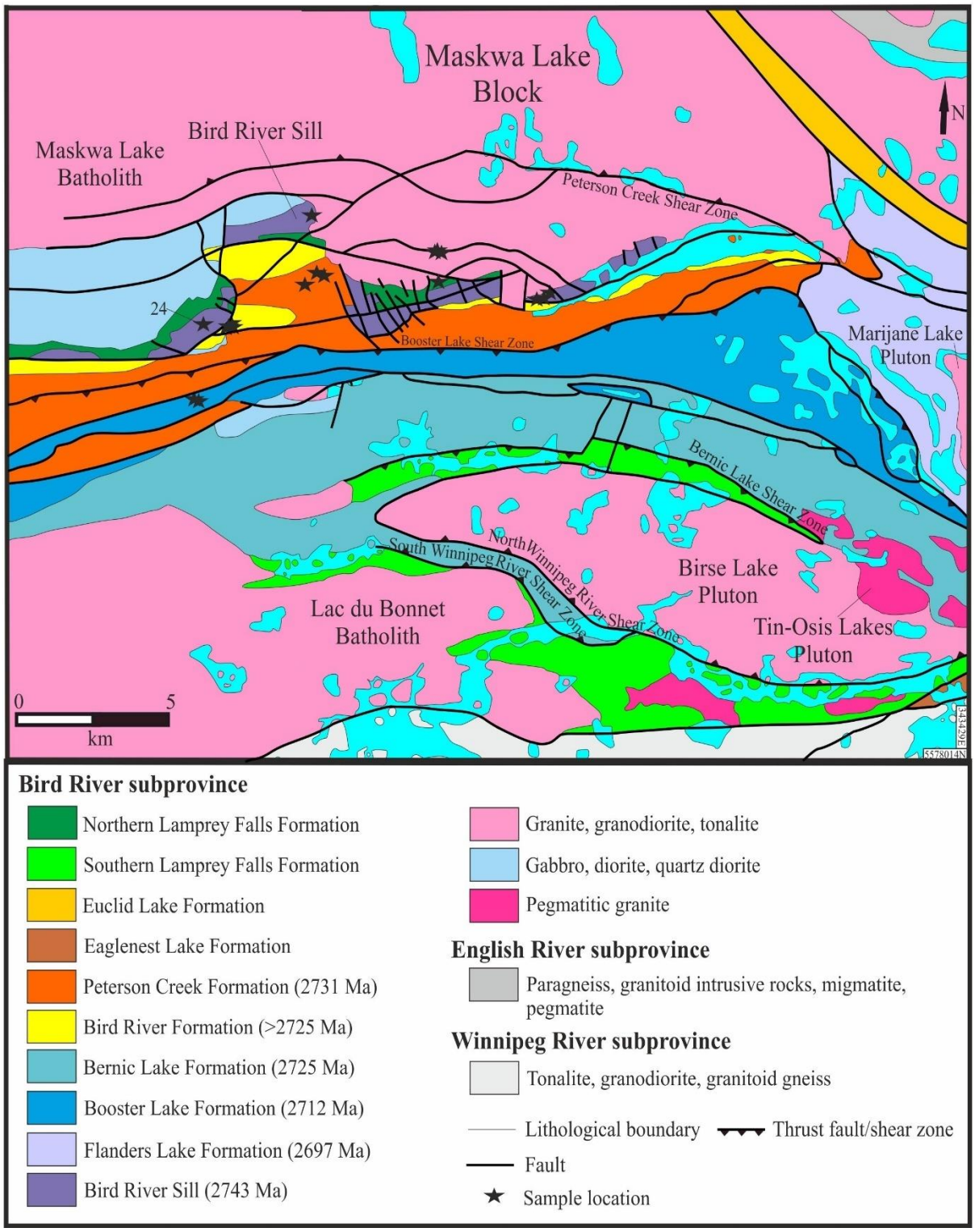

Fig. 3.3. Simplified geological map of the Bird River greenstone belt (modified from Bécu et al., 2013; Yang et al., 2013; Yang and Gilbert, 2014).

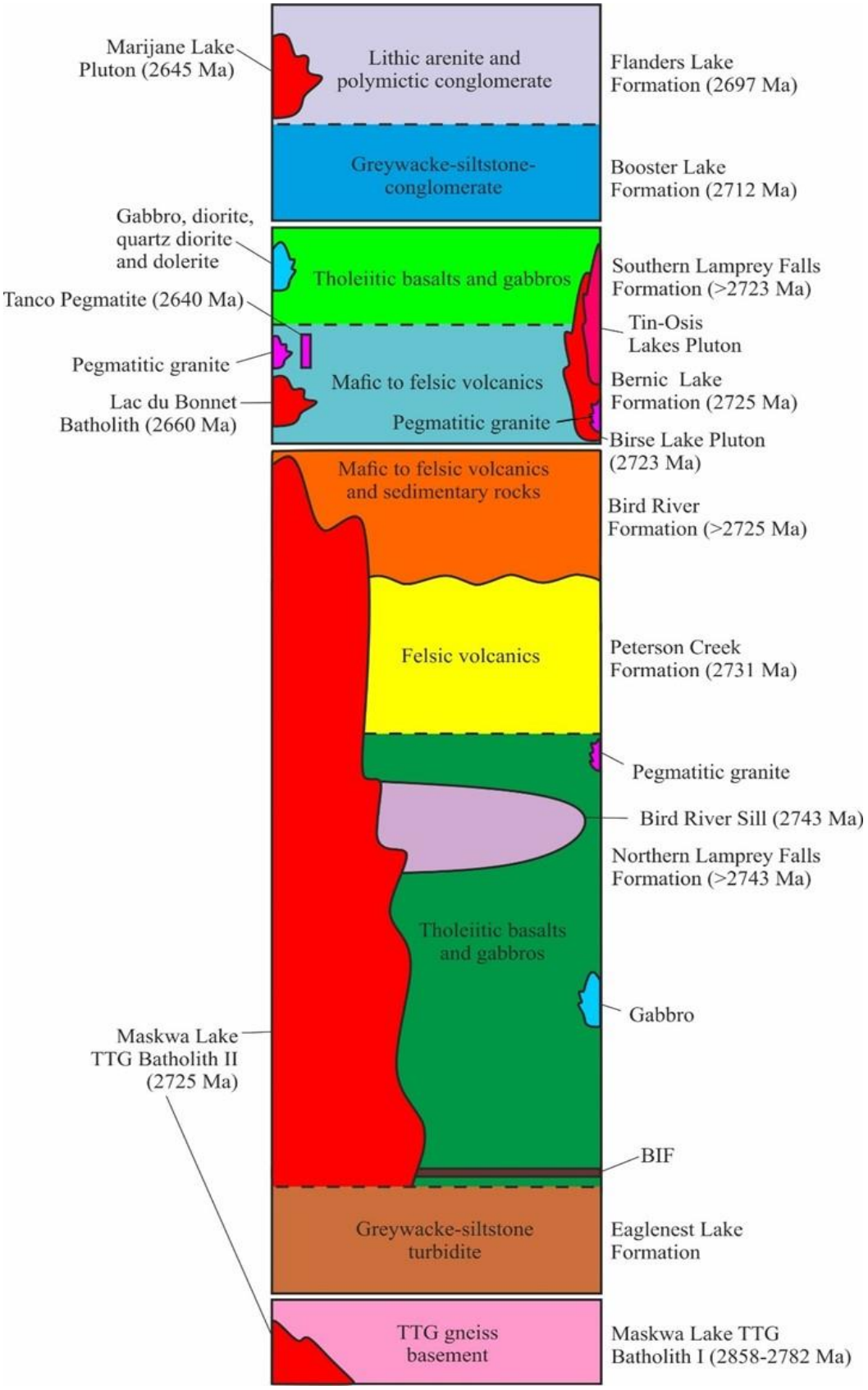

Fig. 3.4. Lithostratigraphy of the southern arm of the Bird River greenstone belt (constructed based on information from Gilbert et al., 2008; Yang et al., 2011, 2012, 2013; Yang and Gilbert, 2014).

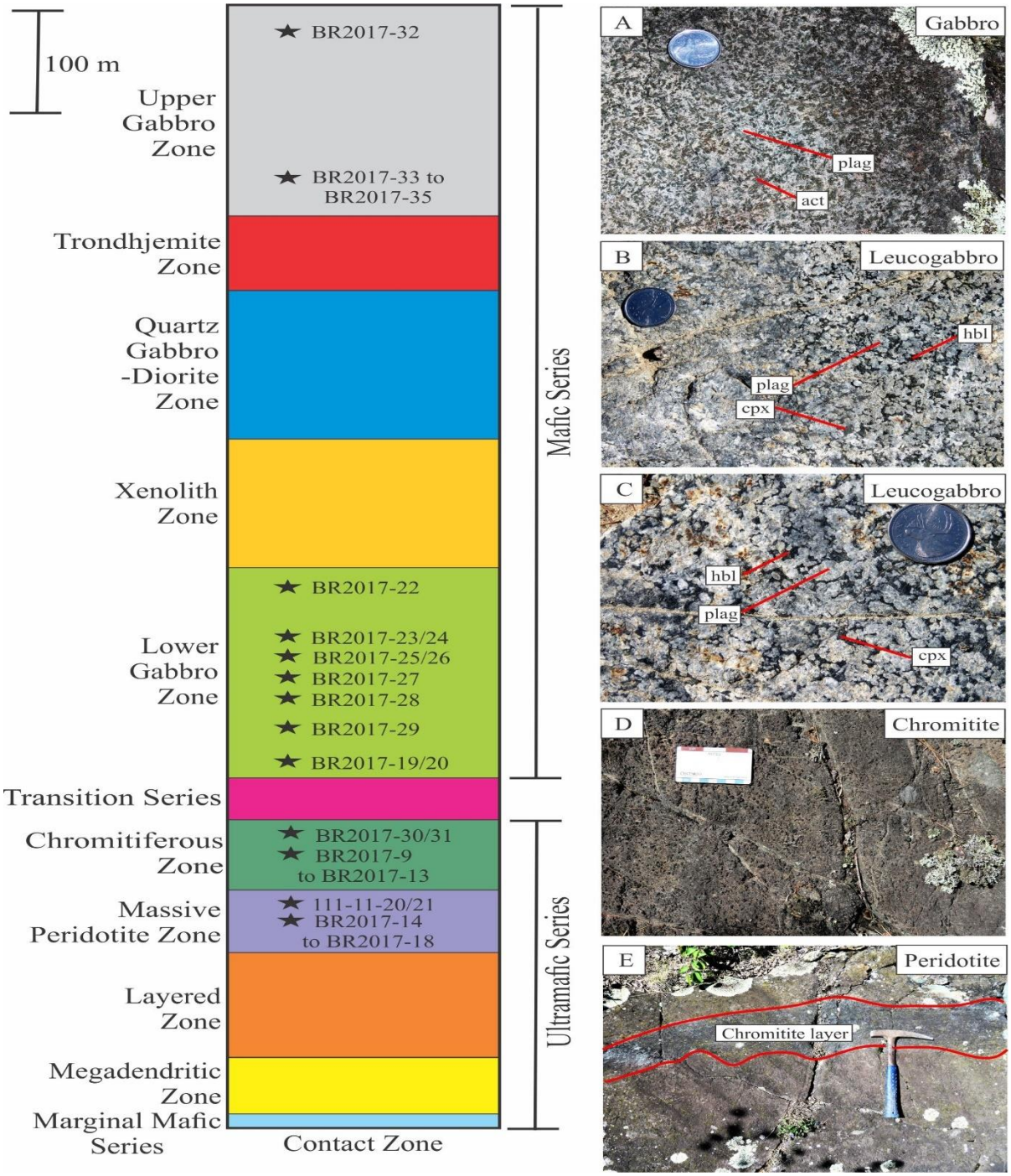

Fig. 3.5. Diagram showing the stratigraphy of the Bird River Sill (modified after Yang and Gilbert. 2014). The approximate stratigraphic locations of samples taken from the Bird River Sill are indicated by the stars. (**a**) Gabbro with a well-preserved cumulate texture and very little primary mineralogy remaining. (**b-c**) Leucogabbros with very well-preserved cumulate textures, magmatic plagioclase megacrysts and magmatic amphibole (hornblende). (**d**) Fragmented and strongly sheared chromites within chromitite. (**e**) Strongly serpentinised peridotites interlayered with a well-preserved chromitite layer. *plag*: plagioclase; *act*: actinolite; *cpx*: clinopyroxene; *hbl*: hornblende.

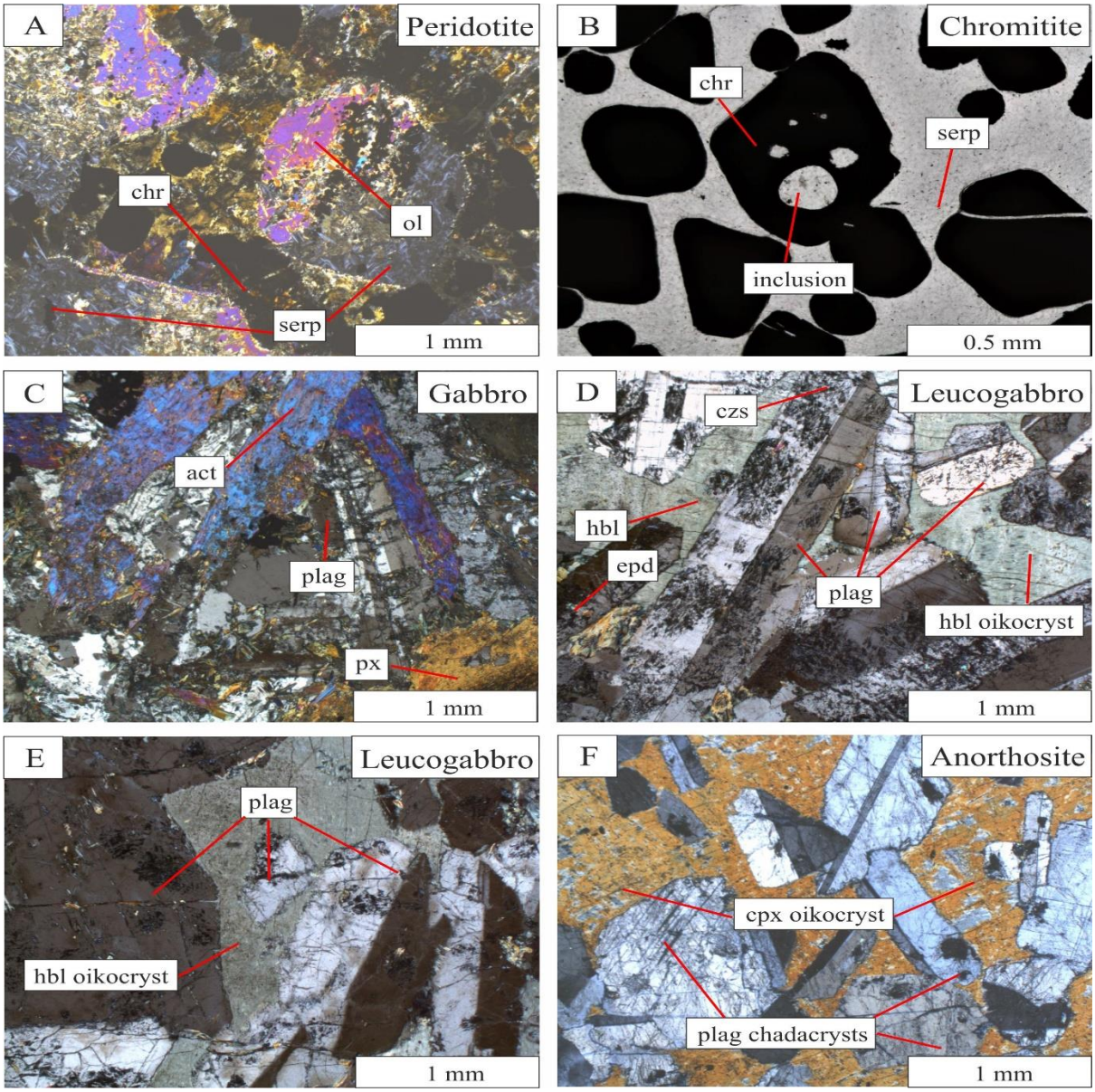

Fig. 3.6. Photomicrographs of lithologies from the Bird River Sill. (**a**) Peridotite from the Ultramafic Series, cross polarised light (XPL). (**b**) Chromitite from the Ultramafic Series, plane polarised light. (**c**) Gabbro from the Mafic Series, XPL. (**d-e**) Leucogabbros from the Mafic Series, XPL. (**f**) Anorthosite from the Mafic Series, XPL. Primary, igneous cumulate textures and minerals are largely well preserved. *plag*: plagioclase; *hbl*: hornblende; *px*: pyroxene; *cpx*: clinopyroxene; *act*: actinolite; *czs*: clinozoisite; *epd*: epidote; *chr*: chromite; *ol*: olivine; *serp*: serpentine.

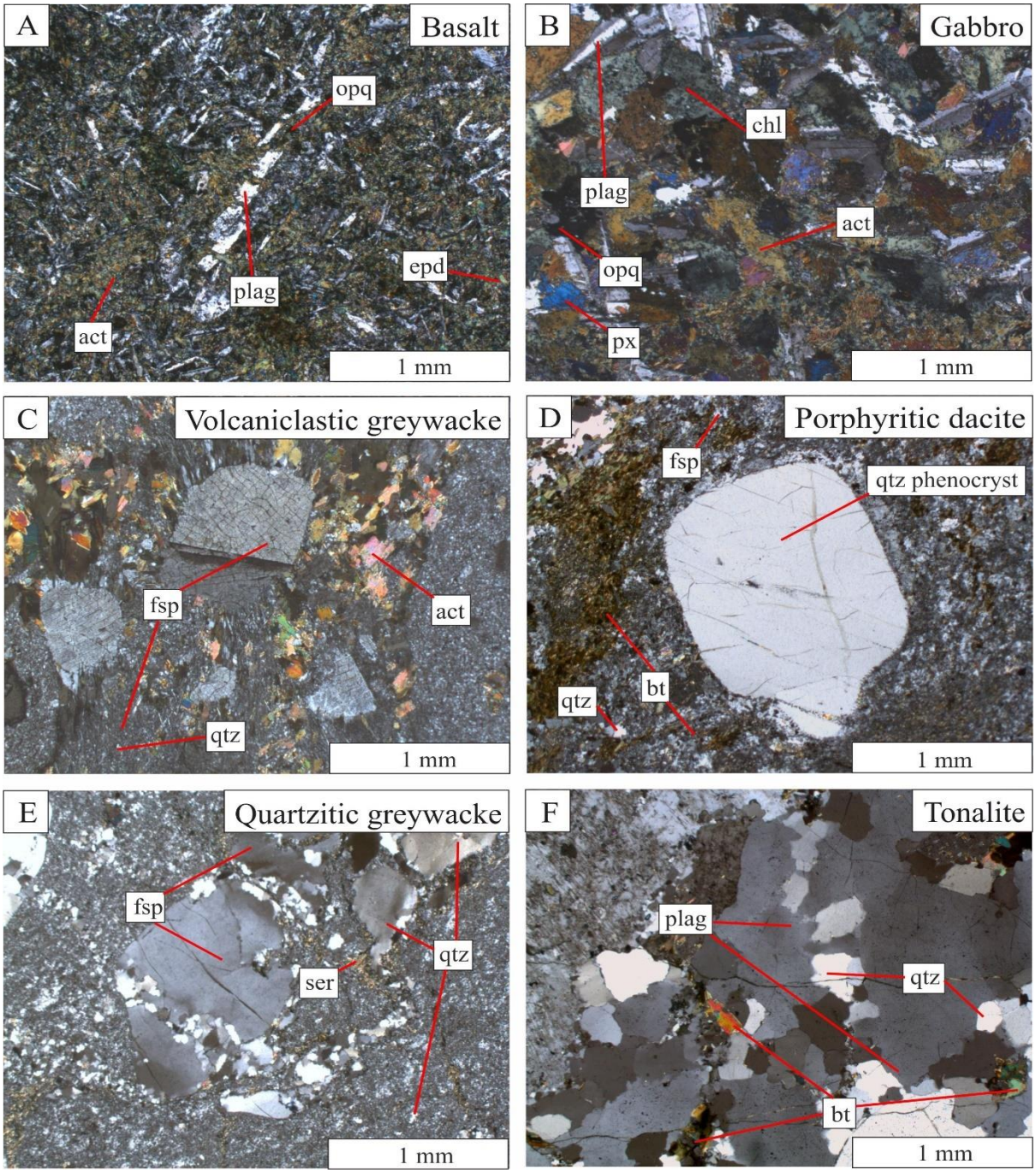

Fig. 3.7. Photomicrographs (all under cross polarised light) of (**a**) a basalt and (**b**) a gabbro from the Northern Lamprey Falls Formation, (**c**) a volcaniclastic greywacke from the Bird River Formation, (**d**) a porphyritic dacite from the Peterson Creek Formation and (**e**) a quartzitic greywacke from the Booster Lake Formation of the Bird River greenstone belt. (**f**) shows a photomicrograph of a tonalite from the Maskwa Lake TTG Batholith I to the north of the southern arm of the Bird River greenstone belt. Primary, igneous textures are generally well preserved; however, metamorphic minerals have largely replaced primary, igneous minerals. *act*: actinolite; *plag*: plagioclase; *opq*: opaque mineral; *px*: pyroxene; *epd*: epidote; *chl*: chlorite; *fsp*: feldspar; *qtz*: quartz; *bt*: biotite; *ser*: sericite.

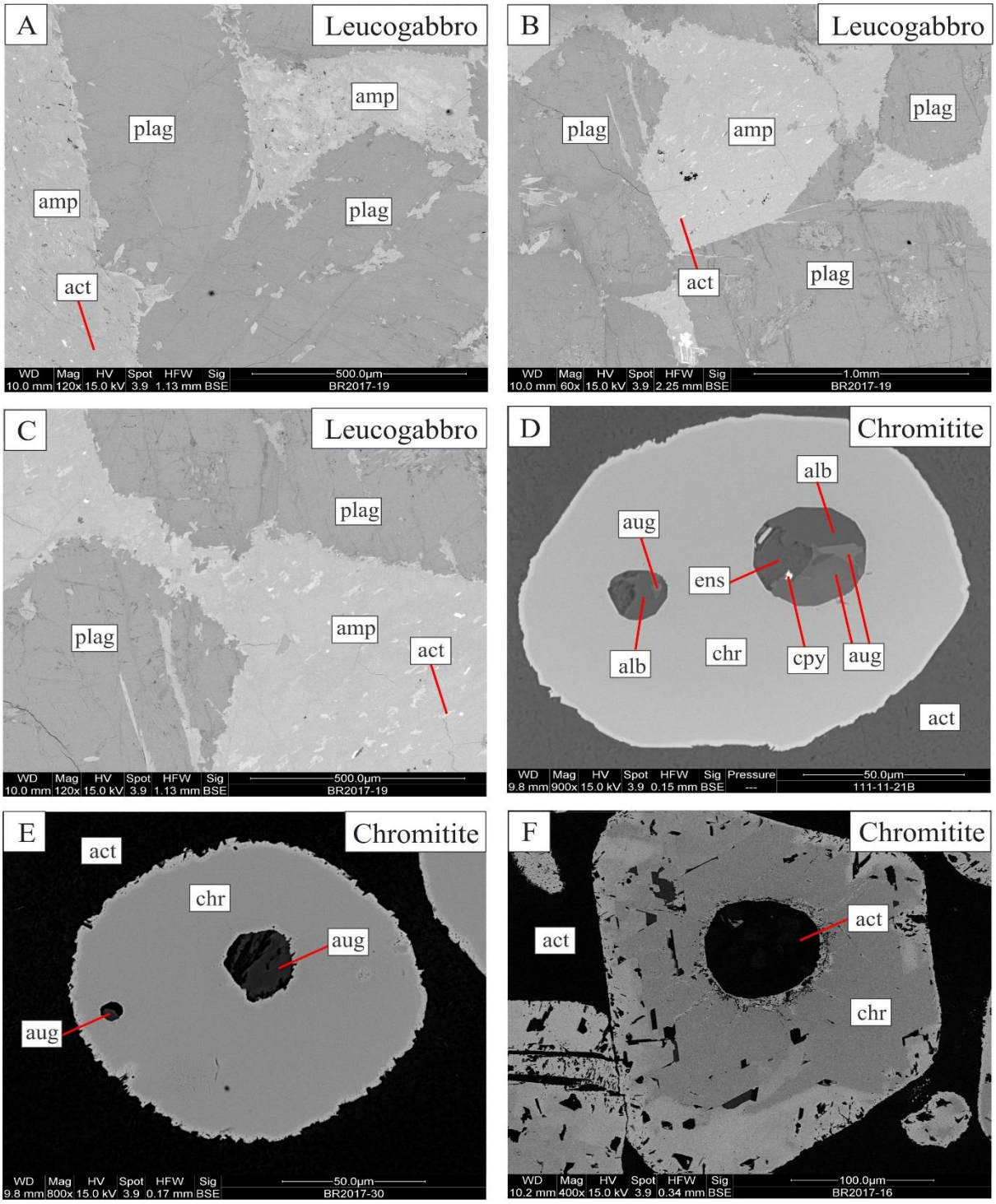

Fig. 3.8. Scanning electron microscope (SEM) back-scatter electron images of (**a-c**) a leucogabbro and (**d-f**) chromitites from the Bird River Sill. Images **a-c** show that cumulate textures and primary minerals are generally well preserved in leucogabbro BR2017-19, however, amphibole (amp) has been partially altered to secondary actinolite (act) and plagioclase (plag) has also been partially altered. The chromites (chr) in the chromitites in **d-f** contain inclusions comprised of augite (aug), albite (alb), enstatite (ens) and chalcopyrite (cpy). The matrix adjacent to the chromites is comprised of secondary actinolite (act).

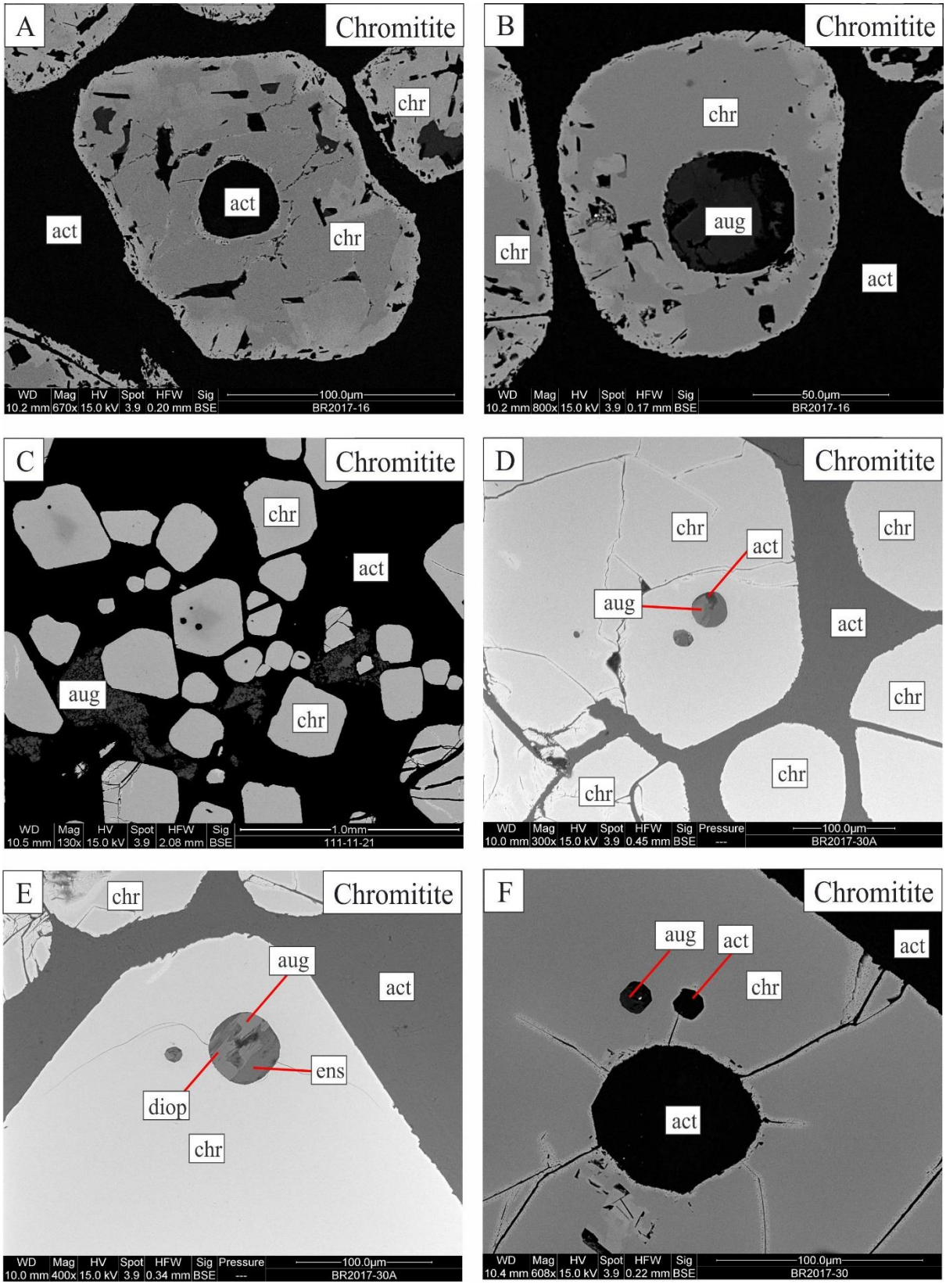

Fig. 3.9. Scanning electron microscope back-scatter electron images of chromitites (**a-f**) from the Bird River Sill. These images show that an actinolite (act) matrix occurs adjacent to chromites (chr) that host inclusions of augite (aug), diopside (diop) and enstatite (ens).

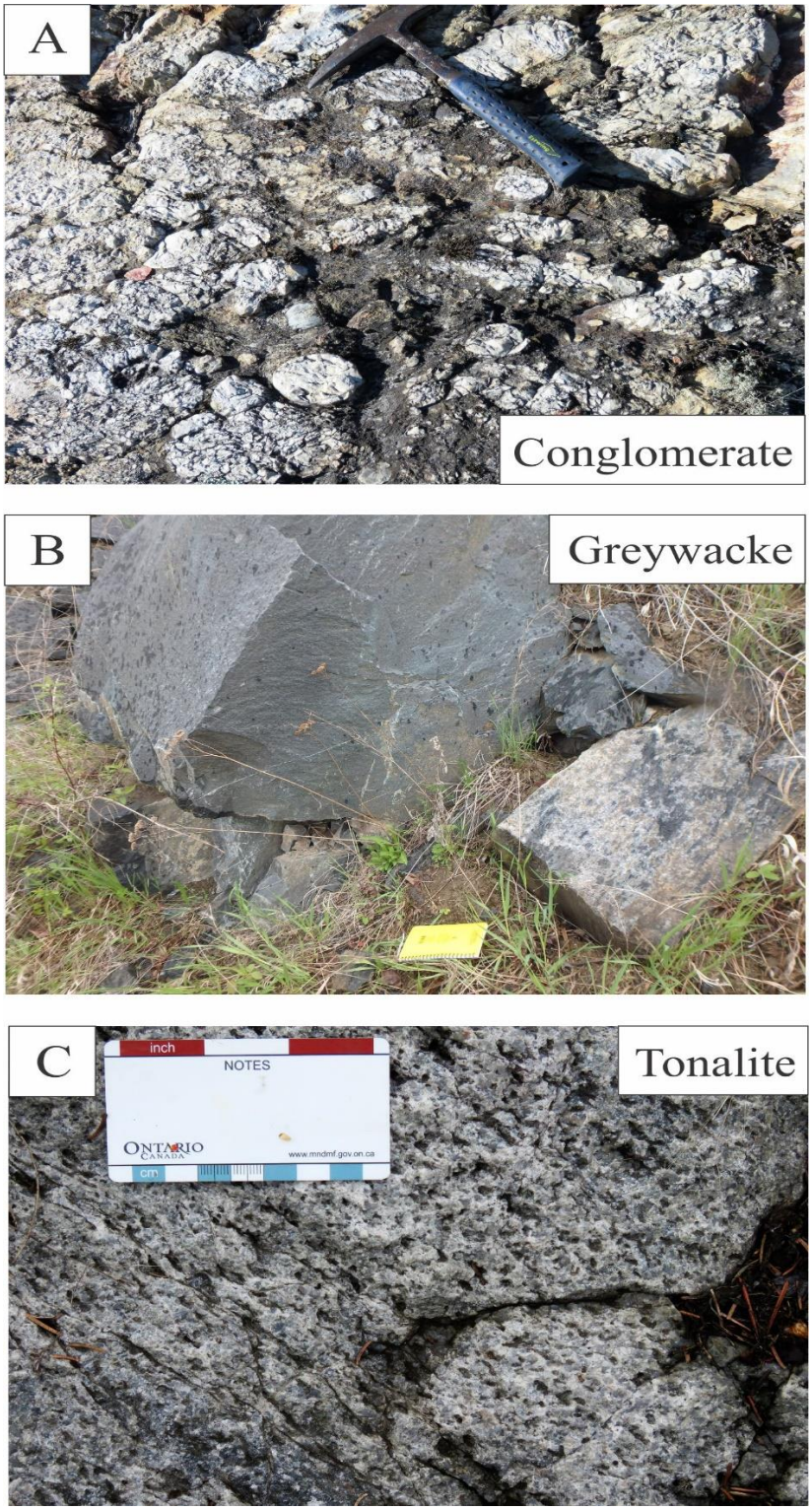

Fig. 3.10. Field photographs of the Bird River greenstone belt and the Maskwa Lake Batholith I. (**a**) Conglomerate with rounded clasts from the Booster Lake Formation. (**b**) Greywacke from the Bird River Formation. (**c**) Coarse-grained tonalite from the Maskwa Lake Batholith I.

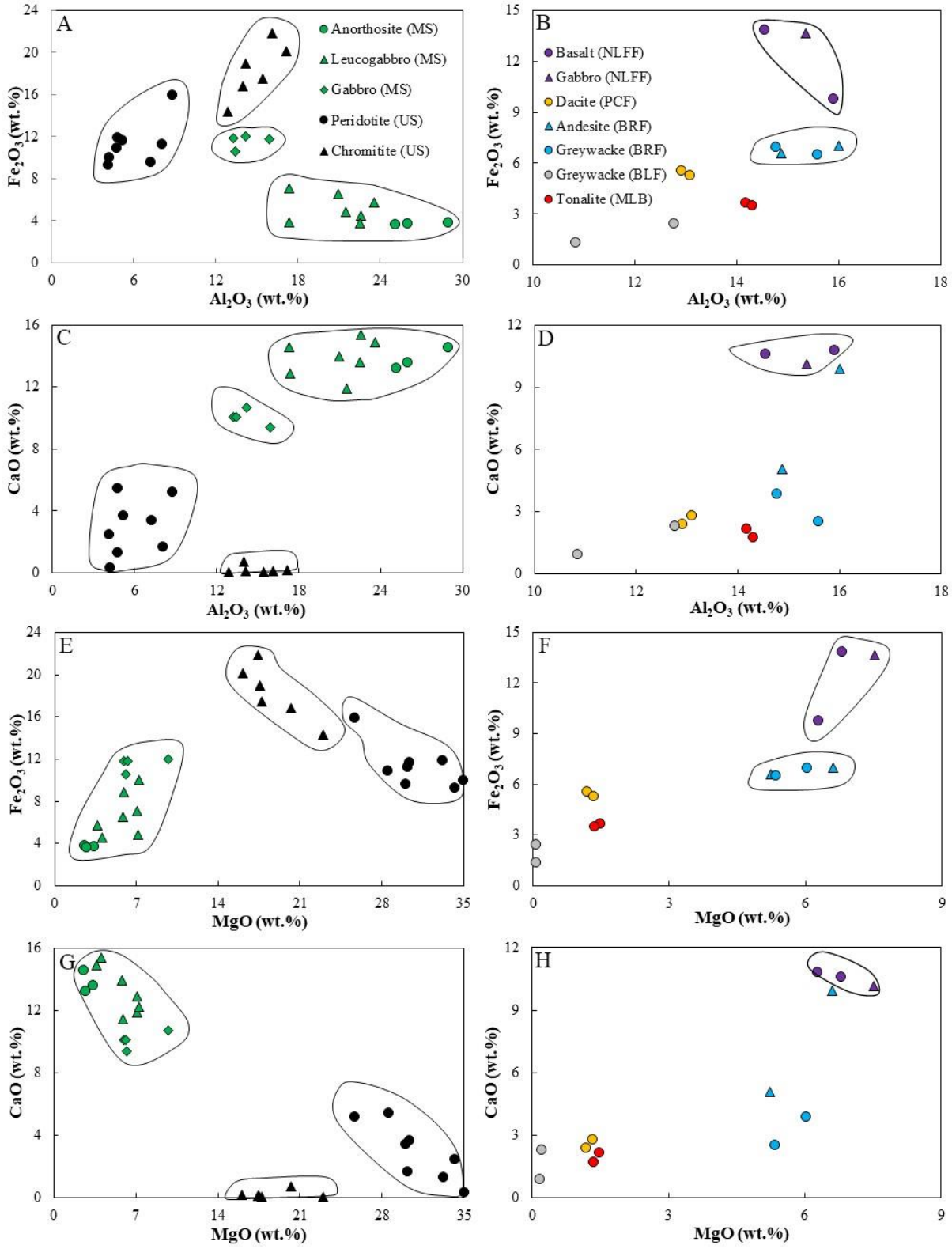

Fig. 3.11. Major element diagrams for the for the Mafic Series (MS) and Ultramafic Series (US) of the Bird River Sill and Northern Lamprey Falls Formation (NLFF), Peterson Creek Formation (PCF), Bird River Formation (BRF), Booster Lake Formation (BLF) and Maskwa Lake Batholith I (MLB). (**a**) $Fe_2O_3^T$ versus Al_2O_3 diagram for the Mafic Series and Ultramafic Series of the Bird River Sill. (**b**) $Fe_2O_3^T$ versus Al_2O_3 diagram for the Northern Lamprey Falls

Formation, Peterson Creek Formation, Bird River Formation, Booster Lake Formation and Maskwa Lake Batholith I. (**c**) CaO versus Al_2O_3 diagram for the Mafic Series and Ultramafic Series of the Bird River Sill. (**d**) CaO versus Al_2O_3 diagram for the Northern Lamprey Falls Formation, Peterson Creek Formation, Bird River Formation, Booster Lake Formation and Maskwa Lake Batholith I. (**e**) $Fe_2O_3^T$ versus MgO diagram for the Mafic Series and the Ultramafic Series of the Bird River Sill. (**f**) $Fe_2O_3^T$ versus MgO diagram for the Northern Lamprey Falls Formation, Peterson Creek Formation, Bird River Formation, Booster Lake Formation and Maskwa Lake Batholith I. (**g**) CaO versus MgO diagram for the Mafic Series and the Ultramafic Series of the Bird River Sill. (**h**) CaO versus MgO diagram for the Northern Lamprey Falls Formation, Peterson Creek Formation, Bird River Formation, Booster Lake Formation and Maskwa Lake Batholith I.

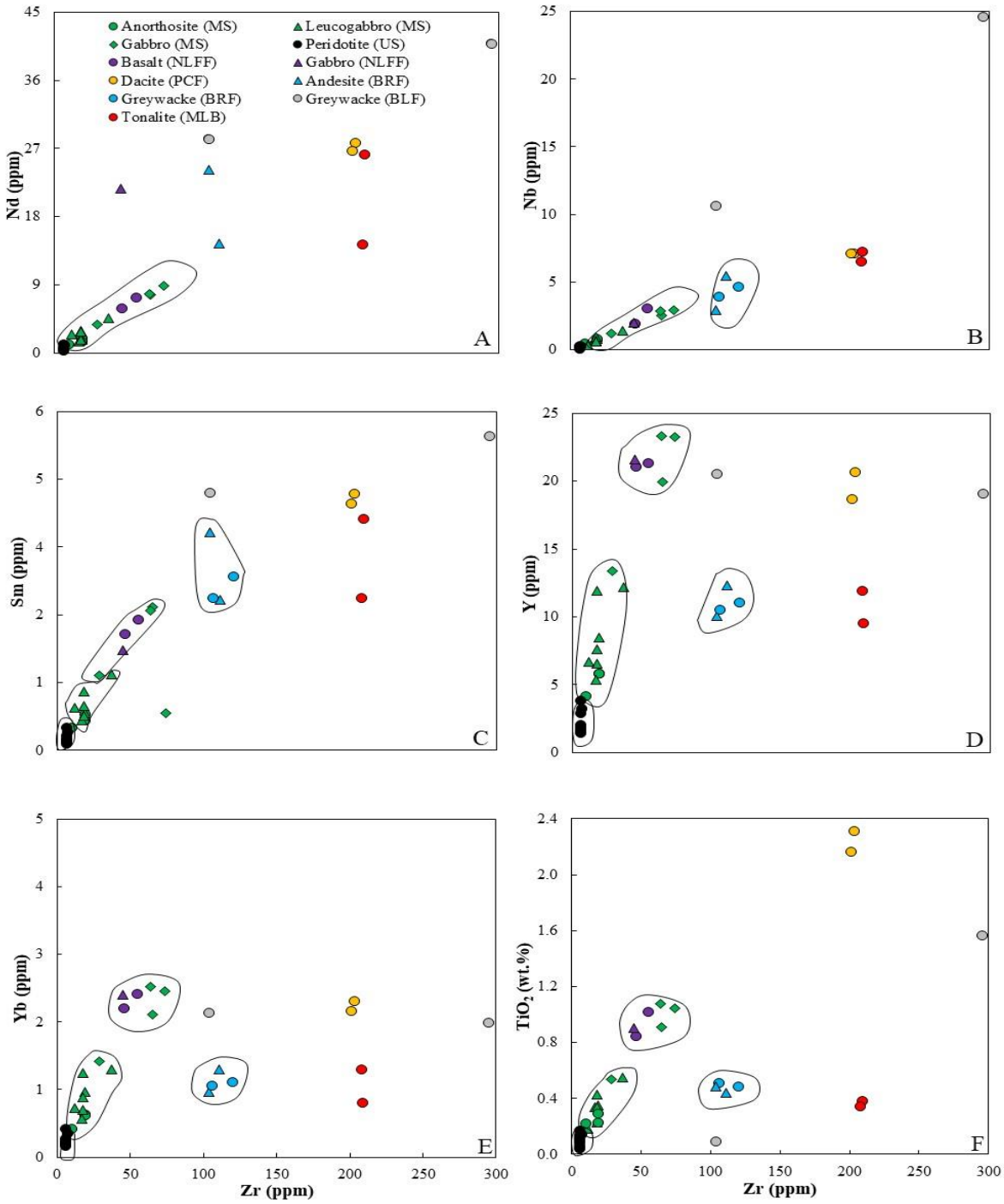

Fig. 3.12. Trace element variation diagrams for the Mafic Series (MS) and the Ultramafic Series (US) of the Bird River Sill and the Northern Lamprey Falls Formation (NLFF), Peterson Creek Formation (PCF), Bird River Formation (BRF), Booster Lake Formation (BLF) and Maskwa Lake Batholith I (MLB). (**a**) Nd versus Zr, (**b**) Nb versus Zr, (**c**) Sm versus Zr, (**d**) Y versus Zr, (**e**) Yb versus Zr and (**f**) TiO_2 versus Zr.

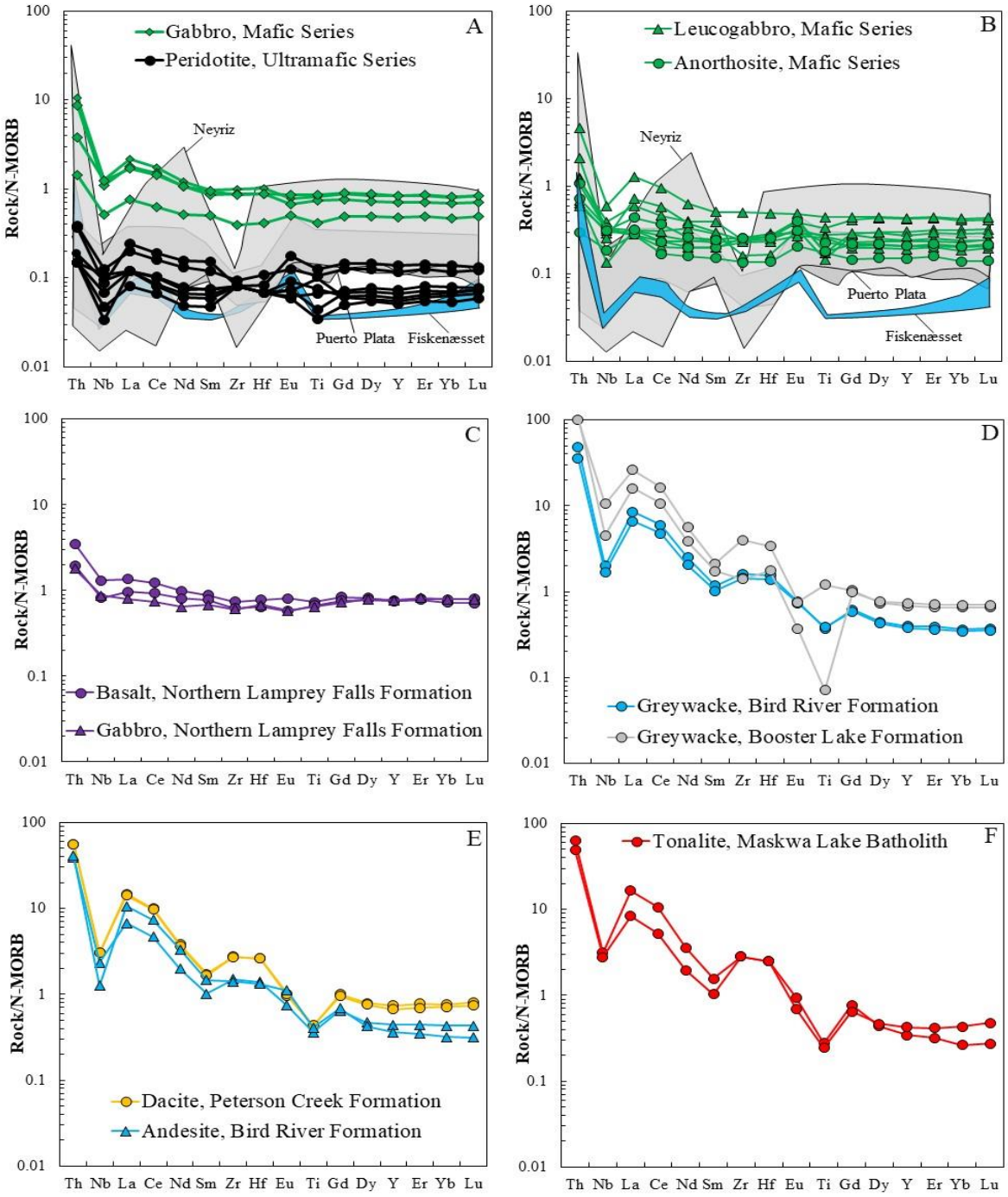

Fig. 3.13. N-MORB-normalised trace element diagrams for the (**a**) Mafic Series gabbros and Ultramafic Series peridotites and (**b**) Mafic Series leucogabbros and anorthosites of the Bird River Sill, (**c**) Northern Lamprey Falls Formation basalts and synvolcanic gabbro, (**d**) Bird River Formation and Booster Lake Formation greywackes, (**e**) Bird River Formation high-magnesian andesites and Peterson Creek Formation dacites and (**f**) Maskwa Lake Batholith I tonalites. Normalisation values are from Sun and McDonough (1989). The fields for the Fiskenæsset Complex (Polat et al., 2011) and the Neyriz (Moghadam et al., 2014) and Puerto Plata (Escuder-Viruete et al., 2014) ophiolites are included in (**a**) and (**b**) for comparison with the Bird River Sill.

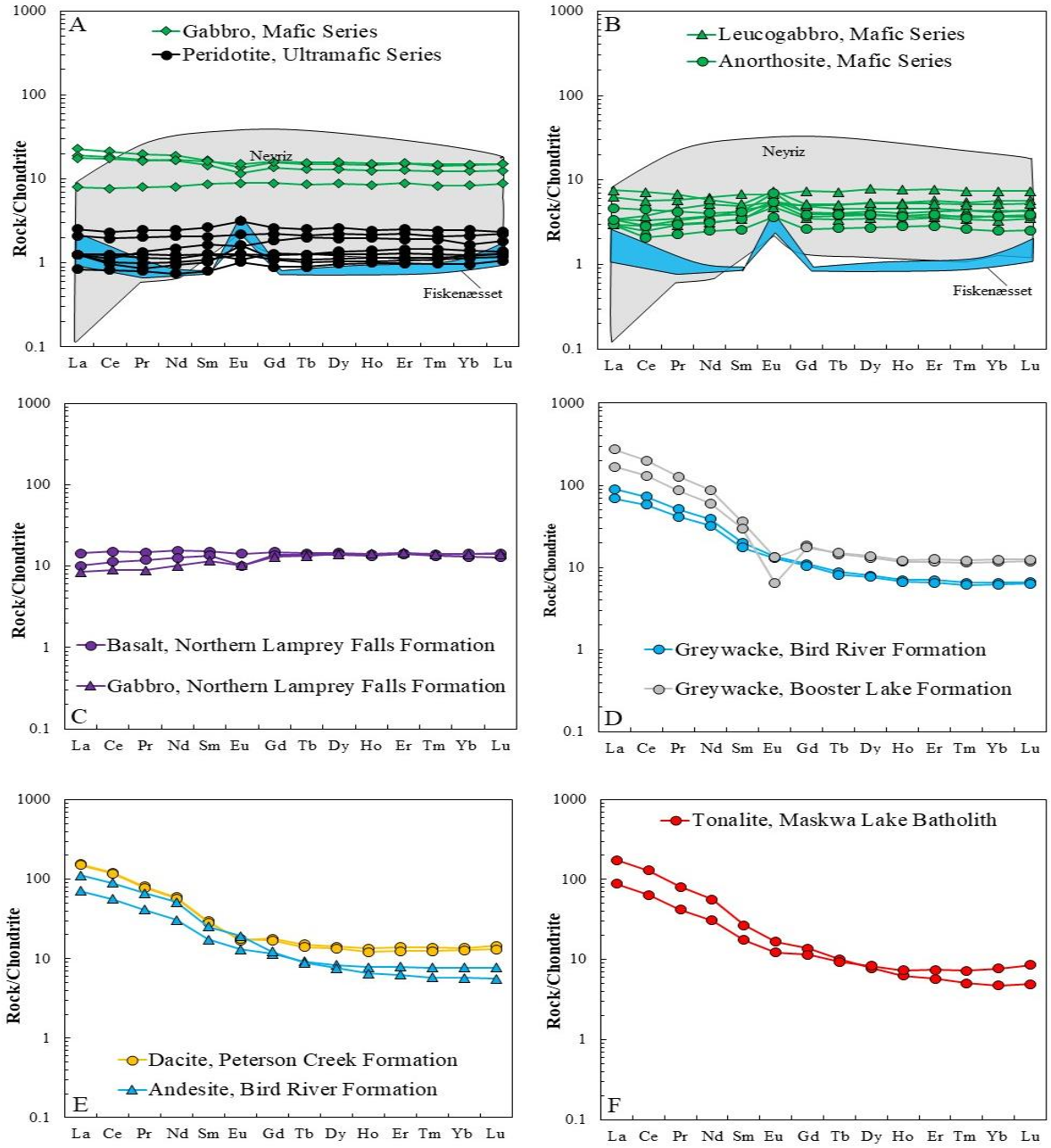

Fig. 3.14. Chondrite-normalised REE diagrams for the (**a**) Mafic Series gabbros and Ultramafic Series peridotites and (**b**) Mafic Series leucogabbros and anorthosites of the Bird River Sill, (**c**) Northern Lamprey Falls Formation basalts and synvolcanic gabbro, (**d**) Bird River Formation and Booster Lake Formation greywackes, (**e**) Bird River Formation high-magnesian andesites and Peterson Creek Formation dacites and (**f**) Maskwa Lake Batholith I tonalites. Normalisation values are from Sun and McDonough (1989). The fields for the Fiskenæsset Complex (Polat et al., 2011) and the Neyriz ophiolite (Moghadam et al., 2014) are included in (**a**) and (**b**) for comparison with the Bird River Sill.

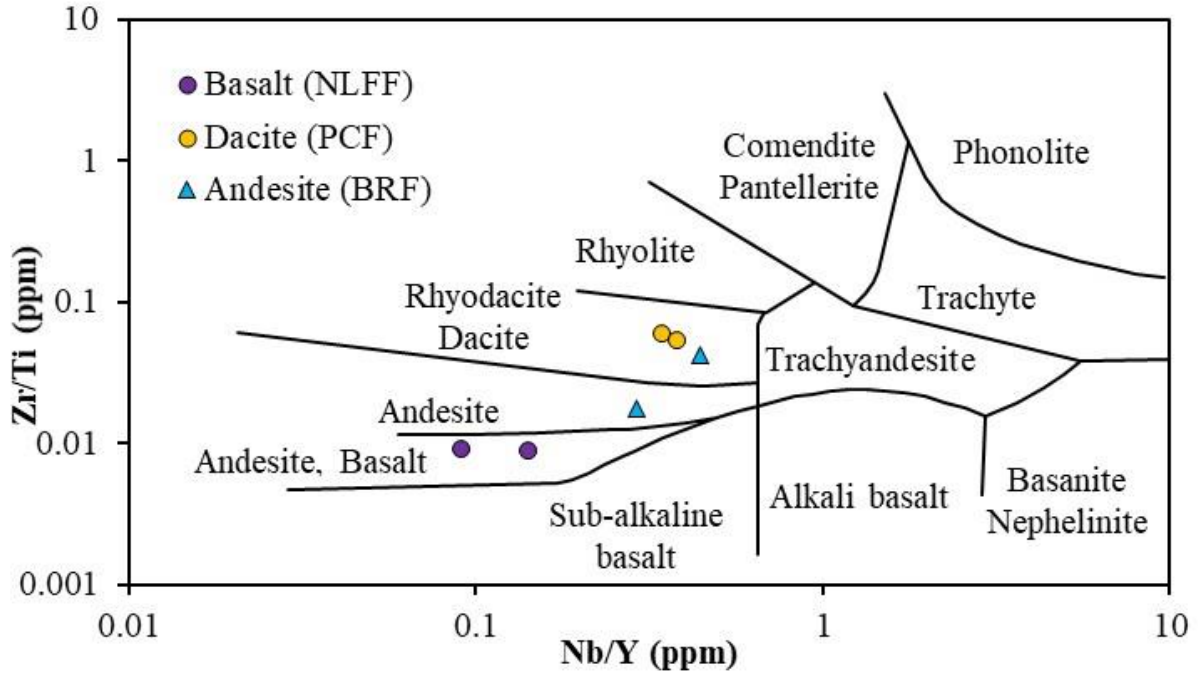

Fig. 3.15. Basalts from the Northern Lamprey Falls Formation (NLFF), dacites from the Peterson Creek Formation (PCF) and andesites from the Bird River Formation (BRF) plotted on a immobile element Zr/Y versus Nb/Y diagram (after Winchester and Floyd, 1977).

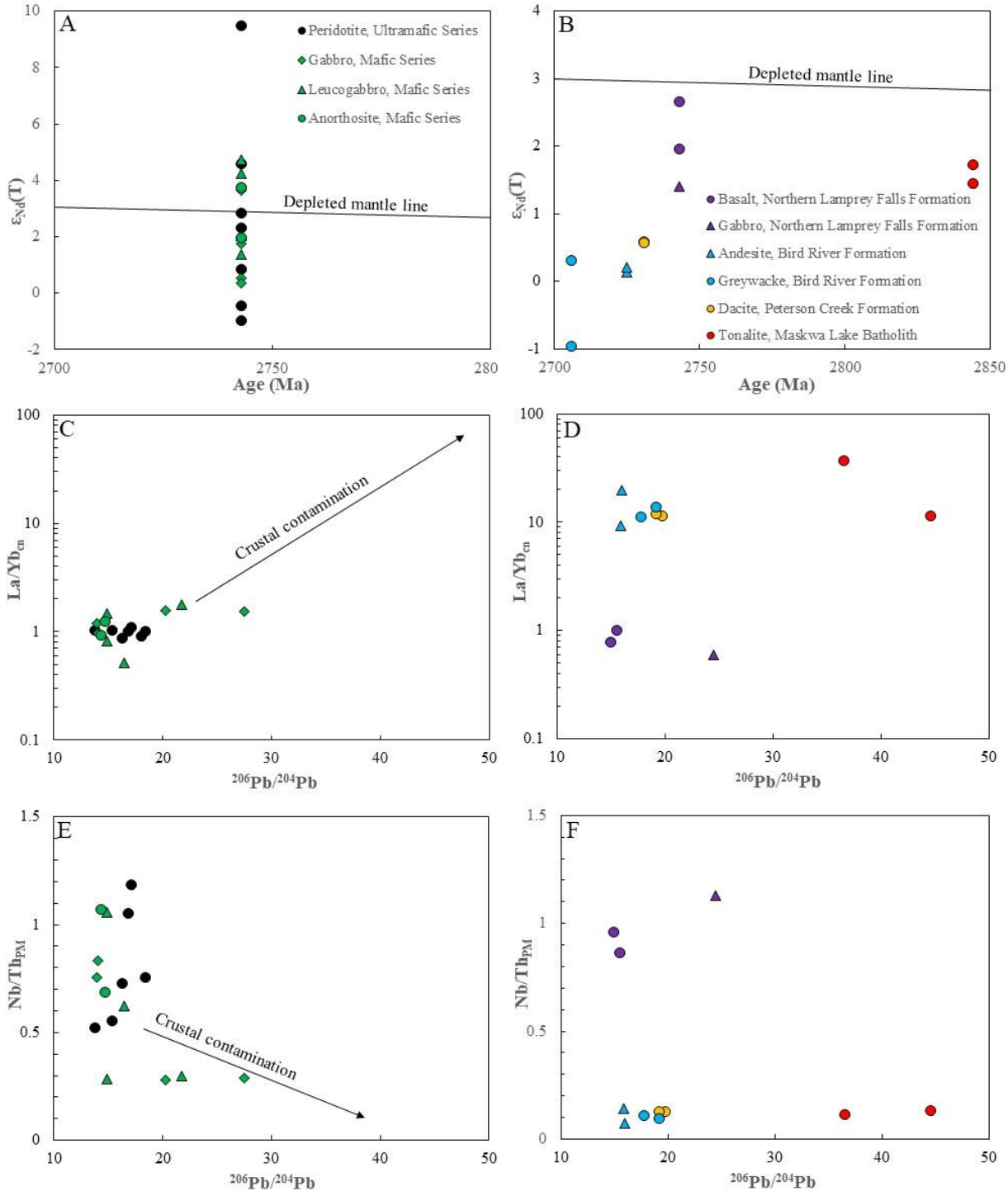

Fig. 3.16. (a) Initial $\varepsilon_{Nd}(T)$ values versus age (Ma) diagram for the lithologies sampled from the Bird River Sill. (**b**) Initial $\varepsilon_{Nd}(T)$ values versus age (Ma) diagram for the lithologies sampled from the Bird River greenstone belt and Maskwa Lake Batholith I. (**c**) Chondrite-normalised La/Yb_{cn} ratio versus $^{206}Pb/^{204}Pb$ ratio diagram for the Bird River Sill. (**d**) Chondrite-normalised La/Yb_{cn} ratio versus $^{206}Pb/^{204}Pb$ ratio diagram for the Bird greenstone belt and Maskwa Lake Batholith I. (**e**) Primitive mantle-normalised Nb/Th_{PM} ratio versus $^{206}Pb/^{204}Pb$ ratio diagram for the Bird River Sill. (**f**) Primitive mantle-normalised Nb/Th_{PM} ratio versus $^{206}Pb/^{204}Pb$ ratio plot for the Bird River greenstone belt and Maskwa Lake Batholith I. The depleted mantle lines in

(**a**) and (**b**) are from Henry et al. (1998). The crustal contamination trend lines in (**c**) and (**e**) are from Lodge et al. (2015).

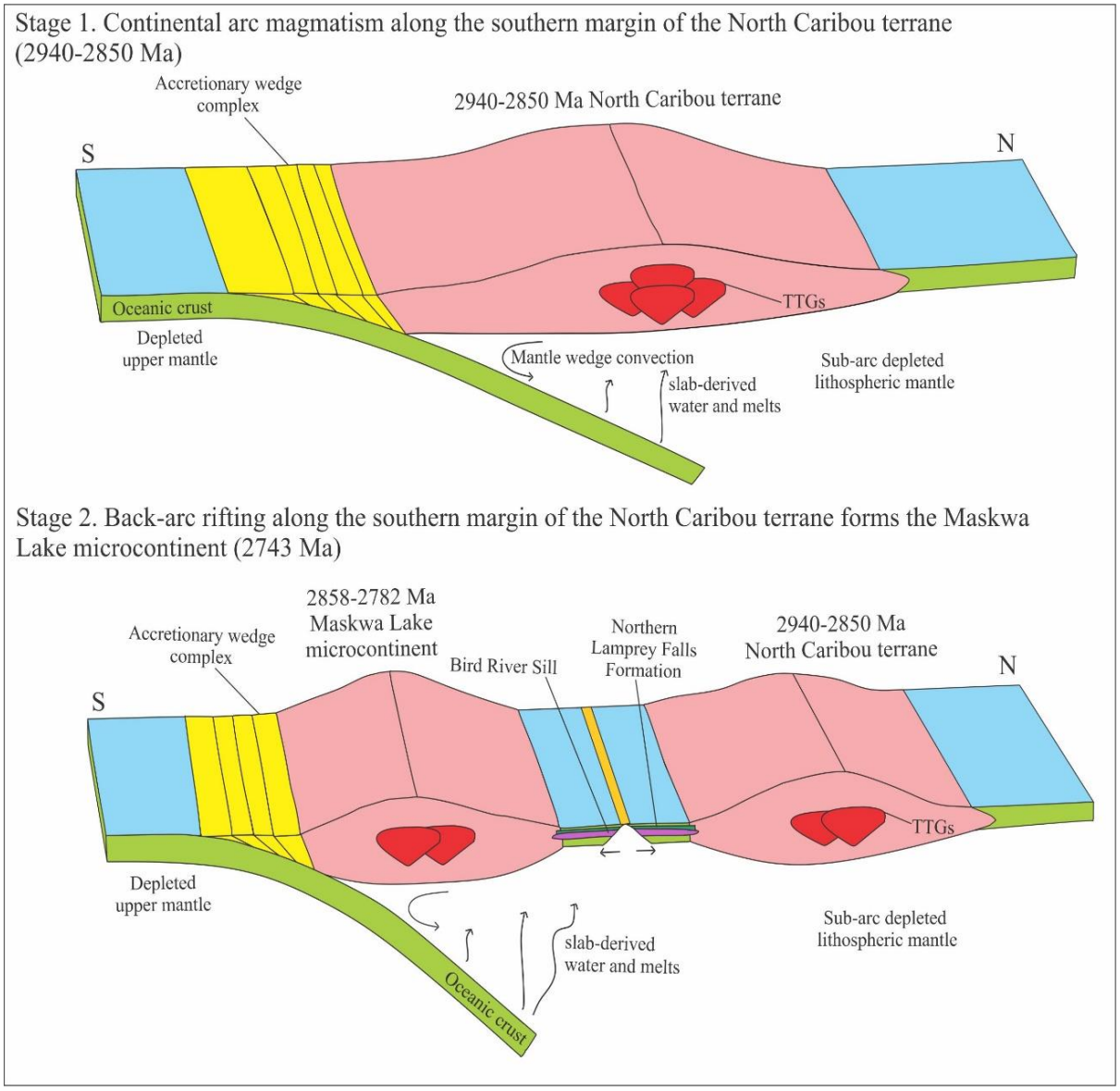

Fig. 3.17. Schematic diagram showing the geodynamic evolution of the Bird River greenstone belt and the Bird River subprovince (see the text for more information).

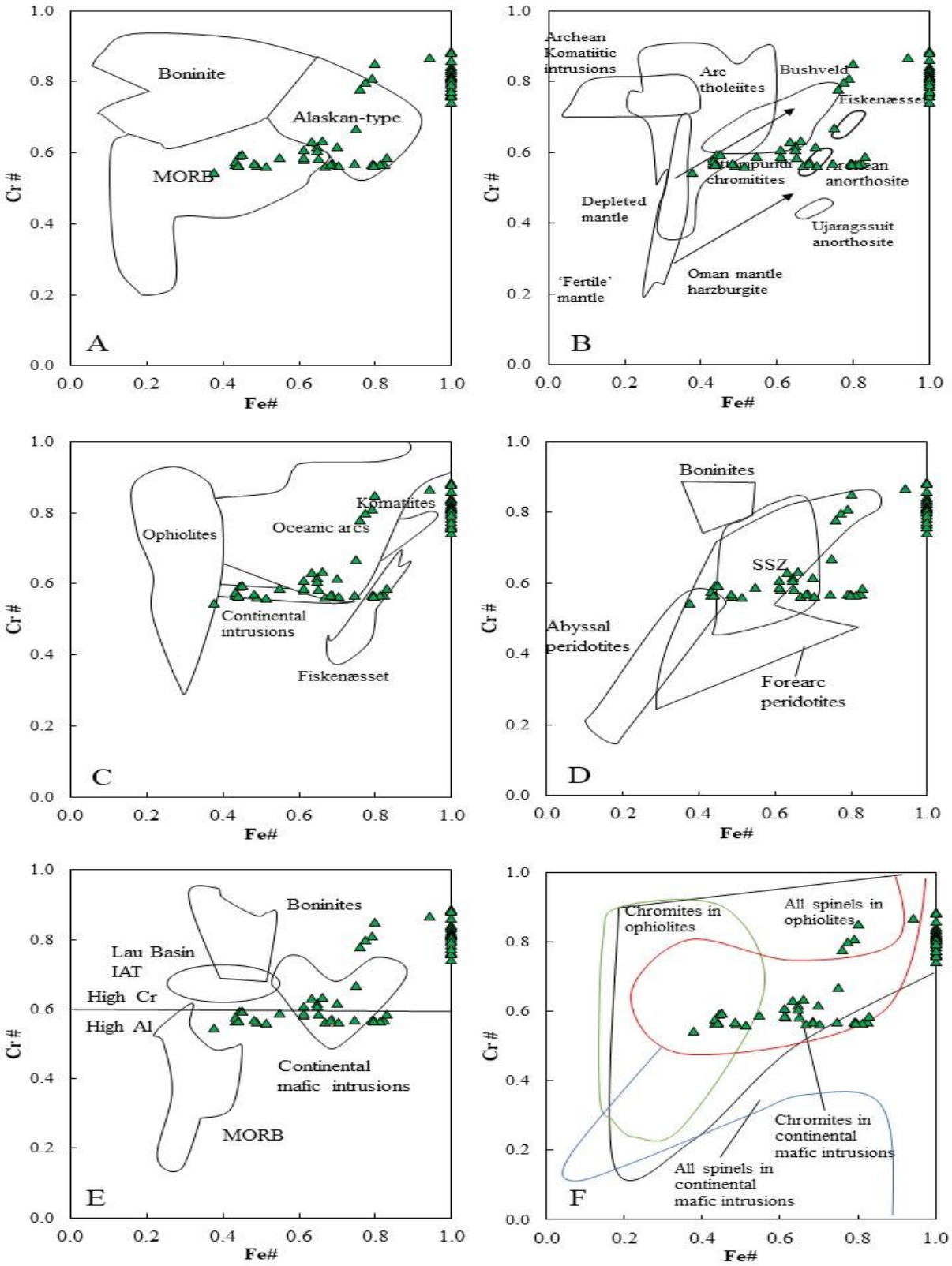

Fig. 4.18. Chromite chemistry diagrams for chromites from the Bird River Sill. (**a**) Cr#(Cr/Cr+Al) versus Mg# (Mg/Mg+Fe^{2+}) diagram that distinguishes between boninitic, Alaskan-type and MORB (mid-ocean ridge basalt) chromites (modified after Kiseleva and Zhmodik, 2017). (**b**) Cr# (Cr/Cr+Al) versus Fe# (Fe^{2+}/Fe^{2+}+Mg) diagram (modified after Rollinson et al., 2010). (**c**) Cr# (Cr/Cr+Al) versus Fe# (Fe^{2+}/Fe^{2+}+Mg) diagram that

distinguishes between chromites in ophiolites, oceanic arcs, continental intrusions, komatiites, and the Fiskenæsset Complex (modified after Lenaz et al., 2018). (**d**) Cr# (Cr/Cr+Al) versus Mg# (Mg/Mg+Fe^{2+}) diagram that distinguishes between suprasubduction zone (SSZ), forearc peridotite, boninitic and abyssal peridotite chromites (modified after Lay et al., 2017). (**e**) Cr# (Cr/Cr+Al) versus Mg# (Mg/Mg+Fe^{2+}) diagram that distinguishes between high Cr and high Al chromites and Lau Basin IAT (island arc tholeiite), boninitic, MORB (mid-ocean ridge basalt), and continental mafic intrusion chromites (modified after Gonzalez-Jimenez et al., 2017). (**f**) Cr# (Cr/Cr+Al) versus Fe# (Fe^{2+}/Fe^{2+}+Mg) diagram that distinguishes between chromites in ophiolites, chromites in continental mafic intrusions, all spinels in continental mafic intrusions and all spinels in ophiolites (modified after Polat et al., 2006).

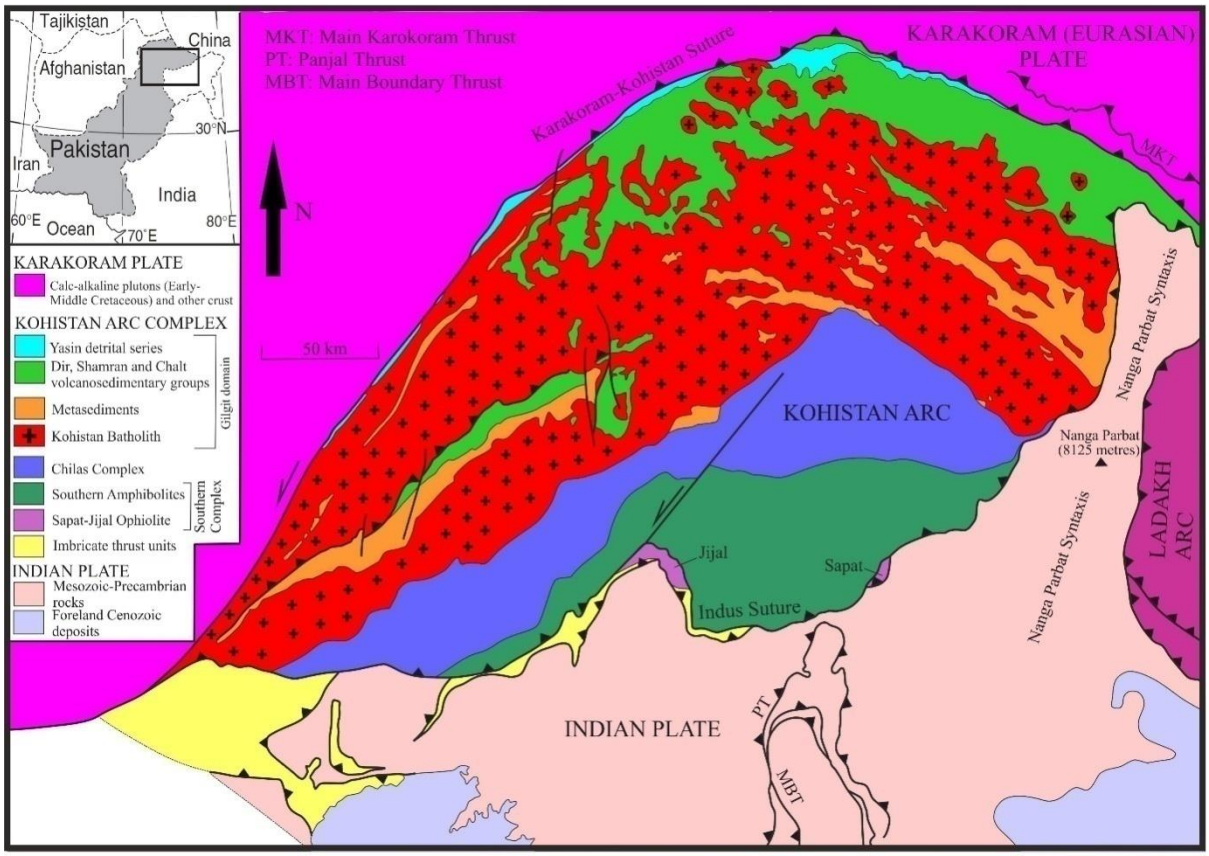

Fig. 3.19. Simplified geological map of the Kohistan arc and the adjacent Indian and Karakoram (Eurasian) plates (modified after Jagoutz et al., 2007, and based on information from Hébert et al., 2012; Petterson, 2018).

Sample ID	Lithology	Age (Ma)	Sm (ppm)	Nd (ppm)	$^{147}Sm/^{144}Nd$	$^{143}Nd/^{144}Nd$	ε_{Nd}
BR2017-9	Peridotite	2743	0.16	0.48	0.197	0.512696±09	0.86
BR2017-10	Peridotite	2743	0.15	0.44	0.201	0.512856±09	2.84
BR2017-11	Peridotite	2743	0.11	0.38	0.184	0.512646±10	4.57
BR2017-12	Peridotite	2743	0.12	0.35	0.213	0.512879±10	-0.99
BR2017-14	Peridotite	2743	0.27	0.80	0.203	0.513241±09	9.47
BR2017-15	Peridotite	2743	0.33	0.98	0.203	0.512861±10	2.31
BR2017-18	Peridotite	2743	0.11	0.30	0.221	0.513049±11	-0.43
BR2017-6	Gabbro	2743	1.63	4.29	0.230	0.513315±06	1.40
BR2017-23	Gabbro	2743	2.26	7.91	0.173	0.512299±04	1.77
BR2017-24	Gabbro	2743	2.18	7.49	0.176	0.512298±07	0.53
BR2017-32	Gabbro	2743	1.37	4.09	0.203	0.512936±07	3.63
BR2017-36	Gabbro	2743	2.20	6.97	0.191	0.512547±05	0.35
BR2017-22	Leucogabbro	2743	0.78	1.98	0.237	0.513615±09	4.72
BR2017-25	Leucogabbro	2743	1.24	4.33	0.173	0.512284±07	1.36
BR2017-27	Leucogabbro	2743	0.56	1.67	0.203	0.512961±07	4.24
BR2017-34	Leucogabbro	2743	0.67	2.22	0.183	0.512496±08	2.04
BR2017-29	Anorthosite	2743	0.67	1.91	0.211	0.51309±08	3.75
BR2017-35	Anorthosite	2743	0.74	2.39	0.188	0.512583±08	1.96
BR2017-8	Basalt	2743	1.83	5.92	0.188	0.512574±06	1.96
BR2017-37	Basalt	2743	1.68	5.13	0.198	0.51280±09	2.66
32-07-1220-1	Andesite	2725	2.45	13.60	0.109	0.511071±06	0.14
32-07-1220-4	Andesite	2725	3.84	23.38	0.099	0.510898±05	0.20
BR2017-3	Dacite	2731	4.23	25.96	0.099	0.510901±05	0.59
BR2017-4	Dacite	2731	4.18	25.71	0.098	0.510894±04	0.58
BR2017-5	Tonalite	2844	3.99	26.08	0.092	0.510769±05	1.73
BR2017-7	Tonalite	2844	1.55	7.98	0.118	0.511226±08	1.44
BR2017-1	Greywacke	2706	3.15	18.72	0.102	0.510961±06	0.31
BR2017-2	Greywacke	2706	2.89	15.67	0.111	0.511066±05	-0.96

The 2σ uncertainty values for the $^{143}Nd/^{144}Nd$ ratios represent absolute values.

Table 3.1. Sm-Nd isotope data from the Neoarchean (2743 Ma) Bird River Sill and associated volcanic, intrusive, and sedimentary rocks.

Sample ID	Lithology	$^{206}Pb/^{204}Pb$	± 2σ	$^{207}Pb/^{204}Pb$	± 2σ	$^{208}Pb/^{204}Pb$	± 2σ	r1**	r2††
BR2017-9	Peridotite	18.064	0.022	15.518	0.020	37.213	0.051	0.97	0.96
BR2017-9-D	Peridotite	18.072	0.028	15.536	0.025	37.297	0.062	0.98	0.97
BR2017-10	Peridotite	16.842	0.019	15.321	0.018	36.214	0.046	0.96	0.95
BR2017-11	Peridotite	17.123	0.022	15.332	0.020	36.170	0.051	0.97	0.96
BR2017-12	Peridotite	13.755	0.016	14.710	0.018	33.552	0.043	0.97	0.96
BR2017-14	Peridotite	18.445	0.025	15.614	0.023	37.982	0.057	0.98	0.96
BR2017-15	Peridotite	15.358	0.017	14.997	0.018	34.911	0.044	0.97	0.95
BR2017-18	Peridotite	16.263	0.022	15.167	0.022	35.709	0.053	0.98	0.97
BR2017-6	Gabbro	24.483	0.026	16.841	0.019	38.150	0.046	0.97	0.95
BR2017-23	Gabbro	20.254	0.031	15.929	0.025	40.057	0.066	0.98	0.97
BR2017-24	Gabbro	27.476	0.045	17.232	0.029	46.764	0.081	0.98	0.97
BR2017-32	Gabbro	14.044	0.014	14.815	0.016	33.800	0.040	0.97	0.95
BR2017-36	Gabbro	14.002	0.012	14.764	0.014	33.865	0.035	0.97	0.93
BR2017-22	Leucogabbro	16.494	0.029	15.196	0.027	36.172	0.067	0.99	0.98
BR2017-25	Leucogabbro	21.721	0.032	16.151	0.025	40.778	0.066	0.98	0.97
BR2017-27	Leucogabbro	14.922	0.023	14.841	0.024	34.439	0.057	0.98	0.97
BR2017-34	Leucogabbro	14.909	0.025	14.938	0.026	34.404	0.060	0.98	0.97
BR2017-29	Anorthosite	14.314	0.025	14.810	0.027	34.061	0.063	0.99	0.98
BR2017-35	Anorthosite	14.717	0.023	14.888	0.024	33.805	0.057	0.99	0.97
BR2017-8	Basalt	15.481	0.016	15.028	0.016	34.939	0.041	0.97	0.95
BR2017-37	Basalt	14.923	0.015	14.921	0.016	34.074	0.040	0.97	0.95
32-07-1220-1	Andesite	15.893	0.017	15.091	0.018	35.544	0.045	0.97	0.94
32-07-1220-4	Andesite	15.959	0.014	15.050	0.015	36.327	0.038	0.96	0.94
BR2017-3	Dacite	19.740	0.020	15.829	0.017	39.454	0.045	0.97	0.96
BR2017-4	Dacite	19.205	0.022	15.746	0.019	39.534	0.050	0.98	0.96
BR2017-5	Tonalite	36.525	0.054	18.844	0.029	54.943	0.087	0.98	0.97
BR2017-7	Tonalite	44.586	0.061	20.294	0.029	49.834	0.075	0.99	0.97
BR2017-1	Greywacke	19.205	0.029	15.620	0.025	37.222	0.060	0.98	0.97
BR2017-2	Greywacke	17.748	0.016	15.401	0.015	36.988	0.039	0.96	0.95

The 2σ uncertainty values represent absolute values.

r1** = $^{206}Pb/^{204}Pb$ vs. $^{207}Pb/^{204}Pb$ error correlation.

r2†† = $^{206}Pb/^{204}Pb$ vs. $^{208}Pb/^{204}Pb$ error correlation.

Table 3.2. Pb isotope data from the Neoarchean (2743 Ma) Bird River Sill and associated volcanic, intrusive, and sedimentary rocks.

Chapter 4: Evidence for hydrous arc magmatism, the Neoarchean anorthosite-bearing Mayville Intrusion, Western Superior Province, Manitoba, Canada

4.1. Introduction

The style of tectonics that operated in the Archean remains highly controversial, with substantial ongoing debate centred around the opposing uniformitarian and non-uniformitarian models (Bédard, 2006, 2018; Condie and Kröner, 2008; Polat et al., 2012, 2015; Bédard et al., 2013; Foley et al., 2014; Foley, 2018; Kusky et al., 2018; Hastie and Fitton, 2019; Wyman, 2019; Roman and Arndt, 2019). Uniformitarian models propose that modern-style plate tectonics processes (e.g., subduction) operated in the Archean (Windley and Garde, 2009; Foley, 2018; Kusky et al., 2018; Wyman, 2019; Liu et al., 2020), whereas non-uniformitarian proponents postulate that vertical tectonics (e.g., sagduction, catalytic delamination) processes operated during this eon (Bédard, 2006, 2018; Hamilton, 2011; Bédard et al., 2013; Thébaud and Rey, 2013; François et al., 2014; Johnson et al., 2014). The occurrence of primary, magmatic amphibole in gabbroic cumulates (anorthosites, troctolites, gabbros, melagabbros and melagabbronorites) with arc signatures is a strong indicator that these lithologies crystallised from hydrous parental magmas in a subduction zone setting (Claeson and Meurer, 2004), as exemplified by the Paleoproterozoic Eriksberg and Rymmen gabbroic arc-derived intrusions in southern Sweden. Magmatic amphibole in anorthosites and leucogabbros in the granulite-facies Fiskenæsset, Naajat Kuuat and Sittampundi Archean megacrystic anorthosite-bearing layered intrusions of Greenland and India has been interpreted to signify that these layered intrusions crystallised from hydrous parental magmas in a suprasubduction zone (Rollinson et al., 2010; Polat et al., 2011; Hoffmann et al., 2012; Mohan et al., 2013). Archean anorthosite-bearing layered intrusions containing magmatic amphibole (e.g., Narndee Igneous Complex, Australia) have also been proposed to form from hydrated mantle plume sources (Ivanic et al., 2010, 2015). As such, the identification of magmatic amphibole in Archean layered intrusions has critical implications for the style of tectonics that operated on the early Earth. Given the controversy surrounding the style of Archean tectonics and the geodynamic settings in which Archean anorthosite-bearing layered intrusions containing magmatic amphibole formed, resolving whether magmatic amphibole formed from hydrous magmas in subduction zone or non-subduction (e.g., plume) in the Archean is of critical importance for

better understanding the geodynamic processes that drove Archean crustal growth and evolution.

The Mayville Intrusion is a well-preserved Archean megacrystic anorthosite-bearing layered intrusion in the Bird River greenstone belt, western Superior Province, Canada (Yang et al., 2011; Percival et al., 2012; Yang and Gilbert, 2014). Compared to other well-preserved and petrologically and geochemically very similar Archean calcic megacrystic anorthosite-bearing layered intrusions (e.g., Fiskenæsset, Naajat Kuuat, Sittampundi), the Mayville Intrusion underwent relatively lower grade, greenschist- to amphibolite-facies metamorphism (Yang et al., 2011; Yang and Gilbert, 2014). As such, it is an ideal location to search for magmatic amphibole and study the field relationships, petrography, and geochemistry of a well-preserved Archean calcic megacrystic anorthosite-bearing layered intrusion. The Mayville Intrusion, therefore, provides a great opportunity to shed light on whether modern-style plate tectonics or sagduction-driven vertical tectonics processes operated in the Archean. Furthermore, constraining the geodynamic setting and petrogenesis of the Mayville Intrusion is critical to better understanding the geodynamic setting, growth, and evolution of the Bird River greenstone belt and, by extension, the Bird River subprovince and the Superior Province.

In order to address the questions outlined above, new fieldwork, petrography, mineral chemistry, whole-rock major and trace element, and whole-rock Sm-Nd and U-Th-Pb isotope geochemical data from anorthosites, leucogabbros, gabbros, pyroxenites, and melagabbros from the Mayville Intrusion were acquired and are presented in this contribution. Similarly, new fieldwork, petrography, and whole-rock major and trace element geochemical data are also presented for basalts and gabbros from the Mayville Assemblage and a gabbro and leucogabbro from the New Manitoba Mine Intrusion of the Bird River greenstone belt, and a dacite dyke from the 2725 Ma phase of the Maskwa Lake tonalite-trondhjemite-granodiorite (TTG) Batholith. The structural characteristics of the Mayville Intrusion and Bird River subprovince will be considered to constrain whether it has structural features consistent with horizontal (e.g., low-angle thrust faults) or vertical (e.g., dome and basin structures) tectonics (Polat et al., 2015; Bédard, 2018; Kusky et al., 2018). This will be combined with the field relationship, petrography, mineral chemistry, and whole-rock major and trace element and radiogenic isotope data presented in this contribution and data from the literature to determine whether the Mayville Intrusion and the Bird River subprovince formed through horizontal (e.g., modern-style plate) or vertical (e.g., sagduction) tectonics.

4.2. Regional geology

4.2.1. Superior Province

The 2.5-3.8 Ga Superior Province (Fig. 4.1) consists of volcanic-plutonic subprovinces or terranes (2.59-3.36 Ga) that alternate with both plutonic (2.65-3.82 Ga) and metasedimentary (2.65-3.00 Ga) subprovinces (Card and Ciesielski, 1986; Percival et al., 2012). High-grade gneissic subprovinces (2.57-3.50 Ga) occur in the northwestern, northeastern and eastern Superior Province (Percival et al., 2012). In the northeastern Superior Province, high-grade gneissic subprovinces (2.70-3.01 Ga) alternate and are juxtaposed with plutonic subprovinces (2.69-3.65 Ga) (Percival et al., 2012). A change in the trend of the subprovince boundaries in the Superior Province occurs through the Superior orocline from W-E-trending subprovinces in the southeastern, central and western Superior Province to NW-SE-trending subprovinces in the northeastern Superior Province (Percival et al., 2012).

Archean megacrystic anorthosite-bearing layered intrusions (e.g., Doré Lake, Bird River, Mayville, Shawmere, Pipestone Lake, Bad Vermilion Lake, Cauchon Lake, Split Lake, Haines) occur in the volcanic-plutonic and high-grade gneissic subprovinces of the Superior Province, and range in age from >2700-2765 Ma (Allard, 1976; Ashwal, 1993, 2010; Percival et al., 2012; Yang and Gilbert, 2014; Polat et al., 2018a, b; Sotiriou et al., 2019a, b). These layered intrusions underwent poly-phase deformation and greenschist- to granulite-facies metamorphism and are intruded by syn- to late-tectonic granitoids (Ashwal, 1993, 2010; Yang and Gilbert, 2014; Ashwal and Bybee, 2017; Polat et al., 2018a; Sotiriou et al., 2019a, b).

4.2.2. Bird River subprovince

The study area is located in the Bird River granite-greenstone subprovince (also known as the Bird River terrane), which is bound by the metasedimentary English River subprovince (also known as the English River belt) and the plutonic Winnipeg River subprovince (also known as the Winnipeg River terrane) to the north and south, respectively (Figs. 4.1 and 4.2; Card and Ciesielski, 1986; Card and Poulsen, 1998; Yang et al., 2011). The Bird River subprovince contains granitoid plutons, which range in age from 2858.1 ± 2.5 Ma (Maskwa Lake TTG

Batholith) to 2645.6 ± 1.3 Ma (Marijane Lake pluton), and the Bird River and Separation Lake greenstone belts (Baadsgaard and Černý, 1993; Wang, 1993; Gilbert et al., 2008; Duguet et al., 2009; Yang, 2014a). Greenschist- to amphibolite-facies metamorphism associated with the convergence between the Winnipeg River subprovince and the Uchi Domain of the North Caribou superterrane during the 2720-2700 Ma Uchian Orogeny affected the Bird River greenstone belt, generating variable folding, shearing and alteration (Gilbert et al., 2008; Percival et al., 2012).

4.2.3. Bird River greenstone belt

The northern arm of the Bird River greenstone belt comprises the volcano-sedimentary Euclid Lake Formation and Mayville Assemblage (>2742.8 ± 0.8 Ma), and the Mayville (2742.8 ± 0.8 Ma), Euclid Lake (2743 ± 1 Ma), New Manitoba Mine and Cat Lake intrusions, which were emplaced into/near to or erupted onto the northern margin of the Mesoarchean Maskwa Lake TTG Batholith I (Fig. 4.2; Houlé et al., 2013; Yang et al., 2013). All of these formations and intrusions were intruded by the 2725 ± 6 Ma phase of the Maskwa Lake TTG Batholith (Wang, 1993; Yang et al., 2012, 2013; Yang, 2014a).

4.2.4. Mayville Intrusion

The 2742.8 ± 0.8 Ma Archean megacrystic anorthosite-bearing Mayville Intrusion is a >10 kilometre-long and 1.1-kilometre-thick sill or lopolith that trends roughly westwards within the northern arm of the Bird River greenstone belt and is cut by a set of late north-northwest- and northeast-trending faults (Figs. 4.2 and 4.3; Yang et al., 2011, 2012). The Mayville Intrusion was emplaced into the Mayville Assemblage and the Maskwa Lake TTG Batholith I (Figs. 4.2 and 4.3; Gilbert et al., 2008; Yang et al., 2011, 2013; Yang and Gilbert, 2014). Despite having been affected by greenschist- to amphibolite-facies metamorphism, the magmatic textures in the Mayville Intrusion are generally well preserved (Peck et al., 2002; Yang et al., 2011; Yang and Gilbert, 2014).

The Mayville Intrusion can be subdivided into two major zones, the lower Heterolithic Breccia Zone and the upper Anorthosite to Leucogabbro Zone (Fig. 4.3; Peck et al., 2002; Yang et al.,

2011). The Anorthosite to Leucogabbro Zone can be further subdivided into the Lower Megacrystic, Layered, Upper Megacrystic, Massive Leucogabbro and Gabbro zones (Yang et al., 2011). Mafic volcanic xenoliths occur in the basal part of the Heterolithic Breccia Zone, however, gneissic and granitoid fragments are more evident in the Massive Leucogabbro and Gabbro zones (Yang et al., 2011). A variety of lithologies are present in the Mayville Intrusion, including anorthosite, leucogabbro, gabbro, melagabbro, chromitite and pyroxenite and, despite being metamorphosed, display well-preserved magmatic textures (Peck et al., 2002; Yang et al., 2011; Yang et al., 2012). The Mayville Intrusion, like the contemporaneous and nearby Bird River Sill and Euclid Lake, Cat Lake, and New Manitoba Mine intrusions, has been interpreted to have formed during the voluminous Bird River mafic magmatic event that occurred in the Bird River subprovince at ~2743 Ma (Fig. 4.2; Yang et al., 2011, 2012, 2013; Houlé et al., 2013).

4.3. Field relationships

Fieldwork carried out in the Mayville Intrusion confirms that it is divided into the Heterolithic Breccia and Anorthosite to Leucogabbro Zones (Figs. 4.3-4.5). The Heterolithic Breccia Zone comprises anorthosite, leucogabbro, gabbro, melagabbro, pyroxenite and chromitite, whereas the Anorthosite to Leucogabbro Zone consists of anorthosite, leucogabbro, and gabbro (Figs. 4.3 and 4.4).

The lithologies of the Heterolithic Breccia Zone have well-preserved cumulate textures and a variably-preserved primary mineralogy (Fig. 4.5). The chromitites exhibit well-pronounced magmatic layering. Autoliths of anorthosites and leucogabbros occur within the Heterolithic Breccia Zone (Fig. 4.5). These autoliths are cut by gabbroic dykes (Fig. 4.5). Magmatic layering is only locally preserved and often disrupted by shearing. Magmatic and tectonic brecciation occurs throughout the Heterolithic Breccia Zone.

The anorthosites and leucogabbros from the Anorthosite to Leucogabbro Zone are characterised by a well-preserved cumulate texture, a distinctive megacrystic texture and have plagioclase megacrysts up to 6 centimetres in diameter (Fig. 4.4). Abundant magmatic amphibole is well-preserved in the anorthosites and leucogabbros. This magmatic amphibole exhibits well-defined cleavage, whole-grain optical continuity and serrated igneous grain boundaries in the field, indicating that it is of igneous origin (Fig. 4.4). Some of the anorthosites

and leucogabbros have undergone partial recrystallisation, yet still preserve their cumulate textures (Fig. 4.5). The magmatic plagioclase and amphibole in these recrystallised anorthosites and leucogabbros have largely recrystallised to metamorphic plagioclase (albite) and amphibole (actinolite). Some of the anorthosites and leucogabbros have been sheared (Fig. 4.5).

The Mayville Intrusion intrudes pillow basalts of the Mayville Assemblage and is intruded by the Neoarchean phase of the Maskwa Lake TTG Batholith (Fig. 4.3). The Mayville Intrusion contains TTG xenoliths belonging to the Mesoarchean phase of the Maskwa Lake TTG Batholith, which represents the only felsic crust in the area older than the Mayville Intrusion (Yang et al., 2011, 2012, 2013). The Mayville Assemblage pillow basalts and gabbros were intruded by the Neoarchean phase of the Maskwa Lake TTG Batholith (Fig. 4.3). These pillow basalts and gabbros were erupted onto and emplaced into the Mesoarchean phase of the Maskwa Lake TTG Batholith, respectively.

4.4. Sampling

Samples were obtained from the Neoarchean Mayville Intrusion (Figs. 4.2 and 4.3) during fieldwork conducted in the Bird River area of southeastern Manitoba in June 2017 and August 2018. Fourteen anorthosites, eight leucogabbros, two chromitites, one pyroxenite and one gabbro were collected from the Anorthosite to Leucogabbro and Heterolithic Breccia Zones of the Mayville Intrusion. This field-based sampling was supplemented by selecting samples at the Geological Survey of Manitoba in Winnipeg, where samples were described and cut for whole-rock analysis and thin section studies. These samples include nine anorthosites, five leucogabbros, five gabbros, five melagabbros, and two pyroxenites. Samples selected from the Mayville Assemblage include five basalts, and one gabbro. Two gabbro samples from the New Manitoba Mine Intrusion were also selected. Field sampling, combined with samples from the Geological Survey of Manitoba, allowed for representative sampling from the bottom to the top of the Mayville Intrusion to understand the genetic relationships between the different units within this intrusion. Furthermore, a dacite dyke sample was selected from the younger, 2725 Ma phase of the Maskwa Lake TTG Batholith. Sampling was conducted from the least to most altered samples to ascertain the effect of hydrothermal alteration associated with metamorphism on the samples' element mobility. The samples' weights ranged from 2 to 4 kg.

The Global Positioning System (GPS) coordinates for the field and Geological Survey of Manitoba sample locations are given in Appendices 3.1 and 3.2.

4.5. Methods

4.5.1. Major and trace elements

Fifty-two samples from the Mayville Intrusion, six samples from the Mayville Assemblage, and two samples from the New Manitoba Mine Intrusion were analysed for major elements. Additionally, one dacite dyke sample from the Maskwa Lake TTG Batholith II was also analysed for major elements. Prior to the major element analysis at Activation Laboratories Ltd. (Actlabs) in Ancaster, Ontario, Canada, using a Fusion inductively-coupled plasma (ICP) mass spectrometer, an agate mill was used to crush the samples down to individual powders, which were then heated for 3 hours at 1100°C. The loss-on-ignition (LOI) values for the samples were calculated using the consequential weight loss. A commixture of lithium metaborate and lithium tetraborate facilitated the fusion of the samples and a 5% nitric acid solution expedited their dissolution. Major element oxides totals are 100 ± 1.5 wt.%. Reproducibility was greater than ±5% for the analysed samples. Appendix 3.3 contains detection limits for the major elements and the results of the standard and duplicate analyses.
Burnham (2017) and Hargreaves (2017) provide a thorough outline of the analytical procedure followed for the trace element ICP mass spectrometer (MS) analyses conducted at Geoscience Laboratories (Geo Labs) in Sudbury, Ontario, Canada. Fifty-one samples from the Mayville Intrusion, six samples from the Mayville Assemblage and two samples from the New Manitoba Mine Intrusion were analysed for trace elements using this analytical technique, alongside one dacite dyke sample from the Maskwa Lake TTG Batholith II. The multiple acids technique was used to dissolve the powder samples produced during the major element analysis process outlined above. The use of this technique produced a greater than ±10% reproducibility for the majority of the trace element analyses (Polat et al., 2016). The methods set out in Taylor and McLennan (1985) were used to calculate the Eu/Eu*, Ce/Ce*, Nb/Nb*, Zr/Zr*, Ti/Ti* and Hf/Hf* anomalous element ratios of the samples. For the petrogenetic interpretation to follow, trace elements were normalised to known normal mid-ocean ridge basalt (N-MORB) and chondrite values (Sun and McDonough, 1989). The $Mg/(Mg + Fe^{2+})$ molecular ratio was used

to calculate the Mg-numbers (#) of the samples (Gill, 2010; Zhou et al., 2016). These Mg# were calculated on the basis that Fe^{2+} represents 90% of total Fe (Gill, 2010; Zhou et al., 2016).

4.5.2. Sm-Nd and Pb isotope analyses

Nineteen samples from the Mayville Intrusion were selected for Sm-Nd and Pb isotope analyses on the basis of having coherent chondrite-normalised rare-earth element (REE) and N-MORB-normalized trace element patterns and being representative of the lithologies of this layered intrusion. Samarium, Nd and Pb isotopic ratios and Sm and Nd isotopic dilution concentrations were determined from dissolved powder aliquots at the Department of Geosciences and Natural Resource Management (IGN), University of Copenhagen, Copenhagen, Denmark, using a VG Sector IT Thermal Ionization Mass Spectrometer (TIMS). A $^{150}Nd/^{147}Sm$ spike was mixed in with the sample powders before acid digestion. This digestion was accomplished and facilitated by the use of concentrated HNO_3-, HCl- and HF-bearing Savillex^{TM} beakers that were placed on a hotplate heated at 130°C for 3 days to dissolve these powder samples (Wu et al., 2016). Rare-earth element separation was ensured using chromatographic separation columns charged with 12 ml AG50W-X 8 (100-200 mesh) cation resin. Eichrom's^{TM} LN resin SPS (Part#LN-B25-S) stored in smaller chromatographic columns facilitated Sm and Nd separation. Lead separation was conducted using 100-200 mesh Bio-Rad AG 1 x 8 resin in conventional glass and miniature glass stem anion exchange columns containing 1 ml and 200 µl of this resin, respectively. The Sm and Nd isotope compositions were determined using a multi-dynamic routine and a static multi-collection mode, respectively. Mass bias necessitated the use of a $^{146}Nd/^{144}Nd$ ratio of 0.7219 to correct the measured Nd isotope ratios for this issue. During the analytical period, a mean value of $^{143}Nd/^{144}Nd = 0.5120948 \pm 0.0000089$ (2σ; $n = 8$) was yielded by measurements of the JNdi standard. Additionally, a greater than 2% (2σ) precision for the $^{147}Sm/^{144}Nd$ ratio analyses persisted throughout the analytical period's duration. Quantification of the Pb isotope compositions of the samples was facilitated using a static multi-collection mode. Throughout the analyses of the Pb isotope ratio compositions, fractionation was controlled by the repeated analysis of the NBS 981 standard (using the values of Todt et al., 1993). Total procedural blanks of <200 pg Pb demonstrated that the Pb isotope ratio compositions were not influenced beyond the third significant digit.

4.5.3. Scanning electron microscope energy dispersive X-ray spectroscopy (SEM-EDS) analyses

The mineralogical compositions and textures of the samples were characterised at the University of Windsor using an FEI Quanta 200 field emission gun (FEG) scanning electron microscope (SEM), equipped with a back-scattered electron (BSE) imaging unit. A spot size of 3.9 μm, a voltage of 15 kV and an analysis duration of 30 seconds per analysis spot were used to acquire qualitative and quantitative SEM-EDS data on the chemistry and textures of plagioclase, amphibole, chromite, and chromite-hosted mineral inclusions from the Mayville Intrusion. The error percentage values for these minerals are inversely proportional to their weight percentage values.

4.5.4. Raman spectrometer analyses

In order to corroborate data obtained using petrographic and scanning electron microscopy, a WiTec confocal Raman spectrometer at the Great Lakes Institute for Environmental Research, University of Windsor, was used. Operating conditions included a 40 mW laser power, a 7 μm laser spot size, a 532 nm excitation wavelength, and an analysis duration of 10 seconds per analysis. The spots analysed were chosen based on the location of the SEM-EDS analysis spots. Plagioclase, amphibole, and chromite grains from the Mayville Intrusion were analysed using this analytical technique.

4.6. Petrography

4.6.1. Mayville Intrusion

The anorthosites and leucogabbros from the Anorthosite to Leucogabbro Zone and leucogabbros from the Heterolithic Breccia Zone of the Mayville Intrusion are coarse grained to megacrystic (≤6 cm) and generally exhibit fresh cumulate textures and primary igneous minerals (Figs. 4.4-4.7). Small plagioclase grains and megacrysts form 70 to 95% of these lithologies, and mainly occur as euhedral, well-preserved primary crystals (Figs. 4.4-4.7). Primary, magmatic ferromagnesian minerals form 5 to 30% of the anorthosites and

leucogabbros and include amphibole, clinopyroxene and orthopyroxene that have serrated grain boundaries with cumulus plagioclase (Figs. 4.4-4.8). These ferromagnesian minerals are interstitial to the plagioclase megacrysts, fine to coarse grained (≤2 mm) and are generally very well preserved (Figs. 4.4-4.7). Amphibole often occurs as oikocrysts enveloping poikilitic cumulus plagioclase (Figs. 4.4-4.7). Opaque minerals form ≤3% of the anorthosites and leucogabbros, with the more altered samples containing ≤10% secondary actinolite. Based on textural relationships, plagioclase crystallised prior to the formation of interstitial pyroxene and amphibole, which was followed by the crystallisation of opaque minerals that contain inclusions of these minerals. The compositions of the plagioclase crystals in the anorthosites, a chromitite and a gabbro ranges from An_0 to An_{100}. Textural observations indicate that the more calcic plagioclases (An_{70-100}) are considered to be of primary origin, whereas the more sodic plagioclases (An_{0-50}) are interpreted as being of metamorphic origin (Ashwal, 1993; Polat et al., 2018). The anorthite content of the cores of plagioclase crystals from the anorthosites ranges from An_{63} to An_{99}. The igneous amphibole in the anorthosites and leucogabbros has undergone between 10% and 100% recrystallisation by volume to actinolite (Figs. 4.4-4.7).

The anorthosites of the Anorthosite to Leucogabbro Zone range from very altered to very fresh. The very altered anorthosites are not as common as the very fresh anorthosites and are comprised of coarse-grained (≤4 mm), secondary sericite (65-70%), zoisite (15-25%), and epidote (1-5%), and primary, relict orthopyroxene (5-10%) and clinopyroxene (5%) crystals. Sericite almost completely replaces primary plagioclase, with zoisite replacing any plagioclase not replaced by sericite (Fig. 4.7). Orthopyroxene and clinopyroxene are partly replaced by secondary epidote and actinolite. Primary cumulate textures are not very well preserved. The majority of the anorthosites from the Anorthosite to Leucogabbro Zone exhibit generally fresh cumulate textures and primary igneous minerals and comprise magmatic plagioclase (60-90%), orthopyroxene (2-25%), clinopyroxene (~1-12%), amphibole (1-40%) and opaques (≤2%), and secondary actinolite (≤10%) porphyroblasts (Figs. 4.6-4.8). Plagioclase occurs as 2 to 3 cm diameter, spherical megacrysts that comprise more numerous, ≤1 cm plagioclase crystals (Figs. 4.5 and 4.6). Magmatic orthopyroxene, clinopyroxene, amphibole and the opaques are fine grained (<1 mm) and are predominantly interstitial to the larger plagioclase megacrysts. Opaques occur as small inclusions within plagioclase and pyroxene, and contain small inclusions of orthopyroxene, clinopyroxene, amphibole and olivine. Some plagioclase crystals are separated by string-like accumulations of primary orthopyroxene and amphibole crystals. Fine grained (<1 mm thick) amphibole-dominated melt veins sometimes occur between the

plagioclase megacrysts. Some plagioclase crystals are partially or completely replaced by clinozoisite and/or sericite. The interstitial, ferromagnesian minerals are more altered than the plagioclase megacrysts with some orthopyroxene, clinopyroxene and amphibole crystals partly or completed altered to actinolite. Rare, <1 mm-thick quartz veins are present and are associated with the more altered parts of these generally fresh anorthosites.

The leucogabbros of the Anorthosite to Leucogabbro Zone are coarse grained (≤5 mm) to megacrystic and have a distinctive megacrystic texture (Fig. 4.6). Euhedral and well-preserved plagioclase crystals and megacrysts form 70 to 75% of the leucogabbros (Fig. 4.6). The plagioclase crystals and megacrysts contain small inclusions (<1 mm) of magmatic, euhedral amphibole, clinopyroxene, orthopyroxene and opaques. Opaque minerals form <1% of the leucogabbros. Sericite and clinozoisite form 2 to 4% of the leucogabbros and have partly replaced plagioclase. Magmatic amphibole occurs as oikocrysts enveloping poikilitic plagioclase chadacrysts (Figs. 4.6-4.8). The leucogabbros of the Heterolithic Breccia Zone are coarse grained (≤5 mm), have well-defined and well-preserved cumulate textures and are generally quite fresh. Euhedral, primary plagioclase forms 50 to 70% of these leucogabbros, with subordinate, interstitial, euhedral magmatic orthopyroxene (15-45%), amphibole (10-15%) and clinopyroxene (3-10%) also present. Opaques form ≤3% of the leucogabbros. Small inclusions of magmatic amphibole and orthopyroxene occur within the plagioclase crystals and the opaques. Some of the larger orthopyroxenes in one of the more orthopyroxene-rich (40-45%) leucogabbros are altered and have undergone partial recrystallisation to secondary actinolite.

The gabbros of the Anorthosite to Leucogabbro Zone are finer grained (1-5 mm) and generally have well-preserved cumulate textures and primary minerals. These gabbros also have a very similar primary mineralogy (plagioclase, amphibole, clinopyroxene and orthopyroxene) to the anorthosites and leucogabbros. Euhedral, magmatic plagioclase forms 25 to 65% of the gabbros. Ferromagnesian minerals, such as magmatic orthopyroxene (20-40%), clinopyroxene (5-15%) and amphibole (1-15%), are mostly subordinate to plagioclase. Secondary chlorite (1-10%) replaces these ferromagnesian minerals. Metamorphic quartz forms 1 to 5% of the more altered gabbros. Primary quartz makes up 15 to 20% of one of the gabbros. Orthopyroxene oikocrysts enclose numerous poikilitic plagioclase chadacrysts. Compared to these gabbros, a gabbro dyke and pyroxenites from the Heterolithic Breccia Zone have a similar grain size (1-5 mm) and primary mineralogy, however, they are more altered. The gabbro dyke from the Heterolithic Breccia Zone is dominated by fine grained (<1 mm), euhedral, primary plagioclase

(~45%) and secondary actinolite (~45%), with coarser-grained (≤3 mm), euhedral magmatic orthopyroxene, clinopyroxene and opaques (5-11%) and secondary actinolite and chlorite (5-10%) being subordinate. Orthopyroxene and clinopyroxene form ≤5% of this gabbro and primarily occur as relicts. This gabbro exhibits a transition from a finer-grained, crystal-free area to a coarser-grained, relatively crystal-rich area and possibly displays a metamorphic foliation.

Pyroxenites from the Heterolithic Breccia Zone exhibit a fine to coarse grained (1-5 mm) texture and comprise euhedral, fine- to coarse-grained, magmatic clinopyroxene (35-40%), plagioclase (35-40%) and orthopyroxene (~20%) crystals and minor (<15) opaque crystals. Cumulate textures and primary igneous minerals are well preserved, however, in some instances, crystals are either partially to completely replaced or recrystallised. Indeed, actinolite forms 15 to 20% of these pyroxenites and mainly replaces fine-grained clinopyroxene and orthopyroxene. A chromitite from the Heterolithic Breccia Zone exhibits a fine- to medium-grained (<2 mm) texture and is dominated by subhedral to euhedral chromite (30-70%) crystals (<2 mm) and fine-grained (<1 mm) serpentine (50%) pseudomorphing olivine, with relict pyroxene being subordinate (Figs. 4.7 and 4.9). The chromites have small inclusions (clinopyroxene, orthopyroxene and albite) and ultra-thin fractures (Figs. 4.7 and 4.9). Lizardite is the predominant serpentine group mineral in this chromitite (Figs. 4.7 and 4.9). Fine-grained (<1 mm), euhedral clinopyroxene (5%) is subordinate to chromite and lizardite (Figs. 4.7 and 4.9). Scanning electron microscope and Raman analyses indicate that the chromites host primary mineral inclusions that consist of primary augite, enstatite, apatite and feldspar and secondary amphibole and calcite (Figs. 4.7 and 4.9; Appendices 3.4 and 3.5).

4.6.2. Mayville Assemblage

A basalt from the Mayville Assemblage comprises 50 to 55% pyroxene, 45 to 50% plagioclase and <1% opaques. This basalt is porphyritic with the coarser-grained plagioclase phenocrysts being larger than the finer-grained pyroxene that forms the fine-grained groundmass. Some of the pyroxenes have been partially altered to actinolite.

4.6.3. Acme Intrusion

One gabbro sampled from the Acme Intrusion in the Mayville Assemblage to the SE of the Mayville Intrusion (Fig. 4.2) has undergone some alteration and recrystallisation, however, some parts of it are relatively fresh. There are numerous quartz veins and 40 to 50% of the sample is secondary sericite after primary plagioclase. Chlorite forms 5 to 15% of the sample and replaces magmatic orthopyroxene, clinopyroxene and amphibole. Magmatic orthopyroxene (20-30%), clinopyroxene (20-25%), opaques (<10%) and plagioclase (<5%) comprise the remainder of the sample.

4.6.4. Dacite dyke (Maskwa Lake TTG Batholith II)

A dacite dyke sampled from the Maskwa Lake TTG Batholith II is fine grained with subordinate, numerous, coarser-grained, larger phenocrysts. Porphyritic euhedral biotite phenocrysts form 20 to 30% of this dacite, with subordinate, finer-grained magmatic quartz (20-30%), plagioclase (30-40%), alkali feldspar (10-20%) and opaques (<1%), and secondary epidote (1-2%) replacing plagioclase. The quartz phenocrysts exhibit undulose extinction and quartz veins form >1% of the dacite.

4.7. Geochemical results

4.7.1. Chromite, plagioclase, amphibole, and chromite-hosted mineral inclusion mineral chemistry

4.7.1.1. Chromite

The cores of the chromite grains from the chromitites of the Mayville Intrusion have variable Cr (26.12-53.15 wt.%) and Fe (0.00-40.18 wt.%) and narrow-ranging Al (6.84-12.72 wt.%) and MgO (0.00-1.53 wt.%) contents, and narrow-ranging Cr# (56-69) and Mg# (0-11) (Appendix 3.4). The rims of these chromite grains have narrow-ranging Al (6.29-11.38 wt.%) and Mg (0.00-1.49 wt.%) and Cr (25.96-32.36 wt.%) and higher Fe (28.08-41.34 wt.%) contents and overlapping Cr# (55-69) and Mg# (0-11) (Appendix 3.4). The rims bordering the

inclusions in the chromite grains have narrow-ranging Al (6.76-12.33 wt.%) and Mg (0.00-1.43 wt.%) and variable Cr (26.50-53.67 wt.%) and Fe (0.00-39.56 wt.%) contents and narrow-ranging Cr# (60-70) and Mg# (0-10) (Appendix 3.4). The chemistry of the chromite grains from the Mayville Intrusion suggest that they are chromite *sensu stricto* to hercynite in composition (Appendix 3.4; Deer et al., 2013).

4.7.1.2. Plagioclase

The cores of the plagioclase grains from the anorthosites of the Mayville Intrusion have variable Ca (7.44-20.52 wt.%), Na (0.10-5.98 wt.%), Al (13.12-19.56 wt.%) and Si (19.99-26.82 wt.%) contents and variably calcic An (63-99) contents, indicating that they are of labradorite to anorthite composition (Appendix 3.4). The rims of these plagioclase grains have similarly variable Ca (7.00-14.12 wt.%), Na (1.08-6.16 wt.%), Al (15.47-19.56 wt.%) and Si (20.50-26.98 wt.%) contents and variable An (43-88) contents, indicating that they range from andesine to bytownite composition (Appendix 3.4).

The cores of the plagioclase grains from chromitite sample MV2018-13 have narrow-ranging Ca (14.56-15.49 wt.%), Na (0.22-0.83 wt.%), Al (19.87-20.38 wt.%) and Si (19.93-20.90 wt.%) contents and very calcic An (91-98) contents, suggesting that they are of anorthite composition (Appendix 3.4). The rims of these plagioclase grains have overlapping Ca (12.33-15.29 wt.%), Na (0.16-0.91 wt.%), Al (19.82-20.38 wt.%) and Si (19.68-20.62 wt.%) contents and similarly high An (90-98) contents, indicating that they are also of anorthite composition (Appendix 3.4).

The cores of the plagioclase grains from gabbro samples MV2018-12A and MV2018-12B have variable Ca (4.84-19.50 wt.%), Na (0.92-7.37 wt.%), Al (14.02-19.78 wt.%) and Si (18.28-28.86 wt.%) and variable An (29-100) contents, indicating that they are of oligoclase to anorthite composition (Appendix 3.4). The rims of these plagioclase grains have variable Ca (5.15-14.94 wt.%), Na (0.77-11.36 wt.%), Al (11.30-19.84 wt.%) and Si (20.72-32.80 wt.%) contents and very variable An (0-100) contents, suggesting that they range in composition from albite to anorthite (Appendix 3.4).

4.7.1.3. Amphibole

The cores of the amphibole grains from anorthosites from the Mayville Intrusion have variable Mg (0.87-12.03 wt.%), Al (1.92-14.05 wt.%), Si (12.04-24.64 wt.%) and Fe (6.42-16.40 wt.%) and Ca (7.79-18.42 wt.%) and narrow-ranging Na (0.03-1.13 wt.%) contents and moderate to high Mg# (26-75), indicating that they are predominantly of magnesiohornblende composition, with ferrotschermakite being subordinate (Appendix 3.4; Leake et al., 1997). The rims of these amphibole grains have variable Mg (4.50-10.98 wt.%), Al (2.44-15.14 wt.%), Si (12.44-24.64 wt.%), Ca (2.50-18.30 wt.%) and Fe (6.40-19.54 wt.%) and narrow-ranging Na (0.05-0.99 wt.%) contents and Mg# (56-76), suggesting that they are predominantly of magnesiohornblende in composition, with ferrotschermakite being subordinate (Appendix 3.4; Leake et al., 1997).

The cores of the amphibole grains from chromitite sample MV2018-3 have variable Mg (7.17-17.78 wt.%), Al (5.12-12.85 wt.%), Si (12.78-23.28 wt.%), Ca (5.01-10.30 wt.%), Fe (7.40-10.70 wt.%) and Na (0.04-1.86 wt.%) contents and high Mg# (65-82), indicating that they are mostly magnesiohornblende in composition, with tschermakite being subordinate (Appendix 3.4). The rims of these amphibole grains have variable Mg (7.60-17.30 wt.%), Al (4.96-12.84 wt.%) and Si (12.62-23.25 wt.%), Fe (7.02-10.36 wt.%) and Na (0.09-1.81 wt.%) and narrow-ranging Ca (9.46-9.96 wt.%) contents and high Mg# (66-83), suggesting that they are of magnesiohornblende composition (Appendix 3.4).

The cores of the amphibole grains from gabbro samples MV2018-12A and MV2018-12B have variable Al (1.87-12.58 wt.%), Si (11.94-25.19 wt.%) and Fe (10.74-19.86 wt.%) and narrow-ranging Mg (7.56-9.59 wt.%) and Ca (9.50-10.48 wt.%) contents and moderate to high Mg# (55-69), indicating that they are mainly magnesiohornblende in composition, with actinolite being subordinate (Appendix 3.4; Leake et al., 1997). The rims of these amphibole grains have variable Mg (7.71-11.95 wt.%), Al (2.11-12.56 wt.%), Si (12.56-25.04 wt.%) and Fe (11.29-17.75 wt.%) and narrow-ranging Ca (9.66-10.31 wt.%) and Na (0.25-0.61 wt.%) contents and high Mg# (62-67), suggesting that they predominantly of magnesiohornblende composition, with actinolite being subordinate (Appendix 3.4; Leake et al., 1997).

4.7.1.4. Chromite-hosted mineral inclusions

The chromite-hosted clinopyroxene inclusions in the chromitites of the Mayville Intrusion have variable Al (3.1-12.3 wt.%), Si (14.7-25.1 wt.%), Ca (0.7-12.2 wt.%) and Mg (16.6-20.5 wt.%) contents and high Mg# (71-100) (Appendix 3.4). A chromite-hosted rutile inclusion contains

30.3 wt.% Fe and 27.8 wt.% Ti (Appendix 3.4). A chromite-hosted calcite inclusion contains 52.2 wt.% Ca (Appendix 3.4). A chromite-hosted apatite inclusion contains 39 wt.% Ca and 1.7 wt.% P (Appendix 3.4).

4.7.2. Major and trace elements

4.7.2.1. Mayville Intrusion

The pyroxenites have low SiO_2 (42.6-44.9 wt.%), high $Fe_2O_3^T$ (8.7-14.8 wt.%), CaO (11.1-13.6 wt.%), Al_2O_3 (15.7-18.4 wt.%) and MgO (9.0-13.3 wt.%) and low to moderate TiO_2 (0.22-0.54 wt.%) contents, and moderate to high Mg# (52-73) (Fig. 4.10; Appendix 3.1; Gill, 2010). These pyroxenites have variable trace element abundances, and display LREE-enriched and near-flat HREE patterns and negative Nb and Ti and negative to positive Zr and Hf anomalies on the N-MORB-normalised trace element diagram (Figs. 4.11 and 4.12e; Appendix 3.1).

The chromitites have low SiO_2 (32.9-33.2 wt.%), moderate to high Al_2O_3 (10.3-18.8 wt.%) and TiO_2 (0.47-0.73 wt.%), high $Fe_2O_3^T$ (15.2-19.9 wt.%) and MgO (11.6-20.0 wt.%) and low CaO (5.0-7.9 wt.%) contents, and moderate to high Mg# (54-72) (Fig. 4.10; Appendix 3.1).

The melagabbros have low SiO_2 (43.0-50.1 wt.%), moderate to high Al_2O_3 (12.1-18.7 wt.%), high $Fe_2O_3^T$ (11.6-20.7 wt.%), CaO (9.4-11.9 wt.%) and MgO (6.3-9.3 wt.%) and low to high TiO_2 (0.34-1.01 wt.%) contents, and low to moderate Mg# (39-56) (Fig. 4.10; Appendix 3.1). The melagabbro samples exhibit near-flat to LREE-enriched patterns and negative Nb, Zr and Hf and negative to positive Ti anomalies on the N-MORB-normalised trace element diagram (Fig. 4.12d; Appendix 3.1).

The gabbros have low to moderate SiO_2 (49.2-64.4 wt.%), moderate Al_2O_3 (12.3-15.7 wt.%), high $Fe_2O_3^T$ (6.2-15.5 wt.%) and low to high TiO_2 (0.52-1.71 wt.%), CaO (4.7-13.2 wt.%) and MgO (1.9-9.1 wt.%) contents, and low to moderate Mg# (18-61) (Fig. 4.10; Appendix 3.1). On the N-MORB-normalised trace element diagram, these gabbros have enriched and depleted LREE and near-flat HREE patterns and negative Nb and Ti and negative to positive Zr and Hf anomalies (Fig. 4.12c; Appendix 3.1).

The leucogabbros have low SiO_2 (41.5-50.1 wt.%), high Al_2O_3 (18.3-23.9 wt.%) and CaO (11.1-15.0 wt.%), moderate to high $Fe_2O_3^T$ (4.6-10.0 wt.%) and low to high MgO (2.3-7.9

wt.%) and TiO_2 (0.21-0.79 wt.%) contents, and moderate to high Mg# (47-64) (Fig. 4.10; Appendix 3.1). The leucogabbro samples exhibit enriched and depleted LREE and near-flat HREE patterns and negative to positive Nb, Ti, Zr and Hf anomalies on the N-MORB-normalised trace element diagram (Fig. 4.12b; Appendix 3.1).

The anorthosites have high Al_2O_3 (24.3-30.5 wt.%) and CaO (10.9-15.8 wt.%), low to high $Fe_2O_3^T$ (2.3-7.4 wt.%), MgO (1.0-5.4 wt.%) and TiO_2 (0.12-1.29 wt.%) and low SiO_2 (45.4-51.3 wt.%) contents, and moderate Mg# (38-65) (Fig. 4.10; Appendix 3.1). These anorthosites have low immobile element abundances and exhibit enriched to depleted LREE patterns and negative to positive Zr, Hf, Ti and Nb and positive Eu anomalies on the N-MORB-normalised trace element diagram (Figs. 4.11 and 4.12a; Appendix 3.1).

4.7.2. New Manitoba Mine Intrusion

The gabbro and leucogabbro from the New Manitoba Mine Intrusion have low SiO_2 (45.2-49.9 wt.%), high $Fe_2O_3^T$ (8.1-17.7 wt.%), CaO (10.2-12.5 wt.%) and TiO_2 (0.60-0.71 wt.%) and moderate to high Al_2O_3 (14.7-20.7 wt.%), and MgO (4.2-5.9 wt.%) contents, and low to moderate Mg# (37-48) (Fig. 4.10; Appendix 3.2). On the N-MORB-normalised trace element diagram, these lithologies exhibit LREE-enriched and near-flat HREE patterns and negative Nb, Ti, Zr and Hf anomalies (Fig. 4.12f; Appendix 3.2).

4.7.2.3. Bird River greenstone belt

4.7.2.3.1. Mayville Assemblage

The basalts and gabbro from the Mayville Assemblage have low SiO_2 (47.4-52.4 wt.%), moderate Al_2O_3 (13.7-15.7 wt.%), high CaO (8.9-13.8 wt.%), $Fe_2O_3^T$ (11.1-13.1 wt.%) and MgO (4.5-11.6 wt.%) and moderate to high TiO_2 (0.53-1.00 wt.%) contents, and low to high Mg# (39-65) (Fig. 4.10; Appendix 3.2). On the N-MORB-normalised trace element diagram, these basalts and gabbro display LREE-enriched to near-flat HREE patterns and negative Nb, Zr and Hf and negative to positive Ti anomalies (Fig. 4.12f; Appendix 3.2).

4.7.2.4. Maskwa Lake TTG Batholith II

Sample 111-12-412B01 plots in the dacite field on the Zr/Ti versus Nb/Y diagram (Fig. 4.13) of Winchester and Floyd (1977), thereby confirming that this sample was correctly identified as a dacite in the field. This dacite dyke has high SiO_2 (68.4 wt.%), moderate Al_2O_3 (13.9 wt.%), TiO_2 (0.58 wt.%) and $Fe_2O_3^T$ (5.3 wt.%) and low MgO (1.5 wt.%) and CaO (3.4 wt.%) contents, and a low Mg# (34) (Fig. 4.10; Appendix 3.2). The dacite dyke exhibits a strongly LREE-enriched pattern and displays negative Nb and Ti and positive Zr and Hf anomalies relative to REE on the N-MORB-normalised trace element diagram (Fig. 4.12f; Appendix 3.2).

4.7.3. Radiogenic isotopes

4.7.3.1. Sm-Nd isotopes

The pyroxenites (+2.1 to +2.2) and melagabbros (+2.0 to +3.4) from the Heterolithic Breccia Zone have positive $\varepsilon_{Nd\ (2743\ Ma)}$ values (Fig. 4.14a; Table 4.1). An anorthosite (+2.9) and a leucogabbro (+2.8) also have positive $\varepsilon_{Nd\ (2743\ Ma)}$ values (Fig. 4.14a; Table 4.1). The lithologies of the Anorthosite to Leucogabbro Zone have negative to positive $\varepsilon_{Nd\ (2743\ Ma)}$ values (Fig. 4.14; Table 4.1). The anorthosites from the Anorthosite to Leucogabbro Zone have $\varepsilon_{Nd\ (2743\ Ma)}$ values ranging from -6.8 to +2.1 (Fig. 4.14a; Table 4.1). The leucogabbros from the Anorthosite to Leucogabbro Zone have $\varepsilon_{Nd\ (2743\ Ma)}$ values that vary from negative to positive (-1.5 to +3.9) (Fig. 4.14a; Table 4.1). Similarly, the gabbros from the Anorthosite to Leucogabbro Zone have negative to positive $\varepsilon_{Nd\ (2743\ Ma)}$ values that range from -3.5 to +1.7 (Fig. 4.14a; Table 4.1).

4.7.3.2. Pb isotopes

The pyroxenites and melagabbros from the Heterolithic Breccia Zone have overlapping and quite variable $^{206}Pb/^{204}Pb$ (14.187-20.480 and 14.015-19.036), $^{207}Pb/^{204}Pb$ (14.644-15.872 and 14.616-15.701) and $^{208}Pb/^{204}Pb$ (33.828-38.849 and 33.592-37.307) ratios (Fig. 4.14b; Table 4.2). The anorthosites and leucogabbros from the Heterolithic Breccia Zone have similar $^{206}Pb/^{204}Pb$ (14.018 and 14.249),$^{207}Pb/^{204}Pb$ (14.742 and 14.744) and $^{208}Pb/^{204}Pb$ (33.632 and 33.991) ratios (Fig. 4.14b; Table 4.2). The anorthosites and leucogabbros from the Anorthosite to Leucogabbro Zone have moderately variable $^{206}Pb/^{204}Pb$ (14.018-17.561 and 14.569-16.487) and $^{208}Pb/^{204}Pb$ (33.590-37.243 and 34.018-36.011) ratios, and narrow-ranging $^{207}Pb/^{204}Pb$ (14.761-15.394 and 14.895-15.174) ratios (Fig. 4.14b; Table 4.2). The gabbros from the

Anorthosite to Leucogabbro Zone have wide-ranging $^{206}Pb/^{204}Pb$ (19.541-25.609) ratios, and narrow-ranging $^{207}Pb/^{204}Pb$ (15.761-16.828) and $^{208}Pb/^{204}Pb$ (39.301-40.606) ratios (Fig. 4.14b; Table 4.2).

4.8. Discussion

4.8.1. Effects of metamorphism on element mobility

As with other Archean megacrystic anorthosite-bearing layered intrusions and their associated greenstone belts, the Mayville Intrusion and the Bird River greenstone belt have been subjected to metamorphism resulting from orogenic processes (Figs. 4.5-4.7; Yang and Gilbert, 2014; Ashwal and Bybee, 2017; Polat et al., 2018a). The Mayville Intrusion, the adjacent Mayville Assemblage and the contemporaneous nearby New Manitoba Mine Intrusion underwent greenschist- to amphibolite-facies metamorphism (Peck et al., 2002; Gilbert et al., 2008; Yang and Gilbert, 2014) during the 2720-2700 Ma Uchian Orogeny (Percival et al., 2012). These rocks have undergone variable degrees of recrystallisation and hydrothermal alteration during this metamorphic event (Figs. 4.4-4.9). Whilst cumulate textures and primary igneous minerals are generally quite well preserved throughout most of the Mayville Intrusion, the degree of preservation ranges from the occurrence of unaltered magmatic plagioclase, amphibole, clinopyroxene and orthopyroxene to these minerals being completely recrystallised and hydrothermally altered to albite and actinolite (Figs. 4.4-4.9). The Mayville Assemblage and New Manitoba Mine Intrusion are not as well preserved as the Mayville Intrusion, with pyroxene mostly replaced by actinolite and plagioclase partly replaced by metamorphic plagioclase (albite). Therefore, the effects of this metamorphism on the rocks of the Mayville and New Manitoba Mine intrusions and the Bird River greenstone belt are assessed to determine whether they can be used for valid petrogenetic and geodynamic interpretation. Polat and Hofmann (2003) found that when assessing element mobility in Archean volcanic rocks that had been deformed and metamorphosed, anomalous Ce/Ce* ratios (<0.9 and >1.1) are generated as a consequence of REE mobility in altered samples. The vast majority of the samples from the Mayville Intrusion, Mayville Assemblage and New Manitoba Mine Intrusion have Ce/Ce* ratios between 0.9 and 1.1 (Appendices 3.1 and 3.2), indicating that these samples can be used for valid petrogenetic and geodynamic interpretation (Polat and Hofmann, 2003). Two leucogabbros (111-11-16 and 111-11-12) and two anorthosites (111-12-632A01 and 111-

12-629A01) from the Mayville Intrusion have Ce/Ce* ratios of <0.9 and >1.1 (Appendices 3.1 and 3.2), therefore, these samples are interpreted to be altered and will not be used in the following petrogenetic and geodynamic interpretation. This method, in conjunction with plotting Zr against REE and other HFSE (high-field strength elements; Nb and TiO_2) in bivariate diagrams, indicates that the majority of samples from the Mayville Intrusion and all of the samples from the Mayville Assemblage are not extensively altered and are suitable for valid petrogenetic and geodynamic interpretation (Fig. 4.11).

One anorthosite (-6.8), one leucogabbro (-1.5) and one gabbro (-3.5) from the Anorthosite to Leucogabbro Zone have negative $\varepsilon_{Nd\ (2743\ Ma)}$ values that cannot be accounted for by crustal contamination because their N-MORB-normalised trace element patterns and major and trace element compositions do not indicate such a process (Figs. 4.10-4.12 and Fig. 4.14a). These trace element patterns and major and trace element compositions would most likely resemble those of the Maskwa Lake TTG Batholith I (see Yang et al., 2011, 2012, 2013; Sotiriou et al., 2019b), the only known pre-existing felsic crust in the study area older than the Mayville Intrusion, if these samples had experienced crustal contamination. The trace element patterns of these samples, however, are very similar to those of other samples from the Mayville Intrusion that have positive $\varepsilon_{Nd\ (2743\ Ma)}$ values, suggesting that contamination of older crust did not generate their negative $\varepsilon_{Nd\ (2743\ Ma)}$ values (Henry et al., 1998; Lodge et al., 2015). The negative $\varepsilon_{Nd\ (2743\ Ma)}$ values of these samples cannot be accounted for by assimilation of older mafic volcanic rocks because the Mayville Assemblage, the only known mafic volcanic rocks older than the Mayville Intrusion, formed contemporaneously with this layered intrusion during the ~2743 Ma Bird River magmatic event (Henry et al., 1998; Houlé et al., 2013; Yang et al., 2013). These samples show evidence for hydrothermal alteration of their primary mineralogy and cumulate textures, with magmatic amphibole substantially replaced through recrystallisation by actinolite and magmatic calcic plagioclase partially altered to sodic, metamorphic plagioclase, alongside sericite, clinozoisite and epidote. Combined geochemical and petrographic evidence indicate that the Sm-Nd isotope compositions of these samples were reset by alteration (Lahaye et al., 1995; Lahaye and Arndt, 1996). Despite this resetting, the Sm-Nd and Pb isotopic systems of the Mayville Intrusion as a whole were not significantly affected by greenschist- to amphibolite-facies metamorphism associated with the Uchian Orogeny but rather only the Sm-Nd and Pb isotopic compositions of the three aforementioned samples were reset. The resetting of the Sm-Nd and Pb isotopic systems of only these three samples may be due to more localised cases of greater hydrothermal alteration and

recrystallisation. The Mayville Intrusion has a Pb-Pb whole-rock isochron age of 2696 ± 97 Ma, which is in agreement (within error) with its 2742.8 ± 0.8 Ma U-Pb zircon age (Houlé et al., 2013). This Pb-Pb whole-rock isochron age demonstrates that the Mayville Intrusion was not significantly affected by alteration, an interpretation corroborated by the abundance of well-preserved cumulate textures and magmatic plagioclase, amphibole, clinopyroxene and orthopyroxene.

4.8.2. Assessing the degree of crustal contamination

The Mayville Assemblage contains pillow basalts (Yang et al., 2011, 2012, 2013), indicating that it, and, by extension, the Mayville Intrusion and New Manitoba Mine Intrusion, most likely formed in an oceanic setting adjacent to the Maskwa Lake Block (Yang et al., 2011, 2012, 2013). Field relationships between the Mayville Assemblage pillow basalts and the Mesoarchean phase of the Maskwa Lake TTG Batholith suggest that these pillow basalts were partially erupted onto pre-existing continental crust of the Maskwa Lake Block (Gilbert et al., 2008; Yang et al., 2011, 2012, 2013), which will be referred to henceforth as the Maskwa Lake microcontinent. Some of the pillow basalts of the Mayville Assemblage are in contact with and contain xenoliths of the Mesoarchean phase of the Maskwa Lake TTG Batholith (Yang et al., 2011, 2012), thereby substantiating this interpretation.

The emplacement of the Mayville Assemblage and the Mayville and New Manitoba Mine intrusions onto/into the pre-existing crust of the Maskwa Lake microcontinent is further supported by tonalites of the 2832 Ma and 2858 Ma phases of the Maskwa Lake TTG Batholith I being in contact with MORB-type massive and pillow basalts of the Mayville Assemblage (Gilbert et al., 2008; Duguet et al., 2009). Moreover, a dolerite dyke that is of similar composition and is genetically related to the Mayville Assemblage MORB-type basalts occurs at the contact zone between the Maskwa Lake TTG Batholith I and the Mayville Assemblage basalts (Yang et al., 2013). This dolerite dyke has brecciated and fragmented the part of the batholith into which it was emplaced, suggesting that this dyke was emplaced into the continental crust of the Maskwa Lake microcontinent. Furthermore, sporadic synvolcanic gabbroic dykes crosscut the Maskwa Lake TTG Batholith I (Yang et al., 2013), further indicating that the Mayville Assemblage and the Mayville and New Manitoba Mine intrusions formed in an oceanic setting proximal to the Maskwa Lake microcontinent. Indeed, Yang et al.

(2012) used a primitve mantle-normalized $(Th/Nb)_{PM}$ versus $(Nb/Yb)_{PM}$ plot to show that up to 10% contamination by Mesoarchean continental crust occurred during the ascent of the parental magma(s) to the Mayville Intrusion, Mayville Assemblage and New Manitoba Mine Intrusion. The most contaminated lithology according to this plot is the Anorthosite to Leucogabbro Zone gabbros (10% contamination) (Yang et al., 2012). The Mayville Intrusion has positive $\varepsilon_{Nd\ (2743\ Ma)}$ values lower than +2.0 (+0.7 to +1.7), indicating that the parental magma(s) to this intrusion underwent minor crustal contamination (Fig. 4.14a; Table 4.1; Henry et al., 1998; Lodge et al., 2015). This is corroborated by the Mayville Intrusion having samples with high, transitional to calc-alkaline Zr/Y (4.67-11.13), La/Yb (3.42-5.56) and Th/Yb (0.86-3.38) ratios and enriched N-MORB-normalised trace element patterns (see Henry et al., 1998; Ross and Bédard, 2009; Lodge et al., 2015). Some of the anorthosites, leucogabbros and gabbros of the Anorthosite to Leucogabbro Zone have enriched N-MORB-normalised trace element patterns and major and trace element compositions comparable to the Maskwa Lake TTG Batholith I, indicating that their parental magma(s) was most likely contaminated by this batholith (Yang et al., 2011, 2012, 2013; Sotiriou et al., 2019b). The aforementioned field relationships and trace element characteristics, combined with the predominantly positive $\varepsilon_{Nd\ (2743\ Ma)}$ (+0.7 to +3.9) values of the Mayville Intrusion, imply that its parental magma(s) only underwent minor contamination by pre-existing continental crust and is generally representative of its source, and indicate that the major and trace element geochemistry of this intrusion is largely representative of a variably-depleted mantle source (Fig. 4.14a and b; Henry et al., 1998; Yang et al., 2011, 2012, 2013; Lodge et al., 2015).

4.8.3. Magmatic amphibole - evidence for Archean hydrous arc magmatism

The occurrence of magmatic amphibole in Archean igneous rocks has critical implications for the style of tectonics that operated in the Archean and, therefore, how Archean continental crust grew and evolved (see Polat et al., 2015; Kusky et al., 2018; Hastie and Fitton, 2019; Roman and Arndt, 2019). The style of tectonics that operated in the Archean is still a very controversial issue, with some workers preferring uniformitarian-style tectonics akin to the modern-style plate tectonic processes that operate today and other workers invoking non-uniformitarian-style, vertical tectonic processes (Bédard, 2006, 2018; Condie and Kröner, 2008; Kusky et al., 2018; Roman and Arndt, 2019).

Claeson and Meurer (2004) found that the occurrence of magmatic amphibole in gabbroic arc cumulates is a strong indicator of their crystallisation from hydrous magmas in a subduction zone setting. As such, the identification of magmatic amphibole in Archean igneous rocks will shed light on the question of the nature of Archean tectonics, continental growth, and evolution. Magmatic amphibole has been observed in anorthosites and leucogabbros in the Fiskenæsset, Naajat Kuuat, Sittampundi and São José do Jacuipe Archean megacrystic anorthosite-bearing layered intrusions (Rollinson et al., 2010; Polat et al., 2011; Hoffmann et al., 2012; Mohan et al., 2013; Piaia et al., 2017). The occurrence of magmatic amphibole in these Archean megacrystic anorthosite-bearing layered intrusions, combined with their field relationships and suprasubduction zone immobile element patterns, have been interpreted to indicate that they crystallized from hydrous arc magmas in a subduction zone geodynamic setting. The Fiskenæsset, Naajat Kuuat and Sittampundi complexes underwent amphibolite- to granulite-facies metamorphism and were dismembered during polyphase deformation (Polat et al., 2011; Hoffmann et al., 2012; Mohan et al., 2013). Magmatic amphibole in the Mesoarchean Narndee Igneous Complex (Australia) has been proposed to have crystallised from a mantle plume-derived hydrous magma(s) (Ivanic et al., 2010, 2015). The subduction zone and mantle plume settings proposed for magmatic amphibole in Archean anorthosite-bearing layered intrusions indicates that magmatic amphibole may not be restricted to a particular geodynamic setting and may not necessarily be indicative of hydrous arc magmatism. Resolving whether magmatic amphibole in Archean anorthosite-bearing layered intrusions is indicative of a subduction hydrated, metasomatized mantle wedge source or a hydrated mantle plume source is critical to constraining the style of Archean tectonics.

Precise and accurate SEM-EDS analyses indicate that the amphiboles of the Mayville Intrusion are predominantly magnesiohornblende (Appendix 3.4). The anorthosites and leucogabbros of the Mayville Intrusion characteristically contain abundant amphibole that exhibits pronounced optical continuity (Figs. 4.4-4.7). Anhedral to subhedral amphibole up to at least 10 centimetres across occurs interstitially to highly calcic plagioclase megacrysts as large oikocrysts that envelop smaller plagioclase crystals (Figs. 4.4-4.7). The boundary between the plagioclase megacrysts and the amphibole oikocrysts is often serrated (Fig. 4.8). Furthermore, these amphiboles do not have metamorphic reaction rims that would be indicative of a metamorphic origin (Arguin et al., 2018). These observations indicate that these Mayville amphibole oikocrysts are of magmatic origin, as metamorphic recrystallisation cannot account for these magmatic textures (Claeson and Meurer, 2004). Non-oikocrystic magmatic amphibole occurs

interstitially to the plagioclase megacrysts. Magmatic amphibole from the Mayville Intrusion closely resembles those from the Paleoproterozoic Eriksberg and Rymmen gabbroic intrusions that formed as a result of an interstitial melt reacting with pre-existing cumulus plagioclase (Claeson and Meurer, 2004), suggesting that the Mayville amphiboles formed by a similar process. Elongated, well-orientated, euhedral metamorphic amphibole crystals cut across anhedral to subhedral, non-orientated magmatic amphibole crystals in some samples (Fig. 4.6). The anhedral nature of the primary igneous oikocrystic amphiboles, coupled with their higher Si *apfu* values, distinguishes them from the euhedral secondary metamorphic amphiboles (Figs. 4.6-4.8; Appendix 3.4; Leake et al., 1997; Meurer and Claeson, 2002; Claeson and Meurer, 2004). Furthermore, many amphibole oikocrysts exhibit whole-grain optical continuity and extinction, well-developed cleavage, and envelop multiple plagioclase crystals, features that are indicative of their magmatic origin (Figs. 4.6-4.8; Claeson and Meurer, 2004). Magmatic amphiboles in the anorthosites and leucogabbros of the Mayville Intrusion are quite abundant and better preserved than the magmatic amphiboles in the Fiskenæsset, Naajat Kuuat, Sittampundi and São José do Jacuipe complexes (Figs. 4.4-4.8; Rollinson et al., 2010; Polat et al., 2011; Hoffmann et al., 2012; Mohan et al., 2013; Piaia et al., 2017). Moreover, the Mayville Intrusion was metamorphosed to a lower grade (greenschist- to amphibolite-facies) than these texturally, petrologically and geochemically similar amphibolite- to granulite-facies Archean megacrystic anorthosite-bearing layered intrusions and, therefore, was not as affected by deformation and metamorphic alteration (Rollinson et al., 2010; Polat et al., 2011; Hoffmann et al., 2012; Mohan et al., 2013; Yang et al., 2011; Yang and Gilbert, 2014; Piaia et al., 2017).

The occurrence of abundant, well-preserved magmatic amphibole in the anorthosites and leucogabbros of the Mayville Intrusion indicates that they crystallised from a hydrous parental magma(s) (Figs. 4.4-4.8; Claeson and Meurer, 2004). Given that hydrous magmas are predominantly associated with subduction zones (Claeson and Meurer, 2004; Rollinson et al. 2010; Polat et al., 2011; Hoffmann et al., 2012; Mohan et al., 2013; Piaia et al., 2017; Sotiriou et al., 2019b) rather than mantle plume (e.g., Kerr et al., 2004; Ivanic et al., 2015) settings, the observation of abundant, well-preserved magmatic amphibole in the Mayville Intrusion, combined with its field relationships (Figs. 4.2 and 4.3), highly calcic plagioclase (Appendix 3.4), chromite chemistry (Figs. 4.15 and 4.16; Appendix 3.4) and suprasubduction zone trace element patterns (Fig. 4.12), suggests that it formed in a subduction zone setting (Fig. 4.17). This combined evidence indicates that the Mayville Intrusion provides support for hydrous arc magmatism occurring in the Neoarchean, demonstrating that uniformitarian-style tectonics

occurred in the Archean and has therefore been the predominant process controlling crustal growth and evolution ever since (Hildebrand et al., 2018; Kusky et al., 2018; Hastie and Fitton, 2019; Roman and Arndt, 2019). Hydrated mantle plume sources have also been proposed for some Archean anorthosite-bearing layered intrusions containing magmatic amphibole (Ivanic et al., 2010, 2015), however, the field relationships, mineral chemistry, whole-rock major and trace element, and Sm-Nd and Pb isotope geochemistry of the Mayville Intrusion are incompatible with it being derived from a mantle plume.

Lowrey et al. (2020) conducted an integrated high-precision geochemical and field study of ultramafic to felsic volcanic and ultramafic to mafic intrusive rocks of the Meekatharra Formation (Polelle Group) that are spatially and temporally associated with the Narndee Igneous Complex. The Narndee Igneous Complex contains abundant magmatic amphibole and was interpreted to have formed from a hydrated mantle plume source by Ivanic et al. (2010, 2015). Lowrey et al. (2020) inferred that the Narndee Igneous Complex formed in a subduction zone setting. If this inference is correct, it demonstrates that all known Archean anorthosite-bearing layered intrusions containing magmatic amphibole formed in a subduction zone setting and that magmatic amphibole in these intrusions is indicative of Archean hydrous arc magmatism. This would also provide further support for the magmatic amphibole in the Mayville Intrusion being derived from a hydrous arc magma.

4.8.4. Petrogenesis and mantle source characteristics

The Mayville Intrusion, Mayville Assemblage and New Manitoba Mine Intrusion generally have low Zr/Y (0.99-4.42, 2.18-2.86 and 2.54-2.76), La/Yb (0.69-2.17, 1.12-1.55 and 1.40-1.49) and Th/Yb (0.04-0.30, 0.09-0.18 and 0.14-0.18) ratios and predominantly plot along the tholeiitic trend of the AFM diagram, indicating that their parental magmas were tholeiitic in affinity (Fig. 4.18; Irvine and Baragar, 1971; Ross and Bédard, 2009). On various major element and trace element variation diagrams (Figs. 4.10 and 4.11), the lithologies of the Anorthosite to Leucogabbro and Heterolithic Breccia Zones of the Mayville Intrusion, the Mayville Assemblage and New Manitoba Mine Intrusion plot along the same trend. This suggests that the Mayville Intrusion, Mayville Assemblage and New Manitoba Mine Intrusion may have been cogenetic and formed from similar mantle sources (see Stern et al., 2003; Golowin et al., 2017). The Mayville Intrusion has predominantly positive $\varepsilon_{Nd\ (2743\ Ma)}$ values

(+0.7 to +3.9), indicating that these mantle sources had been variably depleted by at least one prior melt extraction event (Stern et al., 2003; Golowin et al., 2017). The variability in the La/Yb ratios of the anorthosites (La/Yb = 0.91-3.71), leucogabbros (La/Yb = 0.81-1.76), gabbros (La/Yb = 0.69-5.56), melagabbros (La/Yb = 0.88-1.41) and pyroxenites (La/Yb = 1.21-1.54) of the Mayville Intrusion and the basalts (La/Yb = 1.12-1.55) of the Mayville Assemblage indicate that these lithologies exhibit more than one type of REE pattern (Fig. 4.12; Appendices 3.1 and 3.2; Lodge et al., 2015). This suggests that these lithologies crystallised from at least two different batches of magmas or crystal mushes of different composition (see Henry et al., 1998; Ross and Bédard, 2009; Lodge et al., 2015). Given that the Mayville Intrusion's parental magma may have undergone minor contamination by Mesoarchean continental crust, these magma batches or crystal mushes may have been compositionally modified to a small degree by Mesoarchean TTG crust. This is corroborated by positive $\varepsilon_{Nd\ (2743\ Ma)}$ values of the anorthosites (+0.7 to +2.9), leucogabbros (+2.1 to +3.9), melagabbros (+2.0 to +3.4), and pyroxenites (+2.1 to +2.2) of the Mayville Intrusion that are below the depleted mantle ε_{Nd} value (+2.8) expected at 2743 Ma (Fig. 4.14a; Henry et al., 1998).

The Mayville and New Manitoba Mine intrusions and pillow basalt-bearing Mayville Assemblage generally have low immobile element ratios, negative Nb and Ti anomalies and back-arc-like trace element patterns (Figs. 4.11 and 4.12; Appendices 3.1 and 3.2; Pearce and Peate, 1995; Stern et al., 2003; Murphy, 2007; Pearce, 2008). These intrusions and the Mayville Assemblage were partially emplaced into the continental arc-derived Maskwa Lake TTG Batholith I and volcaniclastic-bearing Euclid Lake Formation and were intruded by the continental arc-derived Maskwa Lake TTG Batholith II (Yang et al., 2013). These geochemical characteristics and field relationships indicate that their parental magmas were derived by partial melting of a depleted sub-arc mantle source at a continental back-arc geodynamic setting (Fig. 4.18; Stern et al., 2003; Yang et al., 2013; Golowin et al., 2017; Sotiriou et al., 2019a, b). The LREE-enriched N-MORB-normalized trace element patterns and $\varepsilon_{Nd\ (2743\ Ma)}$ <+2.0 values of the Anorthosite to Leucogabbro Zone gabbros (Fig. 4.12; Appendix 3.1) suggest that they crystallised from a parental magma(s) that was derived by partial melting of a depleted sub-arc aesthenospheric mantle source and subsequently underwent minor contamination by Mesoarchean continental arc-derived crust (see Stern et al., 2003; Yang et al., 2013). The involvement of minor crustal contamination and crustal interaction in the petrogenesis of the gabbros is corroborated by the presence of abundant orthogneiss xenoliths derived from the

adjacent Maskwa Lake TTG Batholith I (Yang et al., 2011, 2012, 2013). This contamination enriched the parental magma(s) in both REE and high-field strength elements (HFSE) so that the resulting gabbros have more steeply-dipping, continental arc-like trace element patterns similar to those of the Maskwa Lake TTG Batholith I (Fig. 4.12; Yang et al., 2011, 2012; Sotiriou et al., 2019b). The geochemical characteristics and arc-like trace element pattern (Figs. 4.10-4.12; Appendix 3.2; Mg# = 34; Ni = 11 ppm; Co = 10 ppm; Yb = 2.09 ppm; Y = 19.9 ppm; La = 26.1 ppm; La/Yb_{cn} = 8.98; Nb/Nb* = 0.13; Ti/Ti* = 0.40) of the dacite dyke emplaced into the Maskwa Lake TTG Batholith II are consistent with its derivation by melting of hydrated lower crustal basalts (Pearce and Peate, 1995; Martin, 1999; Martin et al., 2005; Murphy, 2007; Pearce, 2008; Hoffmann et al., 2011; Yang et al., 2012, 2013; Huang et al., 2013).

The high Ca and Al contents and immobile element geochemistry of the anorthosites and leucogabbros of the Mayville Intrusion suggest that the intrusion had an initially primitive arc tholeiitic hydrous parental magma that formed in a subduction zone setting and then evolved to the hydrous Ca- and Al-rich tholeiitic parental magma from which these lithologies crystallised (Pearce and Peate, 1995; Stern et al., 2003; Takagi et al., 2005; Murphy, 2007; Pearce, 2008; Escuder-Viruete et al., 2014; Sotiriou et al., 2019a, b). This interpretation is based on the following reasoning: (1) Archean megacrystic anorthosites and leucogabbros with high Ca and Al abundances ordinarily crystallise from hydrous calcic, aluminous tholeiitic parental magmas in subduction zone settings (Ashwal, 1993, 2010; Sisson and Grove, 1993a, b; Claeson and Meurer, 2004; Takagi et al., 2005; Polat et al., 2011, 2018a, b; Ashwal and Bybee, 2017); (2) low immobile element abundances in igneous rocks signify crystallisation from primitive magmas that were derived from depleted mantle sources (Pearce and Peate, 1995; Stern et al., 2003; Escuder-Viruete et al., 2014; Golowin et al., 2017); and (3) the anorthosites and leucogabbros of the Mayville Intrusion have genuine negative Nb and Ti anomalies, which are indicative of the generation of igneous rocks in a subduction zone setting (Pearce and Peate, 1995; Murphy, 2007; Pearce, 2008). The hydrous primitive arc tholeiitic parental magma to the Mayville Intrusion likely fractionated olivine and pyroxene at a shallow depth to form the hydrous Ca- and Al-rich tholeiitic magma from which the Mayville Intrusion crystallised (Ashwal, 1993; Takagi et al., 2005; Polat et al., 2018a). This hydrous primitive arc tholeiitic parental magma likely formed by high-degree partial melting of a shallow, depleted (e.g., harzburgitic) sub-arc mantle wedge source that was refertilised by slab melts and/or fluids (Escuder-Viruete et al., 2014; Yang and Gilbert, 2014). Such a petrogenetic model corroborates

with the model proposed by Yang and Gilbert (2014) for the Mayville Intrusion. The occurrence of tholeiitic melt extraction is shown by the Mayville Intrusion's depleted N-MORB-normalised trace element patterns and positive $\varepsilon_{Nd\ (2743\ Ma)}$ (+0.7 to +3.9) values (Fig. 4.12) and would have produced a residual, refractory harzburgitic sub-arc mantle wedge source (Golowin et al., 2017).

Olivine and pyroxene fractionation at depth most likely played a major role in generating the Fe-enrichment (tholeiitic) trend that is observed in the geochemistry of the Mayville Intrusion (Ashwal, 1993). The ultramafic (e.g., peridotite, pyroxenite) lithologies that would have formed as a result of this olivine and pyroxene fractionation are largely missing from the Mayville Intrusion, with the exception of pyroxenite layers in the Heterolithic Breccia Zone (Yang et al., 2011). These lithologies may have mostly crystallised at a greater depth than the present level of exposure in the Mayville Intrusion, which might explain why they are not significant in this intrusion. Archean, Paleoproterozoic, Tertiary and modern tholeiitic mafic-ultramafic intrusions and xenoliths have been shown to have crystallised from hydrous parental magmas in subduction zone settings (Irvine, 1974; Arculus and Wills, 1980; Conrad and Kay, 1984; Cigolini and Kudo, 1987; Beard and Borgia, 1989; Tistl et al., 1994; Cigolini, 1998; Claeson and Meurer, 2004; Bacon et al., 2007; Polat et al., 2018a). This indicates that the Mayville Intrusion's hydrous primitive arc tholeiitic parental magma underwent Fe-enrichment as a consequence of olivine and pyroxene fractionation in a shallow hydrous continental back-arc magma chamber (Ashwal, 1993; Polat et al., 2011, 2018a). This fractionation most likely formed olivine (peridotite) and pyroxene (pyroxenite) cumulates at the base of this shallow arc magma chamber before the Mayville Intrusion's anorthosites, leucogabbros and gabbros crystallised at higher levels in this shallow magma chamber (Polat et al., 2018a).

There is considerable debate regarding the composition of the parental magmas to Archean megacrystic anorthosite-bearing layered intrusions (Ashwal, 1993, 2010; Ashwal and Myers, 1994; Ashwal and Bybee, 2017). There is a general consensus that Archean and younger anorthosite-bearing layered intrusions crystallised from Ca- and Al-rich tholeiitic parental magmas, however, it has also been argued that they may have crystallised from more primitive basaltic, picritic or komatiitic parental magmas (Ashwal, 1993, 2010; Ashwal and Myers, 1994; Ashwal and Bybee, 2017; Latypov et al., 2020). Various methods have been used to calculate or estimate the composition of the parental magmas to Archean megacrystic anorthosite-bearing layered intrusions (Ashwal, 1993). Four methods were employed to calculate the composition of the parental magma to the Mayville Intrusion (Fig. 4.19). Method #1 involved

summing the compositions of the lithologies (anorthosite, leucogabbro, gabbro, melagabbro, pyroxenite) present in the Mayville Intrusion to calculate the composition of its parental melt, based on the proportion of each lithology relative to the intrusion's total thickness (Polat et al., 2011). This method was shown to be applicable to the layered (500 metre-thick) ca. 2.97 Ga Fiskenæsset Complex in southwestern Greenland that has been interpreted to have had an original thickness of 1000 metres (Polat et al., 2011). Utilisation of this method indicates that the Mayville Intrusion had a low-silica, moderate-Mg, high-Ca and -Al parental magma (SiO_2 = 47.27 wt.%, MgO = 6.08 wt.%, Al_2O_3 = 20.96 wt.%, CaO = 12.72 wt.%, Mg# = 56, Ni = 316 ppm, Cr = 319 ppm, Nb/Nb* = 0.56, Ti/Ti* = 1.03). Method #2 is similar, however, it involved calculating the average composition of the Mayville Intrusion to infer the composition of the Mayville Intrusion's parental magma (Ashwal, 1993). This calculated average composition of the Mayville Intrusion is very similar to the composition calculated using Method #1 and also indicates that it crystallized from a low-silica, moderate-Mg, high-Ca and -Al parental magma (SiO_2 = 47.31 wt.%, MgO = 5.32 wt.%, Al_2O_3 = 22.01 wt.%, CaO = 12.88 wt.%, Mg# = 51, Ni = 313 ppm, Cr = 272 ppm, Nb/Nb* = 0.61, Ti/Ti* = 1.08). Method #3 utilised the Petrolog3 software of Danyushevsky and Plechov (2011). The Petrolog3 software enables modelling of the initial and post-fractional crystallization compositions of parental magmas based on geochemical data, partition coefficients and input data for various physical parameters. The average compositions of the Mayville Intrusion's constituent lithologies (anorthosite, leucogabbro, gabbro, melagabbro, pyroxenite) were entered into this software to calculate the compositions of their parental magma(s). Partition coefficient (Kd) values from Rollinson (1993) and the Geochemical Earth Reference Model (GERM) Partition Coefficient (Kd) Database were used for this calculation. The main input physical parameters included a melt oxygen fugacity (fO_2) of Ni-NiO + 1, a melt pressure increase from 2 to 5 kbars, and a melt temperature increase from 900 to 1350ºC. These parameters were chosen based on conditions specified in Takagi et al. (2005) for the optimal crystallisation of calcic (An_{70-95}) plagioclase from hydrous Ca- and Al-rich tholeiitic magmas. These calculated melt compositions were subsequently summed to calculate the overall composition of the Mayville Intrusion's parental magma, based on the respective proportions of its constituent lithologies relative to its total thickness (Polat et al., 2011). This calculation indicates that the Mayville Intrusion crystallised from a low-silica, high-Mg, -Ca and -Al parental magma (SiO_2 = 43.95 wt.%, MgO = 13.17 wt.%, Al_2O_3 = 16.80 wt.%, CaO = 10.18 wt.%, Mg# = 75, Ni = 694 ppm, Nb/Nb* = 0.52, Ti/Ti* = 1.00). Method #4 was also based on the use of the Petrolog3 software, except that the melt compositions calculated for the Mayville Intrusion's constituent lithologies were summed

(Ashwal, 1993). The resultant total was subsequently averaged to infer an overall composition for the Mayville Intrusion's parental magma. The utilisation of this method indicates that the Mayville Intrusion crystallised from a low-silica, high-Mg, -Ca and -Al parental magma (SiO_2 = 43.78 wt.%, MgO = 13.25 wt.%, Al_2O_3 = 15.76 wt.%, CaO = 10.08 wt.%, Mg# = 73, Ni = 1066 ppm, Nb/Nb* = 0.52, Ti/Ti* = 0.95).

The melt composition calculation methods described above indicate that the Mayville Intrusion crystallised from a Ca- and Al-rich tholeiitic magma that fractionated from a more primitive parental magma. The stronger similarity between the melt compositions calculated using Methods #3 and #4 and the primitive parental magmas inferred for the Fiskenæsset Complex (Polat et al., 2011) and Puerto Plata Ophiolite (Escuder-Viruete et al., 2014) compared to Methods #1 and #2 suggests that the primitive magma parental to the Mayville Intrusion was a primitive arc tholeiite and formed in a suprasubduction zone geodynamic setting. Furthermore, both the primitive arc tholeiitic (Methods #3 and #4) and Ca- and Al-rich tholeiitic (Methods #1 and #2) parental magmas calculated for the Mayville Intrusion have negative Nb and minimal to negative Ti anomalies, further indicating that they formed in a subduction zone setting (Pearce and Peate, 1995; Murphy, 2007; Pearce, 2008). The decrease in the negative Nb and Ti anomalies and increase in REE and HFSE contents between the Mayville Intrusion's primitive arc tholeiitic and Ca- and Al-rich tholeiitic parental magmas indicates that the former was more primitive and fractionated to form the latter (Fig. 4.19). The fact that the basalts from the Mayville Assemblage plot along a fractionation trend from the calculated parental magma compositions indicate that they were most likely derived by fractionation of the hydrous Ca- and Al-rich tholeiitic parental magma to the Mayville Intrusion (Fig. 4.19). The melt compositions calculated using Methods #3 and #4 are more similar to the Mayville Assemblage basalts than the melt compositions calculated using Methods #1 and #2 (Fig. 4.19). These findings suggest that the Mayville Intrusion and Mayville Assemblage may have been cogenetic and crystallised from the same hydrous Ca- and Al-rich tholeiitic parental magma(s) that fractionated from a primitive arc tholeiitic parental magma very similar in composition to the parental magma compositions calculated using Methods #3 and #4. Utilisation of the Al-in-hornblende geobarometer (see Johnson and Rutherford, 1989) indicates that the Mayville Intrusion crystallised at pressures between 1 and 5 kbars (average: 2.5 kbars), which is equivalent to a depth of 3 to 15 km (average: 7.5 km). These crystallisation pressures and depths are very similar to the pressures (2-3 kbars) and depths (6-9 km) reported in Takagi et al. (2005) for the optimal crystallisation of highly calcic (>An_{88}) plagioclase from hydrous

Ca- and Al-rich tholeiitic melts. Based on these crystallisation depth and pressure constraints, the Mayville Intrusion most likely crystallised over a pressure range of 2 to 5 kbars and a temperature range of 900 to 1350°C (Takagi et al., 2005).

4.8.5. Geodynamic setting

Pronounced negative Nb and Ti anomalies on the N-MORB normalised multi-element diagram (Fig. 4.12; Appendices 3.1 and 3.2), chromite chemistry (Figs. 4.15 and 4.16), the occurrence of highly calcic (An_{59-100}) plagioclase and magmatic amphibole (Figs. 4.4-4.8; Appendix 3.4) and field relationships (Figs. 4.2 and 4.3) collectively suggest that the Mayville Intrusion, New Manitoba Mine Intrusion and Mayville Assemblage formed during a transition between a continental arc and continental back-arc setting when intra-arc rifting occurred at the southern active continental margin of the North Caribou terrane, creating the Maskwa Lake microcontinent in the process (Fig. 4.17; Pearce and Peate, 1995; Takagi et al., 2005; Murphy, 2007; Pearce, 2008). This interpretation broadly corroborates with the pre-existing back-arc setting models proposed for the Mayville Intrusion and the Bird River greenstone belt (Gilbert et al., 2008; Yang et al., 2011, 2013), however, it does not corroborate with the transitional oceanic arc to continental arc setting proposed by Gilbert (2008) as it does not invoke the involvement of an oceanic arc. The interpretation presented here is corroborated by the continental arc affinity of the TTGs and other granitoids that comprise the Mesoarchean to Neoarchean Maskwa Lake microcontinent (Yang et al., 2013). The primitive arc tholeiitic parental magma proposed for the Mayville Intrusion is not contradicted by the continental back-arc setting interpretation postulated for this intrusion because similarly primitive arc volcanic rocks (boninites) have been interpreted to have formed in continental arc to back-arc settings (Piercey et al., 2001). The dacite dyke that was emplaced into the Maskwa Lake TTG Batholith II has negative Nb and Ti anomalies and high La/Yb_{cn} ratios that are indicative of a continental arc setting (Fig. 4.12; Appendix 3.2; Pearce and Peate, 1995; Murphy, 2007; Pearce, 2008; Yang et al., 2013). Given that the Mayville Intrusion was affected to a small degree by crustal contamination and the Mayville Assemblage, New Manitoba Mine Intrusion and Maskwa Lake TTG Batholith dacite dyke were not influenced by crustal contamination, the negative Nb and Ti anomalies exhibited by these lithologies were most likely created due to a combination of slab dehydration, and lower arc crust and slab fluid-hydrated sub-arc

mantle wedge melting (Pearce and Peate, 1995; Murphy, 2007; Pearce, 2008). This is due to the fact that subduction is the most efficient and common mechanism for generating negative Nb and Ti anomalies (Pearce and Peate, 1995; Murphy, 2007; Pearce, 2008). Polat et al. (2009, 2011) showed that all lithological units, including peridotite, pyroxenite, hornblendite, gabbro, leucogabbro and anorthosite, in differentiated sills of the ca. 2.97 Ga Fiskenæsset Complex, western Greenland, have negative Nb anomalies relative to Th and LREE, indicating that negative Nb anomalies in anorthosite-bearing layered intrusions likely reflect parental melt compositions rather than mineral fractionation processes because all of the cumulate layers possess a negative Nb anomaly. The positive Nb anomalies exhibited by the anorthosites of the Heterolithic Breccia Zone may reflect their derivation by low degree partial melting of a back-arc mantle wedge source or the Mayville Intrusion having a heterogeneously depleted sub-arc mantle wedge source(s) (see Hollings and Kerrich, 2004).

The chemistry of chromites from the Mayville Intrusion (Fig. 4.15; Appendices 3.4 and 3.5) indicates that they share similarities with the composition of chromites in podiform and stratiform chromitites (Lay et al., 2017; Qiu et al., 2018). Chromite chemistry diagrams (Figs. 4.15 and 4.16) also show that the Mayville Intrusion formed in a subduction zone setting. The chromite chemistry of the Mayville Intrusion implies that it formed in a continental back-arc setting as its chromites plot in or close to the arc cumulate, mantle array, Alaskan-type, Fiskenæsset Complex, ophiolite and continental mafic intrusion fields in various chromite chemistry diagrams (Figs. 4.15 and 4.16; see Polat et al., 2006; Rollinson et al., 2010; Gonzalez-Jimenez et al., 2017; Kiseleva and Zhmodik, 2017; Lay et al., 2017; Lenaz et al., 2018). The subduction zone setting proposed here for the Mayville Intrusion is corroborated by the interpretation of Edwards et al. (2000) that podiform chromitites have only formed in subduction zone settings. The Mayville chromites in Fig. 4.16b overlap with those in Fig. GS-3-7 from Yang and Gilbert (2014), who postulated that the Mayville Intrusion formed in a back-arc setting. This interpretation is corroborated by the continental back-arc setting proposed here for the Mayville Intrusion (4.17).

The Mayville Intrusion intrudes both the back-arc pillow basalts of the Mayville Assemblage and the continental arc TTGs of the Maskwa Lake TTG Batholith I, indicating that it was emplaced into both back-arc oceanic crust and arc crust. This is suggested by field relationships, and the Mayville Intrusion having hangingwall orthogneiss and granitoid inclusions in the Anorthosite to Leucogabbro Zone and weakly to strongly positive $\varepsilon_{Nd\ (2743\ Ma)}$ (+0.7 to +3.9) values. As such, the Mayville Intrusion was most likely emplaced into a

continental back-arc basin during intra- to back-arc rifting. The continental back-arc geodynamic setting proposed here for the Mayville Intrusion, Mayville Assemblage and New Manitoba Mine Intrusion, combined with field relationships and their location at the northern margin of the Maskwa Lake microcontinent and Bird River subprovince and the continental arc affinity of the adjacent volcano-sedimentary Euclid Lake Formation (Yang et al., 2011, 2012, 2013), indicates that they represent a dismembered Archean subduction-related ophiolite (Dilek and Furnes, 2011). This ophiolite and the Archean megacrystic anorthosite-bearing Mayville layered intrusion mark a suture zone between the Maskwa Lake microcontinent (Bird River subprovince) and the North Caribou terrane.

Dome and basin structures in Archean greenstone-granitoid terrains are interpreted as products of vertical tectonic (e.g., sagduction) processes as an alternative to modern-style plate tectonics processes (Hamilton, 1998, 2013; Lin, 2005; Bédard, 2006, 2018; Robin and Bailey, 2009; Ivanic et al., 2010, 2015; Bédard et al., 2013; Thébaud and Rey, 2013; Gerya, 2014; François et al., 2014; Johnson et al., 2014). Dome and basin structures, however, are not restricted to the Archean and occur throughout the geological record (Lee et al., 2000; Weijermars and Khan, 2000; Kusky et al., 2018; Zulauf et al., 2019), indicating that the presence of such structures cannot be used to rule out the operation of plate tectonics in the Archean. As a matter of fact, Weijermars and Khan (2000) show that the Late Proterozoic (620 Ma) dome and basin structures in Saudi Arabia formed by plate tectonic processes (e.g., island arc accretion). Collectively, structures in the Bird River greenstone belt (Gilbert et al., 2008) and those in the Superior Province (Percival et al., 2012) are consistent mainly with horizontal tectonic movements (e.g., low-angle thrusting) in the Late Archean. We want to point out that we are not suggesting that all Archean greenstone belts formed in a subduction zone setting. Geochemical and field data indicate that, like modern oceanic crust, Archean greenstone belts formed in diverse geodynamic settings, including intra-oceanic and intra-continental settings (Kerrich and Polat, 2006; Polat, 2013; Shellnutt and Dostal, 2019).

The positive $\varepsilon_{Nd\ (2743\ Ma)}$ values exhibited by the Mayville Intrusion signify that the arc-like geochemistry of its parental magma was not inherited by contamination of pre-existing crust, as is often the case with vertical tectonic autochthonous processes (Smithies et al., 2018). That the majority of the samples from the Mayville Intrusion are unaltered suggests that the arc-like geochemistry of the Mayville Intrusion was not generated as a result of element mobility, which has been proposed as evidence against the operation of horizontal tectonics in the Archean (e.g., Bédard, 2006, 2018; Bédard et al., 2013). Anorthosite-bearing layered mafic to ultramafic

intrusions that are interpreted to have formed from such processes (e.g., Windimurra Intrusion, Australia) do not have the very high anorthite contents exhibited by the plagioclase megacrysts in the Mayville Intrusion that are usually associated with arc volcanic rocks and intrusives (Ahmat and de Laeter, 1982; Takagi et al., 2005; Ivanic et al., 2010). This suggests that the Mayville Intrusion was not derived through vertical tectonic processes but rather at a subduction zone setting. There are no dome and basin structures in the Bird River subprovince, and the Bird River greenstone belt does not lie solely on top of older continental crust and has low-angle thrust faults (Gilbert et al., 2008, Duguet et al., 2009). These lines of evidence indicate that the Mayville Intrusion, New Manitoba Mine Intrusion and Mayville Assemblage formed in a subduction zone setting through modern-style plate tectonics rather than sagduction tectonic processes.

4.8.6. A possible genetic relationship between the Mayville and Bird River layered intrusions

The Mayville and Bird River anorthosite-bearing layered intrusions occur at the northern and southern margins of the Maskwa Lake microcontinent, respectively, and are separated (~25 km) by the Maskwa Lake TTG Batholith (Yang et al., 2011; Yang and Gilbert, 2014). These layered intrusions have the same age (ca. 2743 Ma), formed during the Bird River magmatic event and share many geochronological, lithological, petrographical and geochemical characteristics (Yang et al., 2011; Houlé et al., 2013; Yang and Gilbert, 2014; Sotiriou et al., 2019b). Both the Mayville and Bird River layered intrusions have highly calcic (An_{70-85} and An_{63-99}, respectively) plagioclase megacrysts, magmatic amphibole and cumulate textures (Sotiriou et al., 2019b). Both intrusions were emplaced into back-arc pillow basalts and continental arc TTGs and were intruded by continental arc TTGs (Fig. 4.17; Yang et al., 2011, 2012, 2013; Sotiriou et al., 2019b). The generally positive $\varepsilon_{Nd\ (2743\ Ma)}$ (+0.7 to +3.9 and +0.5 to +4.7, respectively) values of both the Mayville and Bird River layered intrusions reflect derivation of their parental magmas from a depleted mantle source followed by subsequent minor contamination of these parental magmas by TTG arc crust (see Henry et al., 1998; Yang et al., 2011; Yang and Gilbert, 2014; Sotiriou et al., 2019b). Furthermore, the Mayville and Bird River layered intrusions have similar back-arc trace element patterns, hydrous primitive arc tholeiitic parental magmas and similar major and trace element trends, indicating that their

parental magmas underwent broadly similar degrees of differentiation (Figs. 4.10-4.12; Yang and Gilbert; Sotiriou et al., 2019b). Collectively, these geological and geochemical similarities indicate that the Mayville and Bird River layered intrusions have a common petrogenetic history and were emplaced into the same continental back-arc basin (Fig. 4.16).

Mesoarchean continental arc magmatism occurred along the southern margin of the North Caribou terrane from 2940 Ma to 2910 Ma, 2870 Ma to 2850 Ma and 2840 Ma to 2825 Ma (Corfu and Stott, 1993; Percival et al., 2012). The Maskwa Lake TTG Batholith I in the Maskwa Lake microcontinent records continental arc magmatism from 2858 Ma to 2782 Ma (Gilbert et al., 2008; Duguet et al., 2009; Yang et al., 2013). The overlapping, predominantly Mesoarchean ages of continental arc magmatism for the now separated North Caribou terrane and Maskwa Lake microcontinent indicate that the latter was derived by intra-arc rifting from the former (Card and Poulsen, 1998; Gilbert et al., 2008; Percival et al., 2012; Sotiriou et al., 2019b). Given that the Mayville and Bird River layered intrusions were emplaced into back-arc oceanic crust and TTG arc crust during intra- to back-arc rifting, the rifting of the Maskwa Lake microcontinent from the North Caribou terrane most likely occurred at ca. 2743 Ma in association with this intra- to back-arc rifting (Fig. 4.17). The Mayville, Bird River, Euclid Lake, Cat Lake and Coppermine Bay layered intrusions formed during the ca. 2743 Ma Bird River magmatic event (Houlé et al., 2013; Yang et al., 2013; Bécu et al., 2015), which most likely resulted from intra- to back-arc rifting of the southern active continental margin of the North Caribou terrane that created the Maskwa Lake microcontinent (Fig. 4.17). The Maskwa Lake microcontinent most likely subsequently collided with the North Caribou terrane during the Uchian Orogeny.

4.9. Conclusions

The cumulate textures and primary mineralogy of the Mayville Intrusion are generally well preserved, with abundant magmatic plagioclase, amphibole, clinopyroxene, orthopyroxene and chromite. The magmatic nature of the amphiboles in the Mayville Intrusion is strongly indicated by their anhedral nature, whole-grain optical continuity and serrated grain boundaries. The occurrence of abundant, well-preserved magmatic amphibole in the anorthosites and leucogabbros of the Mayville Intrusion indicates that it crystallised from a hydrous magma. The field relationships and geochemical characteristics of the Mayville

Intrusion and the spatially and temporally associated Mayville Assemblage and New Manitoba Mine Intrusion suggest that they were derived from similar parental magmas that formed by partial melting of variably-depleted mantle sources. The REE and HFSE systematics of the Mayville Intrusion, Mayville Assemblage and New Manitoba Mine Intrusion are consistent with a suprasubduction zone geodynamic setting.

The Mayville Intrusion anorthosites and leucogabbros crystallised from a hydrous Ca- and Al-rich tholeiitic magma that fractionated from a hydrous primitive arc tholeiitic parental magma. The parental magmas to the anorthosites, leucogabbros and gabbros of the Anorthosite to Leucogabbro Zone of the Mayville Intrusion underwent minor contamination by the Mesoarchean phase of the Maskwa Lake TTG Batholith. The Mayville Intrusion, Mayville Assemblage and New Manitoba Mine Intrusion represent a suture zone-marking Archean subduction-related ophiolite that formed in a Chilean-style continental back-arc geodynamic setting at the southern active continental margin of the North Caribou terrane. The occurrence of abundant magmatic amphibole in the Mayville Intrusion, combined with its back-arc geodynamic setting and proximity to spatially associated continental arc-derived TTGs and volcanics, strongly indicates that hydrous arc magmatism occurred in the Neoarchean.

4.10. References

Ahmat, A.L., Laeter, J.R., 1982. Rb-Sr isotopic evidence for Archaean-Proterozoic crustal evolution of part of the central Yilgarn Block, Western Australia: Constrains on the age and source of the anorthositic Windimurra Gabbroid. Journal of the Geological Society of Australia 29(1-2), 177-190.

Allard, G.O., 1976. Doré Lake Complex and its importance to Chibougamau geology and metallogeny. Ministère des Richesses Naturelles du Québec, DP-338, 446p.

Arculus, R.J., Wills, K.J., 1980. The petrology of plutonic blocks and inclusions from the Lesser Antilles island arc. Journal of Petrology 21(4), 743-799.

Arguin, J.-P., Pagé, P., Barnes, S.-J., Girard, R., Duran, C., 2018. An integrated model for ilmenite, Al-spinel, and corundum exsolutions in titanomagnetite from oxide-rich layers of the Lac Doré Complex (Québec, Canada). Minerals 8 (476), doi: 10.3390/min8110476.

Ashwal, L.D., 1993. Anorthosites. Minerals and Rocks Series 21, Springer-Verlag: Berlin, 422p.

Ashwal, L.D., 2010. The temporality of anorthosites. The Canadian Mineralogist 48(4), 711-728.

Ashwal, L.D., Bybee, G.M., 2017. Crustal evolution and the temporality of anorthosites. Earth Science Reviews 173, 307-330.

Ashwal, L.D., Myers, J.S., 1994. Archean anorthosites. In: Kondie, K.C. (ed.). Elsevier: Amsterdam, Developments in Precambrian Geology 11, 315-355.

Bacon, C.R., Sisson, T.W., Mazdab, F.K., 2007. Young cumulate complex beneath Veniaminof caldera, Aleutian arc, dated by zircon in erupted plutonic blocks. Geology 35, 491-494.

Beard, J.S., Borgia, A., 1989. Temporal variation of mineralogy and petrology in cognate gabbroic enclaves at Arenal Volcano, Costa Rica. Contributions to Mineralogy and Petrology 103, 110-122.

Bécu, V., Houlé, M.G., McNicoll, V.J., Yang, X.M., Gilbert, H.P., 2015. Mafic intrusive rocks from the Bird River intrusive suite, Bird River greenstone belt, southeast Manitoba. In: Ames, D.E., Houlé, M.G. (eds.). Targeted Geoscience Initiative 4: Canadian Nickel-Copper-Platinum Group Elements-Chromium Ore Systems - Fertility, Pathfinders, New and Revised Models. Geological Survey of Canada, Open File 7856, 49-60.

Bédard, J.H., 2006. A catalytic delamination-driven model for coupled genesis of Archaean crust and sub-continental lithospheric mantle. Geochimica et Cosmochimica Acta 70, 1188-1214.

Bédard, J.H., 2018. Stagnant lids and mantle overturns: Implications for Archaean tectonics, magmagenesis, crustal growth, mantle evolution, and the start of plate tectonics. Geoscience Frontiers 9, 19-49.

Bédard, J.H., Harris, L.B., Thurston, P.C., 2013. The hunting of the snArc. Precambrian Research 229, 20-48.

Burnham, O.M., 2017. Inductively coupled plasma mass spectrometry analysis of trace elements in geological sample after *Aqua Regia* extraction at the Geoscience Laboratories: Revised capabilities resulting from new instrumentation In: Summary of Field Work and Other Activities 2017. Ontario Geological Survey, Open File Report 6333, 31-1 - 31-10.

Card, K.D., Ciesielski, A., 1986. Subdivisions of the Superior Province of the Canadian Shield. Geoscience Canada 13(1), 5-13.

Card, K.D., Poulsen, K.H., 1998. Geology and mineral deposits of the Superior Province of the Canadian shield. In: Lucas, S.B., St-Onge, M.R. (eds.). Geology of the Precambrian Superior and Grenville Provinces and Precambrian Fossils in North America. Geological Survey of Canada, Geology of Canada 7, 13-194.

Cigolini, C., 1998. Intracrustal origin of Arenal basaltic andesite in the light of solid–melt interactions and related compositional buffering. Journal of Volcanology and Geothermal Research 86(1), 277-310.

Cigolini, C., Kudo, A.M., 1987. Xenoliths in recent basaltic andesite flows from Arenal Volcano, Costa Rica: inference on the composition of the lower crust. Contributions to Mineralogy and Petrology 96(3), 381-390.

Claeson, D.T., Meurer, W.P., 2004. Fractional crystallization of hydrous basaltic "arc-type" mamas and the formation of amphibole-bearing gabbroic cumulates. Contributions to Mineralogy and Petrology 147, 288-304.

Condie, K.C., Kröner, A., 2008. When did plate tectonics begin? Evidence from the geologic record. In: Condie, K.C., Pease, A. (eds.). When Did Plate Tectonics Begin On Planet Earth? Geological Society of America Special Paper 440, 281-294.

Conrad, W.K., Kay, R.W., 1984. Ultramafic and mafic inclusions from Adak Island: crystallisation history, and implications for the nature of primary magmas and crustal evolution in the Aleutian Arc. Journal of Petrology 25, 88-125.

Corfu, F., Stott, G.M., 1993. U-Pb geochronology of the central Uchi Subprovince, Superior Province. Canadian Journal of Earth Sciences 30, 1179-1196.

Danyushevsky, L.V., Plechov, P., 2011. Petrolog3: Integrated software for modelling crystallization processes. Geochemistry, Geophysics, Geosystems 12 (7), doi: 10.1029/2011gc003516.

Deer, W.A., Howie, R.A., Zussman, J., 2013. An Introduction to the Rock-Forming Minerals. 3rd edition. The Mineralogical Society: London, 498p.

Dilek, Y., Furnes, H., 2011. Ophiolite genesis and global tectonics: Geochemical and tectonic fingerprinting of ancient oceanic lithosphere. GSA Bulletin 123(3-4), 387-411.

Duguet, M., Lin, S., Davis, D.W., Corkery, M.T., McDonald, J., 2009. Long-lived transpression in the Archean Bird River greenstone belt. western Superior Province, southeastern Manitoba. Precambrian Research 174(3-4), 381-407.

Edwards, S.J., Pearce, J.A., Freeman, J., 2000. New insights concerning the influence of water during the formation of podiform chromitite. In: Dilek, Y., Moores, E.M., Elthon, D., Nicolas, A. (eds.). Ophiolites and Oceanic Crust: New Insights from Field Studies and the Ocean Drilling Program. Geological Society of America Special Paper 349, 139-147.

Escuder-Viruete, J., Castillo-Carrión, M., Pérez-Estaún, A., 2014. Magmatic relationships between depleted mantle harzburgites, boninitic cumulate gabbros and subduction-related

tholeiitic basalts in the Puerto Plata ophiolitic complex, Dominican Republic: Implications for the birth of the Caribbean island-arc. Lithos 196, 261-280.

Foley, B.J., 2018. The dependence of planetary tectonics on mantle thermal state: applications to early Earth evolution. Philosophical Transactions of the Royal Society A: Mathematical, Physical and Engineering Sciences 376(2132), 20170409,http://dx.doi.org/10.1098/rsta.2017.0409.

Foley, B.J., Bercovici, D., Elkins-Tanton, L.T., 2014. Initiation of plate tectonics from post-magma ocean thermochemical convection. Journal of Geophysical Research: Solid Earth 119(11), 8538-8561.

François, C., Philippot, P., Rey, P., Rubatto, D., 2014. Burial and exhumation during Archean sagduction in the East Pilbara Granite-Greenstone Terrane. Earth and Planetary Science Letters 396, 235-251.

Gerya, T., 2014. Precambrian geodynamics: Concepts and models. Gondwana Research 25(2), 442-463.

Gilbert, H.P., Davis, D.W., Duguet, M., Kremer, P., Mealin, C.A., MacDonald, J., 2008. Geology of the Bird River Belt, southeastern Manitoba (parts of NTS 52L5, 6). Manitoba Science, Technology, Energy and Mines, Manitoba Geological Survey, Geoscientific Map MAP2008-1, scale 1:20,000.

Gill, R.G., 2010. Igneous Rocks and Processes: A Practical Guide. John Wiley & Sons Ltd.: Chichester, U.K., 428p.

Golowin, R., Portnyagin, M., Hoernle, K., Sobolev, A., Kuzmin, D., Werner, R., 2017. The role and conditions of second-stage mantle melting in the generation of low-Ti tholeiites and boninites: the case of the Manihiki Plateau and the Troodos ophiolite. Contributions to Mineralogy and Petrology 172(11-12): 104.

Gonzalez-Jimenez, J.M., Camprubi, A., Colás, V., Griffin, W.L., Proenza, J.A., O'Reilly, S.Y., Centeno-Garcia, E., Garcia-Casco, A., Belousova, E., Talavera, C., Farre-de-Pablo, J., 2017. The recycling of chromitites in ophiolites from southwestern North America. Lithos 294, 53-72.

Hamilton, W.B., 1998. Archean magmatism and deformation were not products of plate tectonics. Precambrian Research 91(1-2), 143-179.

Hamilton, W.B., 2011. Plate tectonics began in Neoproterozoic time, and plumes from deep mantle have never operated. Lithos123(1-4), pp.1-20.

Hamilton, W.B., 2013. Evolution of the Archean Mohorovičić discontinuity from a synaccretionary 4.5 Ga protocrust. Tectonophysics 609, 706-733.

Hargreaves, J.C., 2017. Summary of quality control data for the Geoscience Laboratories methods EMP-100, IMC-100, 1MO-100 and ISE-R01. instrumentation In: Summary of Field Work and Other Activities 2017. Ontario Geological Survey, Open File Report 6333, 32-1 - 32-15.

Hastie, A.R., Fitton, J.G., 2019. Eoarchaean tectonics: New constraints from high pressure-temperature experiments and mass balance modelling. Precambrian Research 325, 20-38.

Henry, P., Stevenson, R.K., Gariepy, C., 1998. Late Archean mantle composition and crustal growth in the Western Superior Province of Canada: neodymium and lead isotopic evidence from the Wawa, Quetico and Wabigoon subprovinces. Geochimica et Cosmochimica Acta 62, 143-157.

Hildebrand, R.S., Whalen, J.B., Bowring, S.A., 2018. Resolving the crustal composition paradox by 3.8 Ga billion years of slab failure magmatism and collisional recycling of continental crust. Tectonophysics 734-735, 69-88.

Hoffmann, J.E., Münker, C., Næraa, T., Rosing, M.T., Herwartz, D., Garbe-Schönberg, D., Svahnberg, H., 2011. Mechanisms of Archean crust formation inferred from high-precision HFSE systematics in TTGs. Geochimica et Cosmochimica Acta 75, 4157-4178.

Hoffmann, J.E., Svahnberg, H., Piazolo, S., Scherstén, A., Münker, 2012. Geodynamic evolution of Mesoarchean anorthosite complexes inferred from the Naajat Kuuat Complex, southern West Greenland. Precambrian Research 196-197, 149-170.

Hollings, P., Kerrich, R., 2004. Geochemical systematics of tholeiites from the 2.86 Ga Pickle Crow Assemblage, northwestern Ontario: arc basalts with positive and negative Nb-Hf anomalies. Precambrian Research 134(1-2), 1-20.

Houlé, M.G., McNicoll, V.J., Bécu, V., Yang, X.M., Gilbert, H.P., 2013. New age for the Mayville Intrusion: implication for a large mafic-ultramafic event in the Bird River greenstone belt, southeastern Manitoba (abstract); Geological Association of Canada-Mineralogical Association of Canada, Joint Annual Meeting, Winnipeg, Manitoba, May 22-24, 2013, Program with Abstracts, p. 115.

Huang, H., Polat, A., Fryer, B.J., 2013. Origin of Archean tonalite-trondhjemite-granodiorite (TTG) suites and granites in the Fiskenæsset region, southern West Greenland: Implications for continental growth. Gondwana Research 23, 452-470.

Irvine, T.N., 1974. Petrology of the Duke Island ultramafic complex, southeastern Alaska. Geological Society of America Memoir 138, 240p.

Irvine, T.N., Baragar, W.R.A., 1971. A guide to the chemical classification of the common volcanic rocks. Canadian Journal of Earth Sciences 8, 523-548.

Ivanic, T.J., Nebel, O., Jourdan, F., Faure, K., Kirkland, C.L., Belousova, E.A., 2015. Heterogeneously hydrated mantle beneath the late Archean Yilgarn Craton. Lithos 238, 76-85.

Ivanic, T.J., Wingate, M.T.D., Kirkland, C.L., Van Kranendonk, M.J., Wyche, S., 2010. Age and significance of voluminous mafic-ultramafic magmatic events in the Murchison Domain, Yilgarn Craton. Australian Journal of Earth Sciences 57(5), 597-614.

Johnson, M.C., Rutherford, M.J., 1989. Experimental calibration of the aluminum-in-hornblende geobarometer with application to Long Valley caldera (California) volcanic rocks. Geology 17(9), 837-841.

Johnson, T.E., Brown, M., Kaus, B.J.P., Van Tongeren, J.A., 2014. Delamination and recycling of Archaean crust caused by gravitational instabilities. Nature Geosciences 7, 47-52.

Kerr, A.C., Tarney, J., Kempton, P.D., Pringle, M., Nivia, A., 2004. Mafic pegmatites intruding oceanic plateau gabbros and ultramafic cumulates from Bolivar, Colombia: Evidence for a 'wet' mantle plume? Journal of Petrology 45(9), 1877-1906.

Kerrich, R., Polat, A., 2006. Archean greenstone-tonalite duality: thermochemical mantle convection models or plate tectonics in the early Earth global dynamics? Tectonophysics 415, 141-165.

Kiseleva, O., Zhmodik, S., 2017. PGE mineralization and melt composition of chromitites in Proterozoic ophiolite complexes of Eastern Sayan, Southern Siberia. Geoscience Frontiers 8, 721-731.

Kusky, T.M., Windley, B.F., Polat, A., 2018. Geological evidence for the operation of plate tectonics throughout the Archean: Records from Archean paleo-plate boundaries. Journal of Earth Science 29(6), 1291-1303.

Lahaye, Y., Arndt, N., 1996. Alteration of a komatiite flow from Alexo, Ontario, Canada. Journal of Petrology 37, 1261-1284.

Lahaye, Y., Arndt, N., Byerly, G., Chauvel, C., Fourcade, S., Gruau, G., 1995. The influence of alteration on the trace-element and Nd isotopic compositions of komatiites. Chemical Geology 126, 43-64.

Latypov, R., Chistyakova, S., Costin, G., Namur, O., Barnes, S., Kruger, W., 2020. Monomineralic anorthosites in layered intrusions are indicators of the magma chamber replenishment by plagioclase-only-saturated melts. Scientific Reports 10:3839, https://doi.org/10.1038/s41598-020-60778-w.

Lay, A., Graham, I., Cohen, D., Privat, K., González-Jimenez, J.M., Belousova, E., Barnes, S.J., 2017. Ophiolitic chromitites of Timor Leste: Their composition, platinum group

element geochemistry, mineralogy, and evolution. The Canadian Mineralogist 55(5), 875-908.

Leake, B.E., Woolley, A.R., Arps, C.E.S., Birch, W.D., Gilbert, M.C., Grice, J.D., Hawthorne, F.C., Kato, A., Kisch, H.J., Krivovichev, V.G., Linthout, K., Laird, J., Mandarino, J.A., Maresch, W.V., Nickel, E.H., Rock, N.M.S., Schumacher, J.C., Smith, D.C., Stephenson, N.C.N., Ungaretti, L., Whittaker, E.J.W., Youzhi, G., 1997. Nomenclature of amphiboles: Report of the subcommittee on amphiboles of the International Mineralogical Association, Commission on New Minerals and Mineral Names. The Canadian Mineralogist 35, 219-246.

Lee, J., Hacker, B.R., Dinklage, W.S., Wang, Y., Gans, P., Calvert, A., Wan, J.L., Chen, W., Blythe, A.E., McClelland, W., 2000. Evolution of the Kangmar Dome, southern Tibet: Structural, petrologic, and thermochronologic constraints. Tectonics 19, 872-895.

Lenaz, D., Skogby, H., Rigonat, N., Berger, J., 2018. Following the amphibolite to greenschist metamorphic path through the structural parameters of spinels from Amsaga (Mauritania). Minerals 8(1), 27.

Lin, S., 2005. Synchronous vertical and horizontal tectonism in the Neoarchean: Kinematic evidence from a synclinal keel in the northwestern Superior craton, Canada. Precambrian Research 139, 181-194.

Liu, H., Sun, W.D., Deng, J., 2020. Statistical analysis on secular records of igneous geochemistry: Implication for the early Archean plate tectonics. Geological Journal 55, 994-1002.

Lodge, R.W., Gibson, H.L., Stott, G.M., Franklin, J.M., Hudak, G.J., 2015. Geodynamic setting, crustal architecture, and VMS metallogeny of ca. 2720 Ma greenstone belt assemblages of the northern Wawa subprovince, Superior Province. Canadian Journal of Earth Sciences 52(3), 196-214.

Lowrey, J.R., Wyman, D.A., Ivanic, T.J., Smithies, R.H., Maas, R., 2020. Archean boninite-like rocks of the Northwestern Youanmi Terrane, Yilgarn Craton: Geochemistry and genesis. Journal of Petrology, egaa002, https://doi.org/10.1093/petrology/egaa002.

Martin, H., 1999. Adakitic magmas: modern analogues of Archaean granitoids. Lithos 46, 411-429.

Martin, H., Smithies, R.H., Rapp, R., Moyen, J.-F., Champion, D., 2005. An overview of adakite, tonalite-trondhjemite (TTG), and sanukitoid: relationships and some implications for crustal evolution. Lithos 79, 1-24.

Meurer, W.P., Claeson, D.T., 2002. Evolution of crystallizing interstitial liquid in an arc-related cumulate determined by LA-ICP-MS mapping of a large amphibole oikocryst. Journal of Petrology 43, 607-629.

Mohan, M.R., Satyanarayanan, M., Santosh, M., Sylvester, P.J., Tubrett, M., Lam, R., 2013. Neoarchean suprasubduction zone arc magmatism in southern India: Geochemistry, zircon U-Pb geochronology and Hf isotopes of the Sittampundi Anorthosite Complex. Gondwana Research 23, 539-557.

Murphy, J.B., 2007. Igneous Rock Associations 8. Arc magmatism II: Geochemical and isotopic characteristics. Geoscience Canada 34(1), 7-35.

Pearce, J.A., 2008. Geochemical fingerprinting of oceanic basalts with applications to ophiolite classification and the search for Archean oceanic crust. Lithos 100, 14-48.

Pearce, J.A., Peate, D.W., 1995. Tectonic implications of the composition of volcanic arc magmas. Annual Review of Earth and Planetary Sciences 23, 251-286.

Peck, D.C., Scoates, R.F.J., Theyer, P., Desharnais, G., Hulbert, L.J., Huminicki, M.A.E. 2002. Stratiform and contact-type PGE-Cu-Ni mineralization in the Fox River Sill and the Bird River Belt, Manitoba. In: The Geology, Geochemistry, Mineralogy and Mineral Beneficiation of Platinum-Group Elements, L.J. Cabri (ed.), Canadian Institute of Mining and Metallurgy, Special Volume 54, 367–387.

Percival, J.A., Skulski, T., Sanborn-Barrie, M., Stott, G.M., Leclair, A.D., Corkery, M.T., Boily, M., 2012. Geology and tectonic evolution of the Superior Province, Canada. Tectonic styles in Canada: The Lithoprobe Perspective, Special Paper 49, 321-378.

Piaia, P., Oliveira, E.P., Valeriano, C., 2017. The 2.58 Ga São José do Jacuipe Gabbro-Anorthosite Stratiform Complex, Itabuna-Salvador-Curaçá, São Francisco Craton, Brazil: Root of the Neoarchaean Caraiba continental arc? Journal of South American Earth Sciences 79, 326-341.

Piercey, S.J., Murphy, D.C., Mortensen, J.K., Paradis, S., 2001. Boninitic magmatism in a continental margin setting, Yukon-Tanana terrane, southeastern Yukon, Canada. Geology 29(8), 731-734.

Polat, A., 2013. Geochemical variations in Archean volcanic rocks, southwestern Greenland: Traces of diverse tectonic settings in the early Earth. Geology 41, 379-380.

Polat, A., Appel, P.W.U., Fryer, B., Windley, B., Frei, R., Samson, I.M., Huang, H., 2009. Trace element systematics of the Neoarchean Fiskenæsset anorthosite complex and associated meta-volcanic rocks, SW Greenland: Evidence for a magmatic arc origin. Precambrian Research 175, 87-115.

Polat, A., Frei, R., Longstaffe, F.J., Woods, R., 2018b. Petrogenetic and geodynamic origin of the Neoarchean Doré Lake Complex, Abitibi subprovince, Superior Province, Canada. International Journal of Earth Sciences (Geologische Rundschau) 107, 811-843.

Polat, A., Fryer, B.J., Appel, P.W.U., Kalvig, P., Kerrich, R., Dilek, Y., Yang, Z., 2011. Geochemistry of anorthositic differentiated sills in the Archean (~2970 Ma) Fiskenæsset Complex, SW Greenland: Implications for parental magma compositions, geodynamic setting, and secular heat flow in arcs. Lithos 123, 50-72.

Polat, A., Fryer, B.J., Samson, I.M., Weisener, C., Appel, P.W.U., Frei, R., Windley, B.F., 2012. Geochemistry of ultramafic rocks and hornblendite veins in the Fiskenæsset layered anorthosite complex, SW Greenland: Evidence for hydrous upper mantle in the Archean. Precambrian Research 214-215, 124-153.

Polat, A., Herzberg, C., Münker, C., Rodgers, R., Kusky, T., Li, J., Fryer, B., Delaney, J., 2006. Geochemical and petrological evidence for a suprasubduction zone origin of Neoarchean (ca. 2.5 Ga) peridotites, central orogenic belt, North China craton. Geological Society of America Bulletin 118(7-8), 771-784.

Polat, A., Hofmann, A.W., 2003. Alteration and geochemical patterns in the 3.7-3.8 Ga Isua greenstone belt, West Greenland. Precambrian Research 112, 5-25.

Polat, A., Kokfelt, T., Burke, K.C., Kusky, T., Bradley, D., Dziggel, A., Kolb, J., 2016. Lithological, structural, and geochemical characteristics of the Mesoarchean Târtoq greenstone belt, South-West Greenland, and the Chugach-Prince William accretionary complex, southern Alaska: Evidence for uniformitarian plate-tectonic processes. Canadian Journal of Earth Sciences 53, 1336-1371.

Polat, A., Longstaffe, F.J., Frei, R., 2018a. An overview of anorthosite-bearing layered intrusions in the Archaean craton of southern West Greenland and the Superior Province of Canada: implications for Archaean tectonics and the origin of megacrystic plagioclase. Geodinamica Acta 30(1), 84-99.

Polat, A., Wang, L., Appel, P.W.U., 2015. A review of structural patterns and melting processes in the Archean craton of West Greenland: Evidence for crustal growth at convergent plate margins as opposed to non-uniformitarian models. Tectonophysics, 662, 67-94.

Qiu, T., Yang, J., Milushi, I., Wu, W., Mekshiqi, N., Xiong, F., Zhang, C., Shen, T., 2018. Petrology and PGE abundances of high-Cr and high-Al podiform chromitites and peridotites from the Bulqiza Ultramafic Massif, Eastern Mirdita Ophiolite, Albania. Acta Geologica Sinica 92(3), 1063-1081.

Robin, C.M.I., Bailey, R.C., 2009. Simultaneous generation of Archean crust and subcratonic roots by vertical tectonics. Geology 37(6), 523-526.

Rollinson, H.R, Reid, C., Windley, B.F., 2010. Chromitites from the Fiskenæsset anorthositic complex, West Greenland: clues to late Archaean mantle processes. In: Kusky, T.M., Zhai, M.-G., Xiao, W. (eds.). The Evolving Continents: Understanding Processes of Continental Growth. Geological Society of London, Special Publications 338, 197-212.

Roman, A., Arndt, N., 2019. Differentiated Archean oceanic crust: its thermal structure, mechanical stability and a test of the sagduction hypothesis. Geochimica et Cosmochimica Acta, https://doi.org/10.1016/j.gca.2019.07.009.

Ross, P.-S., Bédard, J.H., 2009. Magmatic affinity of modern and ancient subalkaline volcanic rocks determined from trace-element discriminant diagrams. Canadian Journal of Earth Sciences 46, 823-839.

Shellnutt, J.G., Dostal, J., 2019. Haida Gwaii (British Columbia, Canada): a Phanerozoic analogue of a subduction-unrelated Archean greenstone belt. Scientific Reports 9: 3251.

Sisson, T.W., Grove, T.L., 1993a. Experimental investigations of the role of H_2O in calc-alkaline differentiation and subduction zone magmatism. Contributions to Mineralogy and Petrology 113, 143-166.

Sisson, T.W., Grove, T.L., 1993b. Temperatures and H_2O contents of low-MgO high-alumina basalts. Contributions to Mineralogy and Petrology 113, 167-184.

Smithies, R.H., Ivanic, T.J., Lowrey, J.R., Morris, P.A., Barnes, S.J., Wyche, S., Lu, Y.J., 2018. Two distinct origins for Archean greenstone belts. Earth and Planetary Science Letters 487, 106-116.

Sotiriou, P., Polat, A., Frei, R., 2019a. Petrogenesis and geodynamic setting of the Neoarchaean Haines Gabbroic Complex and Shebandowan greenstone belt, Southwestern Superior Province, Ontario, Canada. Lithos 324-325, 1-19.

Sotiriou, P., Polat, A., Frei, R., Yang, X.M., van Vessem, J., 2019b. A back-arc origin for the Neoarchean megacrystic anorthosite-bearing Bird River Sill and the associated greenstone belt, Bird River subprovince, Western Superior Province, Manitoba, Canada. International Journal of Earth Sciences 108(7), 2177-2207.

Stern, R.J., Fouch, M.J., Klemperer, S.L., 2003. An overview of the Izu-Bonin-Mariana subduction factory. In: Eiler, J. (ed.). Inside The Subduction Factory. American Geophysical Union, Geophysical Monograph 138, 175-222.

Sun, S.S., McDonough, W.F., 1989. Chemical and isotopic systematics of oceanic basalts: implications for mantle composition and processes. In: Saunders, A.D. and Norry, M.J.

(eds.). Magmatism in the Ocean Basins. Geological Society of London: London, Special Publication 42, 313-345.

Takagi, D., Sato, H., Nakagawa, M., 2005. Experimental study of a low-alkali tholeiite at 1–5 kbar: optimal condition for the crystallization of high-An plagioclase in hydrous arc tholeiite. Contributions to Mineralogy and Petrology 149(5), 527-540.

Taylor, S.R., McLennan, S.M., 1985. The continental crust: its composition and evolution. Blackwell: Oxford, 312p.

Thébaud, N., Rey, P.F., 2013. Archean gravity-driven tectonics on hot and flooded continents: Controls on long-lived mineralised hydrothermal systems away from continental margins. Precambrian Research 229, 93-104.

Tistl, M., Burgath, K.P., Höhndorf, A., Kreuzer, H., Muñoz, R., Salinas, R., 1994. Origin and emplacement of Tertiary ultramafic complexes in northwest Colombia: evidence from geochemistry and K-Ar, Sm-Nd and Rb-Sr isotopes. Earth and Planetary Science Letters 126, 41-59.

Todt, W., Cliff, R.A., Hanser, A., Hofmann, A.W., 1993. Re-calibration of NBS lead standards using $^{202}Pb+ ^{205}Pb$ double spike. Terra Abstracts 5, 396.

Wang, X., 1993. U-Pb zircon geochronology study of the Bird River Greenstone Belt, Southeastern Manitoba. University of Windsor, Windsor, Ontario, Unpublished M.Sc. thesis, 121p.

Weijermars, R., Khan, M.A., 2000. Mid-crustal dynamics and island-arc accretion in the Arabian Shield: insight from the Earth's natural laboratory. Earth-Science Reviews 49(1-4), 77-120.

Winchester, J.A., Floyd, P.A., 1977. Geochemical discrimination of different magmas series and their differentiation products using immobile elements. Chemical Geology 20, 325-343.

Windley, B.F., Garde, A.A., 2009. Arc-generated blocks with crustal sections in the North Atlantic craton of West Greenland: Crustal growth in the Archean with modern analogues. Earth-Science Reviews 93, 1-30.

Wu, T., Polat, A., Fryer, B.J., Yang, K., Kusky, T. M., 2016. Geochemistry, Nd, Pb and Sr isotope systematics of the Neoarchean Bad Vermilion Lake Greenstone Belt and spatially associated granitic rocks, Western Superior Province, Canada. Precambrian Research 97, 27-42.

Wyman, D.A., 2019. 2.8 Ga Subduction-related magmatism in the Youanmi Terrane and a revised geodynamic model for the Yilgarn Craton. Precambrian Research 327, 14-33.

Yang, X.M., 2014a. Granitoid rocks in southeastern Manitoba: preliminary results of reconnaissance mapping and sampling. In: Report of Activities 2014. Manitoba Mineral Resources, Manitoba Geological Survey, 49-63.

Yang, X.M., 2014b. Bedrock geology of the Cat Creek area, Bird River greenstone belt, southeastern Manitoba (part of NTS 52L12). Manitoba Mineral Resources, Manitoba Geological Survey, Preliminary Map PMAP2014-3, scale 1:10,000.

Yang, X.M., Gilbert, H.P., 2014. Mineral chemistry of chromite in the Mayville Intrusion: evidence for petrogenesis and linkage to the Bird River sill in the Neoarchean Bird River greenstone belt, southeastern Manitoba (NTS 52L5, 6, 12). In: Report of Activities 2014. Manitoba Mineral Resources, Manitoba Geological Survey, 32-48.

Yang, X.M., Gilbert, H.P., Corkery, M.T., Houlé, M.G., 2011. The Mayville mafic-ultramafic intrusion in the Neoarchean Bird River greenstone belt, southeastern Manitoba (part of NTS 52L12): preliminary geochemical investigation and implication for PGE-Ni-Cu-(Cr) mineralization. In: Report of Activities 2011. Manitoba Innovation, Energy and Mines, Manitoba Geological Survey, 127-142.

Yang, X.M., Gilbert, H.P., Houlé, M.G., 2012. Geological investigations of the Cat Creek area in the Neoarchean Bird River greenstone belt, southeastern Manitoba (parts of NTS 52L12): new insights into PGE-Ni-Cu-Cr mineralization. In: Reports of Activities 2012. Manitoba Innovation, Energy and Mines, Manitoba Geological Survey, 32-53.

Yang, X.M., Gilbert, H.P., Houlé, M.G., 2013. Cat Lake-Euclid Lake area in the Neoarchean Bird River greenstone belt, southeastern Manitoba (parts of NTS 52L11, 12): preliminary results of bedrock geological mapping and their implications for geodynamic evolution and metallogeny. In: Report of Activities 2013. Manitoba Mineral Resources, Manitoba Geological Survey, 70-84.

Zhou, S., Polat, A., Longstaffe, F.J., Yang, K., Fryer, B.J., Weisener, C., 2016. Formation of the Neoarchean Bad Vermilion Lake Anorthosite Complex and spatially associated granitic rocks at a convergent plate margin, Superior Province, Western Ontario, Canada. Gondwana Research 33, 134-159.

Zulauf, G., Zulauf, J., Thiessen, A., Hattingen, E., 2019. Formation of dome-in-dome structures: Results from experimental studies and comparison with natural examples. Journal of Structural Geology 118, 324-339.

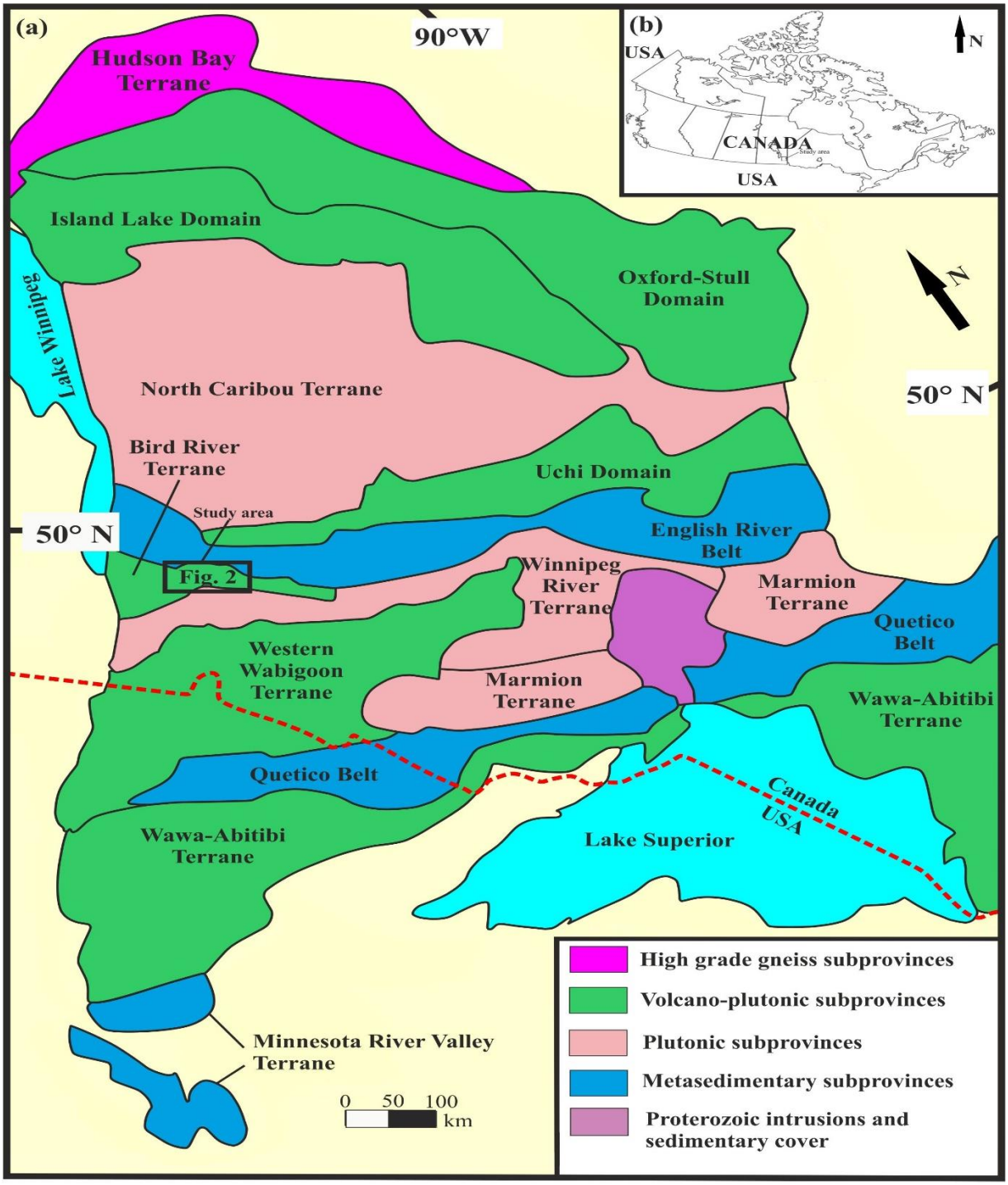

Fig. 4.1. Simplified tectonic map of the western Superior Province (modified after Percival et al., 2012). (**b**) Simplified map of Canada showing its location in North America and the location of the study area.

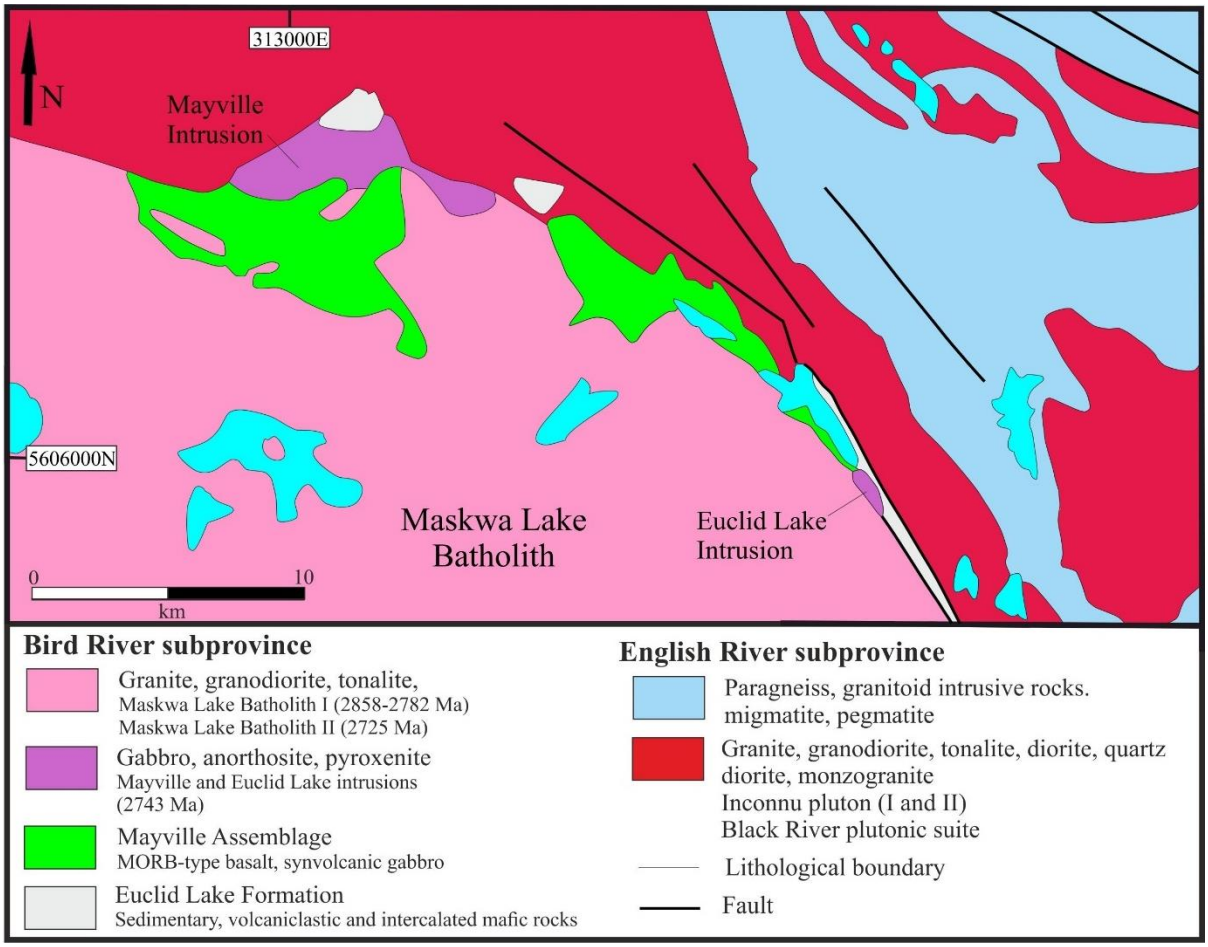

Fig. 4.2. Simplified geological map of the northern arm of the Bird River greenstone belt, showing the Mayville Intrusion, Mayville Assemblage, Euclid Lake Formation and the granitoid batholiths and plutons of the Bird River and English River subprovinces (modified after Yang and Gilbert, 2014).

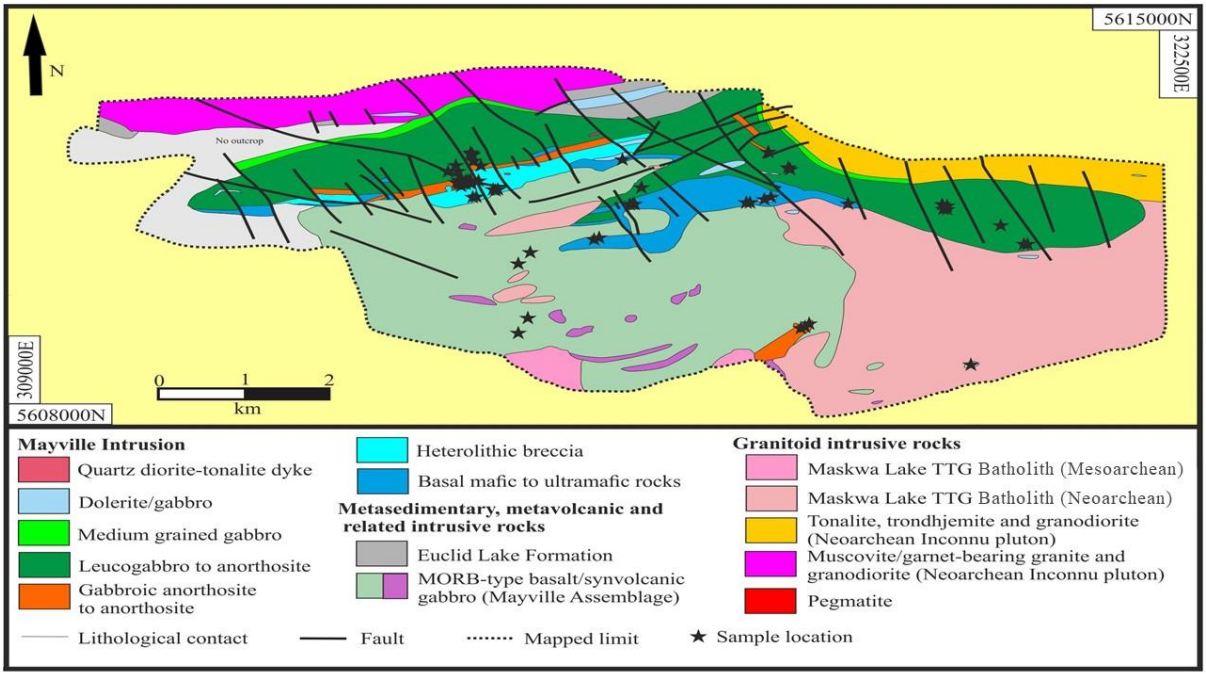

Fig. 4.3. Simplified geological map of the Mayville Intrusion (modified after Yang and Gilbert, 2014).

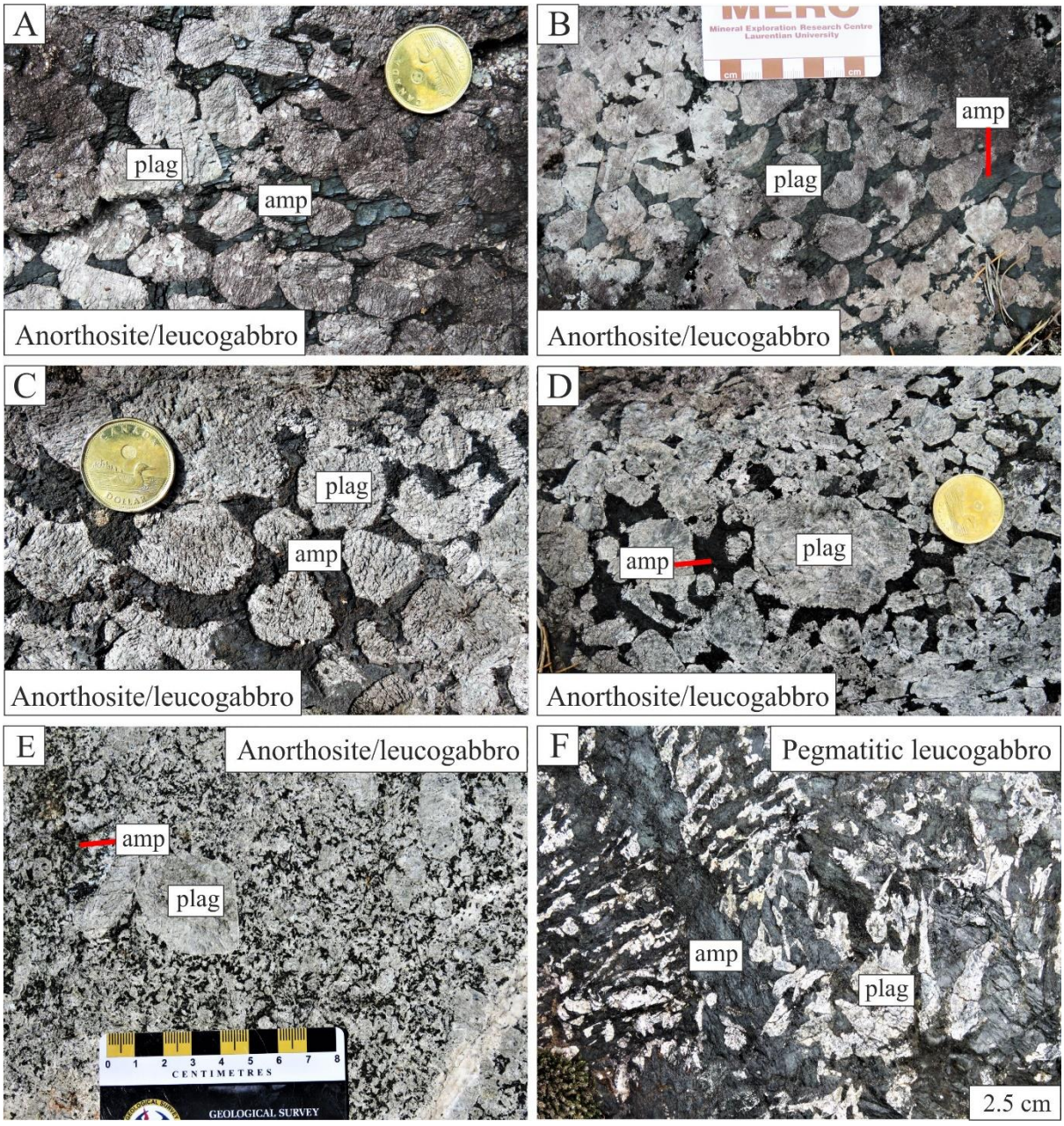

Fig. 4.4. Field photographs from the Mayville Intrusion. (**a-b**) Megacrystic anorthosites/leucogabbros with large magmatic plagioclase megacrysts and large magmatic amphibole oikocrysts that have undergone little recrystallisation. The amphibole oikocrysts have a well-developed primary cleavage and serrated grain boundaries and exhibit whole-grain optical continuity and extinction. (**c**) Megacrystic anorthosite/leucogabbro with magmatic amphibole oikocrysts that envelope plagioclase crystals and have undergone some recrystallisation. (**d**) Megacrystic anorthosite/leucogabbro exhibiting a typical megacrystic texture. (**e**) Megacrystic anorthosite/leucogabbro with a bimodal grain size distribution. (**f**) Pegmatitic leucogabbro with elongate magmatic amphibole and plagioclase crystals that have undergone some recrystallisation. plag: plagioclase; amp: amphibole.

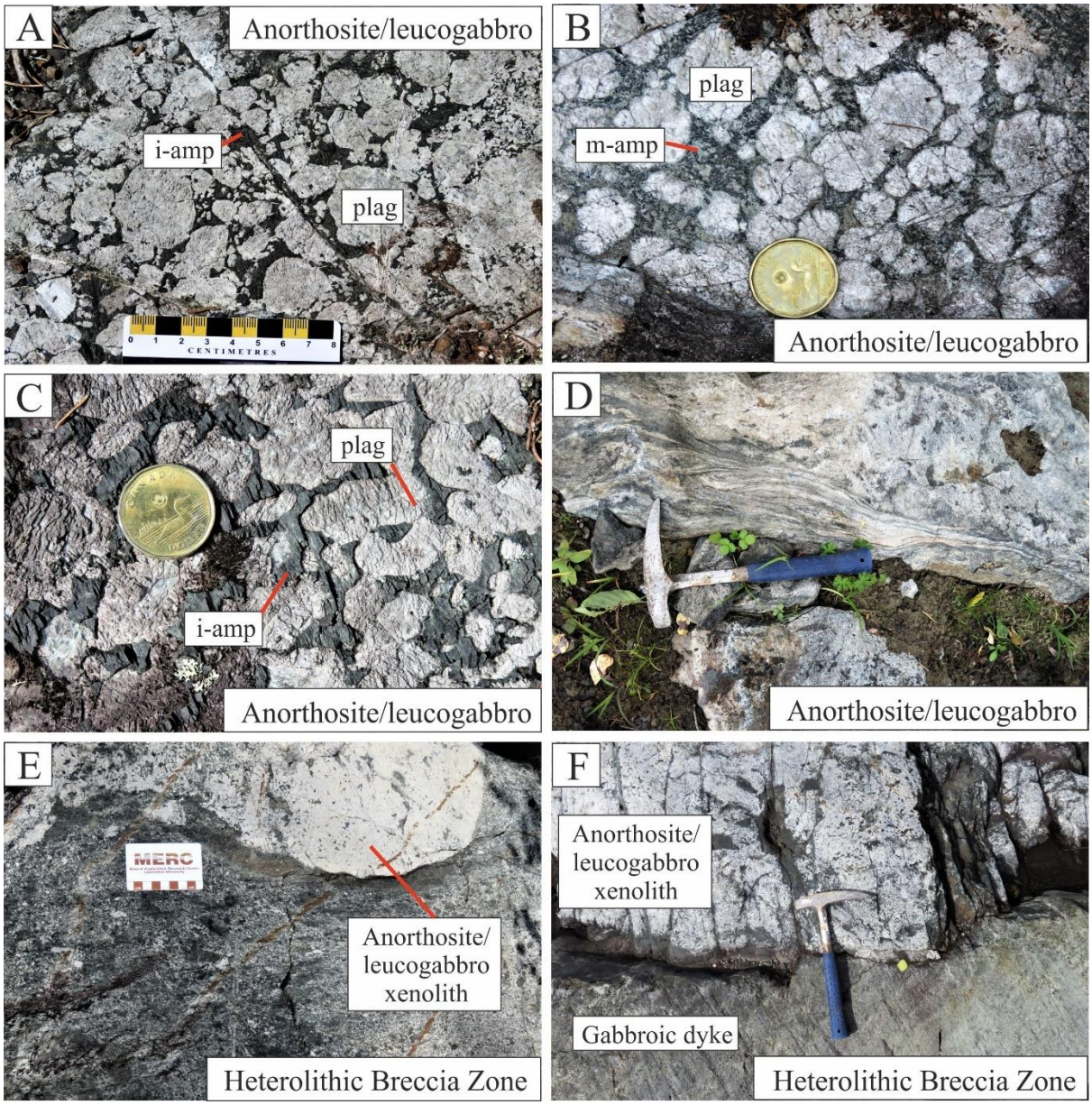

Fig. 4.5. Field photographs from the Mayville Intrusion. (**a**) Megacrystic anorthosite/leucogabbro with a well-preserved megacrystic texture and primary mineralogy. Magmatic plagioclase (plag) megacrysts and interstitial, igneous amphibole (i-amp) are well preserved. (**b**) Megacrystic anorthosite/leucogabbro with a megacrystic texture and a visibly altered primary mineralogy. The plagioclase (plag) megacrysts have been partially altered to sericite and clinozoisite and the interstitial amphibole has been altered to metamorphic amphibole (m-amp). (**c**) Well-preserved megacrystic anorthosite/leucogabbro with relict primary plagioclase (plag) and igneous amphibole (i-amp). (**d**) A mylonitised anorthosite/leucogabbro. (**e**) An anorthosite/leucogabbro xenolith within a sheared part of the Heterolithic Breccia Zone. (**f**) A gabbroic dyke cutting an anorthosite/leucogabbro xenolith within the Heterolithic Breccia Zone.

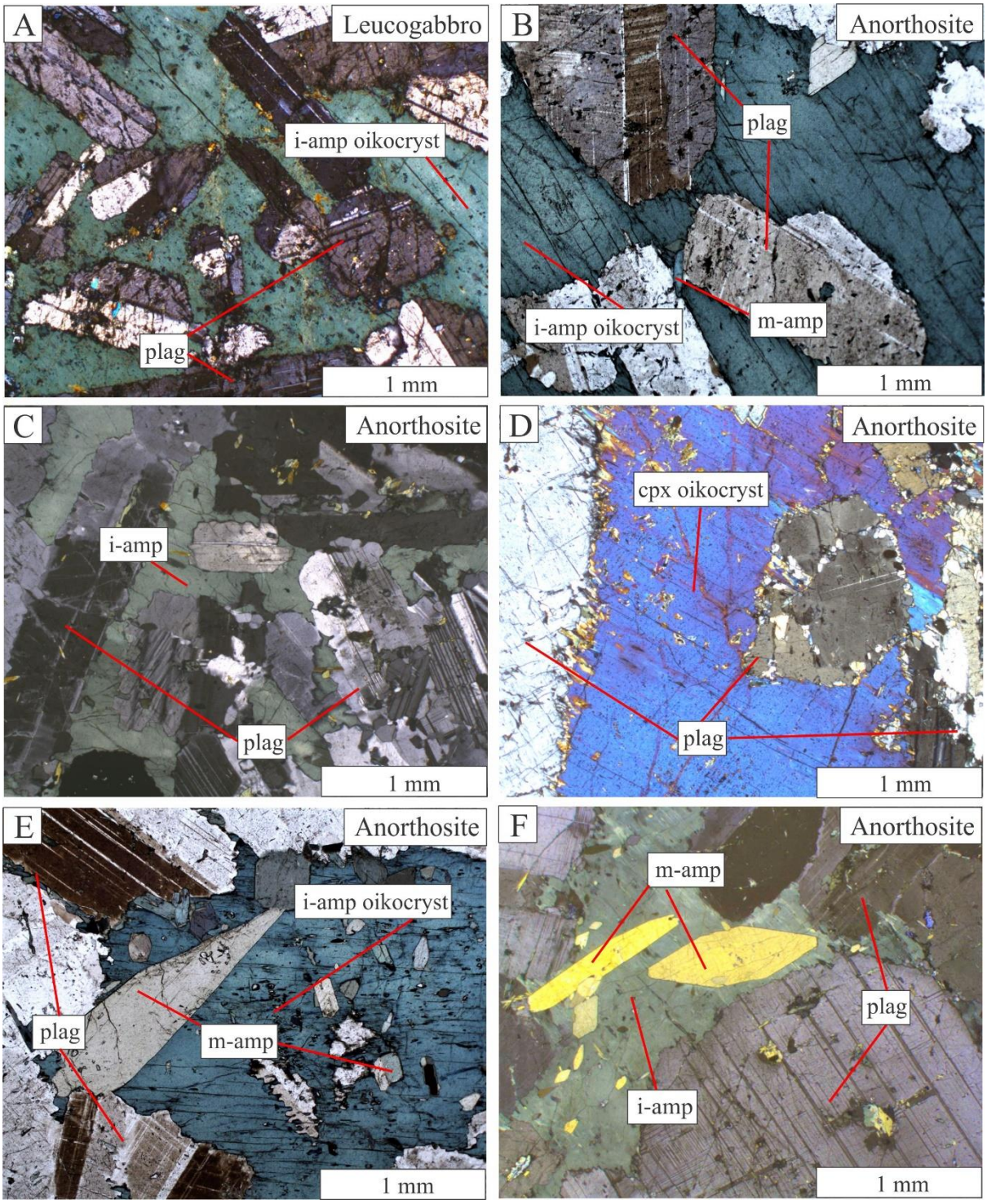

Fig. 4.6. Photomicrographs of anorthosites and leucogabbros from the Anorthosite to Leucogabbro Zone of the Mayville Intrusion. (**a**) Leucogabbro with a magmatic amphibole (i-amp) oikocryst with well-defined primary cleavage enveloping cumulus plagioclase (plag). This magmatic amphibole oikocryst exhibits whole-grain optical continuity and extinction and serrated grain boundaries. (**b**) Anorthosite with a magmatic amphibole (i-amp) oikocryst with well-defined primary cleavage enveloping cumulus plagioclase (plag). (**c**) Anorthosite with a magmatic amphibole (i-amp) oikocryst enveloping cumulus plagioclase (plag). (**d**) Anorthosite with a clinopyroxene (cpx) oikocryst enveloping cumulus plagioclase (plag). (**e**) Anorthosite with metamorphic amphibole (m-amp) overprinting a magmatic amphibole (i-amp) oikocryst.

(**f**) Anorthosite with metamorphic amphiboles (m-amp) overprinting a primary amphibole (i-amp) oikocryst. Cumulate textures are very well preserved and magmatic plagioclase (plag), amphibole (i-amp), and clinopyroxene (cpx) are equally well preserved.

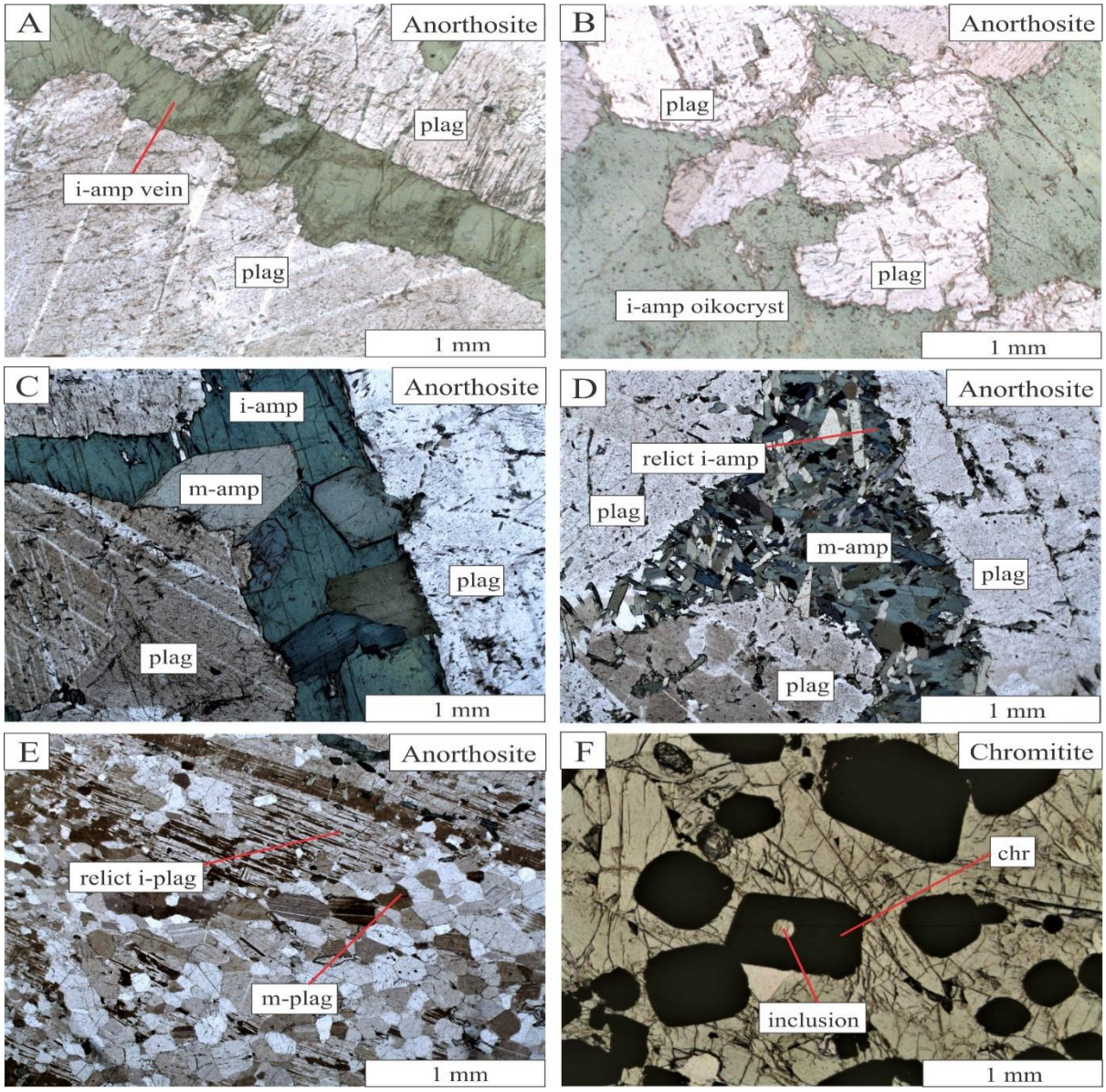

Fig. 4.7. Photomicrographs of lithologies from the Mayville Intrusion. (**a**) Anorthosite with a magmatic amphibole vein (i-amp vein) interstitial to two plagioclase (plag) megacrysts. Note the serrated contacts between the magmatic amphibole vein and the plagioclase megacrysts. (**b**) Anorthosite with an interstitial amphibole (i-amp) oikocryst enveloping cumulus plagioclase (plag). The interstitial amphibole oikocryst is interstitial to cumulus plagioclase and the contact between these minerals is serrated. (**c**) Anorthosite with plagioclase (plag) megacrysts and interstitial magmatic amphibole (i-amp) that has been partially replaced by metamorphic amphibole (m-amp). The magmatic amphibole has well-defined magmatic cleavage. (**d**) Anorthosite with interstitial, now relict magmatic amphibole (i-amp) that has been almost completely replaced by metamorphic amphibole (m-amp). (**e**) Anorthosite with relict plagioclase (relict i-plag) megacrysts that have largely recrystallised to metamorphic plagioclase (m-plag). (**f**) Chromitite with subhedral to euhedral chromite (chr) grains that host mineral inclusions.

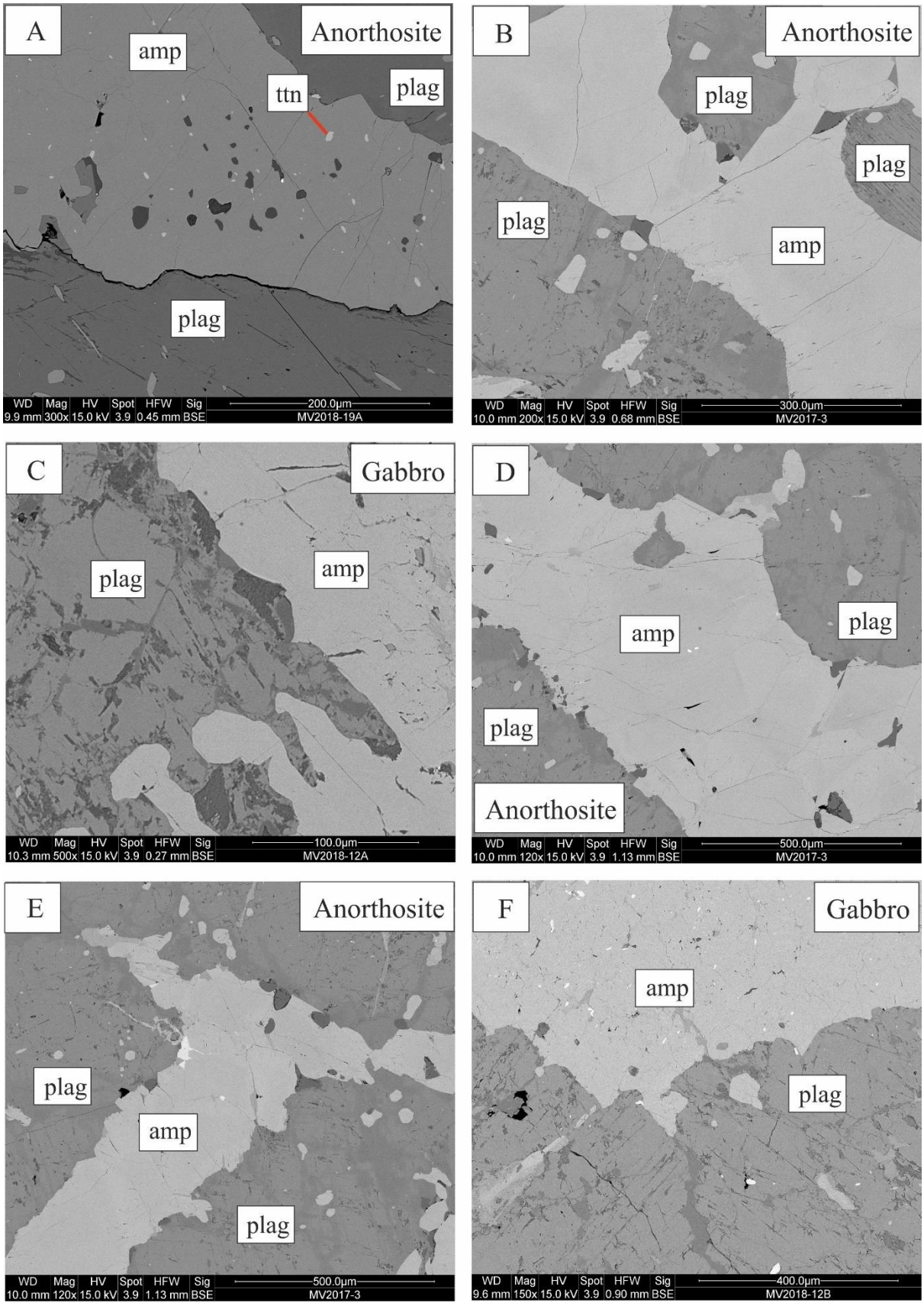

Fig. 4.8. Back-scatter electron scanning electron microscope images from the Mayville Intrusion. (**a**) Anorthosite with interstitial magmatic amphibole (amp) and megacrystic plagioclase (plag). The boundaries between the amphibole and plagioclase are serrated. ttn:

titanite. (**b**) Anorthosite with serrated grain boundaries separating interstitial magmatic amphibole (amp) and megacrystic plagioclase (plag). (**c**) Gabbro with magmatic amphibole and plagioclase. Note the serrated grain boundary between these two minerals. (**d**) Anorthosite with magmatic amphibole (amp) interstitial to plagioclase (plag) megacrysts. (**e**) Anorthosite with interstitial magmatic amphibole (amp) and megacrystic plagioclase (plag). The boundaries between these minerals are serrated. (**f**) Gabbro with magmatic interstitial amphibole (amp) and megacrystic plagioclase (plag).

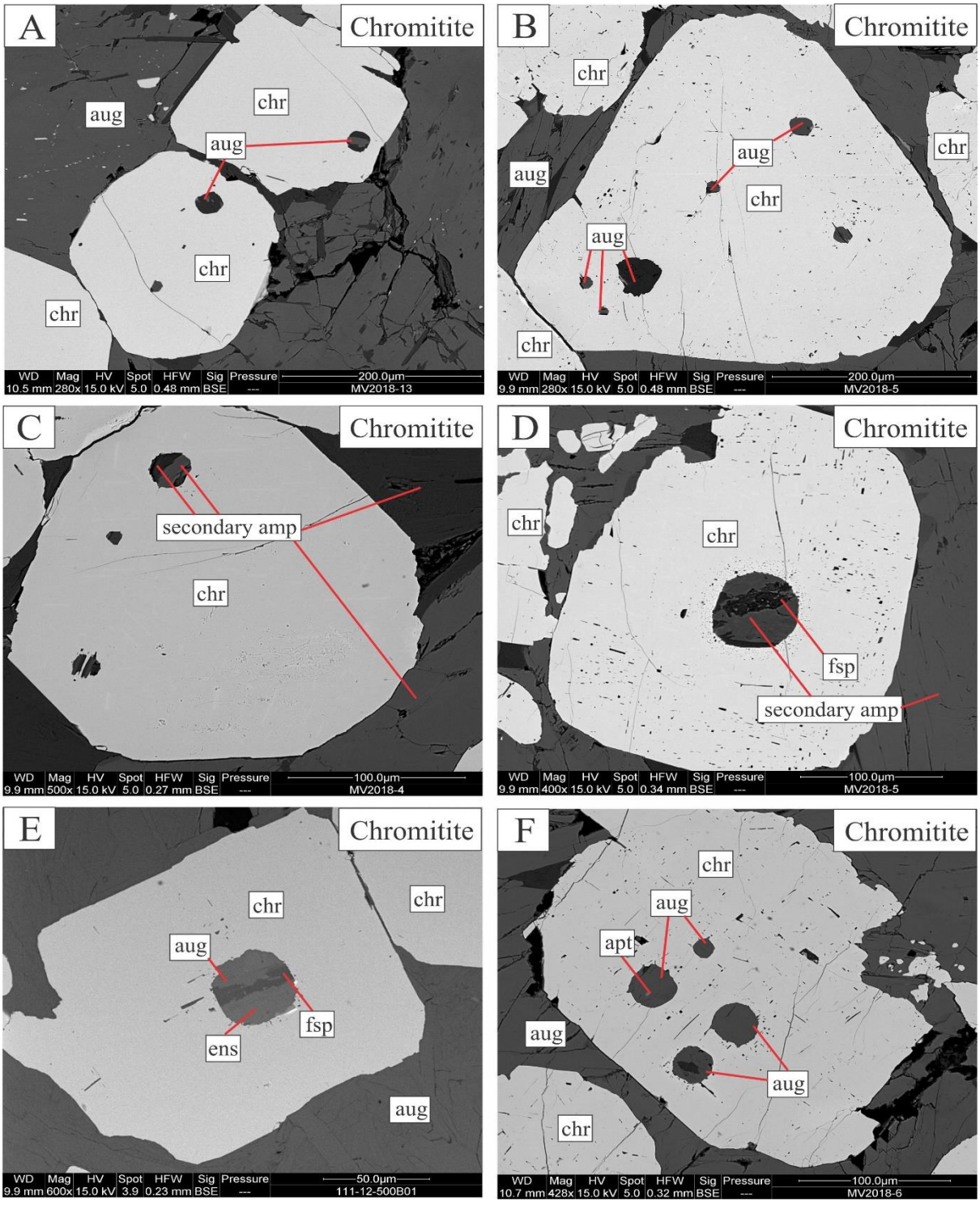

Fig. 4.9. Back-scatter electron scanning electron microscope images from the Mayville Intrusion. (**a**) Chromitite with euhedral chromite (chromite) grains that host augite (aug) inclusions and a matrix comprised of augite. (**b**) Chromitite with multiple chromite (chr) grains hosting augite (aug) inclusions and surrounded by augite. (**c**) Euhedral chromite grain in chromitite. This chromite grain hosts inclusions of secondary amphibole (amp) (most likely after pyroxene) and is surrounded by a matrix of secondary amphibole. (**d**) Chromitite with a euhedral chromite grain that hosts an inclusion comprised of feldspar (fsp) and secondary amphibole (after pyroxene) and is surrounded by secondary amphibole. (**e**) Chromitite with a

subhedral chromite grain that hosts an inclusion comprised of augite, enstatite, and feldspar (fsp) and is surrounded by augite. (**f**) Chromitite with a euhedral chromite grain that hosts augite and apatite (apt) inclusions and is surrounded by augite.

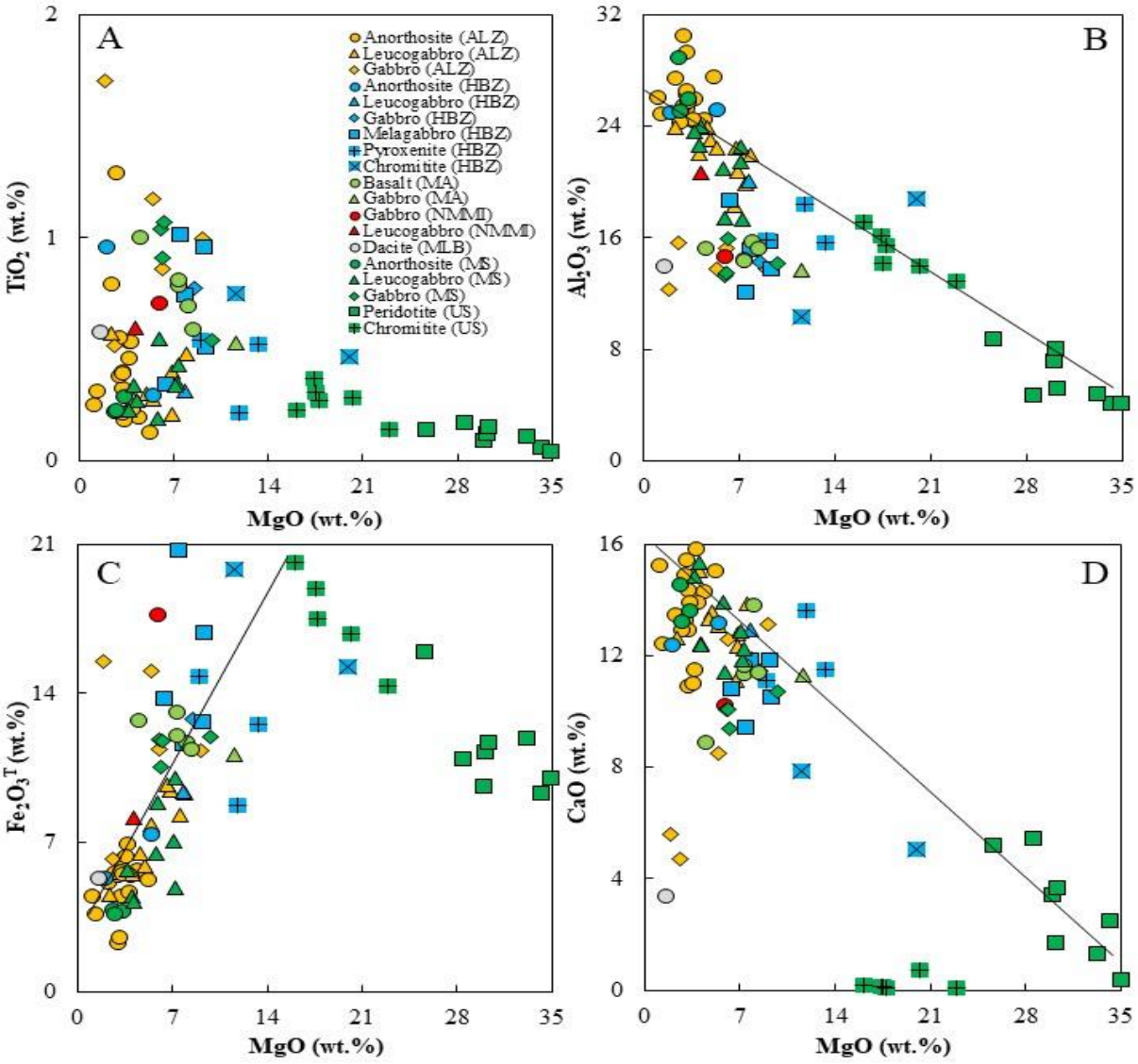

Fig. 4.10. Major element variation diagrams for the Anorthosite to Leucogabbro Zone (ALZ) and Heterolithic Breccia Zone (HBZ) of the Mayville Intrusion, the Mayville Assemblage (MA), the New Manitoba Mine Intrusion (NMMI) and the Maskwa Lake Batholith II (MLB). (**a**) TiO_2 versus MgO, (**b**) Al_2O_3 versus MgO, (**c**) $Fe_2O_3^T$ versus MgO and (**d**) CaO versus MgO. Geochemical data (Sotiriou et al., 2019b) from the anorthosites, leucogabbros and gabbros from the Mafic Series (MS) and peridotites and chromitites from the Ultramafic Series (US) of the Bird River Sill are plotted for comparison.

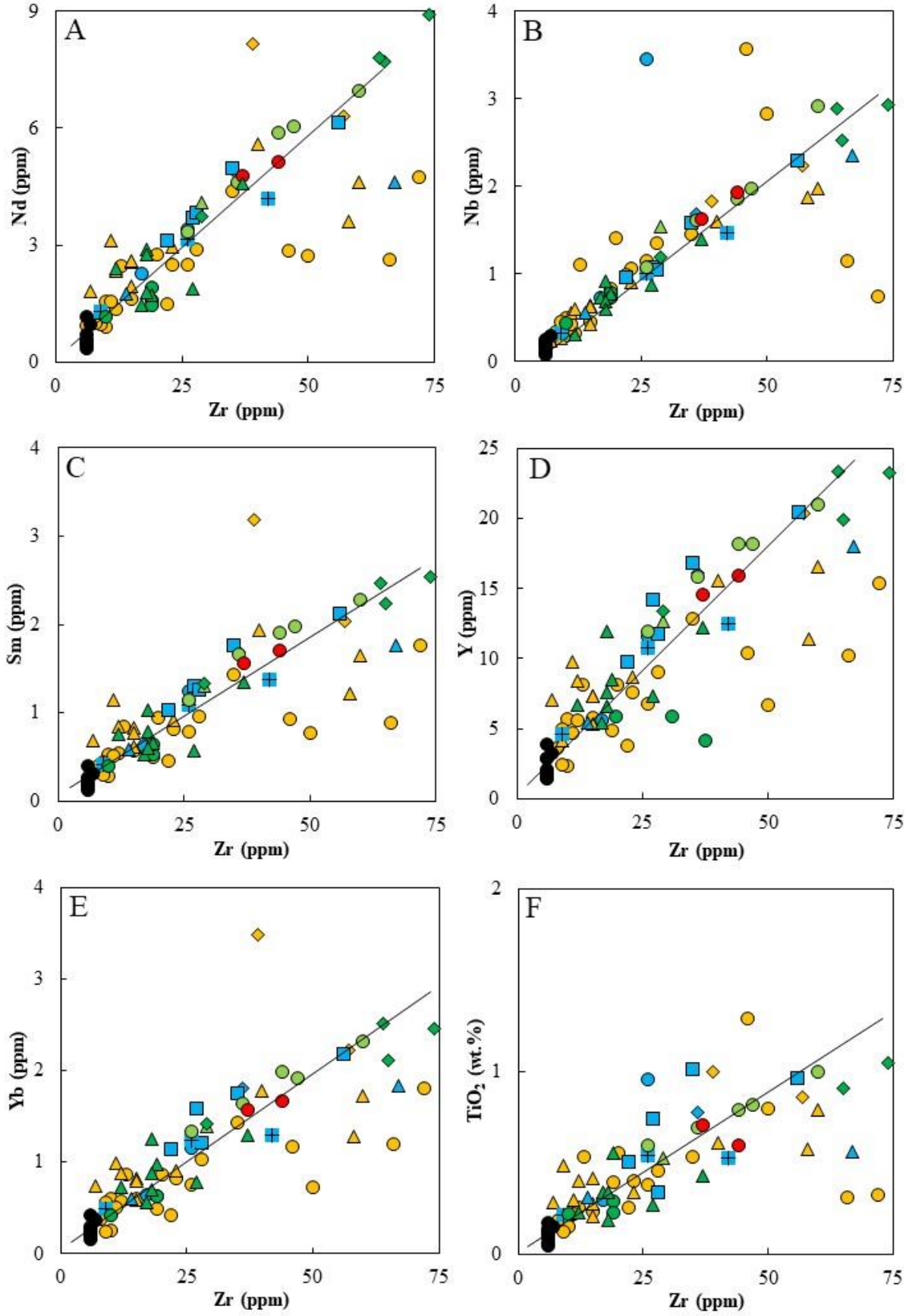

Fig. 4.11. Trace element variation diagrams for the Anorthosite to Leucogabbro Zone (ALZ) and Heterolithic Breccia Zone (HBZ) of the Mayville Intrusion, the Mayville Assemblage

(MA), and the New Manitoba Mine Intrusion (NMMI). (**a**) Nd versus Zr, (**b**) Nb versus Zr, (**c**) Sm versus Zr, (**d**) Y versus Zr, (**e**) Yb versus Zr and (**f**) TiO_2 versus Zr. Geochemical data (Sotiriou et al., 2019b) from the anorthosites, leucogabbros and gabbros from the Mafic Series (MS) and peridotites from the Ultramafic Series (US) of the Bird River Sill are plotted for comparison. The symbols are the same as for Fig. 4.10.

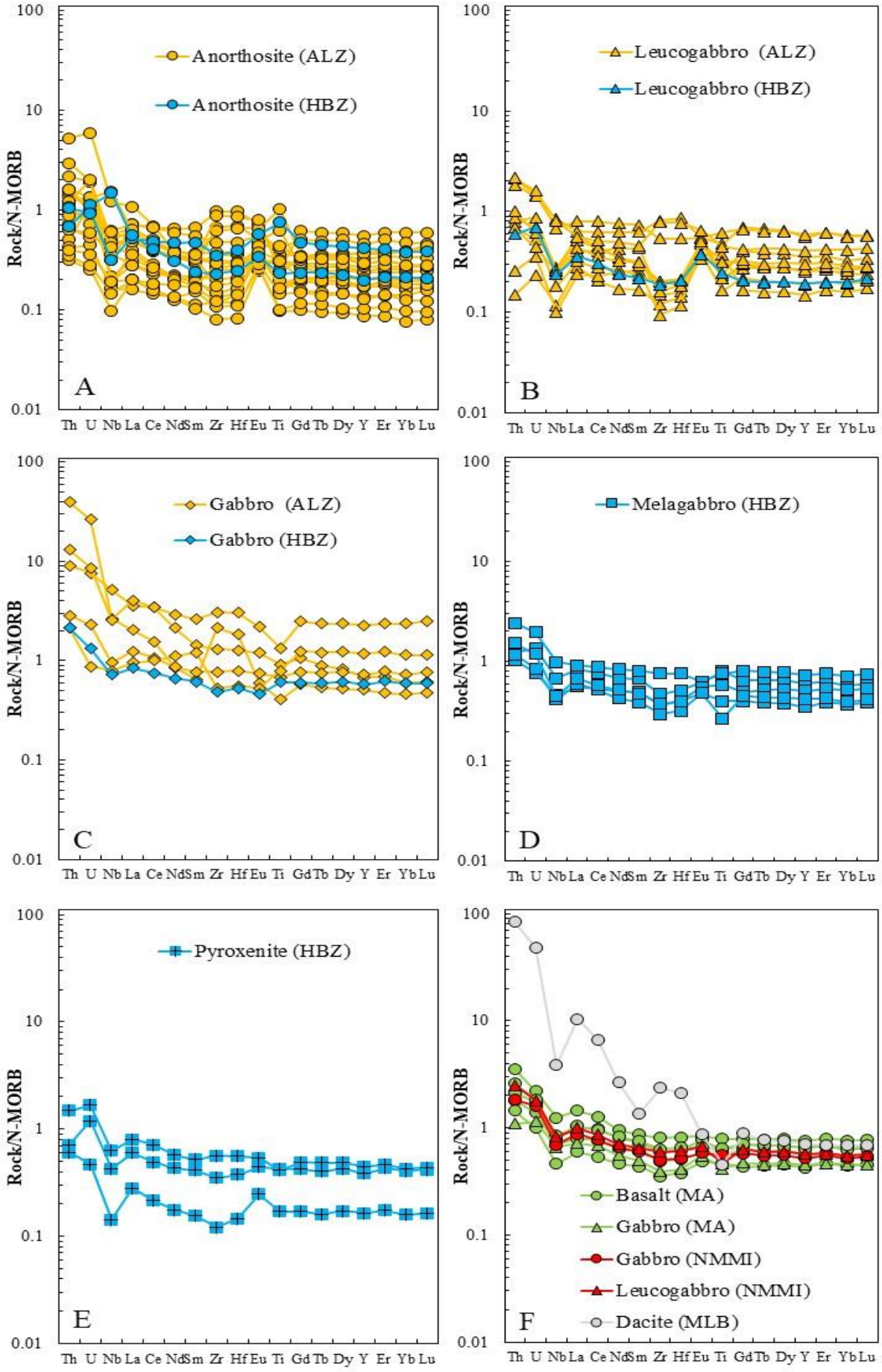
Anorthosite (ALZ)
Anorthosite (HBZ)
A
Leucogabbro (ALZ)
Leucogabbro (HBZ)
B
Gabbro (ALZ)
Gabbro (HBZ)
C
Melagabbro (HBZ)
D
Pyroxenite (HBZ)
E
Basalt (MA)
Gabbro (MA)
Gabbro (NMMI)
Leucogabbro (NMMI)
Dacite (MLB)
F
Rock/N-MORB
100
10
1
0.1
0.01
Th U Nb La Ce Nd Sm Zr Hf Eu Ti Gd Tb Dy Y Er Yb Lu

Fig. 4.12. N-MORB-normalised trace element diagrams for the (**a**) anorthosites from the Anorthosite to Leucogabbro Zone (ALZ) and Heterolithic Breccia Zone (HBZ), (**b**) leucogabbros from the Anorthosite to Leucogabbro Zone (ALZ) and Heterolithic Breccia Zone (HBZ), (**c**) gabbros from the Anorthosite to Leucogabbro Zone (ALZ) and Heterolithic Breccia Zone (HBZ), (**d**) melagabbros from the Heterolithic Breccia Zone (HBZ) and (**e)** pyroxenites from the Heterolithic Breccia Zone (HBZ) from the Mayville Intrusion. (**f**) Basalts and a gabbro from the Mayville Assemblage (MA), a gabbro and leucogabbro from the New Manitoba Mine Intrusion (NMMI) and a dacite dyke from the Maskwa Lake Batholith II (MLB). Normalisation values are from Sun and McDonough (1989).

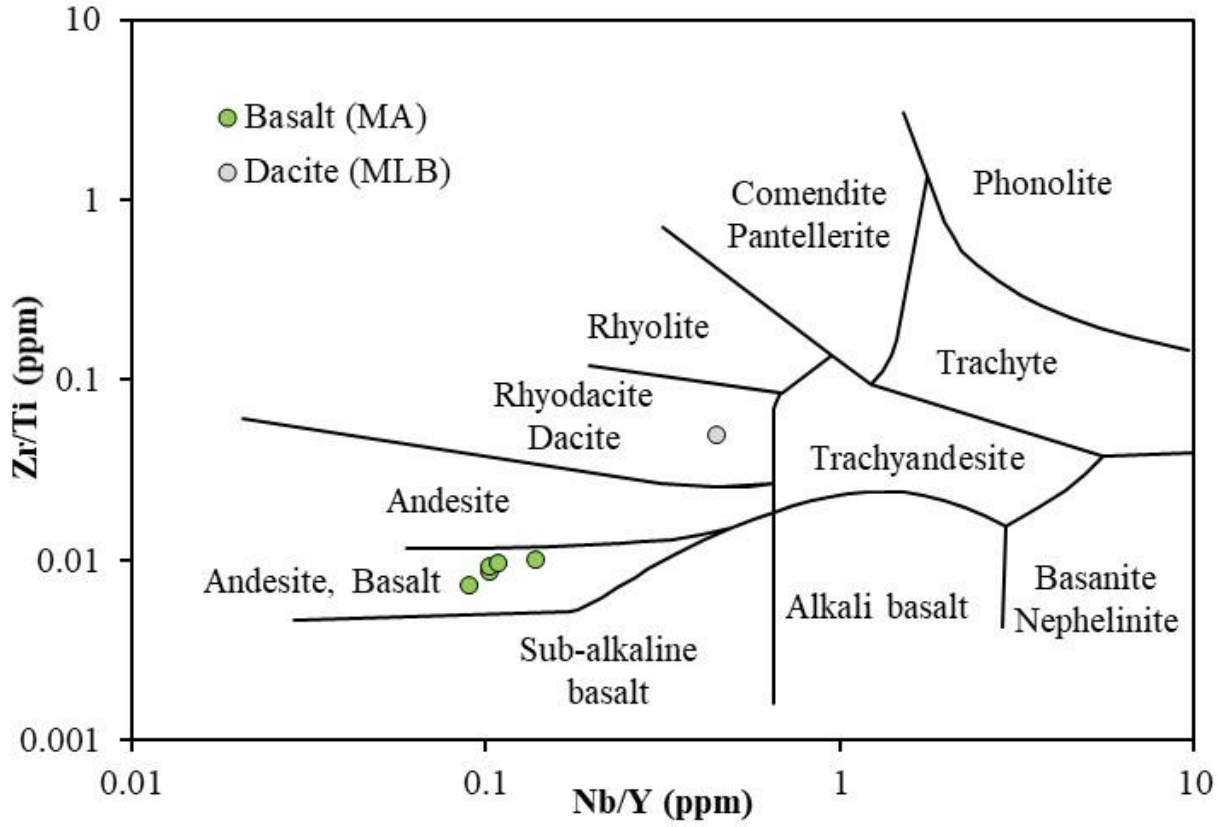

Fig. 4.13. Basalts from the Mayville Assemblage and a dacite dyke from the Maskwa Lake TTG Batholith II (MLB) plotted on a Zr/Ti versus Nb/Y diagram (after Winchester and Floyd, 1977).

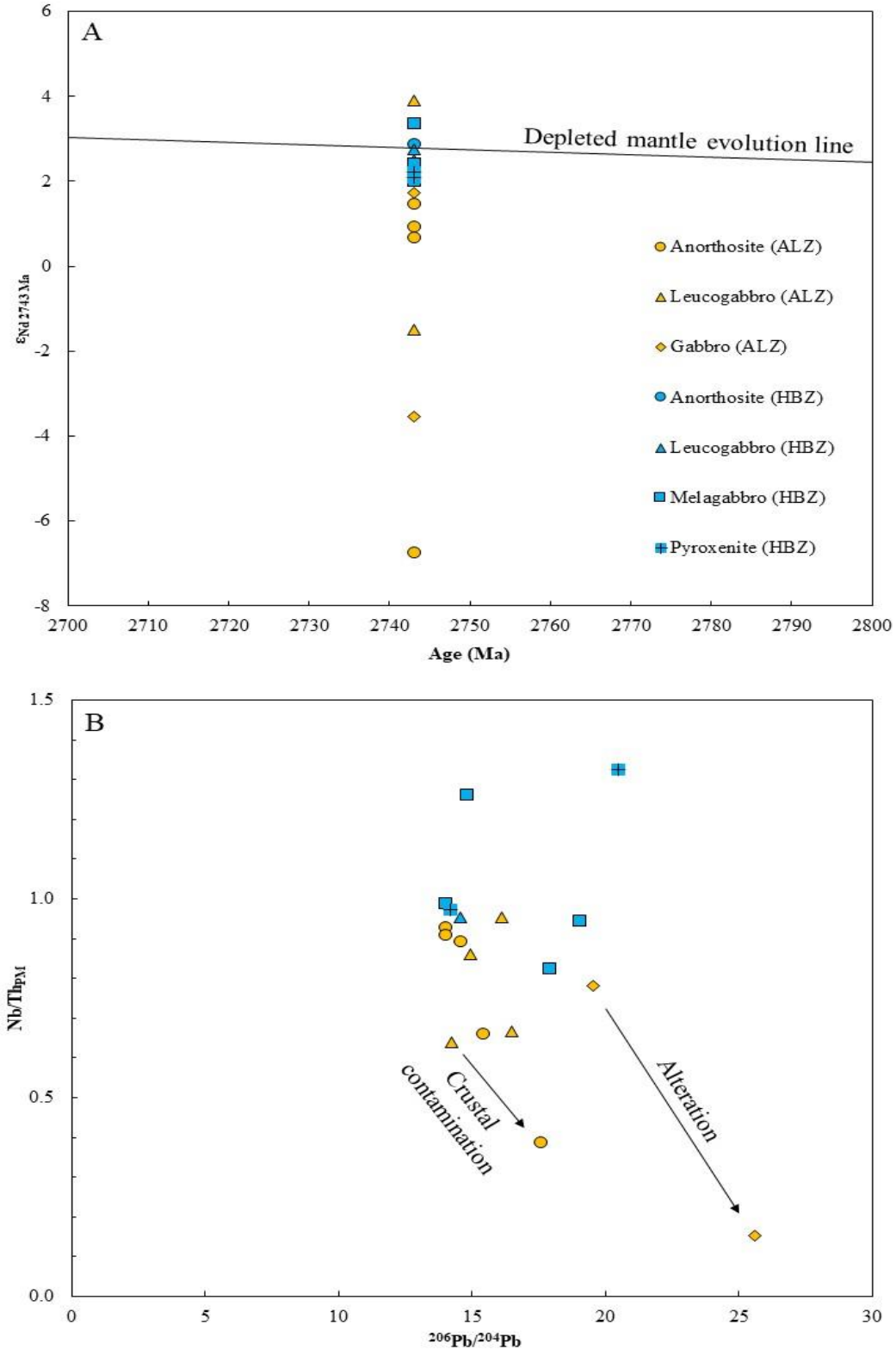

Fig. 4.14. (a) Initial $\varepsilon_{Nd\ (2743\ Ma)}$ values versus age (Ma) diagram for the Mayville Intrusion. The depleted mantle evolution line is from Henry et al. (1998). **(b)** Primitive mantle-normalised Nb/Th_{PM} ratio versus $^{206}Pb/^{204}Pb$ ratio plot for the Mayville Intrusion (modified after Lodge et al. (2015).

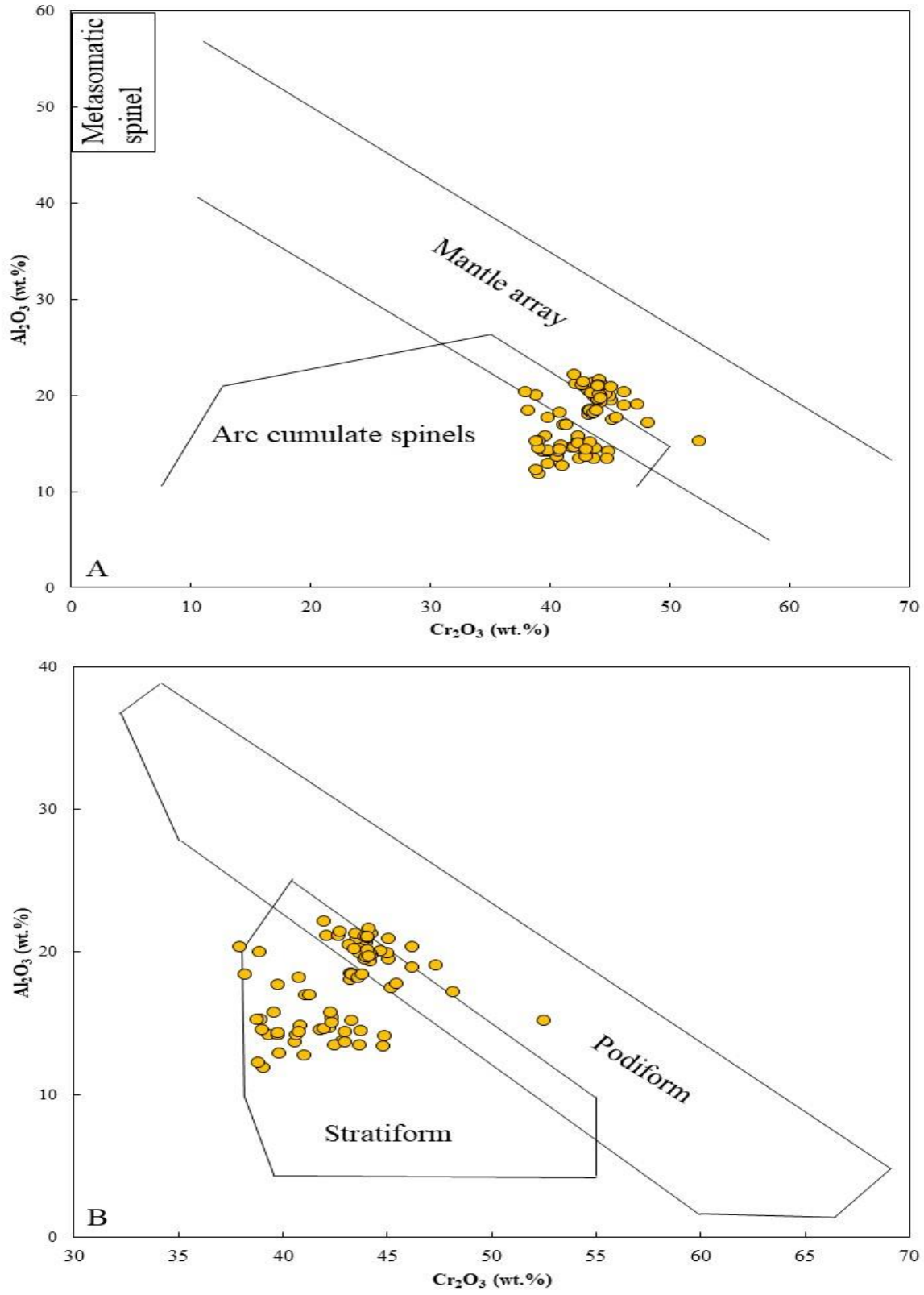

Fig. 4.15. Chromite chemistry diagrams for chromites from the Mayville Intrusion. (**a**) Al_2O_3 versus Cr_2O_3 (wt.%) diagram that distinguishes between mantle array, arc cumulate and metasomatic spinels (after Lay et al., 2017). (**b**) Al_2O_3 versus Cr_2O_3 (wt.%) diagram that distinguishes between podiform and stratiform chromites (after Qiu et al., 2018).

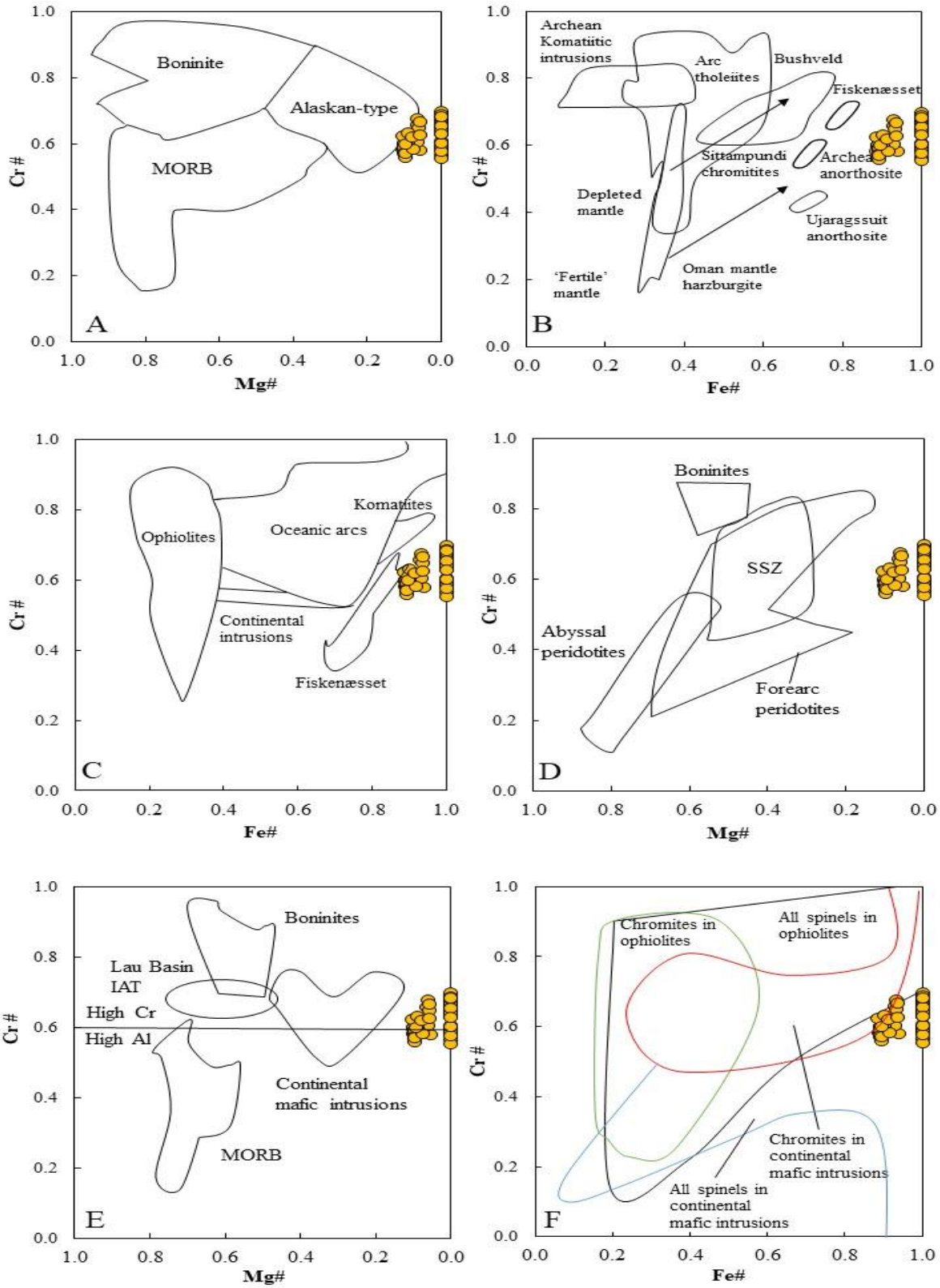

Fig. 4.16. Chromite chemistry diagrams for chromites from the Mayville Intrusion. (**a**) Cr#(Cr/Cr+Al) versus Mg# (Mg/Mg+Fe^{2+}) diagram that distinguishes between boninitic, Alaskan-type and MORB (mid-ocean ridge basalt) chromites (modified after Kiseleva and Zhmodik, 2017). (**b**) Cr# (Cr/Cr+Al) versus Fe# (Fe^{2+}/Fe^{2+}+Mg) diagram (modified after Rollinson et al., 2010). (**c**) Cr# (Cr/Cr+Al) versus Fe# (Fe^{2+}/Fe^{2+}+Mg) diagram that

distinguishes between chromites in ophiolites, oceanic arcs, continental intrusions, komatiites, and the Fiskenæsset Complex (modified after Lenaz et al., 2018). (**d**) Cr# (Cr/Cr+Al) versus Mg# (Mg/Mg+Fe^{2+}) diagram that distinguishes between suprasubduction zone (SSZ), forearc peridotite, boninitic and abyssal peridotite chromites (modified after Lay et al., 2017). (**e**) Cr# (Cr/Cr+Al) versus Mg# (Mg/Mg+Fe^{2+}) diagram that distinguishes between high Cr and high Al chromites and Lau Basin IAT (island arc tholeiite), boninitic, MORB (mid-ocean ridge basalt), and continental mafic intrusion chromites (modified after Gonzalez-Jimenez et al., 2017). (**f**) Cr# (Cr/Cr+Al) versus Fe# (Fe^{2+}/Fe^{2+}+Mg) diagram that distinguishes between chromites in ophiolites, chromites in continental mafic intrusions, all spinels in continental mafic intrusions and all spinels in ophiolites (modified after Polat et al., 2006).

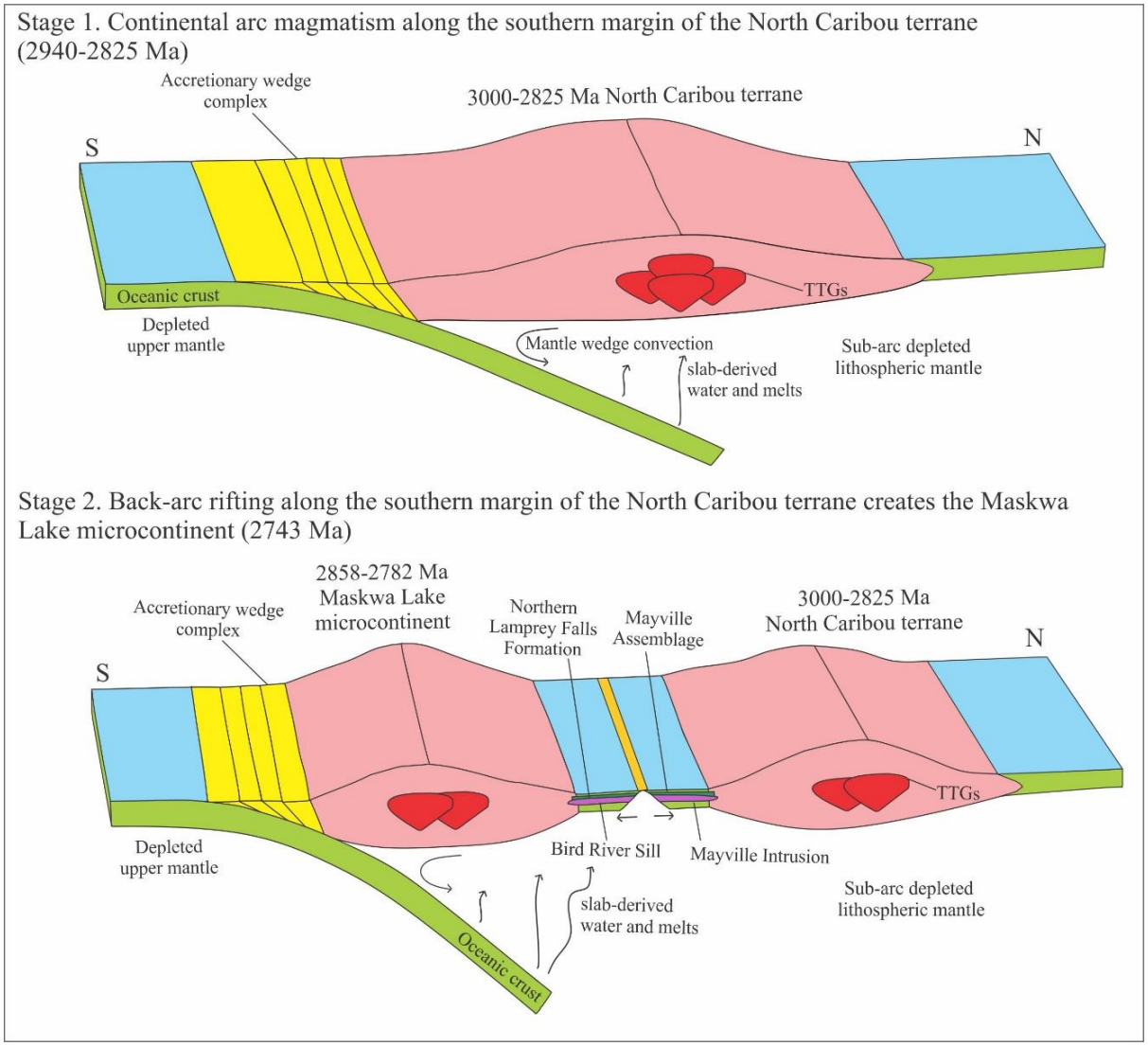

Fig. 4.17. Schematic diagram showing the geodynamic evolution of the Mayville area. Stage 1. Continental arc magmatism occurred along the northern margin of the North Caribou terrane prior to 2743 Ma, forming the 2858 Ma to 2782 Ma phases of the Maskwa Lake TTG Batholith. Stage 2. Continental back-arc rifting along the southern margin of the North Caribou terrane led to continental arc back-arc magmatism that resulted in the creation of the Maskwa Lake microcontinent and the formation of the Northern Lamprey Falls Formation and Mayville Assemblage, the Archean megacrystic anorthosite-bearing Mayville, Euclid Lake and Bird River intrusions and the Cat Lake and New Manitoba Mine intrusions at 2743 Ma during the Bird River magmatic event.

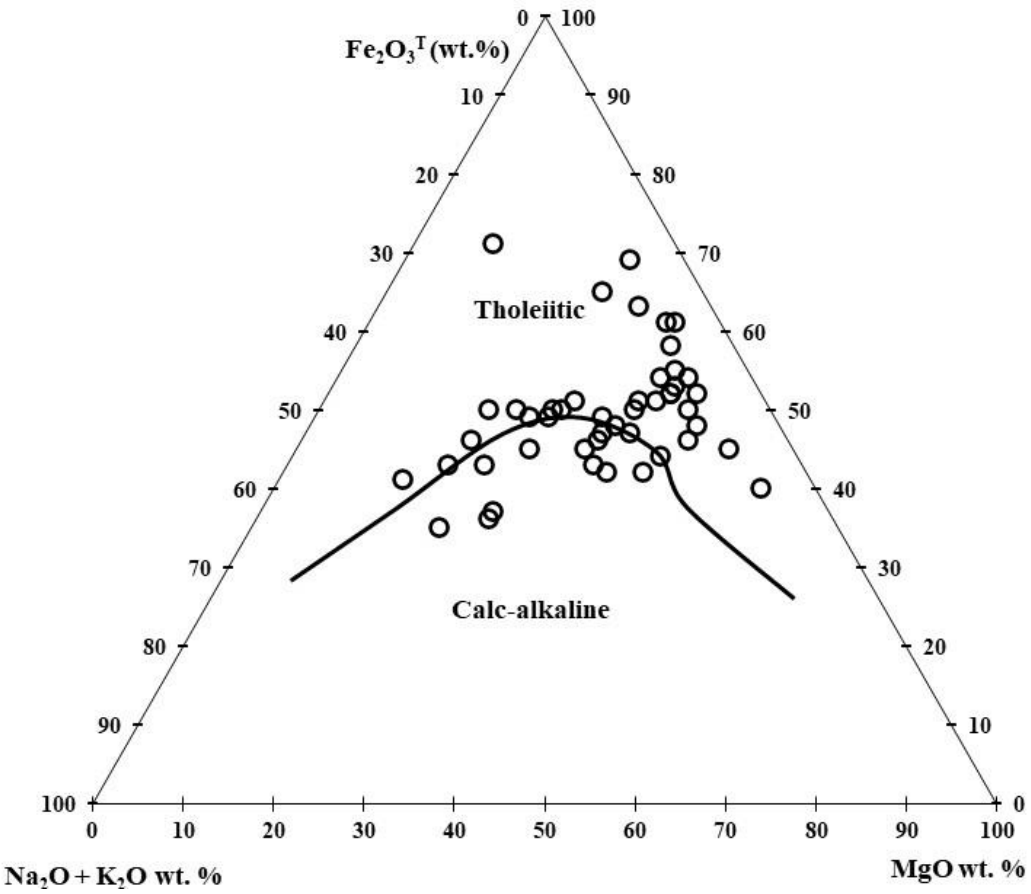

Fig. 4.18. Alkali-iron-magnesium (AFM) oxide diagram (wt.%) for the Mayville Intrusion (after Irvine and Baragar, 1971).

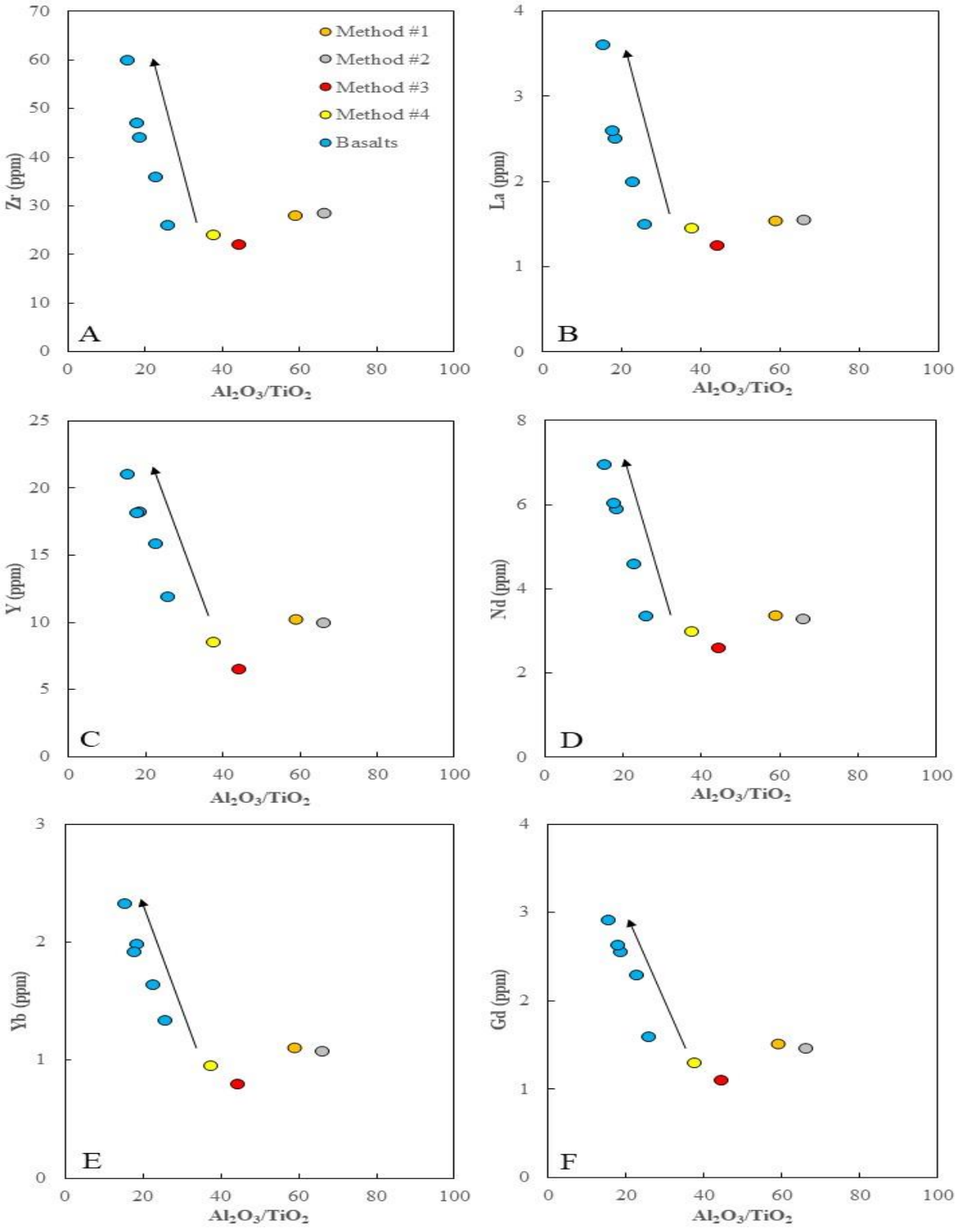

Fig. 4.19. Major element versus trace element diagrams for the basalts of the Mayville Assemblage and the calculated compositions of the parental magma to the Mayville Intrusion. Al_2O_3/TiO_2 versus (**a**) Zr (ppm), (**b**) La (ppm), (**c**) Y (ppm), (**d**) Nd (ppm), (**e**) Yb (ppm) and (**f**) Gd (ppm). The arrows represent the fractionation trends for the basalts of the Mayville Assemblage. Methods #1, #2, #3 and #4 refer to the methods mentioned in the text that were used to calculate the composition of the parental magma to the Mayville Intrusion.

Sample ID	Lithology	Zone	Sm (ppm)	Nd (ppm)	$^{147}Sm/^{144}Nd$	$^{143}Nd/^{144}Nd$	$\varepsilon_{Nd\ (2743\ Ma)}$
111-11-11	Pyroxenite	HBZ	1.519	4.727	0.1945	0.51271±06	2.2
111-11-17	Pyroxenite	HBZ	1.115	3.266	0.2067	0.512924±04	2.1
111-11-05*	Gabbro	ALZ	1.689	6.163	0.1658	0.511898±04	-3.5
111-12-702A01	Gabbro	ALZ	1.875	5.807	0.1955	0.512703±05	1.7
111-11-02	Melagabbro	HBZ	1.468	4.431	0.2006	0.512879±07	3.4
111-11-04	Melagabbro	HBZ	1.861	5.530	0.2038	0.512868±06	2.0
111-11-09	Melagabbro	HBZ	0.624	1.876	0.2014	0.512847±07	2.4
111-11-10	Melagabbro	HBZ	1.152	3.226	0.2161	0.513113±05	2.4
111-12-461A01	Leucogabbro	HBZ	0.517	1.649	0.1896	0.512649±06	2.8
111-12-538A01	Anorthosite	ALZ	0.628	1.779	0.2135	0.513017±07	1.5
111-12-623A01	Leucogabbro	ALZ	1.011	3.139	0.1948	0.512803±08	3.9
111-12-628A01	Leucogabbro	ALZ	0.546	1.738	0.1900	0.512624±08	2.1
MV2017-1	Leucogabbro	ALZ	1.127	3.267	0.2088	0.512984±09	2.5
MV2017-9*	Leucogabbro	ALZ	0.558	2.109	0.1601	0.511898±04	-1.5
111-12-514A01	Anorthosite	HBZ	1.419	4.092	0.2099	0.513024±06	2.9
111-12-547A01*	Anorthosite	ALZ	0.346	0.983	0.2134	0.512596±09	-6.8
111-12-624A01	Anorthosite	ALZ	1.026	3.259	0.1905	0.512573±08	0.9
MV2017-4	Anorthosite	ALZ	0.684	2.083	0.1988	0.512785±07	2.1
MV2017-7	Anorthosite	ALZ	0.809	2.552	0.1918	0.512584±08	0.7

The 2σ uncertainty values represent absolute values. ALZ: Anorthosite to Leucogabbro Zone; HBZ: Heterolithic Breccia Zone.

*Altered samples - reset isotopic compositions

Table 4.1. Sm-Nd isotopic data for the Neoarchean (2743 Ma) Mayville Intrusion.

Sample ID	Lithology	Zone	$^{206}Pb/^{204}Pb$	± 2σ	$^{207}Pb/^{204}Pb$	± 2σ	$^{208}Pb/^{204}Pb$	± 2σ	r1**	r2††
111-11-17	Pyroxenite	HBZ	14.187	0.012	14.644	0.013	33.828	0.034	0.95	0.92
111-11-11	Pyroxenite	HBZ	20.480	0.029	15.872	0.023	38.849	0.059	0.98	0.96
111-11-05*	Gabbro	ALZ	25.609	0.031	16.828	0.022	40.606	0.055	0.98	0.96
111-12-702A01	Gabbro	ALZ	19.541	0.033	15.761	0.027	39.301	0.071	0.99	0.97
111-11-02	Melagabbro	HBZ	14.829	0.012	14.777	0.013	34.359	0.033	0.97	0.95
111-11-04	Melagabbro	HBZ	19.036	0.031	15.701	0.026	37.307	0.065	0.99	0.98
111-11-10	Melagabbro	HBZ	17.930	0.027	15.450	0.024	35.741	0.058	0.98	0.98
111-11-09	Melagabbro	HBZ	14.015	0.013	14.616	0.014	33.592	0.036	0.98	0.94
MV2017-1	Leucogabbro	ALZ	14.588	0.016	14.895	0.017	34.018	0.042	0.96	0.94
MV2017-9*	Leucogabbro	ALZ	14.569	0.020	14.971	0.022	34.346	0.052	0.98	0.96
111-12-538A01	Anorthosite	ALZ	14.935	0.015	14.933	0.016	34.493	0.039	0.97	0.95
111-12-461A01	Leucogabbro	HBZ	14.249	0.019	14.744	0.021	33.991	0.050	0.98	0.96
111-12-628A01	Leucogabbro	ALZ	16.487	0.013	15.138	0.013	36.011	0.035	0.95	0.93
111-12-623A01	Leucogabbro	ALZ	16.139	0.030	15.174	0.029	35.590	0.069	0.99	0.98
MV2017-4	Anorthosite	ALZ	14.705	0.011	14.883	0.012	34.152	0.032	0.96	0.94
MV2017-7	Anorthosite	ALZ	14.018	0.013	14.761	0.015	33.590	0.037	0.97	0.95
111-12-624A01	Anorthosite	ALZ	17.561	0.021	15.394	0.019	37.243	0.049	0.98	0.95
111-12-547A01*	Anorthosite	ALZ	15.414	0.019	15.045	0.019	34.832	0.047	0.97	0.95
111-12-514A01	Anorthosite	HBZ	14.018	0.016	14.742	0.018	33.632	0.043	0.97	0.95

The 2σ uncertainty values represent absolute values. ALZ: Anorthosite to Leucogabbro Zone; HBZ: Heterolithic Breccia Zone.

r1** = $^{206}Pb/^{204}Pb$ vs. $^{207}Pb/^{204}Pb$ error correlation.

r2†† = $^{206}Pb/^{204}Pb$ vs. $^{208}Pb/^{204}Pb$ error correlation.

*Altered samples - reset isotopic compositions

Table 4.2. Pb isotope compositions of the Neoarchean (2743 Ma) Mayville Intrusion.

Chapter 5: Conclusion

This study combines pre-existing literature, field relationship and petrographic observations, mineral chemistry, and whole-rock major and trace element and radiogenic isotope geochemistry data to test the following key hypotheses:

1) The Archean megacrystic anorthosite-bearing layered intrusions in the western Superior Province formed through modern-style plate tectonic processes at subduction zone tectonic settings;
2) Archean anorthosite-bearing layered intrusions formed through sagduction processes (Van Kranendonk et al., 2004; Johnson et al., 2017; Bédard, 2018); and
3) These layered intrusions were cogenetic with spatially and temporally associated volcanic rocks in their host greenstone belts.

Key hypotheses (1) and (2) necessitated the collection, use and interpretation of field relationship and petrographic observations, mineral chemistry, and whole-rock major and trace element and radiogenic isotope geochemistry data to determine the tectonic settings in which the Haines Gabbroic Complex, Bird River Sill and Mayville Intrusion formed and to test previous tectonic setting interpretations proposed for these layered intrusions. Key hypothesis (3) required the collection, use and interpretation of whole-rock major and trace element and radiogenic isotope geochemistry data to ascertain whether these layered intrusions were cogenetic with volcanic rocks in their host greenstone belts.

Testing these hypotheses facilitated the resolution of the following outstanding questions:

1) Why are Archean anorthosite-bearing layered intrusions spatially and temporally associated with greenstone belts?
2) What are the implications of anorthosite studies for the geodynamic evolution of the western Superior Province and continental growth in the Archean?
3) Why are megacrystic anorthosite-bearing layered intrusions restricted to the Archean?
4) Is there a relationship between anorthosite petrogenesis and the secular evolution of the Earth?

5. 1. Tectonic setting of Archean anorthosite-bearing layered intrusions in the western Superior Province

Archean anorthosite-bearing layered intrusions have been interpreted to have formed in a variety of subduction-related and subduction-unrelated tectonic settings, including island arc (Hoffmann et al., 2012), continental arc (Piaia et al., 2017), back-arc (Wiener, 1981; Acosta-Gongora et al., 2018), forearc (Pease et al., 2008), synorogenic (Sharkov et al., 2004, 2006), mantle plume (Ivanic et al., 2010; Spath et al., 2015), mantle plume-derived continental rift (Ivanic et al., 2010), continental rift (Sandeman et al., 2001; Hartlaub et al., 2004), quasi-platform (Vrevskii, 2016), mid-ocean ridge (Kudryashov and Mokrushin, 2011), passive continental margin (Paixão and Oliveira, 1998), post-orogenic (Mukherjee and Das, 2002) and anorogenic (Kudryashov and Mokrushin, 2011) settings. Recently, Polat et al. (2018a) proposed that Archean megacrystic anorthosite-bearing layered intrusions formed in a back-arc or an intra-arc rift tectonic setting.

This study demonstrates through field relationship and petrographic observations, mineral chemistry, and whole-rock major and trace element and radiogenic isotope geochemistry data that the Haines Gabbroic Complex, Bird River Sill and Mayville Intrusion formed in a continental back-arc tectonic setting. This shows that Archean megacrystic anorthosite-bearing layered intrusions in the western Superior Province formed in a subduction zone setting. Indeed, a Japan-style mature intra-oceanic continental arc setting is proposed for the Haines Gabbroic Complex and a Chilean-style continental back-arc setting is proposed for the Bird River Sill and Mayville Intrusion. The tectonic setting interpretations presented in this study corroborate with continental arc, back-arc and intra-arc rift settings proposed by Piaia et al. (2017), Wiener (1981) and Polat et al. (2018a) for Archean megacrystic anorthosite-bearing layered intrusions. Moreover, this study reiterates that the majority of Archean megacrystic anorthosite-bearing layered intrusions formed in subduction zone geodynamic settings.

More than one tectonic setting was previously proposed for the Haines Gabbroic Complex, Bird River Sill and Mayville Intrusion. A plume-derived arc rift (Lodge et al., 2015), rifted active arc or coupled arc-backarc system (Corfu and Stott, 1998), and plume-driven rifting of pre-existing continental crust followed by subduction initiation (Lodge, 2016) have been proposed for the Shebandowan greenstone belt. A rifted active arc or coupled arc-backarc system (Corfu and Stott, 1998) has been specifically proposed for the Haines Gabbroic Complex. It has been demonstrated in this study that the Shebandowan greenstone belt formed

in a Japan-style mature intra-oceanic continental arc to back-arc setting, and the Haines Gabbroic Complex formed in a continental back-arc setting. It has also been shown that a mantle plume accentuated back-arc rifting of this continental arc, which collided with the Western Wabigoon subprovince during the Shebandowanian orogeny (Corfu and Stott, 1998; Percival et al., 2006, 2012; Lodge et al., 2015) These tectonic setting interpretations broadly corroborate with the interpretations of Corfu and Stott (1998), and, to a lesser extent, Lodge et al. (2015).

Both back-arc (Gilbert, 2008; Gilbert et al., 2008; Yang and Gilbert, 2014) and continental rift (Peck et al., 1999a) settings have been proposed for the Bird River Sill. This study shows that the Bird River Sill formed in a Chilean-style continental back-arc basin during intra-arc to back-arc rifting of the North Caribou terrane, creating the Maskwa Lake microcontinent as a separate entity in the process. This interpretation better reaffirms the back-arc setting interpretation of Gilbert (2008), Gilbert et al. (2008) and Yang and Gilbert (2014). The Mayville Intrusion has been proposed to have formed in an extensional back-arc environment in a continental margin setting (Yang et al., 2012) and in a back-arc setting (Gilbert, 2008; Gilbert et al., 2008; Yang et al., 2011; Yang and Gilbert, 2014). These interpretations are corroborated by the present study, which shows that both the Bird River Sill and Mayville Intrusion formed in the same Chilean-style continental back-arc basin during intra-arc to back-arc rifting of the North Caribou terrane. The Birse Lake microcontinent collided with the Maskwa Lake microcontinent during the Uchian orogeny, with both microcontinents being caught up in the collision between the Winnipeg River subprovince and North Caribou terrane towards the end of this orogeny.

The Japan- and Chile-style continental back-arc settings proposed for the Haines Gabbroic, Bird River Sill and Mayville Intrusion indicate that these Archean anorthosite-bearing layered intrusions formed through modern-style plate tectonic processes at subduction zone tectonic settings rather than as a consequence of sagduction processes.

5.2. Archean anorthosite-bearing layered intrusions were cogenetic with spatially and temporally associated volcanic rocks in their host greenstone belts

Archean megacrystic anorthosite-bearing layered intrusions (e.g. Doré Lake Complex, Canada) have been interpreted to be at least partly cogenetic with spatially and temporally associated

volcanic rocks in their host greenstone belts (Polat et al., 2018b). These layered intrusions often intrude pillow basalts in these greenstone belts and have been hypothesised to be genetically related to the latter (Polat et al., 2018a, b). The present study of the Haines Gabbroic Complex, Bird River Sill and Mayville Intrusion shows that these layered intrusions intruded into or are closely spatially associated with pillow basalt-bearing volcanic rocks in their host greenstone belts. This implies that both the layered intrusions and pillow basalts formed in the same environment, in an oceanic setting, and explains why Archean megacrystic anorthosite-bearing layered intrusions are spatially and temporally associated with greenstone belts. The Haines Gabbroic Complex is spatially and temporally associated with the contemporaneous pillow basalt-bearing volcanics of the Greenwater Assemblage and the younger basaltic to rhyolitic volcanics of the Burchell Assemblage. Despite the close spatial and temporal relationship between the Haines Gabbroic Complex and these assemblages, they were not cogenetic.

The Bird River Sill intrudes pillow basalts of the spatially and temporally associated Northern Lamprey Falls Formation. The gabbros of the Bird River Sill were cogenetic with the pillow basalts and gabbros of the Northern Lamprey Falls Formation. The anorthosites, leucogabbros and peridotites of the Bird River Sill were not cogenetic with the pillow basalts and gabbros of the Northern Lamprey Falls Formation. The Mayville Intrusion intrudes pillow basalts and synvolcanic gabbros of the spatially and temporally associated Mayville Assemblage. The Mayville Intrusion was cogenetic with the Mayville Assemblage.

This study demonstrates that Archean megacrystic anorthosite-bearing layered intrusions were either not, partly, or completely genetically related to the spatially and temporally associated volcanic rocks in their host greenstone belts. The findings of this study broadly reaffirm the interpretation of Polat et al. (2018b) that Archean anorthosite-bearing layered intrusions, such as the Doré Lake Complex, were at least in part cogenetic with the spatially and temporally associated mafic volcanic rocks in their host greenstone belts. The present study and other studies (Polat et al., 2011, 2018b) demonstrate that Archean anorthosite-bearing layered intrusions were (Mayville Intrusion), were partly (Bird River Sill, Doré Lake Complex) and were not (Haines Gabbroic Complex, Fiskenæsset Complex) cogenetic with spatially and temporally associated mafic volcanic rocks in their host greenstone belts.

Archean anorthosite-bearing layered intrusions are spatially and temporally associated with greenstone belts (Ashwal, 1993, 2010; Ashwal and Myers, 1994; Ashwal and Bybee, 2017; Polat et al., 2018a). Ashwal (1993) and Polat et al. (2018a) accounted for this by proposing that Archean anorthosite-bearing layered intrusions and spatially and temporally associated pillow basalt-bearing greenstone belts formed in an oceanic setting and a back-arc or intra-arc rift

oceanic setting. The greenstone belts that host the Haines Gabbroic Complex, Bird River Sill and Mayville Intrusion contain pillow basalts. This indicates that these Archean anorthosite-bearing layered intrusions and their host greenstone belts both formed in a continental back-arc oceanic setting, which explains why they are spatially and temporally associated with one another.

Ca- and Al-rich tholeiitic parental magmas have generally been proposed for Archean megacrystic anorthosite-bearing layered intrusions, however, more primitive basaltic, picritic and komatiitic parental magmas have been postulated (Ashwal, 1993, 2010; Ashwal and Myers, 1994; Ashwal and Bybee, 2017; Polat et al., 2018a). This study shows that the Haines Gabbroic Complex, Bird River Sill and Mayville Intrusion crystallised from hydrous Ca- and Al-rich tholeiitic parental magmas that fractionated from hydrous boninitic-like or primitive arc tholeiitic parental magmas.

5.3. Modern-style plate tectonics operated in the western Superior Province in the Neoarchean

There has been and still is considerable debate about the style of tectonics that operated in the Archean, with some workers proposing horizontal tectonics akin to modern-style plate tectonics (e.g., subduction) and other workers advocating vertical (e.g. sagduction) tectonics (Bédard, 2006, 2018; Bédard et al., 2003, 2013; Polat et al., 2015; Kusky et al., 2018; Hastie and Fitton, 2019; Roman and Arndt, 2019). There is a growing consensus that some form of plate tectonics has operated since the Archean, however, when plate tectonics started and the style of plate tectonics in the Archean is heavily debated (Bédard, 2006, 2018; Bédard et al., 2003, 2013; Polat et al., 2015; Kusky et al., 2018; Hastie and Fitton, 2019; Roman and Arndt, 2019). Despite this, vertical sagduction-based tectonic models (Bédard, 2006, 2018; Bédard et al., 2003, 2013) have been proposed recently for the style of tectonics that operated in the Archean in the Superior Province specifically and on the Archean Earth in general that challenge the predominantly horizontal tectonics models that have been postulated to explain the style of tectonics that operated in the Archean.

Plate tectonics has been proposed by Card (1990), Percival et al. (2006, 2012) and Polat et al. (2018a) to account for the style of tectonics that operated in and drove the growth and evolution

of the Superior Province in the Archean. This study demonstrates that the negative Nb and Ti anomalies exhibited by the Haines Gabbroic Complex, Bird River Sill and Mayville Intrusion and spatially and temporally associated volcanic rocks in their host greenstone belts did not result from trace element mobility or crustal contamination and reflect their sub-arc mantle wedge sources. A major argument against Archean subduction put forward by advocates of Archean vertical tectonics is that Archean oceanic crust was too thick to subduct (Bédard et al., 2003, 2013; Bédard 2006, 2018). Hastie and Fitton (2019) found that subduction of thick oceanic crust resulted in the generation of TTG batholiths as early as the Eoarchean. This study shows that Archean megacrystic anorthosite-bearing layered intrusions and their host greenstone belts in the Wawa and Bird River subprovinces of the western Superior Province formed in Japan- and Chilean-style continental arc to continental back-arc tectonic settings. This demonstrates that these layered intrusions and their host greenstone belts formed as a result of modern-style plate tectonics processes in subduction zone settings akin to the Circum-Pacific subduction zones. This suggests that modern-style plate tectonics processes operated in the western Superior Province in the Neoarchean. Indeed, the Bad Vermilion Lake and Doré Lake anorthosite-bearing layered intrusions in the Western Wabigoon and Abitibi subprovince in the western and eastern Superior Province, respectively, were interpreted to have formed in subduction zone settings as a result of modern-style plate tectonics processes (Polat et al., 2018a). This study demonstrates that Archean anorthosite-bearing layered intrusions form through modern-style plate tectonics processes rather than as a result of sagduction processes. This study shows that the western Superior Province and other Archean cratons grew and evolved in subduction zone settings through modern-style plate tectonics processes (Percival et al., 2006, 2012; Polat et al., 2015; Kusky et al., 2018; Polat et al, 2018a; Hastie and Fitton, 2019; Roman and Arndt, 2019).

5.4. The temporal restriction of Archean megacrystic anorthosite-bearing layered intrusions and the relationship between anorthosite petrogenesis and the secular evolution of the Earth

Calcic megacrystic anorthosite-bearing layered intrusions are largely restricted to the Archean (Rollinson et al., 2010; Polat et al., 2011, 2018a). The restriction of these layered intrusions to the Archean has been linked to the secular evolution of the Earth, as higher mantle potential temperatures and higher-degree partial melting of the mantle in the Archean relative to the

post-Archean have been proposed to be critical requirements for their genesis (Rollinson et al., 2010; Polat et al., 2011, 2018a). These processes facilitated the formation of the siliceous Al-rich slab melts that were required to metasomatise and refertilise the highly-depleted sub-arc harzburgitic mantle wedge source to calcic megacrystic anorthosite-bearing layered intrusions (Rollinson et al., 2010; Polat et al., 2011, 2018a). High-degree partial melting of this refertilised sub-arc mantle wedge generated the large volumes of the hydrous boninitic-like or primitive arc tholeiitic parental magmas, and in turn, hydrous Ca- and Al-rich tholeiitic parental magmas from which these layered intrusions and their synonymous calcic plagioclase megacrysts crystallised (Rollinson et al., 2010; Polat et al., 2011, 2018a). The petrogenesis and tectonic settings of the Haines Gabbroic Complex, Bird River Sill and Mayville Intrusion suggest that Archean megacrystic anorthosite-bearing layered intrusions formed as a consequence of the aforementioned magmatic processes in a subduction zone setting. Lower mantle potential temperatures and lower degrees of partial melting of the mantle at the end of the Archean led to the near cessation of the genesis of calcic megacrystic anorthosite-bearing layered intrusions by this time (Rollinson et al., 2010; Polat et al., 2011, 2018a). This near cessation in the genesis of calcic megacrystic anorthosite-bearing layered intrusions marks a very important transitional event in the secular evolution of the Earth that led to a switch from slab-dominant to mantle wedge-dominant crust formation (Rollinson et al., 2010; Polat et al., 2011). This study demonstrates that the refertilisation of a depleted sub-arc mantle wedge source by siliceous Al-rich slab melts was involved in the genesis of calcic megacrystic anorthosite-bearing layered intrusions and corroborates the models of Rollinson et al. (2010) and Polat et al. (2011, 2018a). Whilst the genesis of calcic megacrystic anorthosite-bearing layered intrusions largely ceased at the end of the Archean, close Phanerozoic analogues in the Peruvian Andes, the Peninsular Ranges of California and the Black Giants Anorthosite Complex in New Zealand (Walawender and Smith, 1980; Regan, 1985; Gibson and Ireland, 1999) indicate that this process did not completely cease at the end of the Archean and has been in operation right up until the present day.

5. 5. References

Acosta-Gongora, P., Pehrsson, S.J., Sandeman, H., Martel, E., Peterson, T., 2018. The Ferguson Lake deposit: an example of Ni–Cu–Co–PGE mineralization emplaced in a back-arc basin setting?. Canadian Journal of Earth Sciences 55(8), 958-979.

Ashwal, L.D., 1993. Anorthosites. Springer-Verlag: Berlin, Germany, Minerals and Rocks 21, 422p.

Ashwal, L.D., 2010. The temporality of anorthosites. The Canadian Mineralogist 48(4), 711-728.

Ashwal, L.D., Bybee, G.M., 2017. Crustal evolution and the temporality of anorthosites. Earth-Science Reviews 173, 307-330.

Ashwal, L.D., Myers, J.S., 1994. Archean anorthosites. In: Condie, K.C. (ed.). Archean Crustal Evolution. Elsevier: Amsterdam, Developments in Precambrian Geology 11, 315-355.

Bédard, J.H., 2006. A catalytic delamination-driven model for coupled genesis of Archaean crust and sub-continental lithospheric mantle. Geochimica et Cosmochimica Acta 70(5), 1188-1214.

Bédard, J.H., 2018. Stagnant lids and mantle overturns: Implications for Archaean tectonics, magmagenesis, crustal growth, mantle evolution, and the start of plate tectonics. Geoscience Frontiers 9(1), 19-49.

Bédard, J.H., Brouillette, P., Madore, L., Berclaz, A., 2003. Archaean cratonization and deformation in the northern Superior Province, Canada: an evaluation of plate tectonic versus vertical tectonic models. Precambrian Research 127(1-3), 61-87.

Bedard, J.H., Harris, L.B., Thurston, P.C., 2013. The hunting of the snArc. Precambrian Research 229, 20-48.

Card, K.D., 1990. A review of the Superior Province of the Canadian Shield, a production of Archean accretion. Precambrian Research 48, 99-156.

Corfu, F., Stott, G.M.,1998. Shebandowan greenstone belt, western Superior Province: U-Pb ages, tectonic implications, and correlations. Geological Society of America Bulletin 110, 1467-1484.

Gibson, G.M., Ireland, T.R., 1999. Black Giants Anorthosite, New Zealand: A Paleozoic analogue of Archean stratiform anorthosites and implications for the formation of Archean high-grade gneiss terranes. Geology 27(2), 131-134.

Gilbert, H.P., 2008. Stratigraphic investigations in the Bird River greenstone belt, Manitoba (part of NTS 52L5, 6). In: Report of Activities 2008. Manitoba Science, Technology, Energy and Mines, Manitoba Geological Survey, 121-138.

Gilbert, H.P., Davis, D.W., Duguet, M., Kremer, P., Mealin, C.A., MacDonald, J., 2008. Geology of the Bird River Belt, southeastern Manitoba (parts of NTS 52L5, 6). Manitoba Science, Technology, Energy and Mines, Manitoba Geological Survey, Geoscientific Map MAP2008-1, scale 1:20,000.

Hartlaub, R.P., Heaman, L.M., Ashton, K.E., Chacko, T., 2004. The Archean Murmac Bay Group: evidence for a giant archean rift in the Rae Province, Canada. Precambrian Research 131(3-4), 345-372.

Hastie, A.R., Fitton, J.G., 2019. Eoarchaean tectonics: New constraints from high pressure-temperature experiments and mass balance modelling. Precambrian Research 325, 20-38.

Hoffmann, J.E., Svahnberg, H., Piazolo, S., Scherstén, A., Münker, C., 2012. The geodynamic evolution of Mesoarchean anorthosite complexes inferred from the Naajat Kuuat Complex, southern West Greenland. Precambrian Research 196, 149-170.

Ivanic, T.J., Wingate, M.T.D., Kirkland, C.L., Van Kranendonk, M.J., Wyche, S., 2010. Age and significance of voluminous mafic–ultramafic magmatic events in the Murchison Domain, Yilgarn Craton. Australian Journal of Earth Sciences 57(5), 597-614.

Kudryashov, N.M., Mokrushin, A.V., 2011. Mesoarchean gabbroanorthosite magmatism of the Kola Region: petrochemical, geochronological, and isotope-geochemical data. Petrology 19(2), 167-182.

Kusky, T.M., Windley, B.F., Polat, A., 2018. Geological evidence for the operation of plate tectonics throughout the Archean: Records from Archean paleo-plate boundaries. Journal of Earth Science 29(6), 1291-1303.

Lodge, R.W.D., 2016. Petrogenesis of intermediate volcanic assemblages from the Shebandowan greenstone belt, Superior Province: Evidence for subduction during the Neoarchean. Precambrian Research 272, 150-167.

Lodge, R.W.D., Gibson, H.L., Stott, G.M., Franklin, J.M., Hudak, G.J., 2015. Geodynamic setting, crustal architecture, and VMS metallogeny of ca. 2720 Ma greenstone belt assemblages of the northern Wawa subprovince, Superior Province. Canadian Journal of Earth Sciences 52(3), 196-214.

Mukherjee, A., Das, S., 2002. Anorthosites, granulites and the supercontinent cycle. Gondwana Research 5(1), 147-156.

Paixão, M.A.P., Oliveira, E.P., 1998. The Lagoa da Vaca complex: an Archaean layered anorthosite body on the western edge of the Uauá Block, Bahia, Brazil. Revista Brasileira de Geociencias 28(2), 201-208.

Pease, V., Percival, J., Smithies, H., Stevens, G., Van Kranendonk, M., 2008. When did plate tectonics begin? Evidence from the orogenic record. In: Condie, K.C., Pease, V. (ed.). When Did Plate Tectonic Begin On Planet Earth? The Geological Society of America, Special Paper 440, 199-228.

Peck, D.C., Halden, N.M., Jobin-Bevans, S., Cameron, H.D.M., Theyer, P., 1999a. Summary of metallogenetic and petrogenetic features of Archean anorthosites and associated mafic and ultramafic rocks in the Superior Province, Manitoba (parts of NTS 63I, 63J, 63P and 64A). In: Report of Activities 1999. Manitoba Industry, Trade and Mines, Geological Services, 94-96.

Percival, J.A., Sanborn-Barrie, M., Skulski, T., Stott, G.M., Helmstaedt, H., White, D.J., 2006. Tectonic evolution of the western Superior Province from NATMAP and Lithoprobe studies. Canadian Journal of Earth Sciences 43(7), 1085-1117.

Percival, J.A., Skulski, T., Sanborn-Barrie, M., Stott, G.M., Leclair, A.D., Corkery, M.T., Boily, M., 2012. Geology and tectonic evolution of the Superior Province, Canada. Tectonic styles in Canada: The Lithoprobe Perspective, Special Paper 49, 321-378.

Piaia, P., Oliveira, E.P., Valeriano, C.M., 2017. The 2.58 Ga São José do Jacuipe gabbro-anorthosite stratiform complex, Itabuna-Salvador-Curaçá Orogen, São Francisco Craton, Brazil: Root of the Neoarchaean Caraiba continental arc?. Journal of South American Earth Sciences 79, 326-341.

Polat, A., Frei, R., Longstaffe, F.J., Woods, 2018b. Petrogenetic and geodynamic origin of the Neoarchaean Doré Lake Complex, Abitibi subprovince, Superior Province, Canada. International Journal of Earth Sciences (Geol Rundsch) 107(3), 811-843.

Polat, A., Fryer, B.J., Appel, P.W., Kalvig, P., Kerrich, R., Dilek, Y., Yang, Z., 2011. Geochemistry of anorthositic differentiated sills in the Archean (~ 2970 Ma) Fiskenæsset Complex, SW Greenland: Implications for parental magma compositions, geodynamic setting, and secular heat flow in arcs. Lithos 123(1-4), 50-72.

Polat, A., Longstaffe, F.J., Frei, R., 2018a. An overview of anorthosite-bearing layered intrusions in the Archaean craton of southern West Greenland and the Superior Province of Canada: implications for Archaean tectonics and the origin of megacrystic plagioclase. Geodinamica Acta 30(1), 84-99.

Polat, A., Wang, L., Appel, P.W.U., 2015. A review of structural patterns and melting processes in the Archean craton of West Greenland: Evidence for crustal growth at convergent plate margins as opposed to non-uniformitarian models. Tectonophysics 662, 67-94.

Regan, P.F., 1985. The early basic intrusions. In: Pitcher, W.S., Atherton, M.P., Cobbing, E.J., Beckinsale, R.D. (eds.). Magmatism at a Plate Edge: the Peruvian Andes. Blackie: Glasgow, 72-89.

Rollinson, H.R, Reid, C., Windley, B.F., 2010. Chromitites from the Fiskenæsset anorthositic complex, West Greenland: clues to late Archaean mantle processes. In: Kusky, T.M., Zhai, M.-G., Xiao, W. (eds.). The Evolving Continents: Understanding Processes of Continental Growth. Geological Society of London, Special Publications 338, 197-212.

Roman, A., Arndt, N., 2019. Differentiated Archean oceanic crust: its thermal structure, mechanical stability and a test of the sagduction hypothesis. Geochimica et Cosmochimica Acta, https://doi.org/10.1016/j.gca.2019.07.009.

Sandeman, H.A., Brown, J., Studnicki-Gizbert, C., MacHattie, T., Hyde, D., Johnstone, S., Greiner, E., Plaza, D., 2001. Bedrock mapping in the Committee Bay belt, Laughland Lake area, central mainland, Nunavut. Natural Resources Canada, Geological Survey of Canada, 28p.

Sharkov, E.V., Krassivskaya, I.S., Chistyakov, A.V., 2004. Dispersed mafic–ultramafic intrusive magmatism in Early Paleoproterozoic mobile zones of the Baltic Shield: an example of the Belomorian drusite (coronite) complex. Petrology 12(6), 561-582.

Sharkov, E.V., Smol'kin, V.F., Belyatskii, V.B., Chistyakov, A.V., Fedotov, Z.A., 2006. Age of the Moncha Tundra fault, Kola Peninsula: Evidence from the Sm-Nd and Rb-Sr isotopic systematics of metamorphic assemblages. Geochemistry International 44(4), 317-326.

Spath, C.S. III, Lesher, C.M., Houlé, M.G., 2015. Hybridized ultramafic rocks in the Black Label hybrid zone of the Black Thor intrusive complex, McFaulds Lake greenstone belt, Ontario, In: Ames, D.E., Houlé, M.G. (eds.). Targeted Geoscience Initiative 4: Canadian Nickel-Copper-Platinum Group Elements-Chromium Ore Systems - Fertility, Pathfinders, New and Revised Models. Geological Survey of Canada, Open File 7856, 103–114.

Vrevskii, A.B., 2016. Age and sources of the anorthosites of the Neoarchean Kolmozero-Voron'ya greenstone belt (Fennoscandian Shield). Petrology 24(6), 527-542.

Walawender, M.J., 1976. Petrology and emplacement of the Los Pinos pluton, southern California. Canadian Journal of Earth Sciences 13(9), 1288-1300.

Walawender, M.J., Smith, T.E., 1980. Geochemical and petrologic evolution of the basic plutons of the Peninsular Ranges batholith, southern California. The Journal of Geology 88(2), 233-242.

Wiener, R.W., 1981. Tectonic setting, rock chemistry, and metamorphism of an Archean gabbro–anorthosite complex, Tessiuyakh Bay, Labrador. Canadian Journal of Earth Sciences 18(9), 1409-1421.

Yang, X.M., Gilbert, H.P., 2014. Mineral chemistry of chromite in the Mayville intrusion: evidence for petrogenesis and linkage to the Bird River sill in the Neoarchean Bird River greenstone belt, southeastern Manitoba (NTS 52L5, 6, 12). In: Report of Activities 2014. Manitoba Mineral Resources, Manitoba Geological Survey, 32-48.

Yang, X.M., Gilbert, H.P., Corkery, M.T., Houlé, M.G., 2011. The Mayville mafic-ultramafic intrusion in the Neoarchean Bird River greenstone belt, southeastern Manitoba (part of NTS 52L12): preliminary geochemical investigation and implication for PGE-Ni-Cu-(Cr) mineralization. In: Report of Activities 2011. Manitoba Innovation, Energy and Mines, Manitoba Geological Survey, 127-142.

Yang, X.M., Gilbert, H.P., Houlé, M.G., 2012. Geological investigations of the Cat Creek area in the Neoarchean Bird River greenstone belt, southeastern Manitoba (parts of NTS 52L12): new insights into PGE-Ni-Cu-Cr mineralization. In: Reports of Activities 2012. Manitoba Innovation, Energy and Mines, Manitoba Geological Survey, 32-53.

Zhou, S., Polat, A., Longstaffe, F.J., Yang, K., Fryer, B.J., Weisener, C., 2016. Formation of the Neoarchean Bad Vermilion Lake Anorthosite Complex and spatially associated granitic rocks at a convergent plate margin, Superior Province, Western Ontario, Canada. Gondwana Research 33, 134-159.

Appendices

Appendix 1

Appendix 1.1. Major (wt.%) and trace element (ppm) data for anorthosites, leucogabbros and gabbros from the Haines Gabbroic Complex.

Sample ID	Lithology	SiO_2	Al_2O_3	$Fe_2O_3^T$	MnO	MgO	CaO
SP04-002-1	Anorthosite	48.35	24.20	4.58	0.09	2.65	13.76
SP04-002-4	Anorthosite	49.93	26.92	2.18	0.05	1.16	13.36
SP04-002-5	Leucogabbro	49.51	23.90	3.72	0.08	1.09	16.56
SP04-002-6	Anorthosite	48.38	25.86	3.12	0.06	1.42	15.74
SP04-002-8	Gabbro	48.65	17.90	6.51	0.12	7.73	12.59
SP04-002-11	Leucogabbro	64.11	18.35	1.74	0.03	1.31	3.03
SP04-002-13	Gabbro	49.28	16.36	7.35	0.14	8.29	13.57
SP04-002-14	Leucogabbro	48.41	21.54	5.75	0.11	5.81	12.81
SP04-002-15	Gabbro	46.92	16.43	6.84	0.13	8.02	11.86
SP04-002-16	Gabbro	47.42	17.00	6.29	0.12	7.56	12.69
SP04-002-17	Gabbro	48.59	19.05	7.13	0.14	8.14	12.12
SP04-002-20	Gabbro	43.48	14.56	6.04	0.12	6.98	11.59
SP04-002-21	Gabbro	39.44	11.05	8.21	0.14	11.46	12.38
SP04-002-23	Anorthosite	48.08	24.35	4.51	0.08	3.11	13.96
SP04-002-24	Leucogabbro	48.77	23.15	4.94	0.08	3.57	14.43
SP04-002-25	Gabbro	49.79	14.48	8.45	0.17	9.90	12.43
SP04-002-26	Anorthosite	50.42	24.04	3.82	0.07	2.56	13.21
SP04-002-27	Gabbro	49.74	13.69	8.58	0.18	10.08	13.11
SP04-002-29	Anorthosite	47.93	26.11	4.15	0.07	2.39	13.41
SP04-002-30	Anorthosite	48.65	24.46	3.20	0.07	2.47	14.60
SP04-002-31	Leucogabbro	49.48	22.79	3.63	0.07	3.27	12.30

Sample ID	Na_2O	K_2O	TiO_2	P_2O_5	LOI	Total	Mg#	Ba	Sr	Y
SP04-002-1	2.78	0.03	0.34	0.04	2.80	99.61	53	14.00	157.00	10.00
SP04-002-4	4.22	0.37	0.13	0.01	1.96	100.30	51	79.00	191.00	3.00
SP04-002-5	2.19	0.01	0.24	0.01	2.12	99.43	37	4.00	160.00	7.00
SP04-002-6	2.99	0.02	0.26	0.03	2.34	100.20	47	7.00	188.00	7.00
SP04-002-8	1.61	0.07	0.19	< 0.01	3.57	98.94	70	12.00	115.00	6.00
SP04-002-11	8.80	0.22	0.12	< 0.01	2.77	100.50	60	73.00	112.00	2.00
SP04-002-13	1.50	0.03	0.22	< 0.01	2.56	99.30	69	4.00	97.00	7.00
SP04-002-14	2.06	0.14	0.21	< 0.01	3.16	100.00	67	25.00	138.00	6.00
SP04-002-15	1.24	0.06	0.20	< 0.01	8.90	100.60	70	17.00	87.00	7.00
SP04-002-16	1.27	0.09	0.18	< 0.01	6.42	99.03	70	18.00	112.00	6.00
SP04-002-17	2.24	0.07	0.24	< 0.01	2.66	100.40	69	9.00	125.00	7.00
SP04-002-20	0.16	2.39	0.20	< 0.01	13.42	98.95	70	72.00	51.00	6.00
SP04-002-21	0.96	0.16	0.60	0.10	15.03	99.54	73	50.00	170.00	10.00
SP04-002-23	3.09	0.02	0.41	0.03	2.85	100.50	58	9.00	153.00	10.00
SP04-002-24	2.38	0.01	0.39	0.03	2.80	100.60	59	< 2	143.00	10.00
SP04-002-25	1.14	0.09	0.23	0.02	3.20	99.89	70	10.00	96.00	8.00
SP04-002-26	3.40	0.04	0.26	0.04	2.33	100.20	57	12.00	181.00	10.00
SP04-002-27	1.41	0.08	0.30	0.01	3.03	100.20	70	24.00	120.00	10.00
SP04-002-29	3.24	0.09	0.27	0.01	2.62	100.30	53	18.00	156.00	9.00
SP04-002-30	2.92	0.01	0.13	< 0.01	2.28	98.78	60	4.00	164.00	4.00
SP04-002-31	3.71	0.01	0.13	< 0.01	3.25	98.64	64	6.00	150.00	4.00

Sample ID	Sc	Zr	V	Ba	Be	Bi	Cd	Ce	Co	Cr
SP04-002-1	19.00	28.00	93.00	13.91	0.22	<DL	0.02	5.07	21.33	95.85
SP04-002-4	6.00	12.00	33.00	75.22	0.47	<DL	0.04	2.08	6.28	22.71
SP04-002-5	14.00	23.00	76.00	3.81	0.12	<DL	0.03	2.94	12.93	38.57
SP04-002-6	12.00	26.00	73.00	6.83	0.36	<DL	0.06	3.78	14.38	30.29
SP04-002-8	33.00	8.00	110.00	12.01	0.19	<DL	0.05	1.70	34.76	132.91
SP04-002-11	8.00	10.00	24.00	70.04	0.91	<DL	0.01	1.02	10.99	28.16
SP04-002-13	39.00	9.00	133.00	5.25	0.15	<DL	0.05	1.68	39.31	157.85
SP04-002-14	23.00	19.00	91.00	25.16	0.20	<DL	0.01	2.71	26.52	83.42
SP04-002-15	37.00	6.00	126.00	18.08	0.16	<DL	0.04	1.38	36.20	147.94
SP04-002-16	33.00	7.00	112.00	18.32	0.18	<DL	0.04	1.50	32.86	134.58
SP04-002-17	40.00	12.00	137.00	9.62	0.30	<DL	0.03	2.07	33.79	141.48
SP04-002-20	32.00	12.00	111.00	70.95	0.44	<DL	0.04	1.44	33.92	130.13
SP04-002-21	16.00	106.00	123.00	49.06	1.02	<DL	0.09	47.39	41.42	404.17
SP04-002-23	21.00	38.00	111.00	3.60	0.27	<DL	0.14	5.59	18.53	56.58
SP04-002-24	26.00	30.00	119.00	2.61	0.21	<DL	0.15	4.01	24.78	72.70
SP04-002-25	43.00	9.00	148.00	11.80	0.30	<DL	0.06	1.83	48.67	164.48
SP04-002-26	12.00	30.00	65.00	12.22	0.37	<DL	0.03	6.33	15.08	26.43
SP04-002-27	49.00	13.00	172.00	25.47	0.26	<DL	0.08	2.66	46.70	196.16
SP04-002-29	18.00	20.00	82.00	17.91	0.34	<DL	0.05	3.85	19.84	44.63
SP04-002-30	16.00	7.00	60.00	4.05	0.16	<DL	0.05	1.54	14.02	61.37
SP04-002-31	15.00	8.00	58.00	5.99	0.28	<DL	0.03	1.65	17.39	53.09

Sample ID	Cs	Cu	Dy	Er	Eu	Ga	Gd	Hf	Ho	In
SP04-002-1	0.06	23.50	1.84	1.22	0.52	18.85	1.60	0.74	0.41	0.02
SP04-002-4	0.31	2.23	0.56	0.35	0.39	20.00	0.48	0.29	0.12	0.01
SP04-002-5	0.02	3.50	1.22	0.78	0.49	22.33	1.01	0.53	0.26	0.02
SP04-002-6	0.02	104.78	1.35	0.82	0.49	21.26	1.14	0.54	0.28	0.02
SP04-002-8	0.20	59.80	1.21	0.79	0.35	14.88	0.90	0.23	0.26	0.03
SP04-002-11	0.11	4.88	0.47	0.29	0.11	6.97	0.32	0.26	0.10	0.01
SP04-002-13	0.03	36.66	1.31	0.89	0.36	13.79	0.99	0.31	0.29	0.03
SP04-002-14	0.27	20.93	1.15	0.80	0.40	16.13	0.96	0.42	0.25	0.02
SP04-002-15	0.16	30.68	1.22	0.80	0.46	13.68	0.94	0.23	0.27	0.03
SP04-002-16	0.23	30.81	1.07	0.74	0.36	14.54	0.80	0.22	0.25	0.02
SP04-002-17	0.19	15.84	1.35	0.85	0.35	14.66	1.05	0.36	0.28	0.03
SP04-002-20	1.46	226.39	1.13	0.78	0.24	12.90	0.86	0.30	0.25	0.03
SP04-002-21	0.22	108.60	2.47	1.16	1.26	11.45	3.88	2.17	0.43	0.03
SP04-002-23	0.01	170.49	1.81	1.15	0.55	18.06	1.55	0.84	0.38	0.03
SP04-002-24	0.01	168.19	1.71	1.14	0.55	18.66	1.46	0.66	0.38	0.03
SP04-002-25	0.49	117.56	1.41	0.97	0.33	12.86	1.08	0.30	0.31	0.03
SP04-002-26	0.09	39.77	1.80	1.09	0.54	18.80	1.52	0.65	0.37	0.02
SP04-002-27	0.27	90.68	1.84	1.20	0.41	12.02	1.40	0.43	0.40	0.04
SP04-002-29	0.07	85.64	1.48	0.90	0.49	19.20	1.30	0.52	0.32	0.02
SP04-002-30	<DL	12.59	0.71	0.45	0.39	21.40	0.63	0.20	0.16	0.01
SP04-002-31	0.02	11.34	0.70	0.43	0.36	18.70	0.56	0.20	0.15	0.02

Sample ID	La	Li	Lu	Mo	Nb	Nd	Ni	Pb	Pr	Rb
SP04-002-1	1.99	3.70	0.18	1.59	1.41	3.97	43.40	<DL	0.80	0.80
SP04-002-4	0.97	1.96	0.05	0.47	0.52	1.59	15.50	1.03	0.31	7.91
SP04-002-5	1.16	2.15	0.12	0.40	0.84	2.53	20.79	0.75	0.51	0.29
SP04-002-6	1.62	2.77	0.11	0.30	0.96	2.90	24.41	1.18	0.61	0.31
SP04-002-8	0.72	5.62	0.11	0.26	0.24	1.75	94.32	<DL	0.33	1.62
SP04-002-11	0.46	2.03	0.04	0.75	0.34	0.82	15.57	0.74	0.16	4.55
SP04-002-13	0.70	3.36	0.13	0.30	0.26	1.74	105.68	<DL	0.33	0.46
SP04-002-14	1.12	5.13	0.12	0.32	0.54	2.18	67.94	<DL	0.42	2.90
SP04-002-15	0.57	10.09	0.13	0.28	0.16	1.51	101.66	0.71	0.26	1.57
SP04-002-16	0.59	8.00	0.11	0.19	0.16	1.43	96.19	0.70	0.26	1.88
SP04-002-17	0.81	4.65	0.13	0.21	0.39	1.91	120.90	<DL	0.36	1.37
SP04-002-20	0.57	16.41	0.11	0.15	0.36	1.32	110.75	<DL	0.23	65.99
SP04-002-21	19.28	6.64	0.16	0.11	12.09	27.50	230.89	1.37	6.55	2.99
SP04-002-23	2.14	3.97	0.16	0.40	1.72	4.31	48.76	<DL	0.86	0.25
SP04-002-24	1.50	4.11	0.16	0.40	1.38	3.21	62.92	<DL	0.65	<DL
SP04-002-25	0.66	4.82	0.14	0.23	0.28	1.84	134.98	<DL	0.31	2.13
SP04-002-26	2.48	3.68	0.16	0.42	1.36	4.48	40.58	<DL	0.90	0.90
SP04-002-27	0.93	3.79	0.18	0.27	0.44	2.53	146.06	1.04	0.44	1.83
SP04-002-29	1.42	4.33	0.13	0.33	0.89	3.13	31.87	<DL	0.63	2.33
SP04-002-30	0.65	2.97	0.07	0.35	0.23	1.33	36.70	<DL	0.26	0.25
SP04-002-31	0.73	5.15	0.06	0.21	0.27	1.38	41.54	<DL	0.27	<DL

Sample ID	Sb	Sc	Sm	Sn	Sr	Ta	Tb	Th	Ti	Tl
SP04-002-1	0.12	18.45	1.26	0.50	169.07	0.09	0.28	0.15	2075.61	<DL
SP04-002-4	0.71	5.06	0.42	0.38	189.00	0.04	0.08	0.07	770.11	0.05
SP04-002-5	0.57	11.27	0.79	0.49	165.52	0.05	0.18	0.11	1441.65	<DL
SP04-002-6	1.55	11.26	0.86	0.40	186.97	0.06	0.20	0.11	1538.11	<DL
SP04-002-8	0.27	32.91	0.63	0.35	119.02	<DL	0.17	0.04	1152.64	0.01
SP04-002-11	0.05	7.63	0.24	0.38	103.46	0.02	0.06	0.14	622.57	0.03
SP04-002-13	0.26	38.32	0.65	0.31	99.48	<DL	0.18	0.04	1321.15	0.01
SP04-002-14	0.26	22.33	0.67	0.46	132.55	0.04	0.17	0.07	1227.65	0.02
SP04-002-15	0.16	34.24	0.60	0.31	80.94	<DL	0.17	0.03	1099.42	0.01
SP04-002-16	0.19	30.51	0.54	0.31	105.74	<DL	0.15	0.02	1059.76	0.01
SP04-002-17	0.26	38.69	0.68	0.35	114.88	<DL	0.19	0.06	1364.62	0.01
SP04-002-20	0.08	32.65	0.53	0.32	51.07	<DL	0.16	0.04	1273.62	0.27
SP04-002-21	0.17	16.06	4.98	0.72	165.82	0.62	0.48	2.56	3571.37	0.02
SP04-002-23	0.27	20.99	1.27	0.57	149.73	0.11	0.28	0.19	2465.25	<DL
SP04-002-24	0.25	25.27	1.07	0.47	142.50	0.08	0.25	0.11	2278.31	0.01
SP04-002-25	0.15	43.94	0.68	0.35	97.99	<DL	0.20	0.03	1468.33	0.02
SP04-002-26	0.34	12.29	1.25	0.46	178.62	0.09	0.27	0.23	1598.85	0.01
SP04-002-27	0.19	48.77	0.91	0.39	117.58	0.03	0.26	0.06	1763.65	0.01
SP04-002-29	0.11	16.97	0.99	0.45	153.30	0.06	0.22	0.09	1596.86	0.01
SP04-002-30	0.41	14.14	0.45	0.42	170.71	<DL	0.10	0.03	781.91	<DL
SP04-002-31	0.37	15.44	0.44	0.32	152.16	<DL	0.10	0.03	793.73	<DL

Sample ID	Tm	U	W	Y	Yb	Zn	Zr	Zr/Y	La/Yb	Th/Yb
SP04-002-1	0.17	0.05	0.26	11.68	1.19	32.96	26.98	2.31	1.68	0.12
SP04-002-4	0.05	0.02	0.24	3.16	0.34	10.37	10.71	3.39	2.84	0.19
SP04-002-5	0.11	0.03	0.32	7.37	0.77	11.05	19.03	2.58	1.51	0.14
SP04-002-6	0.12	0.03	0.50	7.48	0.74	13.08	18.46	2.47	2.19	0.15
SP04-002-8	0.12	<DL	0.12	7.07	0.78	44.24	6.71	0.95	0.92	0.05
SP04-002-11	0.04	0.09	1.19	2.50	0.27	10.49	9.07	3.63	1.71	0.52
SP04-002-13	0.13	0.01	0.16	7.83	0.87	52.57	9.44	1.21	0.80	0.04
SP04-002-14	0.11	0.02	0.18	6.51	0.79	31.69	13.68	2.10	1.42	0.09
SP04-002-15	0.12	<DL	0.21	6.79	0.83	45.18	6.18	0.91	0.69	0.03
SP04-002-16	0.11	<DL	0.19	6.16	0.73	41.31	6.36	1.03	0.80	0.03
SP04-002-17	0.13	0.02	0.12	7.66	0.87	40.96	11.47	1.50	0.93	0.07
SP04-002-20	0.11	0.02	0.31	6.57	0.78	41.91	9.88	1.50	0.73	0.05
SP04-002-21	0.16	0.28	0.46	11.51	1.09	62.81	105.63	9.17	17.77	2.36
SP04-002-23	0.17	0.05	0.24	10.35	1.08	30.22	29.75	2.88	1.97	0.17
SP04-002-24	0.16	0.03	0.19	10.02	1.05	34.22	23.60	2.36	1.42	0.10
SP04-002-25	0.14	0.01	0.08	8.21	0.93	48.29	9.35	1.14	0.71	0.03
SP04-002-26	0.16	0.06	0.18	10.28	1.07	20.58	22.36	2.18	2.31	0.22
SP04-002-27	0.18	0.01	0.11	10.75	1.19	52.52	13.38	1.24	0.78	0.05
SP04-002-29	0.13	0.03	0.22	8.71	0.91	21.09	18.77	2.15	1.56	0.10
SP04-002-30	0.07	<DL	0.13	4.22	0.43	19.93	6.38	1.51	1.49	0.07
SP04-002-31	0.06	<DL	0.09	3.96	0.43	21.56	6.63	1.67	1.72	0.07

Sample ID	Nd/Sm	La/Nb	Dy/Yb	La/Sm_{cn}	La/Yb_{cn}	Gd/Yb_{cn}	Nb/Nb*	Zr/Zr*	Ti/Ti*	Eu/Eu*	Ce/Ce*
SP04-002-1	3.14	1.41	1.55	1.02	1.21	1.11	0.61	0.71	0.60	1.13	0.98
SP04-002-4	3.77	1.88	1.64	1.49	2.04	1.15	0.48	0.77	0.70	2.65	0.93
SP04-002-5	3.21	1.38	1.58	0.95	1.08	1.08	0.56	0.80	0.66	1.67	0.94
SP04-002-6	3.36	1.69	1.83	1.21	1.57	1.27	0.53	0.69	0.64	1.50	0.93
SP04-002-8	2.76	3.04	1.55	0.73	0.66	0.95	0.32	0.38	0.63	1.40	0.86
SP04-002-11	3.39	1.34	1.74	1.21	1.22	0.98	0.32	1.20	0.92	1.16	0.92
SP04-002-13	2.69	2.74	1.50	0.70	0.57	0.93	0.36	0.53	0.68	1.38	0.86
SP04-002-14	3.27	2.07	1.46	1.08	1.02	1.01	0.45	0.67	0.63	1.52	0.97
SP04-002-15	2.49	3.62	1.48	0.61	0.49	0.94	0.30	0.38	0.60	1.85	0.88
SP04-002-16	2.67	3.67	1.45	0.71	0.57	0.90	0.33	0.43	0.66	1.66	0.94
SP04-002-17	2.83	2.06	1.54	0.77	0.66	0.99	0.43	0.60	0.66	1.25	0.94
SP04-002-20	2.49	1.58	1.45	0.69	0.53	0.91	0.57	0.70	0.77	1.07	0.97
SP04-002-21	5.53	1.60	2.28	2.50	12.75	2.95	0.40	0.53	0.33	0.87	1.03
SP04-002-23	3.40	1.24	1.67	1.09	1.42	1.18	0.64	0.75	0.72	1.21	1.01
SP04-002-24	3.00	1.08	1.62	0.90	1.02	1.15	0.80	0.75	0.75	1.35	1.00
SP04-002-25	2.69	2.38	1.51	0.62	0.51	0.96	0.49	0.49	0.70	1.18	0.99
SP04-002-26	3.60	1.82	1.68	1.29	1.66	1.17	0.42	0.56	0.48	1.21	1.04
SP04-002-27	2.79	2.13	1.55	0.66	0.56	0.97	0.45	0.52	0.64	1.11	1.02
SP04-002-29	3.14	1.59	1.62	0.92	1.12	1.18	0.59	0.63	0.57	1.32	1.00
SP04-002-30	2.94	2.84	1.63	0.92	1.07	1.21	0.38	0.49	0.60	2.23	0.91
SP04-002-31	3.12	2.72	1.65	1.07	1.23	1.08	0.42	0.50	0.66	2.23	0.91

Appendix 1.2. Major (wt.%) and trace element (ppm) data for basalts, basaltic andesites, andesites, picrites, serpentinites, gabbros, olivine websterites and harzburgites from the Greenwater and Burchell assemblages of the Shebandowan greenstone belt.

Sample ID	Lithology	Assemblage	Latitude/Longitude Location Coordinates	
SD2016-02	Serpentinite	Greenwater	48°35.791'N	090°14.923'W
SD2016-08	Serpentinite	Greenwater	48°35.767'N	090°14.824'W
SD2016-09	Serpentinite	Greenwater	48°35.767'N	090°14.824'W
SD2016-11	Serpentinite	Greenwater	48°35.368'N	090°16.774'W
SD2016-14	Gabbro	Greenwater	48°35.468'N	090°14.366'W
SD2016-15	Basaltic andesite	Greenwater	48°35.151'N	090°13.404'W
SD2016-16	Basaltic andesite	Greenwater	48°35.151'N	090°13.404'W
SD2016-18	Basalt	Greenwater	48°35.246'N	090°13.725'W
SD2016-20	Basalt	Greenwater	48°35.246'N	090°13.725'W
SD2016-21	Gabbro	Burchell	48°37.955'N	090°29.342'W
SD2016-23	Gabbro	Burchell	48°37.876'N	090°29.727'W
SD2016-25	Gabbro	Burchell	48°37.258'N	090°31.787'W
SD2016-27	Andesite	Burchell	48°36.889'N	090°32.754'W
SD2016-29	Andesite	Burchell	48°37.171'N	090°31.719'W
SD2016-30	Gabbro	Burchell	48°36.523'N	090°32.172'W
SD2016-34	Gabbro	Burchell	48°35.640'N	090°32.730'W
SD2016-36	Andesite	Burchell	48°35.179'N	090°33.205'W
SD2016-37	Gabbro	Burchell	48°35.198'N	090°33.307'W
SD2016-41	Gabbro	Greenwater	48°30.680'N	090°35.144'W
SD2016-43	Gabbro	Greenwater	48°30.188'N	090°23.064'W
SP06-015-32	Pyroxenite	Greenwater	N/A	N/A
SP06-015-33	Pyroxenite	Greenwater	N/A	N/A
SP05-006-34	Picrite	Greenwater	N/A	N/A
SP06-006-37	Picrite	Greenwater	N/A	N/A
SP06-004-39	Picrite	Greenwater	N/A	N/A
SP06-003-40	Pyroxenite	Greenwater	N/A	N/A
SP04-007-42	Peridotite	Greenwater	N/A	N/A
SP04-007-43	Peridotite	Greenwater	N/A	N/A
SP04-007-44	Peridotite	Greenwater	N/A	N/A

Sample ID	SiO_2	Al_2O_3	$Fe_2O_3^T$	MnO	MgO	CaO	Na_2O	K_2O	TiO_2	P_2O_5
SD2016-02	39.00	1.04	10.79	0.08	33.10	2.00	0.02	0.02	0.06	0.04
SD2016-08	44.02	8.96	12.02	0.18	20.34	7.43	0.31	0.03	0.30	0.02
SD2016-09	44.60	9.20	11.94	0.18	20.52	7.66	0.36	0.05	0.35	< 0.01
SD2016-11	37.72	3.26	14.27	0.18	31.10	2.43	0.03	0.03	0.20	0.02
SD2016-14	48.01	13.84	15.27	0.23	6.88	10.10	1.48	0.03	1.44	0.09
SD2016-15	50.64	13.90	14.72	0.18	5.81	9.22	1.35	0.06	1.48	0.12
SD2016-16	53.88	12.69	12.86	0.15	6.56	7.18	2.33	0.06	1.25	0.12
SD2016-18	50.33	14.12	13.90	0.19	6.79	7.02	3.34	0.05	1.23	0.10
SD2016-20	47.94	13.01	14.38	0.23	6.36	9.98	2.01	0.06	1.10	0.09
SD2016-21	46.87	15.81	10.60	0.16	4.86	9.08	3.44	0.53	1.40	0.15
SD2016-23	52.04	13.74	12.32	0.18	5.84	8.58	3.53	0.17	0.76	0.10
SD2016-25	48.61	15.56	10.34	0.16	7.70	11.66	2.02	0.12	0.68	0.05
SD2016-27	54.64	14.09	9.15	0.13	8.41	7.02	2.05	0.22	0.71	0.14
SD2016-29	52.89	17.45	7.52	0.12	5.11	4.42	5.45	1.24	0.90	0.20
SD2016-30	55.72	13.71	7.27	0.13	5.29	9.28	4.16	0.28	1.49	0.03
SD2016-34	49.01	16.82	9.56	0.14	7.08	11.96	2.32	0.11	0.74	0.05
SD2016-36	57.53	16.17	9.24	0.14	4.56	5.62	3.23	1.42	1.13	0.16
SD2016-37	48.03	15.70	11.93	0.21	7.29	10.98	1.89	0.10	0.88	0.06
SD2016-41	48.10	18.48	8.15	0.14	7.04	11.74	2.25	0.80	0.49	0.04
SD2016-43	50.88	14.60	9.68	0.13	8.01	8.71	3.22	0.71	0.77	0.08
SP06-015-32	43.76	6.33	15.52	0.17	21.23	7.18	0.43	0.05	0.95	0.08
SP06-015-33	45.13	7.91	13.26	0.20	18.77	9.31	0.68	0.07	1.08	0.10
SP05-006-34	45.96	10.26	12.95	0.20	15.82	9.78	1.01	0.47	0.51	0.04
SP06-006-37	46.05	10.86	12.61	0.19	16.08	9.43	0.98	0.39	0.65	0.05
SP06-004-39	46.75	11.21	11.99	0.20	14.48	9.69	0.84	0.60	0.55	0.04
SP06-003-40	48.86	5.96	11.89	0.19	17.65	11.37	0.59	0.09	0.88	0.05
SP04-007-42	40.28	4.72	13.01	0.19	27.92	3.02	0.17	0.08	0.28	0.03
SP04-007-43	39.28	3.71	13.69	0.21	30.23	1.58	0.09	0.08	0.29	0.07
SP04-007-44	39.24	4.28	14.16	0.19	29.79	2.34	0.18	0.06	0.28	0.04

Sample ID	LOI	Total	Mg#	Ba	Sr	Y	Sc	Zr	V	Ba
SD2016-02	12.39	98.55	86	< 2	12.00	2.00	7.00	4.00	38.00	3.40
SD2016-08	5.26	98.89	77	< 2	15.00	6.00	24.00	12.00	124.00	3.16
SD2016-09	5.17	100.10	77	< 2	15.00	7.00	24.00	15.00	129.00	2.99
SD2016-11	9.40	98.63	81	< 2	4.00	4.00	13.00	13.00	74.00	2.89
SD2016-14	2.74	100.10	47	28.00	91.00	21.00	56.00	66.00	406.00	31.74
SD2016-15	2.83	100.30	44	26.00	143.00	38.00	42.00	127.00	340.00	28.56
SD2016-16	3.12	100.20	50	26.00	97.00	31.00	42.00	113.00	333.00	39.77
SD2016-18	2.83	99.88	49	25.00	68.00	22.00	45.00	72.00	326.00	27.21
SD2016-20	3.51	98.67	47	20.00	150.00	21.00	42.00	69.00	340.00	22.96
SD2016-21	6.35	99.26	48	93.00	246.00	25.00	32.00	89.00	277.00	95.77
SD2016-23	2.47	99.73	48	28.00	118.00	24.00	42.00	68.00	197.00	29.32
SD2016-25	3.10	100.00	60	20.00	135.00	13.00	36.00	38.00	230.00	21.26
SD2016-27	3.51	100.10	65	32.00	139.00	14.00	22.00	101.00	151.00	32.22
SD2016-29	4.42	99.73	57	114.00	132.00	18.00	21.00	140.00	142.00	113.97
SD2016-30	2.12	99.46	59	180.00	146.00	43.00	42.00	153.00	256.00	178.72
SD2016-34	2.55	100.30	59	24.00	128.00	14.00	41.00	39.00	248.00	23.82
SD2016-36	1.15	100.30	49	375.00	242.00	19.00	24.00	131.00	197.00	372.82
SD2016-37	2.58	99.67	55	18.00	169.00	16.00	40.00	44.00	274.00	20.46
SD2016-41	2.10	99.32	63	124.00	258.00	9.00	31.00	26.00	185.00	123.41
SD2016-43	1.73	98.52	62	114.00	255.00	24.00	39.00	84.00	222.00	114.34
SP06-015-32	3.81	99.50	73	6.00	67.00	12.00	21.00	63.00	203.00	8.81
SP06-015-33	3.26	99.76	74	8.00	73.00	14.00	28.00	62.00	218.00	9.86
SP05-006-34	3.27	100.30	71	79.00	39.00	9.00	34.00	22.00	204.00	76.38
SP06-006-37	3.04	100.30	72	57.00	24.00	14.00	34.00	39.00	217.00	55.30
SP06-004-39	3.08	99.42	71	107.00	67.00	11.00	37.00	29.00	209.00	104.61
SP06-003-40	2.74	100.30	75	8.00	35.00	11.00	29.00	50.00	214.00	9.69
SP04-007-42	8.79	98.50	81	4.00	20.00	6.00	17.00	24.00	98.00	6.53
SP04-007-43	9.63	98.86	81	5.00	13.00	5.00	16.00	21.00	93.00	7.69
SP04-007-44	9.01	99.57	81	3.00	15.00	6.00	16.00	19.00	95.00	5.42

Sample ID	Be	Bi	Cd	Ce	Co	Cr	Cs	Cu	Dy	Er
SD2016-02	0.12	0.47	0.02	0.76	110.25	3791.00	0.04	253.50	0.21	0.12
SD2016-08	0.19	0.15	0.03	2.05	96.31	1990.65	0.24	79.22	1.25	0.78
SD2016-09	0.18	<DL	0.04	2.42	90.97	2046.83	0.39	61.30	1.56	0.99
SD2016-11	0.16	<DL	<DL	1.98	130.17	3004.13	0.44	5.08	0.82	0.56
SD2016-14	0.46	<DL	0.14	10.54	50.98	258.00	0.18	131.68	4.43	2.83
SD2016-15	0.65	<DL	0.12	22.86	47.97	47.34	0.15	124.47	7.48	4.65
SD2016-16	0.72	<DL	0.19	19.79	45.28	44.23	0.22	125.03	6.21	3.93
SD2016-18	0.45	<DL	0.09	10.87	47.24	66.27	0.33	129.66	4.44	2.82
SD2016-20	0.52	<DL	0.10	10.45	51.99	59.06	0.12	157.47	4.31	2.74
SD2016-21	0.72	<DL	0.04	15.40	40.31	104.88	2.42	7.26	4.99	3.12
SD2016-23	0.57	<DL	0.09	12.40	40.39	66.15	0.20	152.55	4.59	2.91
SD2016-25	0.38	<DL	0.03	5.67	44.26	382.16	0.12	84.60	2.56	1.63
SD2016-27	0.61	<DL	0.02	20.81	40.62	350.29	0.21	55.50	2.98	1.77
SD2016-29	0.76	<DL	0.07	32.04	27.05	57.14	4.51	12.46	3.66	2.14
SD2016-30	0.80	<DL	0.02	34.96	23.12	12.89	0.17	2.43	8.23	5.19
SD2016-34	0.29	<DL	0.07	6.31	36.39	363.47	0.11	181.71	2.66	1.75
SD2016-36	0.68	<DL	0.06	28.25	29.33	48.96	1.79	30.89	3.83	2.27
SD2016-37	0.32	<DL	0.04	7.32	44.39	332.67	0.10	46.04	3.20	2.06
SD2016-41	0.25	<DL	0.06	4.22	36.07	685.68	4.44	72.98	1.88	1.20
SD2016-43	0.45	<DL	0.04	14.71	39.62	498.99	0.80	30.76	4.77	3.08
SP06-015-32	0.60	<DL	0.09	8.78	86.65	1752.98	0.13	72.25	2.79	1.49
SP06-015-33	0.72	<DL	0.08	12.85	75.72	1736.38	0.13	56.18	3.08	1.71
SP05-006-34	0.41	<DL	0.08	3.36	73.78	1328.08	0.51	77.66	1.81	1.13
SP06-006-37	0.39	<DL	0.07	5.61	73.95	1795.52	0.28	12.07	2.60	1.63
SP06-004-39	0.35	<DL	0.34	3.87	74.32	1347.94	0.57	89.87	2.12	1.34
SP06-003-40	0.55	<DL	0.07	10.45	61.22	1531.66	0.30	50.52	2.53	1.38
SP04-007-42	0.21	<DL	0.03	4.66	108.65	2816.35	1.25	4.05	1.43	0.94
SP04-007-43	0.20	<DL	<DL	3.04	121.03	2961.20	1.01	3.61	1.10	0.71
SP04-007-44	0.30	<DL	0.04	2.92	121.26	2948.34	1.33	22.29	1.19	0.74

Sample ID	Eu	Ga	Gd	Hf	Ho	In	La	Li	Lu	Mo
SD2016-02	0.03	1.53	0.21	0.14	0.04	0.01	0.40	1.00	0.02	0.34
SD2016-08	0.30	8.34	0.99	0.41	0.26	0.03	0.68	10.24	0.12	0.12
SD2016-09	0.35	9.24	1.30	0.45	0.33	0.04	0.76	19.66	0.14	0.09
SD2016-11	0.19	3.93	0.67	0.34	0.17	0.02	0.77	1.88	0.09	0.10
SD2016-14	1.06	18.76	3.66	1.92	0.95	0.09	3.84	15.22	0.43	0.32
SD2016-15	1.46	20.32	6.41	3.64	1.59	0.10	8.75	18.06	0.68	0.79
SD2016-16	1.30	18.77	5.48	3.35	1.33	0.10	7.91	23.98	0.56	0.53
SD2016-18	0.95	15.40	3.68	2.14	0.95	0.08	3.95	14.09	0.42	0.30
SD2016-20	0.96	17.66	3.63	1.93	0.92	0.08	3.81	18.19	0.40	0.25
SD2016-21	1.32	18.08	4.53	2.43	1.05	0.08	6.03	21.61	0.46	0.27
SD2016-23	1.03	19.00	3.94	1.91	0.97	0.08	4.73	9.48	0.43	0.19
SD2016-25	0.61	15.07	2.05	1.06	0.55	0.04	1.92	18.34	0.24	0.27
SD2016-27	0.87	15.61	2.87	2.59	0.61	0.04	8.53	31.79	0.26	0.49
SD2016-29	1.06	13.78	3.64	3.62	0.74	0.04	12.88	22.31	0.30	1.41
SD2016-30	2.20	16.10	7.00	4.34	1.79	0.07	12.52	6.67	0.76	0.24
SD2016-34	0.63	14.22	2.25	1.05	0.59	0.05	2.21	8.66	0.25	0.42
SD2016-36	1.21	19.32	3.85	3.52	0.77	0.06	11.56	16.78	0.32	0.88
SD2016-37	0.71	15.67	2.61	1.34	0.69	0.06	2.72	9.36	0.30	0.46
SD2016-41	0.48	14.53	1.52	0.73	0.40	0.04	1.63	32.42	0.17	0.27
SD2016-43	0.90	14.07	3.96	2.26	1.03	0.06	5.32	13.21	0.45	0.31
SP06-015-32	0.78	11.10	2.84	1.69	0.54	0.05	2.47	1.84	0.20	0.15
SP06-015-33	0.98	11.83	3.32	1.69	0.62	0.06	4.40	2.48	0.21	2.23
SP05-006-34	0.45	11.07	1.45	0.62	0.38	0.05	1.14	26.96	0.16	1.41
SP06-006-37	0.66	12.04	2.12	1.11	0.57	0.05	2.07	23.33	0.24	0.19
SP06-004-39	0.48	11.74	1.74	0.82	0.45	0.04	1.43	18.93	0.19	0.22
SP06-003-40	0.75	10.15	2.64	1.33	0.48	0.05	3.41	7.11	0.17	0.58
SP04-007-42	0.32	5.67	1.20	0.65	0.30	0.03	1.82	2.21	0.13	0.10
SP04-007-43	0.22	4.19	0.93	0.65	0.23	0.03	1.27	1.67	0.11	<DL
SP04-007-44	0.25	4.77	0.99	0.54	0.26	0.03	1.29	1.74	0.12	0.09

Sample ID	Nb	Nd	Ni	Pb	Pr	Rb	Sb	Sc	Sm	Sn
SD2016-02	0.14	0.61	1971.70	0.91	0.13	0.65	1.21	7.30	0.17	0.20
SD2016-08	0.38	2.05	1581.92	0.76	0.36	0.88	0.11	24.10	0.72	0.31
SD2016-09	0.50	2.52	1225.65	<DL	0.44	1.88	0.08	24.73	0.93	0.34
SD2016-11	0.51	1.51	1137.96	<DL	0.31	1.86	<DL	13.29	0.49	0.26
SD2016-14	3.05	8.74	66.55	<DL	1.62	0.49	0.07	55.40	2.78	0.76
SD2016-15	5.98	17.51	38.43	1.29	3.44	1.08	0.34	41.43	5.13	1.43
SD2016-16	5.53	14.87	39.18	2.09	2.98	1.61	0.55	40.67	4.30	2.68
SD2016-18	3.17	9.05	55.30	<DL	1.72	0.89	0.13	44.68	2.85	0.72
SD2016-20	2.88	8.51	72.16	0.79	1.62	1.03	0.13	42.24	2.65	1.34
SD2016-21	4.28	11.52	68.05	1.34	2.31	16.73	0.50	32.05	3.51	1.49
SD2016-23	3.04	9.13	66.95	<DL	1.82	2.54	0.21	42.33	2.88	0.76
SD2016-25	1.65	4.58	138.24	1.17	0.87	3.26	0.40	35.20	1.45	0.45
SD2016-27	4.51	11.19	261.22	1.06	2.60	5.24	0.26	21.30	2.67	0.95
SD2016-29	6.25	16.37	73.32	1.75	3.84	51.01	0.07	21.24	3.63	1.04
SD2016-30	6.28	20.27	38.37	0.62	4.48	4.77	0.25	41.25	5.52	2.85
SD2016-34	1.68	4.77	96.28	0.85	0.92	2.53	0.17	39.93	1.56	0.62
SD2016-36	5.21	15.22	44.17	2.50	3.47	28.26	0.06	23.90	3.57	1.26
SD2016-37	2.08	5.83	100.84	1.15	1.10	1.87	0.12	40.59	1.90	0.64
SD2016-41	1.15	3.39	116.14	<DL	0.65	37.08	<DL	30.79	1.11	0.44
SD2016-43	3.60	9.99	78.19	1.39	2.06	23.93	0.21	38.28	2.98	0.95
SP06-015-32	4.65	8.83	1329.94	<DL	1.66	0.59	0.07	21.61	2.58	0.78
SP06-015-33	4.88	10.38	973.90	<DL	2.13	0.56	0.07	27.97	3.00	0.96
SP05-006-34	0.86	3.10	459.87	1.11	0.56	11.17	0.07	33.26	1.09	0.59
SP06-006-37	1.42	4.85	508.57	<DL	0.87	9.94	0.05	33.26	1.60	0.66
SP06-004-39	1.01	3.64	445.33	5.62	0.67	14.56	0.07	36.02	1.26	0.44
SP06-003-40	3.64	8.30	928.51	2.15	1.67	1.31	0.07	27.67	2.34	1.02
SP04-007-42	1.00	3.19	985.11	0.83	0.66	3.47	0.25	16.22	0.92	0.52
SP04-007-43	0.80	2.14	1083.63	0.95	0.46	3.55	0.22	14.49	0.67	0.47
SP04-007-44	0.84	2.31	1057.85	<DL	0.45	3.59	0.16	15.36	0.74	0.45

Sample ID	Sr	Ta	Tb	Th	Ti	Tl	Tm	U	W	Y
SD2016 02	10.10	0.01	0.03	0.08	323.00	0.01	0.02	0.07	0.46	1.00
SD2016-08	15.33	0.03	0.19	0.04	1827.78	0.01	0.11	0.02	0.24	6.70
SD2016-09	15.46	0.03	0.24	0.05	2132.42	0.02	0.14	0.03	0.21	8.57
SD2016-11	4.03	0.03	0.12	0.06	1184.70	<DL	0.08	0.02	0.07	4.72
SD2016-14	92.40	0.19	0.66	0.28	8269.17	0.01	0.41	0.07	0.07	24.57
SD2016-15	146.39	0.40	1.11	0.70	8427.27	0.02	0.68	0.20	0.24	42.32
SD2016-16	133.39	0.36	0.95	0.87	7633.54	0.02	0.58	0.25	0.27	34.29
SD2016-18	68.23	0.20	0.66	0.32	7280.26	0.01	0.42	0.09	0.08	24.97
SD2016-20	159.36	0.19	0.64	0.32	7229.73	<DL	0.39	0.08	0.09	24.36
SD2016-21	254.71	0.28	0.76	0.43	8740.91	0.06	0.46	0.12	0.52	27.93
SD2016-23	121.04	0.20	0.68	0.41	4647.46	0.01	0.43	0.11	0.16	26.55
SD2016-25	135.53	0.10	0.37	0.20	4053.35	0.01	0.23	0.06	0.33	14.43
SD2016-27	139.25	0.31	0.47	0.89	4219.21	0.01	0.26	0.22	0.25	15.87
SD2016-29	131.93	0.44	0.59	1.76	5339.39	0.18	0.30	0.49	0.61	20.02
SD2016-30	145.21	0.46	1.21	0.84	8870.33	0.01	0.77	0.20	0.18	46.71
SD2016-34	126.96	0.11	0.40	0.20	4221.63	0.01	0.25	0.06	0.31	15.16
SD2016-36	232.37	0.38	0.62	1.52	6426.79	0.07	0.32	0.40	0.21	20.63
SD2016-37	168.32	0.14	0.46	0.22	5089.40	0.01	0.30	0.08	0.18	18.13
SD2016-41	265.59	0.07	0.27	0.11	3069.85	0.25	0.17	0.05	0.15	10.48
SD2016-43	257.88	0.23	0.71	0.49	4664.76	0.09	0.45	0.16	0.14	27.05
SP06-015-32	63.87	0.31	0.45	0.47	5688.12	0.01	0.20	0.12	0.43	14.04
SP06-015-33	69.62	0.32	0.50	0.46	6097.75	0.01	0.23	0.12	0.81	15.58
SP05-006-34	38.04	0.05	0.26	0.08	2952.66	0.07	0.16	0.02	0.39	10.09
SP06-006-37	23.76	0.09	0.38	0.14	3808.04	0.06	0.24	0.04	0.29	14.53
SP06-004-39	67.54	0.06	0.31	0.10	3238.19	0.05	0.20	0.03	0.25	11.94
SP06-003-40	35.67	0.24	0.41	0.37	5241.47	0.01	0.19	0.09	0.72	12.56
SP04-007-42	20.15	0.07	0.21	0.13	1654.32	0.03	0.13	0.03	0.14	7.74
SP04-007-43	12.74	0.05	0.17	0.11	1614.99	0.02	0.11	0.03	0.10	5.92
SP04-007-44	14.58	0.05	0.17	0.10	1564.67	0.03	0.11	0.04	0.12	6.86

Sample ID	Yb	Zn	Zr	Zr/Y	La/Yb	Th/Yb	Nd/Sm	La/Nb	Dy/Yb	Zr/Ti
SD201602	0.13	57.20	6.00	6.00	3.05	0.60	3.61	2.94	1.56	0.02
SD2016-08	0.74	86.67	13.56	2.02	0.91	0.05	2.87	1.79	1.68	0.01
SD2016-09	0.92	91.29	14.21	1.66	0.83	0.06	2.71	1.54	1.70	0.01
SD2016-11	0.56	84.09	12.37	2.62	1.37	0.10	3.07	1.52	1.47	0.01
SD2016-14	2.78	102.92	66.52	2.71	1.38	0.10	3.15	1.26	1.59	0.01
SD2016-15	4.44	107.98	130.97	3.10	1.97	0.16	3.41	1.46	1.68	0.02
SD2016-16	3.83	101.89	118.08	3.44	2.07	0.23	3.46	1.43	1.62	0.02
SD2016-18	2.70	88.75	74.67	2.99	1.47	0.12	3.18	1.25	1.65	0.01
SD2016-20	2.52	98.72	67.59	2.77	1.51	0.13	3.21	1.32	1.71	0.01
SD2016-21	2.97	57.21	90.61	3.24	2.03	0.15	3.28	1.41	1.68	0.01
SD2016-23	2.79	76.28	69.63	2.62	1.70	0.15	3.18	1.56	1.64	0.01
SD2016-25	1.58	45.78	36.65	2.54	1.22	0.12	3.16	1.16	1.62	0.01
SD2016-27	1.68	75.15	101.85	6.42	5.09	0.53	4.20	1.89	1.78	0.02
SD2016-29	1.99	81.88	143.46	7.17	6.49	0.89	4.51	2.06	1.84	0.03
SD2016-30	5.03	28.55	152.86	3.27	2.49	0.17	3.67	1.99	1.64	0.02
SD2016-34	1.64	46.51	37.03	2.44	1.35	0.12	3.05	1.32	1.62	0.01
SD2016-36	2.10	74.05	132.89	6.44	5.51	0.73	4.26	2.22	1.82	0.02
SD2016-37	1.97	54.03	46.51	2.56	1.38	0.11	3.07	1.31	1.62	0.01
SD2016-41	1.14	48.91	25.49	2.43	1.43	0.10	3.04	1.41	1.65	0.01
SD2016-43	2.96	39.74	79.48	2.94	1.80	0.16	3.35	1.48	1.61	0.02
SP06-015-32	1.35	49.06	60.55	4.31	1.83	0.35	3.42	0.53	2.08	0.01
SP06-015-33	1.44	56.61	61.41	3.94	3.05	0.32	3.46	0.90	2.13	0.01
SP05-006-34	1.08	78.70	20.92	2.07	1.06	0.08	2.86	1.33	1.68	0.01
SP06-006-37	1.55	87.75	37.65	2.59	1.34	0.09	3.04	1.46	1.68	0.01
SP06-004-39	1.29	82.21	27.76	2.32	1.11	0.08	2.89	1.42	1.65	0.01
SP06-003-40	1.21	50.60	47.31	3.77	2.81	0.30	3.56	0.93	2.09	0.01
SP04-007-42	0.89	80.88	22.01	2.84	2.04	0.15	3.48	1.83	1.60	0.01
SP04-007-43	0.69	89.82	22.51	3.80	1.85	0.17	3.19	1.58	1.61	0.01
SP04-007-44	0.77	91.27	18.90	2.76	1.66	0.13	3.13	1.53	1.54	0.01

Sample ID	Nb/Y	La/Sm_{cn}	La/Yb_{cn}	Gd/Yb_{cn}	Nb/Nb*	Zr/Zr*	Ti/Ti*	Eu/Eu*	Ce/Ce*
SD2016 02	0.14	1.53	2.19	1.33	0.18	1.11	0.70	0.51	0.82
SD2016-08	0.06	0.61	0.65	1.10	0.54	0.66	0.89	1.09	1.02
SD2016-09	0.06	0.53	0.60	1.17	0.58	0.55	0.79	0.96	1.02
SD2016-11	0.11	1.01	0.99	0.99	0.57	0.85	0.85	0.99	1.00
SD2016-14	0.12	0.89	0.99	1.09	0.69	0.80	1.06	1.01	1.04
SD2016-15	0.14	1.10	1.41	1.19	0.57	0.82	0.60	0.78	1.02
SD2016-16	0.16	1.19	1.48	1.18	0.50	0.87	0.64	0.81	1.00
SD2016-18	0.13	0.90	1.05	1.13	0.66	0.87	0.92	0.89	1.02
SD2016-20	0.12	0.93	1.08	1.19	0.61	0.84	0.95	0.95	1.03
SD2016-21	0.15	1.11	1.46	1.26	0.62	0.84	0.90	1.01	1.01
SD2016-23	0.11	1.06	1.22	1.17	0.51	0.80	0.57	0.93	1.04
SD2016-25	0.11	0.86	0.87	1.08	0.63	0.84	0.96	1.08	1.07
SD2016-27	0.28	2.06	3.65	1.42	0.39	1.10	0.62	0.95	1.08
SD2016-29	0.31	2.29	4.65	1.52	0.31	1.10	0.60	0.89	1.12
SD2016-30	0.13	1.46	1.78	1.15	0.46	0.86	0.58	1.08	1.14
SD2016-34	0.11	0.91	0.97	1.14	0.59	0.80	0.92	1.02	1.08
SD2016-36	0.25	2.09	3.95	1.52	0.29	1.07	0.71	1.00	1.09
SD2016-37	0.11	0.92	0.99	1.10	0.62	0.83	0.94	0.97	1.04
SD2016-41	0.11	0.95	1.03	1.11	0.63	0.78	0.96	1.12	1.00
SD2016-43	0.13	1.15	1.29	1.11	0.53	0.86	0.56	0.80	1.09
SP06-015-32	0.33	0.62	1.32	1.75	1.02	0.75	0.86	0.88	1.06
SP06-015-33	0.31	0.95	2.19	1.90	0.80	0.65	0.79	0.95	1.03
SP05-006-34	0.09	0.68	0.76	1.11	0.65	0.67	0.96	1.09	1.03
SP06-006-37	0.10	0.84	0.96	1.13	0.61	0.80	0.85	1.09	1.02
SP06-004-39	0.08	0.73	0.80	1.12	0.63	0.77	0.90	0.99	0.97
SP06-003-40	0.29	0.94	2.02	1.80	0.76	0.64	0.86	0.93	1.08
SP04-007-42	0.13	1.28	1.46	1.11	0.48	0.76	0.64	0.93	1.05
SP04-007-43	0.14	1.22	1.33	1.12	0.49	1.11	0.84	0.85	0.97
SP04-007-44	0.12	1.13	1.19	1.06	0.55	0.86	0.75	0.90	0.94

Appendix 1.3. Standard and duplicate analyses results for the Haines Gabbroic Complex and Shebandowan greenstone belt.

	LIMS ID	Ba	Be	Bi	Cd	Ce	Co
	Unit	ppm	Ppm	ppm	Ppm	ppm	Ppm
	LLoD	0.8	0.04	0.47	0.013	0.12	0.13
	UL	1740	360	47	4	2420	187
17-0038-0002	SD2016-08	3.1552	0.1909	0.154	0.0294	2.0538	96.3106
17-0038-0003	SD2016-09	2.9878	0.1794	<DL	0.0438	2.4152	90.9729
17-0038-0004	SD2016-11	2.8911	0.1594	<DL	<DL	1.977	130.1738
17-0038-0005	SD2016-14	31.7419	0.4574	<DL	0.138	10.5358	50.9761
17-0038-0006	SD2016-15	28.5554	0.6511	<DL	0.1159	22.8582	47.9653
17-0038-0007	SD2016-16	39.7737	0.7182	<DL	0.1893	19.7917	45.2824
17-0038-0008	SD2016-18	27.2052	0.4486	<DL	0.0935	10.8674	47.2445
17-0038-0009	SD2016-20	22.9552	0.5228	<DL	0.104	10.4538	51.9908
17-0038-0010	SD2016-21	95.7688	0.7185	<DL	0.0401	15.3964	40.3133
17-0038-0010D	SD2016-21 DUP	95.1714	0.7508	<DL	0.0368	15.4501	40.5376
MRB-29	QC-IHST	290.0222	1.0271	<DL	0.0949	48.097	49.2004
BHVO-2	QC-INST	133.7766	1.1177	<DL	0.0958	36.4867	45.7754
BLANK	QC-BLANK	<DL	0.0595	<DL	<DL	<DL	<DL
17-0038-0011	SD2016-23	29.3156	0.5666	<DL	0.0865	12.3954	40.3935
17-0038-0012	SD2016-25	21.2587	0.3752	<DL	0.0293	5.6658	44.2576
17-0038-0013	SD2016-27	32.2161	0.6083	<DL	0.0245	20.8051	40.6203
17-0038-0014	SD2016-29	113.9653	0.7637	<DL	0.0693	32.0395	27.0459
17-0038-0015	SD2016-30	178.7201	0.8043	<DL	0.021	34.9593	23.1213
17-0038-0016	SD2016-34	23.8155	0.287	<DL	0.0679	6.3113	36.393
17-0038-0017	SD2016-36	372.8202	0.6782	<DL	0.0621	28.2496	29.3277
17-0038-0018	SD2016-37	20.4611	0.3201	<DL	0.0385	7.318	44.3915
17-0038-0019	SD2016-41	123.4115	0.2519	<DL	0.0553	4.2191	36.0689
17-0038-0020	SD2016-43	114.34	0.4486	<DL	0.0417	14.7079	39.6243
17-0038-0020D	SD2016-43 DUP	113.2701	0.4879	<DL	0.044	14.4301	39.922
17-0038-0021	SP04-002-1	13.9146	0.2197	<DL	0.0214	5.0683	21.3312
17-0038-0022	SP04-002-4	75.2239	0.4706	<DL	0.0363	2.077	6.282
17-0038-0023	SP04-002-5	3.8102	0.1229	<DL	0.0317	2.9388	12.9272
17-0038-0024	SP04-002-6	6.833	0.3577	<DL	0.0551	3.7833	14.3789
17-0038-0025	SP04-002-8	12.0096	0.1913	<DL	0.0479	1.6994	34.7576
17-0038-0026	SP04-002-11	70.0435	0.9129	<DL	0.0145	1.0209	10.9936
17-0038-0027	SP04-002-13	5.2471	0.1497	<DL	0.0451	1.6815	39.3082
17-0038-0028	SP04-002-14	25.1561	0.2023	<DL	0.0142	2.711	26.5241
17-0038-0029	SP04-002-15	18.0755	0.1553	<DL	0.0387	1.3787	36.1971
17-0038-0030	SP04-002-16	18.3174	0.1801	<DL	0.0353	1.5035	32.8577
17-0038-0030D	SP04-002-16 DUP	18.9468	0.1718	<DL	0.0443	1.4459	33.3384

Cr	Cs	Cu	Dy	Er	Eu	Ga	Gd	Hf	Ho
ppm	ppm	ppm	ppm	ppm	ppm	ppm	Ppm	ppm	Ppm
3	0.013	1.4	0.009	0.007	0.0031	0.04	0.009	0.14	0.0025
4500	600	2900	135	87	19	58	118	29	29
1990.65	0.2435	79.2164	1.2506	0.7835	0.3023	8.3364	0.9899	0.412	0.264
2046.83	0.3881	61.2985	1.5593	0.9923	0.3456	9.2388	1.3	0.4496	0.3346
3004.13	0.4365	5.0822	0.8198	0.5592	0.1851	3.9269	0.6673	0.3432	0.1747
257.9991	0.1842	131.6752	4.4317	2.8281	1.0575	18.7587	3.6617	1.9205	0.9476
47.3414	0.1486	124.4674	7.4781	4.6498	1.4642	20.3222	6.4064	3.6423	1.5908
44.2308	0.2157	125.0325	6.2086	3.9306	1.2957	18.7747	5.4781	3.3548	1.3282
66.2709	0.3295	129.6617	4.4449	2.8248	0.9468	15.4002	3.6775	2.1354	0.9548
59.0609	0.1204	157.4727	4.3055	2.7365	0.9626	17.6614	3.6256	1.9313	0.9208
104.8834	2.4177	7.2613	4.9907	3.1152	1.3207	18.0762	4.5292	2.4282	1.0541
105.0453	2.3991	7.2873	5.1201	3.1493	1.2842	18.091	4.4258	2.4878	1.0774
268.1984	0.2388	148.6821	5.4555	2.8528	1.9144	19.1832	6.1088	4.6374	1.0689
306.7754	0.0988	133.2767	5.5369	2.6123	2.1187	21.2866	6.5108	4.4728	1.011
<DL	<DL	<DL	<DL	<DL	<DL	<DL	<DL	<DL	<DL
66.1512	0.2014	152.553	4.5858	2.9107	1.0252	18.9972	3.94	1.9069	0.9728
382.1641	0.1154	84.596	2.5582	1.63	0.6118	15.0702	2.0528	1.0632	0.545
350.2899	0.2116	55.5007	2.9788	1.7744	0.8658	15.6051	2.8722	2.5926	0.6079
57.1382	4.5116	12.4585	3.6571	2.1431	1.0601	13.7824	3.6382	3.6154	0.7431
12.8924	0.1652	2.4328	8.2314	5.1879	2.2015	16.0991	7.0029	4.3359	1.7874
363.4673	0.1051	181.706	2.657	1.7501	0.63	14.2206	2.2512	1.0463	0.588
48.9579	1.7911	30.8924	3.8284	2.2672	1.2147	19.3247	3.854	3.5161	0.7733
332.6657	0.1016	46.0407	3.1955	2.0615	0.7082	15.6702	2.6122	1.3361	0.6928
685.6766	4.4442	72.9797	1.8785	1.1969	0.4804	14.5301	1.5242	0.7308	0.3968
498.9879	0.7969	30.7623	4.7694	3.0783	0.9019	14.0694	3.9583	2.2616	1.0272
497.2086	0.8012	31.114	4.724	3.0517	0.8985	14.1768	3.9112	2.2269	1.0074
95.8485	0.0648	23.5044	1.8438	1.2161	0.5239	18.8471	1.596	0.7439	0.4067
22.71	0.3065	2.2305	0.5635	0.3503	0.3897	20.0013	0.4771	0.2913	0.1157
38.5656	0.0186	3.5026	1.2156	0.783	0.4881	22.3334	1.0076	0.5307	0.2626
30.2921	0.0157	104.7784	1.3528	0.8237	0.4879	21.2615	1.1359	0.5391	0.2763
132.9112	0.1958	59.8042	1.2128	0.7946	0.3463	14.8807	0.8964	0.2261	0.2608
28.1571	0.111	4.8827	0.4663	0.2876	0.106	6.9697	0.3179	0.2647	0.0973
157.8451	0.034	36.6625	1.3081	0.8946	0.3622	13.7857	0.9853	0.311	0.2945
83.4187	0.2673	20.9322	1.1472	0.7954	0.3998	16.1266	0.9604	0.4211	0.2495
147.9435	0.1599	30.6763	1.2211	0.798	0.4568	13.6848	0.9378	0.2286	0.2683
134.5835	0.2314	30.81	1.0671	0.7412	0.3582	14.5418	0.8024	0.2204	0.2473
134.9278	0.2399	31.0666	1.0725	0.7198	0.3581	14.5196	0.8187	0.2172	0.2413
280.6714	0.2481	156.5265	5.3387	2.7919	1.8705	19.6982	5.9141	4.4194	1.0402

In	La	Li	Lu	Mo	Nb	Nd	Ni	Pb	Pr
ppm	ppm	Ppm	ppm	ppm	ppm	ppm	Ppm	ppm	Ppm
0.0018	0.1	0.4	0.002	0.08	0.028	0.06	0.7	0.18	0.014
1.9	1380	207	9	44	277	760	4100	700	240
0.0347	0.6775	10.2448	0.1181	0.1236	0.3794	2.0525	1581.923	0.7609	0.3622
0.0403	0.7641	19.6622	0.1431	0.088	0.4966	2.5175	1225.654	<DL	0.4415
0.0205	0.7661	1.8825	0.0913	0.1046	0.5054	1.5119	1137.958	<DL	0.3097
0.0878	3.8384	15.2166	0.4275	0.317	3.0532	8.7447	66.5462	<DL	1.6155
0.1028	8.7496	18.0647	0.6843	0.7871	5.9828	17.513	38.4282	1.2945	3.4361
0.0978	7.9063	23.9839	0.5632	0.5269	5.5254	14.8749	39.1805	2.093	2.9819
0.0772	3.9523	14.087	0.4214	0.2995	3.1661	9.0509	55.2951	<DL	1.7243
0.0768	3.8102	18.187	0.3957	0.2506	2.882	8.5086	72.16	0.7945	1.6188
0.0819	6.0259	21.6065	0.455	0.2688	4.2811	11.5182	68.0468	1.3392	2.3057
0.0814	6.0557	21.6644	0.4556	0.2266	4.3126	11.6286	68.4548	1.3577	2.3087
0.0744	21.7009	9.478	0.3648	0.8544	12.3202	28.61	106.9956	5.1239	6.5169
0.0855	15.4965	4.6068	0.2835	4.0494	17.6908	25.758	121.7914	2.1395	5.4743
<DL	<DL	<DL	<DL	<DL	<DL	<DL	<DL	<DL	<DL
0.0764	4.729	9.4761	0.4282	0.1926	3.0358	9.1335	66.951	<DL	1.8156
0.0416	1.9199	18.3436	0.2424	0.2747	1.6494	4.5793	138.2411	1.1717	0.8723
0.0414	8.5251	31.7949	0.2553	0.4938	4.5071	11.1944	261.2164	1.0608	2.599
0.0429	12.8796	22.3114	0.3027	1.4083	6.2535	16.3738	73.3166	1.7466	3.841
0.068	12.5195	6.6716	0.7628	0.24	6.2775	20.2716	38.3699	0.6249	4.4842
0.0492	2.2118	8.6592	0.2546	0.4229	1.6797	4.7731	96.2837	0.8519	0.9207
0.0581	11.5627	16.7846	0.3195	0.8765	5.2115	15.2166	44.1655	2.4992	3.4719
0.0583	2.7183	9.3552	0.2964	0.4565	2.0779	5.8257	100.8443	1.1492	1.0957
0.035	1.6316	32.4236	0.1718	0.2659	1.1536	3.3868	116.1423	<DL	0.6506
0.0588	5.3204	13.209	0.4452	0.3095	3.6007	9.9921	78.1911	1.3929	2.0564
0.0583	5.3078	13.4619	0.4519	0.2918	3.5733	9.8465	77.3345	1.2672	1.9796
0.0177	1.9947	3.6991	0.181	1.5851	1.4149	3.9704	43.4034	<DL	0.803
0.0086	0.9729	1.9603	0.0506	0.4664	0.5176	1.5892	15.5019	1.0336	0.3064
0.0199	1.1604	2.1481	0.1152	0.3992	0.8405	2.5288	20.7937	0.7548	0.5098
0.0158	1.619	2.771	0.113	0.3021	0.9576	2.8994	24.4125	1.1791	0.6094
0.0286	0.7156	5.6158	0.1148	0.2629	0.2356	1.7466	94.3205	<DL	0.3273
0.0077	0.4566	2.0328	0.0365	0.7506	0.3395	0.8235	15.5692	0.736	0.1604
0.0306	0.7004	3.3599	0.1324	0.2955	0.2556	1.7443	105.6782	<DL	0.327
0.0233	1.1189	5.1256	0.119	0.3168	0.5411	2.1759	67.9365	<DL	0.4212
0.0298	0.5676	10.0863	0.1303	0.2809	0.1566	1.5052	101.6581	0.7097	0.2621
0.0246	0.5876	8.0034	0.1107	0.185	0.1602	1.4341	96.1923	0.7022	0.2629
0.0259	0.5828	8.0833	0.1125	0.1888	0.1784	1.594	96.564	0.7154	0.2621
0.0715	21.7511	10.2044	0.3468	0.8802	12.6744	27.9554	111.643	4.6878	6.4351

Rb	Sb	Sc	Sm	Sn	Sr	Ta	Tb	Th	Ti
ppm	ppm	ppm	ppm	Ppm	ppm	ppm	ppm	ppm	Ppm
0.11	0.04	1.1	0.026	0.16	0.6	0.007	0.0023	0.018	7
3800	28	63	128	14	1560	320	21	109	25000
0.8825	0.1134	24.0978	0.7164	0.3147	15.3252	0.0297	0.1869	0.0397	1827.781
1.8755	0.0797	24.7301	0.9281	0.3442	15.4588	0.03	0.2365	0.0539	2132.417
1.8567	<DL	13.2907	0.4921	0.264	4.0325	0.032	0.1231	0.0565	1184.698
0.4886	0.0741	55.3997	2.7773	0.7586	92.4017	0.1943	0.6553	0.2819	8269.173
1.0835	0.3435	41.4297	5.132	1.4283	146.3891	0.4017	1.1137	0.7002	8427.267
1.6089	0.5521	40.6698	4.2962	2.68	133.3876	0.3616	0.9538	0.8697	7633.543
0.8876	0.1283	44.6774	2.8478	0.7196	68.2314	0.2046	0.6601	0.3238	7280.259
1.0251	0.1338	42.2364	2.653	1.3443	159.3596	0.1934	0.6437	0.3242	7229.729
16.7283	0.4994	32.0482	3.5099	1.4888	254.711	0.2775	0.7589	0.433	8740.908
17.023	0.4866	32.077	3.4732	1.6137	253.7104	0.2786	0.7574	0.4437	8863.935
13.7766	0.053	30.3059	6.3299	2.6723	302.7322	0.8145	0.9189	2.6006	11006.57
9.7285	0.0943	31.9571	6.278	1.98	403.6106	1.1514	0.9757	1.2251	16965.63
<DL	<DL	<DL	<DL	<DL	<DL	<DL	<DL	<DL	<DL
2.5421	0.2059	42.3253	2.8765	0.7627	121.0373	0.1953	0.6755	0.4082	4647.464
3.2595	0.4019	35.2049	1.4493	0.4546	135.5326	0.1013	0.371	0.1958	4053.35
5.2378	0.2551	21.3034	2.666	0.9458	139.2475	0.3108	0.4712	0.8878	4219.208
51.0115	0.0742	21.2363	3.6278	1.0384	131.9345	0.442	0.5934	1.7636	5339.388
4.7724	0.2496	41.2459	5.5211	2.8524	145.2059	0.4597	1.2096	0.8354	8870.333
2.532	0.1682	39.9306	1.5637	0.6195	126.9566	0.11	0.4019	0.2045	4221.633
28.2638	0.0552	23.9015	3.574	1.2621	232.3709	0.3763	0.6153	1.5239	6426.793
1.8682	0.1178	40.5943	1.8995	0.6364	168.3155	0.1377	0.4613	0.2247	5089.395
37.0778	<DL	30.792	1.1132	0.4432	265.5917	0.071	0.2717	0.1131	3069.845
23.932	0.2115	38.2797	2.9805	0.9492	257.8785	0.2343	0.7076	0.4877	4664.758
23.7907	0.1434	38.2914	2.9481	0.9589	258.7802	0.2267	0.7063	0.5088	4668.845
0.8008	0.1183	18.4518	1.2638	0.5031	169.0652	0.0899	0.2759	0.1479	2075.614
7.9148	0.711	5.0563	0.422	0.3845	189.0004	0.0353	0.083	0.0662	770.1144
0.2944	0.57	11.2662	0.7866	0.4872	165.5197	0.0523	0.1774	0.106	1441.651
0.3121	1.545	11.2575	0.8619	0.4036	186.9727	0.0643	0.1957	0.1097	1538.114
1.6208	0.2696	32.9079	0.632	0.3527	119.0221	<DL	0.1666	0.0411	1152.644
4.5464	0.046	7.6314	0.2429	0.3794	103.463	0.0246	0.0614	0.1384	622.5706
0.4616	0.2585	38.3247	0.6492	0.3129	99.4785	<DL	0.1813	0.0393	1321.154
2.897	0.2554	22.3321	0.6659	0.4591	132.5517	0.0352	0.1655	0.0705	1227.652
1.5734	0.1564	34.2429	0.6039	0.3059	80.9401	<DL	0.1692	0.026	1099.417
1.8833	0.1927	30.5071	0.5374	0.3079	105.7418	<DL	0.1508	0.0228	1059.755
1.9375	0.1941	31.0522	0.5258	0.2935	106.022	<DL	0.1535	<DL	1056.274
14.727	0.0571	32.3407	6.0923	2.6992	306.7111	0.8068	0.8876	2.608	11603.31

Tl	Tm	U	V	W	Y	Yb	Zn	Zr	
Ppm	ppm	ppm	ppm	ppm	ppm	ppm	ppm	ppm	
0.002	0.0019	0.011	0.8	0.05	0.05	0.009	1.8	6	
20	13	1620	370	141	740	70	9100	1450	Comments
0.0078	0.1121	0.0243		0.2369	6.7048	0.7444	86.6713	13.5621	**Cr correction on V**
0.0152	0.1438	0.0317		0.2132	8.5651	0.9155	91.2881	14.2067	**Cr correction on V**
<DL	0.0837	0.0178		0.0736	4.7187	0.5573	84.0914	12.3734	**Cr correction on V**
0.0144	0.4128	0.0742	>UL	0.0662	24.5669	2.7826	102.9207	66.5224	
0.0222	0.6795	0.2022	338.925	0.2379	42.3169	4.4402	107.9754	130.9717	
0.0163	0.5768	0.2509	327.919	0.2706	34.2881	3.8272	101.8938	118.0772	
0.005	0.4194	0.0864	337.1889	0.0839	24.9657	2.695	88.7511	74.666	
<DL	0.3919	0.0791	351.7928	0.0914	24.3593	2.5204	98.7158	67.589	
0.0627	0.4557	0.1234	282.3585	0.5181	27.9335	2.9706	57.2083	90.6108	
0.0653	0.4637	0.1323	284.4047	0.5295	28.3119	2.9533	56.9311	92.0505	
0.0657	0.4007	0.6253	302.5962	0.2104	26.5763	2.5134	105.9996	167.9015	
0.0187	0.3391	0.4263	310.6714	0.2162	26.507	2.0307	91.3419	175.238	
<DL	<DL	<DL	<DL	<DL	<DL	<DL	<DL	<DL	
0.0131	0.43	0.1105	198.7824	0.1576	26.5469	2.7884	76.2795	69.6263	
0.0132	0.2327	0.0563	234.1734	0.3281	14.4253	1.5773	45.7809	36.6533	
0.0127	0.2557	0.2244	150.3439	0.2487	15.8669	1.6756	75.1477	101.8526	
0.1809	0.3034	0.486	143.4913	0.6095	20.0195	1.9856	81.883	143.461	
0.0081	0.7678	0.1982	263.3596	0.1833	46.7113	5.032	28.5529	152.8645	
0.0099	0.2497	0.0585	252.3662	0.3083	15.1626	1.6407	46.513	37.03	
0.0665	0.3162	0.4002	201.7232	0.2131	20.6293	2.0979	74.0492	132.8926	
0.0052	0.3005	0.075	285.4029	0.1764	18.1333	1.9697	54.0346	46.5063	
0.2455	0.1694	0.0492	187.8679	0.1486	10.4839	1.1385	48.9105	25.4911	
0.0911	0.4512	0.159	225.5394	0.1437	27.0489	2.9578	39.7403	79.4826	
0.0894	0.4428	0.163	229.1882	0.1489	26.9764	2.8701	39.8162	79.5483	
<DL	0.1746	0.0504	92.1927	0.2595	11.6841	1.1865	32.961	26.9846	
0.0509	0.0523	0.0248	31.9647	0.2362	3.158	0.3429	10.3728	10.7112	
<DL	0.114	0.0327	71.4502	0.3196	7.3663	0.7686	11.0529	19.0276	
<DL	0.1184	0.0326	68.7422	0.5017	7.4774	0.7401	13.0837	18.4638	
0.011	0.1158	<DL	113.1141	0.1152	7.0659	0.78	44.2425	6.7147	
0.0305	0.0438	0.0879	21.3537	1.1894	2.4978	0.2678	10.4891	9.0691	
0.0053	0.131	0.0117	131.7884	0.1555	7.8298	0.8748	52.5668	9.4363	
0.0217	0.1122	0.0208	88.2695	0.1833	6.5111	0.7858	31.6887	13.6807	
0.0136	0.1156	<DL	116.2801	0.2148	6.7877	0.8265	45.175	6.1766	
0.0139	0.1087	<DL	106.7474	0.1914	6.1572	0.7342	41.3096	6.3571	
0.0158	0.1088	<DL	107.4202	0.1716	6.0506	0.7298	41.0466	6.0485	
0.0677	0.389	0.6322	316.4571	0.1988	27.0755	2.4761	104.5975	170.8978	

	LIMS ID	Ba	Be	Bi	Cd	Ce	Co
	Unit	Ppm	ppm	ppm	ppm	ppm	Ppm
	LLoD	0.8	0.04	0.47	0.013	0.12	0.13
	UL	1740	360	47	4	2420	187
AGV-2	QC-INST	1142.575	2.1177	<DL	0.0896	69.1714	15.8928
BLANK	QC-BLANK	<DL	0.0716	<DL	<DL	<DL	<DL
17-0038-0031	SP04-002-17	9.6238	0.3026	<DL	0.0294	2.0668	33.7878
17-0038-0032	SP04-002-20	70.9495	0.4356	<DL	0.0421	1.4396	33.9218
17-0038-0033	SP04-002-21	49.0624	1.0176	<DL	0.0912	47.3903	41.4232
17-0038-0034	SP04-002-23	3.6039	0.2724	<DL	0.1364	5.5909	18.5288
17-0038-0035	SP04-002-24	2.6091	0.2072	<DL	0.1463	4.0082	24.7762
17-0038-0036	SP04-002-25	11.8031	0.2961	<DL	0.0612	1.8253	48.6726
17-0038-0037	SP04-002-26	12.2227	0.3701	<DL	0.0338	6.3282	15.0842
17-0038-0038	SP04-002-27	25.4739	0.2605	<DL	0.0779	2.6613	46.6991
17-0038-0039	SP04-002-29	17.905	0.3407	<DL	0.0535	3.8527	19.8425
17-0038-0040	SP04-002-30	4.0516	0.1629	<DL	0.0506	1.5366	14.0234
17-0038-0040D	SP04-002-30 DUP	4.2935	0.1608	<DL	0.0569	1.6598	13.812
17-0038-0041	SP04-002-31	5.9945	0.2844	<DL	0.031	1.6533	17.3918
17-0038-0042	SP06-015-32	8.809	0.6025	<DL	0.0918	8.7826	86.6474
17-0038-0043	SP06-015-33	9.8576	0.7225	<DL	0.0791	12.8461	75.7208
17-0038-0044	SP05-006-34	76.3757	0.4109	<DL	0.0793	3.3599	73.7793
17-0038-0045	SP06-006-37	55.2953	0.3929	<DL	0.0711	5.612	73.953
17-0038-0046	SP06-004-39	104.6097	0.3535	<DL	0.344	3.8689	74.3189
17-0038-0047	SP06-003-40	9.6929	0.5456	<DL	0.0698	10.4534	61.2192
17-0038-0048	SP04-007-42	6.5341	0.2123	<DL	0.0317	4.6615	108.6512
17-0038-0049	SP04-007-43	7.6879	0.1962	<DL	<DL	3.0356	121.0311
17-0038-0050	SP04-007-44	5.4152	0.3038	<DL	0.0378	2.9193	121.2613
17-0038-0050D	SP04-007-44 DUP	5.4868	0.3516	<DL	0.0335	3.1074	119.4457
MRB-29	QC-IHST	290.0937	1.0818	<DL	0.11	47.679	49.9229
GSP-2	QC-INST	1365.336	1.5199	<DL	0.1402	430.1568	7.1928
BLANK	QC-BLANK	<DL	<DL	<DL	<DL	<DL	<DL

Cr	Cs	Cu	Dy	Er	Eu	Ga	Gd	Hf	Ho
ppm	ppm	ppm	ppm	Ppm	ppm	ppm	ppm	ppm	Ppm
3	0.013	1.4	0.009	0.007	0.0031	0.04	0.009	0.14	0.0025
4500	600	2900	135	87	19	58	118	29	29
16.8217	1.1526	51.7184	3.5745	1.8084	1.5515	20.43	4.526	5.0922	0.6682
<DL	<DL	<DL	<DL	<DL	<DL	<DL	<DL	<DL	<DL
141.4792	0.1931	15.8424	1.346	0.8508	0.3464	14.6562	1.0514	0.3552	0.2807
130.1266	1.4627	226.3938	1.1266	0.7792	0.2361	12.9024	0.8562	0.303	0.2536
404.1734	0.2177	108.6027	2.4713	1.1649	1.258	11.4463	3.8764	2.1739	0.4326
56.5816	0.0138	170.4947	1.8075	1.1541	0.5536	18.0579	1.5469	0.8377	0.3825
72.6984	0.0138	168.1882	1.7081	1.1371	0.554	18.6561	1.4618	0.6625	0.38
164.4849	0.4916	117.5635	1.4062	0.9669	0.3335	12.8558	1.0801	0.2983	0.3052
26.4295	0.0922	39.7743	1.8027	1.09	0.5441	18.8012	1.5226	0.646	0.3711
196.1627	0.2703	90.681	1.8409	1.1954	0.4115	12.0203	1.4023	0.4324	0.4027
44.6318	0.0722	85.6372	1.4778	0.9004	0.4924	19.1974	1.3015	0.5177	0.3155
61.3716	<DL	12.5923	0.7092	0.4511	0.3914	21.402	0.6344	0.2023	0.1562
62.0612	0.0149	12.5174	0.7185	0.4747	0.3823	21.2942	0.5994	0.1895	0.1568
53.0881	0.015	11.3378	0.703	0.4301	0.3624	18.6976	0.5559	0.1982	0.1523
1752.98	0.1283	72.2546	2.7938	1.4896	0.777	11.1006	2.8406	1.6907	0.5421
1736.38	0.1286	56.1772	3.0808	1.7124	0.9829	11.8278	3.3208	1.6927	0.6183
1328.08	0.5068	77.6551	1.8133	1.1276	0.449	11.0731	1.4489	0.623	0.3784
1795.52	0.2819	12.0705	2.603	1.6347	0.657	12.0364	2.1218	1.1144	0.5734
1347.94	0.5663	89.8739	2.1225	1.3448	0.4788	11.7365	1.7413	0.8171	0.4511
1531.66	0.3032	50.5168	2.5311	1.3819	0.7549	10.1487	2.6383	1.3331	0.4823
2816.35	1.2528	4.0529	1.4318	0.9367	0.3211	5.6664	1.203	0.6528	0.3046
2961.2	1.0131	3.6133	1.1036	0.7083	0.2196	4.1915	0.9297	0.6455	0.2347
2948.34	1.3267	22.2907	1.1938	0.7369	0.2534	4.7747	0.9902	0.5415	0.2633
2941.05	1.3439	21.6343	1.1808	0.759	0.2594	4.7164	1.0061	0.5406	0.2549
268.4044	0.2362	149.1803	5.2374	2.8267	1.9114	19.6259	5.9838	4.4298	1.0444
21.2707	1.1831	45.4691	5.787	2.3089	2.3252	22.8686	11.9766	12.5897	0.9547
<DL	<DL	<DL	<DL	<DL	<DL	<DL	<DL	<DL	<DL

In	La	Li	Lu	Mo	Nb	Nd	Ni	Pb	Pr
Ppm	ppm	ppm	ppm	Ppm	ppm	ppm	ppm	ppm	Ppm
0.0018	0.1	0.4	0.002	0.08	0.028	0.06	0.7	0.18	0.014
1.9	1380	207	9	44	277	760	4100	700	240
0.0427	38.2714	9.7652	0.2415	2.2119	13.1421	30.8431	18.7932	12.7091	8.0812
<DL	<DL	<DL	<DL	<DL	<DL	<DL	<DL	<DL	<DL
0.0333	0.8093	4.6467	0.134	0.2138	0.3925	1.9126	120.8963	<DL	0.3565
0.027	0.5697	16.4141	0.1124	0.1516	0.3613	1.3175	110.7488	<DL	0.232
0.0341	19.2839	6.6382	0.1588	0.1112	12.0888	27.5033	230.8904	1.3713	6.5484
0.0278	2.1369	3.9704	0.157	0.4011	1.7243	4.3062	48.7598	<DL	0.855
0.027	1.4969	4.1101	0.1575	0.4024	1.3807	3.2121	62.9161	<DL	0.6493
0.0307	0.6602	4.8226	0.1436	0.2288	0.2776	1.8375	134.9828	<DL	0.3101
0.0172	2.4806	3.6755	0.159	0.4206	1.3636	4.4803	40.5773	<DL	0.9046
0.0392	0.9317	3.7895	0.1809	0.2735	0.4376	2.5285	146.06	1.0413	0.4391
0.0248	1.4207	4.3318	0.1324	0.3339	0.8938	3.1263	31.8651	<DL	0.6276
0.0128	0.6455	2.9656	0.0653	0.353	0.2273	1.3275	36.6974	<DL	0.2643
0.0149	0.6836	3.0696	0.0647	0.3184	0.2368	1.3259	37.0096	<DL	0.2653
0.015	0.7337	5.1455	0.0616	0.2117	0.2702	1.3815	41.5444	<DL	0.2678
0.0467	2.4682	1.8373	0.1954	0.1507	4.6501	8.8311	1329.937	<DL	1.6634
0.0581	4.4031	2.4825	0.209	2.2283	4.8796	10.3835	973.902	<DL	2.13
0.0483	1.1435	26.9623	0.1593	1.4078	0.8598	3.102	459.8651	1.1107	0.5584
0.0539	2.0745	23.3297	0.2385	0.1885	1.4185	4.8467	508.5703	<DL	0.8714
0.0431	1.4323	18.9322	0.1862	0.2242	1.0071	3.6396	445.3346	5.622	0.666
0.0548	3.4065	7.1139	0.1749	0.5784	3.6443	8.3046	928.5083	2.1541	1.6654
0.0316	1.8191	2.2051	0.1315	0.0962	0.996	3.1852	985.1107	0.8323	0.6562
0.025	1.2708	1.6703	0.1067	<DL	0.8026	2.141	1083.632	0.9513	0.4643
0.0252	1.2882	1.7408	0.1186	0.0937	0.8433	2.3066	1057.853	<DL	0.4494
0.0247	1.214	1.7191	0.1218	<DL	0.818	2.3351	1051.281	<DL	0.4466
0.0717	21.7822	9.9824	0.3532	0.8321	12.5074	28.1399	108.866	4.6686	6.4987
0.0484	181.858	34.4592	0.2172	2.2605	25.2786	204.1852	16.4892	40.3214	54.7005
<DL	<DL	<DL	<DL	<DL	<DL	<DL	<DL	<DL	<DL

Rb	Sb	Sc	Sm	Sn	Sr	Ta	Tb	Th	Ti
Ppm	ppm	ppm	ppm	ppm	ppm	ppm	ppm	ppm	Ppm
0.11	0.04	1.1	0.026	0.16	0.6	0.007	0.0023	0.018	7
3800	28	63	128	14	1560	320	21	109	25000
67.9602	0.4542	12.8378	5.5651	2.3158	644.3419	0.8317	0.6184	6.2273	6159.186
<DL	<DL	<DL	<DL	<DL	<DL	<DL	<DL	<DL	<DL
1.3731	0.2616	38.6865	0.6754	0.3508	114.8777	<DL	0.193	0.058	1364.62
65.9857	0.0775	32.6511	0.53	0.3164	51.0692	<DL	0.156	0.0385	1273.621
2.9934	0.171	16.0596	4.9778	0.7232	165.8189	0.6152	0.4815	2.5557	3571.368
0.2489	0.274	20.9948	1.2675	0.5674	149.7303	0.1073	0.2759	0.188	2465.248
<DL	0.2501	25.2689	1.069	0.4727	142.5025	0.0842	0.2532	0.1092	2278.311
2.1276	0.1534	43.9372	0.6836	0.3502	97.991	<DL	0.1975	0.0266	1468.332
0.9013	0.3432	12.2886	1.245	0.4633	178.6204	0.0945	0.2743	0.2338	1598.852
1.8258	0.1898	48.7746	0.9058	0.3921	117.5758	0.0282	0.259	0.0555	1763.646
2.3292	0.1124	16.9742	0.9941	0.4468	153.3049	0.0608	0.2211	0.0905	1596.862
0.2513	0.4107	14.1441	0.4519	0.419	170.7085	<DL	0.0998	0.0309	781.9105
0.2693	0.4078	15.095	0.4374	0.4302	173.1583	<DL	0.1086	0.0264	792.0706
<DL	0.3728	15.4413	0.4425	0.3154	152.1627	<DL	0.1008	0.0306	793.7307
0.5904	0.0689	21.6117	2.5816	0.7845	63.8669	0.3078	0.4459	0.4659	5688.115
0.5647	0.0658	27.9673	3.0039	0.9584	69.6156	0.3238	0.5013	0.4613	6097.747
11.1703	0.0693	33.2626	1.0864	0.5917	38.0416	0.0502	0.2618	0.0839	2952.661
9.9376	0.0543	33.2641	1.5956	0.6553	23.7626	0.0904	0.3816	0.1447	3808.04
14.5622	0.0721	36.0243	1.2593	0.4416	67.5384	0.0637	0.3131	0.0976	3238.185
1.3145	0.0726	27.6702	2.3356	1.0155	35.6731	0.2387	0.4149	0.3682	5241.467
3.4685	0.2483	16.2157	0.9166	0.5201	20.152	0.0657	0.2092	0.1298	1654.316
3.5525	0.2158	14.4918	0.671	0.4709	12.7416	0.0544	0.1668	0.1149	1614.989
3.5894	0.1607	15.3596	0.7378	0.4459	14.5785	0.0516	0.1736	0.0994	1564.666
3.561	0.1641	14.5462	0.7291	0.4016	14.1985	0.0541	0.1735	0.1014	1567.652
15.0549	0.0565	31.2743	6.2904	2.6806	310.3136	0.8104	0.8889	2.5748	11426.52
246.1832	0.3863	6.6359	25.9403	6.9966	236.5261	0.8634	1.2852	106.9958	3958.272
<DL	<DL	<DL	<DL	<DL	<DL	<DL	<DL	<DL	<DL

Tl	Tm	U	V	W	Y	Yb	Zn	Zr	
Ppm	ppm	ppm	ppm	ppm	ppm	ppm	ppm	ppm	
0.002	0.0019	0.011	0.8	0.05	0.05	0.009	1.8	6	
20	13	1620	370	141	740	70	9100	1450	Comments
0.2629	0.257	1.8788	120.4415	0.4804	19.1196	1.6597	84.067	227.9023	
<DL	<DL	<DL	<DL	<DL	<DL	<DL	<DL	<DL	
0.0075	0.1264	0.0157	137.3578	0.1178	7.6604	0.8749	40.9608	11.4717	
0.2678	0.113	0.0174	115.6038	0.3102	6.5693	0.7754	41.9103	9.8772	
0.0205	0.1637	0.2757	120.8921	0.4594	11.5129	1.0852	62.8113	105.6284	
<DL	0.1655	0.0504	111.8043	0.24	10.3476	1.0827	30.2182	29.7528	
0.0059	0.1576	0.0261	121.1219	0.1938	10.0164	1.0548	34.2186	23.5966	
0.0195	0.1408	0.0136	152.8717	0.0771	8.2089	0.9336	48.2867	9.35	
0.0076	0.1597	0.0586	65.0946	0.1763	10.2781	1.0725	20.5751	22.3617	
0.0111	0.1762	0.0134	175.0721	0.113	10.7508	1.1907	52.5163	13.3766	
0.0138	0.1309	0.0334	84.8264	0.2187	8.7142	0.9108	21.0921	18.7711	
<DL	0.0669	<DL	61.9219	0.1277	4.2225	0.4343	19.934	6.376	
<DL	0.0662	<DL	62.3862	0.1389	4.2406	0.4261	19.3253	6.4125	
<DL	0.0635	<DL	60.5342	0.0934	3.9599	0.4262	21.5615	6.6253	
0.005	0.2044	0.1188		0.4332	14.0407	1.346	49.0575	60.5524	**Cr correction on V**
0.0051	0.2325	0.1242		0.8143	15.5773	1.4445	56.6137	61.4055	**Cr correction on V**
0.068	0.1643	0.0231		0.3882	10.0906	1.0805	78.6981	20.9159	**Cr correction on V**
0.0571	0.2364	0.0409		0.291	14.5272	1.5523	87.7546	37.6465	**Cr correction on V**
0.052	0.1957	0.034		0.2518	11.9444	1.2881	82.2093	27.7562	**Cr correction on V**
0.0111	0.1881	0.0942		0.722	12.5565	1.2103	50.6047	47.3125	**Cr correction on V**
0.0259	0.1347	0.0303		0.1351	7.7408	0.8929	80.8846	22.0078	**Cr correction on V**
0.0223	0.1068	0.025		0.1041	5.9243	0.6876	89.815	22.5079	**Cr correction on V**
0.0253	0.1086	0.0404		0.1206	6.8568	0.7743	91.2733	18.8994	**Cr correction on V**
0.0284	0.1214	0.046		0.0965	6.8685	0.7635	92.879	19.3653	**Cr correction on V**
0.065	0.3874	0.6357	306.9357	0.2089	27.4316	2.3806	108.623	169.9802	
1.2354	0.2856	2.4306	53.1114	0.3486	25.886	1.6137	107.7292	488.3333	
<DL	<DL	<DL	<DL	<DL	<DL	<DL	<DL	<DL	

<DL = below lower detection limit

>UL = above upper detection limit

Cr values highlighted in **bold** indicate where V has had an influence on Cr values

Appendix 2

Appendix 2.1. Major (wt.%) and trace (ppm) element data for anorthosites, leucogabbros, gabbros, peridotites and chromitites from the Bird River Sill.

Lithology	Peridotite	Peridotite	Peridotite	Peridotite	Peridotite	Peridotite
Series	Ultramafic	Ultramafic	Ultramafic	Ultramafic	Ultramafic	Ultramafic
	BR2017-9	BR2017-10	BR2017-11	BR2017-12	BR2017-13	BR2017-14
SiO_2	34.19	38.63	33.08	37.41	36.15	36.63
Al_2O_3	7.20	4.14	8.05	4.78	8.78	5.17
$Fe_2O_3^T$	9.63	9.32	11.28	11.92	15.97	11.70
MnO	0.06	0.08	0.17	0.19	0.13	0.16
MgO	29.99	34.19	30.15	33.20	25.63	30.30
CaO	3.43	2.47	1.71	1.33	5.22	3.69
Na_2O	0.03	0.03	0.02	0.03	0.05	0.02
K_2O	< 0.01	< 0.01	< 0.01	< 0.01	< 0.01	< 0.01
TiO_2	0.09	0.06	0.12	0.11	0.14	0.15
P_2O_5	0.01	< 0.01	0.02	< 0.01	0.02	0.02
LOI	10.34	10.28	9.43	10.35	7.66	9.96
Total	94.97	99.23	94.03	99.31	99.76	97.80
Mg#	85	87	83	83	74	82
Ni	1390	1306	1339	2700	1268	2550
Cr	4500	4500	4500	4500	1042	3139
Co	107	86	128	172	109	144
V	129	53	192	71	62	66
Sc	8	14	6	10	17	14
Li	0.90	1.50	1.20	0.90	2.70	0.40
Rb	0.32	0.30	0.26	0.30	0.35	0.46
Ba	2	1	2	1	2	1
Sr	2	1	2	1	2	3
Ga	8	4	11	5	7	5
Zr	6	6	6	6	6	7
Hf	0.14	0.14	0.14	0.14	0.14	0.22
Nb	0.25	0.16	0.22	0.08	0.19	0.29
Ta	0.01	0.01	0.01	0.01	0.01	0.01
U	0.01	0.01	0.01	<0.011	0.01	0.03
Th	0.02	0.02	0.02	0.02	0.02	0.05
Y	2.04	1.88	1.52	1.63	2.89	3.23
Pb	0.24	0.23	0.22	1.82	0.18	1.32
Cu	181	17	16	623	7	957
Zn	71	29	142	159	60	76
La	0.30	0.30	0.30	0.30	0.30	0.50
Ce	0.77	0.76	0.63	0.60	0.69	1.20
Pr	0.12	0.11	0.09	0.08	0.13	0.19
Nd	0.58	0.53	0.48	0.44	0.70	0.97

Lithology	Peridotite	Peridotite	Peridotite	Peridotite	Peridotite	Peridotite
Series	Ultramafic	Ultramafic	Ultramafic	Ultramafic	Ultramafic	Ultramafic
	BR2017-9	BR2017-10	BR2017-11	BR2017-12	BR2017-13	BR2017-14
Sm	0.20	0.20	0.17	0.16	0.25	0.32
Eu	0.06	0.07	0.07	0.09	0.09	0.13
Gd	0.27	0.25	0.22	0.23	0.38	0.46
Tb	0.05	0.05	0.04	0.04	0.07	0.08
Dy	0.35	0.32	0.26	0.29	0.50	0.56
Ho	0.08	0.07	0.06	0.06	0.11	0.12
Er	0.24	0.22	0.18	0.19	0.32	0.37
Tm	0.04	0.03	0.03	0.03	0.05	0.05
Yb	0.24	0.21	0.20	0.21	0.28	0.36
Lu	0.04	0.03	0.03	0.03	0.05	0.06
Al_2O_3/TiO_2	81	66	66	45	65	35
Sr/Y	1.03	0.53	0.99	0.86	0.55	0.93
Nb/Ta	25.00	22.71	27.38	11.29	26.57	22.38
Zr/Y	2.94	3.19	3.95	3.68	2.08	2.17
La/Yb	1.26	1.42	1.54	1.45	1.07	1.40
Th/Yb	0.08	0.08	0.11	0.09	0.06	0.13
Nd/Sm	2.97	2.70	2.84	2.82	2.77	3.07
La/Nb	1.20	1.89	1.37	3.80	1.61	1.72
Dy/Yb	1.47	1.51	1.35	1.38	1.77	1.58
Th/Ta	1.80	2.57	2.75	2.57	2.57	3.54
Ti/Zr	88.92	62.95	121.90	105.91	135.88	125.89
La/Sm_{cn}	0.99	0.99	1.15	1.24	0.77	1.02
La/Yb_{cn}	0.90	1.02	1.10	1.04	0.77	1.00
Gd/Yb_{cn}	0.92	0.98	0.95	0.92	1.11	1.05
Nb/Nb*	0.80	0.51	0.63	0.25	0.60	0.45
Zr/Zr*	1.06	1.10	1.25	1.36	0.84	0.75
Hf/Hf*	0.89	0.93	1.05	1.14	0.71	0.85
Ti/Ti*	0.90	0.61	1.58	1.24	0.96	0.86
Eu/Eu*	0.85	1.02	1.16	1.52	0.91	1.02
Ce/Ce*	0.99	1.02	0.91	0.93	0.85	0.94
North	50°27.493'	50°27.503'	50°27.503'	50°27.531'	50°27.547'	50°27.569'
West	095°33.456'	095°33.469'	095°33.469'	095°33.501'	095°33.481'	095°33.477'

Lithology	Peridotite	Chromitite	Chromitite	Peridotite	Leucogabbro	Leucogabbro
Series	Ultramafic	Ultramafic	Ultramafic	Ultramafic	Mafic	Mafic
	BR2017-15	BR2017-16	BR2017-17	BR2017-18	BR2017-19	BR2017-20
SiO_2	38.27	13.35	20.59	37.16	47.27	49.09
Al_2O_3	4.74	17.17	12.90	4.17	22.59	24.01
$Fe_2O_3^T$	10.96	20.15	14.35	10.04	4.53	4.26
MnO	0.16	1.47	0.53	0.12	0.08	0.06
MgO	28.50	16.08	22.95	34.98	4.04	4.18
CaO	5.46	0.19	0.06	0.36	15.34	12.37
Na_2O	0.03	0.01	0.01	< 0.01	1.88	2.66
K_2O	< 0.01	< 0.01	< 0.01	< 0.01	0.12	0.35
TiO_2	0.17	0.23	0.14	0.04	0.34	0.27
P_2O_5	< 0.01	0.03	< 0.01	< 0.01	0.02	< 0.01
LOI	10.15	5.70	8.45	11.48	2.45	1.95
Total	98.46	74.37	79.98	98.36	98.67	99.20
Mg#	82	59	74	86	61	64
Ni	1588			1919	64	61
Cr	1663			3135	118	49
Co	117			114	23	17
V	78			37	113	54
Sc	14			7	13	14
Li	1.30			0.40	4.00	12.00
Rb	0.70			0.30	1.49	3.65
Ba	2			1	17	39
Sr	6			1	125	156
Ga	4			4	15	16
Zr	6			6	17	27
Hf	0.17			0.14	0.48	0.74
Nb	0.20			0.11	0.72	0.87
Ta	0.02			0.01	0.04	0.08
U	0.02			0.02	0.03	0.05
Th	0.04			0.02	0.07	0.07
Y	3.83			1.44	5.37	7.30
Pb	0.82			0.40	0.63	0.56
Cu	30			56	137	8
Zn	89			53	47	39
La	0.60			0.20	0.70	2.50
Ce	1.42			0.50	1.53	3.80
Pr	0.23			0.08	0.28	0.43
Nd	1.15			0.35	1.46	1.88
Sm	0.40			0.12	0.53	0.57

Lithology	Peridotite	Chromitite	Chromitite	Peridotite	Leucogabbro	Leucogabbro
Series	Ultramafic	Ultramafic	Ultramafic	Ultramafic	Mafic	Mafic
	BR2017-15	BR2017-16	BR2017-17	BR2017-18	BR2017-19	BR2017-20
Eu	0.18			0.06	0.28	0.49
Gd	0.54			0.18	0.72	0.83
Tb	0.09			0.03	0.13	0.15
Dy	0.67			0.25	0.89	1.11
Ho	0.14			0.06	0.19	0.25
Er	0.42			0.16	0.60	0.77
Tm	0.06			0.02	0.09	0.12
Yb	0.42			0.16	0.56	0.79
Lu	0.06			0.03	0.09	0.13
Al_2O_3/TiO_2	28	74	96	95	67	89
Sr/Y	1.67			0.69	23.24	21.40
Nb/Ta	12.75			15.71	17.24	11.46
Zr/Y	1.57			4.17	3.17	3.70
La/Yb	1.44			1.23	1.24	3.18
Th/Yb	0.11			0.11	0.13	0.09
Nd/Sm	2.85			2.85	2.76	3.29
La/Nb	2.94			1.82	0.97	2.87
Dy/Yb	1.59			1.52	1.58	1.41
Th/Ta	2.75			2.57	1.71	0.93
Ti/Zr	168.85			43.96	118.49	59.95
La/Sm_{cn}	0.96			1.05	0.85	2.83
La/Yb_{cn}	1.03			0.88	0.89	2.28
Gd/Yb_{cn}	1.06			0.93	1.06	0.87
Nb/Nb*	0.30			0.43	0.76	0.49
Zr/Zr*	0.52			1.71	1.15	1.54
Hf/Hf*	0.53			1.44	1.17	1.53
Ti/Ti*	0.85			0.71	1.32	0.98
Eu/Eu*	1.19			1.21	1.36	2.16
Ce/Ce*	0.92			0.98	0.84	0.89
North	50°27.551'	50°27.499'	50°27.499'	50°27.471'	50°27.433'	50°27.432'
West	095°33.477'	095°33.596'	095°33.596'	095°33.636'	095°33.587'	095°33.583'

Lithology	Leucogabbro	Gabbro	Gabbro	Leucogabbro	Leucogabbro	Leucogabbro
Series	Mafic	Mafic	Mafic	Mafic	Mafic	Mafic
	BR2017-22	BR2017-23	BR2017-24	BR2017-25	BR2017-26	BR2017-27
SiO_2	49.72	53.58	54.12	51.20	49.04	45.37
Al_2O_3	21.49	13.27	13.45	17.37	17.33	22.50
$Fe_2O_3^T$	4.87	11.83	10.56	8.88	10.05	7.07
MnO	0.05	0.15	0.15	0.13	0.14	0.11
MgO	7.15	5.97	6.11	5.93	7.26	7.10
CaO	11.86	10.08	10.08	11.41	12.24	12.88
Na_2O	1.24	2.30	2.15	2.20	1.67	1.60
K_2O	0.31	0.20	0.14	0.23	0.16	0.12
TiO_2	0.35	1.04	0.91	0.55	0.43	0.34
P_2O_5	0.04	0.09	0.09	0.04	0.03	0.03
LOI	2.38	0.97	1.16	1.27	1.25	2.16
Total	99.45	99.49	98.91	99.20	99.60	99.27
Mg#	72	47	51	54	56	64
Ni	71	77	83	138	105	199
Cr	95	96	98	264	309	45
Co	24	46	43	39	43	42
V	156	332	317	212	215	104
Sc	30	44	44	39	55	16
Li	18.70	13.90	14.30	16.10	12.50	12.30
Rb	5.46	1.78	1.78	2.87	1.50	1.64
Ba	33	38	41	39	20	13
Sr	95	121	122	150	92	125
Ga	16	17	17	16	15	14
Zr	19	74	65	37	18	18
Hf	0.59	2.10	1.81	1.01	0.55	0.51
Nb	0.77	2.93	2.52	1.39	0.92	0.68
Ta	0.05	0.22	0.18	0.09	0.05	0.04
U	0.04	0.31	0.27	0.13	0.05	0.03
Th	0.15	1.25	1.04	0.55	0.14	0.08
Y	8.49	23.25	19.94	12.19	11.90	6.55
Pb	0.41	1.17	0.76	0.69	0.36	0.51
Cu	1	63	38	287	39	32
Zn	12	70	57	67	60	50
La	0.70	5.40	4.50	3.20	1.50	0.80
Ce	1.78	12.91	11.24	7.22	3.46	2.04
Pr	0.32	1.86	1.59	1.02	0.55	0.34
Nd	1.73	8.90	7.71	4.59	2.89	1.77
Sm	0.66	2.54	2.23	1.34	1.03	0.60
Eu	0.30	0.79	0.68	0.49	0.40	0.33

Lithology	Leucogabbro	Gabbro	Gabbro	Leucogabbro	Leucogabbro	Leucogabbro
Series	Mafic	Mafic	Mafic	Mafic	Mafic	Mafic
	BR2017-22	BR2017-23	BR2017-24	BR2017-25	BR2017-26	BR2017-27
Gd	1.04	3.23	2.79	1.65	1.52	0.85
Tb	0.19	0.56	0.49	0.29	0.27	0.15
Dy	1.37	3.83	3.28	2.03	1.98	1.07
Ho	0.30	0.83	0.71	0.44	0.43	0.23
Er	0.95	2.51	2.11	1.32	1.29	0.71
Tm	0.14	0.37	0.32	0.19	0.19	0.11
Yb	0.97	2.46	2.11	1.30	1.25	0.70
Lu	0.15	0.38	0.32	0.20	0.19	0.11
Al_2O_3/TiO_2	62	13	15	32	40	67
Sr/Y	11.19	5.20	6.12	12.26	7.74	19.02
Nb/Ta	16.43	13.57	13.71	14.79	16.96	18.97
Zr/Y	2.24	3.18	3.26	3.04	1.51	2.75
La/Yb	0.72	2.20	2.14	2.46	1.20	1.14
Th/Yb	0.15	0.51	0.49	0.43	0.11	0.11
Nd/Sm	2.63	3.50	3.45	3.42	2.80	2.93
La/Nb	0.91	1.84	1.78	2.30	1.64	1.17
Dy/Yb	1.41	1.56	1.56	1.56	1.59	1.53
Th/Ta	3.15	5.80	5.66	5.88	2.63	2.14
Ti/Zr	109.80	84.49	83.84	89.27	142.88	111.90
La/Sm_{cn}	0.69	1.37	1.30	1.54	0.94	0.86
La/Yb_{cn}	0.52	1.58	1.53	1.77	0.86	0.82
Gd/Yb_{cn}	0.89	1.09	1.10	1.05	1.01	1.00
Nb/Nb*	0.56	0.26	0.27	0.25	0.47	0.65
Zr/Zr*	1.05	0.92	0.93	0.88	0.62	1.03
Hf/Hf*	1.18	0.94	0.93	0.87	0.68	1.05
Ti/Ti*	1.05	0.88	0.92	0.92	0.83	1.15
Eu/Eu*	1.09	0.84	0.83	1.01	0.96	1.41
Ce/Ce*	0.91	0.99	1.02	0.97	0.93	0.95
North	50°27.245'	50°27.296'	50°27.299'	50°27.312'	50°27.322'	50°27.347'
West	095°33.410'	095°33.476'	095°33.468'	095°33.519'	095°33.573'	095°33.635'

Lithology	Anorthosite	Anorthosite	Chromitite	Chromitite	Gabbro	Leucogabbro
Series	Mafic	Mafic	Ultramafic	Ultramafic	Mafic	Mafic
	BR2017-28	BR2017-29	BR2017-30	BR2017-31	BR2017-32	BR2017-33
SiO_2	44.90	47.70	13.69	13.36	48.79	48.31
Al_2O_3	28.93	25.96	14.17	15.44	14.18	20.95
$Fe_2O_3^T$	3.86	3.77	18.94	17.48	11.99	6.52
MnO	0.05	0.06	0.42	0.29	0.26	0.11
MgO	2.55	3.32	17.53	17.74	9.76	5.82
CaO	14.58	13.60	0.12	0.07	10.70	13.94
Na_2O	1.81	2.37	0.03	0.01	1.75	2.34
K_2O	0.50	0.29	< 0.01	< 0.01	0.50	0.16
TiO_2	0.22	0.29	0.31	0.27	0.54	0.19
P_2O_5	< 0.01	0.04	0.01	< 0.01	0.03	< 0.01
LOI	2.10	1.79	5.28	5.01	1.67	1.77
Total	99.49	99.19	70.50	69.67	100.20	100.10
Mg#	54	61	62	64	59	61
Ni	44	40			235	94
Cr	110	44			725	629
Co	15	17			49	32
V	80	83			230	125
Sc	13	12			40	36
Li	13.50	9.50			16.50	7.80
Rb	9.58	4.64			10.54	2.51
Ba	59	27			113	11
Sr	117	123			139	110
Ga	17	16			14	14
Zr	10	19			29	12
Hf	0.28	0.55			0.85	0.34
Nb	0.44	0.78			1.19	0.31
Ta	0.03	0.05			0.08	0.02
U	0.03	0.04			0.06	0.05
Th	0.04	0.09			0.17	0.08
Y	4.18	5.84			13.41	6.72
Pb	1.57	1.62			3.26	1.31
Cu	72	30			8	19
Zn	38	31			148	39
La	0.70	0.80			1.90	0.80
Ce	1.27	1.75			4.71	2.30
Pr	0.22	0.29			0.76	0.44
Nd	1.17	1.47			3.75	2.41
Sm	0.40	0.52			1.33	0.76
Eu	0.21	0.32			0.52	0.32

Lithology	Anorthosite	Anorthosite	Chromitite	Chromitite	Gabbro	Leucogabbro
Series	Mafic	Mafic	Ultramafic	Ultramafic	Mafic	Mafic
	BR2017-28	BR2017-29	BR2017-30	BR2017-31	BR2017-32	BR2017-33
Gd	0.54	0.76			1.82	1.02
Tb	0.10	0.14			0.32	0.17
Dy	0.69	0.98			2.24	1.17
Ho	0.16	0.21			0.48	0.26
Er	0.47	0.61			1.47	0.75
Tm	0.07	0.10			0.21	0.11
Yb	0.42	0.62			1.42	0.73
Lu	0.06	0.09			0.22	0.11
Al_2O_3/TiO_2	132	89	45	58	26	113
Sr/Y	27.89	21.13			10.37	16.37
Nb/Ta	17.40	17.38			15.11	15.70
Zr/Y	2.39	3.25			2.16	1.79
La/Yb	1.65	1.28			1.34	1.09
Th/Yb	0.08	0.14			0.12	0.11
Nd/Sm	2.95	2.81			2.81	3.18
La/Nb	1.61	1.02			1.59	2.55
Dy/Yb	1.64	1.56			1.58	1.60
Th/Ta	1.44	1.93			2.16	4.15
Ti/Zr	131.29	91.82			111.01	92.42
La/Sm_{cn}	1.14	0.99			0.92	0.68
La/Yb_{cn}	1.18	0.92			0.96	0.79
Gd/Yb_{cn}	1.05	1.01			1.06	1.15
Nb/Nb*	0.64	0.70			0.49	0.29
Zr/Zr*	0.87	1.28			0.77	0.53
Hf/Hf*	0.88	1.34			0.81	0.54
Ti/Ti*	1.18	1.13			0.82	0.52
Eu/Eu*	1.39	1.53			1.01	1.12
Ce/Ce*	0.79	0.89			0.95	0.94
North	50°27.366'	50°27.397'	50°27.477'	50°27.477'	50°29.111'	50°28.012'
West	095°33.655'	095°33.645'	095°33.487'	095°33.487'	095°30.437'	095°25.434'

Lithology	Leucogabbro	Anorthosite	Gabbro	Chromitite	Chromitite
Series	Mafic	Mafic	Mafic	Ultramafic	Ultramafic
	BR2017-34	BR2017-35	BR2017-36	111-11-21	111-11-20
SiO_2	48.31	49.59	50.14	13.16	16.23
Al_2O_3	23.59	25.09	15.92	16.12	14.01
$Fe_2O_3^T$	5.74	3.66	11.77	21.81	16.80
MnO	0.09	0.06	0.39	0.45	0.45
MgO	3.68	2.71	6.23	17.42	20.23
CaO	14.86	13.22	9.40	0.11	0.71
Na_2O	1.75	3.21	3.25	0.03	0.02
K_2O	0.16	0.21	0.35	< 0.01	< 0.01
TiO_2	0.23	0.23	1.07	0.37	0.28
P_2O_5	0.04	0.02	0.09	< 0.01	< 0.01
LOI	0.97	1.36	0.87	5.00	7.03
Total	99.41	99.34	99.49	74.47	75.76
Mg#	53	57	49	59	68
Ni	64	73	99		
Cr	949	170	208		
Co	25	14	45		
V	101	77	308		
Sc	28	14	42		
Li	1.50	5.70	16.60		
Rb	1.53	3.83	3.41		
Ba	11	42	201		
Sr	147	167	147		
Ga	17	18	17		
Zr	18	19	64		
Hf	0.56	0.53	1.82		
Nb	0.61	0.74	2.89		
Ta	0.05	0.05	0.19		
U	0.09	0.14	0.11		
Th	0.25	0.13	0.46		
Y	7.62	5.86	23.33		
Pb	2.20	3.68	11.74		
Cu	11	8	208		
Zn	31	20	522		
La	1.80	1.10	4.20		
Ce	4.39	2.76	10.65		
Pr	0.64	0.40	1.56		
Nd	2.75	1.91	7.82		
Sm	0.79	0.65	2.47		
Eu	0.43	0.41	0.88		

Lithology	Leucogabbro	Anorthosite	Gabbro	Chromitite	Chromitite
Series	Mafic	Mafic	Mafic	Ultramafic	Ultramafic
	BR2017-34	BR2017-35	BR2017-36	111-11-21	111-11-20
Gd	1.07	0.81	3.28		
Tb	0.19	0.15	0.58		
Dy	1.35	1.00	4.03		
Ho	0.30	0.21	0.86		
Er	0.87	0.65	2.54		
Tm	0.13	0.09	0.38		
Yb	0.88	0.63	2.52		
Lu	0.13	0.10	0.38		
Al_2O_3/TiO_2	104	110	15	43	51
Sr/Y	19.29	28.48	6.30		
Nb/Ta	12.87	13.63	15.59		
Zr/Y	2.36	3.24	2.74		
La/Yb	2.04	1.74	1.67		
Th/Yb	0.29	0.20	0.18		
Nd/Sm	3.49	2.95	3.16		
La/Nb	2.98	1.49	1.46		
Dy/Yb	1.53	1.58	1.60		
Th/Ta	5.36	2.37	2.46		
Ti/Zr	75.27	71.94	100.60		
La/Sm_{cn}	1.47	1.10	1.10		
La/Yb_{cn}	1.46	1.25	1.20		
Gd/Yb_{cn}	1.00	1.05	1.08		
Nb/Nb*	0.21	0.46	0.49		
Zr/Zr*	0.72	1.01	0.86		
Hf/Hf*	0.81	1.02	0.88		
Ti/Ti*	0.59	0.77	0.95		
Eu/Eu*	1.41	1.72	0.94		
Ce/Ce*	0.99	1.00	1.01		
North	50°28.002'	50°27.975'	N/A	50°27.284'	50°27.282'
West	095°25.454'	095°25.437'	N/A	095°33.303'	095°33.301'

Appendix 2.2. Major (wt.%) and trace (ppm) element data for basalts, gabbros, dacites, andesites, and greywackes from the Bird River greenstone belt and tonalites from the Maskwa Lake TTG Batholith I (MLB).

Lithology	Greywacke	Greywacke	Dacite	Dacite	Tonalite	Gabbro
Formation	Bird River	Bird River	Peterson Creek	Peterson Creek	MLB	Lamprey Falls
	BR2017-1	BR2017-2	BR2017-3	BR2017-4	BR2017-5	BR2017-6
SiO_2	61.11	60.71	69.15	70.43	70.38	48.70
Al_2O_3	15.57	14.76	12.90	13.08	14.17	15.36
$Fe_2O_3^T$	6.54	6.99	5.57	5.28	3.71	13.67
MnO	0.10	0.11	0.07	0.06	0.03	0.19
MgO	5.33	6.02	1.19	1.33	1.48	7.53
CaO	2.54	3.89	2.40	2.80	2.18	10.14
Na_2O	4.35	3.41	2.93	3.19	4.29	1.21
K_2O	1.80	2.62	3.49	2.36	1.69	1.23
TiO_2	0.49	0.51	0.57	0.62	0.38	0.91
P_2O_5	0.13	0.09	0.17	0.17	0.07	0.08
LOI	1.44	1.09	1.33	1.00	0.81	0.98
Total	99.39	100.20	99.77	100.30	99.21	100.00
Mg#	59	61	28	31	42	50
Ni	127	162	5	6	20	149
Cr	307	519	6	77	66	214
Co	37	30	12	15	10	50
V	95	110	53	58	35	297
Sc	16	18	14	14	7	48
Li	32	37	24	19	15	11
Rb	47	65	70	47	41	47
Ba	329	528	658	741	146	121
Sr	81	165	93	145	108	108
Ga	17	16	17	17	13	16
Zr	120	106	203	201	209	45
Hf	3.19	2.83	5.33	5.35	5.10	1.39
Nb	4.68	3.93	7.11	7.09	7.24	2.02
Ta	0.42	0.34	0.58	0.58	0.60	0.13
U	1.53	1.08	1.70	1.72	1.34	0.24
Th	5.83	4.25	6.70	6.69	7.54	0.21
Y	11.09	10.53	20.67	18.68	9.56	21.64
Pb	5.27	5.61	8.20	9.85	1.67	1.17
Cu	70	51	13	22	26	128
Zn	71	71	73	53	10	38
La	21.30	16.50	36.70	35.60	41.40	2.00
Ce	44.67	35.55	74.34	72.33	79.08	5.53

Lithology	Greywacke	Greywacke	Dacite	Dacite	Tonalite	Gabbro
Formation	Bird River	Bird River	Peterson Creek	Peterson Creek	MLB	Lamprey Falls
	BR2017-1	BR2017-2	BR2017-3	BR2017-4	BR2017-5	BR2017-6
Pr	4.90	3.93	7.71	7.47	7.70	0.85
Nd	18.21	15.03	27.72	26.74	26.21	4.70
Sm	3.08	2.70	4.55	4.37	4.10	1.78
Eu	0.79	0.76	0.98	1.03	0.96	0.60
Gd	2.28	2.16	3.68	3.49	2.83	2.66
Tb	0.33	0.31	0.57	0.52	0.38	0.50
Dy	2.02	1.94	3.59	3.44	1.98	3.58
Ho	0.40	0.38	0.76	0.68	0.36	0.81
Er	1.17	1.09	2.31	2.07	0.95	2.42
Tm	0.17	0.16	0.35	0.32	0.13	0.36
Yb	1.11	1.06	2.32	2.16	0.81	2.40
Lu	0.17	0.16	0.37	0.34	0.13	0.36
Al_2O_3/TiO_2	32	29	23	21	37	17
Sr/Y	9.67	17.40	4.67	8.88	11.30	6.50
Nb/Ta	11.16	11.60	12.28	12.29	12.08	15.10
Zr/Y	10.82	10.07	9.82	10.76	21.86	2.08
La/Yb	19.17	15.64	15.85	16.47	51.36	0.83
Th/Yb	5.24	4.03	2.90	3.10	9.36	0.09
Nd/Sm	5.90	5.58	6.10	6.12	6.40	2.64
La/Nb	4.56	4.20	5.16	5.02	5.72	0.99
Dy/Yb	1.82	1.84	1.55	1.59	2.46	1.49
Th/Ta	13.91	12.53	11.58	11.60	12.59	1.60
Ti/Zr	24.23	28.79	16.89	18.55	10.90	120.56
La/Sm_{cn}	4.46	3.95	5.21	5.26	6.52	0.72
La/Yb_{cn}	13.75	11.22	11.37	11.82	36.84	0.60
Gd/Yb_{cn}	1.70	1.69	1.32	1.33	2.90	0.92
Nb/Nb*	0.10	0.11	0.11	0.11	0.10	0.73
Zr/Zr*	0.95	0.99	1.07	1.10	1.19	0.92
Hf/Hf*	0.91	0.95	1.01	1.06	1.05	1.03
Ti/Ti*	0.44	0.50	0.32	0.35	0.25	0.92
Eu/Eu*	0.90	0.96	0.73	0.81	0.86	0.84
Ce/Ce*	1.06	1.07	1.07	1.07	1.07	1.03
North	50°27.619'	50°27.605'	50°27.809'	50°27.786'	50°28.276'	50°28.272'
West	095°32.536'	095°32.520'	095°30.225'	095°29.952'	095°27.064'	095°27.038'

Lithology	Tonalite	Basalt	Rhyolite	Basalt	Greywacke	Greywacke
Formation	MLB BR2017-7	Lamprey Falls BR2017-8	Peterson Creek BR2017-21	Lamprey Falls BR2017-37	Booster Lake BR2017-38	Booster Lake BR2017-39
SiO_2	71.58	49.78	81.35	51.53	72.61	78.96
Al_2O_3	14.29	14.54	10.02	15.90	12.76	10.84
$Fe_2O_3^T$	3.51	13.89	0.94	9.81	2.43	1.37
MnO	0.03	0.25	0.02	0.18	0.05	0.06
MgO	1.34	6.79	0.69	6.28	0.20	0.16
CaO	1.75	10.63	0.20	10.84	2.30	0.92
Na_2O	4.86	2.21	0.14	3.30	3.01	3.67
K_2O	1.25	0.16	4.46	0.43	3.76	2.55
TiO_2	0.35	1.02	0.03	0.85	1.57	0.10
P_2O_5	0.06	0.08	0.02	0.06	0.12	< 0.01
LOI	0.70	0.51	1.61	0.94	1.47	1.06
Total	99.73	99.86	99.47	100.10	100.30	99.68
Mg#	40	47	57	53	13	17
Ni	11	76	1	110	20	4
Cr	94	173	10	371	106	110
Co	13	49	0	40	16	1
V	36	311	< 5	287	130	< 5
Sc	6	41	3	45	9	4
Li	13	7	22	10	10	9
Rb	33	1	126	6	110	63
Ba	284	52	158	274	800	600
Sr	101	96	19	180	115	41
Ga	15	16	14	15	16	12
Zr	208	55	95	46	295	104
Hf	5.12	1.59	4.34	1.32	6.93	3.62
Nb	6.52	3.03	12.03	1.90	24.60	10.61
Ta	0.89	0.19	1.99	0.12	1.62	1.12
U	2.04	0.13	6.68	0.12	9.86	3.28
Th	5.88	0.42	17.75	0.24	11.99	13.15
Y	11.92	21.33	30.99	21.05	19.08	20.55
Pb	2.64	1.50	18.21	2.52	22.19	13.33
Cu	12	53	4	3	32	6
Zn	18	56	25	39	34	9
La	20.90	3.40	2.10	2.40	65.10	39.80
Ce	39.10	9.21	7.56	6.97	123.03	79.88

Lithology	Tonalite	Basalt	Rhyolite	Basalt	Greywacke	Greywacke
Formation	MLB BR2017-7	Lamprey Falls BR2017-8	Peterson Creek BR2017-21	Lamprey Falls BR2017-37	Booster Lake BR2017-38	Booster Lake BR2017-39
Pr	4.01	1.40	0.94	1.13	12.20	8.21
Nd	14.33	7.26	4.01	5.89	40.86	28.25
Sm	2.70	2.32	1.45	2.06	5.56	4.57
Eu	0.71	0.83	0.00	0.59	0.77	0.38
Gd	2.37	3.08	2.14	2.81	3.81	3.61
Tb	0.35	0.54	0.52	0.51	0.54	0.57
Dy	2.12	3.72	4.13	3.53	3.35	3.49
Ho	0.42	0.80	0.93	0.76	0.66	0.69
Er	1.23	2.37	3.08	2.31	1.94	2.11
Tm	0.19	0.35	0.50	0.34	0.29	0.31
Yb	1.31	2.42	3.34	2.21	2.00	2.14
Lu	0.22	0.37	0.49	0.33	0.30	0.32
Al_2O_3/TiO_2	41	14	304	19	8	113
Sr/Y	9.45	5.65	0.58	11.24	6.78	2.15
Nb/Ta	7.30	15.72	6.05	16.25	15.17	9.47
Zr/Y	17.45	2.58	3.07	2.19	15.46	5.06
La/Yb	16.00	1.41	0.63	1.09	32.62	18.62
Th/Yb	4.50	0.17	5.31	0.11	6.00	6.16
Nd/Sm	5.31	3.14	2.76	2.86	7.34	6.18
La/Nb	3.21	1.12	0.17	1.26	2.65	3.75
Dy/Yb	1.62	1.54	1.24	1.60	1.68	1.63
Th/Ta	6.58	2.17	8.92	2.02	7.39	11.73
Ti/Zr	10.00	110.96	2.08	110.38	31.84	5.53
La/Sm_{cn}	5.00	0.95	0.93	0.75	7.55	5.62
La/Yb_{cn}	11.48	1.01	0.45	0.78	23.39	13.36
Gd/Yb_{cn}	1.50	1.06	0.53	1.05	1.58	1.40
Nb/Nb*	0.14	0.60	0.46	0.59	0.21	0.11
Zr/Zr*	1.98	0.79	2.33	0.78	1.16	0.54
Hf/Hf*	1.76	0.83	3.84	0.81	0.98	0.68
Ti/Ti*	0.30	0.85	0.05	0.86	0.81	0.05
Eu/Eu*	0.85	0.95	0.01	0.75	0.51	0.28
Ce/Ce*	1.04	1.02	1.30	1.02	1.06	1.07
North	50°28.314'	50°27.898'	50°27.781'	N/A	50°26.362'	50°26.320'
West	095°27.042'	095°27.355'	095°31.557'	N/A	095°33.615'	095°33.606'

Lithology	Andesite	Andesite
Formation	Bird River	Bird River
	32-07-1220-1	32-07-1220-4
SiO_2	54.17	60.08
Al_2O_3	16.01	14.87
$Fe_2O_3^T$	7.01	6.59
MnO	0.15	0.09
MgO	6.61	5.23
CaO	9.92	5.07
Na_2O	3.69	4.22
K_2O	0.20	1.55
TiO_2	0.44	0.49
P_2O_5	0.09	0.14
LOI	1.33	1.22
Total	99.62	99.54
Mg#	63	59
Ni	179	98
Cr	321	237
Co	31	25
V	115	121
Sc	24	16
Li	9	26
Rb	3	32
Ba	94	881
Sr	485	815
Ga	17	20
Zr	111	104
Hf	2.86	2.72
Nb	5.45	2.92
Ta	0.42	0.22
U	1.10	1.02
Th	4.67	4.88
Y	12.30	10.06
Pb	12.31	9.93
Cu	3	48
Zn	87	75
La	16.90	26.50
Ce	34.81	55.41

Lithology	Andesite	Andesite
Formation	Bird River	Bird River
	32-07-1220-1	32-07-1220-4
Pr	3.94	6.40
Nd	14.41	24.23
Sm	2.67	3.87
Eu	0.76	1.12
Gd	2.36	2.53
Tb	0.35	0.33
Dy	2.13	1.93
Ho	0.44	0.37
Er	1.31	1.04
Tm	0.20	0.15
Yb	1.31	0.97
Lu	0.20	0.14
Al_2O_3/TiO_2	36	30
Sr/Y	55.22	89.56
Nb/Ta	13.09	13.39
Zr/Y	9.02	10.34
La/Yb	12.94	27.32
Th/Yb	3.57	5.03
Nd/Sm	5.39	6.27
La/Nb	3.10	9.08
Dy/Yb	1.63	1.98
Th/Ta	11.21	22.38
Ti/Zr	23.87	28.13
La/Sm_{cn}	4.08	4.43
La/Yb_{cn}	9.28	19.60
Gd/Yb_{cn}	1.50	2.16
Nb/Nb*	0.14	0.06
Zr/Zr*	1.06	0.64
Hf/Hf*	0.99	0.60
Ti/Ti*	0.45	0.41
Eu/Eu*	0.92	1.10
Ce/Ce*	1.03	1.03
North	50°28.312'	50°28.312'
West	095°32.274'	095°32.274'

Appendix 2.3. Standard and duplicate analyses results.

Sample ID	Client Sample ID	QC Name	Analyte	Units	Measured Value	Cert/Dup Value
BLANK-18-19380		BLANK	Ba	ppm	0.1	
BLANK-18-19380		BLANK	Be	ppm	0.02	
BLANK-18-19380		BLANK	Bi	ppm	0	
BLANK-18-19380		BLANK	Cd	ppm	0.005	
BLANK-18-19380		BLANK	Ce	ppm	0.01	
BLANK-18-19380		BLANK	Co	ppm	0.01	
BLANK-18-19380		BLANK	Cr	ppm	1	
BLANK-18-19380		BLANK	Cs	ppm	0.001	
BLANK-18-19380		BLANK	Cu	ppm	0	
BLANK-18-19380		BLANK	Dy	ppm	0.003	
BLANK-18-19380		BLANK	Er	ppm	0.002	
BLANK-18-19380		BLANK	Eu	ppm	0.0015	
BLANK-18-19380		BLANK	Ga	ppm	0	
BLANK-18-19380		BLANK	Gd	ppm	0.003	
BLANK-18-19380		BLANK	Hf	ppm	0.02	
BLANK-18-19380		BLANK	Ho	ppm	0.0001	
BLANK-18-19380		BLANK	In	ppm	0.0001	
BLANK-18-19380		BLANK	La	ppm	0	
BLANK-18-19380		BLANK	Li	ppm	0	
BLANK-18-19380		BLANK	Lu	ppm	0.001	
BLANK-18-19380		BLANK	Mo	ppm	0.02	
BLANK-18-19380		BLANK	Nb	ppm	0.001	
BLANK-18-19380		BLANK	Nd	ppm	0.01	
BLANK-18-19380		BLANK	Ni	ppm	0.1	
BLANK-18-19380		BLANK	Pb	ppm	0.01	
BLANK-18-19380		BLANK	Pr	ppm	0.001	
BLANK-18-19380		BLANK	Rb	ppm	0.01	
BLANK-18-19380		BLANK	Sb	ppm	0	
BLANK-18-19380		BLANK	Sc	ppm	0.5	
BLANK-18-19380		BLANK	Sm	ppm	0.001	
BLANK-18-19380		BLANK	Sn	ppm	0.01	
BLANK-18-19380		BLANK	Sr	ppm	0	
BLANK-18-19380		BLANK	Ta	ppm	-0.002	
BLANK-18-19380		BLANK	Tb	ppm	0	
BLANK-18-19380		BLANK	Th	ppm	0.004	
BLANK-18-19380		BLANK	Ti	ppm	1	
BLANK-18-19380		BLANK	Tl	ppm	0.001	
BLANK-18-19380		BLANK	Tm	ppm	0.0007	
BLANK-18-19380		BLANK	U	ppm	0.002	
BLANK-18-19380		BLANK	V	ppm	0	
BLANK-18-19380		BLANK	W	ppm	0	
BLANK-18-19380		BLANK	Y	ppm	0	
BLANK-18-19380		BLANK	Yb	ppm	0.004	

Sample ID	Client Sample ID	QC Name	Analyte	Units	Measured Value	Cert/Dup Value
BLANK-18-19380		BLANK	Zn	ppm	1.6	
BLANK-18-19380		BLANK	Zr	ppm	1	
BLANK-18-19381		BLANK	Ba	ppm	0.1	
BLANK-18-19381		BLANK	Be	ppm	0.06	
BLANK-18-19381		BLANK	Bi	ppm	0	
BLANK-18-19381		BLANK	Cd	ppm	0.004	
BLANK-18-19381		BLANK	Ce	ppm	0.02	
BLANK-18-19381		BLANK	Co	ppm	0.02	
BLANK-18-19381		BLANK	Cr	ppm	1	
BLANK-18-19381		BLANK	Cs	ppm	0.002	
BLANK-18-19381		BLANK	Cu	ppm	0	
BLANK-18-19381		BLANK	Dy	ppm	0.006	
BLANK-18-19381		BLANK	Er	ppm	0.005	
BLANK-18-19381		BLANK	Eu	ppm	0.0014	
BLANK-18-19381		BLANK	Ga	ppm	0.01	
BLANK-18-19381		BLANK	Gd	ppm	0.002	
BLANK-18-19381		BLANK	Hf	ppm	0.04	
BLANK-18-19381		BLANK	Ho	ppm	0.0011	
BLANK-18-19381		BLANK	In	ppm	0.0004	
BLANK-18-19381		BLANK	La	ppm	0	
BLANK-18-19381		BLANK	Li	ppm	0	
BLANK-18-19381		BLANK	Lu	ppm	0.001	
BLANK-18-19381		BLANK	Mo	ppm	0.03	
BLANK-18-19381		BLANK	Nb	ppm	0.001	
BLANK-18-19381		BLANK	Nd	ppm	0.01	
BLANK-18-19381		BLANK	Ni	ppm	0.1	
BLANK-18-19381		BLANK	Pb	ppm	0.03	
BLANK-18-19381		BLANK	Pr	ppm	0.001	
BLANK-18-19381		BLANK	Rb	ppm	0.02	
BLANK-18-19381		BLANK	Sb	ppm	0	
BLANK-18-19381		BLANK	Sc	ppm	0.4	
BLANK-18-19381		BLANK	Sm	ppm	0.005	
BLANK-18-19381		BLANK	Sn	ppm	0	
BLANK-18-19381		BLANK	Sr	ppm	0.1	
BLANK-18-19381		BLANK	Ta	ppm	-0.003	
BLANK-18-19381		BLANK	Tb	ppm	0.0004	
BLANK-18-19381		BLANK	Th	ppm	0.006	
BLANK-18-19381		BLANK	Ti	ppm	1	
BLANK-18-19381		BLANK	Tl	ppm	0.002	
BLANK-18-19381		BLANK	Tm	ppm	0.0009	
BLANK-18-19381		BLANK	U	ppm	0.002	
BLANK-18-19381		BLANK	V	ppm	0.1	
BLANK-18-19381		BLANK	W	ppm	0.01	

Sample ID	Client Sample ID	QC Name	Analyte	Units	Measured Value	Cert/Dup Value
BLANK-18-19381		BLANK	Y	ppm	0.01	
BLANK-18-19381		BLANK	Yb	ppm	0.003	
BLANK-18-19381		BLANK	Zn	ppm	1.4	
BLANK-18-19381		BLANK	Zr	ppm	1	
BLANK-18-19382		BLANK	Ba	ppm	0.1	
BLANK-18-19382		BLANK	Be	ppm	0.02	
BLANK-18-19382		BLANK	Bi	ppm	0	
BLANK-18-19382		BLANK	Cd	ppm	0.002	
BLANK-18-19382		BLANK	Ce	ppm	0.03	
BLANK-18-19382		BLANK	Co	ppm	0.03	
BLANK-18-19382		BLANK	Cr	ppm	2	
BLANK-18-19382		BLANK	Cs	ppm	0	
BLANK-18-19382		BLANK	Cu	ppm	0	
BLANK-18-19382		BLANK	Dy	ppm	0.002	
BLANK-18-19382		BLANK	Er	ppm	0.002	
BLANK-18-19382		BLANK	Eu	ppm	0.0015	
BLANK-18-19382		BLANK	Ga	ppm	0	
BLANK-18-19382		BLANK	Gd	ppm	0.002	
BLANK-18-19382		BLANK	Hf	ppm	0.03	
BLANK-18-19382		BLANK	Ho	ppm	0.0003	
BLANK-18-19382		BLANK	In	ppm	0.0004	
BLANK-18-19382		BLANK	La	ppm	0	
BLANK-18-19382		BLANK	Li	ppm	0	
BLANK-18-19382		BLANK	Lu	ppm	0.001	
BLANK-18-19382		BLANK	Mo	ppm	0.02	
BLANK-18-19382		BLANK	Nb	ppm	0.002	
BLANK-18-19382		BLANK	Nd	ppm	0.01	
BLANK-18-19382		BLANK	Ni	ppm	0.3	
BLANK-18-19382		BLANK	Pb	ppm	0.01	
BLANK-18-19382		BLANK	Pr	ppm	0.001	
BLANK-18-19382		BLANK	Rb	ppm	0.02	
BLANK-18-19382		BLANK	Sb	ppm	0	
BLANK-18-19382		BLANK	Sc	ppm	0.3	
BLANK-18-19382		BLANK	Sm	ppm	0.003	
BLANK-18-19382		BLANK	Sn	ppm	0	
BLANK-18-19382		BLANK	Sr	ppm	0	
BLANK-18-19382		BLANK	Ta	ppm	0	
BLANK-18-19382		BLANK	Tb	ppm	0	
BLANK-18-19382		BLANK	Th	ppm	0.002	
BLANK-18-19382		BLANK	Ti	ppm	1	
BLANK-18-19382		BLANK	Tl	ppm	0.001	
BLANK-18-19382		BLANK	Tm	ppm	0.0001	
BLANK-18-19382		BLANK	U	ppm	0.002	
BLANK-18-19382		BLANK	V	ppm	0.2	
BLANK-18-19382		BLANK	W	ppm	0	
BLANK-18-19382		BLANK	Y	ppm	0.01	
BLANK-18-19382		BLANK	Yb	ppm	0	

Sample ID	Client Sample ID	QC Name	Analyte	Units	Measured Value	Cert/Dup Value
BLANK-18-19382		BLANK	Zn	ppm	1.5	
BLANK-18-19382		BLANK	Zr	ppm	1	
BLANK-18-19383		BLANK	Ba	ppm	0.2	
BLANK-18-19383		BLANK	Be	ppm	0.02	
BLANK-18-19383		BLANK	Bi	ppm	0	
BLANK-18-19383		BLANK	Cd	ppm	0.001	
BLANK-18-19383		BLANK	Ce	ppm	0.01	
BLANK-18-19383		BLANK	Co	ppm	0.05	
BLANK-18-19383		BLANK	Cr	ppm	1	
BLANK-18-19383		BLANK	Cs	ppm	0.002	
BLANK-18-19383		BLANK	Cu	ppm	0.1	
BLANK-18-19383		BLANK	Dy	ppm	0.003	
BLANK-18-19383		BLANK	Er	ppm	0.005	
BLANK-18-19383		BLANK	Eu	ppm	0.001	
BLANK-18-19383		BLANK	Ga	ppm	0.03	
BLANK-18-19383		BLANK	Gd	ppm	0.002	
BLANK-18-19383		BLANK	Hf	ppm	0.15	
BLANK-18-19383		BLANK	Ho	ppm	0.0003	
BLANK-18-19383		BLANK	In	ppm	0.0001	
BLANK-18-19383		BLANK	La	ppm	0	
BLANK-18-19383		BLANK	Li	ppm	0.1	
BLANK-18-19383		BLANK	Lu	ppm	0.001	
BLANK-18-19383		BLANK	Mo	ppm	0.1	
BLANK-18-19383		BLANK	Nb	ppm	0.009	
BLANK-18-19383		BLANK	Nd	ppm	0.01	
BLANK-18-19383		BLANK	Ni	ppm	0	
BLANK-18-19383		BLANK	Pb	ppm	0.05	
BLANK-18-19383		BLANK	Pr	ppm	0.003	
BLANK-18-19383		BLANK	Rb	ppm	0.04	
BLANK-18-19383		BLANK	Sb	ppm	0.01	
BLANK-18-19383		BLANK	Sc	ppm	1.7	
BLANK-18-19383		BLANK	Sm	ppm	0.001	
BLANK-18-19383		BLANK	Sn	ppm	0.02	
BLANK-18-19383		BLANK	Sr	ppm	0.1	
BLANK-18-19383		BLANK	Ta	ppm	0	
BLANK-18-19383		BLANK	Tb	ppm	0.0005	
BLANK-18-19383		BLANK	Th	ppm	0.011	
BLANK-18-19383		BLANK	Ti	ppm	3	
BLANK-18-19383		BLANK	Tl	ppm	0	
BLANK-18-19383		BLANK	Tm	ppm	0.0001	
BLANK-18-19383		BLANK	U	ppm	0.008	
BLANK-18-19383		BLANK	V	ppm	0.2	
BLANK-18-19383		BLANK	W	ppm	0.01	

Sample ID	Client Sample ID	QC Name	Analyte	Units	Measured Value	Cert/Dup Value
BLANK-18-19383		BLANK	Y	ppm	0.03	
BLANK-18-19383		BLANK	Yb	ppm	0.004	
BLANK-18-19383		BLANK	Zn	ppm	0.6	
BLANK-18-19383		BLANK	Zr	ppm	6	
BLANK-18-19384		BLANK	Ba	ppm	0.1	
BLANK-18-19384		BLANK	Be	ppm	0.01	
BLANK-18-19384		BLANK	Bi	ppm	0	
BLANK-18-19384		BLANK	Cd	ppm	0.011	
BLANK-18-19384		BLANK	Ce	ppm	0.02	
BLANK-18-19384		BLANK	Co	ppm	0.02	
BLANK-18-19384		BLANK	Cr	ppm	1	
BLANK-18-19384		BLANK	Cs	ppm	0.002	
BLANK-18-19384		BLANK	Cu	ppm	0.1	
BLANK-18-19384		BLANK	Dy	ppm	0.002	
BLANK-18-19384		BLANK	Er	ppm	0.001	
BLANK-18-19384		BLANK	Eu	ppm	0.0011	
BLANK-18-19384		BLANK	Ga	ppm	0.04	
BLANK-18-19384		BLANK	Gd	ppm	0.002	
BLANK-18-19384		BLANK	Hf	ppm	0.03	
BLANK-18-19384		BLANK	Ho	ppm	0.001	
BLANK-18-19384		BLANK	In	ppm	0.0001	
BLANK-18-19384		BLANK	La	ppm	0	
BLANK-18-19384		BLANK	Li	ppm	0	
BLANK-18-19384		BLANK	Lu	ppm	0	
BLANK-18-19384		BLANK	Mo	ppm	0.06	
BLANK-18-19384		BLANK	Nb	ppm	0.001	
BLANK-18-19384		BLANK	Nd	ppm	0.01	
BLANK-18-19384		BLANK	Ni	ppm	0	
BLANK-18-19384		BLANK	Pb	ppm	0.06	
BLANK-18-19384		BLANK	Pr	ppm	0.002	
BLANK-18-19384		BLANK	Rb	ppm	0.02	
BLANK-18-19384		BLANK	Sb	ppm	0	
BLANK-18-19384		BLANK	Sc	ppm	0.6	
BLANK-18-19384		BLANK	Sm	ppm	0.003	
BLANK-18-19384		BLANK	Sn	ppm	0	
BLANK-18-19384		BLANK	Sr	ppm	0.1	
BLANK-18-19384		BLANK	Ta	ppm	0.003	
BLANK-18-19384		BLANK	Tb	ppm	0.0004	
BLANK-18-19384		BLANK	Th	ppm	0.007	
BLANK-18-19384		BLANK	Ti	ppm	1	
BLANK-18-19384		BLANK	Tl	ppm	0	

Sample ID	Client Sample ID	QC Name	Analyte	Units	Measured Value	Cert/Dup Value
BLANK-18-19384		BLANK	Tm	ppm	0.0005	
BLANK-18-19384		BLANK	U	ppm	0.001	
BLANK-18-19384		BLANK	V	ppm	0	
BLANK-18-19384		BLANK	W	ppm	0.01	
BLANK-18-19384		BLANK	Y	ppm	0.01	
BLANK-18-19384		BLANK	Yb	ppm	0.003	
BLANK-18-19384		BLANK	Zn	ppm	0.5	
BLANK-18-19384		BLANK	Zr	ppm	1	
BLANK-18-19385		BLANK	Ba	ppm	0.2	
BLANK-18-19385		BLANK	Be	ppm	0.03	
BLANK-18-19385		BLANK	Bi	ppm	0	
BLANK-18-19385		BLANK	Cd	ppm	0	
BLANK-18-19385		BLANK	Ce	ppm	0.01	
BLANK-18-19385		BLANK	Co	ppm	0.05	
BLANK-18-19385		BLANK	Cr	ppm	1	
BLANK-18-19385		BLANK	Cs	ppm	0.001	
BLANK-18-19385		BLANK	Cu	ppm	0.1	
BLANK-18-19385		BLANK	Dy	ppm	0.005	
BLANK-18-19385		BLANK	Er	ppm	0.004	
BLANK-18-19385		BLANK	Eu	ppm	0.0003	
BLANK-18-19385		BLANK	Ga	ppm	0.03	
BLANK-18-19385		BLANK	Gd	ppm	0.002	
BLANK-18-19385		BLANK	Hf	ppm	0.13	
BLANK-18-19385		BLANK	Ho	ppm	0.0006	
BLANK-18-19385		BLANK	In	ppm	0	
BLANK-18-19385		BLANK	La	ppm	0	
BLANK-18-19385		BLANK	Li	ppm	0.1	
BLANK-18-19385		BLANK	Lu	ppm	0.001	
BLANK-18-19385		BLANK	Mo	ppm	0.08	
BLANK-18-19385		BLANK	Nb	ppm	0.007	
BLANK-18-19385		BLANK	Nd	ppm	0.01	
BLANK-18-19385		BLANK	Ni	ppm	0.2	
BLANK-18-19385		BLANK	Pb	ppm	0.04	
BLANK-18-19385		BLANK	Pr	ppm	0.003	
BLANK-18-19385		BLANK	Rb	ppm	0.04	
BLANK-18-19385		BLANK	Sb	ppm	0.01	
BLANK-18-19385		BLANK	Sc	ppm	1.4	
BLANK-18-19385		BLANK	Sm	ppm	0.003	
BLANK-18-19385		BLANK	Sn	ppm	0.02	
BLANK-18-19385		BLANK	Sr	ppm	0.1	
BLANK-18-19385		BLANK	Ta	ppm	0	

Sample ID	Client Sample ID	QC Name	Analyte	Units	Measured Value	Cert/Dup Value
BLANK-18-19385		BLANK	Tb	ppm	0.0005	
BLANK-18-19385		BLANK	Th	ppm	0.01	
BLANK-18-19385		BLANK	Ti	ppm	2	
BLANK-18-19385		BLANK	Tl	ppm	0.001	
BLANK-18-19385		BLANK	Tm	ppm	0.0007	
BLANK-18-19385		BLANK	U	ppm	0.007	
BLANK-18-19385		BLANK	V	ppm	0.2	
BLANK-18-19385		BLANK	W	ppm	0.01	
BLANK-18-19385		BLANK	Y	ppm	0.03	
BLANK-18-19385		BLANK	Yb	ppm	0.006	
BLANK-18-19385		BLANK	Zn	ppm	0.3	
BLANK-18-19385		BLANK	Zr	ppm	6	
Dup-18-45457	BR2017-1	DUP	Ba	ppm	333.2	
Dup-18-45457	BR2017-1	DUP	Be	ppm	0.79	
Dup-18-45457	BR2017-1	DUP	Bi	ppm	0.75	
Dup-18-45457	BR2017-1	DUP	Cd	ppm	0.056	
Dup-18-45457	BR2017-1	DUP	Ce	ppm	45.71	
Dup-18-45457	BR2017-1	DUP	Co	ppm	36.84	
Dup-18-45457	BR2017-1	DUP	Cr	ppm	302	
Dup-18-45457	BR2017-1	DUP	Cs	ppm	0.97	
Dup-18-45457	BR2017-1	DUP	Cu	ppm	70.3	
Dup-18-45457	BR2017-1	DUP	Dy	ppm	2.049	
Dup-18-45457	BR2017-1	DUP	Er	ppm	1.158	
Dup-18-45457	BR2017-1	DUP	Eu	ppm	0.7792	
Dup-18-45457	BR2017-1	DUP	Ga	ppm	16.66	
Dup-18-45457	BR2017-1	DUP	Gd	ppm	2.284	
Dup-18-45457	BR2017-1	DUP	Hf	ppm	3.19	
Dup-18-45457	BR2017-1	DUP	Ho	ppm	0.3968	
Dup-18-45457	BR2017-1	DUP	In	ppm	0.0329	
Dup-18-45457	BR2017-1	DUP	La	ppm	21.5	
Dup-18-45457	BR2017-1	DUP	Li	ppm	32.1	
Dup-18-45457	BR2017-1	DUP	Lu	ppm	0.168	
Dup-18-45457	BR2017-1	DUP	Mo	ppm	0.83	
Dup-18-45457	BR2017-1	DUP	Nb	ppm	4.727	
Dup-18-45457	BR2017-1	DUP	Nd	ppm	18.49	
Dup-18-45457	BR2017-1	DUP	Ni	ppm	126.6	
Dup-18-45457	BR2017-1	DUP	Pb	ppm	5.26	
Dup-18-45457	BR2017-1	DUP	Pr	ppm	5.017	
Dup-18-45457	BR2017-1	DUP	Rb	ppm	47.6	
Dup-18-45457	BR2017-1	DUP	Sb	ppm	1.86	
Dup-18-45457	BR2017-1	DUP	Sc	ppm	16.7	
Dup-18-45457	BR2017-1	DUP	Sm	ppm	3.037	
Dup-18-45457	BR2017-1	DUP	Sn	ppm	1.99	

Sample ID	Client Sample ID	QC Name	Analyte	Units	Measured Value	Cert/Dup Value
Dup-18-45457	BR2017-1	DUP	Sr	ppm	80.9	
Dup-18-45457	BR2017-1	DUP	Ta	ppm	0.425	
Dup-18-45457	BR2017-1	DUP	Tb	ppm	0.3321	
Dup-18-45457	BR2017-1	DUP	Th	ppm	5.847	
Dup-18-45457	BR2017-1	DUP	Ti	ppm	2836	
Dup-18-45457	BR2017-1	DUP	Tl	ppm	0.379	
Dup-18-45457	BR2017-1	DUP	Tm	ppm	0.1681	
Dup-18-45457	BR2017-1	DUP	U	ppm	1.496	
Dup-18-45457	BR2017-1	DUP	V	ppm	93.8	
Dup-18-45457	BR2017-1	DUP	W	ppm	0.2	
Dup-18-45457	BR2017-1	DUP	Y	ppm	11.15	
Dup-18-45457	BR2017-1	DUP	Yb	ppm	1.126	
Dup-18-45457	BR2017-1	DUP	Zn	ppm	69.3	
Dup-18-45457	BR2017-1	DUP	Zr	ppm	121	
Dup-18-45458	BR2017-10	DUP	Ba	ppm	1.2	
Dup-18-45458	BR2017-10	DUP	Be	ppm	0.09	
Dup-18-45458	BR2017-10	DUP	Bi	ppm	0.02	
Dup-18-45458	BR2017-10	DUP	Cd	ppm	0.026	
Dup-18-45458	BR2017-10	DUP	Ce	ppm	0.72	
Dup-18-45458	BR2017-10	DUP	Co	ppm	85.6	
Dup-18-45458	BR2017-10	DUP	Cr	ppm	4786	
Dup-18-45458	BR2017-10	DUP	Cs	ppm	0.123	
Dup-18-45458	BR2017-10	DUP	Cu	ppm	14.7	
Dup-18-45458	BR2017-10	DUP	Dy	ppm	0.331	
Dup-18-45458	BR2017-10	DUP	Er	ppm	0.218	
Dup-18-45458	BR2017-10	DUP	Eu	ppm	0.0759	
Dup-18-45458	BR2017-10	DUP	Ga	ppm	3.93	
Dup-18-45458	BR2017-10	DUP	Gd	ppm	0.275	
Dup-18-45458	BR2017-10	DUP	Hf	ppm	0.11	
Dup-18-45458	BR2017-10	DUP	Ho	ppm	0.0692	
Dup-18-45458	BR2017-10	DUP	In	ppm	0.0154	
Dup-18-45458	BR2017-10	DUP	La	ppm	0.3	
Dup-18-45458	BR2017-10	DUP	Li	ppm	1.5	
Dup-18-45458	BR2017-10	DUP	Lu	ppm	0.033	
Dup-18-45458	BR2017-10	DUP	Mo	ppm	0.06	
Dup-18-45458	BR2017-10	DUP	Nb	ppm	0.131	
Dup-18-45458	BR2017-10	DUP	Nd	ppm	0.58	
Dup-18-45458	BR2017-10	DUP	Ni	ppm	1320.9	
Dup-18-45458	BR2017-10	DUP	Pb	ppm	0.22	
Dup-18-45458	BR2017-10	DUP	Pr	ppm	0.114	
Dup-18-45458	BR2017-10	DUP	Rb	ppm	0.3	
Dup-18-45458	BR2017-10	DUP	Sb	ppm	0.5	
Dup-18-45458	BR2017-10	DUP	Sc	ppm	14.4	

Sample ID	Client Sample ID	QC Name	Analyte	Units	Measured Value	Cert/Dup Value
Dup-18-45458	BR2017-10	DUP	Sm	ppm	0.18	
Dup-18-45458	BR2017-10	DUP	Sn	ppm	0.11	
Dup-18-45458	BR2017-10	DUP	Sr	ppm	0.9	
Dup-18-45458	BR2017-10	DUP	Ta	ppm	0.002	
Dup-18-45458	BR2017-10	DUP	Tb	ppm	0.0467	
Dup-18-45458	BR2017-10	DUP	Th	ppm	0.017	
Dup-18-45458	BR2017-10	DUP	Ti	ppm	341	
Dup-18-45458	BR2017-10	DUP	Tl	ppm	0.004	
Dup-18-45458	BR2017-10	DUP	Tm	ppm	0.0318	
Dup-18-45458	BR2017-10	DUP	U	ppm	0.007	
Dup-18-45458	BR2017-10	DUP	W	ppm	0.03	
Dup-18-45458	BR2017-10	DUP	Y	ppm	1.89	
Dup-18-45458	BR2017-10	DUP	Yb	ppm	0.21	
Dup-18-45458	BR2017-10	DUP	Zn	ppm	30.6	
Dup-18-45458	BR2017-10	DUP	Zr	ppm	4	
Dup-18-45459	BR2017-22	DUP	Ba	ppm	32.9	
Dup-18-45459	BR2017-22	DUP	Be	ppm	0.2	
Dup-18-45459	BR2017-22	DUP	Bi	ppm	0.01	
Dup-18-45459	BR2017-22	DUP	Cd	ppm	0.026	
Dup-18-45459	BR2017-22	DUP	Ce	ppm	1.71	
Dup-18-45459	BR2017-22	DUP	Co	ppm	24.77	
Dup-18-45459	BR2017-22	DUP	Cr	ppm	99	
Dup-18-45459	BR2017-22	DUP	Cs	ppm	1.402	
Dup-18-45459	BR2017-22	DUP	Cu	ppm	0.8	
Dup-18-45459	BR2017-22	DUP	Dy	ppm	1.365	
Dup-18-45459	BR2017-22	DUP	Er	ppm	0.921	
Dup-18-45459	BR2017-22	DUP	Eu	ppm	0.2962	
Dup-18-45459	BR2017-22	DUP	Ga	ppm	16.38	
Dup-18-45459	BR2017-22	DUP	Gd	ppm	1.037	
Dup-18-45459	BR2017-22	DUP	Hf	ppm	0.63	
Dup-18-45459	BR2017-22	DUP	Ho	ppm	0.307	
Dup-18-45459	BR2017-22	DUP	In	ppm	0.0233	
Dup-18-45459	BR2017-22	DUP	La	ppm	0.6	
Dup-18-45459	BR2017-22	DUP	Li	ppm	19.2	
Dup-18-45459	BR2017-22	DUP	Lu	ppm	0.148	
Dup-18-45459	BR2017-22	DUP	Mo	ppm	1.27	
Dup-18-45459	BR2017-22	DUP	Nb	ppm	0.743	
Dup-18-45459	BR2017-22	DUP	Nd	ppm	1.85	
Dup-18-45459	BR2017-22	DUP	Ni	ppm	72.1	
Dup-18-45459	BR2017-22	DUP	Pb	ppm	0.41	
Dup-18-45459	BR2017-22	DUP	Pr	ppm	0.303	
Dup-18-45459	BR2017-22	DUP	Rb	ppm	5.56	

Sample ID	Client Sample ID	QC Name	Analyte	Units	Measured Value	Cert/Dup Value
Dup-18-45459	BR2017-22	DUP	Sb	ppm	0.44	
Dup-18-45459	BR2017-22	DUP	Sc	ppm	30.3	
Dup-18-45459	BR2017-22	DUP	Sm	ppm	0.73	
Dup-18-45459	BR2017-22	DUP	Sn	ppm	0.16	
Dup-18-45459	BR2017-22	DUP	Sr	ppm	97	
Dup-18-45459	BR2017-22	DUP	Ta	ppm	0.048	
Dup-18-45459	BR2017-22	DUP	Tb	ppm	0.188	
Dup-18-45459	BR2017-22	DUP	Th	ppm	0.148	
Dup-18-45459	BR2017-22	DUP	Ti	ppm	2133	
Dup-18-45459	BR2017-22	DUP	Tl	ppm	0.033	
Dup-18-45459	BR2017-22	DUP	Tm	ppm	0.1441	
Dup-18-45459	BR2017-22	DUP	U	ppm	0.042	
Dup-18-45459	BR2017-22	DUP	V	ppm	157.5	
Dup-18-45459	BR2017-22	DUP	W	ppm	0.04	
Dup-18-45459	BR2017-22	DUP	Y	ppm	8.55	
Dup-18-45459	BR2017-22	DUP	Yb	ppm	0.973	
Dup-18-45459	BR2017-22	DUP	Zn	ppm	11.8	
Dup-18-45459	BR2017-22	DUP	Zr	ppm	21	
Dup-18-45460	BR2017-34	DUP	Ba	ppm	11.3	
Dup-18-45460	BR2017-34	DUP	Be	ppm	0.22	
Dup-18-45460	BR2017-34	DUP	Bi	ppm	0.04	
Dup-18-45460	BR2017-34	DUP	Cd	ppm	0.06	
Dup-18-45460	BR2017-34	DUP	Ce	ppm	4.16	
Dup-18-45460	BR2017-34	DUP	Co	ppm	24.17	
Dup-18-45460	BR2017-34	DUP	Cr	ppm	930	
Dup-18-45460	BR2017-34	DUP	Cs	ppm	0.07	
Dup-18-45460	BR2017-34	DUP	Cu	ppm	10.8	
Dup-18-45460	BR2017-34	DUP	Dy	ppm	1.369	
Dup-18-45460	BR2017-34	DUP	Er	ppm	0.896	
Dup-18-45460	BR2017-34	DUP	Eu	ppm	0.4296	
Dup-18-45460	BR2017-34	DUP	Ga	ppm	16.63	
Dup-18-45460	BR2017-34	DUP	Gd	ppm	1.049	
Dup-18-45460	BR2017-34	DUP	Hf	ppm	0.55	
Dup-18-45460	BR2017-34	DUP	Ho	ppm	0.3012	
Dup-18-45460	BR2017-34	DUP	La	ppm	1.7	
Dup-18-45460	BR2017-34	DUP	Li	ppm	1.4	
Dup-18-45460	BR2017-34	DUP	Lu	ppm	0.134	
Dup-18-45460	BR2017-34	DUP	Mo	ppm	1.52	
Dup-18-45460	BR2017-34	DUP	Nb	ppm	0.613	
Dup-18-45460	BR2017-34	DUP	Nd	ppm	2.7	
Dup-18-45460	BR2017-34	DUP	Ni	ppm	63	
Dup-18-45460	BR2017-34	DUP	Pb	ppm	2.22	

Sample ID	Client Sample ID	QC Name	Analyte	Units	Measured Value	Cert/Dup Value
Dup-18-45460	BR2017-34	DUP	Pr	ppm	0.618	
Dup-18-45460	BR2017-34	DUP	Rb	ppm	1.39	
Dup-18-45460	BR2017-34	DUP	Sb	ppm	0.38	
Dup-18-45460	BR2017-34	DUP	Sc	ppm	26.9	
Dup-18-45460	BR2017-34	DUP	Sm	ppm	0.815	
Dup-18-45460	BR2017-34	DUP	Sn	ppm	0.22	
Dup-18-45460	BR2017-34	DUP	Sr	ppm	148.4	
Dup-18-45460	BR2017-34	DUP	Ta	ppm	0.044	
Dup-18-45460	BR2017-34	DUP	Tb	ppm	0.198	
Dup-18-45460	BR2017-34	DUP	Th	ppm	0.22	
Dup-18-45460	BR2017-34	DUP	Ti	ppm	1303	
Dup-18-45460	BR2017-34	DUP	Tl	ppm	0.006	
Dup-18-45460	BR2017-34	DUP	Tm	ppm	0.1304	
Dup-18-45460	BR2017-34	DUP	U	ppm	0.094	
Dup-18-45460	BR2017-34	DUP	W	ppm	0.19	
Dup-18-45460	BR2017-34	DUP	Y	ppm	7.7	
Dup-18-45460	BR2017-34	DUP	Yb	ppm	0.872	
Dup-18-45460	BR2017-34	DUP	Zn	ppm	31	
Dup-18-45460	BR2017-34	DUP	Zr	ppm	18	
IHST-18-25522		MRB-29	Ba	ppm	292.3	
IHST-18-25522		MRB-29	Be	ppm	1.01	
IHST-18-25522		MRB-29	Bi	ppm	0.03	
IHST-18-25522		MRB-29	Cd	ppm	0.123	
IHST-18-25522		MRB-29	Ce	ppm	49.69	
IHST-18-25522		MRB-29	Co	ppm	48.91	
IHST-18-25522		MRB-29	Cr	ppm	270	
IHST-18-25522		MRB-29	Cs	ppm	0.25	
IHST-18-25522		MRB-29	Cu	ppm	159.4	
IHST-18-25522		MRB-29	Dy	ppm	5.144	
IHST-18-25522		MRB-29	Er	ppm	2.755	
IHST-18-25522		MRB-29	Eu	ppm	1.8822	
IHST-18-25522		MRB-29	Ga	ppm	18.99	
IHST-18-25522		MRB-29	Gd	ppm	5.733	
IHST-18-25522		MRB-29	Hf	ppm	4.35	
IHST-18-25522		MRB-29	Ho	ppm	0.9968	
IHST-18-25522		MRB-29	In	ppm	0.0744	
IHST-18-25522		MRB-29	La	ppm	21.4	
IHST-18-25522		MRB-29	Li	ppm	9.3	
IHST-18-25522		MRB-29	Lu	ppm	0.34	
IHST-18-25522		MRB-29	Mo	ppm	0.82	
IHST-18-25522		MRB-29	Nb	ppm	12.367	
IHST-18-25522		MRB-29	Nd	ppm	27.93	

Sample ID	Client Sample ID	QC Name	Analyte	Units	Measured Value	Cert/Dup Value
IHST-18-25522		MRB-29	Ni	ppm	105.5	
IHST-18-25522		MRB-29	Pb	ppm	5.74	
IHST-18-25522		MRB-29	Pr	ppm	6.346	
IHST-18-25522		MRB-29	Rb	ppm	14.83	
IHST-18-25522		MRB-29	Sb	ppm	0.06	
IHST-18-25522		MRB-29	Sc	ppm	31.5	
IHST-18-25522		MRB-29	Sm	ppm	6.118	
IHST-18-25522		MRB-29	Sn	ppm	2.61	
IHST-18-25522		MRB-29	Sr	ppm	306.6	
IHST-18-25522		MRB-29	Ta	ppm	0.806	
IHST-18-25522		MRB-29	Tb	ppm	0.8588	
IHST-18-25522		MRB-29	Th	ppm	2.543	
IHST-18-25522		MRB-29	Ti	ppm	10765	
IHST-18-25522		MRB-29	Tl	ppm	0.07	
IHST-18-25522		MRB-29	Tm	ppm	0.3755	
IHST-18-25522		MRB-29	U	ppm	0.619	
IHST-18-25522		MRB-29	V	ppm	298.9	
IHST-18-25522		MRB-29	W	ppm	0.2	
IHST-18-25522		MRB-29	Y	ppm	26.37	
IHST-18-25522		MRB-29	Yb	ppm	2.367	
IHST-18-25522		MRB-29	Zn	ppm	106.7	
IHST-18-25522		MRB-29	Zr	ppm	165	
IHST-18-25523		MRB-29	Ba	ppm	285.9	
IHST-18-25523		MRB-29	Be	ppm	1.09	
IHST-18-25523		MRB-29	Bi	ppm	0.03	
IHST-18-25523		MRB-29	Cd	ppm	0.125	
IHST-18-25523		MRB-29	Ce	ppm	50.17	
IHST-18-25523		MRB-29	Co	ppm	51.77	
IHST-18-25523		MRB-29	Cr	ppm	286	
IHST-18-25523		MRB-29	Cs	ppm	0.243	
IHST-18-25523		MRB-29	Cu	ppm	151	
IHST-18-25523		MRB-29	Dy	ppm	5.234	
IHST-18-25523		MRB-29	Er	ppm	2.807	
IHST-18-25523		MRB-29	Eu	ppm	1.8802	
IHST-18-25523		MRB-29	Ga	ppm	19.6	
IHST-18-25523		MRB-29	Gd	ppm	5.903	
IHST-18-25523		MRB-29	Hf	ppm	4.44	
IHST-18-25523		MRB-29	Ho	ppm	1.0139	
IHST-18-25523		MRB-29	In	ppm	0.0791	
IHST-18-25523		MRB-29	La	ppm	21.5	
IHST-18-25523		MRB-29	Li	ppm	9.9	
IHST-18-25523		MRB-29	Lu	ppm	0.361	
IHST-18-25523		MRB-29	Mo	ppm	0.85	

Sample ID	Client Sample ID	QC Name	Analyte	Units	Measured Value	Cert/Dup Value
IHST-18-25523		MRB-29	Nb	ppm	12.654	
IHST-18-25523		MRB-29	Nd	ppm	27.88	
IHST-18-25523		MRB-29	Ni	ppm	112	
IHST-18-25523		MRB-29	Pb	ppm	4.72	
IHST-18-25523		MRB-29	Pr	ppm	6.487	
IHST-18-25523		MRB-29	Rb	ppm	15.15	
IHST-18-25523		MRB-29	Sb	ppm	0.06	
IHST-18-25523		MRB-29	Sc	ppm	33.9	
IHST-18-25523		MRB-29	Sm	ppm	6.21	
IHST-18-25523		MRB-29	Sn	ppm	2.4	
IHST-18-25523		MRB-29	Sr	ppm	307.7	
IHST-18-25523		MRB-29	Ta	ppm	0.808	
IHST-18-25523		MRB-29	Tb	ppm	0.8709	
IHST-18-25523		MRB-29	Th	ppm	2.576	
IHST-18-25523		MRB-29	Ti	ppm	11457	
IHST-18-25523		MRB-29	Tl	ppm	0.068	
IHST-18-25523		MRB-29	Tm	ppm	0.393	
IHST-18-25523		MRB-29	U	ppm	0.658	
IHST-18-25523		MRB-29	V	ppm	319.5	
IHST-18-25523		MRB-29	W	ppm	0.2	
IHST-18-25523		MRB-29	Y	ppm	26.7	
IHST-18-25523		MRB-29	Yb	ppm	2.474	
IHST-18-25523		MRB-29	Zn	ppm	111.9	
IHST-18-25523		MRB-29	Zr	ppm	168	
IHST-18-25528		MRB-29	Ba	ppm	287.7	
IHST-18-25528		MRB-29	Be	ppm	1.06	
IHST-18-25528		MRB-29	Bi	ppm	0.03	
IHST-18-25528		MRB-29	Cd	ppm	0.124	
IHST-18-25528		MRB-29	Ce	ppm	48.86	
IHST-18-25528		MRB-29	Co	ppm	50.56	
IHST-18-25528		MRB-29	Cr	ppm	277	
IHST-18-25528		MRB-29	Cs	ppm	0.245	
IHST-18-25528		MRB-29	Cu	ppm	162.3	
IHST-18-25528		MRB-29	Dy	ppm	5.332	
IHST-18-25528		MRB-29	Er	ppm	2.798	
IHST-18-25528		MRB-29	Eu	ppm	1.8834	
IHST-18-25528		MRB-29	Ga	ppm	19.43	
IHST-18-25528		MRB-29	Gd	ppm	5.909	
IHST-18-25528		MRB-29	Hf	ppm	4.41	
IHST-18-25528		MRB-29	Ho	ppm	1.0171	
IHST-18-25528		MRB-29	In	ppm	0.0777	
IHST-18-25528		MRB-29	La	ppm	21.7	
IHST-18-25528		MRB-29	Li	ppm	9.1	

Sample ID	Client Sample ID	QC Name	Analyte	Units	Measured Value	Cert/Dup Value
IHST-18-25528		MRB-29	Lu	ppm	0.358	
IHST-18-25528		MRB-29	Mo	ppm	0.97	
IHST-18-25528		MRB-29	Nb	ppm	12.592	
IHST-18-25528		MRB-29	Nd	ppm	28.04	
IHST-18-25528		MRB-29	Ni	ppm	109.4	
IHST-18-25528		MRB-29	Pb	ppm	4.81	
IHST-18-25528		MRB-29	Pr	ppm	6.462	
IHST-18-25528		MRB-29	Rb	ppm	15.15	
IHST-18-25528		MRB-29	Sb	ppm	0.06	
IHST-18-25528		MRB-29	Sc	ppm	32.9	
IHST-18-25528		MRB-29	Sm	ppm	6.266	
IHST-18-25528		MRB-29	Sn	ppm	2.33	
IHST-18-25528		MRB-29	Sr	ppm	307.9	
IHST-18-25528		MRB-29	Ta	ppm	0.809	
IHST-18-25528		MRB-29	Tb	ppm	0.8809	
IHST-18-25528		MRB-29	Th	ppm	2.628	
IHST-18-25528		MRB-29	Ti	ppm	11389	
IHST-18-25528		MRB-29	Tl	ppm	0.067	
IHST-18-25528		MRB-29	Tm	ppm	0.3821	
IHST-18-25528		MRB-29	U	ppm	0.65	
IHST-18-25528		MRB-29	V	ppm	311.7	
IHST-18-25528		MRB-29	W	ppm	0.21	
IHST-18-25528		MRB-29	Y	ppm	26.73	
IHST-18-25528		MRB-29	Yb	ppm	2.425	
IHST-18-25528		MRB-29	Zn	ppm	109.3	
IHST-18-25528		MRB-29	Zr	ppm	169	
IHST-18-25529		MRB-29	Ba	ppm	290.1	
IHST-18-25529		MRB-29	Be	ppm	1.1	
IHST-18-25529		MRB-29	Bi	ppm	0.44	
IHST-18-25529		MRB-29	Cd	ppm	0.122	
IHST-18-25529		MRB-29	Ce	ppm	48.54	
IHST-18-25529		MRB-29	Co	ppm	52.55	
IHST-18-25529		MRB-29	Cr	ppm	293	
IHST-18-25529		MRB-29	Cs	ppm	0.239	
IHST-18-25529		MRB-29	Cu	ppm	157.9	
IHST-18-25529		MRB-29	Dy	ppm	5.282	
IHST-18-25529		MRB-29	Er	ppm	2.817	
IHST-18-25529		MRB-29	Eu	ppm	1.8746	
IHST-18-25529		MRB-29	Ga	ppm	19.49	
IHST-18-25529		MRB-29	Gd	ppm	5.884	
IHST-18-25529		MRB-29	Hf	ppm	4.56	
IHST-18-25529		MRB-29	Ho	ppm	1.018	
IHST-18-25529		MRB-29	In	ppm	0.0762	

Sample ID	Client Sample ID	QC Name	Analyte	Units	Measured Value	Cert/Dup Value
IHST-18-25529		MRB-29	La	ppm	21.9	
IHST-18-25529		MRB-29	Li	ppm	10.8	
IHST-18-25529		MRB-29	Lu	ppm	0.353	
IHST-18-25529		MRB-29	Mo	ppm	0.88	
IHST-18-25529		MRB-29	Nb	ppm	12.757	
IHST-18-25529		MRB-29	Nd	ppm	28.04	
IHST-18-25529		MRB-29	Ni	ppm	113.5	
IHST-18-25529		MRB-29	Pb	ppm	4.78	
IHST-18-25529		MRB-29	Pr	ppm	6.444	
IHST-18-25529		MRB-29	Rb	ppm	14.82	
IHST-18-25529		MRB-29	Sb	ppm	0.08	
IHST-18-25529		MRB-29	Sc	ppm	35.9	
IHST-18-25529		MRB-29	Sm	ppm	6.207	
IHST-18-25529		MRB-29	Sn	ppm	2.33	
IHST-18-25529		MRB-29	Sr	ppm	309.9	
IHST-18-25529		MRB-29	Ta	ppm	0.816	
IHST-18-25529		MRB-29	Tb	ppm	0.8807	
IHST-18-25529		MRB-29	Th	ppm	2.583	
IHST-18-25529		MRB-29	Ti	ppm	12046	
IHST-18-25529		MRB-29	Tl	ppm	0.071	
IHST-18-25529		MRB-29	Tm	ppm	0.3799	
IHST-18-25529		MRB-29	U	ppm	0.655	
IHST-18-25529		MRB-29	V	ppm	315.2	
IHST-18-25529		MRB-29	W	ppm	0.21	
IHST-18-25529		MRB-29	Y	ppm	27.26	
IHST-18-25529		MRB-29	Yb	ppm	2.405	
IHST-18-25529		MRB-29	Zn	ppm	109.2	
IHST-18-25529		MRB-29	Zr	ppm	179	
IHST-18-25539		MRB-29	Ba	ppm	294.4	
IHST-18-25539		MRB-29	Be	ppm	1.03	
IHST-18-25539		MRB-29	Bi	ppm	0.04	
IHST-18-25539		MRB-29	Cd	ppm	0.108	
IHST-18-25539		MRB-29	Ce	ppm	46.19	
IHST-18-25539		MRB-29	Co	ppm	51.86	
IHST-18-25539		MRB-29	Cr	ppm	283	
IHST-18-25539		MRB-29	Cs	ppm	0.245	
IHST-18-25539		MRB-29	Cu	ppm	151.2	
IHST-18-25539		MRB-29	Dy	ppm	5.373	
IHST-18-25539		MRB-29	Er	ppm	2.813	
IHST-18-25539		MRB-29	Eu	ppm	1.9215	
IHST-18-25539		MRB-29	Ga	ppm	19.59	
IHST-18-25539		MRB-29	Gd	ppm	6.088	
IHST-18-25539		MRB-29	Hf	ppm	4.38	

Sample ID	Client Sample ID	QC Name	Analyte	Units	Measured Value	Cert/Dup Value
IHST-18-25539		MRB-29	Ho	ppm	1.0468	
IHST-18-25539		MRB-29	In	ppm	0.0784	
IHST-18-25539		MRB-29	La	ppm	21.5	
IHST-18-25539		MRB-29	Li	ppm	9.3	
IHST-18-25539		MRB-29	Lu	ppm	0.354	
IHST-18-25539		MRB-29	Mo	ppm	0.85	
IHST-18-25539		MRB-29	Nb	ppm	12.667	
IHST-18-25539		MRB-29	Nd	ppm	28.13	
IHST-18-25539		MRB-29	Ni	ppm	112.6	
IHST-18-25539		MRB-29	Pb	ppm	4.64	
IHST-18-25539		MRB-29	Pr	ppm	6.429	
IHST-18-25539		MRB-29	Rb	ppm	14.88	
IHST-18-25539		MRB-29	Sb	ppm	0.06	
IHST-18-25539		MRB-29	Sc	ppm	33.1	
IHST-18-25539		MRB-29	Sm	ppm	6.215	
IHST-18-25539		MRB-29	Sn	ppm	2.1	
IHST-18-25539		MRB-29	Sr	ppm	309.3	
IHST-18-25539		MRB-29	Ta	ppm	0.824	
IHST-18-25539		MRB-29	Tb	ppm	0.9007	
IHST-18-25539		MRB-29	Th	ppm	2.562	
IHST-18-25539		MRB-29	Ti	ppm	11580	
IHST-18-25539		MRB-29	Tl	ppm	0.069	
IHST-18-25539		MRB-29	Tm	ppm	0.3852	
IHST-18-25539		MRB-29	U	ppm	0.615	
IHST-18-25539		MRB-29	V	ppm	319.9	
IHST-18-25539		MRB-29	W	ppm	0.22	
IHST-18-25539		MRB-29	Y	ppm	27.08	
IHST-18-25539		MRB-29	Yb	ppm	2.447	
IHST-18-25539		MRB-29	Zn	ppm	116	
IHST-18-25539		MRB-29	Zr	ppm	169	
IHST-18-25540		MRB-29	Ba	ppm	289.2	
IHST-18-25540		MRB-29	Be	ppm	1.18	
IHST-18-25540		MRB-29	Bi	ppm	0.03	
IHST-18-25540		MRB-29	Cd	ppm	0.119	
IHST-18-25540		MRB-29	Ce	ppm	47.51	
IHST-18-25540		MRB-29	Co	ppm	54.07	
IHST-18-25540		MRB-29	Cr	ppm	286	
IHST-18-25540		MRB-29	Cs	ppm	0.234	
IHST-18-25540		MRB-29	Cu	ppm	152.6	
IHST-18-25540		MRB-29	Dy	ppm	5.413	
IHST-18-25540		MRB-29	Er	ppm	2.857	
IHST-18-25540		MRB-29	Eu	ppm	1.92	
IHST-18-25540		MRB-29	Ga	ppm	19.32	

Sample ID	Client Sample ID	QC Name	Analyte	Units	Measured Value	Cert/Dup Value
IHST-18-25540		MRB-29	Gd	ppm	6.024	
IHST-18-25540		MRB-29	Hf	ppm	4.51	
IHST-18-25540		MRB-29	Ho	ppm	1.0295	
IHST-18-25540		MRB-29	In	ppm	0.077	
IHST-18-25540		MRB-29	La	ppm	21.7	
IHST-18-25540		MRB-29	Li	ppm	10.1	
IHST-18-25540		MRB-29	Lu	ppm	0.359	
IHST-18-25540		MRB-29	Mo	ppm	0.85	
IHST-18-25540		MRB-29	Nb	ppm	12.617	
IHST-18-25540		MRB-29	Nd	ppm	28.09	
IHST-18-25540		MRB-29	Ni	ppm	116.4	
IHST-18-25540		MRB-29	Pb	ppm	4.86	
IHST-18-25540		MRB-29	Pr	ppm	6.465	
IHST-18-25540		MRB-29	Rb	ppm	14.44	
IHST-18-25540		MRB-29	Sb	ppm	0.06	
IHST-18-25540		MRB-29	Sc	ppm	36.4	
IHST-18-25540		MRB-29	Sm	ppm	6.327	
IHST-18-25540		MRB-29	Sn	ppm	2.25	
IHST-18-25540		MRB-29	Sr	ppm	306.4	
IHST-18-25540		MRB-29	Ta	ppm	0.818	
IHST-18-25540		MRB-29	Tb	ppm	0.8923	
IHST-18-25540		MRB-29	Th	ppm	2.577	
IHST-18-25540		MRB-29	Ti	ppm	12108	
IHST-18-25540		MRB-29	Tl	ppm	0.067	
IHST-18-25540		MRB-29	Tm	ppm	0.387	
IHST-18-25540		MRB-29	U	ppm	0.628	
IHST-18-25540		MRB-29	V	ppm	327	
IHST-18-25540		MRB-29	W	ppm	0.22	
IHST-18-25540		MRB-29	Y	ppm	27.34	
IHST-18-25540		MRB-29	Yb	ppm	2.462	
IHST-18-25540		MRB-29	Zn	ppm	105.8	
IHST-18-25540		MRB-29	Zr	ppm	173	
INTL-18-31270		BHVO-2	Ba	ppm	128.6	130
INTL-18-31270		BHVO-2	Be	ppm	1.06	
INTL-18-31270		BHVO-2	Bi	ppm	0.01	
INTL-18-31270		BHVO-2	Cd	ppm	0.113	
INTL-18-31270		BHVO-2	Ce	ppm	37.16	38
INTL-18-31270		BHVO-2	Co	ppm	45.91	45
INTL-18-31270		BHVO-2	Cr	ppm	305	280
INTL-18-31270		BHVO-2	Cs	ppm	0.098	
INTL-18-31270		BHVO-2	Cu	ppm	135.6	127
INTL-18-31270		BHVO-2	Dy	ppm	5.252	
INTL-18-31270		BHVO-2	Er	ppm	2.538	

Sample ID	Client Sample ID	QC Name	Analyte	Units	Measured Value	Cert/Dup Value
INTL-18-31270		BHVO-2	Eu	ppm	2.0399	
INTL-18-31270		BHVO-2	Ga	ppm	20.96	21.7
INTL-18-31270		BHVO-2	Gd	ppm	6.09	
INTL-18-31270		BHVO-2	Hf	ppm	4.37	4.1
INTL-18-31270		BHVO-2	Ho	ppm	0.9712	
INTL-18-31270		BHVO-2	In	ppm	0.0861	
INTL-18-31270		BHVO-2	La	ppm	14.7	15
INTL-18-31270		BHVO-2	Li	ppm	4.1	
INTL-18-31270		BHVO-2	Lu	ppm	0.277	
INTL-18-31270		BHVO-2	Mo	ppm	4.52	
INTL-18-31270		BHVO-2	Nb	ppm	17.107	
INTL-18-31270		BHVO-2	Nd	ppm	24.38	
INTL-18-31270		BHVO-2	Ni	ppm	122.6	119
INTL-18-31270		BHVO-2	Pb	ppm	1.52	
INTL-18-31270		BHVO-2	Pr	ppm	5.268	
INTL-18-31270		BHVO-2	Rb	ppm	9.33	9.8
INTL-18-31270		BHVO-2	Sb	ppm	0.11	
INTL-18-31270		BHVO-2	Sc	ppm	32.8	32
INTL-18-31270		BHVO-2	Sm	ppm	6.094	
INTL-18-31270		BHVO-2	Sn	ppm	1.75	
INTL-18-31270		BHVO-2	Sr	ppm	381.3	389
INTL-18-31270		BHVO-2	Ta	ppm	1.141	
INTL-18-31270		BHVO-2	Tb	ppm	0.8913	
INTL-18-31270		BHVO-2	Th	ppm	1.151	
INTL-18-31270		BHVO-2	Ti	ppm	15629	
INTL-18-31270		BHVO-2	Tl	ppm	0.019	
INTL-18-31270		BHVO-2	Tm	ppm	0.3262	
INTL-18-31270		BHVO-2	U	ppm	0.413	
INTL-18-31270		BHVO-2	V	ppm	327	317
INTL-18-31270		BHVO-2	W	ppm	0.2	
INTL-18-31270		BHVO-2	Y	ppm	24.98	26
INTL-18-31270		BHVO-2	Yb	ppm	1.96	
INTL-18-31270		BHVO-2	Zn	ppm	105	103
INTL-18-31270		BHVO-2	Zr	ppm	164	172
INTL-18-31271		GSP-2	Ba	ppm	1346	1340
INTL-18-31271		GSP-2	Be	ppm	1.44	1.5
INTL-18-31271		GSP-2	Bi	ppm	0.03	
INTL-18-31271		GSP-2	Cd	ppm	0.146	
INTL-18-31271		GSP-2	Ce	ppm	458.46	410
INTL-18-31271		GSP-2	Co	ppm	7.43	7.3
INTL-18-31271		GSP-2	Cr	ppm	22	20
INTL-18-31271		GSP-2	Cs	ppm	1.198	1.2
INTL-18-31271		GSP-2	Cu	ppm	46.8	43

Sample ID	Client Sample ID	QC Name	Analyte	Units	Measured Value	Cert/Dup Value
INTL-18-31271		GSP-2	Dy	ppm	5.862	6.1
INTL-18-31271		GSP-2	Er	ppm	2.354	2.2
INTL-18-31271		GSP-2	Eu	ppm	2.2394	2.3
INTL-18-31271		GSP-2	Ga	ppm	23.6	22
INTL-18-31271		GSP-2	Gd	ppm	11.05	12
INTL-18-31271		GSP-2	Hf	ppm	13.37	14
INTL-18-31271		GSP-2	Ho	ppm	0.9702	1
INTL-18-31271		GSP-2	In	ppm	0.0521	
INTL-18-31271		GSP-2	La	ppm	184.8	180
INTL-18-31271		GSP-2	Li	ppm	32.1	
INTL-18-31271		GSP-2	Lu	ppm	0.233	0.23
INTL-18-31271		GSP-2	Mo	ppm	2.42	2.1
INTL-18-31271		GSP-2	Nb	ppm	25.258	27
INTL-18-31271		GSP-2	Nd	ppm	209.86	200
INTL-18-31271		GSP-2	Ni	ppm	16.8	17
INTL-18-31271		GSP-2	Pb	ppm	41.3	42
INTL-18-31271		GSP-2	Pr	ppm	57.356	51
INTL-18-31271		GSP-2	Rb	ppm	252.35	245
INTL-18-31271		GSP-2	Sb	ppm	0.37	
INTL-18-31271		GSP-2	Sc	ppm	7	6.3
INTL-18-31271		GSP-2	Sm	ppm	26.88	27
INTL-18-31271		GSP-2	Sn	ppm	7.04	
INTL-18-31271		GSP-2	Sr	ppm	235.3	240
INTL-18-31271		GSP-2	Ta	ppm	0.862	
INTL-18-31271		GSP-2	Tb	ppm	1.1673	
INTL-18-31271		GSP-2	Th	ppm	108.449	105
INTL-18-31271		GSP-2	Ti	ppm	3974	
INTL-18-31271		GSP-2	Tl	ppm	1.27	1.1
INTL-18-31271		GSP-2	Tm	ppm	0.2888	0.29
INTL-18-31271		GSP-2	U	ppm	2.461	2.4
INTL-18-31271		GSP-2	V	ppm	52.7	52
INTL-18-31271		GSP-2	W	ppm	0.35	
INTL-18-31271		GSP-2	Y	ppm	26.15	28
INTL-18-31271		GSP-2	Yb	ppm	1.659	1.6
INTL-18-31271		GSP-2	Zn	ppm	120.5	120
INTL-18-31271		GSP-2	Zr	ppm	517	550
INTL-18-31275		AGV-2	Ba	ppm	1088.5	1140
INTL-18-31275		AGV-2	Be	ppm	2.14	2.3
INTL-18-31275		AGV-2	Bi	ppm	0.05	
INTL-18-31275		AGV-2	Cd	ppm	0.097	
INTL-18-31275		AGV-2	Ce	ppm	68.78	68
INTL-18-31275		AGV-2	Co	ppm	15.99	16
INTL-18-31275		AGV-2	Cr	ppm	17	17

Sample ID	Client Sample ID	QC Name	Analyte	Units	Measured Value	Cert/Dup Value
INTL-18-31275		AGV-2	Cs	ppm	1.159	1.16
INTL-18-31275		AGV-2	Cu	ppm	53.4	53
INTL-18-31275		AGV-2	Dy	ppm	3.431	3.6
INTL-18-31275		AGV-2	Er	ppm	1.775	1.79
INTL-18-31275		AGV-2	Eu	ppm	1.4665	1.54
INTL-18-31275		AGV-2	Ga	ppm	20.64	20
INTL-18-31275		AGV-2	Gd	ppm	4.309	4.69
INTL-18-31275		AGV-2	Hf	ppm	5.16	5.08
INTL-18-31275		AGV-2	Ho	ppm	0.6545	0.71
INTL-18-31275		AGV-2	In	ppm	0.0445	
INTL-18-31275		AGV-2	La	ppm	36.5	38
INTL-18-31275		AGV-2	Li	ppm	8.8	11
INTL-18-31275		AGV-2	Lu	ppm	0.247	0.25
INTL-18-31275		AGV-2	Mo	ppm	2.31	
INTL-18-31275		AGV-2	Nb	ppm	13.49	15
INTL-18-31275		AGV-2	Nd	ppm	29.26	30
INTL-18-31275		AGV-2	Ni	ppm	19.2	19
INTL-18-31275		AGV-2	Pb	ppm	13.24	13
INTL-18-31275		AGV-2	Pr	ppm	7.908	8.3
INTL-18-31275		AGV-2	Rb	ppm	70.28	68.6
INTL-18-31275		AGV-2	Sb	ppm	0.48	0.6
INTL-18-31275		AGV-2	Sc	ppm	13	13
INTL-18-31275		AGV-2	Sm	ppm	5.381	5.7
INTL-18-31275		AGV-2	Sn	ppm	2.03	2.3
INTL-18-31275		AGV-2	Sr	ppm	649.2	658
INTL-18-31275		AGV-2	Ta	ppm	0.84	0.89
INTL-18-31275		AGV-2	Tb	ppm	0.5851	0.64
INTL-18-31275		AGV-2	Th	ppm	6.071	6.1
INTL-18-31275		AGV-2	Ti	ppm	6240	6019
INTL-18-31275		AGV-2	Tl	ppm	0.272	0.27
INTL-18-31275		AGV-2	Tm	ppm	0.248	0.26
INTL-18-31275		AGV-2	U	ppm	1.893	1.88
INTL-18-31275		AGV-2	V	ppm	118.9	120
INTL-18-31275		AGV-2	W	ppm	0.51	
INTL-18-31275		AGV-2	Y	ppm	18.81	20
INTL-18-31275		AGV-2	Yb	ppm	1.596	1.6
INTL-18-31275		AGV-2	Zn	ppm	91.1	86
INTL-18-31275		AGV-2	Zr	ppm	230	230
INTL-18-31276		BHVO-2	Ba	ppm	131.8	130
INTL-18-31276		BHVO-2	Be	ppm	1.05	
INTL-18-31276		BHVO-2	Bi	ppm	0.02	
INTL-18-31276		BHVO-2	Cd	ppm	0.112	
INTL-18-31276		BHVO-2	Ce	ppm	37.19	38

Sample ID	Client Sample ID	QC Name	Analyte	Units	Measured Value	Cert/Dup Value
INTL-18-31276		BHVO-2	Co	ppm	45.86	45
INTL-18-31276		BHVO-2	Cr	ppm	295	280
INTL-18-31276		BHVO-2	Cs	ppm	0.095	
INTL-18-31276		BHVO-2	Cu	ppm	133.8	127
INTL-18-31276		BHVO-2	Dy	ppm	5.419	
INTL-18-31276		BHVO-2	Er	ppm	2.566	
INTL-18-31276		BHVO-2	Eu	ppm	2.0641	
INTL-18-31276		BHVO-2	Ga	ppm	20.74	21.7
INTL-18-31276		BHVO-2	Gd	ppm	6.279	
INTL-18-31276		BHVO-2	Hf	ppm	4.49	4.1
INTL-18-31276		BHVO-2	Ho	ppm	0.9926	
INTL-18-31276		BHVO-2	In	ppm	0.0854	
INTL-18-31276		BHVO-2	La	ppm	15.2	15
INTL-18-31276		BHVO-2	Li	ppm	4.3	
INTL-18-31276		BHVO-2	Lu	ppm	0.276	
INTL-18-31276		BHVO-2	Mo	ppm	4.85	
INTL-18-31276		BHVO-2	Nb	ppm	17.497	
INTL-18-31276		BHVO-2	Nd	ppm	25.31	
INTL-18-31276		BHVO-2	Ni	ppm	121.6	119
INTL-18-31276		BHVO-2	Pb	ppm	1.76	
INTL-18-31276		BHVO-2	Pr	ppm	5.274	
INTL-18-31276		BHVO-2	Rb	ppm	9.15	9.8
INTL-18-31276		BHVO-2	Sb	ppm	0.1	
INTL-18-31276		BHVO-2	Sc	ppm	32.3	32
INTL-18-31276		BHVO-2	Sm	ppm	6.213	
INTL-18-31276		BHVO-2	Sn	ppm	1.83	
INTL-18-31276		BHVO-2	Sr	ppm	385.2	389
INTL-18-31276		BHVO-2	Ta	ppm	1.168	
INTL-18-31276		BHVO-2	Tb	ppm	0.922	
INTL-18-31276		BHVO-2	Th	ppm	1.206	
INTL-18-31276		BHVO-2	Ti	ppm	16206	
INTL-18-31276		BHVO-2	Tl	ppm	0.02	
INTL-18-31276		BHVO-2	Tm	ppm	0.3309	
INTL-18-31276		BHVO-2	U	ppm	0.424	
INTL-18-31276		BHVO-2	V	ppm	322.6	317
INTL-18-31276		BHVO-2	W	ppm	0.22	
INTL-18-31276		BHVO-2	Y	ppm	25.46	26
INTL-18-31276		BHVO-2	Yb	ppm	1.997	
INTL-18-31276		BHVO-2	Zn	ppm	100.1	103
INTL-18-31276		BHVO-2	Zr	ppm	172	172
INTL-18-31284		AGV-2	Ba	ppm	1174.4	1140
INTL-18-31284		AGV-2	Be	ppm	2.18	2.3
INTL-18-31284		AGV-2	Bi	ppm	0.05	

Sample ID	Client Sample ID	QC Name	Analyte	Units	Measured Value	Cert/Dup Value
INTL-18-31284		AGV-2	Cd	ppm	0.108	
INTL-18-31284		AGV-2	Ce	ppm	65.24	68
INTL-18-31284		AGV-2	Co	ppm	16.5	16
INTL-18-31284		AGV-2	Cr	ppm	17	17
INTL-18-31284		AGV-2	Cs	ppm	1.171	1.16
INTL-18-31284		AGV-2	Cu	ppm	53.8	53
INTL-18-31284		AGV-2	Dy	ppm	3.496	3.6
INTL-18-31284		AGV-2	Er	ppm	1.839	1.79
INTL-18-31284		AGV-2	Eu	ppm	1.5174	1.54
INTL-18-31284		AGV-2	Ga	ppm	20.74	20
INTL-18-31284		AGV-2	Gd	ppm	4.558	4.69
INTL-18-31284		AGV-2	Hf	ppm	5.11	5.08
INTL-18-31284		AGV-2	Ho	ppm	0.6693	0.71
INTL-18-31284		AGV-2	In	ppm	0.0441	
INTL-18-31284		AGV-2	La	ppm	37.6	38
INTL-18-31284		AGV-2	Li	ppm	9.3	11
INTL-18-31284		AGV-2	Lu	ppm	0.253	0.25
INTL-18-31284		AGV-2	Mo	ppm	2.23	
INTL-18-31284		AGV-2	Nb	ppm	13.527	15
INTL-18-31284		AGV-2	Nd	ppm	31.19	30
INTL-18-31284		AGV-2	Ni	ppm	19.3	19
INTL-18-31284		AGV-2	Pb	ppm	12.96	13
INTL-18-31284		AGV-2	Pr	ppm	8.092	8.3
INTL-18-31284		AGV-2	Rb	ppm	70.27	68.6
INTL-18-31284		AGV-2	Sb	ppm	0.49	0.6
INTL-18-31284		AGV-2	Sc	ppm	13.3	13
INTL-18-31284		AGV-2	Sm	ppm	5.577	5.7
INTL-18-31284		AGV-2	Sn	ppm	2.07	2.3
INTL-18-31284		AGV-2	Sr	ppm	655	658
INTL-18-31284		AGV-2	Ta	ppm	0.839	0.89
INTL-18-31284		AGV-2	Tb	ppm	0.6297	0.64
INTL-18-31284		AGV-2	Th	ppm	6.009	6.1
INTL-18-31284		AGV-2	Ti	ppm	6182	6019
INTL-18-31284		AGV-2	Tl	ppm	0.268	0.27
INTL-18-31284		AGV-2	Tm	ppm	0.2542	0.26
INTL-18-31284		AGV-2	U	ppm	1.845	1.88
INTL-18-31284		AGV-2	V	ppm	122.2	120
INTL-18-31284		AGV-2	W	ppm	0.5	
INTL-18-31284		AGV-2	Y	ppm	19.43	20
INTL-18-31284		AGV-2	Yb	ppm	1.638	1.6
INTL-18-31284		AGV-2	Zn	ppm	94.6	86
INTL-18-31284		AGV-2	Zr	ppm	232	230
INTL-18-31285		AGV-2	Ba	ppm	1185.9	1140

Sample ID	Client Sample ID	QC Name	Analyte	Units	Measured Value	Cert/Dup Value
INTL-18-31285		AGV-2	Be	ppm	2.44	2.3
INTL-18-31285		AGV-2	Bi	ppm	0.05	
INTL-18-31285		AGV-2	Cd	ppm	0.119	
INTL-18-31285		AGV-2	Ce	ppm	70.25	68
INTL-18-31285		AGV-2	Co	ppm	16.16	16
INTL-18-31285		AGV-2	Cr	ppm	17	17
INTL-18-31285		AGV-2	Cs	ppm	1.155	1.16
INTL-18-31285		AGV-2	Cu	ppm	54.5	53
INTL-18-31285		AGV-2	Dy	ppm	3.485	3.6
INTL-18-31285		AGV-2	Er	ppm	1.838	1.79
INTL-18-31285		AGV-2	Eu	ppm	1.5205	1.54
INTL-18-31285		AGV-2	Ga	ppm	20.5	20
INTL-18-31285		AGV-2	Gd	ppm	4.358	4.69
INTL-18-31285		AGV-2	Hf	ppm	5.25	5.08
INTL-18-31285		AGV-2	Ho	ppm	0.6699	0.71
INTL-18-31285		AGV-2	In	ppm	0.0461	
INTL-18-31285		AGV-2	La	ppm	38.7	38
INTL-18-31285		AGV-2	Li	ppm	10.1	11
INTL-18-31285		AGV-2	Lu	ppm	0.247	0.25
INTL-18-31285		AGV-2	Mo	ppm	2.14	
INTL-18-31285		AGV-2	Nb	ppm	13.304	15
INTL-18-31285		AGV-2	Nd	ppm	31.51	30
INTL-18-31285		AGV-2	Ni	ppm	19.5	19
INTL-18-31285		AGV-2	Pb	ppm	12.82	13
INTL-18-31285		AGV-2	Pr	ppm	8.269	8.3
INTL-18-31285		AGV-2	Rb	ppm	67.63	68.6
INTL-18-31285		AGV-2	Sb	ppm	0.53	0.6
INTL-18-31285		AGV-2	Sc	ppm	14	13
INTL-18-31285		AGV-2	Sm	ppm	5.743	5.7
INTL-18-31285		AGV-2	Sn	ppm	2.17	2.3
INTL-18-31285		AGV-2	Sr	ppm	630.3	658
INTL-18-31285		AGV-2	Ta	ppm	0.847	0.89
INTL-18-31285		AGV-2	Tb	ppm	0.6086	0.64
INTL-18-31285		AGV-2	Th	ppm	6.096	6.1
INTL-18-31285		AGV-2	Ti	ppm	6377	6019
INTL-18-31285		AGV-2	Tl	ppm	0.267	0.27
INTL-18-31285		AGV-2	Tm	ppm	0.2526	0.26
INTL-18-31285		AGV-2	U	ppm	1.847	1.88
INTL-18-31285		AGV-2	V	ppm	120.1	120
INTL-18-31285		AGV-2	W	ppm	0.51	
INTL-18-31285		AGV-2	Y	ppm	19.01	20
INTL-18-31285		AGV-2	Yb	ppm	1.632	1.6

Sample ID	Client Sample ID	QC Name	Analyte	Units	Measured Value	Cert/Dup Value
INTL-18-31285		AGV-2	Zn	ppm	99.3	86
INTL-18-31285		AGV-2	Zr	ppm	230	230

Appendix 2.4. Selected SEM-EDS analyses of plagioclases, amphiboles and chromites and chromite-hosted inclusions from the Bird River Sill.

Sample ID	Lithology	Series	Mineral	Core/Rim/Inclusion
BR2017-19	Leucogabbro	Mafic Series	Plagioclase	Rim
BR2017-19	Leucogabbro	Mafic Series	Plagioclase	Core
BR2017-19	Leucogabbro	Mafic Series	Plagioclase	Rim
BR2017-19	Leucogabbro	Mafic Series	Plagioclase	Rim
BR2017-19	Leucogabbro	Mafic Series	Plagioclase	Core
BR2017-19	Leucogabbro	Mafic Series	Plagioclase	Rim
BR2017-19	Leucogabbro	Mafic Series	Plagioclase	Rim
BR2017-19	Leucogabbro	Mafic Series	Plagioclase	Core
BR2017-19	Leucogabbro	Mafic Series	Plagioclase	Rim
BR2017-19	Leucogabbro	Mafic Series	Plagioclase	Core
BR2017-19	Leucogabbro	Mafic Series	Plagioclase	Core
BR2017-19	Leucogabbro	Mafic Series	Plagioclase	Core
BR2017-19	Leucogabbro	Mafic Series	Plagioclase	Core
BR2017-19	Leucogabbro	Mafic Series	Plagioclase	Rim
BR2017-19	Leucogabbro	Mafic Series	Plagioclase	Core
BR2017-19	Leucogabbro	Mafic Series	Plagioclase	Core
BR2017-19	Leucogabbro	Mafic Series	Plagioclase	Rim
BR2017-19	Leucogabbro	Mafic Series	Plagioclase	Rim
BR2017-19	Leucogabbro	Mafic Series	Plagioclase	Core
BR2017-19	Leucogabbro	Mafic Series	Plagioclase	Core
BR2017-19	Leucogabbro	Mafic Series	Plagioclase	Rim
BR2017-19	Leucogabbro	Mafic Series	Plagioclase	Rim
BR2017-19	Leucogabbro	Mafic Series	Amphibole	Rim
BR2017-19	Leucogabbro	Mafic Series	Amphibole	Core
BR2017-19	Leucogabbro	Mafic Series	Amphibole	Rim
BR2017-19	Leucogabbro	Mafic Series	Amphibole	Core
BR2017-19	Leucogabbro	Mafic Series	Amphibole	Core
BR2017-19	Leucogabbro	Mafic Series	Amphibole	Core
BR2017-19	Leucogabbro	Mafic Series	Amphibole	Rim
BR2017-19	Leucogabbro	Mafic Series	Amphibole	Core
BR2017-19	Leucogabbro	Mafic Series	Amphibole	Rim
BR2017-19	Leucogabbro	Mafic Series	Amphibole	Core
BR2017-19	Leucogabbro	Mafic Series	Amphibole	Core
111-11-20	Chromitite	Ultramafic Series	Chromite	Core
111-11-20	Chromitite	Ultramafic Series	Chromite	Core
111-11-20	Chromitite	Ultramafic Series	Chromite	Core

Oxygen			Aluminium		
Weight %	Atomic %	Error %	Weight %	Atomic %	Error %
44.92	60.18	8.58	19.00	15.09	4.08
44.79	60.02	8.57	18.97	15.07	4.07
44.86	60.08	8.56	18.76	14.90	4.08
44.55	59.71	8.55	18.84	14.97	4.08
44.95	60.01	8.44	18.69	14.80	4.09
44.80	60.01	8.56	18.76	14.90	4.09
44.85	60.08	8.56	18.93	15.04	4.08
45.15	60.37	8.55	18.80	14.90	4.08
45.23	60.16	8.41	18.30	14.43	4.13
44.86	60.15	8.59	19.02	15.12	4.07
45.17	60.43	8.56	19.00	14.20	4.07
45.28	60.31	8.45	18.39	14.53	4.11
45.05	60.11	8.48	18.58	14.70	4.10
44.76	60.01	8.58	18.66	14.83	4.09
44.42	59.73	8.67	19.09	15.22	4.11
44.40	59.67	8.65	19.01	15.15	4.12
44.26	59.54	8.64	19.00	15.16	4.09
44.43	59.69	8.62	18.97	15.11	4.09
44.41	59.63	8.58	19.02	15.15	4.07
44.44	59.75	8.62	19.08	15.21	4.07
44.51	59.54	8.48	18.96	15.04	4.08
44.76	59.65	8.41	18.16	14.35	4.13
43.84	59.93	8.14	0.94	12.47	25.94
43.46	59.61	8.14	2.32	7.98	25.20
44.14	60.09	8.15	0.91	12.99	26.04
43.64	59.73	8.13	1.39	9.98	25.81
43.34	59.71	8.10	0.52	17.64	26.38
43.28	59.75	8.11	1.71	9.03	25.45
42.99	59.65	8.13	3.31	7.32	24.21
43.28	59.73	8.13	2.22	8.07	24.96
43.20	59.62	8.12	1.90	8.74	25.50
43.12	59.55	8.08	0.01	8.57	25.40
43.22	59.60	8.15	1.46	9.91	25.66
28.84	52.48	5.62	10.32	11.13	7.27
29.36	53.10	5.57	10.36	11.11	7.23
28.11	54.43	5.26	3.84	4.41	9.36

Silicon			Calcium		
Weight %	Atomic %	Error %	Weight %	Atomic %	Error %
21.11	16.11	4.54	13.44	7.19	3.60
21.49	16.40	4.50	13.21	7.07	3.63
21.64	16.51	4.50	13.13	7.02	3.66
21.82	16.66	4.51	12.90	6.90	3,68
22.06	16.78	4.51	11.26	6.00	3.88
21.61	16.49	4.51	13.12	7.01	3.63
21.35	16.29	4.53	13.25	7.09	3.57
21.34	16.26	4.51	13.16	7.03	3.66
22.43	17.00	4.49	11.62	6.17	3.81
21.15	16.15	4.52	13.58	7.27	3.54
20.96	15.97	4.53	13.40	7.16	3.59
21.89	16.61	4.49	12.22	6.50	3.69
22.01	16.73	4.50	12.34	6.57	3.72
21.66	16.54	4.48	13.33	7.13	3.66
21.34	16.35	4.59	13.71	7.36	3.72
21.53	16.48	4.59	13.52	7.26	3.74
21.61	16.56	4.54	13.58	7.29	3.67
21.61	16.54	4.56	13.46	7.22	3.69
21.67	16.58	4.49	13.24	7.09	3.62
21.36	16.36	4.52	13.69	7.35	3.55
22.18	16.90	4.51	12.23	6.53	3.71
22.76	17.28	4.48	11.54	6.14	3.86
20.20	4.15	10.21	5.57	4.18	7.10
19.69	4.25	9.93	5.44	4.33	7.50
20.20	4.15	10.23	5.56	4.27	6.54
20.13	4.17	10.07	5.50	4.21	7.20
20.70	4.09	9.91	5.45	4.20	8.38
20.02	4.20	9.96	5.49	4.28	8.66
19.13	4.33	9.87	5.46	4.38	9.39
19.62	4.24	10.09	5.56	4.26	8.54

Sodium			Magnesium		
Weight %	Atomic %	Error %	Weight %	Atomic %	Error %
1.53	1.43	12.51			
1.54	1.43	11.99			
1.61	1.50	12.09			
1.89	1.76	11.24			
1.98	1.84	11.22			
1.71	1.60	12.03			
1.61	1.50	12.32			
1.55	1.45	12.36			
2.41	2.24	10.32			
1.39	1.30	12.64			
1.47	1.37	12.47			
2.21	2.05	10.49			
2.03	1.89	11.09			
1.59	1.48	11.91			
1.44	1.35	13.39			
1.55	1.45	12.64			
1.55	1.45	12.40			
1.53	1.43	12.35			
1.66	1.55	11.82			
1.43	1.34	12.50			
2.14	1.99	10.45			
2.79	2.58	9.97			
0.19	0.18	52.08	11.55	10.39	5.90
0.37	0.36	30.42	10.68	9.64	5.99
0.14	0.13	65.53	11.78	10.56	5.87
0.26	0.25	44.14	11.30	10.18	5.91
0.27	0.26	35.35	11.09	10.06	5.98
0.27	0.26	40.17	10.30	9.36	6.05
0.40	0.39	32.24	9.12	8.32	6.37
0.48	0.46	25.71	9.95	9.04	6.09
0.29	0.28	37.25	10.30	9.34	6.06
0.31	0.30	31.58	10.42	9.47	6.01
0.24	0.23	40.18	10.71	9.72	6.04
			5.06	6.07	9.30
			4.84	5.76	9.42
			2.32	2.96	12.60

Iron			Chromium			Total	
Weight %	Atomic %	Error %	Weight %	Atomic %	Error %	Weight %	Error %
						100.00	100.00
						100.00	99.99
						100.00	100.01
						100.00	100.00
						98.94	99.43
						100.00	100.01
						99.99	100.00
						100.00	100.01
						99.99	100.00
						100.00	99.99
						100.00	99.13
						99.99	100.00
						100.01	100.00
						100.00	99.99
						100.00	100.01
						100.01	100.01
						100.00	100.00
						100.00	99.99
						100.00	100.00
						100.00	100.01
						100.02	100.00
						100.01	100.00
7.10	2.78	8.76				99.99	99.99
7.50	2.95	9.14				99.99	100.01
6.54	2.55	11.72				100.00	100.00
7.20	2.82	9.47				99.99	100.00
8.38	3.31	8.03				100.00	100.01
8.66	3.43	7.93				100.01	100.02
9.39	3.73	7.38				100.00	99.99
8.54	3.38	7.98				100.01	100.01
8.48	3.35	7.98				100.02	99.99
8.69	3.44	7.58				100.01	98.16
8.28	3.27	8.44				100.01	100.00
23.65	12.33	5.23	32.13	17.99	3.61	100.00	100.00
21.33	11.05	5.45	34.11	18.98	3.60	100.06	100.00
23.69	13.14	5.46	42.04	25.05	3.61	100.00	100.00

Plagioclase		Amphibole		Chromite	
An content	Plagioclase type	Mg#	Amphibole type	Mg#	Cr#
83	Bytownite				
83	Bytownite				
82	Bytownite				
80	Bytownite				
77	Bytownite				
81	Bytownite				
83	Bytownite				
83	Bytownite				
73	Bytownite				
85	Bytownite				
84	Bytownite				
76	Bytownite				
78	Bytownite				
83	Bytownite				
85	Bytownite				
83	Bytownite				
83	Bytownite				
83	Bytownite				
82	Bytownite				
85	Bytownite				
77	Bytownite				
70	Bytownite				
		81	Magnesiohornblende		
		78	Magnesiohornblende		
		82	Magnesiohornblende		
		80	Magnesiohornblende		
		77	Magnesiohornblende		
		75	Magnesiohornblende		
		71	Magnesiohornblende		
		75	Magnesiohornblende		
		76	Magnesiohornblende		
		75	Magnesiohornblende		
		77	Magnesiohornblende		
				35	62
				37	63
				20	85

Sample ID	Lithology	Series	Mineral	Core/Rim/Inclusion
111-11-20	Chromitite	Ultramafic Series	Chromite	Rim
111-11-20	Chromitite	Ultramafic Series	Chromite	Core
111-11-20	Chromitite	Ultramafic Series	Chromite	Core
111-11-20	Chromitite	Ultramafic Series	Chromite	Rim
111-11-20	Chromitite	Ultramafic Series	Chromite	Core
111-11-20	Chromitite	Ultramafic Series	Chromite	Core
111-11-20	Chromitite	Ultramafic Series	Chromite	Core
111-11-20	Chromitite	Ultramafic Series	Chromite	Rim
111-11-21	Chromitite	Ultramafic Series	Chromite	Core
111-11-21	Chromitite	Ultramafic Series	Chromite	Rim
111-11-21	Chromitite	Ultramafic Series	Chromite	Rim
111-11-21	Chromitite	Ultramafic Series	Chromite	Core
111-11-21	Chromitite	Ultramafic Series	Chromite	Core
111-11-21	Chromitite	Ultramafic Series	Chromite	Core
111-11-21	Chromitite	Ultramafic Series	Chromite	Core
111-11-21	Chromitite	Ultramafic Series	Chromite	Core
111-11-21	Chromitite	Ultramafic Series	Chromite	Core
111-11-21	Chromitite	Ultramafic Series	Chromite	Rim
111-11-21	Chromitite	Ultramafic Series	Chromite	Rim
111-11-21	Chromitite	Ultramafic Series	Chromite	Rim
111-11-21	Chromitite	Ultramafic Series	Chromite	Rim
111-11-21	Chromitite	Ultramafic Series	Chromite	Core
111-11-21	Chromitite	Ultramafic Series	Chromite	Core
111-11-21	Chromitite	Ultramafic Series	Chromite	Rim
111-11-21	Chromitite	Ultramafic Series	Chromite	Rim
111-11-21	Chromitite	Ultramafic Series	Chromite	Core
111-11-21	Chromitite	Ultramafic Series	Chromite	Core
111-11-21	Chromitite	Ultramafic Series	Chromite	Rim
111-11-21	Chromitite	Ultramafic Series	Chromite	Core
111-11-21	Chromitite	Ultramafic Series	Chromite	Rim
111-11-21	Chromitite	Ultramafic Series	Chromite	Core
111-11-21	Chromitite	Ultramafic Series	Chromite	Rim
111-11-21	Chromitite	Ultramafic Series	Chromite	Rim
111-11-21	Chromitite	Ultramafic Series	Chromite	Core
111-11-21	Chromitite	Ultramafic Series	Chromite	Core
111-11-21	Chromitite	Ultramafic Series	Chromite	Rim

Oxygen			Aluminium		
Weight %	Atomic %	Error %	Weight %	Atomic %	Error %
28.04	53.99	5.32	4.83	5.51	8.64
28.77	52.63	5.57	9.83	10.67	7.26
28.88	52.43	5.62	10.74	11.56	7.19
28.68	53.42	5.51	8.41	9.29	7.59
29.29	52.70	5.61	10.54	11.24	7.21
28.34	52.22	5.64	10.25	11.20	7.28
27.71	53.14	5.38	5.76	6.55	8.23
27.27	52.83	5.36	5.26	6.04	8.48
28.65	52.06	5.60	11.90	12.82	6.87
25.96	53.41	5.40	2.73	3.33	9.95
25.45	52.72	5.41	2.85	3.50	9.85
27.71	51.60	5.62	11.76	12.99	6.89
28.41	52.16	5.60	11.78	12.82	6.94
28.07	52.01	5.61	11.72	12.88	6.92
27.91	52.07	5.60	11.52	12.74	6.89
28.17	52.17	5.60	11.79	12.95	6.85
28.08	52.15	5.60	11.68	12.86	6.89
25.94	53.26	5.40	3.04	3.71	9.72
25.99	53.31	5.42	3.12	3.80	9.69
26.00	53.54	5.39	2.42	2.96	10.14
25.35	52.89	5.39	1.91	2.37	11.26
29.15	51.22	5.59	11.53	12.01	6.98
29.73	51.86	5.59	11.45	11.84	7.13
25.78	53.42	5.37	1.98	2.43	11.21
25.41	52.41	5.39	2.31	2.83	10.80
29.15	52.33	5.59	11.44	12.17	6.99
28.53	51.59	5.59	11.47	12.30	6.98
25.91	52.66	5.41			
28.37	51.64	5.59	11.45	12.35	6.97
26.32	53.62	5.42	3.46	4.18	9.07
29.35	51.48	5.60	11.49	11.96	7.13
26.63	53.84	5.40	3.92	4.70	8.84
24.77	51.61	5.42	3.41	4.21	9.34
27.95	52.26	5.59	11.09	12.30	6.99
29.25	52.02	5.58	11.48	12.10	7.03
27.03	54.40	5.39	3.73	4.45	8.93

Sodium			Magnesium		
Weight %	Atomic %	Error %	Weight %	Atomic %	Error %
			2.60	3.30	11.83
			4.79	5.77	9.34
			5.00	5.97	9.28
			3.51	4.30	10.16
			5.72	6.78	8.93
			4.28	5.18	9.79
			3.05	3.85	10.99
			2.81	3.58	11.47
			4.43	5.30	9.24
			0.00	0.00	
			0.00	0.00	
			2.80	3.44	10.41
			3.51	4.24	9.80
			2.87	3.50	10.44
			2.42	2.97	11.03
			2.73	3.32	10.76
			2.57	3.14	10.89
			8.70	10.06	7.96
			8.83	10.13	8.01
			1.01	1.37	17.24
			5.68	6.71	8.79
			5.70	6.78	8.73
			4.73	5.71	8.69
			5.07	6.08	9.08
			8.63	9.97	8.02
			2.29	2.81	11.30
			6.79	7.95	8.56

Iron			Chromium			Total	
Weight %	Atomic %	Error %	Weight %	Atomic %	Error %	Atomic %	Weight %
25.03	13.80	5.12	39.50	23.40	3.49	100.00	100.00
23.85	12.50	5.09	32.75	18.44	3.56	100.00	100.00
23.46	12.20	5.11	31.92	17.83	3.57	100.00	100.00
26.73	14.26	4.84	32.67	18.72	3.59	100.00	100.00
22.93	11.82	5.22	31.52	17.45	3.59	100.00	100.00
25.42	13.42	4.89	31.72	17.98	3.63	100.00	100.00
24.56	13.49	5.24	38.92	22.97	3.44	100.00	100.00
24.51	13.60	5.25	40.15	23.94	3.41	100.00	100.00
24.59	12.80	4.90	30.44	17.02	3.63	100.00	100.00
43.33	25.54	4.18	27.98	17.71	3.97	100.00	100.00
43.45	25.78	4.04	28.25	18.00	3.83	100.00	100.00
27.93	14.90	4.67	29.80	17.08	3.61	100.00	100.00
26.35	13.86	4.74	29.95	16.92	3.61	100.00	100.00
27.70	14.71	4.72	29.64	16.90	3.65	100.00	100.00
29.02	15.51	4.47	29.12	16.71	3.60	100.00	100.00
27.82	14.76	4.64	29.49	16.80	3.62	100.00	100.00
28.30	15.06	4.69	29.37	16.79	3.70	100.00	100.00
42.06	24.74	4.19	28.95	18.29	3.89	100.00	100.00
42.52	24.99	4.26	28.36	17.90	4.05	100.00	100.00
42.76	25.23	4.20	28.82	18.27	4.00	100.00	100.00
44.20	26.42	4.12	28.54	18.32	3.95	100.00	100.00
18.08	9.10	5.73	32.55	17.60	3.56	100.00	100.00
17.84	8.92	5.88	32.14	17.25	3.63	100.00	100.00
43.30	25.70	4.21	28.93	18.45	3.94	100.00	100.00
42.22	24.95	4.09	29.05	18.44	3.82	100.00	100.00
23.05	11.85	5.23	30.69	16.95	3.68	100.00	100.00
22.86	11.84	5.10	31.43	17.49	3.56	100.00	100.00
40.65	23.67	4.11	28.71	17.96	3.74	100.00	100.00
24.12	12.58	4.99	30.99	17.36	3.57	100.00	100.00
42.01	24.51	4.29	28.21	17.69	4.05	100.00	100.00
18.12	9.11	5.86	32.40	17.49	3.63	100.00	100.00
40.41	23.40	4.20	29.03	18.06	3.89	100.00	100.00
42.20	25.19	3.96	29.62	18.99	3.66	100.00	100.00
28.37	15.20	4.70	30.31	17.44	3.70	100.00	100.00
20.96	10.68	5.33	31.52	17.25	3.64	100.00	100.00
40.57	23.40	4.21	28.67	17.76	3.94	100.00	100.00

Plagioclase			Amphibole	Chromite	
An content	Plagioclase type	Mg#	Amphibole type	Mg#	Cr#
				21	81
				34	63
				35	61
				25	67
				39	61
				30	62
				24	78
				23	80
				32	57
				14	84
				14	84
				20	57
				25	57
				21	57
				18	57
				20	56
				19	57
				0	83
				0	83
				0	86
				0	89
				55	59
				56	59
				0	88
				6	87
				39	58
				39	59
				23	100
				35	58
				0	81
				55	59
				0	79
				0	82
				17	59
				45	59
				0	80

Sample ID	Lithology	Series	Mineral	Core/Rim/Inclusion
111-11-21	Chromitite	Ultramafic Series	Chromite	Core
111-11-21	Chromitite	Ultramafic Series	Chromite	Core
111-11-21	Chromitite	Ultramafic Series	Chromite	Core
111-11-21	Chromitite	Ultramafic Series	Chromite	Core
111-11-21	Chromitite	Ultramafic Series	Chromite	Core
111-11-21	Chromitite	Ultramafic Series	Chromite	Rim
111-11-21	Chromitite	Ultramafic Series	Chromite	Rim
111-11-21	Chromitite	Ultramafic Series	Chromite	Rim
111-11-21	Chromitite	Ultramafic Series	Chromite	Rim
111-11-21	Chromitite	Ultramafic Series	Chromite	Rim
111-11-21	Chromitite	Ultramafic Series	Chromite	Rim
111-11-21	Chromitite	Ultramafic Series	Chromite	Core
111-11-21	Chromitite	Ultramafic Series	Chromite	Core
111-11-21	Chromitite	Ultramafic Series	Chromite	Core
111-11-21	Chromitite	Ultramafic Series	Chromite	Rim
111-11-21	Chromitite	Ultramafic Series	Chromite	Rim
111-11-21	Chromitite	Ultramafic Series	Chromite	Rim
111-11-21	Chromitite	Ultramafic Series	Chromite	Rim
111-11-21	Chromitite	Ultramafic Series	Chromite	Rim
111-11-21	Chromitite	Ultramafic Series	Chromite	Rim
111-11-21	Chromitite	Ultramafic Series	Chromite	Core
111-11-21	Chromitite	Ultramafic Series	Chromite	Core
111-11-21	Chromitite	Ultramafic Series	Chromite	Core
111-11-21	Chromitite	Ultramafic Series	Chromite	Rim
111-11-21	Chromitite	Ultramafic Series	Chromite	Rim
111-11-21B	Chromitite	Ultramafic Series	Chromite	Core
111-11-21B	Chromitite	Ultramafic Series	Chromite	Core
111-11-21B	Chromitite	Ultramafic Series	Chromite	Core
111-11-21B	Chromitite	Ultramafic Series	Chromite	Core
111-11-21B	Chromitite	Ultramafic Series	Chromite	Rim
111-11-21B	Chromitite	Ultramafic Series	Chromite	Core
111-11-21B	Chromitite	Ultramafic Series	Chromite	Core
111-11-21B	Chromitite	Ultramafic Series	Chromite	Rim
111-11-21B	Chromitite	Ultramafic Series	Chromite	Core
111-11-21B	Chromitite	Ultramafic Series	Chromite	Core

Oxygen			Aluminium		
Weight %	Atomic %	Error %	Weight %	Atomic %	Error %
31.18	52.24	5.73	11.76	11.68	7.18
29.82	51.71	5.61	12.38	12.73	6.87
29.80	51.62	5.63	12.49	12.83	6.96
29.94	51.89	5.61	12.08	12.42	7.03
29.58	51.39	5.63	12.54	12.92	6.93
25.98	53.23	5.42	3.31	4.03	9.37
26.13	53.41	5.38	3.37	4.09	9.50
25.86	53.05	5.44	3.40	4.14	9.03
25.87	52.64	5.48	4.69	5.66	8.46
27.95	51.88	5.62	11.77	12.96	6.88
25.09	51.72	5.45	4.45	5.44	8.67
29.06	51.13	5.63	12.47	13.01	6.84
29.50	51.68	5.63	12.24	12.72	6.97
29.52	51.84	5.62	12.36	12.87	6.92
26.13	53.19	5.44	4.03	4.86	8.83
26.38	53.12	5.46	5.15	6.15	8.27
25.06	51.70	5.44	4.34	5.30	8.76
25.73	52.45	5.44	4.73	5.71	8.58
25.38	52.41	5.41	3.48	4.26	9.56
27.02	55.04	5.31	1.92	2.32	11.49
26.80	54.14	5.39	3.63	4.35	9.05
28.63	52.08	5.61	12.10	13.06	6.90
28.49	51.69	5.63	12.16	13.09	6.93
28.55	51.92	5.63	11.92	12.86	6.94
26.09	53.09	5.44	4.22	5.09	8.87
26.85	54.18	5.42	3.78	4.53	8.94
30.12	53.75	5.93	10.28	10.87	8.13
28.08	52.11	6.00	9.65	10.62	8.63
27.99	54.05	5.86	6.45	7.39	9.39
28.15	51.41	6.00	9.69	10.50	8.53
26.14	53.80	5.80	2.11	2.58	14.30
27.19	50.25	5.98	9.80	10.74	8.31
28.15	51.45	6.01	10.59	11.48	8.09
33.04	59.49	5.56	6.65	7.10	10.91
30.10	53.88	5.91	10.34	10.98	8.20
26.85	50.35	6.05	10.48	11.65	8.12

Silicon			Calcium		
Weight %	Atomic %	Error %	Weight %	Atomic %	Error %
1.62	1.55	15.29			

Sodium			Magnesium		
Weight %	Atomic %	Error %	Weight %	Atomic %	Error %
			11.18	12.32	7.57
			8.84	10.09	7.88
			8.94	10.19	7.91
			8.90	10.16	7.96
			8.84	10.11	7.89
			2.81	3.44	10.42
			8.01	9.27	8.10
			7.99	9.21	8.07
			7.53	8.70	8.10
			4.14	4.96	9.56
			4.75	5.67	9.16
			4.51	5.40	9.27
			5.57	6.54	10.27
			4.19	5.11	11.64
			1.50	1.91	19.10
			6.32	7.60	10.16
			6.36	7.73	10.05
			5.47	6.58	10.32
			4.98	5.87	10.77
			4.37	5.39	11.08

Iron			Chromium			Total	
Weight %	Atomic %	Error %	Weight %	Atomic %	Error %	Weight %	Atomic %
17.20	8.26	5.95	27.06	13.95	3.84	100.00	100.00
17.66	8.77	5.87	31.30	16.70	3.60	100.00	100.00
17.34	8.61	5.84	31.42	16.75	3.66	100.00	100.00
17.36	8.62	5.61	31.71	16.91	3.62	100.00	100.00
17.62	8.77	5.78	31.41	16.80	3.61	100.00	100.00
42.54	24.98	4.17	28.17	17.76	3.97	100.00	100.00
42.15	24.68	4.18	28.34	17.82	3.85	100.00	100.00
42.49	24.98	4.17	28.24	17.83	3.95	100.00	100.00
41.07	23.94	4.15	28.37	17.76	3.90	100.00	100.00
28.02	14.90	4.69	29.45	16.82	3.62	100.00	100.00
42.39	25.03	4.04	28.07	17.81	3.82	100.00	100.00
19.50	9.83	5.50	30.97	16.77	3.53	100.00	100.00
19.08	9.58	5.58	31.19	16.81	3.65	100.00	100.00
20.26	10.20	5.31	30.34	16.39	3.61	100.00	100.00
41.46	24.18	4.26	28.38	17.78	4.02	100.00	100.00
39.88	23.01	4.21	28.60	17.72	3.89	100.00	100.00
41.95	24.80	3.98	28.66	18.20	3.67	100.00	100.00
40.92	23.89	4.05	28.62	17.95	3.74	100.00	100.00
42.75	25.29	4.03	28.40	18.04	3.79	100.00	100.00
43.66	25.47	4.10	27.40	17.17	3.96	100.00	100.00
40.88	23.67	4.30	28.69	17.84	4.04	100.00	100.00
25.03	13.05	4.82	30.10	16.85	3.62	100.00	100.00
24.47	12.72	4.89	30.13	16.83	3.62	100.00	100.00
24.84	12.94	4.87	30.17	16.88	3.70	100.00	100.00
42.00	24.48	4.14	27.69	17.34	3.91	100.00	100.00
41.53	24.01	4.30	27.84	17.28	4.07	100.00	100.00
22.37	11.44	7.30	31.67	17.39	4.84	100.00	100.00
25.77	13.70	6.90	32.31	18.45	4.69	100.00	100.00
34.25	18.95	5.86	29.80	17.70	4.99	100.00	100.00
23.04	12.06	7.37	32.79	18.43	4.75	100.00	100.00
41.73	24.61	5.59	30.02	19.01	5.06	100.00	100.00
23.97	12.69	7.37	32.69	18.59	4.57	100.00	100.00
22.81	11.94	7.25	32.98	18.55	4.62	100.00	100.00
			60.31	33.41	4.51	100.00	100.00
20.98	10.76	8.03	33.60	18.51	4.69	100.00	100.00
26.29	14.12	6.47	32.02	18.48	4.54	100.00	100.00

Plagioclase			Amphibole	Chromite	
An content	Plagioclase type	Mg#	Amphibole type	Mg#	Cr#
				62	54
				56	57
				57	57
				57	58
				56	57
				0	82
				0	81
				0	81
				0	76
				20	56
				0	77
				51	56
				52	57
				49	56
				0	79
				0	74
				0	77
				0	76
				0	81
				0	88
				0	80
				30	56
				33	56
				32	57
				0	77
				0	79
				39	62
				29	63
				10	71
				41	64
				0	88
				40	63
				38	62
					82
				38	63
				30	61

Sample ID	Lithology	Series	Mineral	Core/Rim/Inclusion
111-11-21B	Chromitite	Ultramafic Series	Chromite	Core
111-11-21B	Chromitite	Ultramafic Series	Chromite	Rim
111-11-21B	Chromitite	Ultramafic Series	Chromite	Rim
BR2017-16	Chromitite	Ultramafic Series	Chromite	Core
BR2017-16	Chromitite	Ultramafic Series	Chromite	Core
BR2017-16	Chromitite	Ultramafic Series	Chromite	Rim
BR2017-16	Chromitite	Ultramafic Series	Chromite	Rim
BR2017-16	Chromitite	Ultramafic Series	Chromite	Core
BR2017-16	Chromitite	Ultramafic Series	Chromite	Core
BR2017-16	Chromitite	Ultramafic Series	Chromite	Rim
BR2017-16	Chromitite	Ultramafic Series	Chromite	Rim
BR2017-16	Chromitite	Ultramafic Series	Chromite	Core
BR2017-16	Chromitite	Ultramafic Series	Chromite	Rim
BR2017-16	Chromitite	Ultramafic Series	Chromite	Core
BR2017-16	Chromitite	Ultramafic Series	Chromite	Rim
BR2017-16	Chromitite	Ultramafic Series	Chromite	Core
BR2017-30	Chromitite	Ultramafic Series	Chromite	Core
BR2017-30	Chromitite	Ultramafic Series	Chromite	Core
BR2017-30	Chromitite	Ultramafic Series	Chromite	Core
BR2017-30	Chromitite	Ultramafic Series	Chromite	Core
BR2017-30	Chromitite	Ultramafic Series	Chromite	Rim
BR2017-30	Chromitite	Ultramafic Series	Chromite	Rim
BR2017-30	Chromitite	Ultramafic Series	Chromite	Core
BR2017-30	Chromitite	Ultramafic Series	Chromite	Core
BR2017-30	Chromitite	Ultramafic Series	Chromite	Core
BR2017-30	Chromitite	Ultramafic Series	Chromite	Rim
BR2017-30	Chromitite	Ultramafic Series	Chromite	Core
BR2017-30	Chromitite	Ultramafic Series	Chromite	Core
BR2017-30	Chromitite	Ultramafic Series	Chromite	Core
BR2017-30	Chromitite	Ultramafic Series	Chromite	Rim
BR2017-30	Chromitite	Ultramafic Series	Chromite	Rim
BR2017-30	Chromitite	Ultramafic Series	Chromite	Core
BR2017-30	Chromitite	Ultramafic Series	Chromite	Core
BR2017-30	Chromitite	Ultramafic Series	Chromite	Core
BR2017-30	Chromitite	Ultramafic Series	Chromite	Core
BR2017-30	Chromitite	Ultramafic Series	Chromite	Core

Oxygen			Aluminium		
Weight %	Atomic %	Error %	Weight %	Atomic %	Error %
28.48	52.23	5.99	10.35	11.25	8.08
27.16	54.46	5.76	3.92	4.66	11.26
27.74	54.27	5.69	3.97	4.61	11.21
30.57	53.76	5.72	14.53	15.15	6.69
29.51	53.63	5.61	11.89	12.81	6.94
28.97	54.18	5.46	8.72	9.67	7.44
28.59	53.90	5.56	8.57	9.58	7.55
31.38	54.04	5.74	15.99	16.33	6.49
29.96	53.08	5.72	14.39	15.11	6.68
27.71	53.42	5.49	7.09	8.10	7.88
27.77	53.44	5.54	7.26	8.28	7.84
30.30	53.79	5.68	13.80	14.53	6.69
28.18	54.01	5.49	7.38	8.39	7.72
29.23	53.67	5.55	10.80	11.76	7.01
28.26	54.09	5.42	6.99	7.94	7.77
30.47	53.95	5.69	13.97	14.67	6.71
33.25	55.85	6.26	3.26	3.25	9.06
29.71	55.80	5.66	4.12	4.59	9.05
28.08	52.51	5.57	9.82	10.88	7.27
27.68	51.98	5.56	9.55	10.63	7.36
24.95	51.07	5.47	4.08	4.95	9.03
29.04	56.06	5.35	4.16	4.76	9.04
27.79	51.91	5.57	9.45	10.47	7.30
27.97	55.38	5.53	3.83	4.49	8.95
26.34	52.63	5.41	4.51	5.35	8.86
26.28	52.85	5.73	3.43	4.09	9.68
30.81	54.00	6.19	6.16	6.41	7.76
28.72	52.51	5.60	10.99	11.92	7.08
27.24	50.35	5.55	9.45	10.36	7.40
38.08	59.14	5.63	4.96	4.57	8.51
27.65	54.35	5.41	2.60	3.03	10.56
28.43	52.36	5.56	9.10	9.94	7.51
28.87	52.80	5.55	9.42	10.22	7.35
32.91	57.39	5.39	9.97	10.31	7.01
28.21	52.31	5.55	9.30	10.22	7.41
32.55	55.18	5.61	10.87	10.93	7.02

Sodium			Magnesium		
Weight %	Atomic %	Error %	Weight %	Atomic %	Error %
			4.37	5.39	11.08
			4.60	5.56	10.89
			3.75	4.34	9.71
			2.82	3.37	10.98
			2.09	2.57	12.29
			2.14	2.65	11.77
			4.33	4.90	9.30
			3.90	4.55	9.57
			1.80	2.28	13.03
			1.91	2.42	12.96
			3.42	4.00	9.83
			1.52	1.92	14.14
			2.70	3.27	11.00
			1.57	1.98	13.69
			3.34	3.89	9.90
			7.98	8.82	7.97
			2.33	2.88	12.13
			2.98	3.67	10.59
			3.33	4.11	10.36
			1.24	1.67	15.69
			1.33	1.69	15.89
			3.96	4.86	9.90
			1.40	1.84	15.34
			1.38	1.83	14.59
			5.60	6.46	8.74
			4.05	4.87	9.78
			6.19	7.53	8.84
			13.12	13.40	7.27
			1.94	2.51	13.29
			5.05	6.12	9.36
			4.98	5.99	9.37
			4.16	4.78	9.63
			4.30	5.25	9.78

Iron			Chromium			Total	
Weight %	Atomic %	Error %	Weight %	Atomic %	Error %	Weight %	Atomic %
24.85	13.05	6.97	31.73	17.90	4.60	100.00	100.00
38.69	22.22	5.42	30.23	18.65	4.72	100.00	100.00
37.52	21.03	5.49	29.26	17.61	4.87	100.00	100.00
25.13	12.66	4.95	26.02	14.08	3.86	100.00	100.00
26.50	13.80	4.76	29.29	16.38	3.67	100.00	100.00
27.18	14.56	4.96	33.05	19.02	3.61	100.00	100.00
33.71	18.21	4.48	26.99	15.66	3.85	100.00	100.00
23.64	11.66	5.11	24.67	13.07	3.87	100.00	100.00
25.21	12.79	5.02	26.54	14.47	3.86	100.00	100.00
34.59	19.10	4.38	28.81	17.09	3.73	100.00	100.00
36.41	20.08	4.33	26.66	15.79	3.83	100.00	100.00
25.86	13.15	4.92	26.63	14.54	3.84	100.00	100.00
35.06	19.25	4.34	27.86	16.43	3.73	100.00	100.00
27.18	14.30	4.66	30.09	17.00	3.57	100.00	100.00
30.04	16.47	4.76	33.14	19.52	3.63	100.00	100.00
25.40	12.88	4.92	26.81	14.61	3.80	100.00	100.00
20.20	9.72	5.26	24.66	12.74	3.82	100.00	100.00
29.31	15.77	4.96	31.97	18.48	3.90	100.00	100.00
26.90	14.41	4.90	32.22	18.54	3.67	100.00	100.00
26.75	14.39	4.79	32.69	18.89	3.57	100.00	100.00
36.91	21.64	4.41	32.82	20.67	3.67	100.00	100.00
34.05	18.83	4.66	31.42	18.66	3.91	100.00	100.00
26.06	13.94	4.76	32.74	18.82	3.57	100.00	100.00
34.82	19.75	4.54	32.59	19.85	3.77	100.00	100.00
34.51	19.75	4.38	33.24	20.43	3.61	100.00	100.00
34.51	19.88	4.42	33.12	20.49	3.65	100.00	100.00
18.85	9.47	5.68	31.10	16.78	3.59	100.00	100.00
23.84	12.48	5.16	32.40	18.23	3.63	100.00	100.00
18.73	9.92	5.97	38.40	21.84	3.43	100.00	100.00
18.46	8.21	5.28	19.09	9.12	4.23	100.00	100.00
33.11	18.64	4.82	33.78	20.43	3.99	100.00	100.00
24.47	12.91	5.12	32.94	18.67	3.62	100.00	100.00
24.28	12.72	5.19	32.45	18.26	3.65	100.00	100.00
24.11	12.04	4.75	28.85	15.48	3.60	100.00	100.00
24.84	13.19	4.97	33.35	19.02	3.58	100.00	100.00
16.52	8.02	6.12	31.21	16.28	3.69	100.00	100.00

Plagioclase		Amphibole		Chromite	
An content	Plagioclase type	Mg#	Amphibole type	Mg#	Cr#
				32	61
				0	80
				0	79
				28	48
				21	56
				16	66
				14	62
				32	44
				28	49
				12	68
				12	66
				25	50
				10	66
				20	59
				12	71
				25	50
				50	80
				17	80
				22	63
				24	64
				8	81
				9	80
				28	64
				0	82
				9	79
				9	83
				43	72
				30	60
				46	68
				64	67
				13	87
				35	65
				34	64
				31	60
				31	65
				52	60

Sample ID	Lithology	Series	Mineral	Core/Rim/Inclusion
BR2017-30	Chromitite	Ultramafic Series	Chromite	Core
BR2017-30	Chromitite	Ultramafic Series	Chromite	Core
BR2017-30	Chromitite	Ultramafic Series	Chromite	Core
BR2017-30	Chromitite	Ultramafic Series	Chromite	Core
BR2017-30	Chromitite	Ultramafic Series	Chromite	Core
BR2017-30A	Chromitite	Ultramafic Series	Chromite	Core
BR2017-30A	Chromitite	Ultramafic Series	Chromite	Core
BR2017-30A	Chromitite	Ultramafic Series	Chromite	Core
BR2017-30A	Chromitite	Ultramafic Series	Chromite	Rim
BR2017-30A	Chromitite	Ultramafic Series	Chromite	Rim
BR2017-30A	Chromitite	Ultramafic Series	Chromite	Core
BR2017-30A	Chromitite	Ultramafic Series	Chromite	Rim
BR2017-30A	Chromitite	Ultramafic Series	Chromite	Rim
BR2017-30A	Chromitite	Ultramafic Series	Chromite	Core
BR2017-30A	Chromitite	Ultramafic Series	Chromite	Core
BR2017-30A	Chromitite	Ultramafic Series	Chromite	Rim
BR2017-30A	Chromitite	Ultramafic Series	Chromite	Rim
BR2017-31	Chromitite	Ultramafic Series	Chromite	Core
BR2017-31	Chromitite	Ultramafic Series	Chromite	Core
BR2017-31	Chromitite	Ultramafic Series	Chromite	Core
BR2017-31	Chromitite	Ultramafic Series	Chromite	Core
BR2017-31	Chromitite	Ultramafic Series	Chromite	Rim
BR2017-31	Chromitite	Ultramafic Series	Chromite	Core
BR2017-31	Chromitite	Ultramafic Series	Chromite	Core
BR2017-31	Chromitite	Ultramafic Series	Chromite	Core
BR2017-31	Chromitite	Ultramafic Series	Chromite	Rim
BR2017-31	Chromitite	Ultramafic Series	Chromite	Core
BR2017-31	Chromitite	Ultramafic Series	Chromite	Core
BR2017-31	Chromitite	Ultramafic Series	Chromite	Rim
BR2017-31	Chromitite	Ultramafic Series	Chromite	Rim
BR2017-31	Chromitite	Ultramafic Series	Chromite	Rim
BR2017-31	Chromitite	Ultramafic Series	Chromite	Core
BR2017-31	Chromitite	Ultramafic Series	Chromite	Rim
111-11-20	Chromitite	Ultramafic Series	Clinopyroxene	Inclusion
111-11-20	Chromitite	Ultramafic Series	Clinopyroxene	Inclusion
111-11-20	Chromitite	Ultramafic Series	Clinopyroxene	Inclusion

Oxygen			Aluminium		
Weight %	Atomic %	Error %	Weight %	Atomic %	Error %
37.63	59.83	5.38	12.72	11.99	6.75
27.99	51.05	5.70	8.81	9.52	7.34
29.82	54.18	5.47	7.64	8.23	7.70
27.94	54.09	5.41	5.75	6.60	8.29
28.82	52.95	5.54	9.54	10.39	7.33
28.02	51.91	5.96	9.94	10.91	8.17
28.59	54.21	5.94	9.78	11.00	8.48
29.31	52.32	6.00	9.79	10.37	8.38
32.60	57.70	5.82	11.09	11.64	8.60
28.03	52.71	5.86	8.97	10.00	8.28
29.39	52.41	5.83	9.60	10.15	8.18
30.01	55.82	5.77	9.86	10.87	7.98
29.07	52.75	5.88	10.16	10.93	8.00
28.08	52.17	5.89	9.04	9.96	8.38
28.89	52.82	5.89	10.33	11.20	7.99
27.34	53.35	5.78	5.77	6.67	9.30
28.75	53.69	5.81	8.69	9.63	8.35
27.37	50.19	5.52	9.43	10.26	7.46
30.12	52.41	5.58	11.93	12.31	7.01
29.70	52.69	5.62	11.67	12.28	7.06
29.75	52.83	5.60	11.54	12.15	7.11
27.64	52.41	5.56	9.18	10.32	7.42
27.10	52.95	5.36	5.69	6.59	8.26
29.66	52.99	5.62	12.46	13.21	6.92
29.04	52.34	5.60	11.42	12.21	7.02
28.27	54.32	5.39	6.22	7.09	8.11
29.74	52.28	5.56	10.66	11.11	7.28
29.67	52.22	5.56	10.57	11.03	7.28
26.21	52.20	5.43	5.13	6.06	8.60
28.53	53.52	5.50	8.87	9.86	7.48
27.37	53.61	5.39	4.28	4.97	8.97
28.47	51.83	5.56	10.12	10.92	7.19
29.06	54.00	5.48	9.14	10.07	7.38
45.89	60.12	8.28	0.76	0.59	18.65
46.05	59.80	8.00	4.79	3.69	6.95
48.60	61.46	7.32	6.13	4.60	7.43

Silicon			Calcium		
Weight %	Atomic %	Error %	Weight %	Atomic %	Error %
27.24	20.32	4.13	10.44	5.46	4.32
24.14	17.86	4.40	8.56	4.44	4.77
21.34	15.37	4.95	4.10	2.07	10.75

Sodium			Magnesium		
Weight %	Atomic %	Error %	Weight %	Atomic %	Error %
			7.82	8.18	7.97
			4.96	5.95	9.20
			4.50	5.38	9.56
			1.75	2.23	13.20
			4.35	5.26	9.71
			4.30	5.25	11.40
			7.44	8.74	9.92
			2.93	3.63	12.55
			7.55	8.86	9.31
			5.15	6.15	10.20
			4.47	5.46	10.86
			4.23	5.09	11.26
			1.65	2.12	16.31
			2.77	3.41	12.54
			7.06	8.51	8.64
			7.93	9.08	8.25
			6.18	7.22	8.78
			6.03	7.05	8.80
			2.43	3.03	11.40
			1.83	2.35	13.33
			4.51	5.30	9.32
			5.25	6.23	8.93
			1.70	2.15	13.60
			8.19	9.48	8.29
			8.19	9.49	8.32
			1.56	2.04	13.60
			2.50	3.09	11.42
			2.35	3.03	11.99
			5.86	7.02	8.86
			2.61	3.19	11.25
			15.67	13.51	5.34
3.04	2.75	10.20	13.41	11.46	5.59
			19.84	16.51	5.19

Iron			Chromium			Total	
Weight %	Atomic %	Error %	Weight %	Atomic %	Error %	Weight %	Atomic %
13.92	6.34	6.42	27.91	13.65	3.73	100.00	100.00
18.40	9.62	6.01	36.68	20.58	3.50	100.00	100.00
21.71	11.30	5.40	35.05	19.59	3.54	100.00	100.00
33.44	18.54	4.46	31.12	18.54	3.63	100.00	100.00
25.11	13.21	5.01	32.18	18.19	3.63	100.00	100.00
25.01	13.27	6.81	32.61	18.59	4.66	100.00	100.00
28.93	15.72	6.74	32.70	19.08	4.79	100.00	100.00
20.45	10.45	7.93	33.00	18.12	4.76	100.00	100.00
			56.31	30.66	4.50	100.00	100.00
27.49	14.81	6.19	32.57	18.85	4.46	100.00	100.00
19.99	10.21	7.20	33.47	18.37	4.30	100.00	100.00
27.78	14.80	6.14	32.34	18.51	4.46	100.00	100.00
23.12	12.02	6.85	32.50	18.14	4.45	100.00	100.00
25.25	13.44	6.73	33.17	18.97	4.56	100.00	100.00
23.68	12.40	7.04	32.87	18.49	4.54	100.00	100.00
31.69	17.72	6.04	33.56	20.15	4.65	100.00	100.00
27.14	14.52	6.09	32.65	18.76	4.46	100.00	100.00
16.40	8.62	6.53	39.74	22.42	3.41	100.00	100.00
15.99	7.97	6.09	34.03	18.22	3.53	100.00	100.00
21.99	11.18	5.35	30.45	16.62	3.80	100.00	100.00
21.72	11.05	5.36	30.96	16.92	3.74	100.00	100.00
30.00	16.30	4.69	30.75	17.94	3.75	100.00	100.00
29.00	16.24	4.82	36.39	21.88	3.57	100.00	100.00
22.30	11.42	5.28	31.07	17.09	3.68	100.00	100.00
23.12	11.94	5.17	31.17	17.28	3.68	100.00	100.00
31.65	17.42	4.73	32.16	19.02	3.74	100.00	100.00
18.13	9.13	6.05	33.29	18.00	3.66	100.00	100.00
18.19	9.17	5.93	33.38	18.08	3.66	100.00	100.00
33.63	19.19	4.63	33.47	20.51	3.73	100.00	100.00
29.09	15.63	4.68	31.01	17.90	3.73	100.00	100.00
33.22	18.64	4.69	32.78	19.75	3.82	100.00	100.00
22.68	11.83	5.30	32.87	18.41	3.65	100.00	100.00
27.72	14.75	4.78	31.47	17.99	3.66	100.00	100.00
						100.00	100.00
						100.00	100.00
						100.00	100.00

Plagioclase			Amphibole	Chromite	
An content	Plagioclase type	Mg#	Amphibole type	Mg#	Cr#
				59	53
				41	68
				35	70
				12	74
				31	64
				31	63
				0	63
				48	64
					72
				21	65
				49	64
				0	63
				36	62
				31	66
				31	62
				12	75
				21	66
				52	69
				56	60
				42	58
				41	58
				17	63
				14	77
				34	56
				37	59
				12	73
				54	62
				53	62
				11	77
				18	64
				15	80
				40	63
				19	64

Sample ID	Lithology	Series	Mineral	Core/Rim/Inclusion
111-11-21	Chromitite	Ultramafic Series	Clinopyroxene	Inclusion
111-11-21	Chromitite	Ultramafic Series	Clinopyroxene	Inclusion
111-11-21	Chromitite	Ultramafic Series	Clinopyroxene	Inclusion
111-11-21	Chromitite	Ultramafic Series	Clinopyroxene	Inclusion
111-11-21	Chromitite	Ultramafic Series	Clinopyroxene	Inclusion
111-11-21	Chromitite	Ultramafic Series	Clinopyroxene	Inclusion
111-11-21	Chromitite	Ultramafic Series	Clinopyroxene	Inclusion
111-11-21	Chromitite	Ultramafic Series	Clinopyroxene	Inclusion
111-11-21B	Chromitite	Ultramafic Series	Clinopyroxene	Inclusion
111-11-21B	Chromitite	Ultramafic Series	Clinopyroxene	Inclusion
111-11-21B	Chromitite	Ultramafic Series	Clinopyroxene	Inclusion
111-11-21B	Chromitite	Ultramafic Series	Clinopyroxene	Inclusion
111-11-21B	Chromitite	Ultramafic Series	Clinopyroxene	Inclusion
111-11-21B	Chromitite	Ultramafic Series	Clinopyroxene	Inclusion
111-11-21B	Chromitite	Ultramafic Series	Clinopyroxene	Inclusion
BR2017-16	Chromitite	Ultramafic Series	Clinopyroxene	Inclusion
BR2017-16	Chromitite	Ultramafic Series	Clinopyroxene	Inclusion
BR2017-30	Chromitite	Ultramafic Series	Clinopyroxene	Inclusion
BR2017-30	Chromitite	Ultramafic Series	Clinopyroxene	Inclusion
BR2017-30	Chromitite	Ultramafic Series	Clinopyroxene	Inclusion
BR2017-30	Chromitite	Ultramafic Series	Clinopyroxene	Inclusion
BR2017-30	Chromitite	Ultramafic Series	Clinopyroxene	Inclusion
BR2017-30	Chromitite	Ultramafic Series	Clinopyroxene	Inclusion
BR2017-30	Chromitite	Ultramafic Series	Clinopyroxene	Inclusion
BR2017-30	Chromitite	Ultramafic Series	Clinopyroxene	Inclusion
BR2017-30	Chromitite	Ultramafic Series	Clinopyroxene	Inclusion
BR2017-30	Chromitite	Ultramafic Series	Clinopyroxene	Inclusion
BR2017-30A	Chromitite	Ultramafic Series	Clinopyroxene	Inclusion
BR2017-30A	Chromitite	Ultramafic Series	Clinopyroxene	Inclusion
BR2017-30A	Chromitite	Ultramafic Series	Clinopyroxene	Inclusion
BR2017-30A	Chromitite	Ultramafic Series	Clinopyroxene	Inclusion
BR2017-30A	Chromitite	Ultramafic Series	Clinopyroxene	Inclusion
BR2017-31	Chromitite	Ultramafic Series	Clinopyroxene	Inclusion
BR2017-31	Chromitite	Ultramafic Series	Clinopyroxene	Inclusion
BR2017-31	Chromitite	Ultramafic Series	Clinopyroxene	Inclusion
BR2017-31	Chromitite	Ultramafic Series	Clinopyroxene	Inclusion

Oxygen			Aluminium		
Weight %	Atomic %	Error %	Weight %	Atomic %	Error %
44.42	58.16	8.00	3.01	2.34	8.12
45.03	58.91	8.06	5.01	3.89	6.79
43.17	60.20	8.41	9.99	8.26	5.66
45.20	58.97	7.98	2.97	2.30	8.12
44.61	58.39	8.03	4.55	3.53	7.01
44.38	58.34	8.13	5.67	4.42	6.52
49.13	62.94	7.83	7.58	5.76	5.93
44.24	58.12	8.10	4.95	3.86	6.91
48.27	62.19	8.29			
47.49	61.78	8.59	8.14	6.28	7.12
47.69	61.73	8.40	3.50	2.69	9.79
46.53	60.59	8.48	2.97	2.30	10.97
45.11	59.03	8.52	6.11	4.74	7.68
44.34	59.91	9.52	1.20	0.96	16.02
48.82	62.77	8.32	2.99	2.28	10.51
46.41	60.36	8.08	6.38	4.92	6.49
47.07	61.27	8.16	1.54	1.19	10.98
46.81	60.71	8.01	1.92	1.47	10.21
46.85	60.75	8.01	2.51	1.93	9.26
45.59	59.31	7.99	4.50	3.47	7.28
46.66	60.50	7.97	0.60	0.46	22.36
46.77	60.98	8.20	3.76	2.91	7.61
45.51	59.46	8.16	5.71	4.43	6.77
45.27	60.14	8.62	0.96	0.76	14.21
45.40	59.20	8.05	2.65	2.05	8.76
45.27	59.08	8.07	6.68	5.17	6.51
45.72	59.43	7.99	3.67	2.83	7.83
45.56	61.54	9.66	0.93	0.74	20.68
45.13	59.28	8.82	1.72	1.34	16.13
47.48	61.48	8.34			
46.18	59.96	8.31	4.38	3.37	8.50
45.23	59.09	8.41	5.61	4.34	7.86
44.31	58.04	8.06	4.34	3.37	7.35
46.31	60.29	8.05	0.55	0.42	22.46
45.19	59.01	8.04	5.47	4.23	6.71
44.84	58.73	8.11	6.70	5.20	6.45

Silicon			Calcium		
Weight %	Atomic %	Error %	Weight %	Atomic %	Error %
26.08	19.45	4.24	8.63	4.51	4.58
23.98	17.87	4.38	9.42	4.92	4.64
16.20	12.87	4.94	11.57	6.44	3.43
25.74	19.13	4.24	8.75	4.56	4.76
24.19	18.03	4.37	9.13	4.77	4.50
23.82	17.84	4.38	9.86	5.18	4.43
26.31	19.20	4.30	7.16	3.66	6.50
24.58	18.39	4.35	9.43	4.94	4.64
27.38	20.09	4.41	8.75	4.50	6.80
22.04	16.33	5.11	10.41	5.40	6.65
25.54	18.83	4.68	9.18	4.74	6.66
26.05	19.33	4.66	9.38	4.88	6.43
22.57	16.82	4.91	9.92	5.18	5.86
25.73	19.80	4.39	17.79	9.60	4.43
26.66	19.52	4.59	8.36	4.29	6.99
22.52	16.69	4.54	9.58	4.98	4.55
26.61	19.73	4.10	10.15	5.27	4.40
27.22	20.11	4.18	8.40	4.35	5.01
26.47	19.55	4.23	8.51	4.41	4.82
24.44	18.11	4.41	8.50	4.41	4.92
29.13	21.52	4.05	7.81	4.04	5.20
25.23	18.74	4.27	10.13	5.27	4.49
23.07	17.17	4.54	9.82	5.12	4.57
26.74	20.23	4.00	13.84	7.34	3.75
25.72	19.11	4.29	8.88	4.62	4.66
22.21	16.51	4.62	9.25	4.82	4.63
24.83	18.38	4.35	8.55	4.44	4.86
24.33	18.72	4.40	19.87	10.72	4.48
28.45	21.29	4.63	9.61	5.04	7.32
27.34	20.16	4.40	9.25	4.78	6.09
23.85	17.64	4.74	8.95	4.64	6.31
23.63	17.59	4.80	9.31	4.86	6.33
24.65	18.39	4.38	8.96	4.69	4.72
27.65	20.50	4.07	9.06	4.71	4.67
23.49	17.47	4.46	9.19	4.79	4.70
22.43	16.73	4.57	9.68	5.06	4.71

Sodium			Magnesium			Total	
Weight %	Atomic %	Error %	Weight %	Atomic %	Error %	Weight %	Atomic %
3.27	2.98	9.22	14.58	12.56	5.43	100.00	100.00
3.42	3.11	9.45	13.14	11.31	5.54	100.00	100.00
			8.28	7.60	6.36	100.00	100.00
2.97	2.70	10.09	14.38	12.34	5.44	100.00	100.00
3.91	3.56	8.95	13.62	11.73	5.54	100.00	100.00
3.02	2.76	10.02	13.25	11.46	5.48	100.00	100.00
3.17	2.83	10.75	6.65	5.60	6.58	100.00	100.00
3.17	2.90	9.92	13.64	11.79	5.47	100.00	100.00
			15.60	13.23	5.78	100.00	100.00
			11.91	10.20	6.24	100.00	100.00
			14.10	12.01	6.02	100.00	100.00
			15.06	12.91	5.94	100.00	100.00
3.65	3.32	11.04	12.65	10.90	6.31	100.00	100.00
			10.93	9.72	6.38	100.00	100.00
			13.16	11.13	6.12	100.00	100.00
2.74	2.48	10.86	12.37	10.58	5.63	100.00	100.00
			14.63	12.53	5.35	100.00	100.00
			15.66	13.36	5.29	100.00	100.00
			15.65	13.36	5.29	100.00	100.00
3.40	3.08	9.56	13.57	11.62	5.58	100.00	100.00
			15.79	13.48	5.27	100.00	100.00
			14.11	12.10	5.40	100.00	100.00
3.10	2.82	10.47	12.79	11.00	5.65	100.00	100.00
			13.18	11.52	5.48	100.00	100.00
2.95	2.67	10.22	14.39	12.35	5.52	100.00	100.00
3.76	3.41	9.30	12.83	11.02	5.65	100.00	100.00
3.64	3.30	9.29	13.58	11.62	5.60	100.00	100.00
			9.31	8.28	6.81	100.00	100.00
			15.09	13.04	6.04	100.00	100.00
			15.93	13.57	5.70	100.00	100.00
			13.07	11.16	6.22	100.00	100.00
3.58	3.25	10.92	12.64	10.87	6.24	100.00	100.00
4.11	3.74	8.87	13.64	11.76	5.58	100.00	100.00
			16.43	14.08	5.18	100.00	100.00
3.54	3.22	9.29	13.12	11.27	5.58	100.00	100.00
3.70	3.37	9.19	12.65	10.90	5.63	100.00	100.00

Sample ID	Lithology	Series	Mineral	Core/Rim/Inclusion
BR2017-31	Chromitite	Ultramafic Series	Clinopyroxene	Inclusion
111-11-21	Chromitite	Ultramafic Series	Orthopyroxene	Inclusion
111-11-21B	Chromitite	Ultramafic Series	Orthopyroxene	Inclusion
111-11-21B	Chromitite	Ultramafic Series	Orthopyroxene	Inclusion
111-11-21B	Chromitite	Ultramafic Series	Orthopyroxene	Inclusion
BR2017-30A	Chromitite	Ultramafic Series	Orthopyroxene	Inclusion
BR2017-30A	Chromitite	Ultramafic Series	Orthopyroxene	Inclusion
111-11-20	Chromitite	Ultramafic Series	Plagioclase	Inclusion
111-11-21	Chromitite	Ultramafic Series	Plagioclase	Inclusion
111-11-21	Chromitite	Ultramafic Series	Plagioclase	Inclusion
111-11-21	Chromitite	Ultramafic Series	Plagioclase	Inclusion
111-11-21	Chromitite	Ultramafic Series	Plagioclase	Inclusion
111-11-21B	Chromitite	Ultramafic Series	Plagioclase	Inclusion
111-11-21B	Chromitite	Ultramafic Series	Plagioclase	Inclusion
111-11-21B	Chromitite	Ultramafic Series	Plagioclase	Inclusion
111-11-21B	Chromitite	Ultramafic Series	Plagioclase	Inclusion
111-11-21B	Chromitite	Ultramafic Series	Plagioclase	Inclusion
BR2017-30	Chromitite	Ultramafic Series	Plagioclase	Inclusion
BR2017-30	Chromitite	Ultramafic Series	Plagioclase	Inclusion
BR2017-30	Chromitite	Ultramafic Series	Plagioclase	Inclusion
BR2017-30	Chromitite	Ultramafic Series	Plagioclase	Inclusion
BR2017-16	Chromitite	Ultramafic Series	Calcite	Inclusion
BR2017-16	Chromitite	Ultramafic Series	Calcite	Inclusion

Oxygen			Aluminium		
Weight %	Atomic %	Error %	Weight %	Atomic %	Error %
44.96	59.16	8.25	1.06	0.83	14.78
37.31	49.68	7.43			
46.92	59.34	7.10			
47.85	60.09	7.01			
48.27	60.63	7.01			
49.02	61.34	6.86			
49.11	61.41	6.87			
45.31	57.98	6.92	11.28	8.56	4.79
45.21	58.04	6.93	10.34	7.87	4.67
46.24	59.02	6.87	10.57	8.00	4.83
50.24	62.92	6.75	10.71	7.95	5.20
46.51	60.04	7.57	9.17	7.02	5.05
45.84	58.71	7.29	9.49	7.21	5.62
46.01	58.79	7.20	9.94	7.53	5.58
47.20	60.05	7.21	9.09	6.85	5.77
46.46	59.25	7.22	9.94	7.51	5.76
45.52	58.25	7.23	10.54	8.00	5.48
45.13	57.98	7.01	9.95	7.58	4.80
45.70	58.54	6.97	9.74	7.40	4.81
45.57	58.37	6.99	8.02	6.09	5.21
45.91	58.71	6.94	10.26	7.78	4.85
51.22	72.45	10.39			
52.28	73.29	10.33			

Silicon			Calcium		
Weight %	Atomic %	Error %	Weight %	Atomic %	Error %
27.65	20.72	4.11	10.30	5.41	4.36
39.24	29.76	4.09			
31.45	22.66	4.58			
28.77	20.59	4.83			
30.38	21.74	4.64			
29.95	21.35	4.49			
29.71	21.16	4.53			
32.15	23.44	4.14			
34.70	25.38	3.91			
33.36	24.26	4.00			
30.26	21.59	4.25			
32.93	24.22	3.93	3.96	2.04	8.95
35.44	25.85	4.20			
34.05	24.79	4.26			
34.88	25.28	4.21			
33.89	24.62	4.30			
33.27	24.25	4.37			
35.33	25.86	3.92			
34.96	25.51	3.91			
34.95	25.50	3.95			
34.05	24.81	3.98			
			48.78	27.55	2.43
			47.72	26.71	2.44

Sodium			Magnesium		
Weight %	Atomic %	Error %	Weight %	Atomic %	Error %
			16.03	13.88	5.20
			23.46	20.56	4.38
			21.64	18.01	5.23
			23.38	19.32	5.28
			21.34	17.64	5.31
			21.03	17.31	5.23
			21.18	17.43	5.25
11.26	10.03	6.95			
9.75	8.72	6.98			
9.83	8.73	7.10			
6.29	5.48	8.71	2.50	2.06	8.81
7.43	6.67	7.93			
9.23	8.23	8.17			
9.99	8.89	8.04			
8.84	7.82	8.29			
9.70	8.61	8.07			
10.67	9.50	7.74			
9.59	8.58	7.07			
9.59	8.55	7.07			
7.87	7.02	7.45	3.58	3.02	7.04
9.78	8.70	7.08			

Plagioclase	
An content	Plagioclase type
0	Albite
0	Albite
0	Albite
0	Albite
23	Oligoclase
0	Albite
0	Albite
0	Albite
0	Albite
0	Albite
0	Albite
0	Albite
0	Albite
0	Albite

Appendix 2.5. Main Raman spectra peak values for selected chromites and chromite-hosted inclusions from the Bird River Sill.

Sample ID	Lithology	Series	Mineral	
BR2017-9	Peridotite	Ultramafic Series	Clinopyroxene (inclusion)	**667.20**
BR2017-30	Chromitite	Ultramafic Series	Chromite	218.81
BR2017-30	Chromitite	Ultramafic Series	Albite (inclusion)	0.78
BR2017-30	Chromitite	Ultramafic Series	Albite (inclusion)	1.37
BR2017-30	Chromitite	Ultramafic Series	Albite (inclusion)	0.76
BR2017-30	Chromitite	Ultramafic Series	Albite (inclusion)	1.86
BR2017-30	Chromitite	Ultramafic Series	Albite (inclusion)	1.64
BR2017-30	Chromitite	Ultramafic Series	Albite (inclusion)	1.69
BR2017-30	Chromitite	Ultramafic Series	Albite (inclusion)	2.00
BR2017-30	Chromitite	Ultramafic Series	Albite (inclusion)	1.47
BR2017-30	Chromitite	Ultramafic Series	Albite (inclusion)	1.44
BR2017-30	Chromitite	Ultramafic Series	Clinopyroxene (inclusion)	1.18
BR2017-30	Chromitite	Ultramafic Series	Clinopyroxene (inclusion)	1.02
BR2017-30	Chromitite	Ultramafic Series	Clinopyroxene (inclusion)	0.96
BR2017-30	Chromitite	Ultramafic Series	Clinopyroxene (inclusion)	1.12
BR2017-30	Chromitite	Ultramafic Series	Clinopyroxene (inclusion)	197.28
BR2017-30A	Chromitite	Ultramafic Series	Chromite	**584.59**
BR2017-30A	Chromitite	Ultramafic Series	Chromite	**588.83**
BR2017-31	Chromitite	Ultramafic Series	Chromite	91.72
BR2017-31	Chromitite	Ultramafic Series	Clinopyroxene (inclusion)	1.43
BR2017-31	Chromitite	Ultramafic Series	Clinopyroxene (inclusion)	235.09
BR2017-31	Chromitite	Ultramafic Series	Clinopyroxene (inclusion)	87.01

Sample ID	Lithology	Series	Mineral	
BR2017-31	Chromitite	Ultramafic Series	Clinopyroxene (inclusion)	0.58
BR2017-31	Chromitite	Ultramafic Series	Clinopyroxene (inclusion)	0.53
BR2017-31	Chromitite	Ultramafic Series	Clinopyroxene (inclusion)	0.54
BR2017-31	Chromitite	Ultramafic Series	Clinopyroxene (inclusion)	1.31
BR2017-31	Chromitite	Ultramafic Series	Clinopyroxene (inclusion)	1.36
BR2017-31	Chromitite	Ultramafic Series	Clinopyroxene (inclusion)	1.58
BR2017-31	Chromitite	Ultramafic Series	Albite (inclusion)	89.64
BR2017-31	Chromitite	Ultramafic Series	Albite (inclusion)	1.68
BR2017-31	Chromitite	Ultramafic Series	Albite (inclusion)	165.19

Peak values in bold indicate the most important values

Main Raman spectra peak values (cm^{-1})								
1012.20								
279.46	**710.51**							
157.39	197.63	**462.46**	**495.66**	681.32				
156.79	222.94	**461.72**	**494.19**	680.54				
112.28	197.37	365.26	**513.73**	680.69				
197.77	365.89	**494.53**	681.37					
197.04	365.11	680.86	1055.83					
197.22	365.14	681.13	1056.29					
156.31	221.85	**461.52**	**494.12**					
153.38	217.94	**456.84**	**490.55**	682.33				
109.08	156.15	195.89	217.53	360.73	**461.83**	**493.41**	681.88	1110.73
120.00	171.75	236.32	394.19	533.02	**679.34**	**1030.22**	1059.31	
120.44	182.96	228.18	376.82	398.93	**681.19**			
106.59	193.81	360.77	**678.67**	**1051.64**				
192.99	360.60	**678.49**	1139.2					
365.76	**681.14**							
704.34	1220.47	1540.55						
705.76	1540.11	1624.04	1691.62	2088.21				
585.26	**699.60**							
114.90	197.28	365.04	**680.85**					
391.14	**672.37**	1256.58						
123.56	168.05	226.00	391.07	549.44	**675.93**	1056.51		

Main Raman spectra peak values (cm^{-1})								
83.31	182.70	226.27	**679.13**	1064.94				
87.05	202.17	548.41	**679.98**	1247.91				
169.34	228.66	**676.73**	1059.40					
197.97	367.24	**680.81**	1057.90					
114.76	197.14	365.44	**680.44**	1056.66				
197.17	365.28	**680.34**	1055.48					
164.77	295.92	**484.05**	**513.68**	1105.18				
93.40	164.98	294.69	366.64	**482.07**	**512.83**	**681.39**	1248.71	1572.07
295.17	**513.81**	**679.43**						

Appendix 3

Appendix 3.1. Major (wt.%) and trace (ppm) element data for anorthosites, leucogabbros, gabbros, melagabbros and pyroxenites from the Mayville Intrusion.

Lithology	Gabbro	Gabbro	Leucogabbro	Anorthosite	Anorthosite	Anorthosite
Zone	HBZ	ALZ	ALZ	ALZ	ALZ	ALZ
	111-12-612A01	111-12-621A01	MV2017-1	MV2017-2	MV2017-3	MV2017-4
SiO_2	48.47	56.52	48.28	48.93	47.47	48.03
Al_2O_3	14.29	12.31	23.08	25.28	27.46	24.53
$Fe_2O_3^T$	12.79	15.52	5.95	4.49	5.14	5.74
MnO	0.25	0.21	0.09	0.06	0.07	0.09
MgO	8.50	1.86	4.95	3.14	2.28	4.39
CaO	11.47	5.60	13.57	10.89	13.45	14.31
Na_2O	2.35	3.88	1.85	3.38	2.51	1.89
K_2O	0.17	0.57	0.45	1.09	0.28	0.17
TiO_2	0.78	1.71	0.30	0.32	0.80	0.20
P_2O_5	0.05	0.32	0.01	< 0.01	0.10	< 0.01
LOI	0.80	0.50	0.97	0.96	1.01	0.79
Total	99.92	99.01	99.51	98.54	100.60	100.10
Mg#	54	18	60	55	44	58
Ni	154	21	79	60	70	78
Cr	340	74	47	25	38	235
Co	59	38	29	17	21	23
V	275	42	113	74	103	124
Sc	43	36	17	11	9	27
Li	9	23	36	35	21	14
Rb	2	6	7	60	5	3
Ba	44	97	18	85	53	24
Sr	97	116	155	179	160	117
Ga	11	25	18	21	20	18
Zr	36	228	11	72	50	10
Hf	1.08	6.25	0.33	1.99	1.41	0.30
Nb	1.69	11.96	0.56	0.74	2.84	0.50
Ta	0.11	0.72	0.03	0.08	0.22	0.03
U	0.06	0.36	0.04	0.09	0.28	0.05
Th	0.26	1.09	0.10	0.26	0.63	0.09
Y	16.2	64.0	9.8	15.4	6.7	5.7
Pb	0.84	1.91	1.22	1.80	2.21	1.51
Cu	6.2	15.9	32.9	25.2	226.0	2.6
Zn	130.8	51.2	48.0	37.6	28.5	41.5
La	2.10	9.00	1.00	1.80	2.70	0.80

Lithology	Gabbro	Gabbro	Leucogabbro	Anorthosite	Anorthosite	Anorthosite
Zone	HBZ	ALZ	ALZ	ALZ	ALZ	ALZ
	111-12-612A01	111-12-621A01	MV2017-1	MV2017-2	MV2017-3	MV2017-4
Ce	5.68	25.69	3.06	5.08	5.17	1.99
Pr	0.93	4.05	0.58	0.89	0.67	0.32
Nd	4.82	21.44	3.12	4.76	2.73	1.54
Sm	1.63	6.86	1.14	1.76	0.77	0.52
Eu	0.47	2.23	0.56	0.74	0.52	0.44
Gd	2.21	9.16	1.50	2.27	0.97	0.76
Tb	0.40	1.58	0.26	0.40	0.16	0.14
Dy	2.79	10.74	1.74	2.67	1.13	0.96
Ho	0.60	2.33	0.36	0.58	0.24	0.21
Er	1.85	7.01	1.06	1.77	0.71	0.61
Tm	0.27	1.05	0.15	0.26	0.11	0.09
Yb	1.81	7.24	1.00	1.81	0.73	0.60
Lu	0.27	1.14	0.16	0.27	0.12	0.09
Al_2O_3/TiO_2	18.44	7.22	77.45	78.27	34.50	123.89
Sr/Y	7.85	1.95	19.75	13.93	35.40	42.33
Nb/Ta	15.69	16.59	16.44	9.78	13.13	16.73
Zr/Y	2.23	3.56	1.12	4.67	7.46	1.75
La/Yb	1.16	1.24	1.01	0.99	3.71	1.34
Th/Yb	0.14	0.15	0.10	0.14	0.86	0.14
Nd/Sm	2.96	3.13	2.73	2.71	3.54	2.96
La/Nb	1.24	0.75	1.79	2.42	0.95	1.59
Dy/Yb	1.54	1.48	1.74	1.47	1.56	1.61
Th/Ta	2.38	1.50	2.79	3.38	2.90	2.87
Ti/Zr	129.06	44.83	162.41	26.89	95.44	118.70
La/Sm_{cn}	0.83	0.85	0.57	0.66	2.26	0.99
La/Yb_{cn}	0.83	0.89	0.72	0.71	2.66	0.96
Gd/Yb_{cn}	1.01	1.05	1.25	1.04	1.11	1.05
Nb/Nb*	0.54	0.90	0.43	0.26	0.51	0.45
Zr/Zr*	0.76	1.11	0.35	1.47	2.04	0.66
Hf/Hf*	0.82	1.10	0.37	1.47	2.08	0.72
Ti/Ti*	0.99	0.54	0.58	0.39	2.33	0.80
Eu/Eu*	0.76	0.86	1.31	1.12	1.82	2.12
Ce/Ce*	0.98	1.03	0.98	0.97	0.93	0.95
North	50°38.114'	50°38.297'	50°37.817'	50°37.819'	50°37.966'	50°37.966'
West	095°36.332'	095°38.102'	095°33.426'	095°33.421'	095°33.384'	095°33.384'

Lithology	Anorthosite	Anorthosite	Anorthosite	Leucogabbro	Leucogabbro	Anorthosite
Zone	ALZ	ALZ	ALZ	ALZ	ALZ	ALZ
	MV2017-5	MV2017-6	MV2017-7	MV2017-8	MV2017-9	111-12-538A01
SiO_2	46.75	46.62	46.36	45.28	47.29	47.07
Al_2O_3	25.50	24.44	26.32	21.93	22.01	24.25
$Fe_2O_3^T$	5.49	6.97	6.19	9.36	5.53	5.47
MnO	0.09	0.12	0.11	0.14	0.11	0.08
MgO	2.95	3.67	3.21	7.86	4.04	3.93
CaO	13.30	11.48	12.94	11.90	15.04	13.91
Na_2O	2.06	2.75	2.35	1.44	1.39	2.17
K_2O	0.48	0.81	0.56	0.49	0.88	0.30
TiO_2	0.38	0.46	0.40	0.48	0.28	0.24
P_2O_5	0.04	0.06	0.03	0.01	< 0.01	< 0.01
LOI	1.53	1.53	2.23	1.71	2.10	1.36
Total	98.55	98.90	100.70	100.60	98.67	98.78
Mg#	49	48	48	60	57	56
Ni	40	44	55	272	51	51
Cr	102	104	100	14	422	174
Co	22	30	23	57	19	20
V	115	136	122	132	134	111
Sc	14	24	16	15	30	25
Li	92	86	104	36	33	9
Rb	29	33	25	13	35	5
Ba	64	445	139	24	77	26
Sr	180	178	166	124	132	141
Ga	17	14	17	16	19	18
Zr	26	28	23	9	7	15
Hf	0.73	0.77	0.62	0.29	0.24	0.43
Nb	1.14	1.35	1.07	0.27	0.24	0.45
Ta	0.08	0.09	0.06	0.02	0.02	0.03
U	0.06	0.05	0.06	0.01	0.02	0.06
Th	0.17	0.18	0.14	0.02	0.03	0.06
Y	6.8	9.0	7.6	4.2	7.1	5.8
Pb	3.94	3.27	3.05	0.60	1.06	3.37
Cu	35.1	4.8	46.1	20.4	7.1	9.0
Zn	44.9	66.3	72.8	58.9	54.1	40.2
La	1.20	1.60	1.20	0.70	0.60	0.70

Lithology	Anorthosite	Anorthosite	Anorthosite	Leucogabbro	Leucogabbro	Anorthosite
Zone	ALZ	ALZ	ALZ	ALZ	ALZ	ALZ
	MV2017-5	MV2017-6	MV2017-7	MV2017-8	MV2017-9	111-12-538A01
Ce	2.93	3.69	3.10	1.55	1.72	1.70
Pr	0.48	0.58	0.48	0.25	0.34	0.31
Nd	2.49	2.88	2.49	1.25	1.81	1.63
Sm	0.78	0.96	0.81	0.44	0.69	0.57
Eu	0.31	0.25	0.39	0.38	0.51	0.37
Gd	1.01	1.28	1.08	0.61	1.01	0.78
Tb	0.18	0.23	0.19	0.11	0.19	0.14
Dy	1.23	1.56	1.30	0.73	1.26	1.02
Ho	0.26	0.34	0.28	0.16	0.28	0.21
Er	0.77	1.02	0.83	0.50	0.78	0.65
Tm	0.11	0.15	0.12	0.07	0.11	0.09
Yb	0.76	1.03	0.82	0.49	0.74	0.60
Lu	0.11	0.15	0.13	0.08	0.11	0.09
Al_2O_3/TiO_2	67.46	53.25	65.80	45.50	78.89	102.75
Sr/Y	36.60	31.00	29.83	131.00	25.40	36.25
Nb/Ta	15.25	15.91	16.64	15.22	12.42	15.13
Zr/Y	3.83	3.11	3.03	2.17	0.99	2.60
La/Yb	1.59	1.55	1.46	1.42	0.81	1.18
Th/Yb	0.22	0.18	0.18	0.04	0.04	0.10
Nd/Sm	3.19	3.00	3.07	2.84	2.62	2.85
La/Nb	1.05	1.18	1.13	2.55	2.54	1.54
Dy/Yb	1.62	1.51	1.59	1.48	1.70	1.72
Th/Ta	2.21	2.15	2.25	1.00	1.63	2.03
Ti/Zr	87.16	98.27	104.26	321.06	238.94	94.32
La/Sm_{cn}	0.99	1.08	0.96	1.03	0.56	0.79
La/Yb_{cn}	1.14	1.11	1.05	1.02	0.58	0.84
Gd/Yb_{cn}	1.10	1.02	1.09	1.03	1.12	1.08
Nb/Nb*	0.60	0.59	0.60	0.57	0.41	0.52
Zr/Zr*	1.10	1.00	0.96	0.72	0.37	0.92
Hf/Hf*	1.12	0.99	0.93	0.84	0.46	0.95
Ti/Ti*	1.15	1.10	1.08	2.32	0.84	0.90
Eu/Eu*	1.06	0.69	1.26	2.24	1.88	1.68
Ce/Ce*	0.94	0.93	0.99	0.91	0.92	0.88
North	50°36.847'	50°36.847'	50°36.871'	50°37.619'	50°37.624'	50°38.230'
West	095°34.758'	095°34.758'	095°34.718'	095°32.556'	095°32.554'	095°35.163'

Lithology	Anorthosite	Anorthosite	Leucogabbro	Pyroxenite	Melagabbro	Leucogabbro
Zone	ALZ	HBZ	HBZ	HBZ	HBZ	ALZ
	111-12-541A01	111-12-514A01	111-12-461A01	111-11-17	111-11-02	111-11-16
SiO_2	45.38	48.70	45.74	44.91	41.96	46.29
Al_2O_3	24.52	25.05	20.12	15.81	12.12	23.76
$Fe_2O_3^T$	6.40	5.34	9.41	14.77	20.70	7.33
MnO	0.08	0.06	0.14	0.19	0.21	0.12
MgO	3.60	1.98	7.74	8.98	7.47	6.87
CaO	11.02	12.41	12.92	11.13	9.44	12.67
Na_2O	2.14	3.05	1.40	1.50	1.59	1.62
K_2O	1.93	0.29	0.20	0.10	0.17	0.18
TiO_2	0.53	0.96	0.31	0.54	1.01	0.34
P_2O_5	0.06	0.01	< 0.01	0.03	0.07	0.03
LOI	4.50	0.73	1.18	1.41	3.18	1.10
Total	100.20	98.57	99.16	99.37	97.92	100.30
Mg#	50	40	59	52	39	63
Ni	33	30	251	1784	3308	270
Cr	43	35	299	831	406	256
Co	21	21	54	114	187	44
V	135	131	104	226	350	104
Sc	21	19	22	39	46	22
Li	64	28	27	32	16	18
Rb	38	4	9	3	1	2
Ba	159	38	20	21	22	26
Sr	167	148	111	74	59	148
Ga	18	21	15	14	14	17
Zr	35	26	14	26	35	23
Hf	0.98	0.81	0.42	0.77	1.05	0.65
Nb	1.45	3.45	0.56	1.00	1.59	0.90
Ta	0.09	0.25	0.03	0.07	0.10	0.06
U	0.05	0.05	0.03	0.06	0.06	0.04
Th	0.19	0.08	0.07	0.09	0.15	0.12
Y	12.8	11.6	5.4	10.8	16.9	8.7
Pb	0.68	3.19	1.09	2.04	1.11	0.59
Cu	64.3	50.0	98.2	2863.6	2900.0	195.7
Zn	47.5	65.3	55.4	81.4	113.9	52.9
La	1.80	1.30	0.90	1.50	2.10	1.60

Lithology	Anorthosite	Anorthosite	Leucogabbro	Pyroxenite	Melagabbro	Leucogabbro
Zone	ALZ	HBZ	HBZ	HBZ	HBZ	ALZ
	111-12-541A01	111-12-514A01	111-12-461A01	111-11-17	111-11-02	111-11-16
Ce	4.97	3.65	2.34	3.66	5.77	3.41
Pr	0.84	0.64	0.38	0.60	0.94	0.56
Nd	4.37	3.41	1.75	3.16	4.97	2.95
Sm	1.43	1.25	0.58	1.09	1.76	0.92
Eu	0.57	0.59	0.39	0.45	0.64	0.42
Gd	1.86	1.76	0.76	1.56	2.37	1.20
Tb	0.33	0.30	0.13	0.27	0.44	0.22
Dy	2.32	1.99	0.92	1.93	2.96	1.49
Ho	0.49	0.41	0.21	0.42	0.64	0.32
Er	1.50	1.20	0.59	1.28	1.90	0.92
Tm	0.22	0.17	0.09	0.18	0.27	0.14
Yb	1.43	1.15	0.60	1.24	1.76	0.91
Lu	0.21	0.18	0.10	0.19	0.28	0.14
Al_2O_3/TiO_2	45.92	26.12	64.49	29.22	11.95	70.71
Sr/Y	16.00	13.55	40.00	11.14	4.62	28.60
Nb/Ta	15.43	14.08	17.34	14.93	15.69	15.77
Zr/Y	2.73	2.25	2.59	2.41	2.07	2.64
La/Yb	1.26	1.13	1.50	1.21	1.20	1.76
Th/Yb	0.14	0.07	0.12	0.07	0.09	0.13
Nd/Sm	3.05	2.73	3.02	2.91	2.82	3.21
La/Nb	1.24	0.38	1.62	1.50	1.32	1.78
Dy/Yb	1.62	1.73	1.53	1.56	1.69	1.64
Th/Ta	2.05	0.33	2.25	1.27	1.49	2.04
Ti/Zr	91.46	221.12	133.60	124.74	173.68	87.58
La/Sm_{cn}	0.81	0.67	1.00	0.89	0.77	1.12
La/Yb_{cn}	0.91	0.81	1.07	0.87	0.86	1.26
Gd/Yb_{cn}	1.08	1.26	1.05	1.04	1.12	1.09
Nb/Nb*	0.58	2.48	0.51	0.66	0.66	0.49
Zr/Zr*	0.83	0.75	0.82	0.83	0.70	0.83
Hf/Hf*	0.84	0.84	0.89	0.89	0.76	0.84
Ti/Ti*	0.83	1.75	1.13	1.05	1.19	0.89
Eu/Eu*	1.06	1.21	1.77	1.06	0.95	1.22
Ce/Ce*	0.98	0.97	0.97	0.94	1.00	0.87
North	50°38.345'	50°37.594'	50°38.051'	50°38.063'	50°37.500'	50°38.043'
West	095°35.171'	095°34.329'	095°37.415'	095°37.390'	095°35.358'	095°37.247'

Lithology	Melagabbro	Leucogabbro	Pyroxenite	Melagabbro	Melagabbro	Melagabbro
Zone	HBZ	HBZ	HBZ	HBZ	HBZ	HBZ
	111-11-04	111-11-12	111-11-11	111-11-10	111-11-09	111-11-08
SiO_2	45.44	41.52	42.64	50.05	44.50	44.70
Al_2O_3	15.70	23.74	15.69	15.13	13.73	18.73
$Fe_2O_3^T$	12.67	9.96	12.52	11.64	16.89	13.79
MnO	0.23	0.13	0.16	0.18	0.21	0.15
MgO	9.22	7.10	13.29	7.82	9.34	6.33
CaO	11.86	14.10	11.52	11.83	10.52	10.81
Na_2O	0.90	1.39	1.95	1.68	1.24	1.55
K_2O	0.83	0.19	0.21	0.09	0.10	0.10
TiO_2	0.96	0.56	0.52	0.74	0.51	0.34
P_2O_5	0.09	0.13	0.07	0.03	0.02	0.04
LOI	1.27	1.08	1.33	0.89	1.88	1.89
Total	99.17	99.90	99.89	100.10	98.95	98.43
Mg#	56	56	65	54	50	45
Ni	286	243	436	170	2133	831
Cr	347	424	904	530	287	172
Co	54	52	65	54	146	64
V	276	99	137	278	215	119
Sc	40	22	36	49	34	26
Li	17	19	10	39	28	29
Rb	36	2	1	2	3	3
Ba	105	51	30	20	19	16
Sr	70	310	45	80	50	155
Ga	17	14	11	15	13	16
Zr	56	67	42	27	22	28
Hf	1.56	1.81	1.14	0.82	0.66	0.82
Nb	2.30	2.35	1.47	1.08	0.97	1.05
Ta	0.15	0.17	0.10	0.06	0.06	0.07
U	0.09	0.09	0.08	0.04	0.04	0.06
Th	0.29	0.23	0.18	0.13	0.14	0.18
Y	20.4	18.1	12.5	14.2	9.8	11.8
Pb	0.60	0.44	0.37	1.52	1.62	3.14
Cu	80.5	214.7	207.3	98.5	2900.0	2900.0
Zn	92.5	36.7	34.8	71.6	106.9	92.8
La	2.30	3.10	2.00	1.40	1.50	1.70

Lithology	Melagabbro	Leucogabbro	Pyroxenite	Melagabbro	Melagabbro	Melagabbro
Zone	HBZ	HBZ	HBZ	HBZ	HBZ	HBZ
	111-11-04	111-11-12	111-11-11	111-11-10	111-11-09	111-11-08
Ce	6.62	5.96	5.32	3.98	3.92	4.30
Pr	1.17	0.88	0.81	0.69	0.61	0.73
Nd	6.13	4.60	4.18	3.71	3.11	3.82
Sm	2.13	1.76	1.37	1.31	1.03	1.26
Eu	0.64	0.49	0.55	0.56	0.49	0.49
Gd	2.96	2.56	1.81	1.81	1.48	1.66
Tb	0.53	0.44	0.32	0.35	0.26	0.29
Dy	3.53	3.10	2.21	2.41	1.74	1.98
Ho	0.75	0.66	0.47	0.52	0.38	0.43
Er	2.25	1.95	1.38	1.59	1.15	1.27
Tm	0.32	0.28	0.20	0.23	0.16	0.18
Yb	2.18	1.83	1.30	1.59	1.14	1.21
Lu	0.34	0.28	0.20	0.24	0.18	0.19
Al_2O_3/TiO_2	16.32	42.39	29.94	20.39	27.08	54.93
Sr/Y	4.50	22.86	5.11	8.00	10.60	19.25
Nb/Ta	15.64	13.80	15.44	16.81	15.40	14.56
Zr/Y	2.74	3.71	3.37	1.90	2.25	2.38
La/Yb	1.05	1.69	1.54	0.88	1.32	1.41
Th/Yb	0.13	0.13	0.14	0.08	0.12	0.15
Nd/Sm	2.88	2.62	3.04	2.84	3.02	3.02
La/Nb	1.00	1.32	1.36	1.30	1.55	1.62
Dy/Yb	1.62	1.69	1.70	1.52	1.53	1.64
Th/Ta	1.98	1.37	1.87	1.95	2.24	2.54
Ti/Zr	102.98	50.11	74.79	164.75	138.15	73.01
La/Sm_{cn}	0.70	1.14	0.94	0.69	0.94	0.87
La/Yb_{cn}	0.76	1.21	1.11	0.63	0.95	1.01
Gd/Yb_{cn}	1.12	1.15	1.16	0.95	1.08	1.14
Nb/Nb*	0.66	0.65	0.58	0.60	0.50	0.44
Zr/Zr*	0.92	1.40	1.04	0.73	0.73	0.75
Hf/Hf*	0.92	1.36	1.02	0.80	0.79	0.80
Ti/Ti*	0.98	0.68	0.81	1.24	1.02	0.61
Eu/Eu*	0.78	0.71	1.06	1.12	1.22	1.03
Ce/Ce*	0.98	0.87	1.02	0.98	0.99	0.93
North	50°37.485'	50°37.577'	50°37.583'	50°38.096'	50°38.096'	50°38.095'
West	095°35.337'	095°37.341'	095°37.324'	095°36.361'	095°36.363'	095°36.367'

Lithology	Gabbro	Gabbro	Gabbro	Anorthosite	Anorthosite	Leucogabbro
Zone	ALZ	ALZ	ALZ	ALZ	ALZ	ALZ
	111-11-05	111-12-703A01	111-12-702A01	111-12-632A01	111-12-629A01	111-12-628A01
SiO_2	64.40	50.47	51.80	49.65	46.63	45.57
Al_2O_3	15.69	13.82	15.25	26.93	24.74	22.42
$Fe_2O_3^T$	6.24	15.06	11.38	3.68	5.27	9.43
MnO	0.08	0.30	0.20	0.05	0.09	0.15
MgO	2.58	5.43	6.08	2.65	5.05	6.80
CaO	4.70	8.51	12.57	12.71	14.54	12.79
Na_2O	3.45	0.93	0.98	3.61	2.00	1.74
K_2O	1.26	1.61	0.19	0.15	0.36	0.09
TiO_2	0.52	1.17	0.86	0.15	0.25	0.21
P_2O_5	0.11	0.11	0.07	< 0.01	0.01	0.03
LOI	1.00	1.12	0.65	0.86	1.35	1.33
Total	100.00	98.53	100.00	100.40	100.30	100.50
Mg#	42	39	49	56	63	56
Ni	77	90	162	70	62	206
Cr	164	29	289	108	591	33
Co	20	68	55	18	21	55
V	91	266	304	46	150	59
Sc	17	29	51	6	39	10
Li	22	22	13	20	50	11
Rb	48	47	2	2	4	1
Ba	320	139	27	23	36	14
Sr	190	186	93	184	142	108
Ga	18	19	16	19	18	16
Zr	158	97	57	10	12	15
Hf	3.79	2.62	1.63	0.28	0.38	0.38
Nb	6.15	6.03	2.23	0.30	0.33	0.43
Ta	0.52	0.42	0.15	0.02	0.02	0.03
U	1.25	0.40	0.11	0.02	0.02	0.03
Th	4.77	1.57	0.34	0.05	0.04	0.08
Y	14.2	19.0	20.4	2.3	5.6	5.3
Pb	3.01	4.95	0.92	2.50	1.41	0.34
Cu	113.3	118.1	195.2	51.6	6.6	48.4
Zn	58.3	95.1	90.7	26.0	42.3	50.1
La	5.10	10.20	3.10	0.50	0.60	0.80

Lithology	Gabbro	Gabbro	Gabbro	Anorthosite	Anorthosite	Leucogabbro
Zone	ALZ	ALZ	ALZ	ALZ	ALZ	ALZ
	111-11-05	111-12-703A01	111-12-702A01	111-12-632A01	111-12-629A01	111-12-628A01
Ce	11.70	25.70	8.06	1.38	1.32	2.08
Pr	1.47	3.47	1.25	0.18	0.24	0.37
Nd	6.24	15.54	6.31	0.89	1.37	1.94
Sm	1.71	3.75	2.04	0.29	0.54	0.62
Eu	0.61	1.22	0.76	0.26	0.30	0.39
Gd	2.14	3.89	2.83	0.38	0.82	0.81
Tb	0.36	0.61	0.51	0.06	0.15	0.14
Dy	2.39	3.76	3.50	0.41	1.02	0.92
Ho	0.49	0.75	0.75	0.09	0.21	0.20
Er	1.41	2.05	2.32	0.27	0.63	0.60
Tm	0.21	0.29	0.35	0.04	0.09	0.09
Yb	1.41	1.84	2.22	0.25	0.58	0.58
Lu	0.22	0.28	0.35	0.04	0.09	0.10
Al_2O_3/TiO_2	30.35	11.77	17.77	180.74	98.57	107.27
Sr/Y	14.14	12.27	5.71	196.00	37.75	55.00
Nb/Ta	11.80	14.23	15.18	18.81	17.21	17.04
Zr/Y	11.13	5.09	2.79	4.29	2.16	2.84
La/Yb	3.61	5.56	1.39	2.00	1.04	1.37
Th/Yb	3.38	0.86	0.15	0.21	0.06	0.14
Nd/Sm	3.66	4.15	3.09	3.11	2.52	3.14
La/Nb	0.83	1.69	1.39	1.66	1.83	1.88
Dy/Yb	1.69	2.05	1.57	1.65	1.77	1.57
Th/Ta	9.16	3.71	2.34	3.31	1.89	3.32
Ti/Zr	19.62	72.56	90.24	89.32	125.39	83.53
La/Sm_{cn}	1.93	1.76	0.98	1.13	0.71	0.84
La/Yb_{cn}	2.59	3.98	1.00	1.43	0.75	0.98
Gd/Yb_{cn}	1.25	1.75	1.05	1.25	1.18	1.15
Nb/Nb*	0.29	0.35	0.51	0.43	0.52	0.39
Zr/Zr*	2.87	0.75	0.94	1.17	0.82	0.81
Hf/Hf*	2.48	0.73	0.97	1.19	0.94	0.74
Ti/Ti*	0.68	0.81	0.91	1.16	0.99	0.76
Eu/Eu*	0.97	0.97	0.96	2.38	1.38	1.68
Ce/Ce*	1.03	1.05	0.99	1.11	0.84	0.92
North	50°37.493'	50°38.118'	50°38.208'	50°37.567'	50°38.048'	50°38.081'
West	095°35.345'	095°35.264'	095°36.174'	095°38.047'	095°38.085'	095°38.082'

Lithology	Anorthosite	Anorthosite	Leucogabbro	Anorthosite	Anorthosite	Anorthosite
Zone	ALZ	ALZ	ALZ	ALZ	ALZ	HBZ
	111-12-625A01	111-12-624A01	111-12-623A01	111-12-564A01	111-12-547A01	MV2018-1
SiO_2	48.89	51.27	49.70	47.51	47.06	46.15
Al_2O_3	24.35	24.95	23.90	26.01	30.52	25.15
$Fe_2O_3^T$	5.58	3.68	4.59	4.70	2.34	7.39
MnO	0.08	0.04	0.06	0.08	0.03	0.10
MgO	2.72	1.28	2.33	3.26	1.40	5.43
CaO	12.92	12.44	12.65	15.84	14.89	13.16
Na_2O	3.13	3.96	3.44	1.83	2.56	1.55
K_2O	0.07	0.07	0.24	0.22	0.31	0.13
TiO_2	1.29	0.31	0.57	0.22	0.12	0.30
P_2O_5	0.04	0.04	0.02	0.03	0.02	0.02
LOI	0.81	0.85	1.20	0.77	1.22	1.12
Total	99.90	98.91	98.70	100.50	100.50	100.50
Mg#	46	38	47	55	52	59
Ni	29	30	52	46	25	1094
Cr	27	50	7	436	13	70
Co	19	11	19	18	9	78
V	92	68	128	105	38	87
Sc	17	11	13	25	5	10
Li	59	39	54	8	12	13
Rb	2	2	4	2	4	1
Ba	19	22	41	13	14	26
Sr	143	166	167	144	197	156
Ga	20	22	20	20	19	16
Zr	46	66	58	11	9	17
Hf	1.35	1.75	1.58	0.34	0.24	0.51
Nb	3.57	1.14	1.88	0.42	0.39	0.74
Ta	0.28	0.13	0.14	0.03	0.03	0.05
U	0.06	0.09	0.08	0.09	0.02	0.04
Th	0.19	0.35	0.26	0.15	0.05	0.13
Y	10.4	10.3	11.4	4.7	2.5	5.6
Pb	0.63	0.89	1.18	1.47	2.12	0.96
Cu	3.4	4.0	29.6	54.6	4.8	1730.0
Zn	26.9	24.9	28.4	22.4	18.4	48.1
La	1.50	1.60	1.40	1.00	0.40	1.40

Lithology	Anorthosite	Anorthosite	Leucogabbro	Anorthosite	Anorthosite	Anorthosite
Zone	ALZ	ALZ	ALZ	ALZ	ALZ	HBZ
	111-12-625A01	111-12-624A01	111-12-623A01	111-12-564A01	111-12-547A01	MV2018-1
Ce	3.44	3.81	3.87	2.13	1.09	3.05
Pr	0.58	0.55	0.68	0.32	0.18	0.47
Nd	2.84	2.62	3.62	1.55	0.97	2.27
Sm	0.93	0.89	1.22	0.52	0.30	0.63
Eu	0.67	0.81	0.67	0.37	0.27	0.35
Gd	1.27	1.18	1.56	0.71	0.37	0.87
Tb	0.24	0.22	0.29	0.12	0.06	0.16
Dy	1.66	1.64	1.95	0.82	0.43	1.02
Ho	0.37	0.35	0.42	0.18	0.09	0.22
Er	1.15	1.09	1.26	0.53	0.26	0.64
Tm	0.17	0.17	0.19	0.08	0.04	0.09
Yb	1.17	1.19	1.28	0.50	0.23	0.64
Lu	0.19	0.20	0.20	0.08	0.04	0.10
Al_2O_3/TiO_2	18.85	79.71	41.78	119.31	248.13	84.68
Sr/Y	16.11	19.67	17.40	52.00	217.00	27.87
Nb/Ta	12.62	8.94	13.72	15.56	11.70	15.66
Zr/Y	4.42	6.43	5.10	2.34	3.67	3.04
La/Yb	1.28	1.34	1.10	2.01	1.71	2.17
Th/Yb	0.16	0.29	0.20	0.30	0.22	0.19
Nd/Sm	3.06	2.96	2.98	3.00	3.27	3.59
La/Nb	0.42	1.40	0.75	2.38	1.04	1.90
Dy/Yb	1.41	1.37	1.53	1.64	1.83	1.59
Th/Ta	0.68	2.75	1.90	5.48	1.55	2.66
Ti/Zr	168.38	28.43	59.12	118.81	81.93	104.73
La/Sm_{cn}	1.04	1.17	0.74	1.25	0.87	1.43
La/Yb_{cn}	0.92	0.96	0.79	1.44	1.23	1.56
Gd/Yb_{cn}	0.90	0.81	1.01	1.18	1.29	1.12
Nb/Nb*	1.56	0.36	0.73	0.26	0.64	0.41
Zr/Zr*	1.68	2.56	1.64	0.73	0.99	0.84
Hf/Hf*	1.78	2.46	1.61	0.81	0.96	0.91
Ti/Ti*	3.22	0.79	1.11	0.91	0.95	0.97
Eu/Eu*	1.89	2.43	1.48	1.85	2.48	1.43
Ce/Ce*	0.90	0.99	0.96	0.91	0.98	0.92
North	50°38.182'	50°38.235'	50°38.265'	50°38.282'	50°37.457'	50°38.072'
West	095°38.018'	095°38.117'	095°38.091'	095°35.010'	095°33.040'	095°37.411'

Lithology	Pyroxenite	Chromitite	Leucogabbro	Leucogabbro	Leucogabbro	Anorthosite
Zone	HBZ	HBZ	ALZ	ALZ	ALZ	ALZ
	MV2018-2	MV2018-3	MV2018-7	MV2018-8A	MV2018-8B	MV2018-9
SiO_2	44.79	33.23	47.63	47.44	50.08	46.82
Al_2O_3	18.38	18.83	22.49	20.78	18.32	26.54
$Fe_2O_3^T$	8.72	15.23	7.85	9.44	9.73	5.68
MnO	0.17	0.18	0.11	0.15	0.14	0.08
MgO	11.85	19.95	5.43	6.85	6.66	3.74
CaO	13.62	5.03	13.08	12.34	11.10	14.34
Na_2O	1.22	0.62	2.18	1.66	2.48	1.99
K_2O	0.21	0.06	0.13	0.17	0.35	0.16
TiO_2	0.22	0.47	0.61	0.41	0.79	0.53
P_2O_5	0.02	0.03	0.07	0.02	0.12	0.03
LOI	1.26	6.52	0.93	0.91	0.97	0.94
Total	100.40	100.20	100.50	100.20	100.70	100.80
Mg#	73	72	58	59	58	57
Ni	521	218	103	191	110	85
Cr	447	4500	413	141	220	84
Co	62	96	31	43	36	27
V	111	268	198	139	235	139
Sc	27	14	26	21	43	14
Li	12	14	22	18	32	22
Rb	2	0	2	3	3	4
Ba	32	6	14	19	37	27
Sr	107	4	134	105	118	127
Ga	11	14	19	16	17	19
Zr	9	15	40	15	60	13
Hf	0.30	0.46	1.11	0.42	1.78	0.39
Nb	0.33	0.73	1.60	0.65	1.98	1.11
Ta	0.02	0.05	0.11	0.04	0.15	0.06
U	0.02	0.05	0.07	0.03	0.07	0.03
Th	0.07	0.26	0.26	0.10	0.22	0.08
Y	4.6	8.3	15.5	7.4	16.6	8.1
Pb	0.33	0.18	1.10	0.85	0.91	1.40
Cu	48.9	10.4	9.3	54.5	2.3	162.0
Zn	42.3	115.0	39.8	47.2	53.6	22.5
La	0.70	3.20	2.00	1.40	1.60	1.20

Lithology	Pyroxenite	Chromitite	Leucogabbro	Leucogabbro	Leucogabbro	Anorthosite
Zone	HBZ	HBZ	ALZ	ALZ	ALZ	ALZ
	MV2018-2	MV2018-3	MV2018-7	MV2018-8A	MV2018-8B	MV2018-9
Ce	1.61	4.70	6.06	3.40	4.70	3.01
Pr	0.26	0.66	1.05	0.55	0.80	0.50
Nd	1.28	2.91	5.60	2.57	4.61	2.46
Sm	0.41	0.98	1.94	0.83	1.65	0.85
Eu	0.25	0.63	0.57	0.49	0.56	0.48
Gd	0.62	1.25	2.58	1.11	2.47	1.23
Tb	0.11	0.22	0.45	0.20	0.43	0.23
Dy	0.78	1.45	2.97	1.26	2.88	1.55
Ho	0.17	0.32	0.65	0.28	0.61	0.32
Er	0.52	0.95	1.84	0.83	1.83	0.94
Tm	0.08	0.14	0.26	0.12	0.26	0.14
Yb	0.48	0.94	1.78	0.83	1.72	0.86
Lu	0.08	0.16	0.27	0.13	0.26	0.13
Al_2O_3/TiO_2	85.49	39.98	37.11	50.19	23.22	49.79
Sr/Y	23.40	0.47	8.65	14.24	7.10	15.70
Nb/Ta	14.43	16.11	14.77	15.73	13.56	17.31
Zr/Y	1.96	1.81	2.58	2.04	3.62	1.60
La/Yb	1.45	3.42	1.12	1.70	0.93	1.40
Th/Yb	0.15	0.28	0.14	0.13	0.13	0.09
Nd/Sm	3.14	2.98	2.89	3.10	2.80	2.90
La/Nb	2.11	4.41	1.25	2.17	0.81	1.08
Dy/Yb	1.61	1.55	1.67	1.53	1.67	1.80
Th/Ta	3.17	5.78	2.36	2.54	1.52	1.25
Ti/Zr	143.21	188.24	90.82	165.46	78.83	245.79
La/Sm_{cn}	1.11	2.12	0.67	1.09	0.63	0.91
La/Yb_{cn}	1.04	2.45	0.81	1.22	0.67	1.00
Gd/Yb_{cn}	1.06	1.10	1.20	1.11	1.19	1.18
Nb/Nb*	0.35	0.19	0.53	0.40	0.78	0.84
Zr/Zr*	0.74	0.53	0.72	0.61	1.29	0.53
Hf/Hf*	0.89	0.58	0.72	0.62	1.38	0.58
Ti/Ti*	1.02	1.00	0.64	1.04	0.92	1.29
Eu/Eu*	1.53	1.74	0.77	1.56	0.85	1.43
Ce/Ce*	0.92	0.79	1.02	0.95	1.02	0.95
North	50°38.075'	50°38.158'	50°38.169'	50°38.167'	50°38.167'	50°38.163'
West	095°37.389'	095°37.310'	095°37.320'	095°37.319'	095°37.319'	095°37.309'

Lithology	Anorthosite	Leucogabbro	Gabbro	Chromitite	Leucogabbro	Anorthosite
Zone	ALZ	ALZ	ALZ	HBZ	ALZ	ALZ
	MV2018-10	MV2018-11	MV2018-12	MV2018-13	MV2018-14	MV2018-15
SiO_2	46.63	48.58	49.17	32.86	47.48	48.05
Al_2O_3	27.54	23.87	13.76	10.28	19.88	26.11
$Fe_2O_3^T$	5.29	6.52	11.33	19.85	8.32	4.47
MnO	0.08	0.09	0.17	0.31	0.12	0.07
MgO	2.92	4.66	9.05	11.58	7.53	3.19
CaO	15.07	13.35	13.15	7.88	13.86	15.27
Na_2O	1.95	1.93	1.14	0.80	1.44	2.03
K_2O	0.16	0.47	0.37	0.08	0.10	0.15
TiO_2	0.55	0.27	1.00	0.75	0.40	0.39
P_2O_5	0.04	0.01	0.07	< 0.01	0.02	0.03
LOI	0.70	1.06	1.40	0.88	1.03	0.93
Total	100.90	100.80	100.60	85.26	100.20	100.70
Mg#	52	59	61	54	64	59
Ni	60	159	153		179	65
Cr	161	128	834		1634	475
Co	19	33	48		42	19
V	155	93	370		183	124
Sc	13	20	63		39	13
Li	15	43	37		17	15
Rb	2	4	5		1	3
Ba	13	39	36		9	8
Sr	165	186	82		111	140
Ga	19	19	15		15	19
Zr	20	15	39		12	19
Hf	0.57	0.44	1.14		0.38	0.51
Nb	1.41	0.62	1.84		0.60	0.84
Ta	0.09	0.04	0.10		0.04	0.06
U	0.03	0.03	0.04		0.02	0.03
Th	0.13	0.12	0.26		0.08	0.08
Y	8.1	7.4	32.9		8.5	4.9
Pb	1.22	1.04	0.55		0.93	0.66
Cu	17.4	28.1	23.8		32.1	122.8
Zn	30.3	25.6	46.2		56.4	23.8
La	1.30	1.30	2.40		1.10	0.70

Lithology	Anorthosite	Leucogabbro	Gabbro	Chromitite	Leucogabbro	Anorthosite
Zone	ALZ	ALZ	ALZ	HBZ	ALZ	ALZ
	MV2018-10	MV2018-11	MV2018-12	MV2018-13	MV2018-14	MV2018-15
Ce	3.36	3.25	7.51		2.74	1.83
Pr	0.54	0.50	1.42		0.44	0.29
Nd	2.76	2.60	8.16		2.35	1.57
Sm	0.95	0.78	3.19		0.84	0.51
Eu	0.45	0.51	0.54		0.35	0.31
Gd	1.25	1.13	4.60		1.22	0.74
Tb	0.22	0.19	0.81		0.20	0.14
Dy	1.47	1.26	5.59		1.43	0.84
Ho	0.32	0.28	1.22		0.32	0.19
Er	0.94	0.86	3.63		0.93	0.56
Tm	0.13	0.12	0.53		0.13	0.08
Yb	0.86	0.79	3.49		0.88	0.49
Lu	0.13	0.13	0.52		0.13	0.08
Al_2O_3/TiO_2	49.98	87.12	13.79	13.80	49.70	66.27
Sr/Y	20.28	25.32	2.50		13.09	28.65
Nb/Ta	16.23	14.49	18.56		15.84	13.52
Zr/Y	2.46	2.04	1.18		1.42	3.89
La/Yb	1.52	1.64	0.69		1.25	1.42
Th/Yb	0.15	0.15	0.07		0.09	0.15
Nd/Sm	2.90	3.34	2.56		2.80	3.11
La/Nb	0.92	2.09	1.31		1.83	0.84
Dy/Yb	1.71	1.59	1.60		1.63	1.70
Th/Ta	1.48	2.81	2.59		2.18	1.23
Ti/Zr	165.16	109.51	153.41		199.83	124.31
La/Sm_{cn}	0.88	1.08	0.49		0.85	0.89
La/Yb_{cn}	1.09	1.18	0.49		0.90	1.02
Gd/Yb_{cn}	1.20	1.18	1.09		1.15	1.24
Nb/Nb*	0.81	0.37	0.55		0.47	0.85
Zr/Zr*	0.73	0.62	0.45		0.51	1.26
Hf/Hf*	0.75	0.66	0.48		0.58	1.22
Ti/Ti*	1.25	0.72	0.61		0.97	1.54
Eu/Eu*	1.26	1.67	0.43		1.05	1.57
Ce/Ce*	0.99	0.99	1.00		0.97	1.00
North	50°38.164'	50°38.164'	50°38.161'	50°38.158'	50°38.086'	50°38.292'
West	095°37.304'	095°37.304'	095°37.302'	095°37.309'	095°37.687'	095°37.847'

Lithology Zone	Anorthosite ALZ MV2018-16	Anorthosite ALZ MV2018-17	Anorthosite ALZ MV2018-18	Anorthosite ALZ MV2018-19
SiO_2	46.29	48.80	48.21	48.87
Al_2O_3	25.78	29.36	27.14	26.37
$Fe_2O_3^T$	5.51	2.54	3.89	3.97
MnO	0.09	0.04	0.06	0.07
MgO	5.14	1.04	3.29	3.13
CaO	13.90	15.45	15.29	15.39
Na_2O	1.73	2.18	2.00	1.90
K_2O	0.26	0.12	0.05	0.23
TiO_2	0.13	0.25	0.18	0.21
P_2O_5	0.02	0.02	0.01	0.02
LOI	1.44	0.55	0.65	0.75
Total	100.30	100.30	100.80	100.90
Mg#	65	45	63	61
Ni	105	18	48	36
Cr	477	18	384	148
Co	31	9	15	14
V	59	45	86	83
Sc	15	7	13	18
Li	61	24	36	23
Rb	17	4	2	4
Ba	27	14	12	11
Sr	145	158	133	167
Ga	17	21	19	19
Zr	6	22	8	9
Hf	0.17	0.60	0.23	0.29
Nb	0.23	0.99	0.34	0.45
Ta	0.01	0.07	0.03	0.03
U	0.01	0.05	0.01	0.02
Th	0.04	0.11	0.04	0.05
Y	2.9	3.8	3.6	4.9
Pb	0.64	0.33	0.29	0.67
Cu	2.2	4.1	2.5	1.4
Zn	39.5	16.9	23.8	29.4
La	0.50	0.90	0.50	0.50

Lithology	Anorthosite	Anorthosite	Anorthosite	Anorthosite
Zone	ALZ	ALZ	ALZ	ALZ
	MV2018-16	MV2018-17	MV2018-18	MV2018-19
Ce	1.23	2.01	1.17	1.39
Pr	0.19	0.29	0.20	0.25
Nd	0.93	1.49	0.99	1.29
Sm	0.27	0.45	0.40	0.44
Eu	0.26	0.32	0.30	0.39
Gd	0.43	0.58	0.56	0.77
Tb	0.08	0.10	0.09	0.13
Dy	0.47	0.66	0.66	0.89
Ho	0.11	0.13	0.15	0.19
Er	0.32	0.42	0.43	0.59
Tm	0.05	0.06	0.06	0.09
Yb	0.30	0.43	0.38	0.55
Lu	0.04	0.07	0.06	0.08
Al_2O_3/TiO_2	201.41	116.97	147.50	124.39
Sr/Y	50.07	41.55	37.34	33.94
Nb/Ta	16.36	14.94	13.12	16.11
Zr/Y	2.08	5.79	2.24	1.83
La/Yb	1.67	2.12	1.30	0.91
Th/Yb	0.13	0.25	0.11	0.09
Nd/Sm	3.41	3.33	2.46	2.96
La/Nb	2.18	0.91	1.47	1.11
Dy/Yb	1.58	1.56	1.72	1.61
Th/Ta	2.71	1.59	1.62	1.71
Ti/Zr	127.89	68.40	137.88	141.21
La/Sm_{cn}	1.18	1.30	0.80	0.74
La/Yb_{cn}	1.20	1.52	0.93	0.65
Gd/Yb_{cn}	1.18	1.12	1.20	1.15
Nb/Nb*	0.39	0.75	0.55	0.68
Zr/Zr*	0.71	1.59	0.75	0.71
Hf/Hf*	0.72	1.57	0.78	0.83
Ti/Ti*	0.90	1.24	0.96	0.88
Eu/Eu*	2.35	1.95	1.91	2.04
Ce/Ce*	0.97	0.97	0.92	0.97
North	50°38.255'	50°38.344'	50°38.367'	50°38.359'
West	095°37.847'	095°37.854'	095°37.873'	095°37.893'

Appendix 3.2. Major (wt.%) and trace (ppm) element data for basalts and gabbros from the Mayville Assemblage, a gabbro and leucogabbro from the New Manitoba Mine Intrusion and a dacite dyke from the Maskwa Lake TTG Batholith II (MLB).

Lithology	Basalt	Basalt	Gabbro	Leucogabbro	Basalt	Gabbro
Zone	Mayville	Mayville	NMMI	NMMI	Mayville	Mayville
	111-12-490A01	111-12-485A01	111-12-424A01	111-12-423A01	111-11-03	111-12-726A01
SiO_2	47.93	52.41	45.15	49.94	50.17	47.38
Al_2O_3	15.74	15.30	14.67	20.67	14.47	13.67
$Fe_2O_3^T$	11.69	12.73	17.70	8.14	12.02	11.12
MnO	0.26	0.33	0.17	0.12	0.23	0.18
MgO	7.97	4.51	5.91	4.15	7.35	11.62
CaO	13.84	8.88	10.22	12.45	11.36	11.33
Na_2O	1.14	3.28	1.94	2.13	2.18	1.28
K_2O	0.16	0.18	0.18	0.20	0.32	0.23
TiO_2	0.70	1.00	0.71	0.60	0.79	0.53
P_2O_5	0.05	0.06	0.06	0.06	0.06	0.03
LOI	0.70	0.64	2.27	0.89	0.90	1.35
Total	100.20	99.32	98.98	99.35	99.85	98.71
Mg#	55	39	37	48	52	65
Ni	175	82	1925	109	144	340
Cr	414	182	134	148	294	693
Co	53	48	164	30	54	61
V	243	307	252	169	276	205
Sc	40	45	35	27	47	41
Li	9	9	13	11	10	13
Rb	2	2	3	3	3	10
Ba	44	61	28	31	78	47
Sr	103	126	89	135	100	78
Ga	15	15	15	19	15	13
Zr	36	60	37	44	44	29
Hf	1.05	1.68	1.06	1.25	1.27	0.84
Nb	1.62	2.91	1.63	1.93	1.86	1.54
Ta	0.11	0.19	0.11	0.13	0.12	0.09
U	0.07	0.10	0.08	0.09	0.08	0.05
Th	0.22	0.43	0.22	0.30	0.25	0.13
Y	15.9	21.0	14.6	16.0	18.2	12.7
Pb	0.54	1.40	1.27	0.60	0.34	0.55
Cu	3.7	158.1	2900.0	252.1	5.9	123.5

Lithology	Basalt	Basalt	Gabbro	Leucogabbro	Basalt	Gabbro
Zone	Mayville 111-12-490A01	Mayville 111-12-485A01	NMMI 111-12-424A01	NMMI 111-12-423A01	Mayville 111-11-03	Mayville 111-12-726A01
Zn	169.4	213.1	147.0	60.0	70.9	103.6
La	2.00	3.60	2.20	2.50	2.50	1.80
Ce	5.75	9.60	5.81	6.53	7.38	5.14
Pr	0.90	1.41	0.92	1.01	1.15	0.84
Nd	4.60	6.95	4.78	5.12	5.89	4.08
Sm	1.67	2.28	1.57	1.71	1.90	1.30
Eu	0.60	0.85	0.59	0.68	0.78	0.56
Gd	2.29	2.92	2.12	2.34	2.55	1.74
Tb	0.41	0.52	0.37	0.40	0.46	0.30
Dy	2.72	3.58	2.54	2.75	3.09	2.13
Ho	0.58	0.78	0.54	0.59	0.68	0.46
Er	1.72	2.37	1.65	1.71	2.02	1.39
Tm	0.25	0.35	0.24	0.26	0.30	0.20
Yb	1.64	2.32	1.58	1.67	1.98	1.39
Lu	0.24	0.35	0.25	0.26	0.30	0.21
Al_2O_3/TiO_2	22.65	15.30	20.78	34.74	18.41	25.99
Sr/Y	8.23	7.59	8.09	10.00	7.14	8.78
Nb/Ta	15.25	15.49	14.77	15.46	15.38	17.86
Zr/Y	2.27	2.86	2.54	2.76	2.41	2.29
La/Yb	1.22	1.55	1.40	1.49	1.26	1.30
Th/Yb	0.13	0.18	0.14	0.18	0.13	0.09
Nd/Sm	2.76	3.05	3.05	2.99	3.10	3.13
La/Nb	1.24	1.24	1.35	1.29	1.34	1.17
Dy/Yb	1.66	1.54	1.61	1.65	1.56	1.54
Th/Ta	2.04	2.27	2.00	2.41	2.10	1.52
Ti/Zr	115.73	99.91	114.39	81.07	107.09	108.73
La/Sm_{cn}	0.77	1.02	0.91	0.94	0.85	0.89
La/Yb_{cn}	0.88	1.11	1.00	1.07	0.90	0.93
Gd/Yb_{cn}	1.16	1.04	1.11	1.16	1.07	1.04
Nb/Nb*	0.58	0.55	0.55	0.52	0.55	0.74
Zr/Zr*	0.77	0.89	0.80	0.88	0.78	0.74
Hf/Hf*	0.81	0.90	0.83	0.90	0.81	0.78
Ti/Ti*	0.83	0.96	0.94	0.78	0.89	0.89
Eu/Eu*	0.93	1.01	0.99	1.04	1.09	1.13
Ce/Ce*	1.04	1.03	0.99	1.00	1.05	1.01
North	50°37.028'	50°37.376'	50°36.110'	50°36.121'	50°37.505'	50°37.048'
West	095°37.553'	095°37.541'	095°28.467'	095°28.510'	095°37.436'	095°37.453'

Lithology	Basalt	Dacite	Basalt
Zone	Mayville 111-12-570A01	MLB 111-12-412B01	Mayville 111-12-443A01
SiO_2	49.28	68.40	49.12
Al_2O_3	14.41	13.94	15.29
$Fe_2O_3^T$	13.10	5.31	11.39
MnO	0.33	0.05	0.20
MgO	7.32	1.53	8.40
CaO	11.63	3.40	11.39
Na_2O	2.25	3.64	1.56
K_2O	0.49	2.05	0.22
TiO_2	0.81	0.58	0.59
P_2O_5	0.06	0.16	0.03
LOI	0.80	1.01	1.11
Total	100.50	100.10	99.29
Mg#	50	34	57
Ni	139	11	163
Cr	337	58	267
Co	55	10	54
V	287	63	241
Sc	43	10	43
Li	22	18	12
Rb	6	54	4
Ba	106	574	29
Sr	106	170	77
Ga	15	16	14
Zr	47	174	26
Hf	1.35	4.38	0.78
Nb	1.97	8.95	1.07
Ta	0.14	0.83	0.07
U	0.09	2.28	0.05
Th	0.31	10.07	0.17
Y	18.2	19.9	11.9
Pb	2.08	3.70	1.28
Cu	157.7	36.2	153.7

Lithology	Basalt	Dacite	Basalt
Zone	Mayville	MLB	Mayville
	111-12-570A01	111-12-412B01	111-12-443A01
Zn	181.3	48.0	84.0
La	2.60	26.10	1.50
Ce	7.14	50.07	4.03
Pr	1.13	5.38	0.66
Nd	6.04	19.48	3.36
Sm	1.97	3.60	1.14
Eu	0.67	0.89	0.49
Gd	2.63	3.26	1.59
Tb	0.46	0.52	0.29
Dy	3.08	3.41	2.04
Ho	0.67	0.70	0.45
Er	2.01	2.04	1.40
Tm	0.29	0.31	0.20
Yb	1.92	2.09	1.34
Lu	0.29	0.31	0.21
Al_2O_3/TiO_2	17.70	24.08	25.83
Sr/Y	7.40	9.72	9.00
Nb/Ta	14.61	10.74	15.34
Zr/Y	2.58	8.76	2.18
La/Yb	1.36	12.52	1.12
Th/Yb	0.16	4.83	0.13
Nd/Sm	3.06	5.41	2.94
La/Nb	1.32	2.92	1.40
Dy/Yb	1.61	1.64	1.53
Th/Ta	2.30	12.09	2.49
Ti/Zr	103.83	19.95	136.50
La/Sm_{cn}	0.85	4.68	0.85
La/Yb_{cn}	0.97	8.98	0.80
Gd/Yb_{cn}	1.14	1.29	0.98
Nb/Nb*	0.52	0.13	0.49
Zr/Zr*	0.81	1.23	0.79
Hf/Hf*	0.84	1.12	0.85
Ti/Ti*	0.90	0.40	1.06
Eu/Eu*	0.90	0.79	1.12
Ce/Ce*	1.01	1.02	0.98
North	50°36.365'	50°36.399'	50°36.590'
West	095°33.596'	095°28.350'	095°29.312'

Appendix 3.3. Standard and duplicate analyses results.

Sample ID	Client Sample ID	QC Name	Analyte	Units	Measured Value	Cert/Dup Value
BLANK-18-19380		BLANK	Ba	Ppm	0.1	
BLANK-18-19380		BLANK	Be	Ppm	0.02	
BLANK-18-19380		BLANK	Bi	Ppm	0	
BLANK-18-19380		BLANK	Cd	Ppm	0.005	
BLANK-18-19380		BLANK	Ce	ppm	0.01	
BLANK-18-19380		BLANK	Co	ppm	0.01	
BLANK-18-19380		BLANK	Cr	ppm	1	
BLANK-18-19380		BLANK	Cs	ppm	0.001	
BLANK-18-19380		BLANK	Cu	ppm	0	
BLANK-18-19380		BLANK	Dy	ppm	0.003	
BLANK-18-19380		BLANK	Er	ppm	0.002	
BLANK-18-19380		BLANK	Eu	ppm	0.0015	
BLANK-18-19380		BLANK	Ga	ppm	0	
BLANK-18-19380		BLANK	Gd	ppm	0.003	
BLANK-18-19380		BLANK	Hf	ppm	0.02	
BLANK-18-19380		BLANK	Ho	ppm	0.0001	
BLANK-18-19380		BLANK	In	ppm	0.0001	
BLANK-18-19380		BLANK	La	ppm	0	
BLANK-18-19380		BLANK	Li	ppm	0	
BLANK-18-19380		BLANK	Lu	ppm	0.001	
BLANK-18-19380		BLANK	Mo	ppm	0.02	
BLANK-18-19380		BLANK	Nb	ppm	0.001	
BLANK-18-19380		BLANK	Nd	ppm	0.01	
BLANK-18-19380		BLANK	Ni	ppm	0.1	
BLANK-18-19380		BLANK	Pb	ppm	0.01	
BLANK-18-19380		BLANK	Pr	ppm	0.001	
BLANK-18-19380		BLANK	Rb	ppm	0.01	
BLANK-18-19380		BLANK	Sb	ppm	0	
BLANK-18-19380		BLANK	Sc	ppm	0.5	
BLANK-18-19380		BLANK	Sm	ppm	0.001	
BLANK-18-19380		BLANK	Sn	ppm	0.01	
BLANK-18-19380		BLANK	Sr	ppm	0	
BLANK-18-19380		BLANK	Ta	ppm	-0.002	
BLANK-18-19380		BLANK	Tb	ppm	0	
BLANK-18-19380		BLANK	Th	ppm	0.004	
BLANK-18-19380		BLANK	Ti	ppm	1	
BLANK-18-19380		BLANK	Tl	ppm	0.001	

Sample ID	Client Sample ID	QC Name	Analyte	Units	Measured Value	Cert/Dup Value
BLANK-18-19380		BLANK	Tm	ppm	0.0007	
BLANK-18-19380		BLANK	U	ppm	0.002	
BLANK-18-19380		BLANK	V	ppm	0	
BLANK-18-19380		BLANK	W	ppm	0	
BLANK-18-19380		BLANK	Y	ppm	0	
BLANK-18-19380		BLANK	Yb	ppm	0.004	
BLANK-18-19380		BLANK	Zn	ppm	1.6	
BLANK-18-19380		BLANK	Zr	ppm	1	
BLANK-18-19381		BLANK	Ba	ppm	0.1	
BLANK-18-19381		BLANK	Be	ppm	0.06	
BLANK-18-19381		BLANK	Bi	ppm	0	
BLANK-18-19381		BLANK	Cd	ppm	0.004	
BLANK-18-19381		BLANK	Ce	ppm	0.02	
BLANK-18-19381		BLANK	Co	ppm	0.02	
BLANK-18-19381		BLANK	Cr	ppm	1	
BLANK-18-19381		BLANK	Cs	ppm	0.002	
BLANK-18-19381		BLANK	Cu	ppm	0	
BLANK-18-19381		BLANK	Dy	ppm	0.006	
BLANK-18-19381		BLANK	Er	ppm	0.005	
BLANK-18-19381		BLANK	Eu	ppm	0.0014	
BLANK-18-19381		BLANK	Ga	ppm	0.01	
BLANK-18-19381		BLANK	Gd	ppm	0.002	
BLANK-18-19381		BLANK	Hf	ppm	0.04	
BLANK-18-19381		BLANK	Ho	ppm	0.0011	
BLANK-18-19381		BLANK	In	ppm	0.0004	
BLANK-18-19381		BLANK	La	ppm	0	
BLANK-18-19381		BLANK	Li	ppm	0	
BLANK-18-19381		BLANK	Lu	ppm	0.001	
BLANK-18-19381		BLANK	Mo	ppm	0.03	
BLANK-18-19381		BLANK	Nb	ppm	0.001	
BLANK-18-19381		BLANK	Nd	ppm	0.01	
BLANK-18-19381		BLANK	Ni	ppm	0.1	
BLANK-18-19381		BLANK	Pb	ppm	0.03	
BLANK-18-19381		BLANK	Pr	ppm	0.001	
BLANK-18-19381		BLANK	Rb	ppm	0.02	
BLANK-18-19381		BLANK	Sb	ppm	0	
BLANK-18-19381		BLANK	Sc	ppm	0.4	

Sample ID	Client Sample ID	QC Name	Analyte	Units	Measured Value	Cert/Dup Value
BLANK-18-19381		BLANK	Sm	ppm	0.005	
BLANK-18-19381		BLANK	Sn	ppm	0	
BLANK-18-19381		BLANK	Sr	ppm	0.1	
BLANK-18-19381		BLANK	Ta	ppm	-0.003	
BLANK-18-19381		BLANK	Tb	ppm	0.0004	
BLANK-18-19381		BLANK	Th	ppm	0.006	
BLANK-18-19381		BLANK	Ti	ppm	1	
BLANK-18-19381		BLANK	Tl	ppm	0.002	
BLANK-18-19381		BLANK	Tm	ppm	0.0009	
BLANK-18-19381		BLANK	U	ppm	0.002	
BLANK-18-19381		BLANK	V	ppm	0.1	
BLANK-18-19381		BLANK	W	ppm	0.01	
BLANK-18-19381		BLANK	Y	ppm	0.01	
BLANK-18-19381		BLANK	Yb	ppm	0.003	
BLANK-18-19381		BLANK	Zn	ppm	1.4	
BLANK-18-19381		BLANK	Zr	ppm	1	
BLANK-18-19382		BLANK	Ba	ppm	0.1	
BLANK-18-19382		BLANK	Be	ppm	0.02	
BLANK-18-19382		BLANK	Bi	ppm	0	
BLANK-18-19382		BLANK	Cd	ppm	0.002	
BLANK-18-19382		BLANK	Ce	ppm	0.03	
BLANK-18-19382		BLANK	Co	ppm	0.03	
BLANK-18-19382		BLANK	Cr	ppm	2	
BLANK-18-19382		BLANK	Cs	ppm	0	
BLANK-18-19382		BLANK	Cu	ppm	0	
BLANK-18-19382		BLANK	Dy	ppm	0.002	
BLANK-18-19382		BLANK	Er	ppm	0.002	
BLANK-18-19382		BLANK	Eu	ppm	0.0015	
BLANK-18-19382		BLANK	Ga	ppm	0	
BLANK-18-19382		BLANK	Gd	ppm	0.002	
BLANK-18-19382		BLANK	Hf	ppm	0.03	
BLANK-18-19382		BLANK	Ho	ppm	0.0003	
BLANK-18-19382		BLANK	In	ppm	0.0004	
BLANK-18-19382		BLANK	La	ppm	0	
BLANK-18-19382		BLANK	Li	ppm	0	
BLANK-18-19382		BLANK	Lu	ppm	0.001	
BLANK-18-19382		BLANK	Mo	ppm	0.02	

Sample ID	Client Sample ID	QC Name	Analyte	Units	Measured Value	Cert/Dup Value
BLANK-18-19382		BLANK	Nb	ppm	0.002	
BLANK-18-19382		BLANK	Nd	ppm	0.01	
BLANK-18-19382		BLANK	Ni	ppm	0.3	
BLANK-18-19382		BLANK	Pb	ppm	0.01	
BLANK-18-19382		BLANK	Pr	ppm	0.001	
BLANK-18-19382		BLANK	Rb	ppm	0.02	
BLANK-18-19382		BLANK	Sb	ppm	0	
BLANK-18-19382		BLANK	Sc	ppm	0.3	
BLANK-18-19382		BLANK	Sm	ppm	0.003	
BLANK-18-19382		BLANK	Sn	ppm	0	
BLANK-18-19382		BLANK	Sr	ppm	0	
BLANK-18-19382		BLANK	Ta	ppm	0	
BLANK-18-19382		BLANK	Tb	ppm	0	
BLANK-18-19382		BLANK	Th	ppm	0.002	
BLANK-18-19382		BLANK	Ti	ppm	1	
BLANK-18-19382		BLANK	Tl	ppm	0.001	
BLANK-18-19382		BLANK	Tm	ppm	0.0001	
BLANK-18-19382		BLANK	U	ppm	0.002	
BLANK-18-19382		BLANK	V	ppm	0.2	
BLANK-18-19382		BLANK	W	ppm	0	
BLANK-18-19382		BLANK	Y	ppm	0.01	
BLANK-18-19382		BLANK	Yb	ppm	0	
BLANK-18-19382		BLANK	Zn	ppm	1.5	
BLANK-18-19382		BLANK	Zr	ppm	1	
BLANK-18-19383		BLANK	Ba	ppm	0.2	
BLANK-18-19383		BLANK	Be	ppm	0.02	
BLANK-18-19383		BLANK	Bi	ppm	0	
BLANK-18-19383		BLANK	Cd	ppm	0.001	
BLANK-18-19383		BLANK	Ce	ppm	0.01	
BLANK-18-19383		BLANK	Co	ppm	0.05	
BLANK-18-19383		BLANK	Cr	ppm	1	
BLANK-18-19383		BLANK	Cs	ppm	0.002	
BLANK-18-19383		BLANK	Cu	ppm	0.1	
BLANK-18-19383		BLANK	Dy	ppm	0.003	
BLANK-18-19383		BLANK	Er	ppm	0.005	
BLANK-18-19383		BLANK	Eu	ppm	0.001	
BLANK-18-19383		BLANK	Ga	ppm	0.03	

Sample ID	Client Sample ID	QC Name	Analyte	Units	Measured Value	Cert/Dup Value
BLANK-18-19383		BLANK	Gd	ppm	0.002	
BLANK-18-19383		BLANK	Hf	ppm	0.15	
BLANK-18-19383		BLANK	Ho	ppm	0.0003	
BLANK-18-19383		BLANK	In	ppm	0.0001	
BLANK-18-19383		BLANK	La	ppm	0	
BLANK-18-19383		BLANK	Li	ppm	0.1	
BLANK-18-19383		BLANK	Lu	ppm	0.001	
BLANK-18-19383		BLANK	Mo	ppm	0.1	
BLANK-18-19383		BLANK	Nb	ppm	0.009	
BLANK-18-19383		BLANK	Nd	ppm	0.01	
BLANK-18-19383		BLANK	Ni	ppm	0	
BLANK-18-19383		BLANK	Pb	ppm	0.05	
BLANK-18-19383		BLANK	Pr	ppm	0.003	
BLANK-18-19383		BLANK	Rb	ppm	0.04	
BLANK-18-19383		BLANK	Sb	ppm	0.01	
BLANK-18-19383		BLANK	Sc	ppm	1.7	
BLANK-18-19383		BLANK	Sm	ppm	0.001	
BLANK-18-19383		BLANK	Sn	ppm	0.02	
BLANK-18-19383		BLANK	Sr	ppm	0.1	
BLANK-18-19383		BLANK	Ta	ppm	0	
BLANK-18-19383		BLANK	Tb	ppm	0.0005	
BLANK-18-19383		BLANK	Th	ppm	0.011	
BLANK-18-19383		BLANK	Ti	ppm	3	
BLANK-18-19383		BLANK	Tl	ppm	0	
BLANK-18-19383		BLANK	Tm	ppm	0.0001	
BLANK-18-19383		BLANK	U	ppm	0.008	
BLANK-18-19383		BLANK	V	ppm	0.2	
BLANK-18-19383		BLANK	W	ppm	0.01	
BLANK-18-19383		BLANK	Y	ppm	0.03	
BLANK-18-19383		BLANK	Yb	ppm	0.004	
BLANK-18-19383		BLANK	Zn	ppm	0.6	
BLANK-18-19383		BLANK	Zr	ppm	6	
BLANK-18-19384		BLANK	Ba	ppm	0.1	
BLANK-18-19384		BLANK	Be	ppm	0.01	
BLANK-18-19384		BLANK	Bi	ppm	0	
BLANK-18-19384		BLANK	Cd	ppm	0.011	
BLANK-18-19384		BLANK	Ce	ppm	0.02	

Sample ID	Client Sample ID	QC Name	Analyte	Units	Measured Value	Cert/Dup Value
BLANK-18-19384		BLANK	Co	ppm	0.02	
BLANK-18-19384		BLANK	Cr	ppm	1	
BLANK-18-19384		BLANK	Cs	ppm	0.002	
BLANK-18-19384		BLANK	Cu	ppm	0.1	
BLANK-18-19384		BLANK	Dy	ppm	0.002	
BLANK-18-19384		BLANK	Er	ppm	0.001	
BLANK-18-19384		BLANK	Eu	ppm	0.0011	
BLANK-18-19384		BLANK	Ga	ppm	0.04	
BLANK-18-19384		BLANK	Gd	ppm	0.002	
BLANK-18-19384		BLANK	Hf	ppm	0.03	
BLANK-18-19384		BLANK	Ho	ppm	0.001	
BLANK-18-19384		BLANK	In	ppm	0.0001	
BLANK-18-19384		BLANK	La	ppm	0	
BLANK-18-19384		BLANK	Li	ppm	0	
BLANK-18-19384		BLANK	Lu	ppm	0	
BLANK-18-19384		BLANK	Mo	ppm	0.06	
BLANK-18-19384		BLANK	Nb	ppm	0.001	
BLANK-18-19384		BLANK	Nd	ppm	0.01	
BLANK-18-19384		BLANK	Ni	ppm	0	
BLANK-18-19384		BLANK	Pb	ppm	0.06	
BLANK-18-19384		BLANK	Pr	ppm	0.002	
BLANK-18-19384		BLANK	Rb	ppm	0.02	
BLANK-18-19384		BLANK	Sb	ppm	0	
BLANK-18-19384		BLANK	Sc	ppm	0.6	
BLANK-18-19384		BLANK	Sm	ppm	0.003	
BLANK-18-19384		BLANK	Sn	ppm	0	
BLANK-18-19384		BLANK	Sr	ppm	0.1	
BLANK-18-19384		BLANK	Ta	ppm	0.003	
BLANK-18-19384		BLANK	Tb	ppm	0.0004	
BLANK-18-19384		BLANK	Th	ppm	0.007	
BLANK-18-19384		BLANK	Ti	ppm	1	
BLANK-18-19384		BLANK	Tl	Ppm	0	
BLANK-18-19384		BLANK	Tm	Ppm	0.0005	
BLANK-18-19384		BLANK	U	Ppm	0.001	
BLANK-18-19384		BLANK	V	Ppm	0	
BLANK-18-19384		BLANK	W	Ppm	0.01	
BLANK-18-19384		BLANK	Y	Ppm	0.01	

Sample ID	Client Sample ID	QC Name	Analyte	Units	Measured Value	Cert/Dup Value
BLANK-18-19384		BLANK	Yb	Ppm	0.003	
BLANK-18-19384		BLANK	Zn	Ppm	0.5	
BLANK-18-19384		BLANK	Zr	Ppm	1	
BLANK-18-19385		BLANK	Ba	Ppm	0.2	
BLANK-18-19385		BLANK	Be	Ppm	0.03	
BLANK-18-19385		BLANK	Bi	Ppm	0	
BLANK-18-19385		BLANK	Cd	Ppm	0	
BLANK-18-19385		BLANK	Ce	Ppm	0.01	
BLANK-18-19385		BLANK	Co	Ppm	0.05	
BLANK-18-19385		BLANK	Cr	Ppm	1	
BLANK-18-19385		BLANK	Cs	Ppm	0.001	
BLANK-18-19385		BLANK	Cu	Ppm	0.1	
BLANK-18-19385		BLANK	Dy	Ppm	0.005	
BLANK-18-19385		BLANK	Er	Ppm	0.004	
BLANK-18-19385		BLANK	Eu	Ppm	0.0003	
BLANK-18-19385		BLANK	Ga	Ppm	0.03	
BLANK-18-19385		BLANK	Gd	Ppm	0.002	
BLANK-18-19385		BLANK	Hf	Ppm	0.13	
BLANK-18-19385		BLANK	Ho	Ppm	0.0006	
BLANK-18-19385		BLANK	In	Ppm	0	
BLANK-18-19385		BLANK	La	Ppm	0	
BLANK-18-19385		BLANK	Li	Ppm	0.1	
BLANK-18-19385		BLANK	Lu	Ppm	0.001	
BLANK-18-19385		BLANK	Mo	Ppm	0.08	
BLANK-18-19385		BLANK	Nb	Ppm	0.007	
BLANK-18-19385		BLANK	Nd	Ppm	0.01	
BLANK-18-19385		BLANK	Ni	Ppm	0.2	
BLANK-18-19385		BLANK	Pb	Ppm	0.04	
BLANK-18-19385		BLANK	Pr	Ppm	0.003	
BLANK-18-19385		BLANK	Rb	Ppm	0.04	
BLANK-18-19385		BLANK	Sb	Ppm	0.01	
BLANK-18-19385		BLANK	Sc	Ppm	1.4	
BLANK-18-19385		BLANK	Sm	Ppm	0.003	
BLANK-18-19385		BLANK	Sn	Ppm	0.02	
BLANK-18-19385		BLANK	Sr	Ppm	0.1	
BLANK-18-19385		BLANK	Ta	Ppm	0	
BLANK-18-19385		BLANK	Tb	Ppm	0.0005	

Sample ID	Client Sample ID	QC Name	Analyte	Units	Measured Value	Cert/Dup Value
BLANK-18-19385		BLANK	Th	ppm	0.01	
BLANK-18-19385		BLANK	Ti	ppm	2	
BLANK-18-19385		BLANK	Tl	ppm	0.001	
BLANK-18-19385		BLANK	Tm	ppm	0.0007	
BLANK-18-19385		BLANK	U	ppm	0.007	
BLANK-18-19385		BLANK	V	ppm	0.2	
BLANK-18-19385		BLANK	W	ppm	0.01	
BLANK-18-19385		BLANK	Y	ppm	0.03	
BLANK-18-19385		BLANK	Yb	ppm	0.006	
BLANK-18-19385		BLANK	Zn	ppm	0.3	
BLANK-18-19385		BLANK	Zr	ppm	6	
Dup-18-45461	111-12-424A01	DUP	Ba	ppm	27.7	
Dup-18-45461	111-12-424A01	DUP	Be	ppm	0.3	
Dup-18-45461	111-12-424A01	DUP	Bi	ppm	0.92	
Dup-18-45461	111-12-424A01	DUP	Cd	ppm	1.008	
Dup-18-45461	111-12-424A01	DUP	Ce	ppm	5.66	
Dup-18-45461	111-12-424A01	DUP	Co	ppm	167.49	
Dup-18-45461	111-12-424A01	DUP	Cr	ppm	135	
Dup-18-45461	111-12-424A01	DUP	Cs	ppm	0.127	
Dup-18-45461	111-12-424A01	DUP	Cu	ppm	6234	
Dup-18-45461	111-12-424A01	DUP	Dy	ppm	2.511	
Dup-18-45461	111-12-424A01	DUP	Er	ppm	1.63	
Dup-18-45461	111-12-424A01	DUP	Eu	ppm	0.6146	
Dup-18-45461	111-12-424A01	DUP	Ga	ppm	14.9	
Dup-18-45461	111-12-424A01	DUP	Gd	ppm	2.107	
Dup-18-45461	111-12-424A01	DUP	Hf	ppm	1.07	
Dup-18-45461	111-12-424A01	DUP	Ho	ppm	0.5557	
Dup-18-45461	111-12-424A01	DUP	In	ppm	0.1212	
Dup-18-45461	111-12-424A01	DUP	La	ppm	2.2	
Dup-18-45461	111-12-424A01	DUP	Li	ppm	12.8	
Dup-18-45461	111-12-424A01	DUP	Lu	ppm	0.239	
Dup-18-45461	111-12-424A01	DUP	Mo	ppm	0.5	
Dup-18-45461	111-12-424A01	DUP	Nb	ppm	1.658	
Dup-18-45461	111-12-424A01	DUP	Nd	ppm	4.73	
Dup-18-45461	111-12-424A01	DUP	Ni	ppm	1952.7	
Dup-18-45461	111-12-424A01	DUP	Pb	ppm	1.28	
Dup-18-45461	111-12-424A01	DUP	Pr	ppm	0.919	

Sample ID	Client Sample ID	QC Name	Analyte	Units	Measured Value	Cert/Dup Value
Dup-18-45461	111-12-424A01	DUP	Rb	ppm	3.45	
Dup-18-45461	111-12-424A01	DUP	Sb	ppm	0.18	
Dup-18-45461	111-12-424A01	DUP	Sc	ppm	35.6	
Dup-18-45461	111-12-424A01	DUP	Sm	ppm	1.564	
Dup-18-45461	111-12-424A01	DUP	Sn	ppm	1.01	
Dup-18-45461	111-12-424A01	DUP	Sr	ppm	89.2	
Dup-18-45461	111-12-424A01	DUP	Ta	ppm	0.106	
Dup-18-45461	111-12-424A01	DUP	Tb	ppm	0.3732	
Dup-18-45461	111-12-424A01	DUP	Th	ppm	0.229	
Dup-18-45461	111-12-424A01	DUP	Ti	ppm	4267	
Dup-18-45461	111-12-424A01	DUP	Tl	ppm	0.036	
Dup-18-45461	111-12-424A01	DUP	Tm	ppm	0.2388	
Dup-18-45461	111-12-424A01	DUP	U	ppm	0.072	
Dup-18-45461	111-12-424A01	DUP	V	ppm	253.7	
Dup-18-45461	111-12-424A01	DUP	W	ppm	0.22	
Dup-18-45461	111-12-424A01	DUP	Y	ppm	14.56	
Dup-18-45461	111-12-424A01	DUP	Yb	ppm	1.584	
Dup-18-45461	111-12-424A01	DUP	Zn	ppm	150.7	
Dup-18-45461	111-12-424A01	DUP	Zr	ppm	37	
Dup-18-45466	MV2017-2	DUP	Ba	ppm	89.1	
Dup-18-45466	MV2017-2	DUP	Be	ppm	0.4	
Dup-18-45466	MV2017-2	DUP	Bi	ppm	0.26	
Dup-18-45466	MV2017-2	DUP	Cd	ppm	0.065	
Dup-18-45466	MV2017-2	DUP	Ce	ppm	5.08	
Dup-18-45466	MV2017-2	DUP	Co	ppm	17.48	
Dup-18-45466	MV2017-2	DUP	Cr	ppm	26	
Dup-18-45466	MV2017-2	DUP	Cs	ppm	19.704	
Dup-18-45466	MV2017-2	DUP	Cu	ppm	25	
Dup-18-45466	MV2017-2	DUP	Dy	ppm	2.779	
Dup-18-45466	MV2017-2	DUP	Er	ppm	1.85	
Dup-18-45466	MV2017-2	DUP	Eu	ppm	0.7529	
Dup-18-45466	MV2017-2	DUP	Ga	ppm	20.75	
Dup-18-45466	MV2017-2	DUP	Gd	ppm	2.314	
Dup-18-45466	MV2017-2	DUP	Hf	ppm	1.87	
Dup-18-45466	MV2017-2	DUP	Ho	ppm	0.605	
Dup-18-45466	MV2017-2	DUP	In	ppm	0.0195	
Dup-18-45466	MV2017-2	DUP	La	ppm	1.8	

Sample ID	Client Sample ID	QC Name	Analyte	Units	Measured Value	Cert/Dup Value
Dup-18-45466	MV2017-2	DUP	Li	ppm	38.8	
Dup-18-45466	MV2017-2	DUP	Lu	ppm	0.277	
Dup-18-45466	MV2017-2	DUP	Mo	ppm	1.27	
Dup-18-45466	MV2017-2	DUP	Nb	ppm	0.733	
Dup-18-45466	MV2017-2	DUP	Nd	ppm	5.11	
Dup-18-45466	MV2017-2	DUP	Ni	ppm	59.8	
Dup-18-45466	MV2017-2	DUP	Pb	ppm	1.76	
Dup-18-45466	MV2017-2	DUP	Pr	ppm	0.915	
Dup-18-45466	MV2017-2	DUP	Rb	ppm	59.91	
Dup-18-45466	MV2017-2	DUP	Sb	ppm	0.07	
Dup-18-45466	MV2017-2	DUP	Sc	ppm	11	
Dup-18-45466	MV2017-2	DUP	Sm	ppm	1.847	
Dup-18-45466	MV2017-2	DUP	Sn	ppm	0.14	
Dup-18-45466	MV2017-2	DUP	Sr	ppm	179.5	
Dup-18-45466	MV2017-2	DUP	Ta	ppm	0.08	
Dup-18-45466	MV2017-2	DUP	Tb	ppm	0.409	
Dup-18-45466	MV2017-2	DUP	Th	ppm	0.224	
Dup-18-45466	MV2017-2	DUP	Ti	ppm	1922	
Dup-18-45466	MV2017-2	DUP	Tl	ppm	0.522	
Dup-18-45466	MV2017-2	DUP	Tm	ppm	0.2808	
Dup-18-45466	MV2017-2	DUP	U	ppm	0.074	
Dup-18-45466	MV2017-2	DUP	V	ppm	77.1	
Dup-18-45466	MV2017-2	DUP	W	ppm	0.2	
Dup-18-45466	MV2017-2	DUP	Y	ppm	15.77	
Dup-18-45466	MV2017-2	DUP	Yb	ppm	1.848	
Dup-18-45466	MV2017-2	DUP	Zn	ppm	36.9	
Dup-18-45466	MV2017-2	DUP	Zr	ppm	68	
Dup-18-45482	MV2017-9	DUP	Ba	ppm	74.7	
Dup-18-45482	MV2017-9	DUP	Be	ppm	0.13	
Dup-18-45482	MV2017-9	DUP	Bi	ppm	0.1	
Dup-18-45482	MV2017-9	DUP	Cd	ppm	0.023	
Dup-18-45482	MV2017-9	DUP	Ce	ppm	1.71	
Dup-18-45482	MV2017-9	DUP	Co	ppm	18.87	
Dup-18-45482	MV2017-9	DUP	Cr	ppm	408	
Dup-18-45482	MV2017-9	DUP	Cs	ppm	8.399	
Dup-18-45482	MV2017-9	DUP	Cu	ppm	5.4	
Dup-18-45482	MV2017-9	DUP	Dy	ppm	1.206	

Sample ID	Client Sample ID	QC Name	Analyte	Units	Measured Value	Cert/Dup Value
Dup-18-45482	MV2017-9	DUP	Er	ppm	0.755	
Dup-18-45482	MV2017-9	DUP	Eu	ppm	0.4923	
Dup-18-45482	MV2017-9	DUP	Ga	ppm	18.9	
Dup-18-45482	MV2017-9	DUP	Gd	ppm	0.967	
Dup-18-45482	MV2017-9	DUP	Hf	ppm	0.23	
Dup-18-45482	MV2017-9	DUP	Ho	ppm	0.259	
Dup-18-45482	MV2017-9	DUP	In	ppm	0.0327	
Dup-18-45482	MV2017-9	DUP	La	ppm	0.7	
Dup-18-45482	MV2017-9	DUP	Li	ppm	32.4	
Dup-18-45482	MV2017-9	DUP	Lu	ppm	0.106	
Dup-18-45482	MV2017-9	DUP	Mo	ppm	0.25	
Dup-18-45482	MV2017-9	DUP	Nb	ppm	0.221	
Dup-18-45482	MV2017-9	DUP	Nd	ppm	1.85	
Dup-18-45482	MV2017-9	DUP	Ni	ppm	49.3	
Dup-18-45482	MV2017-9	DUP	Pb	ppm	0.99	
Dup-18-45482	MV2017-9	DUP	Pr	ppm	0.322	
Dup-18-45482	MV2017-9	DUP	Rb	ppm	34.72	
Dup-18-45482	MV2017-9	DUP	Sb	ppm	0.22	
Dup-18-45482	MV2017-9	DUP	Sc	ppm	30.3	
Dup-18-45482	MV2017-9	DUP	Sm	ppm	0.703	
Dup-18-45482	MV2017-9	DUP	Sn	ppm	0.27	
Dup-18-45482	MV2017-9	DUP	Sr	ppm	129.2	
Dup-18-45482	MV2017-9	DUP	Ta	ppm	0.016	
Dup-18-45482	MV2017-9	DUP	Tb	ppm	0.1764	
Dup-18-45482	MV2017-9	DUP	Th	ppm	0.018	
Dup-18-45482	MV2017-9	DUP	Ti	ppm	1683	
Dup-18-45482	MV2017-9	DUP	Tl	ppm	0.158	
Dup-18-45482	MV2017-9	DUP	Tm	ppm	0.1087	
Dup-18-45482	MV2017-9	DUP	U	ppm	0.015	
Dup-18-45482	MV2017-9	DUP	V	ppm	138.9	
Dup-18-45482	MV2017-9	DUP	W	ppm	30.54	
Dup-18-45482	MV2017-9	DUP	Y	ppm	6.86	
Dup-18-45482	MV2017-9	DUP	Yb	ppm	0.695	
Dup-18-45482	MV2017-9	DUP	Zn	ppm	52.4	
Dup-18-45482	MV2017-9	DUP	Zr	ppm	7	
Dup-18-45483	111-12-541A01	DUP	Ba	ppm	160.2	
Dup-18-45483	111-12-541A01	DUP	Be	ppm	0.26	

Sample ID	Client Sample ID	QC Name	Analyte	Units	Measured Value	Cert/Dup Value
Dup-18-45483	111-12-541A01	DUP	Bi	ppm	0.05	
Dup-18-45483	111-12-541A01	DUP	Cd	ppm	0.072	
Dup-18-45483	111-12-541A01	DUP	Ce	ppm	5.01	
Dup-18-45483	111-12-541A01	DUP	Co	ppm	20.99	
Dup-18-45483	111-12-541A01	DUP	Cr	ppm	42	
Dup-18-45483	111-12-541A01	DUP	Cs	ppm	3.604	
Dup-18-45483	111-12-541A01	DUP	Cu	ppm	63	
Dup-18-45483	111-12-541A01	DUP	Dy	ppm	2.314	
Dup-18-45483	111-12-541A01	DUP	Er	ppm	1.482	
Dup-18-45483	111-12-541A01	DUP	Eu	ppm	0.5659	
Dup-18-45483	111-12-541A01	DUP	Ga	ppm	18.4	
Dup-18-45483	111-12-541A01	DUP	Gd	ppm	1.851	
Dup-18-45483	111-12-541A01	DUP	Hf	ppm	1.11	
Dup-18-45483	111-12-541A01	DUP	Ho	ppm	0.4923	
Dup-18-45483	111-12-541A01	DUP	In	ppm	0.0246	
Dup-18-45483	111-12-541A01	DUP	La	ppm	1.8	
Dup-18-45483	111-12-541A01	DUP	Li	ppm	63.3	
Dup-18-45483	111-12-541A01	DUP	Lu	ppm	0.223	
Dup-18-45483	111-12-541A01	DUP	Mo	ppm	0.24	
Dup-18-45483	111-12-541A01	DUP	Nb	ppm	1.435	
Dup-18-45483	111-12-541A01	DUP	Nd	ppm	4.44	
Dup-18-45483	111-12-541A01	DUP	Ni	ppm	31.9	
Dup-18-45483	111-12-541A01	DUP	Pb	ppm	0.68	
Dup-18-45483	111-12-541A01	DUP	Pr	ppm	0.844	
Dup-18-45483	111-12-541A01	DUP	Rb	ppm	38.35	
Dup-18-45483	111-12-541A01	DUP	Sb	ppm	0.12	
Dup-18-45483	111-12-541A01	DUP	Sc	ppm	21	
Dup-18-45483	111-12-541A01	DUP	Sm	ppm	1.495	
Dup-18-45483	111-12-541A01	DUP	Sn	ppm	0.14	
Dup-18-45483	111-12-541A01	DUP	Sr	ppm	165.8	
Dup-18-45483	111-12-541A01	DUP	Ta	ppm	0.095	
Dup-18-45483	111-12-541A01	DUP	Tb	Ppm	0.3344	
Dup-18-45483	111-12-541A01	DUP	Th	Ppm	0.196	
Dup-18-45483	111-12-541A01	DUP	Ti	Ppm	3274	
Dup-18-45483	111-12-541A01	DUP	Tl	Ppm	0.286	
Dup-18-45483	111-12-541A01	DUP	Tm	Ppm	0.2185	
Dup-18-45483	111-12-541A01	DUP	U	Ppm	0.051	

Sample ID	Client Sample ID	QC Name	Analyte	Units	Measured Value	Cert/Dup Value
Dup-18-45483	111-12-541A01	DUP	V	ppm	140	
Dup-18-45483	111-12-541A01	DUP	W	ppm	0.68	
Dup-18-45483	111-12-541A01	DUP	Y	ppm	12.85	
Dup-18-45483	111-12-541A01	DUP	Yb	ppm	1.441	
Dup-18-45483	111-12-541A01	DUP	Zn	ppm	48.6	
Dup-18-45483	111-12-541A01	DUP	Zr	ppm	39	
Dup-18-45484	111-11-09	DUP	Ba	ppm	18.6	
Dup-18-45484	111-11-09	DUP	Be	ppm	0.19	
Dup-18-45484	111-11-09	DUP	Bi	ppm	0.3	
Dup-18-45484	111-11-09	DUP	Cd	ppm	0.88	
Dup-18-45484	111-11-09	DUP	Ce	ppm	3.87	
Dup-18-45484	111-11-09	DUP	Co	ppm	146.23	
Dup-18-45484	111-11-09	DUP	Cr	ppm	287	
Dup-18-45484	111-11-09	DUP	Cs	ppm	0.183	
Dup-18-45484	111-11-09	DUP	Cu	ppm	4853.8	
Dup-18-45484	111-11-09	DUP	Dy	ppm	1.768	
Dup-18-45484	111-11-09	DUP	Er	ppm	1.152	
Dup-18-45484	111-11-09	DUP	Eu	ppm	0.4804	
Dup-18-45484	111-11-09	DUP	Ga	ppm	12.92	
Dup-18-45484	111-11-09	DUP	Gd	ppm	1.419	
Dup-18-45484	111-11-09	DUP	Hf	ppm	0.69	
Dup-18-45484	111-11-09	DUP	Ho	ppm	0.3883	
Dup-18-45484	111-11-09	DUP	In	ppm	0.0885	
Dup-18-45484	111-11-09	DUP	La	ppm	1.5	
Dup-18-45484	111-11-09	DUP	Li	ppm	27.2	
Dup-18-45484	111-11-09	DUP	Lu	ppm	0.175	
Dup-18-45484	111-11-09	DUP	Mo	ppm	0.34	
Dup-18-45484	111-11-09	DUP	Nb	ppm	0.957	
Dup-18-45484	111-11-09	DUP	Nd	ppm	3.16	
Dup-18-45484	111-11-09	DUP	Ni	ppm	2137.3	
Dup-18-45484	111-11-09	DUP	Pb	ppm	1.62	
Dup-18-45484	111-11-09	DUP	Pr	ppm	0.611	
Dup-18-45484	111-11-09	DUP	Rb	ppm	2.72	
Dup-18-45484	111-11-09	DUP	Sb	ppm	0.22	
Dup-18-45484	111-11-09	DUP	Sc	ppm	34.4	
Dup-18-45484	111-11-09	DUP	Sm	ppm	1.05	
Dup-18-45484	111-11-09	DUP	Sn	ppm	0.29	

Sample ID	Client Sample ID	QC Name	Analyte	Units	Measured Value	Cert/Dup Value
Dup-18-45484	111-11-09	DUP	Sr	ppm	51.2	
Dup-18-45484	111-11-09	DUP	Ta	ppm	0.059	
Dup-18-45484	111-11-09	DUP	Tb	Ppm	0.2533	
Dup-18-45484	111-11-09	DUP	Th	Ppm	0.146	
Dup-18-45484	111-11-09	DUP	Ti	Ppm	3076	
Dup-18-45484	111-11-09	DUP	Tl	Ppm	0.04	
Dup-18-45484	111-11-09	DUP	Tm	Ppm	0.1663	
Dup-18-45484	111-11-09	DUP	U	Ppm	0.042	
Dup-18-45484	111-11-09	DUP	V	Ppm	224.4	
Dup-18-45484	111-11-09	DUP	W	Ppm	0.03	
Dup-18-45484	111-11-09	DUP	Y	Ppm	9.99	
Dup-18-45484	111-11-09	DUP	Yb	ppm	1.124	
Dup-18-45484	111-11-09	DUP	Zn	ppm	113.7	
Dup-18-45484	111-11-09	DUP	Zr	ppm	23	
Dup-18-45485	111-12-623A01	DUP	Ba	ppm	41.5	
Dup-18-45485	111-12-623A01	DUP	Be	ppm	2.69	
Dup-18-45485	111-12-623A01	DUP	Bi	ppm	0.4	
Dup-18-45485	111-12-623A01	DUP	Cd	ppm	0.095	
Dup-18-45485	111-12-623A01	DUP	Ce	ppm	3.71	
Dup-18-45485	111-12-623A01	DUP	Co	ppm	18.92	
Dup-18-45485	111-12-623A01	DUP	Cr	ppm	7	
Dup-18-45485	111-12-623A01	DUP	Cs	ppm	1.442	
Dup-18-45485	111-12-623A01	DUP	Cu	ppm	29.6	
Dup-18-45485	111-12-623A01	DUP	Dy	ppm	1.965	
Dup-18-45485	111-12-623A01	DUP	Er	ppm	1.294	
Dup-18-45485	111-12-623A01	DUP	Eu	ppm	0.6689	
Dup-18-45485	111-12-623A01	DUP	Ga	ppm	20.61	
Dup-18-45485	111-12-623A01	DUP	Gd	ppm	1.557	
Dup-18-45485	111-12-623A01	DUP	Hf	ppm	1.58	
Dup-18-45485	111-12-623A01	DUP	Ho	ppm	0.4305	
Dup-18-45485	111-12-623A01	DUP	In	ppm	0.0258	
Dup-18-45485	111-12-623A01	DUP	La	ppm	1.5	
Dup-18-45485	111-12-623A01	DUP	Li	ppm	54.7	
Dup-18-45485	111-12-623A01	DUP	Lu	ppm	0.202	
Dup-18-45485	111-12-623A01	DUP	Mo	ppm	0.33	
Dup-18-45485	111-12-623A01	DUP	Nb	ppm	1.908	
Dup-18-45485	111-12-623A01	DUP	Nd	ppm	3.45	

Sample ID	Client Sample ID	QC Name	Analyte	Units	Measured Value	Cert/Dup Value
Dup-18-45485	111-12-623A01	DUP	Ni	ppm	52.2	
Dup-18-45485	111-12-623A01	DUP	Pb	ppm	1.22	
Dup-18-45485	111-12-623A01	DUP	Pr	ppm	0.67	
Dup-18-45485	111-12-623A01	DUP	Rb	ppm	3.92	
Dup-18-45485	111-12-623A01	DUP	Sb	ppm	0.11	
Dup-18-45485	111-12-623A01	DUP	Sc	ppm	13.9	
Dup-18-45485	111-12-623A01	DUP	Sm	ppm	1.222	
Dup-18-45485	111-12-623A01	DUP	Sn	ppm	0.76	
Dup-18-45485	111-12-623A01	DUP	Sr	ppm	167.4	
Dup-18-45485	111-12-623A01	DUP	Ta	ppm	0.133	
Dup-18-45485	111-12-623A01	DUP	Tb	ppm	0.2822	
Dup-18-45485	111-12-623A01	DUP	Th	ppm	0.252	
Dup-18-45485	111-12-623A01	DUP	Ti	ppm	3665	
Dup-18-45485	111-12-623A01	DUP	Tl	ppm	0.031	
Dup-18-45485	111-12-623A01	DUP	Tm	ppm	0.1893	
Dup-18-45485	111-12-623A01	DUP	U	ppm	0.073	
Dup-18-45485	111-12-623A01	DUP	V	ppm	134.8	
Dup-18-45485	111-12-623A01	DUP	W	ppm	0.26	
Dup-18-45485	111-12-623A01	DUP	Y	ppm	11.46	
Dup-18-45485	111-12-623A01	DUP	Yb	ppm	1.254	
Dup-18-45485	111-12-623A01	DUP	Zn	ppm	28.4	
Dup-18-45485	111-12-623A01	DUP	Zr	ppm	58	
IHST-18-25522		MRB-29	Ba	ppm	292.3	
IHST-18-25522		MRB-29	Be	ppm	1.01	
IHST-18-25522		MRB-29	Bi	ppm	0.03	
IHST-18-25522		MRB-29	Cd	ppm	0.123	
IHST-18-25522		MRB-29	Ce	ppm	49.69	
IHST-18-25522		MRB-29	Co	ppm	48.91	
IHST-18-25522		MRB-29	Cr	ppm	270	
IHST-18-25522		MRB-29	Cs	ppm	0.25	
IHST-18-25522		MRB-29	Cu	ppm	159.4	
IHST-18-25522		MRB-29	Dy	ppm	5.144	
IHST-18-25522		MRB-29	Er	ppm	2.755	
IHST-18-25522		MRB-29	Eu	ppm	1.8822	
IHST-18-25522		MRB-29	Ga	ppm	18.99	
IHST-18-25522		MRB-29	Gd	ppm	5.733	
IHST-18-25522		MRB-29	Hf	ppm	4.35	

Sample ID	Client Sample ID	QC Name	Analyte	Units	Measured Value	Cert/Dup Value
IHST-18-25522		MRB-29	Ho	ppm	0.9968	
IHST-18-25522		MRB-29	In	ppm	0.0744	
IHST-18-25522		MRB-29	La	ppm	21.4	
IHST-18-25522		MRB-29	Li	ppm	9.3	
IHST-18-25522		MRB-29	Lu	ppm	0.34	
IHST-18-25522		MRB-29	Mo	ppm	0.82	
IHST-18-25522		MRB-29	Nb	ppm	12.367	
IHST-18-25522		MRB-29	Nd	ppm	27.93	
IHST-18-25522		MRB-29	Ni	ppm	105.5	
IHST-18-25522		MRB-29	Pb	ppm	5.74	
IHST-18-25522		MRB-29	Pr	ppm	6.346	
IHST-18-25522		MRB-29	Rb	ppm	14.83	
IHST-18-25522		MRB-29	Sb	ppm	0.06	
IHST-18-25522		MRB-29	Sc	ppm	31.5	
IHST-18-25522		MRB-29	Sm	ppm	6.118	
IHST-18-25522		MRB-29	Sn	ppm	2.61	
IHST-18-25522		MRB-29	Sr	ppm	306.6	
IHST-18-25522		MRB-29	Ta	ppm	0.806	
IHST-18-25522		MRB-29	Tb	ppm	0.8588	
IHST-18-25522		MRB-29	Th	ppm	2.543	
IHST-18-25522		MRB-29	Ti	ppm	10765	
IHST-18-25522		MRB-29	Tl	ppm	0.07	
IHST-18-25522		MRB-29	Tm	ppm	0.3755	
IHST-18-25522		MRB-29	U	ppm	0.619	
IHST-18-25522		MRB-29	V	ppm	298.9	
IHST-18-25522		MRB-29	W	ppm	0.2	
IHST-18-25522		MRB-29	Y	ppm	26.37	
IHST-18-25522		MRB-29	Yb	ppm	2.367	
IHST-18-25522		MRB-29	Zn	ppm	106.7	
IHST-18-25522		MRB-29	Zr	ppm	165	
IHST-18-25523		MRB-29	Ba	ppm	285.9	
IHST-18-25523		MRB-29	Be	ppm	1.09	
IHST-18-25523		MRB-29	Bi	ppm	0.03	
IHST-18-25523		MRB-29	Cd	ppm	0.125	
IHST-18-25523		MRB-29	Ce	ppm	50.17	
IHST-18-25523		MRB-29	Co	ppm	51.77	
IHST-18-25523		MRB-29	Cr	ppm	286	

Sample ID	Client Sample ID	QC Name	Analyte	Units	Measured Value	Cert/Dup Value
IHST-18-25523		MRB-29	Cs	ppm	0.243	
IHST-18-25523		MRB-29	Cu	ppm	151	
IHST-18-25523		MRB-29	Dy	ppm	5.234	
IHST-18-25523		MRB-29	Er	ppm	2.807	
IHST-18-25523		MRB-29	Eu	ppm	1.8802	
IHST-18-25523		MRB-29	Ga	ppm	19.6	
IHST-18-25523		MRB-29	Gd	ppm	5.903	
IHST-18-25523		MRB-29	Hf	ppm	4.44	
IHST-18-25523		MRB-29	Ho	ppm	1.0139	
IHST-18-25523		MRB-29	In	ppm	0.0791	
IHST-18-25523		MRB-29	La	ppm	21.5	
IHST-18-25523		MRB-29	Li	ppm	9.9	
IHST-18-25523		MRB-29	Lu	ppm	0.361	
IHST-18-25523		MRB-29	Mo	ppm	0.85	
IHST-18-25523		MRB-29	Nb	ppm	12.654	
IHST-18-25523		MRB-29	Nd	ppm	27.88	
IHST-18-25523		MRB-29	Ni	ppm	112	
IHST-18-25523		MRB-29	Pb	ppm	4.72	
IHST-18-25523		MRB-29	Pr	ppm	6.487	
IHST-18-25523		MRB-29	Rb	ppm	15.15	
IHST-18-25523		MRB-29	Sb	ppm	0.06	
IHST-18-25523		MRB-29	Sc	Ppm	33.9	
IHST-18-25523		MRB-29	Sm	Ppm	6.21	
IHST-18-25523		MRB-29	Sn	Ppm	2.4	
IHST-18-25523		MRB-29	Sr	Ppm	307.7	
IHST-18-25523		MRB-29	Ta	Ppm	0.808	
IHST-18-25523		MRB-29	Tb	Ppm	0.8709	
IHST-18-25523		MRB-29	Th	Ppm	2.576	
IHST-18-25523		MRB-29	Ti	Ppm	11457	
IHST-18-25523		MRB-29	Tl	Ppm	0.068	
IHST-18-25523		MRB-29	Tm	Ppm	0.393	
IHST-18-25523		MRB-29	U	Ppm	0.658	
IHST-18-25523		MRB-29	V	Ppm	319.5	
IHST-18-25523		MRB-29	W	Ppm	0.2	
IHST-18-25523		MRB-29	Y	Ppm	26.7	
IHST-18-25523		MRB-29	Yb	Ppm	2.474	
IHST-18-25523		MRB-29	Zn	Ppm	111.9	

Sample ID	Client Sample ID	QC Name	Analyte	Units	Measured Value	Cert/Dup Value
IHST-18-25523		MRB-29	Zr	Ppm	168	
IHST-18-25528		MRB-29	Ba	Ppm	287.7	
IHST-18-25528		MRB-29	Be	Ppm	1.06	
IHST-18-25528		MRB-29	Bi	Ppm	0.03	
IHST-18-25528		MRB-29	Cd	Ppm	0.124	
IHST-18-25528		MRB-29	Ce	Ppm	48.86	
IHST-18-25528		MRB-29	Co	Ppm	50.56	
IHST-18-25528		MRB-29	Cr	Ppm	277	
IHST-18-25528		MRB-29	Cs	Ppm	0.245	
IHST-18-25528		MRB-29	Cu	Ppm	162.3	
IHST-18-25528		MRB-29	Dy	Ppm	5.332	
IHST-18-25528		MRB-29	Er	Ppm	2.798	
IHST-18-25528		MRB-29	Eu	Ppm	1.8834	
IHST-18-25528		MRB-29	Ga	Ppm	19.43	
IHST-18-25528		MRB-29	Gd	Ppm	5.909	
IHST-18-25528		MRB-29	Hf	Ppm	4.41	
IHST-18-25528		MRB-29	Ho	Ppm	1.0171	
IHST-18-25528		MRB-29	In	Ppm	0.0777	
IHST-18-25528		MRB-29	La	Ppm	21.7	
IHST-18-25528		MRB-29	Li	Ppm	9.1	
IHST-18-25528		MRB-29	Lu	Ppm	0.358	
IHST-18-25528		MRB-29	Mo	Ppm	0.97	
IHST-18-25528		MRB-29	Nb	Ppm	12.592	
IHST-18-25528		MRB-29	Nd	Ppm	28.04	
IHST-18-25528		MRB-29	Ni	Ppm	109.4	
IHST-18-25528		MRB-29	Pb	Ppm	4.81	
IHST-18-25528		MRB-29	Pr	Ppm	6.462	
IHST-18-25528		MRB-29	Rb	Ppm	15.15	
IHST-18-25528		MRB-29	Sb	Ppm	0.06	
IHST-18-25528		MRB-29	Sc	Ppm	32.9	
IHST-18-25528		MRB-29	Sm	Ppm	6.266	
IHST-18-25528		MRB-29	Sn	Ppm	2.33	
IHST-18-25528		MRB-29	Sr	Ppm	307.9	
IHST-18-25528		MRB-29	Ta	Ppm	0.809	
IHST-18-25528		MRB-29	Tb	Ppm	0.8809	
IHST-18-25528		MRB-29	Th	Ppm	2.628	
IHST-18-25528		MRB-29	Ti	ppm	11389	

Sample ID	Client Sample ID	QC Name	Analyte	Units	Measured Value	Cert/Dup Value
IHST-18-25528		MRB-29	Tl	ppm	0.067	
IHST-18-25528		MRB-29	Tm	ppm	0.3821	
IHST-18-25528		MRB-29	U	ppm	0.65	
IHST-18-25528		MRB-29	V	ppm	311.7	
IHST-18-25528		MRB-29	W	ppm	0.21	
IHST-18-25528		MRB-29	Y	ppm	26.73	
IHST-18-25528		MRB-29	Yb	ppm	2.425	
IHST-18-25528		MRB-29	Zn	ppm	109.3	
IHST-18-25528		MRB-29	Zr	ppm	169	
IHST-18-25529		MRB-29	Ba	ppm	290.1	
IHST-18-25529		MRB-29	Be	ppm	1.1	
IHST-18-25529		MRB-29	Bi	ppm	0.44	
IHST-18-25529		MRB-29	Cd	ppm	0.122	
IHST-18-25529		MRB-29	Ce	ppm	48.54	
IHST-18-25529		MRB-29	Co	ppm	52.55	
IHST-18-25529		MRB-29	Cr	ppm	293	
IHST-18-25529		MRB-29	Cs	ppm	0.239	
IHST-18-25529		MRB-29	Cu	ppm	157.9	
IHST-18-25529		MRB-29	Dy	ppm	5.282	
IHST-18-25529		MRB-29	Er	ppm	2.817	
IHST-18-25529		MRB-29	Eu	ppm	1.8746	
IHST-18-25529		MRB-29	Ga	ppm	19.49	
IHST-18-25529		MRB-29	Gd	ppm	5.884	
IHST-18-25529		MRB-29	Hf	ppm	4.56	
IHST-18-25529		MRB-29	Ho	ppm	1.018	
IHST-18-25529		MRB-29	In	ppm	0.0762	
IHST-18-25529		MRB-29	La	ppm	21.9	
IHST-18-25529		MRB-29	Li	ppm	10.8	
IHST-18-25529		MRB-29	Lu	ppm	0.353	
IHST-18-25529		MRB-29	Mo	ppm	0.88	
IHST-18-25529		MRB-29	Nb	ppm	12.757	
IHST-18-25529		MRB-29	Nd	ppm	28.04	
IHST-18-25529		MRB-29	Ni	ppm	113.5	
IHST-18-25529		MRB-29	Pb	ppm	4.78	
IHST-18-25529		MRB-29	Pr	ppm	6.444	
IHST-18-25529		MRB-29	Rb	ppm	14.82	
IHST-18-25529		MRB-29	Sb	ppm	0.08	

Sample ID	Client Sample ID	QC Name	Analyte	Units	Measured Value	Cert/Dup Value
IHST-18-25529		MRB-29	Sc	ppm	35.9	
IHST-18-25529		MRB-29	Sm	ppm	6.207	
IHST-18-25529		MRB-29	Sn	ppm	2.33	
IHST-18-25529		MRB-29	Sr	ppm	309.9	
IHST-18-25529		MRB-29	Ta	ppm	0.816	
IHST-18-25529		MRB-29	Tb	ppm	0.8807	
IHST-18-25529		MRB-29	Th	ppm	2.583	
IHST-18-25529		MRB-29	Ti	ppm	12046	
IHST-18-25529		MRB-29	Tl	ppm	0.071	
IHST-18-25529		MRB-29	Tm	ppm	0.3799	
IHST-18-25529		MRB-29	U	ppm	0.655	
IHST-18-25529		MRB-29	V	ppm	315.2	
IHST-18-25529		MRB-29	W	ppm	0.21	
IHST-18-25529		MRB-29	Y	ppm	27.26	
IHST-18-25529		MRB-29	Yb	ppm	2.405	
IHST-18-25529		MRB-29	Zn	ppm	109.2	
IHST-18-25529		MRB-29	Zr	ppm	179	
IHST-18-25539		MRB-29	Ba	ppm	294.4	
IHST-18-25539		MRB-29	Be	ppm	1.03	
IHST-18-25539		MRB-29	Bi	ppm	0.04	
IHST-18-25539		MRB-29	Cd	ppm	0.108	
IHST-18-25539		MRB-29	Ce	ppm	46.19	
IHST-18-25539		MRB-29	Co	ppm	51.86	
IHST-18-25539		MRB-29	Cr	ppm	283	
IHST-18-25539		MRB-29	Cs	ppm	0.245	
IHST-18-25539		MRB-29	Cu	ppm	151.2	
IHST-18-25539		MRB-29	Dy	ppm	5.373	
IHST-18-25539		MRB-29	Er	ppm	2.813	
IHST-18-25539		MRB-29	Eu	ppm	1.9215	
IHST-18-25539		MRB-29	Ga	ppm	19.59	
IHST-18-25539		MRB-29	Gd	ppm	6.088	
IHST-18-25539		MRB-29	Hf	ppm	4.38	
IHST-18-25539		MRB-29	Ho	ppm	1.0468	
IHST-18-25539		MRB-29	In	ppm	0.0784	
IHST-18-25539		MRB-29	La	ppm	21.5	
IHST-18-25539		MRB-29	Li	ppm	9.3	
IHST-18-25539		MRB-29	Lu	ppm	0.354	

Sample ID	Client Sample ID	QC Name	Analyte	Units	Measured Value	Cert/Dup Value
IHST-18-25539		MRB-29	Mo	ppm	0.85	
IHST-18-25539		MRB-29	Nb	ppm	12.667	
IHST-18-25539		MRB-29	Nd	ppm	28.13	
IHST-18-25539		MRB-29	Ni	ppm	112.6	
IHST-18-25539		MRB-29	Pb	ppm	4.64	
IHST-18-25539		MRB-29	Pr	ppm	6.429	
IHST-18-25539		MRB-29	Rb	ppm	14.88	
IHST-18-25539		MRB-29	Sb	ppm	0.06	
IHST-18-25539		MRB-29	Sc	ppm	33.1	
IHST-18-25539		MRB-29	Sm	ppm	6.215	
IHST-18-25539		MRB-29	Sn	ppm	2.1	
IHST-18-25539		MRB-29	Sr	Ppm	309.3	
IHST-18-25539		MRB-29	Ta	Ppm	0.824	
IHST-18-25539		MRB-29	Tb	Ppm	0.9007	
IHST-18-25539		MRB-29	Th	Ppm	2.562	
IHST-18-25539		MRB-29	Ti	Ppm	11580	
IHST-18-25539		MRB-29	Tl	Ppm	0.069	
IHST-18-25539		MRB-29	Tm	Ppm	0.3852	
IHST-18-25539		MRB-29	U	Ppm	0.615	
IHST-18-25539		MRB-29	V	Ppm	319.9	
IHST-18-25539		MRB-29	W	Ppm	0.22	
IHST-18-25539		MRB-29	Y	ppm	27.08	
IHST-18-25539		MRB-29	Yb	ppm	2.447	
IHST-18-25539		MRB-29	Zn	ppm	116	
IHST-18-25539		MRB-29	Zr	ppm	169	
IHST-18-25540		MRB-29	Ba	ppm	289.2	
IHST-18-25540		MRB-29	Be	ppm	1.18	
IHST-18-25540		MRB-29	Bi	ppm	0.03	
IHST-18-25540		MRB-29	Cd	ppm	0.119	
IHST-18-25540		MRB-29	Ce	ppm	47.51	
IHST-18-25540		MRB-29	Co	ppm	54.07	
IHST-18-25540		MRB-29	Cr	ppm	286	
IHST-18-25540		MRB-29	Cs	ppm	0.234	
IHST-18-25540		MRB-29	Cu	ppm	152.6	
IHST-18-25540		MRB-29	Dy	ppm	5.413	
IHST-18-25540		MRB-29	Er	ppm	2.857	
IHST-18-25540		MRB-29	Eu	ppm	1.92	

Sample ID	Client Sample ID	QC Name	Analyte	Units	Measured Value	Cert/Dup Value
IHST-18-25540		MRB-29	Ga	ppm	19.32	
IHST-18-25540		MRB-29	Gd	ppm	6.024	
IHST-18-25540		MRB-29	Hf	ppm	4.51	
IHST-18-25540		MRB-29	Ho	ppm	1.0295	
IHST-18-25540		MRB-29	In	ppm	0.077	
IHST-18-25540		MRB-29	La	ppm	21.7	
IHST-18-25540		MRB-29	Li	ppm	10.1	
IHST-18-25540		MRB-29	Lu	ppm	0.359	
IHST-18-25540		MRB-29	Mo	ppm	0.85	
IHST-18-25540		MRB-29	Nb	ppm	12.617	
IHST-18-25540		MRB-29	Nd	ppm	28.09	
IHST-18-25540		MRB-29	Ni	ppm	116.4	
IHST-18-25540		MRB-29	Pb	ppm	4.86	
IHST-18-25540		MRB-29	Pr	ppm	6.465	
IHST-18-25540		MRB-29	Rb	ppm	14.44	
IHST-18-25540		MRB-29	Sb	ppm	0.06	
IHST-18-25540		MRB-29	Sc	ppm	36.4	
IHST-18-25540		MRB-29	Sm	ppm	6.327	
IHST-18-25540		MRB-29	Sn	ppm	2.25	
IHST-18-25540		MRB-29	Sr	ppm	306.4	
IHST-18-25540		MRB-29	Ta	ppm	0.818	
IHST-18-25540		MRB-29	Tb	ppm	0.8923	
IHST-18-25540		MRB-29	Th	ppm	2.577	
IHST-18-25540		MRB-29	Ti	ppm	12108	
IHST-18-25540		MRB-29	Tl	ppm	0.067	
IHST-18-25540		MRB-29	Tm	ppm	0.387	
IHST-18-25540		MRB-29	U	ppm	0.628	
IHST-18-25540		MRB-29	V	ppm	327	
IHST-18-25540		MRB-29	W	ppm	0.22	
IHST-18-25540		MRB-29	Y	ppm	27.34	
IHST-18-25540		MRB-29	Yb	ppm	2.462	
IHST-18-25540		MRB-29	Zn	ppm	105.8	
IHST-18-25540		MRB-29	Zr	ppm	173	
INTL-18-31270		BHVO-2	Ba	ppm	128.6	130
INTL-18-31270		BHVO-2	Be	ppm	1.06	
INTL-18-31270		BHVO-2	Bi	ppm	0.01	
INTL-18-31270		BHVO-2	Cd	ppm	0.113	

Sample ID	Client Sample ID	QC Name	Analyte	Units	Measured Value	Cert/Dup Value
INTL-18-31270		BHVO-2	Ce	ppm	37.16	38
INTL-18-31270		BHVO-2	Co	ppm	45.91	45
INTL-18-31270		BHVO-2	Cr	ppm	305	280
INTL-18-31270		BHVO-2	Cs	ppm	0.098	
INTL-18-31270		BHVO-2	Cu	ppm	135.6	127
INTL-18-31270		BHVO-2	Dy	ppm	5.252	
INTL-18-31270		BHVO-2	Er	ppm	2.538	
INTL-18-31270		BHVO-2	Eu	ppm	2.0399	
INTL-18-31270		BHVO-2	Ga	ppm	20.96	21.7
INTL-18-31270		BHVO-2	Gd	ppm	6.09	
INTL-18-31270		BHVO-2	Hf	ppm	4.37	4.1
INTL-18-31270		BHVO-2	Ho	ppm	0.9712	
INTL-18-31270		BHVO-2	In	ppm	0.0861	
INTL-18-31270		BHVO-2	La	ppm	14.7	15
INTL-18-31270		BHVO-2	Li	ppm	4.1	
INTL-18-31270		BHVO-2	Lu	ppm	0.277	
INTL-18-31270		BHVO-2	Mo	ppm	4.52	
INTL-18-31270		BHVO-2	Nb	ppm	17.107	
INTL-18-31270		BHVO-2	Nd	ppm	24.38	
INTL-18-31270		BHVO-2	Ni	ppm	122.6	119
INTL-18-31270		BHVO-2	Pb	ppm	1.52	
INTL-18-31270		BHVO-2	Pr	ppm	5.268	
INTL-18-31270		BHVO-2	Rb	ppm	9.33	9.8
INTL-18-31270		BHVO-2	Sb	ppm	0.11	
INTL-18-31270		BHVO-2	Sc	ppm	32.8	32
INTL-18-31270		BHVO-2	Sm	ppm	6.094	
INTL-18-31270		BHVO-2	Sn	ppm	1.75	
INTL-18-31270		BHVO-2	Sr	ppm	381.3	389
INTL-18-31270		BHVO-2	Ta	ppm	1.141	
INTL-18-31270		BHVO-2	Tb	ppm	0.8913	
INTL-18-31270		BHVO-2	Th	ppm	1.151	
INTL-18-31270		BHVO-2	Ti	ppm	15629	
INTL-18-31270		BHVO-2	Tl	ppm	0.019	
INTL-18-31270		BHVO-2	Tm	ppm	0.3262	
INTL-18-31270		BHVO-2	U	ppm	0.413	
INTL-18-31270		BHVO-2	V	ppm	327	317
INTL-18-31270		BHVO-2	W	ppm	0.2	

Sample ID	Client Sample ID	QC Name	Analyte	Units	Measured Value	Cert/Dup Value
INTL-18-31270		BHVO-2	Y	ppm	24.98	26
INTL-18-31270		BHVO-2	Yb	ppm	1.96	
INTL-18-31270		BHVO-2	Zn	ppm	105	103
INTL-18-31270		BHVO-2	Zr	ppm	164	172
INTL-18-31271		GSP-2	Ba	ppm	1346	1340
INTL-18-31271		GSP-2	Be	ppm	1.44	1.5
INTL-18-31271		GSP-2	Bi	ppm	0.03	
INTL-18-31271		GSP-2	Cd	ppm	0.146	
INTL-18-31271		GSP-2	Ce	ppm	458.46	410
INTL-18-31271		GSP-2	Co	ppm	7.43	7.3
INTL-18-31271		GSP-2	Cr	ppm	22	20
INTL-18-31271		GSP-2	Cs	ppm	1.198	1.2
INTL-18-31271		GSP-2	Cu	ppm	46.8	43
INTL-18-31271		GSP-2	Dy	ppm	5.862	6.1
INTL-18-31271		GSP-2	Er	ppm	2.354	2.2
INTL-18-31271		GSP-2	Eu	ppm	2.2394	2.3
INTL-18-31271		GSP-2	Ga	ppm	23.6	22
INTL-18-31271		GSP-2	Gd	ppm	11.05	12
INTL-18-31271		GSP-2	Hf	ppm	13.37	14
INTL-18-31271		GSP-2	Ho	ppm	0.9702	1
INTL-18-31271		GSP-2	In	ppm	0.0521	
INTL-18-31271		GSP-2	La	ppm	184.8	180
INTL-18-31271		GSP-2	Li	ppm	32.1	
INTL-18-31271		GSP-2	Lu	ppm	0.233	0.23
INTL-18-31271		GSP-2	Mo	ppm	2.42	2.1
INTL-18-31271		GSP-2	Nb	ppm	25.258	27
INTL-18-31271		GSP-2	Nd	ppm	209.86	200
INTL-18-31271		GSP-2	Ni	ppm	16.8	17
INTL-18-31271		GSP-2	Pb	ppm	41.3	42
INTL-18-31271		GSP-2	Pr	ppm	57.356	51
INTL-18-31271		GSP-2	Rb	ppm	252.35	245
INTL-18-31271		GSP-2	Sb	ppm	0.37	
INTL-18-31271		GSP-2	Sc	ppm	7	6.3
INTL-18-31271		GSP-2	Sm	ppm	26.88	27
INTL-18-31271		GSP-2	Sn	ppm	7.04	
INTL-18-31271		GSP-2	Sr	ppm	235.3	240
INTL-18-31271		GSP-2	Ta	ppm	0.862	

Sample ID	Client Sample ID	QC Name	Analyte	Units	Measured Value	Cert/Dup Value
INTL-18-31271		GSP-2	Tb	ppm	1.1673	
INTL-18-31271		GSP-2	Th	ppm	108.449	105
INTL-18-31271		GSP-2	Ti	ppm	3974	
INTL-18-31271		GSP-2	Tl	ppm	1.27	1.1
INTL-18-31271		GSP-2	Tm	ppm	0.2888	0.29
INTL-18-31271		GSP-2	U	ppm	2.461	2.4
INTL-18-31271		GSP-2	V	ppm	52.7	52
INTL-18-31271		GSP-2	W	ppm	0.35	
INTL-18-31271		GSP-2	Y	ppm	26.15	28
INTL-18-31271		GSP-2	Yb	ppm	1.659	1.6
INTL-18-31271		GSP-2	Zn	ppm	120.5	120
INTL-18-31271		GSP-2	Zr	ppm	517	550
INTL-18-31275		AGV-2	Ba	ppm	1088.5	1140
INTL-18-31275		AGV-2	Be	ppm	2.14	2.3
INTL-18-31275		AGV-2	Bi	ppm	0.05	
INTL-18-31275		AGV-2	Cd	ppm	0.097	
INTL-18-31275		AGV-2	Ce	ppm	68.78	68
INTL-18-31275		AGV-2	Co	ppm	15.99	16
INTL-18-31275		AGV-2	Cr	ppm	17	17
INTL-18-31275		AGV-2	Cs	ppm	1.159	1.16
INTL-18-31275		AGV-2	Cu	ppm	53.4	53
INTL-18-31275		AGV-2	Dy	ppm	3.431	3.6
INTL-18-31275		AGV-2	Er	ppm	1.775	1.79
INTL-18-31275		AGV-2	Eu	ppm	1.4665	1.54
INTL-18-31275		AGV-2	Ga	ppm	20.64	20
INTL-18-31275		AGV-2	Gd	ppm	4.309	4.69
INTL-18-31275		AGV-2	Hf	ppm	5.16	5.08
INTL-18-31275		AGV-2	Ho	ppm	0.6545	0.71
INTL-18-31275		AGV-2	In	ppm	0.0445	
INTL-18-31275		AGV-2	La	ppm	36.5	38
INTL-18-31275		AGV-2	Li	ppm	8.8	11
INTL-18-31275		AGV-2	Lu	ppm	0.247	0.25
INTL-18-31275		AGV-2	Mo	ppm	2.31	
INTL-18-31275		AGV-2	Nb	ppm	13.49	15
INTL-18-31275		AGV-2	Nd	ppm	29.26	30
INTL-18-31275		AGV-2	Ni	ppm	19.2	19
INTL-18-31275		AGV-2	Pb	ppm	13.24	13

Sample ID	Client Sample ID	QC Name	Analyte	Units	Measured Value	Cert/Dup Value
INTL-18-31275		AGV-2	Pr	ppm	7.908	8.3
INTL-18-31275		AGV-2	Rb	ppm	70.28	68.6
INTL-18-31275		AGV-2	Sb	ppm	0.48	0.6
INTL-18-31275		AGV-2	Sc	ppm	13	13
INTL-18-31275		AGV-2	Sm	ppm	5.381	5.7
INTL-18-31275		AGV-2	Sn	ppm	2.03	2.3
INTL-18-31275		AGV-2	Sr	ppm	649.2	658
INTL-18-31275		AGV-2	Ta	ppm	0.84	0.89
INTL-18-31275		AGV-2	Tb	ppm	0.5851	0.64
INTL-18-31275		AGV-2	Th	ppm	6.071	6.1
INTL-18-31275		AGV-2	Ti	ppm	6240	6019
INTL-18-31275		AGV-2	Tl	ppm	0.272	0.27
INTL-18-31275		AGV-2	Tm	ppm	0.248	0.26
INTL-18-31275		AGV-2	U	ppm	1.893	1.88
INTL-18-31275		AGV-2	V	ppm	118.9	120
INTL-18-31275		AGV-2	W	ppm	0.51	
INTL-18-31275		AGV-2	Y	ppm	18.81	20
INTL-18-31275		AGV-2	Yb	ppm	1.596	1.6
INTL-18-31275		AGV-2	Zn	ppm	91.1	86
INTL-18-31275		AGV-2	Zr	ppm	230	230
INTL-18-31276		BHVO-2	Ba	ppm	131.8	130
INTL-18-31276		BHVO-2	Be	ppm	1.05	
INTL-18-31276		BHVO-2	Bi	ppm	0.02	
INTL-18-31276		BHVO-2	Cd	ppm	0.112	
INTL-18-31276		BHVO-2	Ce	ppm	37.19	38
INTL-18-31276		BHVO-2	Co	ppm	45.86	45
INTL-18-31276		BHVO-2	Cr	ppm	295	280
INTL-18-31276		BHVO-2	Cs	ppm	0.095	
INTL-18-31276		BHVO-2	Cu	ppm	133.8	127
INTL-18-31276		BHVO-2	Dy	ppm	5.419	
INTL-18-31276		BHVO-2	Er	ppm	2.566	
INTL-18-31276		BHVO-2	Eu	ppm	2.0641	
INTL-18-31276		BHVO-2	Ga	ppm	20.74	21.7
INTL-18-31276		BHVO-2	Gd	ppm	6.279	
INTL-18-31276		BHVO-2	Hf	ppm	4.49	4.1
INTL-18-31276		BHVO-2	Ho	ppm	0.9926	
INTL-18-31276		BHVO-2	In	ppm	0.0854	

Sample ID	Client Sample ID	QC Name	Analyte	Units	Measured Value	Cert/Dup Value
INTL-18-31276		BHVO-2	La	ppm	15.2	15
INTL-18-31276		BHVO-2	Li	ppm	4.3	
INTL-18-31276		BHVO-2	Lu	ppm	0.276	
INTL-18-31276		BHVO-2	Mo	ppm	4.85	
INTL-18-31276		BHVO-2	Nb	ppm	17.497	
INTL-18-31276		BHVO-2	Nd	ppm	25.31	
INTL-18-31276		BHVO-2	Ni	ppm	121.6	119
INTL-18-31276		BHVO-2	Pb	ppm	1.76	
INTL-18-31276		BHVO-2	Pr	ppm	5.274	
INTL-18-31276		BHVO-2	Rb	ppm	9.15	9.8
INTL-18-31276		BHVO-2	Sb	ppm	0.1	
INTL-18-31276		BHVO-2	Sc	ppm	32.3	32
INTL-18-31276		BHVO-2	Sm	ppm	6.213	
INTL-18-31276		BHVO-2	Sn	ppm	1.83	
INTL-18-31276		BHVO-2	Sr	ppm	385.2	389
INTL-18-31276		BHVO-2	Ta	ppm	1.168	
INTL-18-31276		BHVO-2	Tb	ppm	0.922	
INTL-18-31276		BHVO-2	Th	ppm	1.206	
INTL-18-31276		BHVO-2	Ti	ppm	16206	
INTL-18-31276		BHVO-2	Tl	ppm	0.02	
INTL-18-31276		BHVO-2	Tm	ppm	0.3309	
INTL-18-31276		BHVO-2	U	ppm	0.424	
INTL-18-31276		BHVO-2	V	ppm	322.6	317
INTL-18-31276		BHVO-2	W	ppm	0.22	
INTL-18-31276		BHVO-2	Y	ppm	25.46	26
INTL-18-31276		BHVO-2	Yb	ppm	1.997	
INTL-18-31276		BHVO-2	Zn	ppm	100.1	103
INTL-18-31276		BHVO-2	Zr	ppm	172	172
INTL-18-31284		AGV-2	Ba	ppm	1174.4	1140
INTL-18-31284		AGV-2	Be	ppm	2.18	2.3
INTL-18-31284		AGV-2	Bi	ppm	0.05	
INTL-18-31284		AGV-2	Cd	ppm	0.108	
INTL-18-31284		AGV-2	Ce	ppm	65.24	68
INTL-18-31284		AGV-2	Co	ppm	16.5	16
INTL-18-31284		AGV-2	Cr	ppm	17	17
INTL-18-31284		AGV-2	Cs	ppm	1.171	1.16
INTL-18-31284		AGV-2	Cu	ppm	53.8	53

Sample ID	Client Sample ID	QC Name	Analyte	Units	Measured Value	Cert/Dup Value
INTL-18-31284		AGV-2	Dy	ppm	3.496	3.6
INTL-18-31284		AGV-2	Er	ppm	1.839	1.79
INTL-18-31284		AGV-2	Eu	ppm	1.5174	1.54
INTL-18-31284		AGV-2	Ga	ppm	20.74	20
INTL-18-31284		AGV-2	Gd	ppm	4.558	4.69
INTL-18-31284		AGV-2	Hf	ppm	5.11	5.08
INTL-18-31284		AGV-2	Ho	ppm	0.6693	0.71
INTL-18-31284		AGV-2	In	ppm	0.0441	
INTL-18-31284		AGV-2	La	ppm	37.6	38
INTL-18-31284		AGV-2	Li	ppm	9.3	11
INTL-18-31284		AGV-2	Lu	ppm	0.253	0.25
INTL-18-31284		AGV-2	Mo	ppm	2.23	
INTL-18-31284		AGV-2	Nb	ppm	13.527	15
INTL-18-31284		AGV-2	Nd	ppm	31.19	30
INTL-18-31284		AGV-2	Ni	ppm	19.3	19
INTL-18-31284		AGV-2	Pb	ppm	12.96	13
INTL-18-31284		AGV-2	Pr	ppm	8.092	8.3
INTL-18-31284		AGV-2	Rb	ppm	70.27	68.6
INTL-18-31284		AGV-2	Sb	ppm	0.49	0.6
INTL-18-31284		AGV-2	Sc	ppm	13.3	13
INTL-18-31284		AGV-2	Sm	ppm	5.577	5.7
INTL-18-31284		AGV-2	Sn	ppm	2.07	2.3
INTL-18-31284		AGV-2	Sr	ppm	655	658
INTL-18-31284		AGV-2	Ta	ppm	0.839	0.89
INTL-18-31284		AGV-2	Tb	ppm	0.6297	0.64
INTL-18-31284		AGV-2	Th	ppm	6.009	6.1
INTL-18-31284		AGV-2	Ti	ppm	6182	6019
INTL-18-31284		AGV-2	Tl	ppm	0.268	0.27
INTL-18-31284		AGV-2	Tm	ppm	0.2542	0.26
INTL-18-31284		AGV-2	U	ppm	1.845	1.88
INTL-18-31284		AGV-2	V	ppm	122.2	120
INTL-18-31284		AGV-2	W	ppm	0.5	
INTL-18-31284		AGV-2	Y	ppm	19.43	20
INTL-18-31284		AGV-2	Yb	ppm	1.638	1.6
INTL-18-31284		AGV-2	Zn	ppm	94.6	86
INTL-18-31284		AGV-2	Zr	ppm	232	230
INTL-18-31285		AGV-2	Ba	ppm	1185.9	1140

Sample ID	Client Sample ID	QC Name	Analyte	Units	Measured Value	Cert/Dup Value
INTL-18-31285		AGV-2	Be	ppm	2.44	2.3
INTL-18-31285		AGV-2	Bi	ppm	0.05	
INTL-18-31285		AGV-2	Cd	ppm	0.119	
INTL-18-31285		AGV-2	Ce	ppm	70.25	68
INTL-18-31285		AGV-2	Co	ppm	16.16	16
INTL-18-31285		AGV-2	Cr	ppm	17	17
INTL-18-31285		AGV-2	Cs	ppm	1.155	1.16
INTL-18-31285		AGV-2	Cu	ppm	54.5	53
INTL-18-31285		AGV-2	Dy	ppm	3.485	3.6
INTL-18-31285		AGV-2	Er	ppm	1.838	1.79
INTL-18-31285		AGV-2	Eu	ppm	1.5205	1.54
INTL-18-31285		AGV-2	Ga	ppm	20.5	20
INTL-18-31285		AGV-2	Gd	ppm	4.358	4.69
INTL-18-31285		AGV-2	Hf	ppm	5.25	5.08
INTL-18-31285		AGV-2	Ho	ppm	0.6699	0.71
INTL-18-31285		AGV-2	In	ppm	0.0461	
INTL-18-31285		AGV-2	La	ppm	38.7	38
INTL-18-31285		AGV-2	Li	ppm	10.1	11
INTL-18-31285		AGV-2	Lu	ppm	0.247	0.25
INTL-18-31285		AGV-2	Mo	ppm	2.14	
INTL-18-31285		AGV-2	Nb	ppm	13.304	15
INTL-18-31285		AGV-2	Nd	ppm	31.51	30
INTL-18-31285		AGV-2	Ni	ppm	19.5	19
INTL-18-31285		AGV-2	Pb	ppm	12.82	13
INTL-18-31285		AGV-2	Pr	ppm	8.269	8.3
INTL-18-31285		AGV-2	Rb	ppm	67.63	68.6
INTL-18-31285		AGV-2	Sb	ppm	0.53	0.6
INTL-18-31285		AGV-2	Sc	ppm	14	13
INTL-18-31285		AGV-2	Sm	ppm	5.743	5.7
INTL-18-31285		AGV-2	Sn	ppm	2.17	2.3
INTL-18-31285		AGV-2	Sr	ppm	630.3	658
INTL-18-31285		AGV-2	Ta	ppm	0.847	0.89
INTL-18-31285		AGV-2	Tb	ppm	0.6086	0.64
INTL-18-31285		AGV-2	Th	ppm	6.096	6.1
INTL-18-31285		AGV-2	Ti	ppm	6377	6019
INTL-18-31285		AGV-2	Tl	ppm	0.267	0.27
INTL-18-31285		AGV-2	Tm	ppm	0.2526	0.26

Sample ID	Client Sample ID	QC Name	Analyte	Units	Measured Value	Cert/Dup Value
INTL-18-31285		AGV-2	U	ppm	1.847	1.88
INTL-18-31285		AGV-2	V	ppm	120.1	120
INTL-18-31285		AGV-2	W	ppm	0.51	
INTL-18-31285		AGV-2	Y	ppm	19.01	20
INTL-18-31285		AGV-2	Yb	ppm	1.632	1.6
INTL-18-31285		AGV-2	Zn	ppm	99.3	86
INTL-18-31285		AGV-2	Zr	ppm	230	230
BLANK-19-20632		BLANK	Ba	ppm	0.1	
BLANK-19-20632		BLANK	Be	ppm	0	
BLANK-19-20632		BLANK	Bi	ppm	0	
BLANK-19-20632		BLANK	Cd	ppm	0	
BLANK-19-20632		BLANK	Ce	ppm	0.01	
BLANK-19-20632		BLANK	Co	ppm	0.02	
BLANK-19-20632		BLANK	Cr	ppm	1	
BLANK-19-20632		BLANK	Cs	ppm	0.001	
BLANK-19-20632		BLANK	Cu	ppm	0	
BLANK-19-20632		BLANK	Dy	ppm	0.001	
BLANK-19-20632		BLANK	Er	ppm	0.001	
BLANK-19-20632		BLANK	Eu	ppm	0.0006	
BLANK-19-20632		BLANK	Ga	ppm	0.01	
BLANK-19-20632		BLANK	Gd	ppm	0	
BLANK-19-20632		BLANK	Hf	ppm	0.05	
BLANK-19-20632		BLANK	Ho	ppm	0.0004	
BLANK-19-20632		BLANK	In	ppm	0.0002	
BLANK-19-20632		BLANK	La	ppm	0	
BLANK-19-20632		BLANK	Li	ppm	0	
BLANK-19-20632		BLANK	Lu	ppm	0	
BLANK-19-20632		BLANK	Mo	ppm	0.03	
BLANK-19-20632		BLANK	Nb	ppm	0.002	
BLANK-19-20632		BLANK	Nd	ppm	0.01	
BLANK-19-20632		BLANK	Ni	ppm	0	
BLANK-19-20632		BLANK	Pb	ppm	0.05	
BLANK-19-20632		BLANK	Pr	ppm	0.002	
BLANK-19-20632		BLANK	Rb	ppm	0.03	
BLANK-19-20632		BLANK	Sb	ppm	0.01	
BLANK-19-20632		BLANK	Sc	ppm	0	
BLANK-19-20632		BLANK	Sm	ppm	0	

Sample ID	Client Sample ID	QC Name	Analyte	Units	Measured Value	Cert/Dup Value
BLANK-19-20632		BLANK	Sn	ppm	0.01	
BLANK-19-20632		BLANK	Sr	ppm	0.3	
BLANK-19-20632		BLANK	Ta	ppm	0	
BLANK-19-20632		BLANK	Tb	ppm	0	
BLANK-19-20632		BLANK	Th	ppm	0.003	
BLANK-19-20632		BLANK	Ti	ppm	1	
BLANK-19-20632		BLANK	Tl	ppm	0	
BLANK-19-20632		BLANK	Tm	ppm	0	
BLANK-19-20632		BLANK	U	ppm	0.003	
BLANK-19-20632		BLANK	V	ppm	0	
BLANK-19-20632		BLANK	W	ppm	0	
BLANK-19-20632		BLANK	Y	ppm	0.01	
BLANK-19-20632		BLANK	Yb	ppm	0.002	
BLANK-19-20632		BLANK	Zn	ppm	0.6	
BLANK-19-20632		BLANK	Zr	ppm	2	
BLANK-19-20633		BLANK	Ba	ppm	0.1	
BLANK-19-20633		BLANK	Be	ppm	0	
BLANK-19-20633		BLANK	Bi	ppm	0	
BLANK-19-20633		BLANK	Cd	ppm	0.002	
BLANK-19-20633		BLANK	Ce	ppm	0	
BLANK-19-20633		BLANK	Co	ppm	0.01	
BLANK-19-20633		BLANK	Cr	ppm	1	
BLANK-19-20633		BLANK	Cs	ppm	0.001	
BLANK-19-20633		BLANK	Cu	ppm	0	
BLANK-19-20633		BLANK	Dy	ppm	0	
BLANK-19-20633		BLANK	Er	ppm	0	
BLANK-19-20633		BLANK	Eu	ppm	0.0003	
BLANK-19-20633		BLANK	Ga	ppm	0.01	
BLANK-19-20633		BLANK	Gd	ppm	0.001	
BLANK-19-20633		BLANK	Hf	ppm	0.03	
BLANK-19-20633		BLANK	Ho	ppm	0.0006	
BLANK-19-20633		BLANK	In	ppm	0.0004	
BLANK-19-20633		BLANK	La	ppm	0	
BLANK-19-20633		BLANK	Li	ppm	0	
BLANK-19-20633		BLANK	Lu	ppm	0	
BLANK-19-20633		BLANK	Mo	ppm	0.02	
BLANK-19-20633		BLANK	Nb	ppm	0.003	

Sample ID	Client Sample ID	QC Name	Analyte	Units	Measured Value	Cert/Dup Value
BLANK-19-20633		BLANK	Nd	ppm	0	
BLANK-19-20633		BLANK	Ni	ppm	0.1	
BLANK-19-20633		BLANK	Pb	ppm	0.02	
BLANK-19-20633		BLANK	Pr	ppm	0	
BLANK-19-20633		BLANK	Rb	ppm	0.01	
BLANK-19-20633		BLANK	Sb	ppm	0.01	
BLANK-19-20633		BLANK	Sc	ppm	0	
BLANK-19-20633		BLANK	Sm	ppm	0.002	
BLANK-19-20633		BLANK	Sn	ppm	0.01	
BLANK-19-20633		BLANK	Sr	ppm	0.3	
BLANK-19-20633		BLANK	Ta	ppm	0.001	
BLANK-19-20633		BLANK	Tb	ppm	0.0002	
BLANK-19-20633		BLANK	Th	ppm	0.002	
BLANK-19-20633		BLANK	Ti	ppm	0	
BLANK-19-20633		BLANK	Tl	ppm	0	
BLANK-19-20633		BLANK	Tm	ppm	0.0003	
BLANK-19-20633		BLANK	U	ppm	0.002	
BLANK-19-20633		BLANK	V	ppm	0	
BLANK-19-20633		BLANK	W	ppm	0	
BLANK-19-20633		BLANK	Y	ppm	0.01	
BLANK-19-20633		BLANK	Yb	ppm	0.002	
BLANK-19-20633		BLANK	Zn	ppm	0.3	
BLANK-19-20633		BLANK	Zr	ppm	1	
Dup-19-48387	MV2018-7	DUP	Ba	ppm	12.5	
Dup-19-48387	MV2018-7	DUP	Be	ppm	0.14	
Dup-19-48387	MV2018-7	DUP	Bi	ppm	0.14	
Dup-19-48387	MV2018-7	DUP	Cd	ppm	0.07	
Dup-19-48387	MV2018-7	DUP	Ce	ppm	6.75	
Dup-19-48387	MV2018-7	DUP	Co	ppm	31.71	
Dup-19-48387	MV2018-7	DUP	Cr	ppm	428	
Dup-19-48387	MV2018-7	DUP	Cs	ppm	1.062	
Dup-19-48387	MV2018-7	DUP	Cu	ppm	9.4	
Dup-19-48387	MV2018-7	DUP	Dy	ppm	3.064	
Dup-19-48387	MV2018-7	DUP	Er	ppm	1.914	
Dup-19-48387	MV2018-7	DUP	Eu	ppm	0.5978	
Dup-19-48387	MV2018-7	DUP	Ga	ppm	17.84	
Dup-19-48387	MV2018-7	DUP	Gd	ppm	2.744	

Sample ID	Client Sample ID	QC Name	Analyte	Units	Measured Value	Cert/Dup Value
Dup-19-48387	MV2018-7	DUP	Hf	ppm	1.17	
Dup-19-48387	MV2018-7	DUP	Ho	ppm	0.6651	
Dup-19-48387	MV2018-7	DUP	In	ppm	0.0397	
Dup-19-48387	MV2018-7	DUP	La	ppm	2.3	
Dup-19-48387	MV2018-7	DUP	Li	ppm	21.3	
Dup-19-48387	MV2018-7	DUP	Lu	ppm	0.285	
Dup-19-48387	MV2018-7	DUP	Mo	ppm	0.16	
Dup-19-48387	MV2018-7	DUP	Nb	ppm	1.6	
Dup-19-48387	MV2018-7	DUP	Nd	ppm	6.23	
Dup-19-48387	MV2018-7	DUP	Ni	ppm	107.8	
Dup-19-48387	MV2018-7	DUP	Pb	ppm	1.04	
Dup-19-48387	MV2018-7	DUP	Pr	ppm	1.189	
Dup-19-48387	MV2018-7	DUP	Rb	ppm	1.6	
Dup-19-48387	MV2018-7	DUP	Sb	ppm	0.13	
Dup-19-48387	MV2018-7	DUP	Sc	ppm	28.8	
Dup-19-48387	MV2018-7	DUP	Sm	ppm	1.996	
Dup-19-48387	MV2018-7	DUP	Sn	ppm	0.18	
Dup-19-48387	MV2018-7	DUP	Sr	ppm	132.4	
Dup-19-48387	MV2018-7	DUP	Ta	ppm	0.107	
Dup-19-48387	MV2018-7	DUP	Tb	ppm	0.464	
Dup-19-48387	MV2018-7	DUP	Th	ppm	0.25	
Dup-19-48387	MV2018-7	DUP	Ti	ppm	3580	
Dup-19-48387	MV2018-7	DUP	Tl	ppm	0.005	
Dup-19-48387	MV2018-7	DUP	Tm	ppm	0.2942	
Dup-19-48387	MV2018-7	DUP	U	ppm	0.062	
Dup-19-48387	MV2018-7	DUP	V	ppm	199	
Dup-19-48387	MV2018-7	DUP	W	ppm	0.25	
Dup-19-48387	MV2018-7	DUP	Y	ppm	15.77	
Dup-19-48387	MV2018-7	DUP	Yb	ppm	1.85	
Dup-19-48387	MV2018-7	DUP	Zn	ppm	41.8	
Dup-19-48387	MV2018-7	DUP	Zr	ppm	39	
Dup-19-48388	MV2018-17	DUP	Ba	ppm	13	
Dup-19-48388	MV2018-17	DUP	Be	ppm	0.16	
Dup-19-48388	MV2018-17	DUP	Bi	ppm	0.05	
Dup-19-48388	MV2018-17	DUP	Cd	ppm	0.036	
Dup-19-48388	MV2018-17	DUP	Ce	ppm	1.81	
Dup-19-48388	MV2018-17	DUP	Co	ppm	8.54	

Sample ID	Client Sample ID	QC Name	Analyte	Units	Measured Value	Cert/Dup Value
Dup-19-48388	MV2018-17	DUP	Cr	ppm	16	
Dup-19-48388	MV2018-17	DUP	Cs	ppm	3.876	
Dup-19-48388	MV2018-17	DUP	Cu	ppm	4.3	
Dup-19-48388	MV2018-17	DUP	Dy	ppm	0.636	
Dup-19-48388	MV2018-17	DUP	Er	ppm	0.42	
Dup-19-48388	MV2018-17	DUP	Eu	ppm	0.311	
Dup-19-48388	MV2018-17	DUP	Ga	ppm	21.38	
Dup-19-48388	MV2018-17	DUP	Gd	ppm	0.557	
Dup-19-48388	MV2018-17	DUP	Hf	ppm	0.86	
Dup-19-48388	MV2018-17	DUP	Ho	ppm	0.1381	
Dup-19-48388	MV2018-17	DUP	In	ppm	0.0138	
Dup-19-48388	MV2018-17	DUP	La	ppm	0.8	
Dup-19-48388	MV2018-17	DUP	Li	ppm	23.5	
Dup-19-48388	MV2018-17	DUP	Lu	ppm	0.074	
Dup-19-48388	MV2018-17	DUP	Mo	ppm	0.1	
Dup-19-48388	MV2018-17	DUP	Nb	ppm	0.99	
Dup-19-48388	MV2018-17	DUP	Nd	ppm	1.38	
Dup-19-48388	MV2018-17	DUP	Ni	ppm	17.2	
Dup-19-48388	MV2018-17	DUP	Pb	ppm	0.33	
Dup-19-48388	MV2018-17	DUP	Pr	ppm	0.297	
Dup-19-48388	MV2018-17	DUP	Rb	ppm	3.9	
Dup-19-48388	MV2018-17	DUP	Sb	ppm	0.09	
Dup-19-48388	MV2018-17	DUP	Sc	ppm	6.3	
Dup-19-48388	MV2018-17	DUP	Sm	ppm	0.456	
Dup-19-48388	MV2018-17	DUP	Sn	ppm	0.11	
Dup-19-48388	MV2018-17	DUP	Sr	ppm	149.7	
Dup-19-48388	MV2018-17	DUP	Ta	ppm	0.07	
Dup-19-48388	MV2018-17	DUP	Tb	ppm	0.1051	
Dup-19-48388	MV2018-17	DUP	Th	ppm	0.099	
Dup-19-48388	MV2018-17	DUP	Ti	ppm	1496	
Dup-19-48388	MV2018-17	DUP	Tl	ppm	0.02	
Dup-19-48388	MV2018-17	DUP	Tm	ppm	0.0614	
Dup-19-48388	MV2018-17	DUP	U	ppm	0.056	
Dup-19-48388	MV2018-17	DUP	V	ppm	42	
Dup-19-48388	MV2018-17	DUP	W	ppm	0.04	
Dup-19-48388	MV2018-17	DUP	Y	ppm	3.72	
Dup-19-48388	MV2018-17	DUP	Yb	ppm	0.428	

Sample ID	Client Sample ID	QC Name	Analyte	Units	Measured Value	Cert/Dup Value
Dup-19-48388	MV2018-17	DUP	Zn	ppm	16.4	
Dup-19-48388	MV2018-17	DUP	Zr	ppm	31	
IHST-19-28027		MRB-29	Ba	ppm	287.8	
IHST-19-28027		MRB-29	Be	ppm	0.94	
IHST-19-28027		MRB-29	Bi	ppm	0.03	
IHST-19-28027		MRB-29	Cd	ppm	0.127	
IHST-19-28027		MRB-29	Ce	ppm	48.43	
IHST-19-28027		MRB-29	Co	ppm	52.44	
IHST-19-28027		MRB-29	Cr	ppm	289	
IHST-19-28027		MRB-29	Cs	ppm	0.243	
IHST-19-28027		MRB-29	Cu	ppm	144.2	
IHST-19-28027		MRB-29	Dy	ppm	5.244	
IHST-19-28027		MRB-29	Er	ppm	2.742	
IHST-19-28027		MRB-29	Eu	ppm	1.9298	
IHST-19-28027		MRB-29	Ga	ppm	19.18	
IHST-19-28027		MRB-29	Gd	ppm	5.983	
IHST-19-28027		MRB-29	Hf	ppm	4.5	
IHST-19-28027		MRB-29	Ho	ppm	1.0062	
IHST-19-28027		MRB-29	In	ppm	0.0786	
IHST-19-28027		MRB-29	La	ppm	21.6	
IHST-19-28027		MRB-29	Li	ppm	10.1	
IHST-19-28027		MRB-29	Lu	ppm	0.361	
IHST-19-28027		MRB-29	Mo	ppm	0.71	
IHST-19-28027		MRB-29	Nb	ppm	12.687	
IHST-19-28027		MRB-29	Nd	ppm	27.86	
IHST-19-28027		MRB-29	Ni	ppm	111.3	
IHST-19-28027		MRB-29	Pb	ppm	4.64	
IHST-19-28027		MRB-29	Pr	ppm	6.603	
IHST-19-28027		MRB-29	Rb	ppm	14.46	
IHST-19-28027		MRB-29	Sb	ppm	0.05	
IHST-19-28027		MRB-29	Sc	ppm	32.8	
IHST-19-28027		MRB-29	Sm	ppm	6.187	
IHST-19-28027		MRB-29	Sn	ppm	2.03	
IHST-19-28027		MRB-29	Sr	ppm	315	
IHST-19-28027		MRB-29	Ta	ppm	0.776	
IHST-19-28027		MRB-29	Tb	ppm	0.878	
IHST-19-28027		MRB-29	Th	ppm	2.638	

Sample ID	Client Sample ID	QC Name	Analyte	Units	Measured Value	Cert/Dup Value
IHST-19-28027		MRB-29	Ti	ppm	11825	
IHST-19-28027		MRB-29	Tl	ppm	0.071	
IHST-19-28027		MRB-29	Tm	ppm	0.3881	
IHST-19-28027		MRB-29	U	ppm	0.672	
IHST-19-28027		MRB-29	V	ppm	328.7	
IHST-19-28027		MRB-29	W	ppm	0.19	
IHST-19-28027		MRB-29	Y	ppm	27.28	
IHST-19-28027		MRB-29	Yb	ppm	2.435	
IHST-19-28027		MRB-29	Zn	ppm	106.4	
IHST-19-28027		MRB-29	Zr	ppm	177	
IHST-19-28028		MRB-29	Ba	ppm	299.6	
IHST-19-28028		MRB-29	Be	ppm	0.96	
IHST-19-28028		MRB-29	Bi	ppm	0.03	
IHST-19-28028		MRB-29	Cd	ppm	0.135	
IHST-19-28028		MRB-29	Ce	ppm	49.89	
IHST-19-28028		MRB-29	Co	ppm	54.26	
IHST-19-28028		MRB-29	Cr	ppm	297	
IHST-19-28028		MRB-29	Cs	ppm	0.241	
IHST-19-28028		MRB-29	Cu	ppm	144.2	
IHST-19-28028		MRB-29	Dy	ppm	5.239	
IHST-19-28028		MRB-29	Er	ppm	2.875	
IHST-19-28028		MRB-29	Eu	ppm	1.9118	
IHST-19-28028		MRB-29	Ga	ppm	20.02	
IHST-19-28028		MRB-29	Gd	ppm	5.966	
IHST-19-28028		MRB-29	Hf	ppm	4.52	
IHST-19-28028		MRB-29	Ho	ppm	1.0241	
IHST-19-28028		MRB-29	In	ppm	0.0806	
IHST-19-28028		MRB-29	La	ppm	22.3	
IHST-19-28028		MRB-29	Li	ppm	10.3	
IHST-19-28028		MRB-29	Lu	ppm	0.358	
IHST-19-28028		MRB-29	Mo	ppm	0.74	
IHST-19-28028		MRB-29	Nb	ppm	12.891	
IHST-19-28028		MRB-29	Nd	ppm	28.89	
IHST-19-28028		MRB-29	Ni	ppm	112.4	
IHST-19-28028		MRB-29	Pb	ppm	4.49	
IHST-19-28028		MRB-29	Pr	ppm	6.909	
IHST-19-28028		MRB-29	Rb	ppm	15.02	

Sample ID	Client Sample ID	QC Name	Analyte	Units	Measured Value	Cert/Dup Value
IHST-19-28028		MRB-29	Sb	ppm	0.06	
IHST-19-28028		MRB-29	Sc	ppm	33.3	
IHST-19-28028		MRB-29	Sm	ppm	6.455	
IHST-19-28028		MRB-29	Sn	ppm	1.81	
IHST-19-28028		MRB-29	Sr	ppm	320	
IHST-19-28028		MRB-29	Ta	ppm	0.78	
IHST-19-28028		MRB-29	Tb	ppm	0.8995	
IHST-19-28028		MRB-29	Th	ppm	2.616	
IHST-19-28028		MRB-29	Ti	ppm	12065	
IHST-19-28028		MRB-29	Tl	ppm	0.074	
IHST-19-28028		MRB-29	Tm	ppm	0.407	
IHST-19-28028		MRB-29	U	ppm	0.66	
IHST-19-28028		MRB-29	V	ppm	336.5	
IHST-19-28028		MRB-29	W	ppm	0.21	
IHST-19-28028		MRB-29	Y	ppm	27.73	
IHST-19-28028		MRB-29	Yb	ppm	2.368	
IHST-19-28028		MRB-29	Zn	ppm	109.8	
IHST-19-28028		MRB-29	Zr	ppm	180	
INTL-19-33779		GSP-2	Ba	ppm	1362.7	1340
INTL-19-33779		GSP-2	Be	ppm	1.39	1.5
INTL-19-33779		GSP-2	Bi	ppm	0.04	
INTL-19-33779		GSP-2	Cd	ppm	0.116	
INTL-19-33779		GSP-2	Ce	ppm	430.88	410
INTL-19-33779		GSP-2	Co	ppm	7.24	7.3
INTL-19-33779		GSP-2	Cr	ppm	21	20
INTL-19-33779		GSP-2	Cs	ppm	1.175	1.2
INTL-19-33779		GSP-2	Cu	ppm	45.4	43
INTL-19-33779		GSP-2	Dy	ppm	5.63	6.1
INTL-19-33779		GSP-2	Er	ppm	2.363	2.2
INTL-19-33779		GSP-2	Eu	ppm	2.3554	2.3
INTL-19-33779		GSP-2	Ga	ppm	21.92	22
INTL-19-33779		GSP-2	Gd	ppm	11.918	12
INTL-19-33779		GSP-2	Hf	ppm	13.45	14
INTL-19-33779		GSP-2	Ho	ppm	0.9605	1
INTL-19-33779		GSP-2	In	ppm	0.0496	
INTL-19-33779		GSP-2	La	ppm	182.8	180
INTL-19-33779		GSP-2	Li	ppm	34	

Sample ID	Client Sample ID	QC Name	Analyte	Units	Measured Value	Cert/Dup Value
INTL-19-33779		GSP-2	Lu	ppm	0.24	0.23
INTL-19-33779		GSP-2	Mo	ppm	1.94	2.1
INTL-19-33779		GSP-2	Nb	ppm	25.533	27
INTL-19-33779		GSP-2	Nd	ppm	206.27	200
INTL-19-33779		GSP-2	Ni	ppm	15.9	17
INTL-19-33779		GSP-2	Pb	ppm	40.75	42
INTL-19-33779		GSP-2	Pr	ppm	57.37	51
INTL-19-33779		GSP-2	Rb	ppm	243.06	245
INTL-19-33779		GSP-2	Sb	ppm	0.45	
INTL-19-33779		GSP-2	Sc	ppm	6.3	6.3
INTL-19-33779		GSP-2	Sm	ppm	25.921	27
INTL-19-33779		GSP-2	Sn	ppm	6.73	
INTL-19-33779		GSP-2	Sr	ppm	237.4	240
INTL-19-33779		GSP-2	Ta	ppm	0.832	
INTL-19-33779		GSP-2	Tb	ppm	1.2728	
INTL-19-33779		GSP-2	Th	ppm	108.516	105
INTL-19-33779		GSP-2	Ti	ppm	3913	
INTL-19-33779		GSP-2	Tl	ppm	1.311	1.1
INTL-19-33779		GSP-2	Tm	ppm	0.2826	0.29
INTL-19-33779		GSP-2	U	ppm	2.481	2.4
INTL-19-33779		GSP-2	V	ppm	53.4	52
INTL-19-33779		GSP-2	W	ppm	0.35	
INTL-19-33779		GSP-2	Y	ppm	26.28	28
INTL-19-33779		GSP-2	Yb	ppm	1.683	1.6
INTL-19-33779		GSP-2	Zn	ppm	114.8	120
INTL-19-33779		GSP-2	Zr	ppm	530	550
INTL-19-33780		AGV-2	Ba	ppm	1069.1	1140
INTL-19-33780		AGV-2	Be	ppm	2.11	2.3
INTL-19-33780		AGV-2	Bi	ppm	0.05	
INTL-19-33780		AGV-2	Cd	ppm	0.093	
INTL-19-33780		AGV-2	Ce	ppm	69	68
INTL-19-33780		AGV-2	Co	ppm	15.94	16
INTL-19-33780		AGV-2	Cr	ppm	17	17
INTL-19-33780		AGV-2	Cs	ppm	1.178	1.16
INTL-19-33780		AGV-2	Cu	ppm	50.1	53
INTL-19-33780		AGV-2	Dy	ppm	3.433	3.6
INTL-19-33780		AGV-2	Er	ppm	1.836	1.79

Sample ID	Client Sample ID	QC Name	Analyte	Units	Measured Value	Cert/Dup Value
INTL-19-33780		AGV-2	Eu	ppm	1.5679	1.54
INTL-19-33780		AGV-2	Ga	ppm	20.73	20
INTL-19-33780		AGV-2	Gd	ppm	4.535	4.69
INTL-19-33780		AGV-2	Hf	ppm	5.48	5.08
INTL-19-33780		AGV-2	Ho	ppm	0.6685	0.71
INTL-19-33780		AGV-2	In	ppm	0.0467	
INTL-19-33780		AGV-2	La	ppm	37.9	38
INTL-19-33780		AGV-2	Li	ppm	10.2	11
INTL-19-33780		AGV-2	Lu	ppm	0.257	0.25
INTL-19-33780		AGV-2	Mo	ppm	1.94	
INTL-19-33780		AGV-2	Nb	ppm	13.928	15
INTL-19-33780		AGV-2	Nd	ppm	30.68	30
INTL-19-33780		AGV-2	Ni	ppm	18.3	19
INTL-19-33780		AGV-2	Pb	ppm	12.77	13
INTL-19-33780		AGV-2	Pr	ppm	8.242	8.3
INTL-19-33780		AGV-2	Rb	ppm	66.63	68.6
INTL-19-33780		AGV-2	Sb	ppm	0.47	0.6
INTL-19-33780		AGV-2	Sc	ppm	12	13
INTL-19-33780		AGV-2	Sm	ppm	5.533	5.7
INTL-19-33780		AGV-2	Sn	ppm	1.96	2.3
INTL-19-33780		AGV-2	Sr	ppm	643.9	658
INTL-19-33780		AGV-2	Ta	ppm	0.832	0.89
INTL-19-33780		AGV-2	Tb	ppm	0.6417	0.64
INTL-19-33780		AGV-2	Th	ppm	6.231	6.1
INTL-19-33780		AGV-2	Ti	ppm	6194	6019
INTL-19-33780		AGV-2	Tl	ppm	0.288	0.27
INTL-19-33780		AGV-2	Tm	ppm	0.2585	0.26
INTL-19-33780		AGV-2	U	ppm	1.959	1.88
INTL-19-33780		AGV-2	V	ppm	121.5	120
INTL-19-33780		AGV-2	W	ppm	0.52	
INTL-19-33780		AGV-2	Y	ppm	19.29	20
INTL-19-33780		AGV-2	Yb	ppm	1.653	1.6
INTL-19-33780		AGV-2	Zn	ppm	89.7	86

Appendix 3.4. SEM-EDS data for plagioclase, amphibole, chromite, ilmenite, rutile and clinopyroxene grains and chromite-hosted mineral inclusions from the Mayville Intrusion.

Sample ID	Lithology	Series	Mineral	Core/Rim/Inclusion
MV2018-18A	Anorthosite	ALZ	Plagioclase	Core
MV2018-18A	Anorthosite	ALZ	Plagioclase	Rim
MV2018-18B	Anorthosite	ALZ	Plagioclase	Core
MV2018-18B	Anorthosite	ALZ	Plagioclase	Rim
MV2018-19A	Anorthosite	ALZ	Plagioclase	Core
MV2018-19A	Anorthosite	ALZ	Plagioclase	Rim
MV2018-19B	Anorthosite	ALZ	Plagioclase	Core
MV2018-19B	Anorthosite	ALZ	Plagioclase	Rim
MV2017-3	Anorthosite	ALZ	Plagioclase	Core
MV2017-3	Anorthosite	ALZ	Plagioclase	Rim
MV2017-4	Anorthosite	ALZ	Plagioclase	Core
MV2017-4	Anorthosite	ALZ	Plagioclase	Rim
MV2018-3	Chromitite	HBZ	Plagioclase	Core
MV2018-3	Chromitite	HBZ	Plagioclase	Rim
MV2018-12A	Gabbro	ALZ	Plagioclase	Core
MV2018-12A	Gabbro	ALZ	Plagioclase	Rim
MV2018-12B	Gabbro	ALZ	Plagioclase	Core
MV2018-12B	Gabbro	ALZ	Plagioclase	Rim
MV2018-18A	Anorthosite	ALZ	Amphibole	Core
MV2018-18A	Anorthosite	ALZ	Amphibole	Rim
MV2018-18B	Anorthosite	ALZ	Amphibole	Core
MV2018-18B	Anorthosite	ALZ	Amphibole	Rim
MV2018-19A	Anorthosite	ALZ	Amphibole	Core
MV2018-19A	Anorthosite	ALZ	Amphibole	Rim
MV2018-19B	Anorthosite	ALZ	Amphibole	Core
MV2018-19B	Anorthosite	ALZ	Amphibole	Rim
MV2017-3	Anorthosite	ALZ	Amphibole	Core
MV2017-3	Anorthosite	ALZ	Amphibole	Rim
MV2017-4	Anorthosite	ALZ	Amphibole	Core
MV2017-4	Anorthosite	ALZ	Amphibole	Rim
MV2018-3	Chromitite	HBZ	Amphibole	Core
MV2018-3	Chromitite	HBZ	Amphibole	Rim
MV2018-12A	Gabbro	ALZ	Amphibole	Core
MV2018-12A	Gabbro	ALZ	Amphibole	Rim
MV2018-12B	Gabbro	ALZ	Amphibole	Core
MV2018-18A	Anorthosite	ALZ	Plagioclase	Core

	Oxygen			Aluminium		
n	Weight %	Atomic %	Error %	Weight %	Atomic %	Error %
7	44.7	59.8	8.5	18.8	14.9	4.1
16	44.7	59.7	8.4	18.3	14.5	4.1
11	44.6	59.8	8.5	18.9	15.0	4.0
13	44.5	59.4	8.4	18.1	14.4	4.1
7	44.8	59.9	8.5	18.6	14.8	4.1
13	44.9	60.0	8.5	18.6	14.8	4.1
11	44.9	60.1	8.6	18.3	14.5	4.1
10	44.9	60.1	8.5	19.0	15.1	3.9
19	44.6	59.6	8.5	18.5	14.7	4.1
23	44.7	59.5	8.3	17.7	14.0	4.1
5	44.2	58.7	8.2	16.9	13.3	4.2
10	44.2	58.5	8.1	16.4	12.9	4.3
5	44.1	59.5	8.8	20.1	16.1	4.0
7	44.2	59.7	8.7	20.1	16.1	4.0
6	44.6	60.1	8.7	19.0	15.2	4.1
12	44.6	59.0	8.0	16.8	13.2	4.2
14	44.1	59.0	8.5	17.7	14.1	4.2
11	44.2	59.2	8.4	18.2	14.5	4.1
14	43.8	60.4	7.7	5.8	4.7	6.6
18	43.4	60.0	7.9	5.1	4.2	6.6
12	43.5	59.9	8.0	3.6	3.0	7.2
16	43.7	60.0	7.9	4.2	3.4	7.2
18	43.7	60.5	8.0	2.7	2.2	8.0
16	43.5	60.3	8.0	3.1	2.5	7.6
11	43.2	60.1	8.0	3.4	2.8	7.4
16	43.1	60.1	8.0	3.7	3.0	7.2
17	42.8	59.8	8.1	6.1	5.1	6.4
8	43.4	59.5	7.6	8.4	7.0	6.1
5	43.1	60.7	7.2	8.8	7.3	6.2
5	41.6	59.1	8.1	6.1	5.2	6.4
26	43.8	59.8	7.7	8.7	7.0	6.0
13	44.4	60.2	7.4	8.7	6.9	6.2
16	43.1	60.2	7.8	3.9	3.2	7.9
8	42.5	58.7	8.1	3.1	2.6	7.6
7	42.3	59.6	8.1	2.7	2.3	8.3

Silicon			Calcium		
Weight %	Atomic %	Error %	Weight %	Atomic %	Error %
21.8	16.6	4.5	12.8	6.9	3.6
22.2	16.8	4.5	12.0	6.4	3.7
21.6	16.5	4.5	13.1	7.0	3.6
22.7	17.3	4.4	11.8	6.3	3.8
21.7	16.5	4.5	12.8	6.8	3.6
21.7	16.5	4.5	12.7	6.8	4.4
21.5	16.4	4.4	13.6	7.3	3.5
21.1	16.1	4.5	13.5	7.2	3.5
22.2	16.9	4.5	12.4	6.6	3.7
23.2	17.6	4.4	11.1	5.9	3.9
25.0	18.9	4.4	9.5	5.0	4.3
25.6	19.3	4.4	8.7	4.6	4.4
20.3	15.7	4.6	15.1	8.2	3.4
20.2	15.5	4.6	14.7	8.0	3.5
20.4	15.7	4.5	15.0	8.1	3.4
24.9	18.7	4.4	8.8	4.7	2.5
23.1	17.6	4.5	12.0	6.5	4.1
23.2	17.6	4.5	11.7	6.3	2.9
21.6	17.0	4.5	8.1	4.5	3.6
22.8	17.9	4.4	8.9	4.9	4.7
23.9	18.7	4.3	9.6	5.3	4.2
24.0	18.8	4.3	9.2	5.0	4.6
24.1	19.0	4.2	9.7	5.4	4.1
23.8	18.8	4.3	9.7	5.4	4.1
23.7	18.8	4.3	9.9	5.5	4.2
23.6	18.7	4.3	9.8	5.5	4.0
22.0	17.5	4.5	10.3	5.8	4.2
18.9	15.1	4.8	8.2	4.6	3.1
17.6	14.2	5.0	5.8	3.3	2.6
21.9	17.7	4.5	9.8	5.6	4.4
19.3	15.1	4.8	7.8	4.3	3.5
19.0	14.8	4.9	6.7	3.7	3.0
22.9	18.3	4.4	8.7	4.9	3.7
24.1	19.3	4.3	9.9	5.6	4.2
24.5	19.7	4.3	10.0	5.6	4.3

Sodium			Magnesium		
Weight %	Atomic %	Error %	Weight %	Atomic %	Error %
2.0	1.8	11.0			
2.6	2.4	10.2			
1.9	1.7	11.3			
2.8	2.6	10.6			
2.1	1.9	10.7			
2.1	1.9	10.9			
1.8	1.7	17.6			
1.5	1.4	12.4			
2.4	2.2	10.4			
3.2	3.0	9.8			
4.4	4.1	9.2			
5.1	4.7	8.2			
0.6	0.5	32.0			
0.4	0.4	39.9			
0.9	0.9	12.0			
4.7	4.3	12.1			
3.0	2.7	10.4			
2.5	2.3	11.6			
0.6	0.6	32.4	9.5	8.6	6.2
0.7	0.7	21.6	9.1	8.2	6.2
0.5	0.5	24.3	9.9	9.0	6.0
0.8	0.7	26.9	9.6	8.7	6.1
0.4	0.4	29.0	9.5	8.7	6.2
0.5	0.5	24.6	9.3	8.5	6.2
0.5	0.5	26.3	8.9	8.2	6.3
0.5	0.5	25.8	8.8	8.0	6.3
0.6	0.6	30.4	7.2	6.6	6.4
0.6	0.6	49.4	7.4	6.8	5.8
0.6	0.6	51.2	7.9	7.3	6.8
0.8	0.8	20.6	6.9	6.4	6.7
1.2	1.1	27.8	10.3	9.2	6.2
0.9	0.9	35.9	11.4	10.1	6.1
0.0	0.0	0.0	8.8	8.1	6.4
0.2	0.2	19.0	8.4	7.8	6.5
0.0	0.0	0.0	8.5	7.9	6.5

Iron			Potassium		
Weight %	Atomic %	Error %	Weight %	Atomic %	Error %
10.6	4.2	6.8			
10.0	4.0	6.9			
8.8	3.5	7.7			
8.5	3.4	8.0			
9.8	3.9	6.8			
10.0	4.0	6.7			
10.5	4.2	6.6			
10.5	4.2	6.7			
11.0	4.4	6.6			
13.2	5.3	6.1			
16.2	6.5	5.4			
12.9	5.3	6.2			
8.9	3.5	8.1			
9.0	3.5	7.9			
12.2	4.9	6.2			
11.8	4.7	6.2			
11.9	4.8	6.4			

Phosphorus			Total		Plagioclase	
Weight %	Atomic %	Error %	Weight %	Atomic %	An content	Plagioclase composition
			100.00	100.00	79	Bytownite
			100.00	100.00	73	Bytownite
			100.00	100.00	80	Bytownite
			100.00	100.00	71	Bytownite
			100.00	100.00	78	Bytownite
			100.00	100.00	78	Bytownite
			100.00	100.00	81	Bytownite
			100.00	100.00	84	Bytownite
			100.00	100.00	75	Bytownite
			100.00	100.00	67	Labradorite
			100.00	100.00	56	Labradorite
			100.00	100.00	49	Andesine
			100.00	100.00	94	Anorthite
			100.00	100.00	95	Anorthite
			100.00	100.00	90	Anorthite
			100.00	100.00	55	Labradorite
			100.00	100.00	70	Bytownite
			100.00	100.00	73	Bytownite
			100.00	100.00		
			100.00	100.00		
			100.00	100.00		
			100.00	100.00		
			100.00	100.00		
			100.00	100.00		
			100.00	100.00		
			100.00	100.00		
			100.00	100.00		
			100.00	100.00		
			100.00	100.00		
			100.00	100.00		
			100.00	100.00		
			100.00	100.00		
			100.00	100.00		
			100.00	100.00		
			100.00	100.00		
			100.00	100.00		
			100.00	100.00		

Amphibole		Chromite		Clinopyroxene	
Mg#	Amphibole type	Mg#	Cr#	Mg#	Fe#
70	Magnesiohornblende				
70	Magnesiohornblende				
74	Magnesiohornblende				
74	Magnesiohornblende				
71	Magnesiohornblende				
70	Magnesiohornblende				
68	Magnesiohornblende				
68	Magnesiohornblende				
58	Magnesiohornblende				
54	Magnesiohornblende				
55	Magnesiohornblende				
58	Magnesiohornblende				
73	Magnesiohornblende				
75	Magnesiohornblende				
65	Magnesiohornblende				
64	Magnesiohornblende				
65	Magnesiohornblende				

Sample ID	Lithology	Series	Mineral	Core/Rim/Inclusion
MV2018-12B	Gabbro	ALZ	Amphibole	Rim
111-12-500B01	Chromitite	HBZ	Chromite	Core
111-12-500B01	Chromitite	HBZ	Chromite	Rim
MV2018-4	Chromitite	HBZ	Chromite	Core
MV2018-4	Chromitite	HBZ	Chromite	Rim
MV2018-5	Chromitite	HBZ	Chromite	Core
MV2018-5	Chromitite	HBZ	Chromite	Rim
MV2018-6	Chromitite	HBZ	Chromite	Core
MV2018-6	Chromitite	HBZ	Chromite	Rim
MV2018-13	Chromitite	HBZ	Chromite	Core
MV2018-13	Chromitite	HBZ	Chromite	Rim
MV2018-3	Chromitite	HBZ	Chromite	Core
MV2018-3	Chromitite	HBZ	Chromite	Rim
111-12-500B01	Chromitite	HBZ	Rutile	Inclusion
MV2018-4	Chromitite	HBZ	Ilmenite	Core
MV2018-4	Chromitite	HBZ	Calcite	Inclusion
MV2018-6	Chromitite	HBZ	Apatite	Inclusion
MV2018-13	Chromitite	HBZ	Clinopyroxene	Matrix
111-12-500B01	Chromitite	HBZ	Clinopyroxene	Inclusion
MV2018-4	Chromitite	HBZ	Clinopyroxene	Inclusion
MV2018-5	Chromitite	HBZ	Clinopyroxene	Inclusion
MV2018-6	Chromitite	HBZ	Clinopyroxene	Inclusion
MV2018-13	Chromitite	HBZ	Clinopyroxene	Inclusion
111-12-500B01	Chromitite	HBZ	Orthopyroxene	Inclusion
MV2018-4	Chromitite	HBZ	Orthopyroxene	Inclusion
MV2018-5	Chromitite	HBZ	Orthopyroxene	Inclusion
MV2018-6	Chromitite	HBZ	Orthopyroxene	Inclusion
MV2018-13	Chromitite	HBZ	Orthopyroxene	Inclusion
111-12-500B01	Chromitite	HBZ	Actinolite	Matrix
MV2018-4	Chromitite	HBZ	Actinolite	Matrix
MV2018-5	Chromitite	HBZ	Actinolite	Matrix
MV2018-6	Chromitite	HBZ	Actinolite	Matrix
MV2018-13	Chromitite	HBZ	Actinolite	Matrix

ALZ: Anorthosite to Leucogabbro Zone
HBZ: Heterolithic Breccia
Zone

	Oxygen			Aluminium		
n	Weight %	Atomic %	Error %	Weight %	Atomic %	Error %
8	42.6	59.9	7.9	3.9	3.2	8.0
8	27.1	52.9	5.9	8.0	9.3	8.6
9	27.0	53.1	5.9	7.5	8.7	8.9
15	28.9	54.0	5.6	9.0	10.0	6.2
5	30.2	52.9	5.9	9.5	9.9	6.4
16	27.3	52.4	5.4	9.6	11.0	6.5
6	27.4	52.6	5.3	10.7	12.2	6.4
17	25.9	49.2	5.4	10.0	11.2	6.9
10	27.7	52.4	5.7	11.1	12.4	7.2
9	29.3	54.9	6.1	9.3	10.2	9.2
8	26.5	52.6	5.9	7.2	8.5	8.7
7	27.5	52.7	5.6	10.5	12.0	7.1
1	28.1	53.2	5.9	10.5	11.8	7.0
1	37.6	64.5	9.7			
14	33.5	60.2	8.2	3.7	4.0	7.7
1	47.8	69.7	10.0			
1	41.9	62.2	10.4			
1	48.7	64.0	9.7			
6	47.5	62.1	8.7	3.1	2.4	10.7
3	42.9	57.5	7.6	5.4	4.3	5.7
8	43.5	59.1	7.6	5.9	4.7	6.0
13	47.3	61.8	8.3	4.3	3.3	7.7
9	47.6	62.7	8.2	5.6	4.4	7.4
15	53.1	65.0	6.6	10.6	7.7	6.6
9	45.5	59.2	6.3	6.9	5.3	7.3
2	44.8	58.6	6.3	6.5	5.0	11.4
2	51.7	64.2	6.1	10.6	7.8	6.8
4	49.6	63.2	6.2	9.7	8.5	10.4
1	53.5	65.2	6.3	12.3	8.9	6.9
11	44.2	58.6	6.8	8.7	6.9	6.5
6	42.8	58.5	7.3	9.4	7.6	5.4
5	49.4	63.5	7.8	8.5	6.4	6.3
6	48.4	63.0	7.6	8.2	6.4	6.6

Silicon			Calcium		
Weight %	Atomic %	Error %	Weight %	Atomic %	Error %
23.0	18.5	4.5	8.9	5.0	3.7
0.1	0.1	0.6			
1.3	1.2	16.1			
			52.2	30.3	1.9
1.7	1.5	9.2	39.5	23.4	2.7
27.0	19.9	5.5	11.0	5.7	10.5
25.1	18.7	4.5	12.2	6.4	5.6
21.6	16.6	4.2	7.0	3.8	3.8
22.8	17.7	4.2	7.8	4.3	5.1
23.1	17.2	4.0	10.0	5.3	4.5
22.5	16.9	4.6	10.5	5.5	5.0
16.6	11.6	6.0	0.7	0.4	0.4
19.1	14.3	4.6			
22.8	16.9	4.6			
14.5	10.2	5.8			
14.7	8.7	4.3			
14.5	10.1	6.3			
18.5	14.3	4.7	2.2	1.2	1.3
19.2	15.0	4.6	6.6	3.6	2.1
20.7	15.3	4.8	8.3	4.3	4.0
19.3	14.4	5.0	7.3	3.8	3.2

Sodium			Magnesium		
Weight %	Atomic %	Error %	Weight %	Atomic %	Error %
0.0	0.0	0.0	9.0	8.4	6.5
			0.4	0.6	7.9
			0.2	0.3	5.1
			1.2	1.4	9.1
			0.3	0.3	6.3
			0.8	1.0	7.8
			1.2	1.5	13.7
			1.2	1.5	13.7
			0.1	0.1	2.1
0.1	0.1	85.7	0.3	0.4	1.6
0.1	0.1	100.0	0.8	1.0	18.0
			3.1	3.5	11.9
			0.2	0.3	3.5
			13.3	11.3	7.9
			12.1	10.4	6.2
1.7	1.5	10.6	10.0	8.8	5.7
			12.7	11.3	5.3
			11.9	10.3	5.7
			11.1	9.6	6.0
			18.9	15.2	5.6
			16.6	14.3	5.2
			19.9	17.1	4.9
			20.5	16.7	5.3
			18.3	13.4	5.4
			19.7	15.8	5.5
0.1	0.1	0.9	13.3	11.4	5.6
0.5	0.5	3.7	12.6	11.3	5.5
			11.8	9.9	5.9
			12.7	10.9	6.0

Iron			Potassium		
Weight %	Atomic %	Error %	Weight %	Atomic %	Error %
12.6	5.1	6.1			
35.5	19.9	5.5			
35.8	20.1	5.5			
33.5	18.0	3.7			
31.4	15.8	3.6			
31.6	17.4	3.5			
31.5	17.3	3.5			
28.6	15.6	4.7			
29.7	16.1	5.0			
25.5	14.4	3.0			
38.8	22.1	5.0			
37.6	20.7	4.1			
35.8	19.4	4.0			
30.3	14.9	5.5			
30.5	16.0	4.5			
9.7	3.8	5.6			
7.5	2.9	5.5			
1.4	0.5	2.5			
4.1	1.5	5.5			

Chromium			Titanium		
Weight %	Atomic %	Error %	Weight %	Atomic %	Error %
28.9	17.4	4.8			
29.5	17.8	4.8			
25.7	14.8	3.4	1.1	0.7	0.6
24.2	13.1	3.2	1.2	0.7	0.7
29.9	17.7	3.0	0.8	0.5	2.0
30.4	17.9	3.0			
28.4	16.6	3.8			
30.2	17.6	4.0			
35.8	20.3	5.3			
27.1	16.6	4.6	0.3	0.2	7.0
24.0	14.2	3.9			
23.8	13.9	3.8	1.0	0.7	18.0
			27.8	15.9	3.9
11.9	6.7	5.6	19.5	11.5	3.5
1.4	0.6	7.8			
1.1	0.5	18.4			

Phosphorus			Total		Plagioclase	
Weight %	Atomic %	Error %	Weight %	Atomic %	An content	Plagioclase composition
			100.00	100.00		
			100.00	100.00		
			100.00	100.00		
			100.00	100.00		
			100.00	100.00		
			100.00	100.00		
			100.00	100.00		
			100.00	100.00		
			100.00	100.00		
			100.00	100.00		
			100.00	100.00		
			100.00	100.00		
			100.00	100.00		
			100.00	100.00		
			100.00	100.00		
			100.00	100.00		
			100.00	100.00		
1.7	1.3	18.2	100.00	100.00		
			100.00	100.00		
			100.00	100.00		
			100.00	100.00		
			100.00	100.00		
			100.00	100.00		
			100.00	100.00		
			100.00	100.00		
			100.00	100.00		
			100.00	100.00		
			100.00	100.00		
			100.00	100.00		
			100.00	100.00		
			100.00	100.00		
			100.00	100.00		
			100.00	100.00		
			100.00	100.00		
			100.00	100.00		
			100.00	100.00		
			100.00	100.00		
			100.00	100.00		
			100.00	100.00		

Amphibole		Chromite		Clinopyroxene	
Mg#	Amphibole type	Mg#	Cr#	Mg#	Fe#
65	Magnesiohornblende				
		3	65		
		1	67		
		7	61		
		2	57		
		6	62		
		0	60		
		9	56		
		9	59		
		1	66		
		0	66		
		2	54		
		5	54		
				100	0
				100	0
				71	29
				81	19
				96	4
				91	9
				10	0
				81	19
				90	10
				94	6
				86	14

Appendix 3.5. Main Raman spectra peak values for plagioclase, amphibole, and chromite grains from the Mayville Intrusion.

Sample ID	Lithology	Zone	Mineral
MV2018-19A	Anorthosite	ALZ	Plagioclase
MV2018-19A	Anorthosite	ALZ	Plagioclase
MV2018-19A	Anorthosite	ALZ	Plagioclase
MV2018-19A	Anorthosite	ALZ	Plagioclase
MV2018-19A	Anorthosite	ALZ	Plagioclase
MV2018-12A	Gabbro	ALZ	Plagioclase
MV2018-12A	Gabbro	ALZ	Plagioclase
MV2018-12A	Gabbro	ALZ	Plagioclase
MV2018-12A	Gabbro	ALZ	Plagioclase
MV2018-12A	Gabbro	ALZ	Plagioclase
MV2018-12A	Gabbro	ALZ	Plagioclase
MV2018-12A	Gabbro	ALZ	Plagioclase
MV2018-12A	Gabbro	ALZ	Plagioclase
MV2018-12A	Gabbro	ALZ	Plagioclase
MV2018-12A	Gabbro	ALZ	Plagioclase
MV2018-12A	Gabbro	ALZ	Plagioclase
MV2018-12B	Gabbro	ALZ	Plagioclase
MV2018-12B	Gabbro	ALZ	Plagioclase
MV2018-12B	Gabbro	ALZ	Plagioclase
MV2018-12B	Gabbro	ALZ	Plagioclase
MV2018-12B	Gabbro	ALZ	Plagioclase
MV2018-12B	Gabbro	ALZ	Plagioclase
111-12-500B01	Chromitite	HBZ	Chromite
111-12-500B01	Chromitite	HBZ	Chromite
111-12-500B01	Chromitite	HBZ	Chromite
MV2018-4	Chromitite	HBZ	Chromite
MV2018-5	Chromitite	HBZ	Chromite
MV2018-6	Chromitite	HBZ	Chromite

Main Raman spectra peak values (cm^{-1})						
191.53	288.96	**508.46**	825.40	1119.42		
96.66	**519.76**					
88.72	**511.17**	826.80	1118.00			
403.57	**509.23**	825.13	1116.23			
508.78	822.96					
87.37	**510.23**	646.33	1121.26			
90.22	**517.29**	1121.60				
98.21	150.68	199.23	289.57	**509.84**	566.23	1119.99
97.31	198.52	**509.29**	567.93			
91.00	204.70	**510.68**	568.19	1118.59		
99.64	201.02	**511.55**	830.94	1117.93		
89.27	**512.92**	674.62				
94.34	**510.07**					
102.13	151.65	201.44	**511.32**	568.54		
101.72	**509.74**					
210.99	293.04	**509.04**	646.77	828.95	1118.85	
509.49	1119.52					
89.62	**512.15**	1118.11				
509.79	825.27	1120.01				
507.55	1119.50					
88.64	**517.20**	674.50				
584.30	**684.00**					
93.52	494.31	**575.56**	**692.00**			
93.10	**574.90**					
84.28	275.34	**667.59**				
585.32	**707.36**					
584.00						

Sample ID	Lithology	Zone	Mineral
MV2018-6	Chromitite	HBZ	Chromite
MV2018-6	Chromitite	HBZ	Chromite
MV2018-13	Chromitite	HBZ	Chromite
MV2018-13	Chromitite	HBZ	Chromite
MV2018-13	Chromitite	HBZ	Chromite
MV2017-3	Anorthosite	ALZ	Amphibole
MV2017-3	Anorthosite	ALZ	Amphibole
MV2017-3	Anorthosite	ALZ	Amphibole
MV2017-3	Anorthosite	ALZ	Amphibole
MV2018-18A	Anorthosite	ALZ	Amphibole
MV2018-18A	Anorthosite	ALZ	Amphibole
MV2018-18A	Anorthosite	ALZ	Amphibole
MV2018-18A	Anorthosite	ALZ	Amphibole
MV2018-18A	Anorthosite	ALZ	Amphibole
MV2018-18A	Anorthosite	ALZ	Amphibole
MV2018-18A	Anorthosite	ALZ	Amphibole
MV2018-18A	Anorthosite	ALZ	Amphibole
MV2018-18A	Anorthosite	ALZ	Amphibole
MV2018-18B	Anorthosite	ALZ	Amphibole
MV2018-18B	Anorthosite	ALZ	Amphibole
MV2018-19A	Anorthosite	ALZ	Amphibole
MV2018-19A	Anorthosite	ALZ	Amphibole
MV2018-19A	Anorthosite	ALZ	Amphibole
MV2018-19A	Anorthosite	ALZ	Amphibole
MV2018-19A	Anorthosite	ALZ	Amphibole
MV2018-19B	Anorthosite	ALZ	Amphibole
MV2018-19B	Anorthosite	ALZ	Amphibole
MV2018-19B	Anorthosite	ALZ	Amphibole
MV2018-19B	Anorthosite	ALZ	Amphibole

Peak values in bold indicate the most important values.

ALZ: Anorthosite to Leucogabbro Zone
HBZ: Heterolithic Breccia
Zone

Main Raman spectra peak values (cm^{-1})				
580.53				
585.69				
91.97	**574.71**			
684.71				
579.38	**680.66**			
674.66				
673.28				
673.45				
674.10				
224.73	**675.10**			
223.86	**675.73**			
88.65	220.44	566.34	**674.48**	
675.19				
675.16				
226.47	**675.57**			
225.66	**674.78**			
224.81	**676.16**			
84.96	311.70	615.10	**675.25**	
227.17	**675.88**	1057.96		
89.09	158.93	219.94	**675.08**	
161.17	473.49	550.52	604.76	**674.41**
158.72	548.84	**674.28**	1062.69	
164.21	472.06	553.15	605.17	**675.31**
164.06	606.58	**675.61**		
158.12	**675.30**			
158.40	**675.14**			
563.73	**673.40**			
574.37	**670.22**			

Vita Auctoris

Paul Sotiriou was born in 1989 in London, United Kingdom. He obtained a B.Sc. (Honours) Geology degree from Kingston University, Kingston upon Thames, United Kingdom, in 2012. He obtained a M.Sc. in Mining Geology from the Camborne School of Mines, University of Exeter, Penryn, United Kingdom in 2013. He commenced his Ph.D. in Earth Sciences at the University of Windsor in January 2017 and successfully defended his Ph.D. thesis in May 2020.